*Physics of Atomic Nuclei, Vol. 66, No. 9, 2003, pp. 1591–1598. From Yadernaya Fizika, Vol. 66, No. 9, 2003, pp. 1637–1645.*


# Clusters and Covalently Bound Nuclear Molecules*

**W. von Oertzen****

*Hahn Meitner Institut, Berlin, and Fachbereich Physik, Freie Universität Berlin, Germany*

Received April 4, 2003

**Abstract**—Nuclear clustering based on $\alpha$ particles and strongly bound substructures with $N = Z$ has been studied for many decades. Of particular interest are excited states close to the decay thresholds into substructures, as described by the Ikeda diagram. This diagram can be extended to neutron-rich nuclei; in these cases strongly deformed isomeric states consisting of clusters and loosely bound neutrons will appear. A possible approach to describe these states is to use explicitly molecular concepts, with neutrons in covalent binding orbits. Examples for molecular structure in beryllium isotopes and in other neutron-rich light nuclei (carbon and neon) are discussed. © *2003 MAIK "Nauka/Interperiodica"*.

## 1. $\alpha$ CLUSTERS, POTENTIALS, AND DIAGRAMS FOR EXOTIC SHAPES

In heavy-ion reactions, resonances have been observed in the excitation functions in various combinations of light $\alpha$-cluster nuclei in the energy regime from the barrier up to regions where the excitation energy in the compound nucleus reaches 30 to 50 MeV. In particular in cases like $^{12}C + {}^{12}C$ [1] and $^{24}Mg + {}^{24}Mg$ [2], the structure of highly excited states can be related to strongly deformed shapes (to super- and hyperdeformation) in the compound nucleus and to the clustering phenomena predicted from cranked $\alpha$-cluster models [3, 4], Hartree–Fock calculations [5], Nilsson–Strutinsky calculations [6], and others [7]. The spectroscopy of strongly deformed shapes in $N = Z$ nuclei has so far been the domain of charged particle spectroscopy. Various decay studies with the emission of $\alpha$ particles, $^8$Be, and heavier fragments are known [2, 8–11]; however, new detector setups with a combined particle–$\gamma$ detection are expected to give new insight into exotic shapes in nuclei related to clustering.

### *A. The Local $\alpha$-Nucleus Potentials*

The formation of molecular structures relies on special properties of the nuclear potential between the two cores (clusters), namely, the occurrence of a "molecular" potential, with attraction at large distances and repulsion at small distances. Thus, in the research on nucleus–nucleus collisions in the last decades, shallow molecular potentials have been used to describe these resonances. For our discussion, we have two quite conspicuous cases with $\alpha$ particles, where the local potentials have a small attractive part and a strong repulsion at small distances. These two cases are shown in Fig. 1, which shows the cases of $\alpha$ particles interacting with $\alpha$ particles and with $^{16}$O. The curves are actually the result of a reduction (using a supersymmetric transformation [14]) of the "true" potential to a phase equivalent shallow potential, which does not exhibit any unphysical bound states. For the case of the $\alpha + \alpha$ potential, the molecular potential created by Ali and Bodmer [12] for $^8$Be (dashed curves) is seen to coincide well with the supersymmetric local potential. For a more detailed discussion of this point, I refer to the survey by Ohkubo *et al.* [13]. The repulsion at small distances can be interpreted as the effect of Pauli blocking; in the case of the $\alpha + \alpha$ potential, the nucleons of the second cluster have to move up into the next major shell. These potentials, which are repulsive at small distances, are needed for nuclei with additional neutrons in order to build covalently bound nuclear cluster structures discussed in the next section.

### *B. Threshold Diagrams*

It has recently been noted that neutron-rich and weakly bound nuclei show a strong tendency to clustering [15–18]. This appears to be a mean field effect, where the residual interaction can saturate better the nuclear forces in a way that a maximum of protons can be shared by the neutrons. But additional quantal effects to be described below lead to the formation of shape isomers as covalent molecular structures for weakly bound nuclei.

As far back as 1968, it was realized by Ikeda [19] that clustering in nuclei will become relevant for states in nuclei close to their thresholds for their

*This article was submitted by the author in English.

** e-mail: oertzen@hmi.de

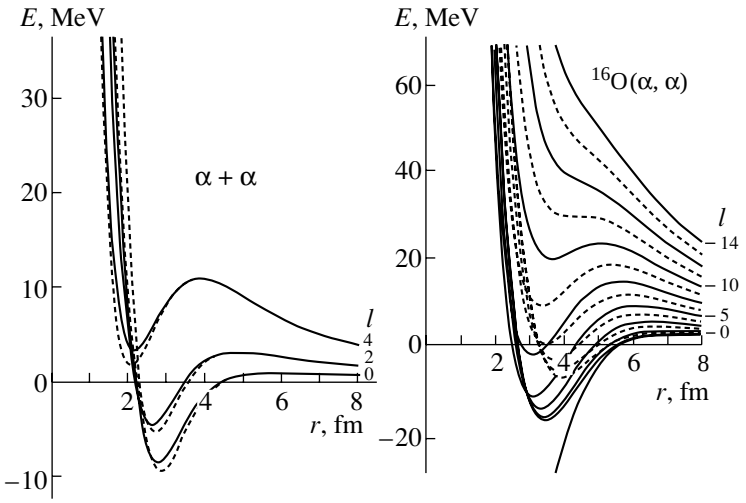


**Fig. 1.** Two examples of shallow local potentials for the interaction of $\alpha$ particles with $\alpha$ particles (the case of $^{8}$Be) and with $^{16}$O (the case of $^{20}$Ne).

decomposition into clusters. This concept is depicted as the Ikeda diagram in Fig. 2, where the threshold energies for the decay into substructures are given in MeV. We observe a systematic change in structure related to $\alpha$ clustering and heavier clusters. Reviews of the work on these clustering phenomena have been published regularly [8–10]; also, for heavier nuclei, like the rotational band structure in $^{20}$Ne and $^{44}$Ti, see [13] for a recent review. Adding neutrons and considering loosely bound threshold states, we will observe molecular structures based on these clusters and covalently bound neutrons.

Using the cluster plus valence neutrons model, we can now discuss the extension of this concept formulated by the author in [17]. The covalent binding of neutrons produces a new diagram as also shown in Fig. 2 (the covalent molecular binding diagram): "covalently bound molecular structures will appear in neutron-rich nuclei close to the thresholds for decomposition into neutrons, $\alpha$ clusters, and other clusters." For reasons of simplicity, only the $^{16}$O cluster is considered in the following, because the structure of $^{12}$C with its large deformation leads to some complications.

## 2. MOLECULAR ORBITALS FOR NEUTRON CONFIGURATIONS

Over the last decades, the molecular orbital model [20–25] for neutrons has been applied to nuclear collisions, in which single nucleons, mostly neutrons, are exchanged between two nuclear cores. This has been done for low-energy reactions and for cases where strongly bound cores (typically $\alpha$-cluster nuclei) and valence nucleons can be defined in a clear way [24]. In a collision process, this approach corresponds to a choice of basis states, which takes the two-center structure of the nuclear reaction into account, and the couplings appear as radial and Coriolis couplings [21, 23]. It can be seen as an equivalent approach to the coupled reaction channel calculations based on the asymptotic basis states of the separated nuclei. A comparison of the two approaches can be found in [25].

The original studies based on the LCNO model of the $^{12}$C + $^{13}$C system and others [20–22] were limited to scattering states, because the core–core potential between two heavier nuclei usually becomes attractive and strongly absorptive once the Coulomb barrier is reached. In this molecular orbital model and in the two-center shell model (in this case, not only valence nucleons, but all nucleons are considered), a correlation diagram has to be drawn, as is well known from the correlation diagrams of atomic physics (see also [26], p. 328). The diagram merges at small distances with the Nilsson diagram of the deformed compound nucleus. The molecular orbitals are classified according to the well-known quantum numbers of molecular valence states: the $K$-quantum number for the projection of the spin, the $\sigma$ and $\pi$ orbitals for the $M = 0$ and $M = 1$ projections of the orbital angular momenta $l$, the parity, and the gerade and ungerade symmetry due to the identity of the two molecular cores. With this correlation diagram, we are able to discuss the structure of the isotopes $^{9}$Be, $^{10}$Be, and $^{11}$Be, if we consider [17] the population of the molecular orbits for a distance corresponding to the potential minimum, or in the Nilsson model to a deformation of $\beta_2 = 0.6$–$0.7$.

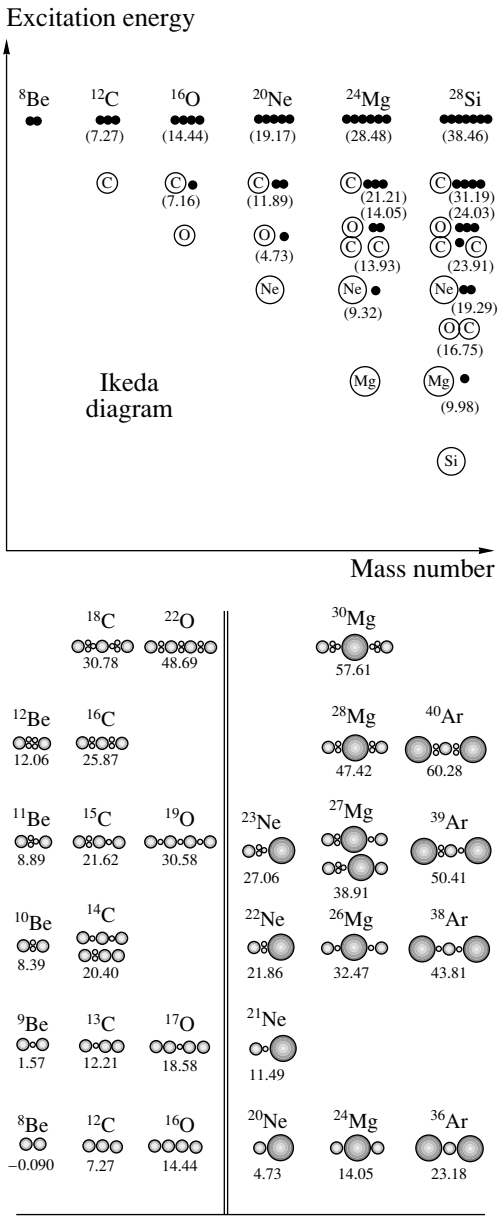


**Fig. 2.** Upper part: the Ikeda diagram for light $\alpha$-cluster nuclei; lower part: the extended threshold diagram of covalently bound nuclear molecules with covalent neutrons. The threshold energies are indicated.

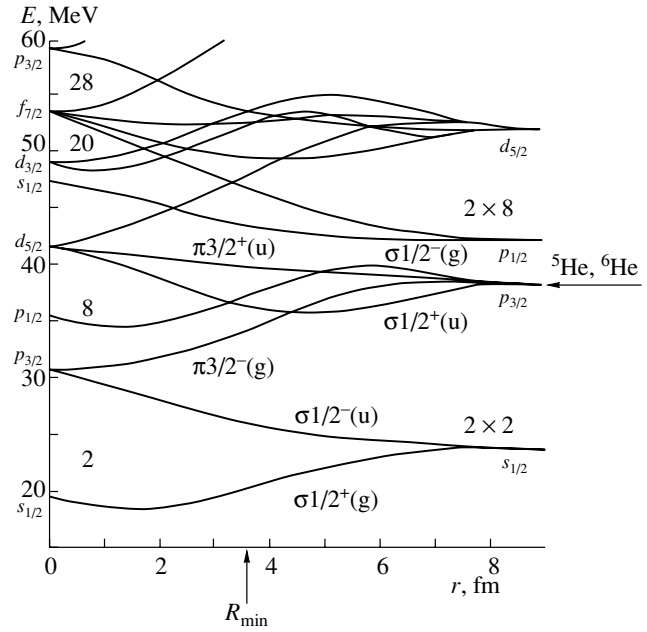


**Fig. 3.** Correlation diagram of molecular orbitals in a two-center shell model picture; the molecular orbitals are labeled by their quantum numbers (see text). The distance between the two centers is denoted by $r$, and $R_{\min}$ is the distance (3.7 fm) where the minimum of the $\alpha + \alpha$ potential occurs, and the states in $^{9-11}$Be are determined by distances of $r = 3.5$–$4.5$ fm.

## 3. BERYLLIUM ISOTOPES, DIMERS

The $^8$Be nucleus can be regarded as the first superdeformed nucleus with an axis ratio of 2 : 1. The situation is quite special for $\alpha$ particles—the $^8$Be is unbound. It has been known for more than two decades that the $^9$Be nucleus is an example of molecular binding in nuclear physics, where two $\alpha$ particles are bound by the covalent neutron. We note (see Fig. 3) that, at the distance where the $\alpha + \alpha$ potential has its minimum, the $K = 3/2^-$ orbit crosses the $K = 1/2^+$ orbit and becomes the lowest state at smaller distances. The first levels of $^9$Be are completely reproduced by this scheme. In a systematic survey of the structure of the beryllium isotopes [17], all(!) known states of the isotopes $^9$Be, $^{10}$Be, and $^{11}$Be can be grouped into rotational bands with molecular configurations by using the diagram of Fig. 3.

The structure of the states in the Be isotopes is thus determined by the "driving forces" of the evolution of the $\pi$ and $\sigma$ orbitals as a function of distance. The ground state of $^{10}$Be can be interpreted as a $(\pi)^2$ configuration with smaller deformation, whereas the excited $0_2^+$ at 6.179 MeV in $^{10}$Be is interpreted as the $(\sigma)^2$ configuration, which attains its lowest energy at much larger distances with a corresponding much larger moment of inertia. The information on excited states in the isotopes of $^9$Be, $^{10}$Be, and $^{11}$Be is compiled in Fig. 4, where the low-lying states of these isotopes are grouped together to form rotational bands. The moments of inertia and thus the deformation of the intrinsic configurations can be deduced from these graphs. For the $K = 1/2^+$, the typical Coriolis decoupling pattern expected for such cases is observed in $^9$Be and also in $^{11}$Be.

Very remarkable is the $K = 3/2^-$ band in $^{11}$Be, with states [27] established to high excitation energy, and which starts at 3.95 MeV, more than 3 MeV

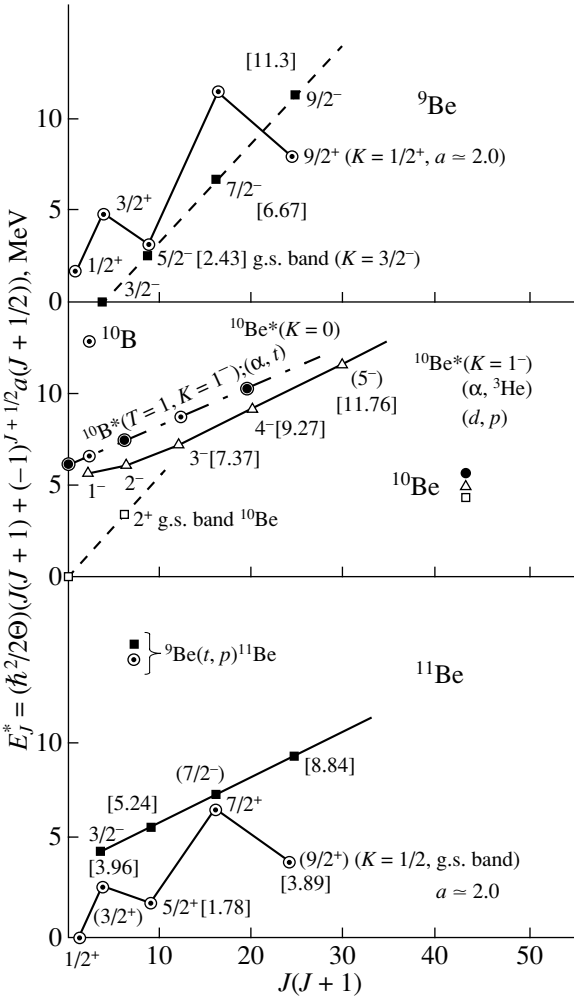


**Fig. 4.** Energy levels of the isotopes of $^9$Be, $^{10}$Be, and $^{11}$Be plotted as function of angular momentum $J(J+1)$.

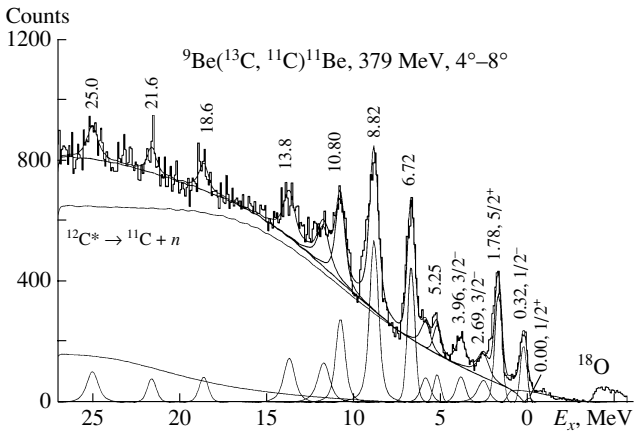


**Fig. 5.** Population of states in $^{11}$Be in a two-neutron transfer reaction on $^9$Be.

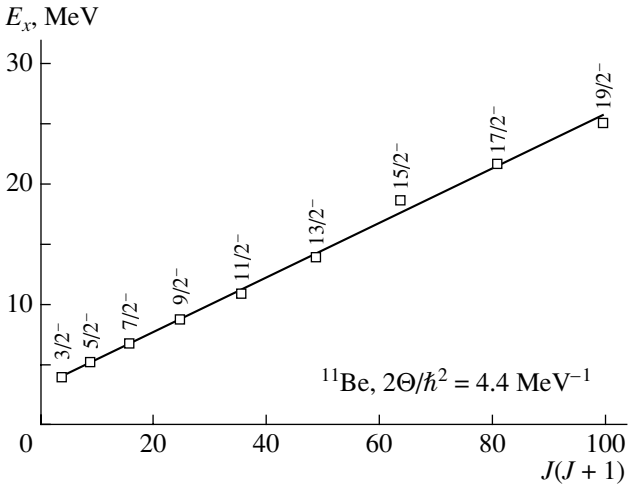


**Fig. 6.** Exitation energies of the $K = 3/2^-$ band (presumed) plotted as function of spin $J(J+1)$.

above the particle threshold (see Figs. 4–6). Inspecting the correlation diagram, we recognize that this band must have the covalent neutron configuration $(\pi) \times (\sigma)^2$, which results in a particular stability and a large deformation due to the properties of the $(\sigma)^2$ bond. The moment of inertia of this band is thus similar to that of the excited $K = 0^+$ band in $^{10}$Be.

These molecular states must be considered as true superdeformed shape isomers. This aspect is observed in a dramatic way through the selectivity for the population of states in $^{11}$Be. We have studied the population of states in $^{11}$Be by (i) single nucleon transfer on $^{10}$Be and (ii) two-neutron transfer on $^9$Be, shown in Fig. 5 from [27]. Whereas for the reaction on $^{10}$Be only three low-lying single particle states (with the configurations $p_{1/2}$, $p_{3/2}$, and $d_{5/2}$) are observed, the two-neutron transfer populates strongly the higher spin members of the $K = 3/2^-$ rotational band, which are completely absent in the one-neutron transfer spectrum.

The two-neutron transfer spectrum shown in Fig. 5 shows a resonant structure, which extends up to a projected spin value of 19/2. We may ponder if this value can still be obtained in a deformed oscillator-shell model by counting the spins of the individual three valence nucleons: in fact the maximum spin of the valence neutrons would be $[(3/2(p_{3/2}) + 8/2(\text{for } 2 \times 5/2)] = 11/2$; the total spin can then only be reached by adding the maximum spin of the $^8$Be system, which is known to be 4, giving the total sum of 19/2!

The proposed molecular properties of the states in Be isotopes have found striking confirmation from model-independent calculations (computer experiments) using the method of antisymmetrized

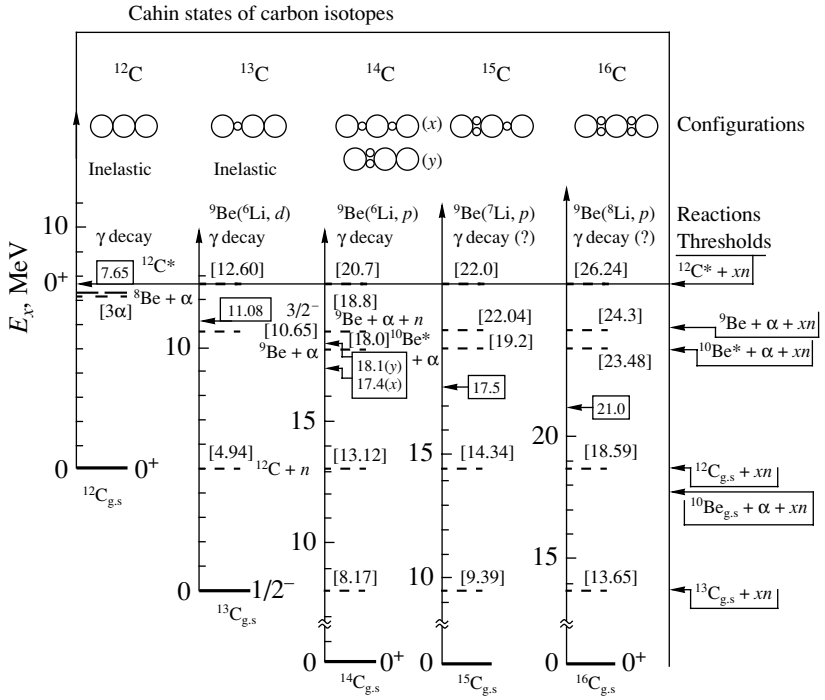


**Fig. 7.** Chain states of carbon isotopes with up to four extra covalent valence neutrons. The thresholds for the decay into $\alpha$ particles and neutrons are aligned to the same level.

molecular dynamics (AMD) of Horiuchi and Kanada-En'yo [15, 16]. Particularly impressive are the density distributions obtained for the ground state $0^+$ and second $0^+$ state of $^{10}$Be, which have been obtained by projection on spin and parity [16]. The formation of covalent bonds with the $(\sigma)^2$ and $(\pi)^2$ configurations according to the correlation diagram in Fig. 3 is very conspicuous in the density distributions obtained from these calculations [16].

The molecular structure is still visible in heavier isotopes of Be, like $^{12}$Be, where the persistence of the strong clustering of the $\alpha$ particles prevents the formation of a closed shell with $N = 8$, and at higher excitation energies, experiments suggest the formation of a rotating dimer decaying into two $^6$He fragments [28]. The properties of these strongly deformed configurations can be traced to excited states of heavier isotopes of Be and, by using the concept of isospin, also to structures in boron isotopes.

## 4. POLYMERS, CHAIN STATES IN CARBON ISOTOPES

Based on the covalently bound structures of the system of two $\alpha$ particles, we can continue the discussion of extreme deformations with three $\alpha$ particles by showing the schematic diagrams for the shape isomers of the carbon isotopes in Fig. 7. The three-$\alpha$-particle threshold state correspondingly is taken to be the second $0_2^+$ in $^{12}$C (a more detailed discussion is given in [17]). The trimers are built with the covalent binding of two times two neutrons by using the well-established knowledge of the covalent bonds in $^{10}$Be. Actually, we may expect that covalently bound shape isomers in $^{16}$C are indeed rather stable configurations (as is the case in atomic molecules). Two bonds in the covalent configuration between the $\alpha$ particles will influence each other so as to increase the total binding energy of the chain, which is expected to be more than 5 MeV. More recent calculations for $^{14}$C and $^{16}$C are discussed in [29, 30]. A detailed discussion of the experimental evidence has recently been published [31].

There are many other nuclear molecules and polymers that can be built on the repulsive $\alpha$-nucleus potentials and additional covalent neutrons. A particular conspicuous example is discussed in the next section (see also [32]).

## 5. MOLECULAR STRUCTURE BASED ON THE $\alpha + {}^{16}$O POTENTIAL, STRUCTURE OF NEON $^{20,21}$Ne

The structure of $\alpha$-cluster nuclei, in particular, of $^{20}$Ne, has been discussed in the $\alpha + {}^{16}$O cluster model over the last decades [8, 33]. It is connected to an octupole degree of freedoms [33]; two bands with $K = 0^{+,-}$ are observed. The particular feature of the inversion doublet with two bands of $K = 0^+$

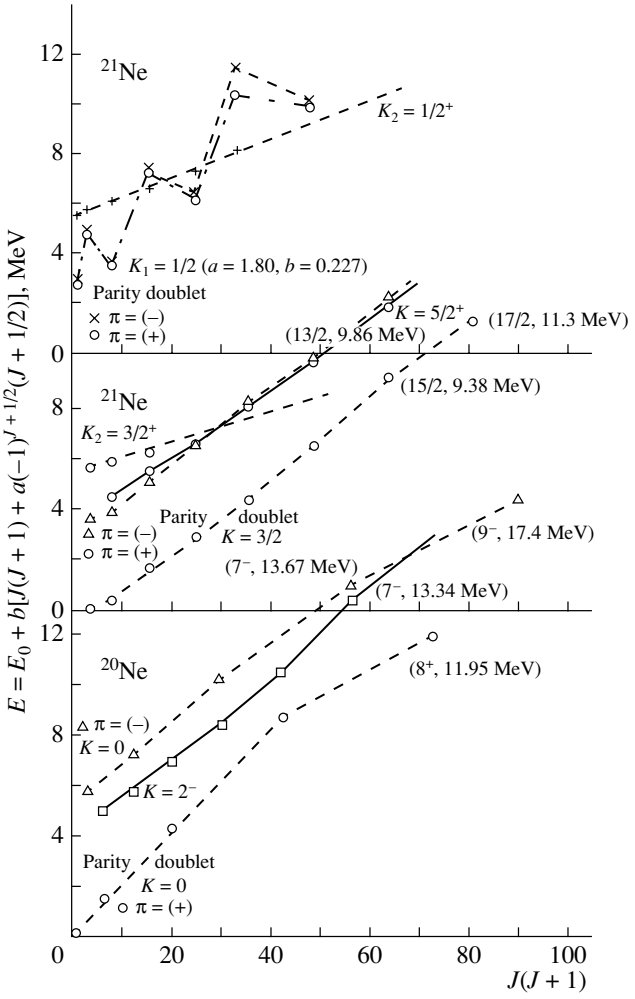


**Fig. 8.** Plot of the excitation energies of known states in $^{20}$Ne and in $^{21}$Ne as rotational bands. The compilation is made in order to compare the band doublets expected from the intrinsic reflection asymmetric shapes and the signature inversion of the structures shown below in Fig. 9.

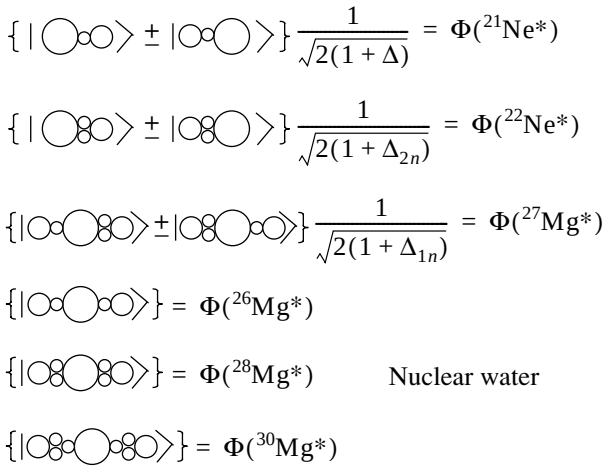


**Fig. 9.** Schematic illustration of the structure of molecular shape isomers in the neon and magnesium isotopes based on the ($\alpha + {}^{16}$O) cluster model plus some neutrons. For the odd mass isotopes, each $K$-quantum number gives rise to a doublet of bands due to the two signs of the signature. The splitting of the bands will be proportional to the overlap $\Delta$.

and $K = 0^-$ (actually $K = 1^-$) is also well described by an angular-momentum-dependent $\alpha + {}^{16}$O local potential; this point has been summarized recently by Ohkubo [13]. This peculiar feature of inversion doublets in nuclear structure arises for the case of an intrinsic asymmetric shape, which has no good parity. For $K$-quantum number zero, $K = 0$, we would have a band with states of alternating parity $J^\pi = (0^+, 1^-, 2^+, 3^-,$ etc.). The fact that this band is split into two bands of definite parity is due to a large probability to change between the two reflection asymmetric shapes by some tunneling process. This case is discussed in volume II of the book by Bohr and Mottelson [34] and also, for example, for molecules in the book by Herzberg [26] (p. 129). A particular case occurs for odd nuclei and for the case of $K \neq 0$, where two parallel bands with equal spin but opposite parity (parity doublets) will occur, a phenomenon also known as signature splitting [26, 34]. This will be the case of $^{21}$Ne. In Fig. 8, rotational bands are plotted in such a manner that the doublets, which may occur due to signature splitting, become visible [32].

In order to study the structure of $^{21}$Ne in a model that consists of one neutron bound in a two-center system with two unequal cores, namely, $\alpha$ and $^{16}$O, we have to look into the structure of an asymmetric top with $K \neq 0$, with an intrinsic violation of parity, as illustrated in Fig. 9. For these structures, a parity projection is obtained with the superposition of two reflection asymmetric states, as shown in Fig. 9. The model resembles in its main structure that of Descouvement [35]; however, the molecular orbital (LCNO) model mentioned in the previous sections is used directly. For this purpose, a correlation diagram must be constructed; however, some of the most important features can be deduced from a threshold diagram, as shown in Fig. 10. This diagram shows the positions (binding energies) of the single-particle orbits of the neutron at the two centers, namely, for $\alpha$ and $^{16}$O. For this system, a remarkable coincidence occurs: the $p_{3/2}$ resonance of $^5$He (at 890 keV) is almost degenerate with the $d_{3/2}$ state, also a resonance at 941 keV in $^{17}$O. We note that this particular situation is known as the quasi-resonance condition for the sharing of valence particles in covalent structures in molecular science.

For the molecular two-center states in $^{21}$Ne, we take these two degenerate $j = 3/2$ orbits at the $\alpha$ and

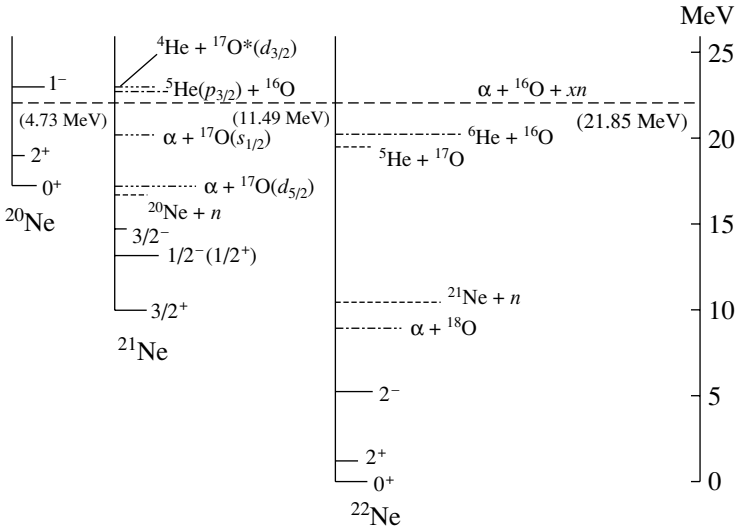


**Fig. 10.** Illustration of the thresholds (aligned to the same level) for the neon isotopes for the ($\alpha + xn +$ $^{16}$O) cluster model. The $J^\pi$ values of band heads in $^{21}$Ne with their $K$-quantum numbers are indicated.

$^{16}$O clusters and construct the $K = 1/2$ and $3/2$ two-center states. These configurations are schematically shown in Fig. 9. There is no reflection symmetry in these intrinsic states; therefore, states with definite parity are constructed by using superpositions, which produce a definite signature. The outcome of these considerations is [32] that there must be in the cluster model, with ($\alpha +$ $^{16}$O + neutron) two parity doublets of bands with $K = 1/2$ and $3/2$, i.e., for each spin, the two parities (+ and −). This situation of a finite $K$ value is also well known in asymmetric atomic molecules as cited by Herzberg [26]. The interesting question of the size of the energy (signature) splitting and of the purity of these configurations can possibly answered experimentally.

Gamma spectroscopy of the neon/magnesium isotopes has been reported over the last 10–20 years [36, 37]. The experimental systematics suggests two $K = 1/2$ bands with opposite parity and very small splitting. This result could be interpreted as due to a rather stable molecular structure based on the $\sigma$ bond between the $\alpha$ particle and the $^{16}$O clusters (see [32]). For $K = 3/2$ bands, we also have two candidates; however, a definite answer for these states is more difficult; they most likely will exhibit strong mixing with other configurations. The splitting is very similar to that in the case of $^{20}$Ne. I mention an interesting finding [37] about the extreme retardation by four orders of magnitude of the $E1$ transition from the excited $1/2^-$ state to the $3/2^+$ ground state, a fact which supports that the $K = 1/2^-$ state has indeed a very different structure.

To conclude the above considerations, we can state that there is in light nuclei strong evidence for dimers, trimers based on $\alpha$ particles, and asymmetric molecules based on $\alpha$ + $^{16}$O clustering. In accordance with the Ikeda diagram (Fig. 2), I can construct more extended molecules, whose band heads can be estimated by using the information from the neon isotopes. The existence of an intrinsic symmetric stable molecule, which I call "nuclear water," $(He)_2O$, can be predicted. The wave functions are schematically shown in Fig 9. These shapes are true shape isomers, with complicated deformations, which cannot be easily described by a few terms in the Legendre function expansions for nuclear shapes. A search for $\gamma$ transitions from such configurations is an interesting challenge for nuclear spectroscopy. Radioactive beam facilities will give access to the more neutron-rich nuclei. With these considerations, it is possible to predict that, in light neutron-rich nuclei, many shape isomers must be observed, which are strongly related to clustering, i.e., with structures which go well beyond usual shell model approaches.

## REFERENCES

1. E. Almquist, D. A. Bromley, and I. A. Kuehner, Phys. Rev. Lett. **4**, 515 (1960); K. A. Erb and D. A. Bromley (Plenum Press, New York, 1984), Vol. 3, p. 201.
2. R. W. Zurmuehle *et al.*, Phys. Lett. B **129B**, 348 (1983); in *Proceedings of the 5th Conference on Clustering Aspects in Nuclear Physics, 1988*; J. Phys. Soc. Jpn. **58**, 37 (1989).
3. S. Marsh and W. D. M. Rae, Phys. Lett. B **180**, 185 (1986).
4. J. Zhang, W. D. M. Rae, and A. C. Merchant, Nucl. Phys. A **575**, 61 (1994).
5. H. Flocard, P. H. Heenen, S. J. Krieger, and M. S. Weiss, Prog. Theor. Phys. **72**, 1000 (1984).

6. G. Leander and S. E. Larsson, Nucl. Phys. A **239**, 93 (1975).
7. S. Aberg and L. O. Joensson, Z. Phys. A **349**, 205 (1994).
8. M. Freer and A. C. Merchant, J. Phys. G **23**, 261 (1997).
9. B. R. Fulton and W. D. M. Rae, J. Phys. G **16**, 333 (1990); B. R. Fulton, Z. Phys. A **349**, 227 (1994) and references therein.
10. *Proceedings of the 5th International Conference on Clustering Aspects in Nuclear and Subnuclear Systems, Kyoto, Japan, 1988,* Ed. by K. Ikeda (Phys. Soc. Japan, Tokyo, 1989).
11. D. Baye, Phys. Rev. Lett. **58**, 2738 (1987).
12. S. Ali and A. R. Bodmer, Nucl. Phys. **80**, 99 (1966).
13. S. Ohkubo *et al.*, Prog. Theor. Phys. Suppl. **132**, 1 (1998); in particular, F. Michel, S. Ohkubo, and G. Reidemeister, Prog. Theor. Phys. Suppl. **132**, 7 (1998).
14. *Proceedings of the 4th International Conference on Radioactive Nuclear Beams, Omiya, Japan, 1996*; Nucl. Phys. A **616**, 3c (1997).
15. H. Horiuchi, K. Ikeda, and Y. Suzuki, Prog. Theor. Phys. Suppl. **52**, Chap. 3 (1972).
16. Y. K. Kanada-En'yo, H. Horiuchi, and A. Dote, J. Phys. G **24**, 1499 (1998); Phys. Rev. C **60**, 064304 (1999).
17. W. von Oertzen, Z. Phys. A **354**, 37 (1996); **357**, 355 (1997); Nuovo Cimento A **110**, 895 (1997).
18. Y. K. Kanada-En'yo, H. Horiuchi, and A. Ono, Phys. Rev. C **52**, 628 (1995); **56**, 1844 (1997).
19. K. Ikeda, N. Tagikawa, and H. Horiuchi, Prog. Theor. Phys. Suppl. 464 (1968).
20. W. von Oertzen, Nucl. Phys. A **148**, 529 (1970); W. von Oertzen and H. G. Bohlen, Phys. Rep. **19C**, 1 (1975).
21. B. Imanishi and W. von Oertzen, Phys. Rep. **155C**, 29 (1987).
22. N. Bischof *et al.*, Nucl. Phys. A **490**, 490 (1988) and references therein.
23. J. Y. Park, W. Greiner, and W. Scheid, Phys. Rev. C **21**, 958 (1980); A. Thiel, J. Phys. G **16**, 867 (1990).
24. *Proceedings of the International Conference on Nuclear and Atomic Clusters, EPS Topical Conf., Turku, Finland, 1991,* Ed. by M. Brenner and T. Loennroth (Springer, Berlin, 1992), p. 88.
25. W. von Oertzen, Th. Wilpert, B. Bilwes, *et al.*, Z. Phys. A **353**, 373 (1996).
26. G. Herzberg, *Molecular Spectra and Molecular Structure*, Vol. I: *Spectra of Diatomic Molecules* (Van Nostrand, Princeton, 1950).
27. H. G. Bohlen *et al.*, Nuovo Cimento A **111**, 841 (1998).
28. M. Freer *et al.*, Phys. Rev. Lett. **82**, 1383 (1999).
29. N. Itagaki *et al.*, Phys. Rev. C **61**, 044306 (2000).
30. N. Itagaki *et al.*, Phys. Rev. C **64**, 014301 (2001).
31. M. Milin and W. von Oertzen, Eur. Phys. J. A **14**, 295 (2002).
32. W. von Oertzen, Eur. Phys. J. A **11**, 403 (2001).
33. P. A. Butler and W. Nazarewicz, Rev. Mod. Phys. **68**, 349 (1996).
34. A. Bohr and B. Mottelson, *Nuclear Structure* (Benjamin, New York, 1975), Vol. II.
35. P. Descouvement, Phys. Rev. C **48**, 2746 (1993).
36. P. M. Endt, Nucl. Phys. A **521**, 1 (1990) and references therein.
37. A. A. Pilt, R. H. Speak, R. V. Elliott, *et al.*, Can. J. Phys. **50**, 1826 (1972).

*Physics of Atomic Nuclei, Vol. 66, No. 9, 2003, pp. 1599–1606. From Yadernaya Fizika, Vol. 66, No. 9, 2003, pp. 1646–1653.*


# Memory Effects in Nuclear Friction*

**I. N. Mikhailov[1], Ch. Briançon[2], T. I. Mikhailova[1]**, and M. Di Toro[3]**

[1] *Joint Institute for Nuclear Research, Dubna, Moscow oblast, 141980 Russia*
[2] *CSNSM, Orsay, France*
[3] *LNS–INFN, Catania, Italy*

Received August 28, 2002

**Abstract**—The status of the problem of describing the dissipative phenomena in nuclear reactions is discussed from experimental and theoretical points of view. Dynamical effects in the initial phase of a fusion reaction are presented showing the evolution of two colliding $^{100}$Mo ions. The role of elastic forces associated with the Fermi surface deformation is shown by comparing the results obtained with and without taking into account the memory effects. The evolution of the unified nuclear system formed after establishing contact between ions is shown to be also strongly influenced by elastic forces associated with the Fermi surface deformations and with related memory effects. Examples are given in which the Fermi surface deformations lead to phenomena usually attributed to the excitation energy and deformation dependence of the friction parameter. © *2003 MAIK "Nauka/Interperiodica".*

## 1. INFORMATION ON FRICTION

The sources of information on nuclear friction are numerous. They are related to the following aspects of friction:

Friction regulates **the time scales of collective processes**: the larger the friction, the stronger the force slowing down the collective motion. The time scales in nuclear fusion are known from the following:

*The rate of collective energy decrease.* It was found at the very beginning of studies of heavy-ion reactions that the bulk of excitation energy in the composite system formed in heavy-ion collisions is transformed fast into the energy of statistical excitation [1]. The friction estimated from this information is large.

*Neutron and $\gamma$-ray multiplicities in fusion* [2, 3]. When the fusion is followed by a fission of a compound nucleus, the multiplicities of emitted particles and $\gamma$ rays prior to fission provide information on the time scales of intermediate processes. From this information, one concludes that the formation of compound state takes much time. Thus, friction, estimated from this observation turns out to be also large (with an important exclusion of cold fusion events where the friction is found to be negligible).

*Anisotropy of $\gamma$ radiation from the fission in low L states.* An analysis of shape and temperature evolution of the composite system formed in the collision of identical ions [4] shows that the equilibration of shape is a slow process. The approach used in this analysis does not include the friction parameter, but the results may be interpreted as the action of a large friction during the bulk of compound nucleus formation time. Unfortunately, this possibility of studying the dissipation in nuclear motion has not been properly used yet in experimental studies.

Friction regulates **fluctuations of collective observables**: from the fluctuation–dissipation theorem of statistical mechanics [5], it follows that the greater the friction, the larger the amplitude of fluctuation of collective observables. Among the different sources of information on the friction coming from this side are *the dispersion in mass and charge distribution of fission fragments* and *the dispersion in their total kinetic energy* [6].

Numerical values for the friction parameter deduced from different sources differ very strongly and the conciliation of experimental information on the friction turns out to be a very delicate problem. It pushes some experts to introduce an unexpected shape dependence of the friction parameter [6] and/or a strong temperature dependence of it [7]. But all attempts to establish the experimental value of the friction parameter with some reasonable accuracy fail when one adds to the sources of information on it also **the cross section of fusion**. The dependence of the latter on friction also follows from the dissipation–fluctuation theorem: the greater the friction, the larger

*This article was submitted by the authors in English.

** e-mail: tmikh@cv.jinr.ru

1063-7788/03/6609-1599$24.00 

the probability of a shape fluctuation leading to the reseparation of ions after the collision.

A very interesting piece of information on the friction provides for **collisions at energies just below the value needed for fusion**. Analyzing the data of [2] on the neutron multiplicity in such events, the authors of [8] conclude that the friction changes during the collision: it is moderately weak at the beginning and increases by about a factor of 10 toward the end of the collision.

The difficulties in describing the fusion probability and the neutron multiplicity in collisions at small energies seem to be symptomatic. They are most probably related to the breakdown of conditions allowing one to consider the changes of nuclear state during the collision as being adiabatically slow. The fast variations of the state cannot be described within theoretical approaches operating with the friction understood in a usual way.

Of various theoretical estimations of friction we mention two:

The classical *wall formula* by Blocki [9] giving the rate of kinetic energy decrease of Fermi gas confined by the wall and moving with respect to it. Note that the wall estimate for friction is often used as a standard indicating its force. In particular, saying that friction is strong or weak, we mean that it is stronger or weaker than predicted by this estimate (see Section 2).

The study of nuclear *linear response* to a perturbation periodic in time [10, 11] and matching it to the response of a dampened linear oscillator.

In both approaches (as in almost all the others) the theory involves an hypothesis of adiabaticity of collective motion: in the Blocki model, the motion of gas is assumed to be much slower than typical velocities of particles; in the linear response theory, the friction is deduced from calculation of energy dissipated in nuclei in the zero-frequency limit.

Among theoretical approaches of fusion free from the adiabaticity hypothesis, we mention our studies based on the virial theorems method [4, 12, 13]. Instead of making assumptions on the friction, we introduce a hypothesis on the collision term in the kinetic equation underlying our studies: we use for it the mean-relaxation-time approximation improved in order to fulfill the invariance properties of the collision integral of macroscopic statistical mechanics [5].

In this approach, the most important part of retardation or memory effects in the collective energy dissipation is taken into account. Their role in the fusion of heavy ions was shown in [4] within rather simplified assumptions on the process. The memory effects turn out to be the most pronounced at the instant of collision of heavy ions. The following long phase of the fusion process leading to the compound nucleus formation and to its fission fulfills the adiabaticity conditions and may be well described using the notion of friction forces.

The value of the friction parameter and the conditions under which its application is justified may, in fact, be estimated from the approach based on the virial theorems method. It is shown, in particular, in [14], where the preparatory steps for systematic studies of the fusion process in realistic conditions are reported and an analysis is made of the fusion dynamics prior to the moment when the contact between the colliding ions is established. Spectacular manifestations of memory effects in heavy-ion collisions have been shown in this way.

## 2. MEMORY EFFECTS PRIOR TO HEAVY-ION COLLISION

### *2.1. Elastoplastic Model of Fusion*

A physical picture of processes taking place just before a unification of heavy ions has been obtained in [14], analyzing the head-on collision of two $^{100}$Mo ions. The matter distribution is described by two collective coordinates: the elongation parameter $L(t)$ defined as the distance between the centers of mass of colliding ions and by the intrinsic quadrupole moment of each of them:

$$q(t) = m \int\limits_{V_1} d\mathbf{r} n(\mathbf{r}) \left[2z^2 - x^2 - y^2\right].$$

In this expression, $V_1$ is the volume of one of ions and $\mathbf{r}$ is the coordinate in the reference frame with the origin at the center of mass of the ion.

One more variable enters into the model: the $(\lambda, \mu) = (2, 0)$ component of the pressure tensor integrated over the volume of one ion:

$$\pi(t) = \int\limits_{V_1} d\mathbf{r}(2P_z(\mathbf{r}, t) - P_x(\mathbf{r}, t) - P_y(\mathbf{r}, t)) \quad (1)$$

(here $P_i(\mathbf{r}, t)$, $i = x, y, z$, are diagonal components of pressure tensor). The quantity $\pi(t)$ appears in the equations of motion under the guise of a generalized velocity in the direction of the cyclic collective coordinate $Z$: $\pi = \dot{Z}$ [15].

The introduction of the $Z$ variable [15] allows one to cast the theory into the Lagrange–Rayleigh form with the Lagrangian function given by

$$\mathcal{L}_c = \mathcal{L}_{\text{ad}} + \mathcal{L}_{\text{dyn}} = \frac{\mu}{2}\dot{L}^2 + M(q)\dot{q}^2 \quad (2)$$

$$- U(L, q) + \frac{2M(0)}{F_{\text{fs}}^{(0)}}\dot{Z}^2 + 4\dot{Z}\int\limits^{q} dq' M(q').$$

The Lagrange–Rayleigh equations

$$\frac{d}{dt}\frac{\partial \mathcal{L}_c}{\partial \dot{Q}_i} - \frac{\partial \mathcal{L}_c}{\partial Q_i} = -\frac{\partial \mathcal{R}}{\partial \dot{Q}_i}$$

($Q_i = L,\ q,\ Z$) involve the dissipation Rayleigh function, which is taken as

$$\mathcal{R} = \frac{2M(0)\pi^2}{\tau F_{\rm fs}^{(0)}}. \qquad (3)$$

In Eq. (2), $\mu = mA_1/2$ is the reduced mass for two Mo ions, and the mass parameter $M(q)$ is found assuming the ellipsoidal deformation of ions and velocity field linear in coordinates within them:

$$M(q) = \frac{5}{8mR_1^2A_1}\ \frac{1}{f^2(1+2/f^6)}$$

with the deformation parameter $f(q)$ defined by

$$q = \frac{2}{5}mR_1^2A_1\left(\frac{1}{f^4} - f^2\right).$$

The Coulomb potential and the generalized surface potential of [16, 17] are used to calculate the potential energy

$$U(L,q) = \frac{1}{2}\int\limits_V\int\limits_V d\mathbf{r}d\mathbf{r}' n(\mathbf{r})n(\mathbf{r}')V(|\mathbf{r}-\mathbf{r}'|). \qquad (4)$$

In Eq. (4), the integration goes over the volume of both ions, $V = V_1 + V_2$.

The quantity $F_{\rm fs}^{(0)}$ measuring the dependence of intrinsic kinetic energy on $\pi$ and the value of relaxation time parameter $\tau$ are fixed using the arguments of [18], where the giant multipole resonances were studied on the same basis as in our approach to nuclear reactions. In the quoted paper, it is found that the centroids and the widths of the first two isoscalar resonances with $\lambda = 2$ and $\lambda = 4$ are correctly reproduced when

$$F_{\rm fs}^{(0)} = \left[\frac{v_F}{r_0A_1^{1/3}}\right]^2$$

and

$$\tau = \left(\frac{4}{3}\right)^2\frac{r_0A_1^{1/3}}{v_F}\left(\hbar/\tau = 24.9A_1^{-1/3}\ \text{MeV}\right).$$

Our calculations show that the deformation of ions remains very small up to the moment of collision and their heating is quite moderate. This choice of $\tau$ and the stability of parameters describing giant resonances exclude any noticeable influence of possible shape and temperature dependences of the relaxation time parameter. Consequently, $\tau$ is considered to be constant.

The collective energy [19] $E_c = \sum_i \dot{Q}_i\partial\mathcal{L}_c/\partial\dot{Q}_i - \mathcal{L}_c$ is equal to

$$E_c = \frac{\mu}{2}\dot{L}^2 + M(q)\dot{q}^2 + U(L,q) + \frac{2M(0)}{F_{\rm fs}^{(0)}}\pi^2 \equiv E_{\rm ad} + E_{\rm dia}, \qquad (5)$$

where

$$E_{\rm dia} = \frac{2M(0)}{F_{\rm fs}^{(0)}}\pi^2.$$

It contains the kinetic energy of translational motion of ions $\mu\dot{L}^2/2$, the sum of kinetic energies originated by the collective flow in two ions $M(q)\dot{q}^2$, and the potential energy $U(L,q)$. In adiabatically slow processes, nucleons have sufficient time to reach an equilibrium distribution over momenta. Then the quantity $\pi$ vanishes together with the last term in the expression for $E_c$. For this reason, the sum of the first three terms in Eq. (5) may be called an adiabatic collective energy and the last term may be named a diabatic contribution to the collective energy.

The Rayleigh dissipation function determines the work produced by the friction on the heat bath. The rate of heating is given by

$$dE_c/dt = -2\mathcal{R}. \qquad (6)$$

From Eqs. (3) and (6), it follows that $E_{\rm stat}(t) \equiv E_c(t=-\infty) - E_c(t)$ is a monotonically rising function of time, as it should be.

The dissipation of collective energy is small when the motion is fast in the time scale given by $\tau$. It may be ignored altogether in the limit of $\tau \to \infty$. In this case, the motion is quasi-elastic. In the opposite case of slow motion, the shape of ions changes with time as if they were plastic. This double-faced nature of the system puts it among elastoplastic systems introduced in the nuclear theory by Nörenberg [20]. The extension of collective space for the coordinate $Z$ marks the difference between our approach and the other well-known approaches of fusion dynamics: the currently used adiabatic approach with the inclusion of dissipation via the friction force and the diabatic dynamics model originated by Nörenberg [20, 21].

### *2.2. Adiabatic Limit*

When the motion is slow, the quantity $\pi$ becomes

$$\pi = -\tau(v_F/r_0A^{1/3})^2(M(q)/M(0))\dot{q}. \qquad (7)$$

The corresponding dynamics, which we call viscous is described by the adiabatic Lagrangian ($E_{\rm ad}$ in Eq. (2)) and by the viscous Rayleigh function

$$\mathcal{R}_{\rm visc} = M(q)\beta_{\rm visc}\dot{q}^2. \qquad (8)$$

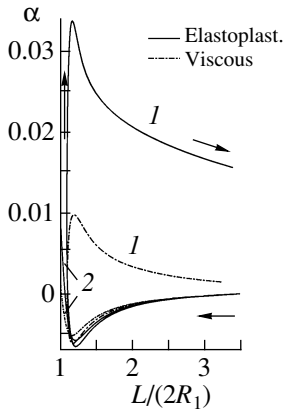


**Fig. 1.** Trajectories of the two-molybdenum system in $\alpha-L$ plane. Here and in Fig. 2, solid curves are obtained with the use of the elastoplastic model, dash-dotted curves correspond to the viscous approximation. Curves *1* and *2* correspond, respectively, to $E_{\text{in}} = 4$ and 4.4 MeV/nucl. Arrows beside the curves indicate the time evolution.

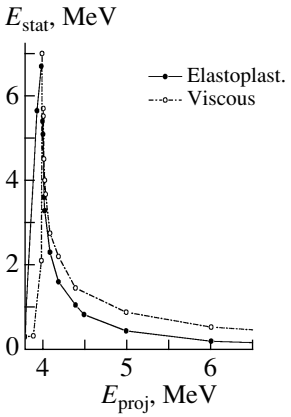


**Fig. 2.** Statistical excitation energy as a function of $E_{\text{in}}$ (see text, Subsection 2.3).

In Eq. (8), there appears a friction parameter

$$\beta_{\text{visc}} = \tau \left( \frac{v_F}{r_0 A^{1/3}} \right)^2 \frac{M(q)}{M(0)}. \qquad (9)$$

Our parametrization of relaxation time parameter $\tau$ makes the friction parameter $\beta_{\text{visc}}$ close to the friction parameter $\beta_{\text{wall}}$ estimated using the wall formula [9] applied to a spherical nucleus of radius $R_1$:

$$\beta_{\text{visc}}/\beta_{\text{wall}} = (4/3)^3 \qquad (\beta_{\text{wall}} = (3/4)v_F/R_1).$$

The expression for adiabatic collective energy $E_{\text{ad}}$ is given in Eq. (5). In the case of motion with an arbitrary speed, one has

$$dE_{\text{ad}}/dt = 4M(q)\pi\dot{q}. \qquad (10)$$

In the general case, the time derivative of $E_{\text{ad}}$ is not a positively defined function of time (as is the total collective energy $E_c$). Then, the variations of $E_{\text{ad}}$ are not related in a simple way to the transformation of collective energy in the energy of statistical excitation. Only in the adiabatic case, when Eq. (7) is valid, are the properties of total collective energy shared by $E_{\text{ad}}$.

### *2.3. Elastoplastic versus Viscous Scenarios of Collision*

Description of fusion and fission reactions using the friction forces is typical of theoretical studies, although the conditions for the application of the adiabatic approach are not always fulfilled. Having this in mind, we present the discussion of differences between the viscous and the elastoplastic scenarios of two $^{100}$Mo ions colliding. The following illustrations allow one to see the memory effects in the collision.

In Figs. 1 and 2, the trajectories drawn in solid lines correspond to the elastoplastic dynamics; the dash-dotted curves give the results of calculations in the viscous approximation. The value of $L$ is given in units of $2R_1$, $R_1$ being the radius of the Mo nucleus. In the following illustrations, we use the parameter $\alpha = 1 - f$ instead of the quadrupole moment $q$.

A comment is due on the potential energy surfaces corresponding to the model. When the distance between the surfaces of two ions is large in comparison with the range of nucleon–nucleon interaction, the potential energy $U(L, \alpha)$ has a valley with a bottom in the region of oblate deformations ($\partial_q U = 0$ when $\alpha < 0$). The valley disappears at $L/(2R_1) = 1.2$, giving way to a surface sloping towards the prolate shapes. For small values of $|\alpha|$, the potential energy ridge ($L_r(\alpha)$), where $\partial U_L = 0$, is situated at $L > 2R_1$. At $\alpha = 0$, $L_r(0) = 2R_1 \cdot 1.07$ and $U(L_r, 0) = 199.16$ MeV.

In Fig. 1, the trajectories of colliding ions are shown in the $L-\alpha$ plot for two different values of incident energy $E_{\text{in}}$. Curves *1* and *2* correspond to $E_{\text{in}}$ equal to 4 and 4.4 MeV/nucl., respectively; the arrows beside the curves indicate the evolution of $L$ in time. Calculations show that the trajectories do not follow the valley in the potential energy landscape and that the shape of approaching nuclei remains very close to spherical: $|\alpha|$ never exceeds 0.04 in all considered cases. The small spheroidal deformation is, however, important, because it engenders the collective energy dissipation.

Figure 2 shows the statistical excitation energy accumulated in the system as a function of incident energy. The results given for energies smaller than 4.013 MeV/nucl. correspond to cases when no contact between the nuclei is established. The statistical energy shown for these trajectories is calculated by

integrating Eq. (6) in the whole time interval of scattering. Calculations made for greater energies correspond to events at which the contact is established. Here, the data are given for the statistical energy accumulated up to the moment of contact. The lowest energy at which the contact is established is equal to $E_{\rm in}^{\rm min} = 4.013$ MeV/nucl. According to calculations, $E_{\rm stat}$ at this point is equal to 7 MeV. The sum of $E_{\rm in}^{\rm min}$ and $E_{\rm stat}$ determines an effective potential energy ridge met by the system during its evolution. This potential energy ridge is found to be equal to 193.16 MeV, which is in remarkable agreement with the estimates of the Bass barrier for $^{100}$Mo + $^{100}$Mo fusion given in [22] ($E_b = 194$ MeV).

The decrease in dissipated energy with increasing $E_{\rm in}$ at energies greater than 4 MeV/nucl. follows from the relation

$$E_{\rm stat}(L) \sim \frac{1}{4\beta}\left\{\int_{\infty}^{L}\frac{dL'}{dL'/dt}F(L')\right\}^2, \qquad (11)$$

which is known from the adiabatic theory [23]. The relative motion velocity $dL'/dt$ increases with the incident energy, causing the integral to decrease.

The maximal value of statistical excitation energy accumulated before the contact is not much different for two lines: the bulk of it is generated when the nuclei slow down and the motion becomes adiabatic. Important differences between the two types of calculations are seen at energies greater than critical for the contact: under these conditions, the memory effects reduce the dissipation of collective energy as compared with the frictional mechanism of the viscous approximation. In fact, the retardation effects in the considered model with the energy independent relaxation time parameter produce phenomena explained elsewhere as coming from the energy dependence of friction. Note that the temperature dependence of the friction parameter is claimed to be an important factor determining the fusion dynamics [24].

Consider the differences in the calculations of $E_{\rm stat}$ corresponding to the elastoplastic and viscous dynamics. Let us suppose that the statistical energy estimates made within the elastoplastic model are exact, and let us reproduce the same estimates within the viscous approximation using a renormalized excitation-energy-dependent friction parameter $\beta_{\rm eff}(E_{\rm in})$. The calculation presented in Fig. 2 shows that the difference in the two estimates of $E_{\rm stat}$ ($E_{\rm in}$) is small at $E_{\rm in} = 4$ MeV/nucl. and increases up to a factor of 3 when $E_{\rm in} = 7$ MeV/nucl. From Eq. (11), it follows that $E_{\rm stat}$ ($E_{\rm in}$), as found in the viscous approximation, is, roughly speaking, in an inverse proportion to the friction parameter $\beta$. Then, to reconcile the viscous and elastoplastic pictures, one must gradually increase $\beta_{\rm eff}(E_{\rm in})$ with increasing $E_{\rm in}$ by the same factor of 3 in this energy interval.

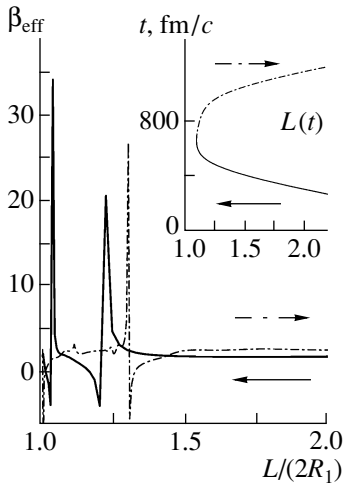


**Fig. 3.** An effective shape-dependent friction parameter $\beta_{\rm eff}(L) = -\pi/\dot{q}$ calculated for the case of scattering at $E_{\rm in} = 4$ MeV/nucl. The corresponding trajectory is shown in the upper right corner. The arrows indicate the time evolution. $\beta_{\rm eff}(L)$ is given in units of $(3/4)v_F/R_1$.

For any arbitrarily chosen trajectory the reconciliation of elasoplastic and viscous dynamics can be done by playing with the shape dependence of the friction parameter. Consider, e.g., the $L$-dependent effective friction parameter

$$\beta_{\rm eff}(L) = -\pi(L)/(dq/dt)_L,$$

where $\pi(L(t))$, $(dq/dt)_{L(t)}$, and $L(t)$ are parametrically defined by their dependence on the time following from the elastoplastic model. As argued before [see Eq. (9)], this quantity represents the action of friction force in the adiabatic regime.

Such an effective friction parameter for the trajectory corresponding to the scattering of two $^{100}$Mo nuclei at 4 MeV/nucl. incident energy is shown in Fig. 3. One sees that $\beta_{\rm eff}(L)$ experiences variations of about two orders of magnitude showing that the dynamics at the moment of collision is not at all adiabatic. At some values of $L$, it reaches much larger values than predicted by the wall formula and becomes negative at some other values of $L$ passing through zero. It is different for the incoming and outgoing parts of the trajectory, reflecting the findings of Wilczinski [8]. The strange behavior of $\beta_{\rm eff}(L)$ shown in this figure could be made in parallel with the very strange shape dependence of the friction parameter suggested in [6] as an optimal fit to a large amount of experimental data on fusion.

The dynamical effects in the collective energy dissipation are discussed in this paper within the model

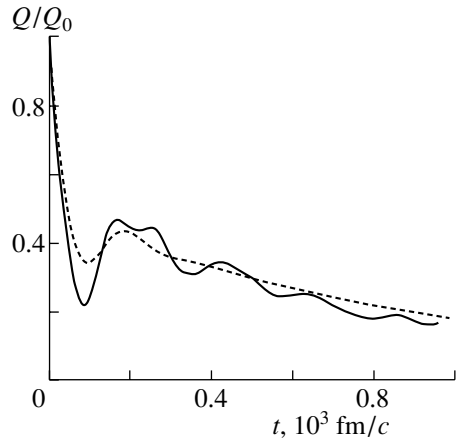


**Fig. 4.** Time dependence of mass quadrupole moment $Q(t)$ for two $^{58}$Ni nuclei after central collision at 6-MeV/nucl. incident energy. Solid curve corresponds to the test particle method; dashed curve corresponds to the elastoplastic model (see [4] for more details).

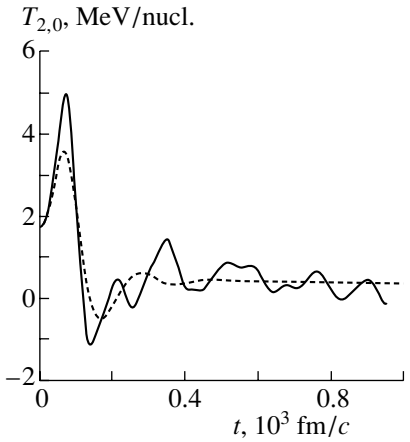


**Fig. 5.** Time dependence of the function $T_{2,0}$ for two $^{58}$Ni nuclei after central collision at 6-MeV/nucl. incident energy. Solid curve corresponds to the test particle method; dashed curve corresponds to the elastoplastic model.

that formally belongs to the transport theory approaches of nuclear dynamics. For casting them into the transport theory approach, an extension of collective space for the collective coordinate ($Z$) is crucial. The conjugated momentum (the quadrupole moment $\pi(t)$ in the distribution of nucleons over momenta) represents the Fermi surface deformation. One of the advantages of our theory is that it does not contain any ambiguity in the estimation of statistical excitation energy. Comparing the calculations done considering $\pi$ as a kinematically independent variable (elastoplastic regime) with calculations made in an approximation in which $\pi$ is considered as a function of state (viscous regime), we have found the following:

Only for slow collective motion is the viscous approximation good.

In this case, one arrives at the description of fusion in terms of a friction force whose strength is comparable with the wall-formula estimation.

In different cases, the viscous approximation becomes deficient.

It is a commonly used practice to treat the dynamical effects associated with the retardation in the action of dissipative forces on the nuclear shape by introducing the excitation energy and/or shape dependence of the friction force. In the examples given here, this technique turns out to be nothing but the simulation of more involved collective dynamics. We show that the name retarded friction is in a way misleading, standing behind a phenomenon combining the effects of elastic and dissipative forces.

Our model is very economic in the choice of parameters. Still, without any fitting procedure, we reproduce the Bass barrier in $^{100}$Mo + $^{100}$Mo collisions. The estimated lower bound of extra push energy (the energy excess needed to put the nuclei into contact) is equal to about half of its experimental value.

## 3. MEMORY EFFECTS IN THE COMPOSITE SYSTEM

The "history" of two $^{100}$Mo ions experiencing a head-on collision and forming a composite system is being studied within the model compatible with the one used to describe their approach and presented in the previous section. Although the end of this study is still far away, some important issues could tentatively be anticipated by recollecting the results of a somewhat more schematic description within the elastoplastic model of fusion of another pair of identical ions: that of two $^{58}$Ni nuclei [4, 13].

The description of two $^{58}$Ni fusion (following a head-on collision) starts in the quoted papers from the moment of their coming to contact. Their shape at this moment is supposed to be spherical. In view of findings reported in the previous section, this approximation does not seem to introduce large errors in our reasoning concerning the memory effects in dissipation. The shape of the composite system formed in the collision is restricted to a one-parametric family of lemniscatoids of rotation. Dynamical equations involve the quadrupole moment $Q$ and the $\lambda, \mu = 2, 0$ component of the pressure tensor integrated over the volume ($\Pi$). The Coulomb and surface potentials (ignoring the proximity contribution of nuclear forces) are used. The quality of such a description of fusion was controlled by comparing results with the results

of large-scale numerical calculations using the test-particle method for resolution of the kinetic equation [25].

Figure 4 shows the time dependence of $Q$ found in [4] by two methods: the solid line corresponds to the test-particle method, and the dashed line follows from the elastoplastic model. In Fig. 5, we show the function $T_{2,0} = (\Pi_{2,0} + K_{2,0})/2$, where $K_{2,0}$ is the component of the intrinsic kinetic energy tensor, again calculated with the two methods. The correspondence is good enough to give a confidence to the latter model.

What interests us here is the oscillatory pattern of curves at the beginning of unification of two ions giving way to a smooth decrease at larger time. Important also is the fact that the oscillations of $Q$ and $\Pi$ are out of phase: the peaks in one variable correspond to the valleys in the other. From our studies, it follows that this behavior does not change after varying the collision energy, the potential, effective mass, and other elements of the model (see, for example, [13]). The oscillatory time dependence of collective variables $Q$ and $\Pi$ means that the adiabatic collective energy contains an important contribution from the elastic forces associated with the Fermi surface deformation caused by the collision (see Eq. (10)). This contribution is nonnegative: from the out-of-phase oscillation pattern of $Q$ and $\Pi$, it follows that $\dot{Q} \cdot \Pi > 0$.

One may try to interpret this type of evolution in terms of effective friction as we did at the end of the previous section. The friction measuring the decrease in adiabatic collective energy within the adiabatic approach and reproducing the results of the elastoplastic model must contain a strong reduction of friction at the beginning of fusion. The reconciliation of two dynamics demands admission of negative values of "effective" friction (which is not physical). The reduction of friction is no longer needed to describe the following phase of fusion where no oscillation of collective observables is present and relation (7) is satisfied.

The foregoing discussion concerned one aspect of friction force, that of damping the collective motion. The friction can be discussed from the point of view of fluctuations also. In the introduction to this paper, we mentioned that accounting for fluctuations in adiabatic approaches meets a serious difficulty: for reasonably strong friction, they lead to an overestimation of the quasifission probability. A very important reduction of the fluctuation amplitude at the beginning of fusion is needed to overcome the difficulty.

The description of fluctuations in the elastoplastic approach does not present any formal difficulty but demands quite a lot of calculations. The method of treating fluctuations in the elastoplastic models and the results of its application are presented in [13]. From the quoted paper, one learns that the memory effects play an important role in the installation of the shape fluctuations: it turns out to be a long process. The shape fluctuations acquire their full strength corresponding to the dissipation-fluctuation theorem only when the shape of the composite system becomes spherical. Before this, the amplitude of shape fluctuations is smaller than that given by the equilibrium statistical mechanics prediction and their role in leading to quasifission is reduced. The first estimates of quasifission probability made within the elastoplastic approach without changing the relaxation time parameter led us to a satisfactory description of experimental results.

## 4. CONCLUDING REMARKS

It seems that much of the uncertainty in the understanding of nuclear dissipation lies in the fact that the friction, often discussed in the literature, is not a universally well-defined physical quantity. It is a commonly used practice to treat the dynamical effects associated with the retardation in the action on the nuclear shape of dissipative forces by introducing the excitation energy and/or shape dependence of the friction force. In the examples given here, this technique turns out to be nothing but a simulation of more involved collective dynamics. We show that the name retarded friction is in a way misleading, standing behind a phenomenon combining the effects of elastic and dissipative forces. The calculations presented before hint strongly that these uncertainties may be eliminated or at least largely reduced by including in the collective space the coordinates representing the distribution of nucleons in the momentum space. This allows one to account for the retardation effects in friction produced by the coupling between the geometrical and Fermi surfaces. Our paper shows that this can be done keeping intact the general structure and methods of currently used approaches to the nuclear reactions.

## ACKNOWLEDGMENTS

This work is based on the material obtained in a scientific collaboration of JINR with France and Italy. Part of the work was done in CSNSM–IN2P3 (Orsay, France) and in INFN–LNS (Catania, Italy). The scientific staff and the administration of these laboratories are gratefully acknowledged.

## REFERENCES


1. J. Wilczynski, Phys. Lett. B **47B**, 484 (1973).
2. D. J. Hinde *et al.*, Phys. Rev. C **45**, 1229 (1992).
3. P. Paul and M. Thoennessen, Annu. Rev. Nucl. Sci. **44**, 65 (1994).
4. I. N. Mikhailov, T. I. Mikhailova, M. Di Toro, *et al.*, Nucl. Phys. A **604**, 358 (1996).
5. R. Balescu, *Equilibrium and Nonequilibrium Statistical Mechanics* (Wiley, New York, 1975).
6. P. Fröbrich and I. I. Gontchar, Phys. Rep. **292** (3–4), 131 (1998).
7. D. Berdichevski, A. Lukasiak, W. Nörenberg, and P. Rozmej, Nucl. Phys. A **499**, 609 (1989).
8. J. Wilczinski, K. Sivek-Wilczinska, and H. W. Wilschut, Phys. Rev. C **54**, 325 (1996).
9. J. Blocki, Y. Boneh, J. R. Nix, and W. J. Swiatecki, Ann. Phys. (N. Y.) **113**, 330 (1978).
10. H. Hofmann, F. A. Ivanyuk, and S. Yamaji, Nucl. Phys. A **598**, 187 (1996).
11. F. A. Ivanyuk, H. Hofmann, V. V. Pashkevich, and S. Yamaji, Phys. Rev. C **55**, 1730 (1997).
12. I. N. Mikhailov, J. Libert, J. Piperova, and E. Kh. Yuldashbaeva, Nucl. Phys. A **574**, 593 (1994).
13. T. I. Mikhailova, I. N. Mikhailov, M. Di Toro, and G. Do Dang, Nucl. Phys. A **641**, 64 (1998).
14. I. N. Mikhailov, T. I. Mikhailova, I. V. Molodtsova, and M. Di Toro, Part. Nucl., Lett., No. 1 [110], 13 (2002).
15. I. N. Mikhailov, Part. Nucl. **31**, 838 (2000).
16. K. T. R. Davies and J. R. Nix, Phys. Rev. C **14**, 1977 (1976).
17. H. J. Krappe, J. R. Nix, and A. J. Sierk, Phys. Rev. C **20**, 992 (1979).
18. E. B. Balbutsev and I. N. Mikhailov, in *Collective Nuclear Dynamics,* Ed. by R. V. Jolos (Nauka, Leningrad, 1990), p. 3.
19. H. Goldstein, *Classical Mechanics* (Addison-Wesley, Reading, 1959), p. 21.
20. W. Nörenberg, Phys. Lett. B **104B**, 107 (1981).
21. P. Rozmej and W. Nörenberg, Phys. Lett. B **177**, 278 (1986).
22. A. B. Quint *et al.*, Z. Phys. A **346**, 119 (1993).
23. Y. Abe, S. Ayik, P. G. Reinhard, and E. Suraud, Phys. Rep. **275** (2–3), 49 (1996).
24. V. M. Kolomietz, V. A. Plujko, and S. Shlomo, Phys. Rev. C **52**, 2480 (1995).
25. P. Chomaz, M. Di Toro, and A. Smerzi, Nucl. Phys. A **563**, 509 (1993).

*Physics of Atomic Nuclei, Vol. 66, No. 9, 2003, pp. 1607–1614. From Yadernaya Fizika, Vol. 66, No. 9, 2003, pp. 1654–1661.*


# The Deformation and Orientation Effect on Reaction Cross Section with Deformed Targets*

**M. Y. Ismail, A. Y. Ellithi**, M. M. Osman, and M. M. Botros**

*Department of Physics, Faculty of Science, University of Cairo, Cairo, Egypt*

Received February 25, 2003

**Abstract**—The reaction cross section ($\sigma_R$) for a deformed target nucleus and spherical projectile is calculated using the optical-limit approximation of the Glauber–Sitenko theory. A method is presented to include both the density-dependent $NN$ interaction and the higher order deformations of the target nucleus in the collision process. We studied both the orientation and the deformation dependence of $\sigma_R$ within the energy range 30–900 MeV/$A$. We found that the orientation of the heavy target nucleus ($A \geq 120$) can produce a difference in the calculated $\sigma_R$ up to 30%. The averaged $\sigma_R$ over all directions of the symmetry axis of the deformed nucleus differs by less than 1% compared with $\sigma_R$ calculated for a spherical target with the same rms matter radius as the deformed nucleus. For certain orientation, it was found that $\sigma_R$ is highly dependent on the hexadecapole deformation. The orientation-averaged cross sections show almost no variation with either the sign or the value of the hexadecapole deformation. We compared the average cross section with the experimental data for several mass numbers; fair agreement is obtained.


## 1. INTRODUCTION

The total reaction cross section $\sigma_R$ is one of the most important physical quantities that characterizes a nuclear reaction; also it has a wide range of fundamental and practical applications. It is useful for gaining information about the nuclear size [1, 2] and the neutron and proton density distribution in nuclei [3]. The large increase in $\sigma_R$ for exotic nuclei poses a question as to its reasons [4]. There are also applications to the radiation effects in biology and designs of radiation shielding.

Neutron halo nuclei have also been studied by measuring the total reaction cross section induced by radioactive nuclear beams [5, 6]. The optical-limit approximation to the Glauber theory has been used to extract the rms matter radii of nuclei from the reaction cross section measurement [7]. For a deformed target or projectile nucleus, the reaction cross section is usually calculated using spherical density distributions, and the effects of deformation are then discussed, using a mean square radius formula for the deformed nucleus.

The first trial to take explicit account of the effects of target (or projectile) deformation in calculating the reaction cross section was done in [8]. The authors considered a projectile nucleus with the quadrupole deformation parameter $\delta_2$. They used the multipole expansion for the deformed nucleus density distribution together with the optical limit to Glauber theory to calculate the reaction cross section for the $^{12}C + {}^{17}N$ reaction. They found that the explicit treatment of the deformed structure leads to a reduction of 0.8% in the calculated cross section compared to the optical-limit (OL) calculations for a spherical projectile with the same rms matter radius. Variations corresponding to the largest and smallest cross section values are +7.2% and −5.6% of the corresponding spherical results, respectively, while their orientation angles for the largest one are $\theta = \pi/2$, $\phi = 0$ and for the smallest one are $\theta = \pi/2$, $\phi = \pi/2$.

This means that the reaction cross section calculated using the OL approximation is not sensitive to the quadrupole deformation except for the case when the projectile (or target) has a significant degree of alignment.

The aim of the present paper is to study the reaction cross section for different pairs of interacting nuclei where one of the two colliding nuclei is deformed. We study the orientation, deformation, energy, and mass number dependence of the reaction cross section. For this purpose, we developed the method considered in [8] for the calculation of reaction cross section when one of the two interacting nuclei is deformed. This development is done by introducing both density and energy dependence in the $NN$ cross section. The density will be considered a constant

*This article was submitted by the authors in English.

**e-mail: ali@mailer.eun.eg

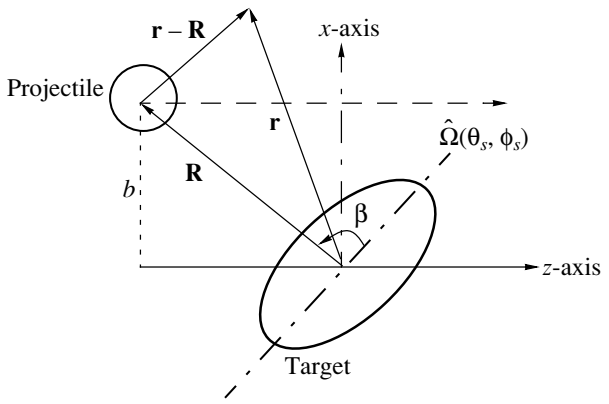


**Fig. 1.** The coordinate system, the centers of the projectile and target exist at $x$–$z$ plane.

value of 0.16 fm$^{-3}$, which is the normal nuclear matter density. We describe a method for calculating $\sigma_R$ for the deformed target (or projectile) nucleus.

## 2. THEORY

The reaction cross section $\sigma_R$ in the framework of the optical-limit approximation to the Glauber–Sitenko theory is written as

$$\sigma_R(\delta, \hat{\mathbf{\Omega}}_s) = 2\pi \int_0^\infty dbb[1 - T(b, \hat{\mathbf{\Omega}}_s)], \qquad (1)$$

where $\delta$ is the set of deformation parameters of the target nucleus and $\hat{\mathbf{\Omega}}_s$ denotes the direction of its symmetry axis with respect to coordinate system, shown in Fig. 1. $T$ is the transparency of the collision at impact parameter $b$, and it is given by

$$T(b, \hat{\mathbf{\Omega}}_s) = \exp[-\chi'(b, \hat{\mathbf{\Omega}}_s)], \qquad (2)$$

where

$$\chi'(b, \hat{\mathbf{\Omega}}_s) = \int_{-\infty}^{+\infty} dz \qquad (3)$$

$$\times \int d\mathbf{r}\rho_T(\mathbf{r}, \hat{\mathbf{\Omega}}_s)\rho_P(|\mathbf{r} - \mathbf{R}|)\sigma_{NN}\left(\rho_T + \rho_P, \frac{E_L}{A_P}\right);$$

$\rho_T$ and $\rho_P$ are the density distributions of the deformed target and the spherical projectile, respectively; $\mathbf{R}$ is the c.m. separation vector; and $E_L/A_P$ is the incident energy per projectile nucleon in the laboratory system. If the $NN$ cross section $\sigma_{NN}$ is density independent, or if it is evaluated at a constant value of $\rho = \rho_P + \rho_T$, then $\chi'$ could be factorized as

$$\chi'(b, \hat{\mathbf{\Omega}}_s) = \sigma_{NN}(E_L/A_P)\chi(b, \hat{\mathbf{\Omega}}_s), \qquad (4)$$

where the integration over $\mathbf{r}$ in $\chi(b, \hat{\mathbf{\Omega}}_s)$ is exactly the overlap integral of the two density distributions. To calculate $\chi(b, \hat{\mathbf{\Omega}}_s)$, we consider first the integral over $\mathbf{r}$

$$O(\mathbf{R}, \beta) = \int d\mathbf{r}\rho_T(\mathbf{r}, \hat{\mathbf{\Omega}}_s)\rho_P(|\mathbf{r} - \mathbf{R}|), \qquad (5)$$

where $\beta$ is the angle between the c.m. separation vector $\mathbf{R}$ and the direction of the symmetry axis $\hat{\mathbf{\Omega}}_s$. We assume the following Fermi shape (for $\rho_T$):

$$\rho_T(\mathbf{r}, \hat{\mathbf{\Omega}}_s) = \frac{\rho_0}{1 + \exp\left[\dfrac{r - R(\theta_1)}{a}\right]}, \qquad (6)$$

$$R(\theta_1) = R_0[1 + \delta_2 Y_{20}(\theta_1) + \delta_4 Y_{40}(\theta_1)], \qquad (7)$$

where $a$ is the diffuseness parameter of the density, $R_0$ is the radius parameter, $\delta_2$ and $\delta_4$ are the quadrupole and hexadecapole deformation parameters, and $\cos\theta_1 = \mathbf{r} \cdot \hat{\mathbf{\Omega}}_s$; then, we substitute

$$|\mathbf{r} - \mathbf{R}| = \sqrt{r^2 + R^2 - 2rR\cos\theta_{rR}} \qquad (8)$$

for the spherical projectile. One can easily calculate $O(\mathbf{R}, \beta)$ for every separation distance $R$ and every orientation angle $\beta$ of the deformed nucleus. It should be noted that the calculation of $O(\mathbf{R}, \beta)$ is similar to the calculation of the interaction potential between deformed nuclei, by using the multipole expansion method for $\rho_T$ [9]. Assuming the approximation of Eq. (4), one can write

$$\chi'(b, \hat{\mathbf{\Omega}}_s) = \sigma_{NN}\left(\frac{E_L}{A_P}, \rho\right) \int_{-\infty}^{\infty} dz O(\mathbf{R}, \beta). \qquad (9)$$

Thus, the method of evaluating $O(\mathbf{R}, \beta)$ is well known and has been used several times. By making the transformations

$$\beta = \cos^{-1}[(b\sin\theta_s\cos\phi_s + z\cos\theta_s)/R], \qquad (10)$$
$$R = \sqrt{b^2 + z^2},$$

one can perform integration with respect to $z$ in Eq. (9) to get $\chi'(b, \hat{\mathbf{\Omega}}_s)$. Introducing $\chi'$ into Eq. (2) and then Eq. (1) and performing the integration over the impact parameter $b$, one obtains the total reaction cross section $\sigma_R(\delta, \hat{\mathbf{\Omega}}_s)$ for specific orientation angles $\hat{\mathbf{\Omega}}_s \equiv (\theta_s, \phi_s)$ and for given deformation parameters $\delta_2$, $\delta_4$. The reaction cross section averaged over all orientations of the symmetry axis of the deformed target is given by

$$\sigma_R^{\text{av}}(\delta) = \frac{1}{4\pi}\int \sigma_R(\delta, \theta_s, \phi_s)d\Omega. \qquad (11)$$

In the present work, we consider the deformed target nuclei $^{238}$U, $^{154}$Sm, and $^{120}$Sn, which interact with spherical projectile nuclei $^{12}$C, $^{16}$O, $^{28}$Si,

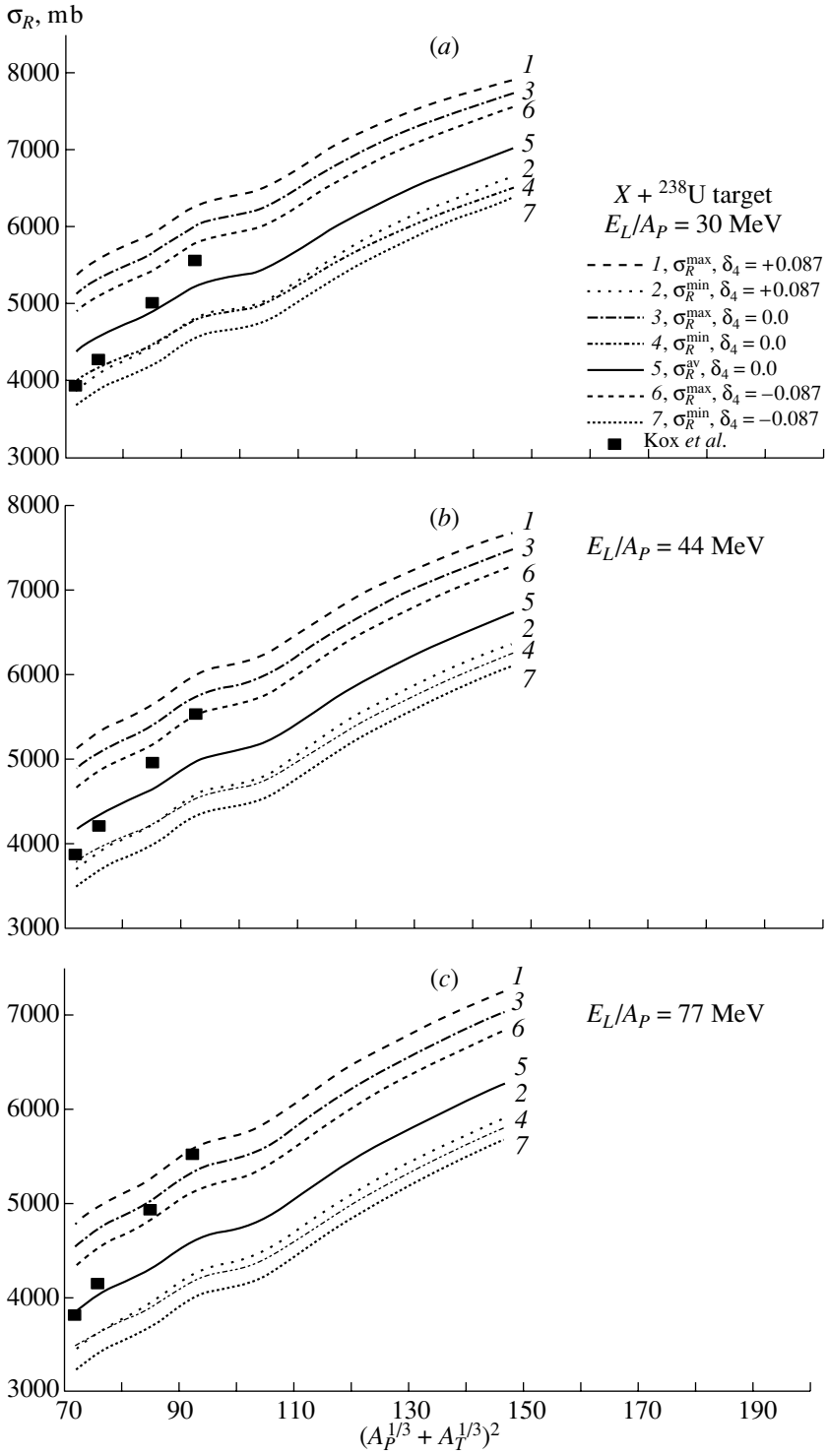


**Fig. 2.** The reaction cross section vs. the squared sum $(A_P^{1/3} + A_T^{1/3})^2$ for $^{238}$U target at projectile energy (*a*) 30, (*b*) 44, and (*c*) 77 MeV.

$^{40}$Ca, $^{60}$Ni, $^{90}$Zr, and $^{208}$Pb. For $^{238}$U, we take the density and deformation parameters as those in [9], namely, the quadrupole deformation parameter $\delta_2 = 0.261$; for $^{154}$Sm, $\delta_2 = 0.331$; and for $^{120}$Sn, $\delta_2 = 0.15$; and the hexadecapole deformation parameter $\delta_4 = 0.0, \pm 0.087$ for all targets.

For spherical nuclei, we assume the Fermi shape density distribution with parameters taken from [10].

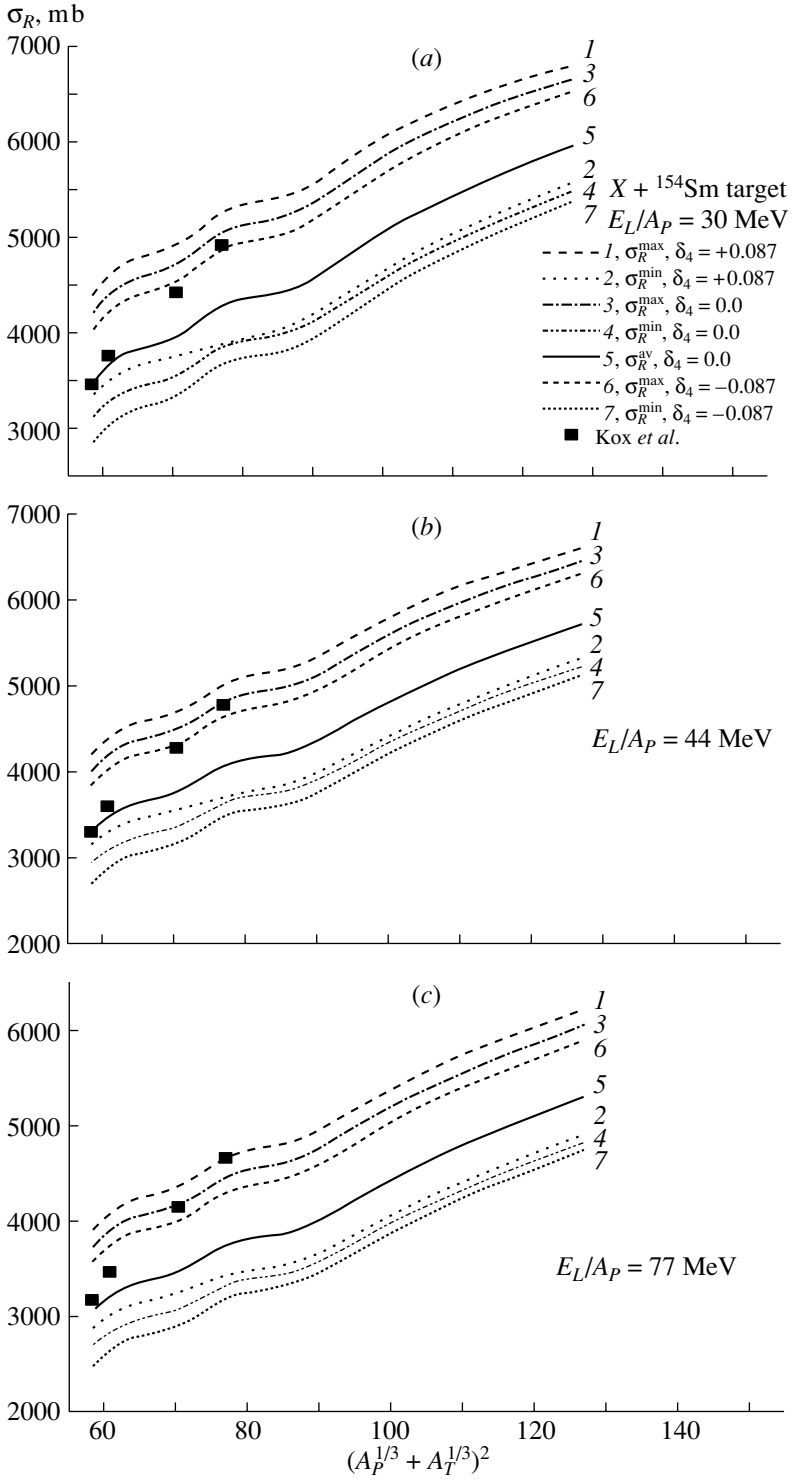


**Fig. 3.** The reaction cross section vs. the squared sum $(A_P^{1/3} + A_T^{1/3})^2$ for $^{154}$Sm target at projectile energy (*a*) 30, (*b*) 44, and (*c*) 77 MeV.

The in-medium $NN$ cross section used in the present work is that derived recently in [11], where the density was assumed to have a constant value $\rho = \rho_P + \rho_T = 0.16$ fm$^{-3}$.

## 3. RESULTS

We calculate the reaction cross section $\sigma_R$ for each projectile with certain energy and a target with specific deformation and different sets of orientations. We

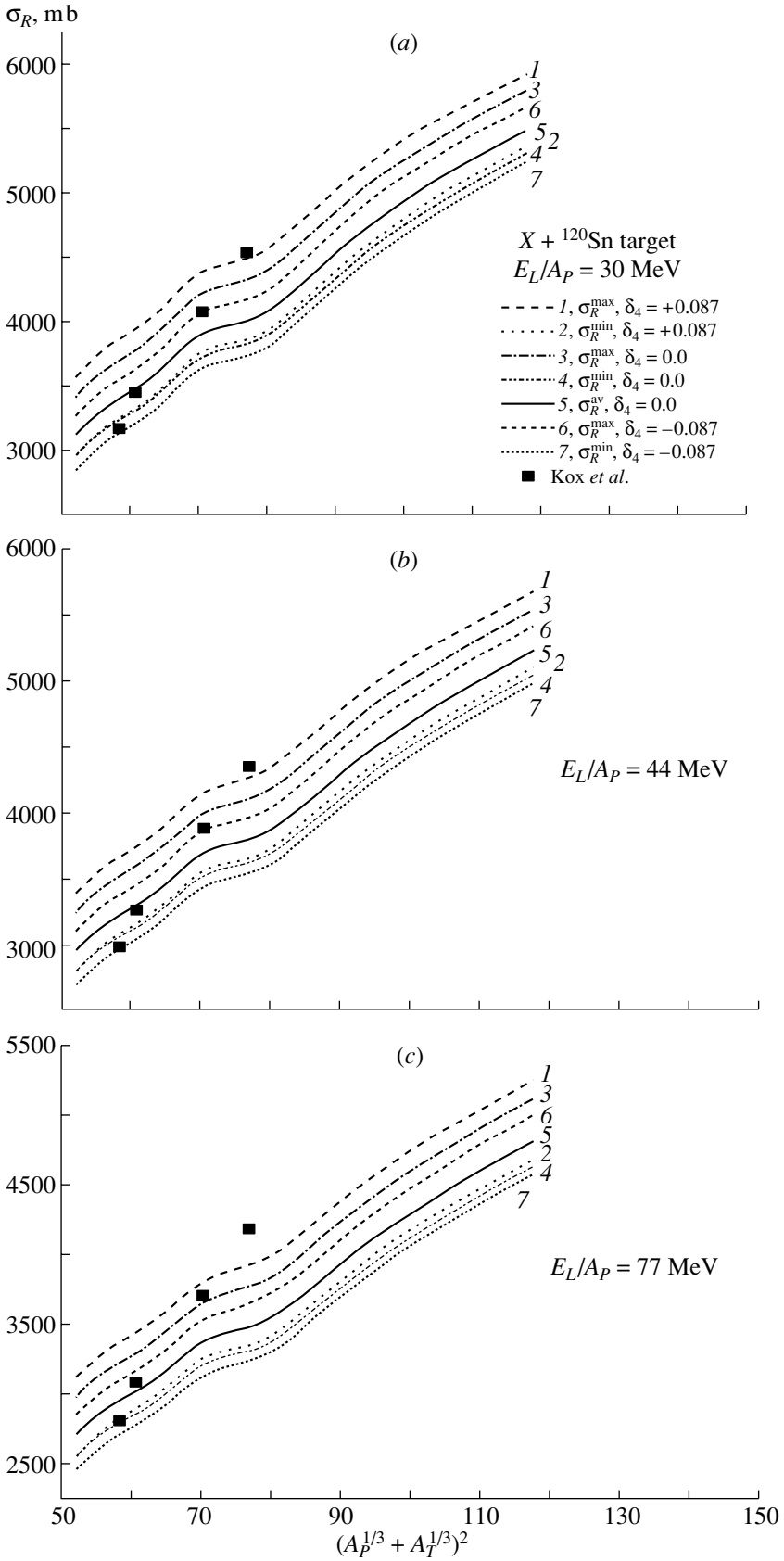


**Fig. 4.** The reaction cross section vs. the squared sum $(A_P^{1/3} + A_T^{1/3})^2$ for $^{120}$Sn target at projectile energy (*a*) 30, (*b*) 44, and (*c*) 77 MeV.

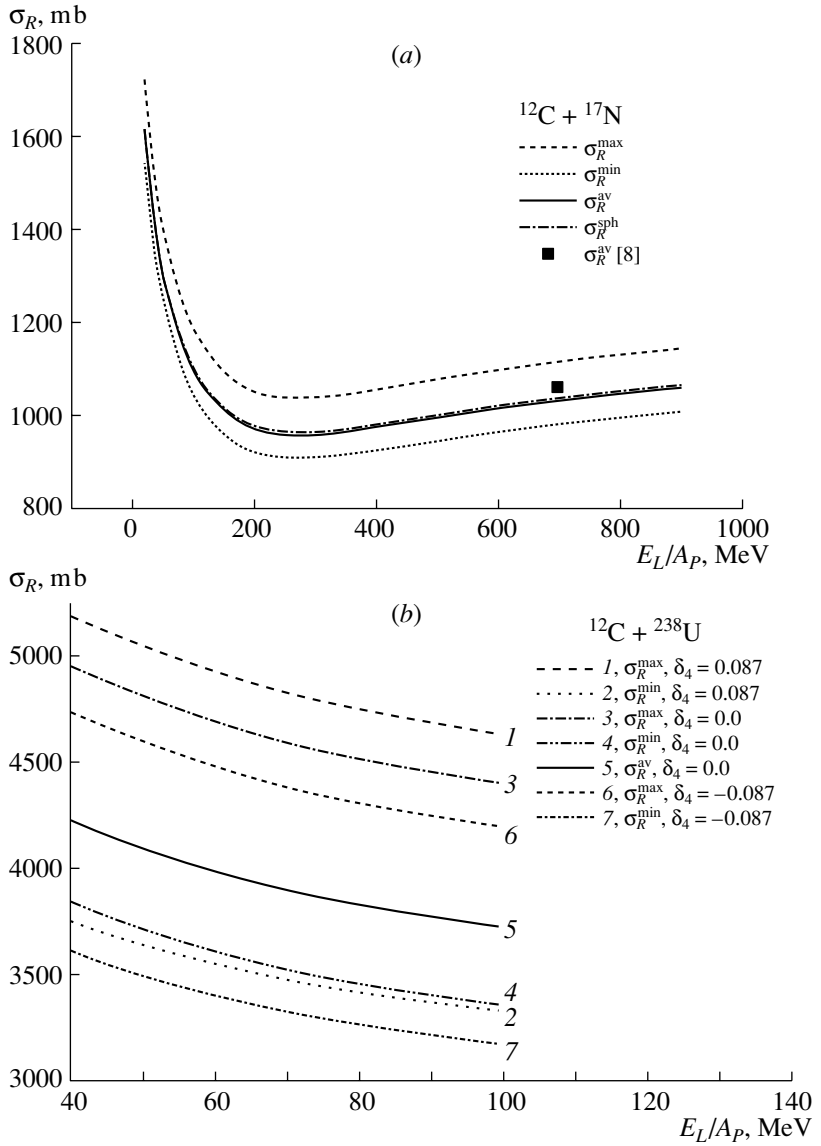


**Fig. 5.** The reaction cross section vs. the projectile energy of the reaction (*a*) $^{12}C + {}^{17}N$ and (*b*) $^{12}C + {}^{238}U$.

find the maximum value of the reaction cross section $\sigma_R^{\max}$ and the minimum value $\sigma_R^{\min}$ for each case. It was found in all cases that $\sigma_R^{\max}$ occurs at the orientation angles $\theta_s = \pi/2$, $\phi_s = 0$, and the minimum value $\sigma_R^{\min}$ occurs at $\theta_s = \pi/2$ and around $\phi = \pi/2$.

The variation of $\sigma_R$ with the square of the sum $(A_P^{1/3} + A_T^{1/3})^2$ for different spherical projectile nuclei with each target nucleus is studied. The extreme values $\sigma_R^{\min}$, $\sigma_R^{\max}$ and the average value $\sigma_R^{\text{av}}$ are shown in Figs. 2*a*, 2*b*, and 2*c* for $^{238}U$ target at projectile energies per nucleon of 30, 44, and 77 MeV. In Fig. 2*a*, the calculations are performed at a value of energy per projectile nucleon $E_L/A_P = 30$ MeV and the values of hexadecapole deformation parameter $\delta_4 = 0.0, \pm 0.087$. The difference between the maximum (which depends on the target orientation) and average cross sections may vary up to 22% (=1000 mb) of the average value for the lightest projectile, $^{12}C$, and decreases to 12% for the heaviest one, $^{208}Pb$, this for deformation parameter $\delta_4 = 0.087$. This difference decreases for $\delta_4 = 0.0$ and even more for $\delta_4 = -0.087$.

The difference between the minimum (which again depends on the target orientation) and the average values may decrease to 16 and 9% of the average value for the lightest and heaviest projectiles, respectively. The square dots represent the values of the reaction cross section calculated with the form parametrized by Kox *et al.* [12] with the neutron thickness correction, within the domain of

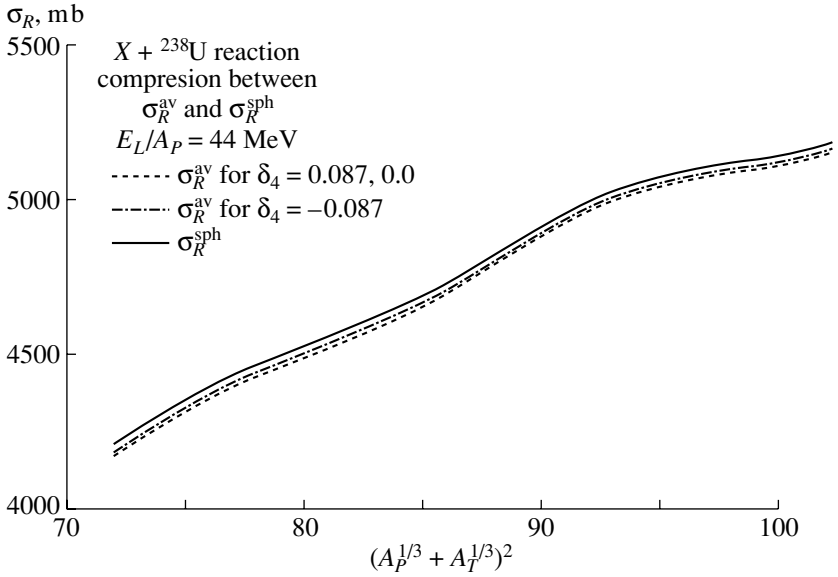


**Fig. 6.** The average reaction cross section vs. the squared sum $(A_P^{1/3} + A_T^{1/3})^2$ for $^{238}$U target and different projectiles for different values of the hexadecapole deformation parameter and the equivalent spherical target.

$(A_P^{1/3} + A_T^{1/3})^2 < 100$, to indicate how close our calculations are to the experimental value. Considering the error in the experimental or parametrized form within 10%, our calculations stay within such an error range. Figures 2*b* and 2*c* are the same as Fig. 2*a*, but for projectile energies of 44 and 77 MeV/$A$, respectively. The minimum (or maximum) difference decreases as the projectile energy per nucleon increases. Figures 3*a*–3*c* are the same as Figs. 2*a*–2*c*, but for $^{154}$Sm; and Figs. 4*a*–4*c*, for $^{120}$Sn. Clearly, the orientation significantly influences the value of the reaction cross section at different projectile masses and target deformations, the maximum or minimum values of the reaction cross section depending strongly on the value and sign of $\delta_4$.

The common feature of the set of curves in each figure (Figs. 2–4) is that they are approximately parallel lines, i.e., they have almost the same slope and almost the same behavior. This indicates that the differences between $\sigma_R^{\max}$ or $\sigma_R^{\min}$ and $\sigma_R^{\text{av}}$ at all values of $(A_P^{1/3} + A_T^{1/3})^2$ with a specific target remain almost constant over all the mass numbers of the projectiles considered. This constant difference depends mainly on the orientation of the target and does not depend on the projectile mass number. The calculations for the cases of $\delta_4 = \pm 0.087$ and the case of $\delta_4 = 0.0$ indicate that the percentage difference produced in $\sigma_R$ is slightly affected by switching on the hexadecapole deformation in all of Figs. 2–4. Moreover, the calculations show that the reaction cross section averaged over all orientations $\sigma_R^{\text{av}}$ is not sensitive to the value of $\delta_4$ or its sign (less than 1%), so their representative curves are expected to coincide and the curves for the average values are limited to that of $\delta_4 = 0.0$ for all of Figs. 2–4.

Figure 5*a* shows the energy variation of $\sigma_R^{\max}$, $\sigma_R^{\min}$, and $\sigma_R^{\text{av}}$ with the laboratory projectile energy per nucleon for $^{12}$C + $^{17}$N pair. It covers wide range of energies (30–900 MeV/$A$). The average value at 700 MeV/$A$ is compared with that of Christley *et al.* [8], and the difference is less than 1%. The curves show that the difference between extreme values $\sigma_R^{\max}$, $\sigma_R^{\min}$ increases with energy and the reaction cross section monotonically decreases until 300 MeV/$A$; then, the difference remains almost constant for higher energies. Figure 5*b* shows the reaction cross section variation with the same projectile but reacting with the heavier $^{238}$U target. The three values of $\delta_4$ for the $^{238}$U nucleus are considered. As Fig. 5*b* indicates, the cross section variation with energy is nearly the same for the three cases of $\delta_4 = \pm 0.087, 0.0$. The curves show that all the values of the cross section decrease according to the same trend as the energy per projectile nucleon increases. As the target mass increases for the case for $^{238}$U, the cross section values also increase.

To test the sensitivity of $\sigma_R^{\text{av}}$, which is averaged over all orientations of the deformed target nucleus, to its deformation parameters, we introduced the reaction cross section of the equivalent spherical target, $\sigma_R^{\text{sph}}$, whose mean square radius is equal to the mean square radius of the deformed target. The mean

square radius is

$$\langle R^2 \rangle = \frac{\int \rho(\mathbf{r}) r^2 d\mathbf{r}}{\int \rho(\mathbf{r}) d\mathbf{r}}.$$

The equivalent spherical target nucleus is assumed to have a density distribution of the form

$$\rho_s = \frac{\rho_0}{1 + \exp \dfrac{r - R_0^s}{a}},$$

where $\rho_0$ can be obtained from

$$\int \rho_s(r) d\mathbf{r} = A_T.$$

We assume that the spherical nucleus has the same diffuseness parameter $a$ as the deformed one, and we get $R_0^s$ from the condition

$$\langle R^2 \rangle_{\text{sph}} = \frac{\int \rho_s(r) r^2 d\mathbf{r}}{A_T} = \langle R^2 \rangle_{\text{def}}.$$

Figure 6 shows the average cross sections $\sigma_R^{\text{av}}$ at $E_L/A_P = 44$ MeV for $\delta_4 = +0.087,\ 0.0,\ -0.087$ and $\sigma_R^{\text{sph}}$ calculated for the equivalent spherical target nucleus for a limited range of projectile mass numbers (to enhance the small differences in the values of the cross sections). The figure indicates that the difference between $\sigma_R^{\text{av}}$ and $\sigma_R^{\text{sph}}$ is small for all $A_P$ values. The difference between $\sigma_R^{\text{av}}$ and $\sigma_R^{\text{sph}}$ is found to be from $0.3\%$ to less than $1.1\%$ in our calculations. This difference depends on the projectile and on the value of $\delta_4$, but it is weakly dependent on $E_L/A_P$.

## REFERENCES


1. W. Shen, B. Wang, J. Feng, *et al.*, Nucl. Phys. A **491**, 130 (1989).
2. T. Suzuki *et al.*, Nucl. Phys. A **630**, 661 (1998).
3. H. Kitagawa, N. Tajima, and H. Sagawa, Z. Phys. A **358**, 381 (1997).
4. J. Feng, W. Q. Shen, Y. G. Ma, and Z. Y. Zhu, Phys. Lett. B **305**, 9 (1993).
5. I. Tanihata *et al.*, Phys. Lett. B **206**, 592 (1988).
6. I. Tanihata, D. Hirata, T. Kobayashi, *et al.*, Phys. Lett. B **289**, 261 (1992).
7. S. K. Charagi and S. K. Gupta, Phys. Rev. C **41**, 1610 (1990).
8. J. A. Christley and J. A. Tostevin, Phys. Rev. C **59**, 2309 (1999).
9. M. J. Rhoades-Brown, V. E. Oberacker, M. Seiwerl, and W. Greiner, Z. Phys. A **310**, 287 (1983).
10. D. T. Khoa and G. R. Satchler, Nucl. Phys. A **668**, 3 (2000).
11. Cai Xiangzhow, F. Jum, S. Wenqing, *et al.*, Phys. Rev. C **58**, 572 (1998).
12. S. Kox, A. Gamp, C. Perrin, *et al.*, Phys. Rev. C **35**, 1678 (1987).

*Physics of Atomic Nuclei, Vol. 66, No. 9, 2003, pp. 1615–1617. From Yadernaya Fizika, Vol. 66, No. 9, 2003, pp. 1662–1664.*


# Total Reaction Cross Section from the Interaction of $^4$He Ions with $^{28}$Si at 10–30 MeV*

**M. K. Baktybaev[1)], A. Duisebaev[1)], B. A. Duisebaev[1)], K. M. Ismailov[1)], M. G. Itkis[2)], K. K. Kadyrzhanov[1)], R. Kalpakchieva[2)], I. V. Kuznetsov[2)**], K. A. Kuterbekov[1)], I. N. Kukhtina[2)], S. M. Lukyanov[1)], A. Mukhamedzhan[1)], Yu. E. Penionzhkevich[1)], B. M. Sadykov[1)], Yu. G. Sobolev[2)], and V. Yu. Ugryumov[2)]**

[1)] *Institute of Nuclear Physics, National Nuclear Center, Almaty, Kazakhstan*

[2)] *Joint Institute for Nuclear Research, Dubna, Moscow oblast, 141980 Russia*

Received August 28, 2002

**Abstract**—New results have been obtained for the energy dependence of the total reaction cross section $\sigma_R$ of $^4$He on $^{28}$Si in the energy range $E_\alpha \leq 30$ MeV. © *2003 MAIK "Nauka/Interperiodica".*

## 1. INTRODUCTION

The elastic scattering of $^4$He ions at bombarding energies $E_\alpha \leq 50$ MeV on target nuclei with $A \leq 50$ has a characteristic feature—an unusually large value of the cross section for scattering at large angles [1]. A consistent description of the experimental data in the considered energy and target-mass regions using the standard optical model with a Woods–Saxon type of potential, as is well known, is not possible. It has been shown in [2] that, using a potential of molecular type or a "quadratic" Woods–Saxon one, it is possible to describe the experimental data in the low-energy region.

It is supposed that of great help in choosing one or another potential might be the experimental results on inelastic reactions, in particular, the data on total reaction cross sections. The total reaction cross section ($\sigma_R$) is one of the fundamental observables characterizing a nuclear collision since it determines the imaginary part of the potential. The measurement of $\sigma_R$ can help in resolving some uncertainties in the parameters of the interaction potential, for which reason it is also considered complimentary to elastic-scattering experiments. However, direct measurements of $\sigma_R$ for $^4$He in the energy range $E_\alpha \leq 50$ MeV are rather scarce [3–5]. Moreover, it is quite difficult to find experiments in which both elastic scattering and $\sigma_R$ have been measured on the same target at the same energy.

In the present work, we report on measurements of $\sigma_R$ in the $^4$He + $^{28}$Si reaction in the energy region $E_\alpha \leq 30$ MeV. The reason for this is that data on elastic scattering are available [6, 7] and it is comparatively easy to perform total reaction cross section measurements on a $^{28}$Si target.

## 2. EXPERIMENTAL METHOD

The experiments were performed at the isochronous cyclotron U-150M (INP, Almaty) at energy $E_\alpha = 29.3$ MeV and intensity of 10 nA. The total reaction cross section was measured using a multilayer semiconductor telescope as described in [8]. The detectors of the telescope, in addition to registration of the reaction products, simultaneously played the role of active targets and energy degraders. The counting rate due to the $^4$He ions should not exceed about $(3–5) \times 10^3$ pps. For this reason, $^4$He ions elastically scattered at 40° on a $^{208}$Pb target (2.3 mg/cm$^2$ thick) were used in the experiments. The telescope $dE_1$–$dE_2$–$E$, consisting of 63-, 115-, and 450-$\mu$m-thick Si detectors, was mounted on a rotatable platform, the angle of which with respect to the beam direction was remotely controlled. In front of the telescope, a collimator ($\varnothing = 4$ mm and $l = 15$ mm) with additional aluminium foils to lower the initial beam energy was installed.

A schematic view of the setup and data acquisition system is presented in Fig. 1. The first $dE_1$ detector gives the start signal for the data acquisition. The signals from the charge-sensitive preamplifier (PA) are divided between the energy and the time section of the electronic system and are then amplified by a spectrometric amplifier (AFA) and by a fast amplifier (TFA), respectively. The signal formed by the

*This article was submitted by the authors in English.

**e-mail: kuzn@nrsun.jinr.ru

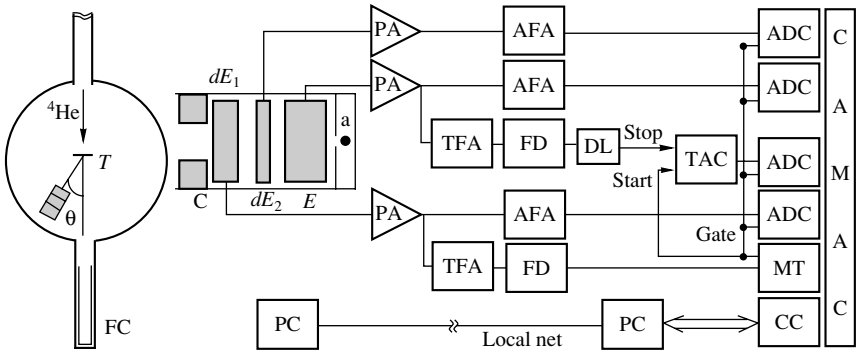


**Fig. 1.** A schematic view of the setup and the data acquisition system.

TFA then enters the discriminator (FD), whose time-reference logical signal is sent to the input of the master trigger (MT) of the acquisition system. As soon as a signal from the FD comes to the open input of the MT (i.e., when the previous event has been completely analyzed), the latter closes and provides the necessary signals defined in a duration and time-delay gate allowing the analog-to-digital convertors (ADCs) to open and also start signals for the time-to-amplitude converter (TAC). The output signal from the MT produces a LAM signal on the CAMAC bus with a time delay equal to the digitization time of the ADCs. After the LAM signal, all information from the CAMAC system is read out, after which the MT input is opened to take the signal created by the next event.

An example of the measured two-dimentional plots is shown in Fig. 2, from where one can see that it is mainly the $^4$He ions that enter the telescope. The cross section was deduced in the following way.

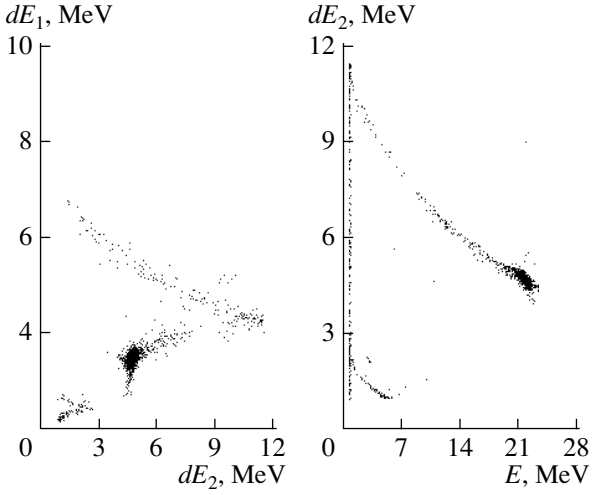


**Fig. 2.** Two-dimentional identification plots showing the energy release of $^4$He in the different detectors used to separate the number of reaction products from elastic scattering events.

Narrow gates were drawn on the energy spectra $dE_1$ and $dE_2$ to include only those events that correspond to the energy loss of $^4$He ions which have not undergone nuclear interactions in these two detectors. In this case, in the third detector, only events of lower energy are observed. The ratio of these events and the total number of events defines the probability of the nuclear reaction induced by the $^4$He ions in the third detector. Knowing the energy of the $^4$He ions entering $E$ (thereby, their range), it is easy to estimate the average total energy in the third detector.

Another approach in determining $\sigma_R$ consists in defining very narrow energy and timing gates on the first $dE_1$ detector; hence, the two-dimensional plot $dE_2$–$E$ allowed separating the events due to reac-

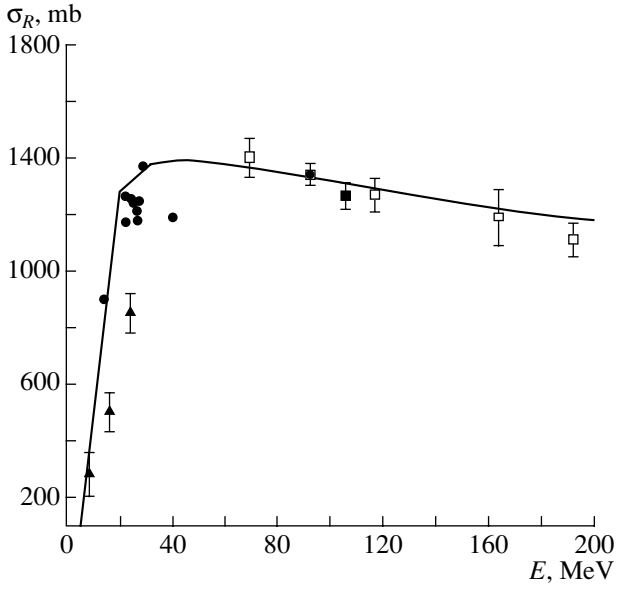


**Fig. 3.** Total reaction cross sections, $\sigma_R$, for the $^4$He + $^{28}$Si reaction: (▲) present work; (□, ■) at higher energies [9, 10]; (●) deduced from $^4$He elastic scattering on $^{28}$Si [6]. The solid curve shows the calculations of $\sigma_R$ based on the double-folding model [11].

tions in the second and third detectors. The thickness of the second detector is well known, the total number of $^4$He ions entering the telescope is measured, and $\sigma_R$ in the second detector is thus easily determined.

## 3. EXPERIMENTAL RESULTS AND DISCUSSION

The $\sigma_R$ values for the $^4\mathrm{He} + {}^{28}\mathrm{Si}$ reaction obtained in the present work at three values of the bombarding energy are presented in Fig. 3 as triangles. The results of direct measurements of $\sigma_R$ carried out at higher energies [9, 10] are shown by open and solid squares. The values of $\sigma_R$ denoted by solid dots have been deduced in [6] in the analysis of $^4$He elastic scattering differential cross sections on $^{28}$Si. The solid curve shows the calculations of $\sigma_R$ based on the double-folding model [11] on the condition of best fit of the $\sigma_R$ data at high energies. As is seen from Fig. 3, in the studied energy range 10–30 MeV, the experimental values of $\sigma_R$ differ noticeably from the theoretical predictions. One possible explanation is that scattering via a compound nucleus formation contributes at low energies and this leads to a decrease in $\sigma_R$.

Obviously, new measurements simultaneously of $\sigma_{\mathrm{el}}$ and $\sigma_R$ and their theoretical analysis are necessary in the energy range 10–80 MeV.

## ACKNOWLEDGMENTS

This work has been performed with partial support from the Russian Foundation for Basic Research (project nos. 01-02-22001 and 0001 00617).

## REFERENCES

1. K. A. Gridnev and A. A. Ogloblin, Fiz. Élem. Chastits At. Yadra **6**, 393 (1975) [Sov. J. Part. Nucl. **6**, 158 (1975)].
2. A. S. Tarig *et al.*, Phys. Rev. C **59**, 2558 (1999).
3. G. Igo and B. D. Wilkins, Phys. Rev. **131**, 1251 (1963).
4. L.V. Dubar *et al.*, Preprint KINR-75-3 (Kiev, 1975).
5. R. E. Warner *et al.*, Phys. Rev. C **40**, 2473 (1989).
6. P. Manngard *et al.*, Nucl. Phys. A **504**, 130 (1989).
7. S. Roy *et al.*, Phys. Rev. C **45**, 2904 (1992).
8. I. V. Kuznetsov *et al.*, Izv. RAN, Ser. Fiz. **63**, 13 (1999).
9. I. V. Kuznetsov *et al.*, Yad. Fiz. **65**, 1609 (2002) [Phys. At. Nucl. **65**, 1569 (2002)].
10. A. Ingemarsson, J. Nyberg, P. U. Renberg, *et al.*, Nucl. Phys. A **676**, 3 (2000).
11. O. M. Knyazkov *et al.*, Fiz. Élem. Chastits At. Yadra **30**, 870 (1999) [Phys. Part. Nucl. **30**, 369 (1999)].

*Physics of Atomic Nuclei, Vol. 66, No. 9, 2003, pp. 1618–1621. From Yadernaya Fizika, Vol. 66, No. 9, 2003, pp. 1665–1668.*


# The Present State of Cluster Radioactivity Research*

**S. P. Tretyakova[1)], A. A. Ogloblin[2)], and G. A. Pik-Pichak[2)]**

[1)] *Flerov Laboratory of Nuclear Reactions, Joint Institute for Nuclear Research, Dubna, Moscow oblast, 141980 Russia*

[2)] *Russian Research Centre Kurchatov Institute, pl. Kurchatova 1, Moscow, 123182 Russia*

Received August 28, 2002

**Abstract**—Complete mass distributions of the energetically allowed decays of nuclei with $A > 112$ were calculated including the known regions of cluster radioactivity and cold fission. These processes represent different branches of the more general family of cold decays. A short review of the current experimental situation is given. The existing data indicate that the transition between the sudden ($\alpha$-decay-like) and adiabatic (fission-like) mechanisms of the fragments formation takes place at the fragments mass values $A \sim 35$–$40$. The study of elastic scattering or fusion–fission reaction of the decay products could serve as a sensitive tool for investigation of the decay mechanism. Some new experiments to be carried out and planned are listed. © *2003 MAIK "Nauka/Interperiodica".*

The term "cluster radioactivity" (CR) is applied to spontaneous emission of light fragments (clusters) heavier than an $\alpha$ particle. Up to now, 19 nuclides from $^{221}$Fr to $^{242}$Cm emitting light nuclei from $^{14}$C to $^{34}$Si have been discovered. The heavy counterparts are grouped in the vicinity of the double magic $^{208}$Pb nucleus, which allows one to consider the known domain of CR as lead radioactivity.

There remain many open problems in the study of this phenomenon, among which the most important are the following ones:

Which domains of CR different from the lead one can exist?

What is the connection between CR and cold fission?

Which nuclear properties (shell effects, deformations, etc.) define the probabilities of cold processes?

What is the mechanism of cluster emission: is it $\alpha$-decay-like (sudden, nonadiabatic) or fission-like (adiabatic)?

In order to get a general view of the problem, we calculated complete mass distributions of a number of cold decays (ground to ground transitions) of nuclei with $A > 112$ using the model [1]. As an example, the calculated mass spectrum of $^{234}$U is shown in Fig. 1. Besides emission of nuclei $^{24,25}$Ne and $^{28}$Mg observed experimentally, a broad group at $A \sim 80$–$110$ is present in the theoretical mass distribution with comparable intensity. One part of it is connected with the formation of fragments with $Z$ and $N$ close to the double magic numbers $Z = 50$ and $N = 82$ (e.g., the decay to $^{100}$Zr + $^{134}$Te) and could be identified as tin CR. In the other part of the spectrum, strongly deformed fragments are seen (say, $^{82}$Ge + $^{152}$Nd). The $^{48}$Ca peak and symmetric decays also exist. To check the model in the region of heavy fragments, we constructed quasiexperimental $^{234}$U cold fission data. This was done by the normalization of the induced cold fission mass spectrum [2] to $T_{1/2}$ of spontaneous fission. The agreement is strikingly good.

The conclusion of our study is that the phenomenon called CR today is not distinguished from the other modes either by nature of its origin or by its probability. One can speak about lead, tin, and calcium CRs depending on the vicinity of $Z$ and $N$ values to the corresponding magic numbers. The most widespread CR (but practically undetectable) is the tin one due to the fact that the ratio 82/50 is close to the average $N/Z$ ratio of decaying parent nuclei (this provides on average the maximum $Q$ values).

Another source of enhancement of the decay probability is the formation of fragments having prolate static deformations. Orientation of the big axis along the direction of movement results in lowering of the Coulomb barrier and diminishing the path under it. The part of mass spectra attributed to cold fission usually is a combination of tin and deformation activities.

Although there is no fundamental difference between cold fission and diverse types of CR, the dynamics of fragment formation in various parts of mass distributions can be not the same. Two extreme mechanisms are known: (i) adiabatic (fission-like)

*This article was submitted by the authors in English.

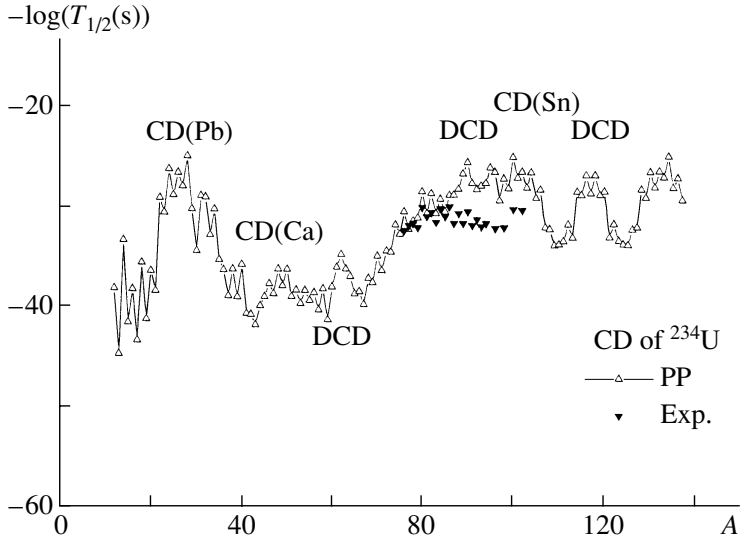


**Fig. 1.** Mass distribution of cold decays of $^{234}$U. Calculations were done using the Pik-Pichak model [1]. Only the light fragment part is shown with the prolongation of about 20 mass units to the region of the corresponding heavy partners.

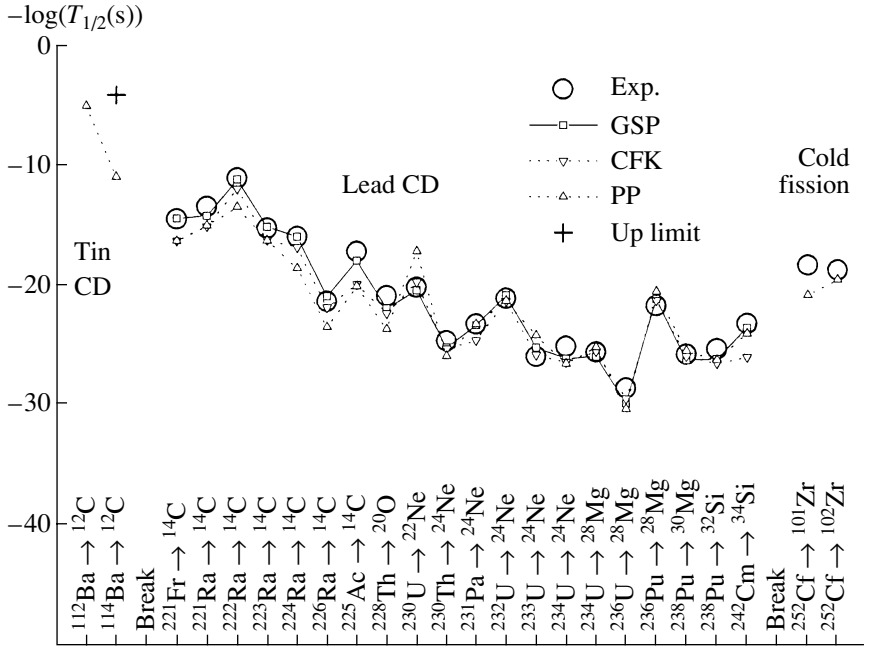


**Fig. 2.** Cluster decay probabilities. Experimental data are marked by ○; □, ▽, and △ are predictions of the models by Greiner–Sandulesku–Poenaru [8], Chuvilski–Furman–Kadmenskii [9], and Pik-Pichak [1], respectively.

and (ii) nonadiabatic or cluster ($\alpha$-decay-like). Obviously, each of them can contribute to the lead CR under study.

During the last few years, the following decays were observed: $^{230}\mathrm{U} \rightarrow {}^{22}\mathrm{Ne} + {}^{208}\mathrm{Pb}$ [3, 4], $^{242}\mathrm{Cm} \rightarrow {}^{34}\mathrm{Si} + {}^{208}\mathrm{Pb}$ [5], and cold fission of $^{252}$Cf [6]; the search for the new domain of cluster emitters near the double magic $^{100}$Sn was undertaken, and the upper limit of $^{114}\mathrm{Ba} \rightarrow {}^{12}\mathrm{C} + {}^{102}\mathrm{Sn}$ decay was established [7]. The solid-state track detector method was used in all experiments except for [6] due to its unprecedented sensitivity and high background rejection capability.

The current experimental data are summarized in Fig. 2. The probabilities of all known decays are shown as a function of the emitted fragment masses. Comparison of the data with the predictions of three models (phenomenological fission-like [8], semimicroscopic fission-like [1], and microscopic $\alpha$-decay-

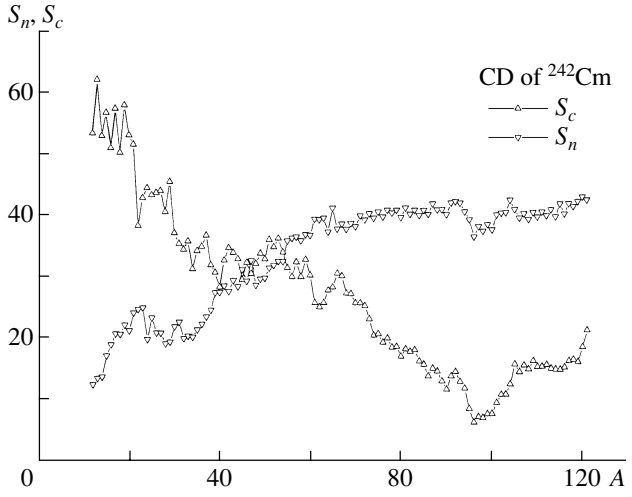


**Fig. 3.** The actions for passing the inner ($S_n$) and outer ($S_c$) barriers of $^{242}$Cm as functions of the emitted fragment masses.

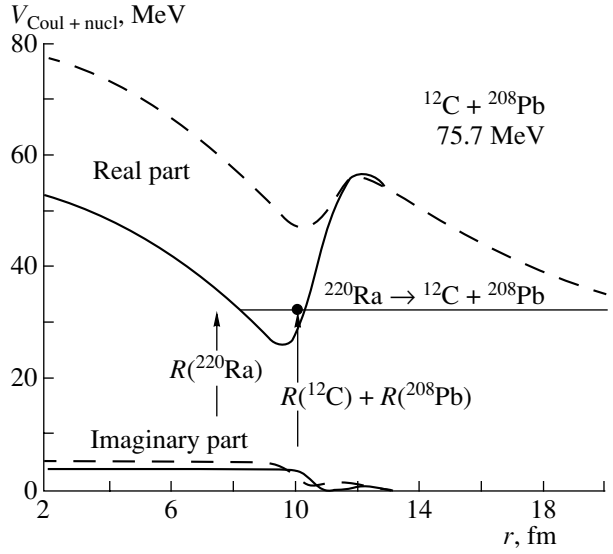


**Fig. 4.** Optical model potentials obtained from $^{12}$C + $^{208}$Pb elastic scattering at $E = 75.7$ MeV [15].

like [9]) is presented. Although the physical grounds of all three models differ very strongly, their predictions are very similar, and they reproduce the data with accuracy of 1–2 orders of magnitude in the domain of lead CR. However, in the region of tin ($Z \cong N \cong 50$) CR, the model [9] predicts $^{114}\text{Ba} \rightarrow {}^{12}\text{C} + {}^{102}\text{Sn}$ decay probability to be ~7 orders of magnitude larger than [1]. On the other hand, the nonadiabatic models (e.g., [10]) predict probabilities several tens of orders of magnitude lower than the adiabatic ones in the region of cold fission. The fission-like models reproduce the existing cold fission data ($^{252}$Cf [6]) very well (see also Fig. 1 for $^{234}$U). The very fact of experimental observation of cold fission means that the $\alpha$-decay-like mechanism is not valid in the corresponding part of the mass distribution.

As to the emission of the lightest fragments, there are serious arguments in favor of a sudden, nonadiabatic mechanism. The first one comes from the fact that the ground-state transition in $^{223}\text{Ra} \rightarrow {}^{14}\text{C} + {}^{209}\text{Pb}$ decay is strongly hindered [11] by the nuclear structure factors, which are not taken into account by fission-like models. Another argument is connected with the validity of the Geiger–Nuttol law for cluster decays [12]. Its correctness means that the decay probability can be factorized into the penetrability of the Coulomb (external) part of the barrier and the preformation (spectroscopic) factor determined by the distances between the straight lines of the different fragment masses.

The first significant deviation from Geiger–Nuttol law was observed for $^{242}\text{Cm} \rightarrow {}^{34}\text{Si} + {}^{208}\text{Pb}$ decay [5]. The preformation probability turned out to be much larger than one could expect from the systematics. The conclusion was made [12] that the transition between the sudden and adiabatic mechanisms really exists and begins for fragments with $A \sim 35$. The change in the decay mechanism can also be explained in the framework of fission-like models. Using [1], we calculated the action for passing the internal and external parts of the barrier by fragments of different masses (Fig. 3). For the light emitting fragments, the main contribution to the action comes from the external part of the barrier, and this explains the validity of the Geiger–Nuttol law for this mass region. The contribution of the internal part becomes equal at $A \sim 40$ and dominates at $A > 60$. This result is in agreement with [13], where penetrabilities of both parts of the barrier were calculated.

As both products of cluster decay are formed in their ground states, the interaction between them (elastic scattering or fusion) can be considered as some kind of inverse processes, which could give in favorable circumstances some independent information about the shape of the barrier [14]. If so, some selection among the theoretical models giving similar penetrabilities and different barriers could be done.

It was shown in the study of $^{12}\text{C} + {}^{208}\text{Pb}$ scattering at 75.7 MeV [15] that the experimental data are sensitive to the internal part of the barrier if some deviation from the exponential falloff of the Fresnel diffraction cross section is observed at extremely large angles. A similar sensitivity was demonstrated in the study of deep subbarrier fusion–fission $^{12}\text{C} + {}^{208}\text{Pb}$ and $^{16}\text{O} + {}^{208}\text{Pb}$ [16]. At the present time, there are only two cases for which the barriers extracted

from the inverse processes can be directly compared with the measured cluster decay probabilities: $^{222}Ra \rightarrow {}^{14}C + {}^{208}Pb$ and $^{230}U \rightarrow {}^{22}Ne + {}^{208}Pb$.

An especially interesting finding [14] was that the sum of nuclear and Coulomb potentials in both systems form a pocket at a distance close to the sum of the $^{12}C$, $^{16}O + {}^{208}Pb$ radii (Fig. 4). The decay energy of $^{220}Ra \rightarrow {}^{12}C + {}^{208}Pb$ slightly exceeds the minimum of the pocket. Thus, the conditions required for the formation of the exotic quasimolecular state are fulfilled (see [14] for details). The possibility for the actinide nuclei to have quasimolecular states based on a $^{208}Pb$ core was discussed in the literature (e.g., [17]).

A few new experiments are being carried out or are under discussion and preparation:

Search for the decay $^{241}Am \rightarrow {}^{34}Si$ (Kurchatov Inst.–JINR);

Search for the decay $^{238}U \rightarrow {}^{34}Si$ (Milano Univ.–JINR);

Search for the decays $^{223}Ac \rightarrow {}^{14}C, {}^{15}N$ (Kurchatov Inst.–JINR);

Search for the decay $^{112}Ba \rightarrow {}^{12}C$ (Kurchatov Inst.–JINR);

Study of elastic scattering and fusion–fission in the systems $^{14}C, {}^{15}N + {}^{208}Pb$ and $^{22}Ne + {}^{208}Pb$ (Kurchatov Inst.–JINR–Jyväskylä Univ.–Florida State Univ.).

## ACKNOWLEDGMENTS

We are grateful to R. Bonetti, Yu.M. Chuvilski, V.M. Furman, F. Goennenwein, R. Julin, M. Leino, V.M. Mikheev, Yu.T. Oganessian, V.A. Shigin, S. Tabor, and W. Trzaska for fruitful discussions.

This work was partly supported by the Russian Foundation for Basic Research (project nos. 17386 and 02-02-17297) and NATO (project no. 93440).

## REFERENCES

1. G. A. Pik-Pichak, Yad. Fiz. **44**, 1421 (1986) [Sov. J. Nucl. Phys. **44**, 923 (1986)].
2. W. Schwab *et al.*, Nucl. Phys. A **577**, 674 (1994).
3. Qiang-yan Pan *et al.*, Chin. Phys. Lett. **16**, 251 (1999).
4. R. Bonetti *et al.,* Nucl. Phys. A **686**, 64 (2001).
5. A. A. Ogloblin *et al.,* Phys. Rev. C **61**, 034301 (2000).
6. M. Croni *et al.*, in *Proceedings of the International Conference "Fission and Properties of Neutron-Rich Nuclei," Sanibel Insland, Florida, 1997,* Ed. by J. Hamilton and A. Ramayya (World Sci., Singapore, 1998), p. 109.
7. A. Guglielmetti *et al.*, Phys. Rev. C **56**, 2912 (1997).
8. D. N. Poenaru *et al.*, At. Data Nucl. Data Tables **48**, 231 (1991).
9. S. G. Kadmenskii, S. D. Kurgalin, *et al.*, Yad. Fiz. **57**, 1981 (1994) [Phys. At. Nucl. **57**, 1905 (1994)].
10. R. Blendowske and H. Walliser, Phys. Rev. Lett. **61**, 1930 (1988).
11. L. Brillard *et al.*, C. R. Acad. Sci. (Paris), Ser. II **309**, 1105 (1989).
12. A. A. Ogloblin *et al.*, in *Proceedings of the International Conference "Nuclear Shells—50 Years," Dubna, 1999,* Ed. by Yu. Ts. Oganessian and R. Kalpakchieva (World Sci., Singapore, 2000), p. 124.
13. D. N. Poenaru, in *Proceedings of the International Conference on Nuclear Reaction Mechanisms, Varenna, Italy, 1999,* p. 348.
14. A. A. Ogloblin and S. P. Tretyakova, in *Proceedings of the International Workshop on Physics of Isomers, St. Petersburg, 2000,* Ed. by F. F. Karpeshin *et al.* (VNIIÉF, Sarov, 2001), p. 122.
15. V. P. Rudakov *et al.*, Izv. Akad. Nauk, Ser. Fiz. **65**, 637 (2001).
16. S. P. Tretyakova *et al.*, in *Proceedings of the International Conference "Nuclear Shells—50 Years," Dubna, 1999,* Ed. by Yu. Ts. Oganessian and R. Kalpakchieva (World Sci., Singapore, 2000), p. 154.
17. B. Buck and A. C. Merchant, Phys. Rev. C **39**, 2097 (1989).

*Physics of Atomic Nuclei, Vol. 66, No. 9, 2003, pp. 1622–1625. From Yadernaya Fizika, Vol. 66, No. 9, 2003, pp. 1669–1672.*


# Dynamical Model of Fission Fragment Angular Distributions*

**V. A. Drozdov[1], D. O. Eremenko[1]**, O. V. Fotina[1], S. Yu. Platonov[1], O. A. Yuminov[1], and G. Giardina[2]**

[1] *Institute of Nuclear Physics, Moscow State University, Moscow, 119992 Russia*

[2] *Dipartamento di Fisica dell' Universita, Messina, Italy*

Received August 28, 2002

**Abstract**—A dynamical model of fission fragment angular distributions is developed. The experimental data on the angular anisotropy of fission fragments is analyzed for the $^{16}O + ^{208}Pb$, $^{232}Th$, $^{238}U$, and $^{248}Cm$ reactions at energies of the incident $^{16}O$ ions ranging from 90 to 160 MeV. This analysis allows us to extract the relaxation time for the tilting mode. It was also demonstrated that the angular distributions are sensitive to the deformation dependence of the nuclear friction. © *2003 MAIK "Nauka/Interperiodica".*

One of the most interesting problems of nuclear physics is the time scale of equilibrating various degrees of freedom in excited nuclei. This work focuses on the angular momentum degrees of freedom and specifically on the tilting mode associated with the orientation of the symmetry axis of a fissioning nucleus relative to the total angular momentum ($J$). This mode controls the angular distributions (AD) [1] and spins of fission fragments [2]. Usually these observables are described within the statistical model of the transition states [1, 2]. There exist two versions of the model, which identify the transition states with either the saddle point or the scission point of the fission barrier. Correspondingly, these models are based on the different assumptions about the relaxation time of the tilting mode ($\tau_K$). In the saddle point model (SPM), $\tau_K$ is assumed to be larger than the saddle-scission time and shorter than the time spent by the nucleus near the saddle. This model had great success in description of the experimental data for the light-particle-induced reactions [1]. It should be noted that the SPM model loses its validity for very high $J$ and heavy fissioning nuclei, namely, when the angular momentum reduces the fission barrier to a value similar or smaller than the nuclear temperature. For the last case, the scission point model was developed. The scission point model [3] is based on the assumption of very quick equilibration of the tilting mode with the small $\tau_K$ (relative to the saddle-scission time). However, in the case of heavy-ion-induced reactions, experimental anisotropies of AD are spread in between the predictions of these models [4]. In this work, we suggest a dynamical model of AD, which takes into account the stochastic aspects of nuclear fission.

In the framework of our model, the dynamics of induced nuclear fission is considered in the stochastic approach [5] by the one-dimensional Langevin equations for the collective coordinate $r$ (distance between the centers of mass of the forming fission fragments) and the corresponding momentum $p$:

$$\frac{dr}{dt} = \frac{p}{m(r)}, \tag{1}$$

$$\frac{dp}{dt} = -\frac{1}{2}\left(\frac{p}{m(r)}\right)^2 \frac{dm(r)}{dr} - \frac{dV(r)}{dr} - \beta(r)p + f(t). \tag{2}$$

Here, $f(t)$ is a random force with the following properties: $\langle f(t)\rangle = 0$, $\langle f(t_1), f(t_2)\rangle = 2D\delta(t_1 - t_2)$; $D$ is expressed, through the Einstein relation, in terms of the nuclear temperature $T$ and the nuclear viscosity coefficient $\gamma$ as $D = T\gamma$; $\beta = \gamma/m$ is the damping coefficient in the fission mode and $m$ is the inertial parameter, which is calculated in the framework of the Werner–Wheeler approach. The nuclear temperature is defined as $T = (E_{\text{int}}/a)^{1/2}$ with $E_{\text{int}} = E^* - p^2/(2m) - V(r) - E_{\text{rot}}(J)$, where $E^*$ is the total excitation energy and $E_{\text{rot}}(J)$ is the rotational energy. In this work, the level-density parameter is chosen in the form $a(r) = a_1 A + a_2 A^{2/3} B_s(r)$, where $B_s(r)$ is the surface energy of the deformed nucleus, and $a_1$ and $a_2$ are taken from [6]. The initial $p$ values are generated for each Langevin sample under assumption of the normal distribution at $r$ corresponding to the equilibrium deformation. The potential energy $V(r)$ (and

*This article was submitted by the authors in English.

** e-mail: eremenko@p6-lnr.npi.msu.su

1063-7788/03/6609-1622$24.00 

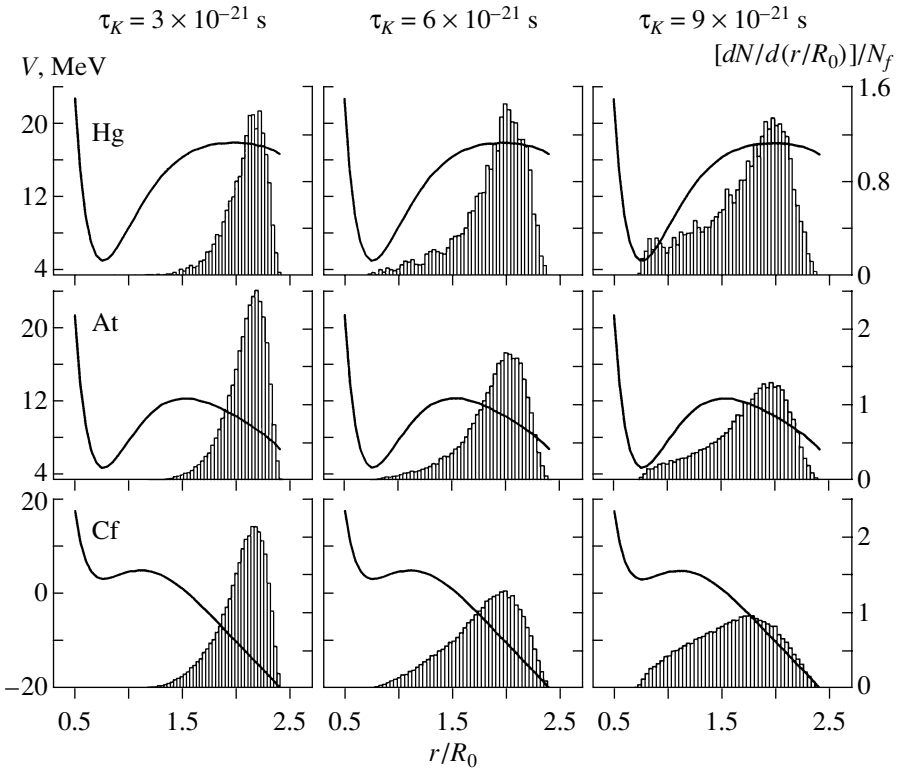


**Fig. 1.** Transition point distributions over deformation for different nuclei. The calculations are performed with $\beta = 4 \times 10^{21}$ s$^{-1}$ at $E^* = 100$ MeV and $J = 30\hbar$. The corresponding fission barriers are also presented.

accordingly $B_s(r)$) is calculated within the liquid-drop model with the Myers–Swiatecki parameters by using the procedure proposed in [7]. The initial $J$ distributions are calculated using the parameterization based on the surface friction model [8]. Light-particle emission is simulated by means of the Monte Carlo method [9]. In the model, the fission time of every Langevin sample is subdivided by intervals that are equal to $\tau_K$. The average deformation for every interval is calculated. The last such point is treated as an effective transition one. The stochastic nature of fission results in an ensemble of such points. The temperature and the moments of inertia at the effective point are determined. Then AD is calculated by the relations

$$W(\theta) = \frac{1}{N_f} \sum_{i=1}^{N_f} \sum_{M=-J_i}^{J_i} \sum_{K=-J_i}^{J_i} \frac{0.5 \exp(-M^2/2M_{0i}^2)(2J_i+1)|d^{J_i}_{M,K}(\theta)|^2 \exp(-K^2/2K_{0i}^2)}{\sum\limits_{M=-J_i}^{J_i} \exp(-M^2/2M_{0i}^2) \sum\limits_{K=-J_i}^{J_i} \exp(-K^2/2K_{0i}^2)}. \quad (3)$$

Here, $N_f$ is the number of Langevin samples that have fissioned, $d^{J_i}_{M,K}(\theta)$ is the symmetric top wave function, and $K_{0i} = (T/\hbar^2)(\Im_{||}^{-1} - \Im_{\perp}^{-1})^{-1}$ and $M_{0i} = \Im_{||} T/\hbar^2$ are the variances of the distributions over projections of $J$ onto the symmetry axis ($K$) and the space fixed axis ($M$). The moments of inertia $\Im_{||}$ and $\Im_{\perp}$ are calculated in the rigid-body approximation. As an illustration of this method, the distributions of the transition points on the deformation axis are presented in Fig. 1 for different nuclei and $\tau_K$ at $E^* = 100$ MeV and $J = 30\hbar$. As one can see, these distributions have substantial variances. The averaged deformations for the transition points are between the saddle and scission deformations. Distribution broadening is also observed with increasing $\tau_K$. It is seen that the lighter the nucleus, the closer the averaged position of the transition point to the saddle deformation.

In the present work, we analyzed the experimental data on the anisotropy of AD and the prescission neu-

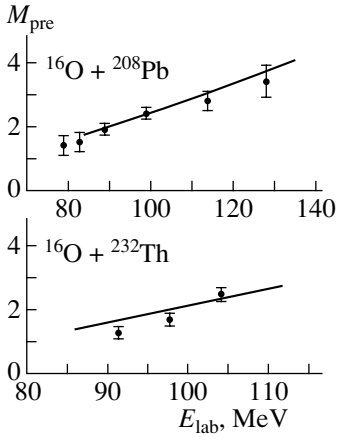


**Fig. 2.** Prescission neutron multiplicities. The solid lines are the calculation results. The points are the experimental data.

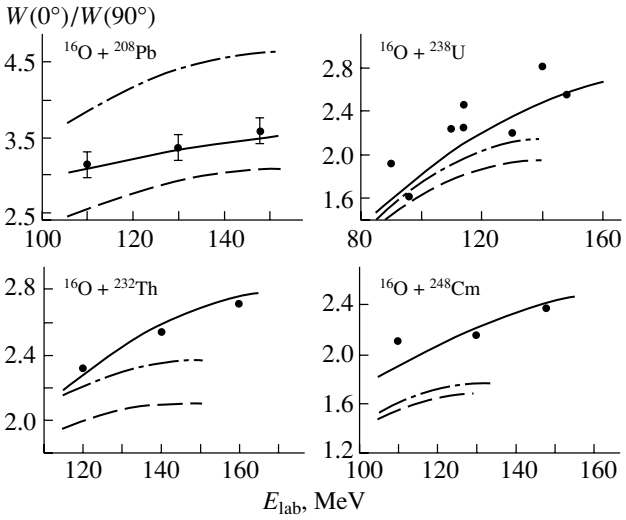


**Fig. 3.** Angular anisotropy of fission fragments. The points are the experimental data. The solid curves are the results of the present calculation; the dash-dotted and dashed curves present the calculations within the saddle point model with and without consideration of the presaddle neutron emission, respecively.

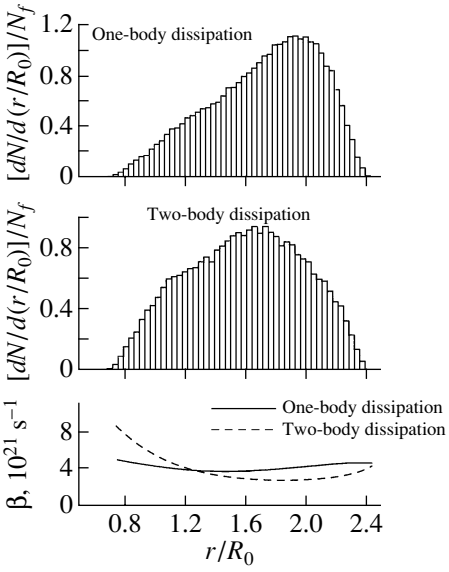


**Fig. 4.** Transition point distributions over deformation for the one-body (upper part) and two-body dissipation (middle part) models. These calculations were performed with $\tau_K = 8 \times 10^{-21}$ s for the $^{248}$Cf nucleus at $E^* = 100$ MeV and $J = 40\hbar$. The lower part of the figure presents the corresponding deformation dependences of $\beta$.

tron multiplicity ($M_{pre}$) for the $^{16}O + ^{208}Pb$, $^{232}Th$, $^{238}U$, and $^{248}Cm$ reactions first assuming deformation independences of $\beta$. Since $M_{pre}$ does not depend on the $\tau_K$ value, we obtained $\beta = 4 \times 10^{21}$ s$^{-1}$ fitting the experimental $M_{pre}$ for the $^{16}O + ^{208}Pb$, $^{232}Th$ reactions [10, 11] (see Fig. 2). Such data is absent for the $^{16}O + ^{238}U$, $^{248}Cm$ reactions. Then, we varied $\tau_K$ to describe the experimental anisotropy of AD as accurately as possible. In Fig. 3, the calculation results are presented in comparison with the experimental data [12]. The best description of the experimental data is achieved with $\tau_K = 6 \times 10^{-21}$ s. It is seen that, for the $^{16}O + ^{208}Pb$, $^{232}Th$, $^{238}U$, and $^{248}Cm$ reactions, our model allows a good description of the experimental data in the energy range under consideration. In addition, Fig. 3 presents the prediction of SPM. It is seen that, for the $^{16}O + ^{208}Pb$ reaction, the experimental data are between two calculations within SPM. It means that SPM in principle can describe the experimental AD for this reaction in this energy range. However, it seems that our calculation reproduces the slope of this energy dependence better than SPM. On the other hand, in the $^{16}O + ^{232}Th$, $^{238}U$, and $^{248}Cm$ reactions, the anisotropy of AD cannot be reproduced in the framework of SPM. It is connected with the formation of compound nuclei having angular-momentum-dependent fission barriers smaller than the temperatures for a considerable part of the initial distributions over angular momentum.

In the framework of the present model, AD is connected with the distribution of the transition points over deformation, which depends on the times spent by the nucleus on different stages of fission. The last means that the AD has to be sensitive to the deformation dependence of nuclear viscosity. In the present work, we used the one-body (only wall contribution) and two-body models of nuclear dissipation to illustrate this sensitivity. Here, we also adjusted $\beta$ to fit $M_{pre}$ as well as possible. In this case, we varied the parameters of the two-body viscosity $\mu$

[13] and the reduction coefficient under the wall formula $k_s$ [14]. Then, to estimate $\tau_K$, we fitted the AD anisotropies. Finally, we obtained $\tau_K = 7 \times 10^{-21}$ s and $\mu = 1.3 \times 10^{-22}$ MeV s fm$^{-3}$ for the two-body model and $\tau_K = 9 \times 10^{-21}$ s and $k_s = 0.26$ for the one-body model. Figure 4 presents the distributions of the transition point positions over deformation for these two models of nuclear dissipation. As is seen, the probability of realization of the effective point for small deformations is higher for the two-body model. This is a result of the fact that the two-body $\beta$ value is larger than the one obtained by the one-body model for the presaddle deformations, but for the saddle-scission deformations, the situation is opposite (see Fig. 4). This behavior of $\beta$ explains the difference in $\tau_K$ obtained in our calculations. All of the preceding allows us to conclude that the AD are sensitive to the deformation dependence of $\beta$.

We conclude that the dynamical model may be useful in the analysis of AD for cases when validity of the transition state models is questionable. Analysis of the experimental data allowed us to obtain $\tau_K$.

## ACKNOWLEDGMENTS

This work was supported by the Russian Foundation for Basic Research (project no. 02-02-17077) and the State Program "Russian Universities" (grant no. UR.02.03.014).

## REFERENCES

1. R. Vandenbosch and J. R. Huizenga, *Nuclear Fission* (Academic, New York, 1973).
2. R. P. Schmitt *et al.*, Nucl. Phys. A **487**, 370 (1988).
3. H. H. Rossner *et al.*, Phys. Rev. Lett. **53**, 38 (1984).
4. J. O. Newton, Fiz. Élem. Chastits At. Yadra **21**, 821 (1990) [Sov. J. Part. Nucl. **21**, 349 (1990)].
5. Y. Abe *et al.*, Phys. Rep. **275**, 49 (1996).
6. A. V. Ignatyuk *et al.*, Yad. Fiz. **21**, 1185 (1975) [Sov. J. Nucl. Phys. **21**, 612 (1975)].
7. J. P. Lestone, Phys. Rev. C **51**, 580 (1995).
8. P. Fröbrich and I. I. Gontchar, Phys. Rep. **292**, 131 (1998).
9. V. A. Drozdov *et al.*, Yad. Fiz. **64**, 221 (2001) [Phys. At. Nucl. **64**, 179 (2001)].
10. H. Rossner *et al.*, Phys. Rev. C **45**, 719 (1992).
11. A. Saxena *et al.*, Phys. Rev. C **49**, 932 (1994).
12. B. B. Back *et al.*, Phys. Rev. C **32**, 195 (1985).
13. K. T. R. Davies *et al.*, Phys. Rev. C **13**, 2385 (1976).
14. J. R. Nix and A. J. Sierk, in *Proceedings of the International School–Seminar on Heavy Ion Physics, Dubna, 1986* (Dubna, 1987), p. 453.

*Physics of Atomic Nuclei, Vol. 66, No. 9, 2003, pp. 1626–1627. From Yadernaya Fizika, Vol. 66, No. 9, 2003, pp. 1673–1675.*


# Influence of the Shell Effects on Fission Fragment Angular Anisotropies*

**V. A. Drozdov****, **D. O. Eremenko**, **O. V. Fotina**, **S. Yu. Platonov**, and **O. A. Yuminov**

*Institute of Nuclear Physics, Moscow State University, Moscow, 119992 Russia*

Received August 28, 2002

**Abstract**—The influence of the damping shell corrections with increasing excitation energy on the fission fragment angular anisotropies is considered. In the framework of the statistical approach to nuclear fission, experimental data on fission fragment angular anisotropies obtained in the $^4$He + $^{238}$U reaction is analyzed. Information about the energy dependence of the shell corrections is obtained from this analysis.


## INTRODUCTION

Shell corrections to the potential energy play an important role in the decay of heavy nuclei at low-excitation energies [1]. Usually information about them was obtained from analysis of experimental data on evaporation residue cross sections, mass distributions of fission fragments, fission probabilities, etc.

The modulation of the nuclear energy surface by the shell corrections leads to the double-humped structure of the fission barrier. However, an increase in excitation energy results in damping of the shell corrections (if the excitation energy is more than 60 MeV, the fission barrier becomes the pure liquid-drop one) [2]. Information about the energy dependence of the shell corrections is very important for description of the fission process and synthesis of superheavy elements [3]. To obtain such a dependence, it is necessary to investigate the energy range where a decrease in the effect with increasing excitation energy is observed. In the present paper, we analyzed fission fragment angular distributions with this purpose.

## ANALYSIS OF EXPERIMENTAL DATA ON FISSION FRAGMENT ANISOTROPIES

The influence of the double-humped structure of the fission barrier on fragment angular distribution was considered in [4]. However, in this work, the case of excitation energies less than 50 MeV was studied and the shell effect damping with increase in the nuclear temperature was neglected. To take into account the decrease in the shell corrections at the characteristic points of the fission barrier (the inner and outer fission barriers and the second well), we analyzed the fission fragment anisotropies in the $\alpha$ + $^{238}$U reaction in the energy range $23 \le E_\alpha \le 100$ MeV.

In this work, we assumed that, in the Pu nuclei, the second well coincides with the top of the liquid barrier in the deformation space. Thereby, the fission fragment angular distributions were calculated as a superposition of the second barrier contribution and the second well one:

$$W(\theta) = \frac{\sum\limits_i P_i \sigma_i W_{\mathrm{SB}i}(\theta)}{\sum\limits_i \sigma_i} + \frac{\sum\limits_i (1-P_i)\sigma_i W_{\mathrm{SW}i}(\theta)}{\sum\limits_i \sigma_i}, \quad (1)$$

where $\sigma_i$ is the partial fission cross section, $P_i$ is the probability of populating the second well of the $i$th nucleus of the neutron-emission cascade, $W_{\mathrm{SB}i}(\theta)$ is the contribution to the angular distribution of the second barrier, and $W_{\mathrm{SW}i}$ is the angular distribution connected with the second well. $W_{\mathrm{SB}i}(\theta)$ and $W_{\mathrm{SW}i}$ are given as

$$W_i(\theta) = \sum_{J=0}^{\infty} \frac{\sigma_{i,J}}{\sigma_i} \times \sum_{K=-J}^{J} \frac{0.5(2J+1)|d^J_{M=0,K}(\theta)|^2 \rho_i(K)}{\sum\limits_{K=-J}^{J} \rho_i(K)}, \quad (2)$$

where $J$ is the total angular momentum of the nuclear system;

$$\rho_i(K) = \exp\{-(\hbar^2 K^2/2T_i)[(1/\Im_{||}) - (1/\Im_\perp)]\}; \quad (3)$$

and $T_i$, $\Im_{||}$, and $\Im_\perp$ are the nuclear temperature and the parallel and perpendicular inertia moments, respectively. These values are calculated at the second barrier and at the second well.

*This article was submitted by the authors in English.

**e-mail: drozdov@p6-lnr.npi.msu.su

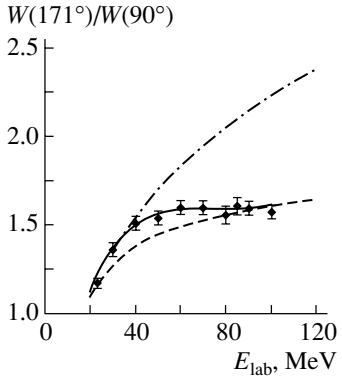


**Fig. 1.** Fission fragments angular anisotropies in the $\alpha + {}^{238}\mathrm{U}$ reaction. The points are the experimental data [6]. The curves are the results of the calculations with the double-humped barrier (dashed-dotted), with the liquid-drop barrier (dashed), and in the framework of the formalism presented in this paper (solid).

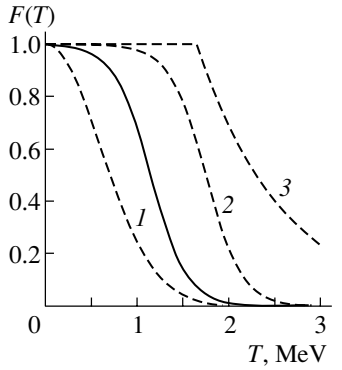


**Fig. 2.** Different types of the shell corrections damping function: *1*—[7], *2*—[2], *3*—[8], and solid curves—the damping function obtained from the best description of the experimental data on the fission fragment anisotropies.

The spin distributions of the initial compound nucleus and the daughter nuclei were calculated using the GFOT code [5].

The probability of populating the second well was calculated as

$$P_i = 1 - \exp\left(-\frac{B_{f\mathrm{II}i}}{T_{\mathrm{II}i}}\right), \qquad (4)$$

where $B_{f\mathrm{II}i} = V_{\mathrm{SB}i} - V_{\mathrm{SW}i} + (\delta W_{\mathrm{SB}i} - \delta W_{\mathrm{SW}i})F(T)$ is the height of the outer fission barrier relative to the second well depth of the $i$th nucleus of the neutron-emission cascade; $T_{\mathrm{II}i}$ is the nuclear temperature at the second well; $V_{\mathrm{SB}i}$ and $V_{\mathrm{SW}i}$ are the liquid-drop potential energies for the second barrier and the second well, respectively; $\delta W_{\mathrm{SB}i}$ and $\delta W_{\mathrm{SW}i}$ are the corresponding shell corrections; and $F(T)$ is a function determining the shell-correction damping with increase in the temperature.

Comparison of the calculation of fission fragment angular anisotropies at the second barrier and at the liquid-drop saddle point with the experimental data is presented in Fig. 1. It is seen that, at low energies, the experimental data is reproduced by the calculation with the double-humped barrier ($P_i \approx 1$) and that, at the highest energies, the data is reproduced by the calculation with the liquid-drop barrier ($P_i \approx 0$). For description of the experimental data on the fission fragment angular anisotropies, we used the damping function of Fermi type in Eq. (1)

$$F(T) = \frac{1}{1 + \exp((T - T_0)/d)}, \qquad (5)$$

where $d = 0.2$ MeV is the rate of washing out (disappearance) of the shell corrections with temperature and $T_0$ was treated as an adjustment parameter. The best description of the experimental data is achieved with use of the value $T_0 = 1.15$ MeV (see Fig. 1).

Figure 2 presents our temperature dependence of the shell corrections in comparison with other temperature dependences of the shell corrections.

## CONCLUSION

It is shown that the damping of the shell corrections with the nuclear temperature can explain the behavior of the fission fragment angular anisotropies in the cases of decay of heavy nuclei with excitation energies ranging from 15 to 100 MeV. In the analyses of the experimental data on the fission fragment angular anisotropies for the $\alpha + {}^{238}\mathrm{U}$ reaction in the energy range $23 \leq E_\alpha \leq 100$ MeV, information about the energy dependence of the shell corrections was obtained.

## ACKNOWLEDGMENTS

This work was supported in part by the Russian Foundation for Basic Research (project no. 02-02-17077) and the State Program "Russian Universities" (grant no. UR.02.03.014).

## REFERENCES

1. V. M. Strutinsky, Nucl. Phys. A **95**, 420 (1967).
2. O. A. Yuminov *et al.*, Nucl. Instrum. Methods Phys. Res. B **164–165**, 963 (2000).
3. G. Giardina *et al.*, in *Proceedings of the International Conference on Nuclear Physics "Nuclear Shells—50 Years," Dubna, Russia, 1999,* Ed. by Yu. Ts. Oganessian and R. Kalpakchieva (World Sci., Singapore, 2000), p. 244.
4. D. O. Eremenko *et al.*, J. Phys. G **22**, 1077 (1996).
5. O. V. Grusha *et al.*, Izv. Akad. Nauk SSSR, Ser. Fiz. **51**, 2055 (1987).
6. S. S. Kapoor *et al.*, Phys. Rev. **149**, 965 (1966).
7. C. C. Sahm *et al.*, Nucl. Phys. A **441**, 316 (1985).
8. A. D'Arrigo *et al.*, J. Phys. G **20**, 365 (1994).

*Physics of Atomic Nuclei, Vol. 66, No. 9, 2003, pp. 1628–1630. From Yadernaya Fizika, Vol. 66, No. 9, 2003, pp. 1676–1678.*


# Decay Time Characteristics of the U-Like Excited Nuclei*

**V. A. Drozdov, D. O. Eremenko, O. V. Fotina, S. Yu. Platonov**, and O. A. Yuminov**

*Institute of Nuclear Physics, Moscow State University, Moscow, 119992 Russia*

Received August 28, 2002

**Abstract**—The unified energy dependence of the induced fission times obtained by the crystal blocking technique for heavy nuclei with $Z = 91$–$94$ in the range of initial excitation energy from 5 to 250 MeV was analyzed. It was demonstrated that, for excitation energies of the investigated heavy fissionable nuclei up to 60–70 MeV, the fission times can be described in the framework of the statistical theory of nuclear reactions taking into account the double-humped structure of the fission barrier and the lifetimes of both classes of excited nuclear states realized in the first and second potential wells. However, for excitation energies above 70 MeV, there is a need to consider the dynamical effects in the fission channel.


The nuclear reaction time is an important characteristic directly associated with both the structural features of the interacting nuclei and the mechanism of decay of the excited nucleus. As it was shown in [1], the double-humped structure of the fission barrier can have a strong influence on the time characteristics of decay of excited heavy nuclei. Moreover, one needs to stress the unique sensitivity of such an observable as the induced fission lifetime to the dynamical properties of the fissioning nuclear system, i.e., magnitude of nuclear matter viscosity and so on.

Here, we present the results of analysis of the large set of experimental data on the induced fission times $\tau_f$ obtained by the crystal blocking technique [2, 3]. We analyze $\tau_f$ for the $^{232}$Th + $p, d, \alpha$ reactions [4] obtained at the U-120 cyclotron of the Institute of Nuclear Physics, Moscow State University, at beam energies in the range from 4 to 7.8 MeV/nucleon. The experimental decay times range from $10^{-17}$ to $10^{-14}$ s, depending on the projectile energy. Our $\tau_f$ data for the $^{28}$Si + $^{\text{nat}}$Pt reaction at the silicon beam energies from 140 to 170 MeV [5] are also analyzed. The last measurements were done with the Tandem-XTU accelerator of the LNL Laboratories (Padova, Italy) and provided experimental decay times ranging from $10^{-18}$ to $10^{-17}$ s. Our own data have been compared with $\tau_f$ for the U-like nuclei produced in the $^{238}$U + $^{28}$Si reaction at the U-beam energy of 24 MeV/nucleon obtained at GANIL [6]. Due to the very large value of the transferred momentum in the last reaction, $\tau_f$ ranges from $10^{-17}$ to $3 \times 10^{-19}$ s for excitation energies in the 10–250 MeV interval. Hence, we have the unified energy dependence of $\tau_f$ for heavy nuclei with $Z = 91$–$94$ in the range of the initial excitation energy from 5 to 250 MeV (see Fig. 1).

As one can see from Fig. 1, the experimental fission times are much longer than that expected from the standard statistical calculations of lifetimes of initial compound nuclei formed in the investigated reactions. Calculations in the framework of the rotating liquid-drop model, taking into account only lifetimes of excited states under equilibrium deformation, underestimate the experimental data by approximately five orders of magnitude at excitation energies about 100 MeV.

The emission of neutrons from the fissioning nuclear system leads to the cooling of nuclei before fission and, as a result, to increasing the mean decay time in the fission channel. Considerations of all possible fission chances during the development of the neutron-emission cascade (each one weighted with its probabilities of occurrence—$\tau_f = \sum \tau_{f_i} \omega_i$, where $\omega_i$ is the relative weight of the fission fragments from the $i$th chance, and $\tau_{fi}$ is the corresponding decay time in the fission channel) improve the fit of the experimental data. But the large difference between theory and experiment (approximately three orders of magnitude) still remains.

Assuming the double-humped fission barrier model with allowance for the lifetimes of the both classes of excited nuclear states in the first and second potential wells [1] makes it possible to improve the fit of $\tau_f$ substantially in the excitation energy region below 60–70 MeV. The reason is that the existence of an additional time delay in the fission channel (connected

*This article was submitted by the authors in English.

**e-mail: platonov@p10-lnr.npi.msu.su

with the lifetime of the second well states) leads to a noticeable increase in $\tau_f$. But for higher initial excitation energies, the influence of this additional time delay diminishes and finally disappears at energies above 70 MeV due to the damping of shell effects with increasing nuclear temperature [5]. In this energy region, the double-humped structure of the fission barrier for heavy nuclei tends to transform into a single-humped one and only one class of excited nuclear states under equilibrium deformation survives.

For an initial excitation energy above 50 MeV, the dynamical aspects of the nuclear fission process begin to play an important role. In this connection, an analysis of the obtained energy dependence of the induced fission times was performed in the framework of the dynamical approach based on the set of stochastic Langevin equations. In the one-dimensional case, it can be represented as

$$\frac{dr}{d\tau} = \frac{p}{m}, \tag{1}$$

$$\frac{dp}{d\tau} = -\frac{p^2}{2}\frac{d}{dr}\left(\frac{1}{m}\right) - \frac{dV}{dr} - \beta p + f(\tau), \tag{2}$$

where $r$ and $p$ are the collective coordinate and the corresponding momentum, respectively. For the $r$, we used the distance between the centers of mass of the formed fission fragments. In Eq. (2), $f(\tau)$ is a random delta-correlated force

$$\langle f(\tau)\rangle = 0, \quad \langle f(\tau_1)f(\tau_2)\rangle = 2D\delta(\tau_1 - \tau_2), \tag{3}$$

where $D$ is expressed, through the Einstein relation, in terms of the nuclear temperature and the coefficient of nuclear friction as $D = t\beta m$, being related to the damping coefficient $\beta$. The inertial parameter $m$ was calculated in the incompressible fluid approximation [7]. In the proposed approach, the damping coefficient $\beta$ was used as an adjustable parameter. The nuclear temperature is defined as $t = (E_{\rm int}/a)^{1/2}$ with $E_{\rm int} = E^* - p^2/(2m) - V(r, J)$, where $E^*$ is the total excitation energy and $a$ is the level-density parameter. In our analysis, the level-density parameter was chosen in the form of $a = A/10$. The potential energy $V(r, J)$ was calculated within the rotating liquid-drop model with the Myers–Swiatecki parameters by using the procedure proposed in [8]. The initial values of $p$ were generated for each trajectory under the assumption of the normal momentum distribution at $r$ corresponding to the equilibrium deformation:

$$F(p) = \frac{1}{\sqrt{2\pi mt}}\exp\left(-\frac{p^2}{2mt}\right). \tag{4}$$

Equations (1), (2) were solved in the framework of the Euler difference scheme. The emission of light particles (neutrons, protons, and $\alpha$ particles) was simulated within the method that is usually used to calculate the multiplicity of prescission light particles in the framework of an approach based on the Langevin equations (see, for example, [9]). The induced fission decay times were calculated by the following relation:

$$\langle\tau_f\rangle = \frac{1}{N_f}\sum_{i=1}^{N_f}\tau_{fi}, \tag{5}$$

where $N_f$ is the number of Langevin samples that have fissioned and $\tau_{fi}$ is the fission time for the $i$th Langevin sample. Other calculation details were described in [9].

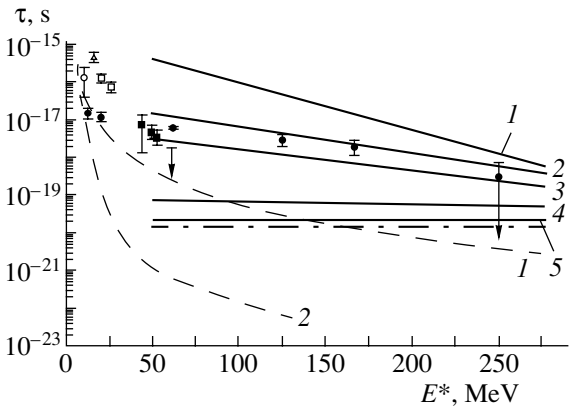


**Fig. 1.** The induced fission times of nuclei with $Z = 91$–$94$ vs. initial excitation energy. Points are experimental data: open circle, triangle, and squares are our data from the $^{232}$Th$(p, xnf)$, $^{232}$Th$(d, xnf)$, and $^{232}$Th$(\alpha, xnf)$ reactions [4]; black squares are our data from the $^{28}$Si + $^{\rm nat}$Pt reaction [5]; black circles are data from [6]. The dashed curves are the results of the statistical calculations (1) with allowance for and (2) with neglect of the contributions of the fissioning nuclei produced in the neutron-evaporation cascade. The solid curves are the results of the dynamical calculations obtained for $\beta = 5 \times 10^{21}$ s$^{-1}$ and $J = 20$ (*1*), 30 (*2*), 40 (*3*), 60 (*4*), and $80\hbar$ (*5*). The dash-dotted curve represents the time for the fissioning system moving from the saddle to the scission for $\beta = 5 \times 10^{21}$ s$^{-1}$ and $J = 40\hbar$.

Because of lack of information on the angular momentum $J$ of the U-like fissioning nuclei formed in the $^{238}$U + $^{28}$Si reaction, we treat this value as a free parameter. Thus, in our calculations, we used two adjustable parameters: $\beta$ and $J$. The best description of the investigated energy dependence of $\tau_f$ was achieved for $\beta = 5 \times 10^{21}$ s$^{-1}$ and $J = (30$–$40)\hbar$ (see Fig. 1). These $J$ values are consistent with the peripheral mechanism of the reaction under study. At higher values of $J = (60$–$80)\hbar$, we obtained $\tau_f$ values very close to the time spent by the fissioning system between the saddle and scission points. This is a result of the fission barrier disappearance at such high $J$ values. In addition, a decrease in $J$ leads to an increase in the $\tau_f$ values due to the cooling of the

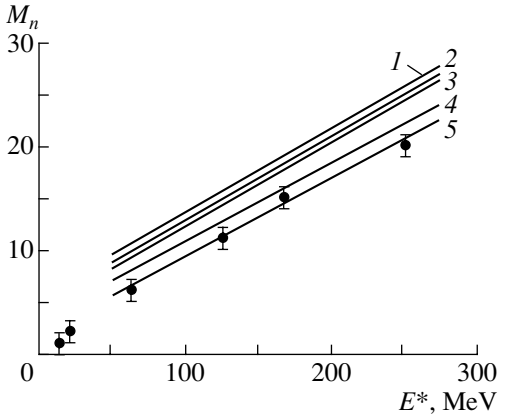


**Fig. 2.** The total neutron multiplicity vs. initial excitation energy of the fissioning U-like nuclei produced in the $^{238}U + {}^{28}Si$ reaction. Points are experimental data from [6]. Curves are the calculation results obtained for $\beta = 5 \times 10^{21}$ s$^{-1}$ and $J = 20$ (*1*), 30 (*2*), 40 (*3*), 60 (*4*), and $80\hbar$ (*5*).

nucleus because of the light-particle emission before the saddle.

In addition, we also tested the obtained $\beta$ and $J$ values using the total neutron multiplicity for the fissioning U-like nuclei formed in the $^{238}U + {}^{28}Si$ reaction (see Fig. 2). Our calculated values of the prescission neutron multiplicity were summed with the data on the postscission neutron multiplicity for the fissioning nuclei with $Z = 91$–$95$ from systematics [10]. As one can see from Fig. 2, our calculation results for $J = (30$–$40)\hbar$ slightly overestimate the experimental data. One of the probable reasons for this difference can be in the fact that, in the systematics [10], it was obtained for complete fusion–fission reactions, while our calculations were done for the concrete initial values of $J$. In any case, the obtained value of the damping coefficient $\beta = 5 \times 10^{21}$ s$^{-1}$ falls into the range of estimates of other authors [10] and corresponds to the concept of "overdamped" collective nuclear motion.

In summary, we analyzed the unified energy dependence of the induced fission decay times for heavy nuclei with $Z = 91$–$94$ in the excitation energy range from 5 to 250 MeV. The analysis allowed us to separate the excitation energy ranges in which the different mechanisms of the excited nucleus decay are dominating. In conclusion, it is necessary to stress the unique sensitivity of the induced fission lifetime to the properties of the fissioning nuclear system, i.e., the magnitude of nuclear matter viscosity, the structure of the excited strongly deformed nuclear states, and so on.

## ACKNOWLEDGMENTS

This work was supported in part by the Russian Foundation for Basic Research (project no. 02-02-17077) and the State Program "Russian Universities" (grant no. UR.02.03.014).

## REFERENCES

1. O. A. Yuminov, S. Yu. Platonov, O. V. Fotina, *et al.*, J. Phys. G **21**, 1243 (1995).
2. A. F. Tulinov, Dokl. Akad. Nauk SSSR **162**, 546 (1965) [Sov. Phys. Dokl. **10**, 463 (1965)].
3. D. O. Eremenko, V. O. Kordyukevich, S. Yu. Platonov, *et al.*, Yad. Fiz. **60**, 206 (1997) [Phys. At. Nucl. **60**, 149 (1997)].
4. D. O. Eremenko, S. Yu. Platonov, O. V. Fotina, and O. A. Yuminov, Yad. Fiz. **61**, 773 (1998) [Phys. At. Nucl. **61**, 695 (1998)].
5. O. A. Yuminov, S. Yu. Platonov, D. O. Eremenko, *et al.*, Nucl. Instrum. Methods Phys. Res. B **164–165**, 973 (2000).
6. F. Goldenbaum, M. Morjean, J. Galin, *et al.*, Phys. Rev. Lett. **82**, 5012 (1999).
7. K. T. R. Davies, A. J. Sierk, and J. R. Nix, Phys. Rev. C **13**, 2385 (1976).
8. J. P. Leston, Phys. Rev. C **51**, 580 (1995).
9. V. A. Drozdov, D. O. Eremenko, S. Yu. Platonov, *et al.*, Yad. Fiz. **64**, 221 (2001) [Phys. At. Nucl. **64**, 179 (2001)].
10. D. Hilsher and H. Rossner, Ann. Phys. (Paris) **17**, 471 (1992).

*Physics of Atomic Nuclei, Vol. 66, No. 9, 2003, pp. 1631–1635. From Yadernaya Fizika, Vol. 66, No. 9, 2003, pp. 1679–1683.*


# New Indications of Collinear Tripartition in $^{252}$Cf(sf) Studied at the Modified FOBOS Setup*

**Yu. V. Pyatkov[1),2)], D. V. Kamanin[1)**], A. A. Alexandrov[1)], I. A. Alexandrova[1)], S. V. Khlebnikov[3)], S. V. Mitrofanov[1)], V. V. Pashkevich[1)], Yu. E. Penionzhkevich[1)], Yu. V. Ryabov[4)], E. A. Sokol[1)], V. G. Tishchenko[1)], A. N. Tjukavkin[2)], A. V. Unzhakova[1)], and S. R. Yamaletdinov[1)]**

[1)] *Joint Institute for Nuclear Research, Dubna, Moscow oblast, 141980 Russia*

[2)] *Moscow Engineering Physics Institute, Kashirskoe sh. 31, Moscow, 115409 Russia*

[3)] *Khlopin Radium Institute, St. Petersburg, 194021 Russia*

[4)] *Institute for Nuclear Research, Russian Academy of Sciences, pr. Shestidesyatiletiya Oktyabrya 7a, Moscow, 117312 Russia*

Received October 18, 2002

**Abstract**—An attempt has been made to search for collinear tripartition in spontaneous fission of $^{252}$Cf by using the FOBOS setup coupled with the neutron detector belt. A group of rare events were detected characterized by reduced total kinetic energy and total nuclear charge gated by the large neutron multiplicity measured. This fact is considered to be an experimental indication of collinear tripartition in $^{252}$Cf. The theoretical indication of the possible existence of the collinear cluster tripartition valley was obtained for the first time. © *2003 MAIK "Nauka/Interperiodica".*

The present paper is devoted to the search for the particular case of true ternary fission at the lowest excitation, i.e., during spontaneous decay. In the early experiments [1] at the FOBOS detector [2] aimed at the study of rare fission modes in spontaneous decays of $^{248}$Cm and $^{252}$Cf, a group of precisely collinear pairs of heavy fragments with a large deficit both of the total mass and of the total kinetic energy was detected. This group lies rather far from the locus connected to conventional binary fission in the correlation plot of the fragment masses (selected area, Fig. 1), and its yield in the lowest limit amounts to $\sim 10^{-6}$–$10^{-5}$ of the whole data body. The mass-energy correlations for these rare events allow one to assign them to fission of the system via an elongated three-body chainlike configuration. In this case, two outside fragments fly apart along the chain axis and can be confused with ordinary fission fragments (FF), while the central fragment can stay almost at rest and, as a result, can hardly be registered. Such an experiment especially suffers from the background of false events due to the partial loss of the FF energy in the construction elements of detector modules. The results obtained have been treated as an indication of collinear cluster tripartition (CCT) of the heavy nuclei under study.

The advanced experiment aimed specially at the investigation of CCT of the $^{252}$Cf nucleus has been

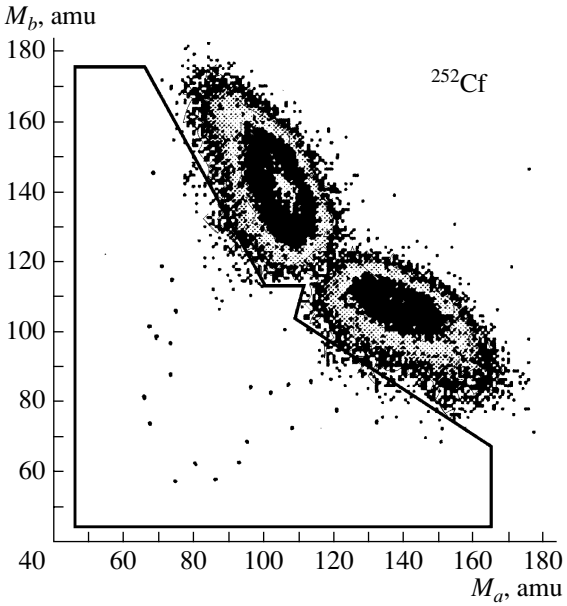


**Fig. 1.** Mass-yield matrix $Y(M_a, M_b)$ of fission fragments for $^{252}$Cf(sf) decay.

*This article was submitted by the authors in English.

**e-mail:kamanin@fobos.jinr.ru

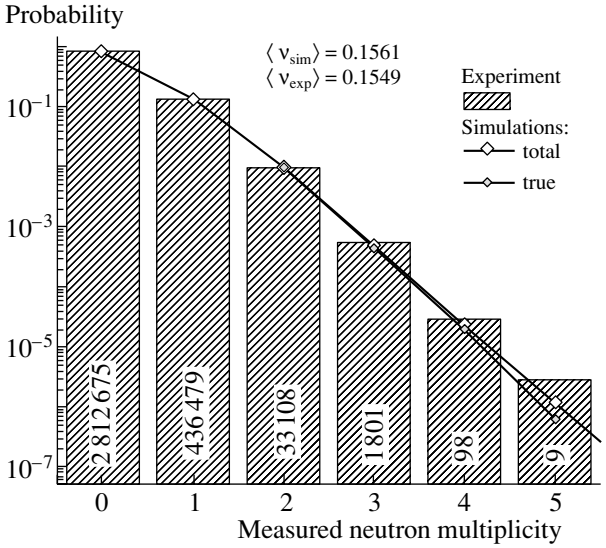


**Fig. 2.** The spectrum of frequency vs. number of tripped neutron counters for the recorded fission events. The actual numbers of counts are labeled. The "true" contribution is conditioned only by the number of emitted neutrons being not less than the measured multiplicity.

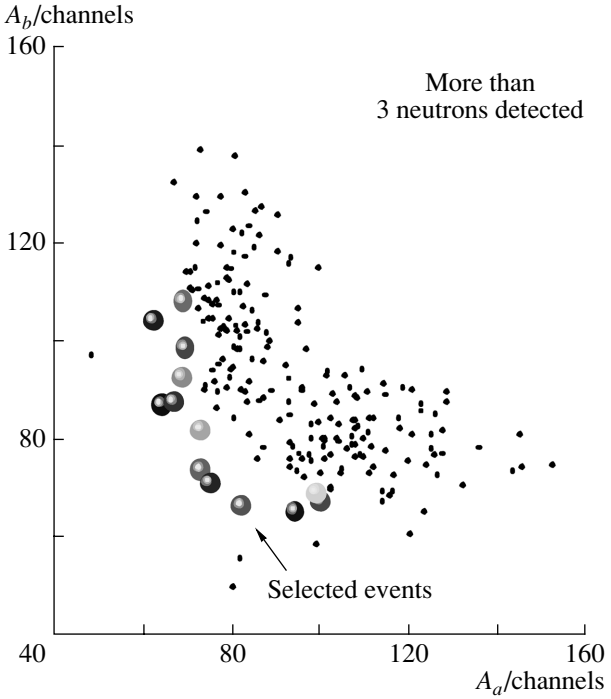


**Fig. 3.** Amplitude distribution $Y(A_a, A_b)$ of the complementary fragments under the condition that at least four neutron counters were fired.

performed at the modified $4\pi$ spectrometer FOBOS at the Flerov Laboratory of the JINR [3]. In order to overcome the above-mentioned methodological obstacles and to improve the quality of the data, some modifications have been introduced into the experimental scheme. These modifications concerned the configuration of the detectors, including the start detector; the electronics; and also the data acquisition system. Some preliminary results of the recent experiment are discussed below.

The FF trigger consisted of two groups each containing six FOBOS modules used as a double-armed spectrometer for measuring the FF velocities ($V$) by means of measuring their time-of-flight and energies ($E$). Thus both the $2{-}V$ and the $V{-}E$ methods are accessible for the calculation of the FF masses. In using the latter method, one does not need to use any a priori assumptions considering the process to be exclusively binary.

The double-armed configuration of the FOBOS spectrometer consisted of the specially designed wide-aperture start detector with an internal FF source [3]. The full symmetrization of the spectrometer arms achieved owing to such a start detector improves the quality of the data substantially.

According to the model of the CCT process proposed in [2], the central fragment of the three-body prescission chain acquires almost the entire deformation energy of the system. Being presumably at rest, it would be an isotropic source of postscission neutrons of a high multiplicity ($\sim$10) in the laboratory system. On the contrary, the neutrons emitted from the moving fission fragments are focused along the fission axis. In order to exploit this phenomenon for revealing the CCT events, a "neutron belt" [4] consisting of 140 separate hexagonal modules based on $^3$He-filled proportional counters was assembled in a plane perpendicular to the symmetry axis of the spectrometer, which serves as the mean fission axis at the same time. The center of this belt coincides with the location of the FF source.

The typical spectrum of frequency vs. the number of tripped neutron counters for the registered fission events is presented in Fig. 2. The function obtained agrees well with the theoretical calculations based on the known probabilities for emitting a certain number of neutrons per fission, meaning the total registration efficiency of about 3.8% [4]. The overall registration efficiency for an isotropic source and, hence, for the neutrons from the CCT events amounts to $\sim$11%. A simple calculation accounting for this difference in the registration efficiencies and in the primary multiplicity spectra ascribed to the processes considered (see [4]) reveals that the registration probability for more than three neutrons from ordinary spontaneous fission in this geometry is two orders of magnitude lower than the same probability for the CCT events.

Our empirical model described in [4] reproduces the shape of the multiplicity distribution from 0 to 3 precisely. In particular, the best fit presented in

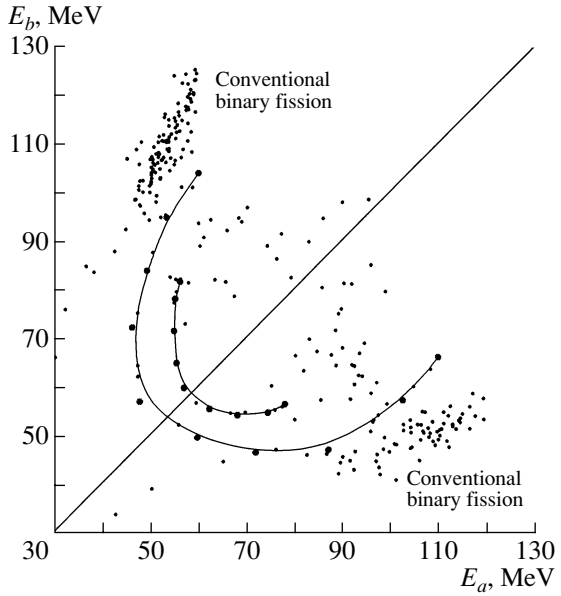


**Fig. 4.** Energy distribution $Y(E_a, E_b)$ of the complementary fragments obtained for the events falling inside the contour marked in Fig. 1.

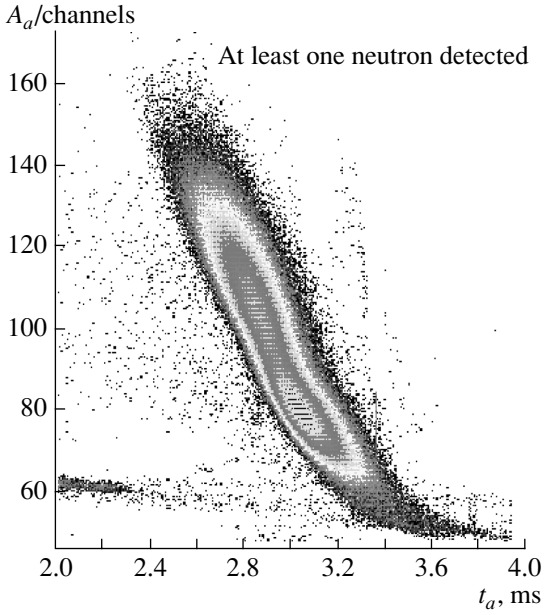


**Fig. 5.** The distribution of the FF amplitude vs. drift time measured in a BIC when at least one neutron detector is fired.

Fig. 2 gives the average multiplicity differing from the experimental one only by the value of 0.001, and such a good reproducibility of the distribution shape is found to be stable against reasonable variations of the parameters of the model. The latter fact is extremely important for the tail of the distribution and, therefore, we checked the most important constants additionally by using simulations with the well-known MCNP code.

One should note that the lowest estimate of $\sim 10^{-6}$–$10^{-5}$ of the yield of CCT with respect to ordinary fission formally assumes the contribution of at least 3–30 CCT events to the multiplicity spectrum in Fig. 2 and these events should contribute mainly to high-multiplicity values. On the other hand, we deliberately did not include the contribution of CCT in our simulations. Although there are no experimental data on multiplicity 6 and higher, the best fit misses surprisingly ~20 events for the measured values of 4 and 5. Based on the statistics of 3 million events presented in Fig. 2, we would not insist on evidence of some additional high-multiplicity process. However, we treat the observed difference between the experiment and simulations as an additional argument for searching the CCT events under the condition of $\nu_{\text{exp}} > 3$.

In addition, according to our simulations, the contribution of the true high-multiplicity events with $\nu_{\text{emitted}} > 3$ to the measured multiplicity greater than 3 amounts to ~80% (Fig. 2), while the rest is mostly due to random coincidences with $\nu_{\text{emitted}} = 3$. This means the reliability of the experimental data selected by such a large number of fired neutron counters.

The first interesting result can already be discussed on the basis of a part of the whole data body counted, $1.4 \times 10^7$ events. Figure 3 shows the amplitude distribution $Y(A_a, A_b)$ of the fragments detected in coincidence in two arms of the spectrometer (labeled $a$ and $b$) gated by the large neutron multiplicity $\nu_{\text{exp}} > 3$, as is discussed above. The set of points that looks like a parabola (denoted as selected events in Fig. 3) attracts one's attention. For comparison, a similar plot obtained for the events falling inside the contour shown in Fig. 1 is given in Fig. 4, although this plot is not gated by the number of fired neutron detectors. The events forming an angle-like structure in Fig. 1, i.e., linked with tripartition, are connected by the parabolic curves.

A serious test of the reliability of the CCT events is the low total charge of both detected fragments, less than $Z_c/2$, where $Z_c$ is the charge number of the fissioning nucleus. Unfortunately Bragg spectroscopy is ruled out for the heavy ions, whose energy is typically lower than 1 $A$ MeV for the FF in spontaneous fission. In order to perform the test for the total charge, an additional parameter was recorded for each fission fragment registered. This alternative method was proposed in [5]. It is based on measuring the delay between the time the fragments enter the Bragg ionization chamber (BIC) and the time the anode pulse crosses a given level, i.e., the parameter connected with the drift time of a charge in a BIC.

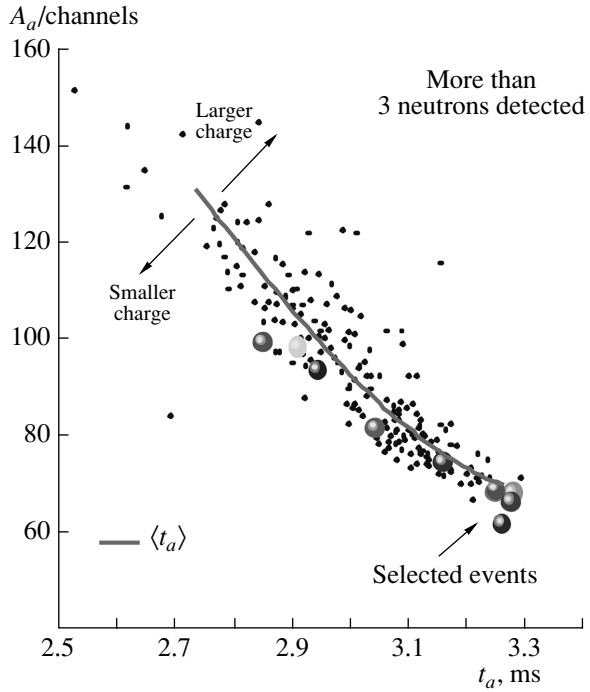


**Fig. 6.** The same distribution as in Fig. 5 when at least four neutron detectors fired. The selected events are the same as in Fig. 3.

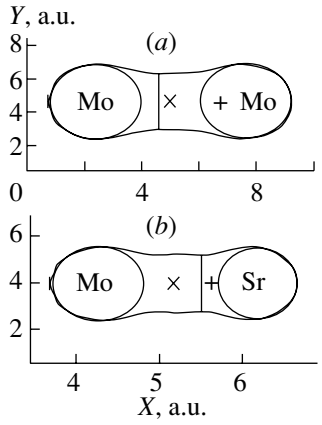


**Fig. 7.** The shape of the nucleus at the bottom of the "symmetric" valley ($Q_2 = 7.52$ a.u., $\eta = 0.074$) (*a*); the same system at the point $Q_2 = 7.52$ a.u., $\eta = -0.208$ (*b*).

The distribution of the FF amplitude $A_a$ vs. drift time $t_a$ obtained in our experiment for one of the detectors is shown in Fig. 5. The FF fall to the light- and the heavy-mass peaks, which are easily distinguished. An individual charge at a given mass should look like a steep power function. Of course, numerical simulations and a direct calibration are needed for an accurate analysis of such a complicated parameter as $t_a$. Indeed, the drift time $t_a$ is a function of the nuclear charge of the FF, its energy, and, less pronounced, its mass simultaneously. However, a preliminary conclusion can be drawn from the drift time vs. amplitude plot shown in Fig. 6, which is accumulated under the same condition of the neutron multiplicity $\nu_{\exp} > 3$ as Fig. 3.

For a usual fission event, one should expect that the measured total charge of the complementary FF is, on the average, equal to the charge of the Cf nucleus, i.e., $\langle Z_a \rangle + \langle Z_b \rangle = 98$. This should mean that the complementary FF has to be found, on the average, on different sides of the line of mean charge $\langle t_a \rangle$ in Fig. 6. However, all the selected events are located on the left and downward from $\langle t_a \rangle$, thus revealing a lower mean fragment charge, whereas no events are found on the other side. Hence, despite a poor charge resolution, the average total charge for the selected events is at least notably lower than 98 with a high probability. In order to make an ultimate conclusion about the total charge, one should consider the correlated FF pairs and trace down the lines of individual charges.

In addition to the experimental work, we continue the theoretical study of CCT. Significant support for the CCT hypothesis was obtained recently in our more detailed calculations of the potential energy surface (PES) of the Cf nucleus carried out in the framework of the procedure presented in [6, 7] based on the Strutinsky method. Figure 7*a* depicts the shape of the fissioning nucleus at the bottom of the "symmetry" valley with the quadrupole moment $Q_2 = 7.52$ a.u. (see Fig. 8 in [7]). As was already pointed out in our previous works [7–10], the system that fissions in the vicinity of the bottom of the potential valley constitutes two magic nuclei (clusters) connected by a neck. In Fig. 7*a*, these clusters are the deformed magic nuclei of $^{106}\mathrm{Mo}_{64}$ ($\beta_2 \sim 0.58$). In the calculations, the shape of the system was varied in such a way that the value of $Q_2$ remained constant while the mass-asymmetry $\eta$ changed starting from the value corresponding to the valley's bottom. By definition,

$$\eta = (M_1 - M_2)/M_c,$$

where $M_{1,2}$ is the mass of the system concentrated, respectively, on the left and on the right sides of the varied boundary, which divides the nuclear body into two parts (marked by vertical lines in Fig. 7), and $M_c$ is the mass of the fissioning nucleus. As a result, the new shape of the system shown in Fig. 7*b* was revealed for the first time. The energy of the system is only slightly higher (by $\sim$2 MeV) than the corresponding value at the bottom. The distinguishing feature of the shape observed is the double waist which vividly divides the system into three parts of comparable sizes. It would appear reasonable to

identify the double rupture of such a configuration as the true ternary fission so long sought. The fact that it was not discovered before may be due to the special kinematics of the process being collinear in nature. As mentioned above, two outside fragments of the three-body chainlike configuration should fly apart along the chain axis, while the central one could stay almost at rest. In addition, one might expect that the scission probability achieves its maximum value when the length of the system is close to the sum of large axes of the constituted clusters. The clusters of Mo, Sr, and, presumably, $^{48}Ar_{30}$ (according to [11], there is a strong shell correction minimum for $N = 30$ at $\beta_2 \sim 0.52$) could be the products of the CCT in this case. For the moment, we have obtained only the first theoretical indication of the possible existence of the Mo–Ar–Sr CCT valley in the $^{252}$Cf nucleus. It seems to us that the possible existence of akin valleys (modes) built on other clusters is not ruled out.

To summarize, we conclude that we observe the structure linked presumably with collinear tripartition just in the raw neutron gated data presented in Fig. 3. This conclusion is confirmed by the preliminary analysis of the FF charge and neutron multiplicity measured as well as by the recent calculations of the PES. That is the most promising result for the moment while processing of the data obtained is still in progress.

## ACKNOWLEDGMENTS

We are grateful to L.V. Pashkevich for her help in preparing the English version of the manuscript. This work is supported in part by the Russian Foundation for Basic Research (project no. 00-02-16577) and by the CRDF (grant no. Mo-011-0).

## REFERENCES

1. H.-G. Ortlepp *et al.*, Nucl. Instrum. Methods Phys. Res. A **403**, 65 (1998).
2. Yu. V. Pyatkov *et al.*, in *Proceedings of the International Conference on Nuclear Physics "Nuclear Shells—50 Years," Dubna, 1999,* Ed. by Yu. Ts. Oganessian and R. Kalpakchieva (World Sci., Singapore, 2000), p. 144.
3. A. A. Alexandrov *et al.*, *Heavy Ion Physics, FLNR JINR Scientific Report 1999–2000,* Ed. by A. G. Popeko, E7-2001-173 (Dubna, 2001), p. 159.
4. D. V. Kamanin *et al.*, this Proceedings.
5. A. Oed *et al.*, Nucl. Instrum. Methods Phys. Res. **205**, 451 (1983).
6. V. V. Pashkevich, Nucl. Phys. A **169**, 275 (1971).
7. Yu. V. Pyatkov *et al.*, Nucl. Phys. A **624**, 140 (1997).
8. Yu. V. Pyatkov and R. A. Shekhmamet'ev, Yad. Fiz. **57**, 1182 (1994) [Phys. At. Nucl. **57**, 1116 (1994)].
9. Yu. V. Pyatkov *et al.*, Izv. Ross. Akad. Nauk, Ser. Fiz. **60** (11), 30 (1996).
10. Yu. V. Pyatkov *et al.*, Nucl. Phys. A **611**, 355 (1996).
11. H. Märten, private communication.

*Physics of Atomic Nuclei, Vol. 66, No. 9, 2003, pp. 1636–1638. From Yadernaya Fizika, Vol. 66, No. 9, 2003, pp. 1684–1686.*


# Applications of the Total Absorption $\gamma$-Ray Spectroscopy for $\beta$-Decay Study*

**I. N. Izosimov[1)]**, A. A. Kazimov[1)], V. G. Kalinnikov[2)], A. A. Solnyshkin[2)], and J. Suhonen[3)]**

[1)] *Khlopin Radium Institute, St. Petersburg, 194021 Russia*

[2)] *Dzelepov Laboratory of Nuclear Problems, Joint Institute for Nuclear Research, Dubna, Moscow oblast, 141980 Russia*

[3)] *Department of Physics, University of Jyväskylä, Jyväskylä, Finland*

Received August 28, 2002

**Abstract**—Applications of total absorption $\gamma$-ray spectroscopy (TAS) for measurements of the beta-decay strength function, for completeness testing of decay schemes, and for determination of total beta-decay energy are discussed. Applications of TAS in combination with high-resolution $\gamma$ spectroscopy for studying the fine structure of the beta-decay strength function are demonstrated. Results for $^{147g}$Tb ($T_{1/2} \simeq 1.6$ h) and for $^{156}$Ho ($T_{1/2} \simeq 56$ min) are presented. © *2003 MAIK "Nauka/Interperiodica".*

## INTRODUCTION

Total absorption $\gamma$-ray spectroscopy (TAS) is applied for measurements of the $\beta$-decay strength function $S_\beta(E)$ [1, 2] and for determination of total energies $Q_\beta$ [1–3]. A combination of TAS with high-resolution $\gamma$ spectroscopy was also used for construction of decay schemes and its completeness testing, and for $S_\beta(E)$ fine-structure study [4–7].

Total absorption spectroscopy is based on summation of cascade $\gamma$-ray energies in $4\pi$ geometry. The population of the levels after $\beta$ decay and the $\beta$-decay strength function are determined from the shape of the accompanying $\beta$-decay TAS $\gamma$ spectra [1]. The end point of the TAS $\gamma$ spectrum is determined by the total energy $Q_\beta$ of the $\beta$ decay [1, 3].

Our TAS $\gamma$ spectrometer (TAGS) [3] consists of two NaI(Tl) crystals $200 \times 110$ and $200 \times 140$ mm$^2$ in size. The larger crystal has a $70 \times 80$-mm$^2$ well into which the nuclei under study are supplied and where the Si(Au) detector is installed. Its sensitive layer is 2 mm thick and allows $\beta$-particle detection. Because the energy resolution of TAGS is not so high, we used $Z$-separated (radiochemically) and $A$-separated (mass separator) sources in our experiments. Contamination from the decay products scarcely influences the results because of their longer half-life and smaller total decay energies.

## STRENGTH FUNCTION STUDY

For $\beta$ transitions of Gamow–Teller type, $S_\beta(E)$ can be written as [1]

$$S_\beta(E) = \frac{B'_\mp(\mathrm{GT}, E)}{D(g_V^2/g_A^2)}, \qquad (1)$$

$$B'_\mp(\mathrm{GT}, E) = \frac{4\pi}{g_A^2} B_\mp(\mathrm{GT}, E) \qquad (2)$$

$$= \frac{1}{2I_i + 1} |\langle I_f || \sum_{k,\mu} t_\mp(k) \sigma_\mu(k) || I_i \rangle|^2,$$

where $I_i$ and $I_f$ are the spins of the initial and final nuclei states, $g_A$ and $g_V$ are the coupling constants of the axial-vector and vector components of the $\beta$ decay, $D = 6260 \pm 60$ s, and $t_\mp\sigma$ is the product of the isospin and spin operators giving the respective operators of the Gamow–Teller $\beta^-$ or $\beta^+$/EC decays.

The charge-changing elementary excitations with isospin $T = 1$ and its $z$ projection $M_T = +1$ can manifest themselves in Gamow–Teller $\beta^+$/EC decay. The Gamow–Teller $M_T = +1$ resonance is a coherent superposition of such elementary excitations at high energy [1]. Using our TAGS, we detected [3] Gamow–Teller $M_T = +1$ resonance for $^{147g}$Tb ($T_{1/2} \simeq 1.6$ h) $\beta^+$/EC decay as a strong peak at $E \simeq 4$ MeV. Using the combination of the TAS and high-resolution, we studied its fine structure [4, 6]. Only qualitative agreement between experimental fine structure and theoretical fine structure (Fig. 1) for the Gamow–Teller $M_T = +1$ resonance was obtained.

*This article was submitted by the authors in English.

** e-mail: izosimov@atom.nw.ru

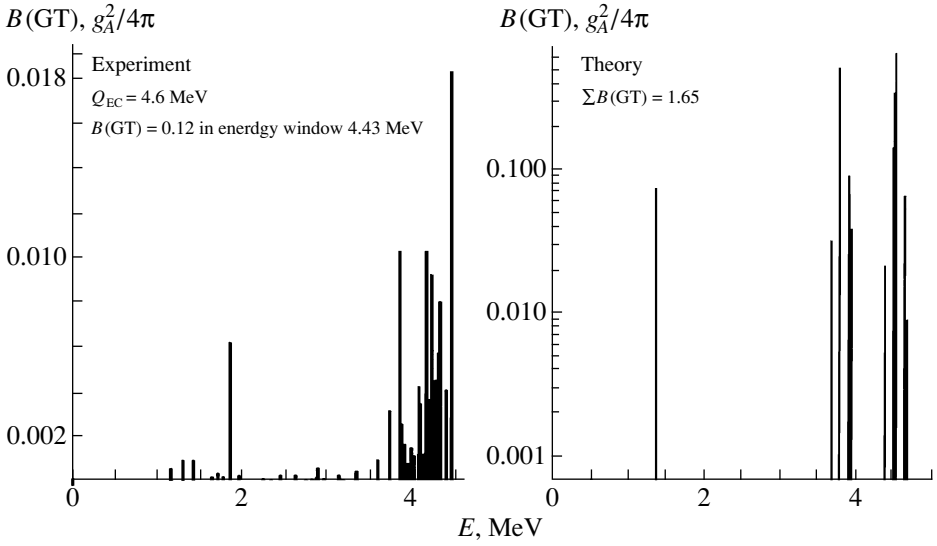


**Fig. 1.** Experimental and theoretical (MQPM model) fine structure of the $^{147g}$Tb $\beta^+$/EC-decay strength function.

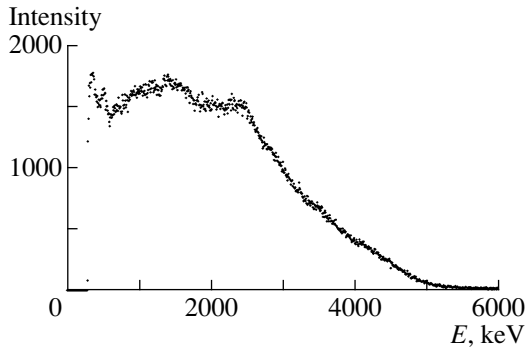


**Fig. 2.** TAS $\gamma$ spectrum for $^{156}$Ho $\beta^+/EC$ decay.

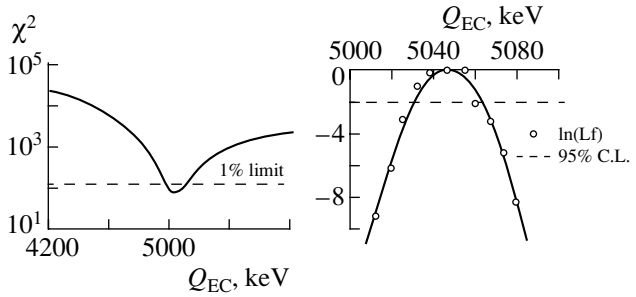


**Fig. 3.** $\chi^2$ (logarithmic scale) and likelihood function (Lf) natural logarithm (ln(Lf)) dependence on the $^{156}$Ho total EC energy. The error connected with the likelihood function width was determined [8] at 68% C.L. (ln(Lf) = −0.5). The analyzing energy interval was 4.27–5.02 MeV.

Theory predicts more strength than was experimentally observed. This is a typical situation for both $\beta^+$/EC and $\beta^-$ decays. For $^{147g}$Tb $\beta^+$/EC decay, not all the strength is in the $Q_{EC}$ window.

For a more detailed analysis of the $\beta^+$/EC-decay strength function in this region, it is necessary to have experimental data on $S_\beta(E)$ in nuclei, where all the $\beta^+$/EC strength lies within the $Q_{EC}$ window. Such a possibility exists for $^{145,143,141}$Tb $\beta^+$/EC decays.

## MEASUREMENT OF THE TOTAL ELECTRON-CAPTURE ENERGY $Q_{EC}$

We used our TAGS for $^{156}$Ho ($T_{1/2} \simeq 56$ min) total $\beta^+$/EC-decay energy $Q_{EC}$ measurements. The $Q_{EC}$ value is connected with the TAS $\gamma$-spectrum end point. The most informative region for determination of the TAS spectrum end point, as a rule, has low counting per channel, and it may be very difficult to determine the end point of the TAS $\gamma$ spectrum directly. The part of the TAS spectrum with enough high statistics is not so informative for end point determination. Thus, there is some optimal TAS spectrum interval for determination of the $Q_{EC}$ value. We use the $\chi^2$ criterion for hypothesis testing and for optimal energy interval selection [3]. For estimation of $Q_{EC}$ and errors, we use the maximum-likelihood method, which gives a result with minimum possible errors [8]. Theoretical spectra are constructed as

$$N(E) = \int_0^{Q_{EC}} S_\beta(e) f(e, Q_{EC}) \epsilon(e) \phi(e, E) de, \quad (3)$$

where $S_\beta(E)$ is the $\beta^+$/EC-decay strength function, $f(e, Q_{EC})$ is the Fermi function for $\beta^+$/EC decay, $\epsilon(e)$ is the spectrometer efficiency, and $\phi(e, E)$ is the re-

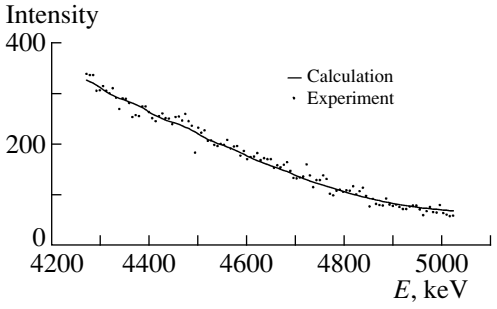


**Fig. 4.** Experimental and calculated TAS $\gamma$ spectra for $^{156}$Ho.

sponse function of the spectrometer calculated using the MCNP code.

The TAS $\gamma$ spectrum for $^{156}$Ho $\beta^+/EC$ decay is shown in Fig. 2. The optimal energy interval for TAS $\gamma$-spectrum analysis was selected using the $\chi^2$ criterion [3] (Figs. 3, 4). From the $\chi^2$ minimum, we estimated the $Q_{\mathrm{EC}}$ value and, after linearization, the error $\delta Q_{\mathrm{EC}}$. We obtained $Q_{\mathrm{EC}} = 5.05 \pm 0.09$ MeV.

As was recommended by Hudson [8] for hypothesis testing, the $\chi^2$ criterion must be used and the maximum-likelihood method must be used for estimation of parameters. The likelihood function for the selected energy interval was constructed using a Poisson distribution and is shown in Fig. 3. Using standard procedures for the maximum-likelihood method, we obtained $Q_{\mathrm{EC}} = 5.05 \pm 0.02$ MeV. The error $\delta Q_{\mathrm{EC}}$ consists of two approximately equal parts. The first part is connected with the uncertainty in determination of the likelihood function maximum and the second one (Fig. 3) is connected with the likelihood function width. Comparing results obtained by the $\chi^2$ method with linearization and by the maximum-likelihood method, we conclude that the maximum-likelihood method is more effective for analysis. Our result is in good agreement with systematics [9].

## ACKNOWLEDGMENTS

This work was supported in part by the Russian Foundation for Basic Research (project no. 00-02-16695).

## REFERENCES

1. Yu. V. Naumov *et al.*, Fiz. Élem. Chastits At. Yadra **14** (2), 420 (1983) [Sov. J. Part. Nucl. **14** (2), 175 (1983)].
2. I. N. Izosimov *et al.*, J. Phys. G **24**, 831 (1998).
3. I. N. Izosimov *et al.*, Phys. Part. Nucl. Lett., No. 2[111], 36 (2002).
4. J. Wawryszczuk *et al.*, Z. Phys. A **375**, 39 (1997).
5. I. N. Izosimov, Fiz. Élem. Chastits At. Yadra **30** (2), 321 (1999) [Phys. Part. Nucl. **30** (2), 131 (1999)].
6. I. N. Izosimov *et al.*, Phys. Part. Nucl. Lett., No. 2[101], 40 (2000).
7. I. N. Izosimov *et al.*, Czech. J. Phys., Sect. A **51**, A277 (2001).
8. D. J. Hudson, *Lectures on Elementary Statistics and Probability* (CERN, Geneva, 1964).
9. G. Audi and A. H. Wapstra, Nucl. Phys. A **595**, 409 (1995).

*Physics of Atomic Nuclei, Vol. 66, No. 9, 2003, pp. 1639–1642. From Yadernaya Fizika, Vol. 66, No. 9, 2003, pp. 1687–1690.*


# Exploring the Neutron Drip Line at the Ne–Mg Region*

**S. M. Lukyanov[1)]**, Yu. E. Penionzhkevich[1)], D. Guillemaud-Mueller[2)], M. Lewitowicz[3)], R. Anne[3)], R. Astabatyan[1)], D. Baiborodin[4)], C. Borcea[5)], A. Buta[5)], F. de Oliveira Santos[3)], Z. Dlouhý[4)], G. Faivre[2)], S. Grevy[6)], G. Georgiev[3)], F. Ibrahim[2)], S. Lobastov[1)], I. Matea[3)], J. Mrazek[4)], A. C. Mueller[2)], F. Negoita[5)], F. Pougheon[2)], O. Perru[2)], Yu. G. Sobolev[1)], I. Stefan[5)], and D. Verney[3)]**

[1)] *Joint Institute for Nuclear Research, Dubna, Moscow oblast, 141980 Russia*

[2)] *IPN, Orsay, France*

[3)] *GANIL, Caen, France*

[4)] *NPI, Řež, Czech Republic*

[5)] *NIPNE, Bucharest, Romania*

[6)] *LPC, Caen, France*

Received August 28, 2002

**Abstract**—The neutron drip line in the neon–magnesium region has been explored by the projectile fragmentation of a $^{48}$Ca(59.8 $A$ MeV) beam using the new fragment separator LISE-2000 at GANIL. New neutron-rich isotopes, $^{34}$Ne and $^{37}$Na, have been observed together with some evidence for the particle instability of $^{33}$Ne and $^{36}$Na. © *2003 MAIK "Nauka/Interperiodica".*

The study of the properties of neutron-rich nuclei far from stability is one of the most exciting areas of modern research in nuclear physics. The progress in our knowledge of the properties of these nuclei has enormously broadened because of the new radioactive ion beam facilities and the development of very sophisticated fragment separators.

One interesting feature has been found in the region of the light neutron-rich nuclei. As was established in 1975 by Thibault *et al.* [1], neutron-rich nuclei with $N \approx 20$ constitute a good example of shape coexistence of spherical and deformed configurations (for example, $^{32}$Mg). In the frame of the shell model, the deformed ground state in $^{32}$Mg is a consequence of the strong correlation energy of $2p$–$2h$ neutron excitations from the *sd* to the *pf* shell. It was suggested that the extra binding energy was gained by the deformation associated with the particle–hole excitation across the $N = 20$ shell gap. If a nucleus gains binding energy through deformation, the drip line extends farther than expected for a closed shell. Recent experiments at GANIL, MSU, and RIKEN were dedicated to the study of the stability of the neutron-rich nuclei with $Z > 7$ and around $N = 20$. The variation of the shell gap and deformation as a function of $N$ and $Z$ could be a major challenge.

Among the recent experiments dedicated to explore the neutron drip line in the region of elements from O to Mg, one could mention those on the particle instability of the neutron-rich oxygen isotopes $^{26,28}$O [2–4] and on the discovery of the particle stability of $^{31}$Ne [5] and $^{31}$F [6]. The appearance of a so-called "island of inversion" with respect to the particle stability of isotopes has been claimed through various theoretical predictions. A particular feature in this region is the progressive development of prolate deformation in spite of the expected effect of spherical stability due to the magicity of the neutron number $N = 20$ [7–10]. It was argued that the deformation might lead to enhanced binding energies in some as yet undiscovered neutron-rich nuclei. The particle stability of $^{31}$F gives strong evidence on the onset of deformation in the region. One may expect that the drip line for the fluorine–magnesium elements could move far beyond the presently known boundaries.

Therefore, there is great interest in studying nuclei in the region of the neutron closure $N = 28$. Experimentally, the properties of $^{44}$S have been studied and it was concluded that the ground state of $^{44}$S is deformed. This result suggested a significant breaking of the $N = 28$ closure for nuclei near $^{44}$S.

*This article was submitted by the authors in English.

**e-mail: lukyanov@flnr.jinr.ru

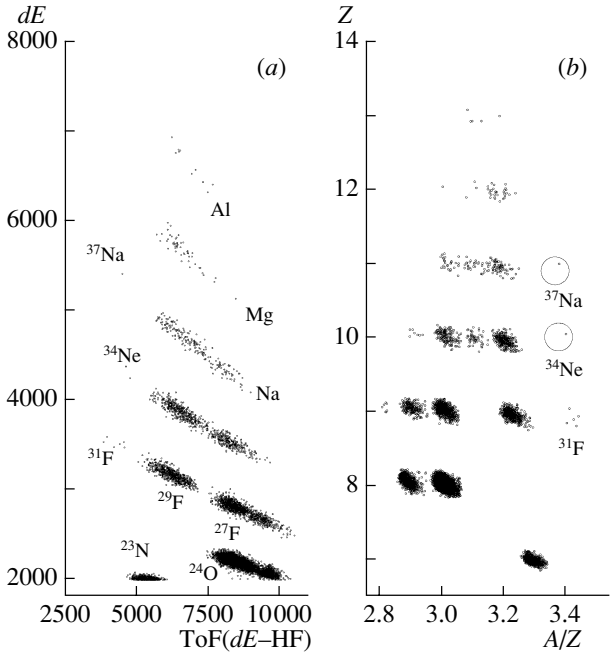


**Fig. 1.** (*a*) Energy loss $dE$ vs. time-of-flight ToF ($de$–HF) identification matrix. (*b*) Two-dimensional $A/Z$ versus $Z$ plot obtained in the reaction of a 58.9$A$ MeV $^{48}$Ca beam on a 161-mg/cm$^2$ tantalum target during a 2.5-d run. The new isotopes $^{34}$Ne (two events) and $^{37}$Na (one event) are clearly visible. No events associated with $^{33}$Ne, $^{36}$Na, and $^{40}$Mg were observed.

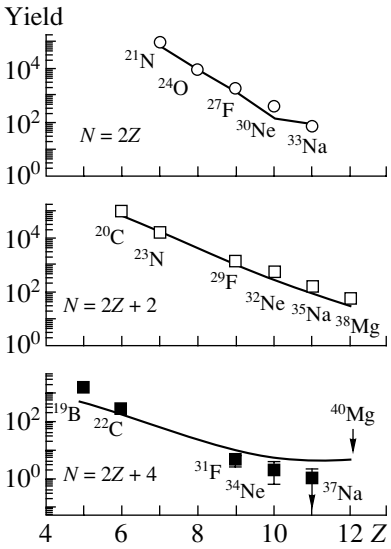


**Fig. 2.** Isotopic production for nuclei with the neutron number $N = 2Z$, $N = 2Z + 2$, and $N = 2Z + 4$. The solid lines present the expected yields according to the LISE code.

In this work, we present the results of our attempt to determine the neutron drip line for the Ne–Mg isotopes in the region of the neutron numbers $N = 20$–28. In particular, our experiment was dedicated to the direct observation of the $^{31}$F, $^{34}$Ne, $^{37}$Na, and $^{40}$Mg nuclei. These nuclei were searched for among the fragmentation products of a 59.8 $A$ MeV $^{48}$Ca beam on a 160-$\mu$m tantalum target. The very neutron-rich beam and target were chosen to optimize the production rate of the drip-line nuclei in accordance with the LISE code [11, 12] and the results of the previous work [13]. The mean intensity of the $^{48}$Ca beam was 150 p nA. The experiment benefited from a recent update of the LISE [14] spectrometer to the LISE-2000 [15] level. The upgrade includes an increase in the maximum magnetic rigidity to 4.3 T m, an increase by a factor of 2.5 in the angular acceptance, and a new line with improved optics. As a consequence, a total increase by a factor of 10 in the production rate of the drip-line nuclei has been achieved with respect to using the standard LISE spectrometer.

The reaction fragments were collected and analyzed by the LISE-2000 spectrometer operated in an achromatic mode and at the maximum values of momentum acceptance (5%) and solid angle (1.9 msr). The magnetic rigidity of the first and the second half of the spectrometer was set at 3.48 and 3.391 T m, respectively. To reduce the overall counting rate due to light isotopes, a beryllium wedge with a mean thickness of 563 mg/cm$^2$ was placed at the momentum dispersive focal plane.

In addition to the standard identification method of the fragments via time-of-flight (ToF), energy loss ($dE$) and total kinetic energy (TKE), a multiwire proportional detector was placed in the dispersive plane of the LISE-2000 spectrometer. This detector allowed measuring the magnetic rigidity of each fragment via its position in the focal plane, improving the mass-to-charge resolution ($A/Q$). The sensitive area of this detector was 10 cm (H) $\times$ 5 cm (V), covering the full momentum acceptance of the spectrometer. The cathode wires were individually read out. A spatial resolution of 0.5 mm was achieved for a counting rate of $10^4$ particles/s. The typical efficiency for this particle detector was about 80%. The mass-to-charge ratio ($A/Q$) was obtained with an accuracy of 0.8%. The selected fragments were implanted in a telescope consisting of seven silicon detectors for the identification of the fragments. In the data analysis, the fully stripped fragments were selected by putting gates on the total kinetic energy measured with the silicon telescope.

The result of the particle identification based only on the $dE$, ToF, and TKE is shown in Fig. 1$a$, where the energy loss measured in the first detector of the telescope is plotted vs. ToF between the $dE$ silicon telescope and the cyclotron radio frequency. This matrix was obtained from the data accumulated over

2.5 d with a mean intensity of the primary beam of 150 p nA. The new isotopes $^{34}$Ne (two events) and $^{37}$Na (one event) are clearly visible. The discovery of $^{31}$F [6] is also confirmed. The $^{34}$Ne and $^{37}$Na isotopes have also been unambiguously identified by using the calculated value of $A/Z$. This value was obtained from the ToF and from $B\rho$, measured by means of the multiwire detector. The two-dimensional $A/Z$ vs. $Z$ plot is shown in Fig. 1*b*. The presence of the events corresponding to $^{34}$Ne and $^{37}$Na confirms that these nuclei are bound. The one event of $^{34}$Ne is absent in Fig. 1*b* due to the fact that the efficiency of the multiwire detector is only 80% for light fragments. No events that could be attributed to $^{33}$Ne, $^{36}$Na, and $^{40}$Mg were observed.

Yields of $N = 2Z$, $N = 2Z + 2$, and $N = 2Z + 4$ nuclei vs. the $Z$ value are shown in Fig. 2. The yield estimates for the fragments were calculated according to the LISE code [12]. An attempt to describe the experimental distributions of the fragments was undertaken by a convolution of Gaussian form of the beam velocity and of an exponential tail at lower energies.

The experimental data were fitted by the same value of $\sigma = 107$ MeV/$c$ (the parameter of the momentum distribution in the convolution [12]) for the three different cases $N = 2Z$, $N = 2Z + 2$, and $N = 2Z + 4$. For nuclei with $N = 2Z$ and $N = 2Z + 2$, we found an agreement between the experimental and calculated values. The calculated values for the nuclei with $N = 2Z + 4$ is higher than the experimental ones for $Z$ greater than 6.

In this region, the most interesting nuclide is $^{40}$Mg, which is probably not bound since no counts have been observed. We estimated the upper limit for the production cross section of $^{40}$Mg to be less than 0.06 pb. However, the present results do not allow drawing a definite conclusion on the instability of $^{40}$Mg; this is also supported by the trend of the calculated yield in Fig. 2. The production cross section for $^{34}$Ne and $^{37}$Na was estimated to be about $0.17 \pm 0.12$ and $0.06 \pm 0.06$ pb, respectively. The cross section for $^{31}$F is estimated to be about 0.7 pb. This value for the production of $^{31}$F in the reaction $^{48}$Ca + $^{\mathrm{nat}}$Ta at 59.8 $A$ MeV is about 5 times higher than in the reaction $^{40}$Ar + Ta at 94.1 $A$ MeV [6].

From the theoretical point of view, the description of the light nuclei in the $sd$–$pf$ shells is still a problem. In particular, the calculation of the binding energy for the very neutron-rich isotopes of O, F, Ne, and Na is a real challenge. There are various theoretical calculations (viz., the finite-range liquid-drop model (FRLD) [16], two versions of the shell model (SM) [17–19], the relativistic mean-field theory [20], and the Hartree–Fock model [21]) that predict the position of the neutron drip line in this region. For instance, the FRLD model gives a very strong binding energy for $^{40}$Mg. In the framework of this model, one- and two-neutron separation energies are even above 3.4 MeV. One may note that the FRLD model gives correct predictions for the stability of $^{31}$Ne and $^{31}$F, implying nuclear deformation effects for both the macroscopic and the microscopic parts. According to the shell-model predictions [18], the last bound isotopes are $^{24}$O, $^{27}$F, $^{34}$Ne, $^{37}$Na, $^{38}$Mg, and $^{43}$Al. However, slight changes of the drip line cannot be excluded since $^{37}$Na was predicted to be bound only by 250 keV, while $^{31}$F, $^{40}$Mg, and $^{43}$Al are unbound by 145, 470, and 550 keV, respectively. According to another shell-model calculation [17], $^{26}$O, $^{34}$Ne, and $^{40}$Mg are the last stable isotopes against two-neutron emission, as indicated by their maximal binding energy. Both SM and HF calculations for even-mass O, Ne, and Mg indicate a disappearance of shell magic numbers and suggest an onset of deformation and a shape coexistence in this region.

The stability/instability of the present nuclei can be explained by taking into account various degrees of mixing in the $sd$ and $fp$ shells, which are related to the deformation effects. According to our results, the neutron drip line is extended beyond $N = 20$ and reaches $N = 24$ for neon and even $N = 26$ for sodium isotopes as a consequence of the mixing of the $d_{3/2}$ and $f_{7/2}$ states, while the $N = 20$ shell closure disappears.

In summary, the neutron-rich isotopes $^{34}$Ne and $^{37}$Na were observed using the newly upgraded LISE-2000 spectrometer and the reaction $^{48}$Ca + $^{\mathrm{nat}}$Ta at 59.8 $A$ MeV. Thus, most probably, the neutron drip line has been reached for the neon and sodium isotopes. However, it seems that, to conclude definitely whether these isotopes do mark the drip line or do not, one will need to pursue further experimental efforts.

## ACKNOWLEDGMENTS

We would like to express our graduate to the members of the FLNR (JINR, Dubna)–GANIL (France) collaboration for the fruitful experimental efforts and discussions of the experimental results obtained in the joint experiments. This work has been carried out with financial support from PICS (IN2P3) project no. 1171, INTAS (grant no. 00-00463), the Russian Foundation for Basic Research (project no. 96-02-17381a), and grant GA ASCR A1048102 of the Czech Republic.

## REFERENCES


1. C. Thibault *et al.*, Phys. Rev. C **12**, 644 (1975).
2. D. Guillemaud-Mueller *et al.*, Z. Phys. A **332**, 189 (1989).
3. O. B. Tarasov *et al.*, Phys. Lett. B **409**, 64 (1997).
4. M. Fauerbach *et al.*, Phys. Rev. C **53**, 647 (1996).
5. H. Sakurai *et al.*, Phys. Rev. C **54**, R2802 (1996).
6. H. Sakurai *et al.*, Phys. Lett. B **448**, 180 (1999).
7. X. Campi *et al.*, Nucl. Phys. A **251**, 193 (1975).
8. R. Nayak and L. Satpathy, Nucl. Phys. A **304**, 64 (1978).
9. A. Poves and J. Retamosa, Nucl. Phys. A **571**, 221 (1994).
10. E. K. Warburton, J. A. Becker, and B. A. Brown, Phys. Rev. C **41**, 1147 (1990).
11. D. Bazin *et al.*, Nucl. Instrum. Methods Phys. Res. A **482**, 307 (2002).
12. ftp://ftp.nscl.msu.edu/lise; http://www.nscl.msu.edu/lise.
13. O. B. Tarasov *et al.*, Nucl. Phys. A **629**, 605 (1998).
14. R. Anne *et al.*, Nucl. Instrum. Methods Phys. Res. A **257**, 215 (1987).
15. R. Anne, Preprint GANIL, GANIL P02 01 (2000).
16. P. Moller *et al.*, At. Data Nucl. Data Tables **39**, 225 (1988).
17. G. A. Lalazissis *et al.*, Phys. Rev. C **60**, 014310 (1999).
18. E. Caurier *et al.*, Phys. Rev. C **58**, 2033 (1998).
19. Y. Utsuno *et al.*, Phys. Rev. C **64**, 011301 (2001).
20. Z. Ren *et al.*, Phys. Rev. C **52**, R20 (1995).
21. J. Terasaki *et al.*, Nucl. Phys. A **621**, 706 (1997).

Physics of Atomic Nuclei, Vol. 66, No. 9, 2003, pp. 1643–1645. From Yadernaya Fizika, Vol. 66, No. 9, 2003, pp. 1691–1693.


# Space Charge Effects of Intense Particle Beams*

**S. Maydanyuk, M. Dolinska, N. Doroshko, and V. Olkchovsky****

*Institute for Nuclear Research, National Academy of Sciences of Ukraine, Kiev, Ukraine*

Received August 28, 2002

**Abstract**—The analytical solutions for the potentials and electrical fields are derived, assuming bunches of spherical shape with homogeneous and parabolic particle distributions to estimate space charge effects of intense particle beams. The trajectories of electrons created within bunches by residual gas ionization have been calculated taking into account the typical parameters of the RF accelerators. © *2003 MAIK "Nauka/Interperiodica".*

## INTRODUCTION

For precise nuclear measurements of beam parameters, it is important to know exact information about the ion beam parameters. For a high ion current, it is necessary to take into account the space charge influence on the longitudinal emittance.

In this paper, the bunched beams that are typical for RF accelerators [1] are described. The bunches are approximated by a sphere with homogeneous and parabolic charge density distribution.

In comparison with the numerical calculations, the presented analytical solutions have some advantages. The potentials and field strengths generated by a bunch are known at any geometrical position. Once the potentials and electromagnetic fields are calculated for a single bunch at rest, the evaluation of time-dependent potentials and fields generated by a moving chain of bunches is straightforward.

## 1. THE ELECTRIC POTENTIAL

In general, in RF accelerators, the geometrical dimensions of a bunch are very similar in the two transverse directions. In the following, we assume a spherical shape for a single bunch. Considering different distributions of the particles within the bunches, we have to find an analytical solution of the Poisson equation.

**1. Charge distribution of bunches.** For spherical bunches, we will consider two cases: homogeneous and parabolic charge distribution within the bunch. In the first case, the spatial density distribution is described by the well-known distribution function of Kapchinskij–Vladimirskij; in the second case, by the Waterberg distribution [2].

**2. The potential of bunches.** The solution of the Poisson equation in the case of a homogeneously charged sphere is straightforward and the result is

$$\phi_{\text{ish}}(r) = \frac{N\zeta e}{4\pi\varepsilon_0}\left(\frac{3}{2R} - \frac{r^2}{2R^3}\right), \qquad (1)$$

$$\phi_{\text{osh}}(r) = \frac{N\zeta e}{4\pi\varepsilon_0}\frac{1}{r}, \qquad (2)$$

where $R$ is the radius of the beam sphere, $N$ is the number of particles within the bunch, $\zeta$ is their charge, $\varepsilon_0$ is the electric constant, and $e$ is the electron charge.

Equation (1) describes the potential inside the spherical bunch and (2) gives the potential outside the bunch.

For a parabolic distribution, the potential inside the sphere becomes

$$\phi_{\text{isp}}(r) = \frac{N\zeta e}{4\pi\varepsilon_0}\left(\frac{15}{8R} - \frac{5r^2}{4R^3} + \frac{3R^4}{8R^5}\right). \qquad (3)$$

Of course, the potential outside the sphere is the same as given by Eq. (2).

## 2. THE ELECTRIC FIELDS OF THE BUNCHES

For the determination of the electric fields of the bunches, we use the equation

$$\mathbf{E}(r) = -\boldsymbol{\nabla}\phi(r).$$

Inside the spherical bunch, it is given by

$$E_{\text{ish}}(r) = \frac{N\zeta e}{4\pi\varepsilon_0}\frac{r}{R^3}, \qquad (4)$$

*This article was submitted by the authors in English.

**e-mail: kinr@kinr.kiev.ua

1063-7788/03/6609-1643$24.00 

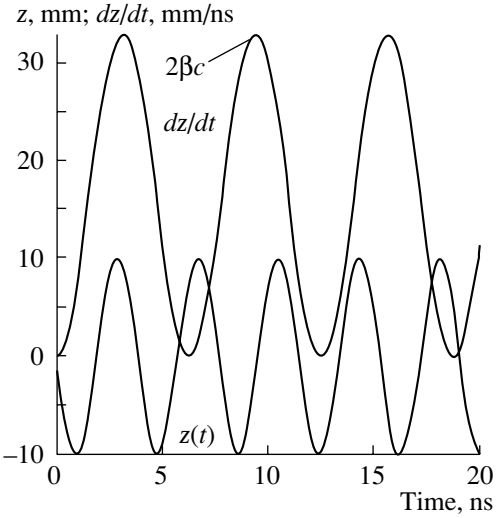


**Fig. 1.** The trajectory and velocity of an electron inside a moving homogeneous charged bunch.

and outside the field, it has to follow immediately from Eq. (2),

$$E_{\rm osh}(r) = \frac{N\zeta e}{4\pi\varepsilon_0}\frac{1}{r^2}. \qquad (5)$$

From Eq. (3), the field inside the parabolic charge bunch is

$$E_{\rm isp}(r) = \frac{N\zeta e}{4\pi\varepsilon_0}\left(\frac{5}{2}\frac{r}{R^3} - \frac{3}{2}\frac{r^3}{R^5}\right), \qquad (6)$$

and outside the bunch the field is the same as given by Eq. (5).

There is an important difference between the location of the maximum field strength in the two cases, which has some consequences concerning the motion of the particles in the phase space. From Eq. (6), it follows that the maximum of the electric field strength occurs at $r = (\sqrt{5}/3)R$ in the case of the parabolic intensity distribution instead of at $r = R$ as in the case of a homogeneous charge distribution.

## 3. THE MOTION OF ELECTRONS IN THE FIELDS OF MOVING BUNCHES

**1. Capture and oscillation of electrons within the homogeneous charged bunch.** Assuming the movement of the bunch in the longitudinal direction, the differential equation for the homogeneously charged sphere can be derived from Eq. (4) as

$$\ddot{z} = -\omega^2(z - \beta ct), \qquad (7)$$

with $\omega^2 = N\zeta e^2/(4\pi\varepsilon_0 m_e R^3)$, where $m_e$ is the mass of the electron and $\beta$ is the relativistic factor.

The trajectory of an electron inside the moving bunch is described by the solution to differential Eq. (7):

$$z(t) = \frac{v_z(0) - \beta c}{\omega}\sin(\omega t) + z(0)\cos(\omega t) + \beta ct, \qquad (8)$$

where $v_z(0)$ and $z(0)$ are the initial velocity and position of the electron.

To derive the condition to catch the electron within the bunch, we consider Eq. (7) for $\beta = 0$ and $\dot{z} = y$. It leads to a simple differential equation. The solution determines the motion of the electron in the phase plane $(z, \dot{z})$:

$$\dot{z} = \pm\sqrt{C_1 - \omega^2 z^2}, \qquad (9)$$

where $C_1$ is a free parameter. It means that the condition for stable oscillation within the bunch can be derived from the relation

$$(\beta c)^2 = \omega^2 R^2, \qquad (10)$$

which leads immediately to the required number of charges

$$N^h_{\rm min} = \frac{4\pi\varepsilon_0 R(\beta c)^2 m_e}{\zeta e^2}. \qquad (11)$$

Figure 1 shows the velocity and trajectory of the electron inside the moving bunch with the following parameters: $N^h_{\rm min} = 2.687 \times 10^9$, $\zeta = 4$, $R = 10$ mm, and $\beta = 0.055$. This result confirms the assumption of deriving the condition for stable oscillation within the bunch by relation (11).

**2. Capture and oscillation of electrons within the parabolic charged bunch.** In this case, Eq. (7) is changed to

$$\ddot{z} = -\omega^2\left(\frac{5}{2}(z - \beta ct) - \frac{3(z - \beta ct)^3}{2R^2}\right). \qquad (12)$$

Then, the movement in the phase plane is

$$\dot{z} = \pm\sqrt{C_2 + \omega_0^2(z^2 - bz^4/2)}, \qquad (13)$$

where $C_2$ is a free parameter, $\omega_0 = \sqrt{5/2}\omega$, and $b = 3/(5R^2)$. Obviously, we have to replace (10) by

$$(\beta c)^2 = \omega_0^2(z^2_{\rm max} - bz^4_{\rm max}/2), \qquad (14)$$

where $\sqrt{5}R/3 < z_{\rm max} < R$.

The relation between $N^h_{\rm min}$ for the homogeneous distribution and $N^p_{\rm min}$ for the parabolic distribution turns out to be

$$N^p_{\rm min} = (270/451)N^h_{\rm min} \approx 0.6N^h_{\rm min}. \qquad (15)$$

The trajectories of electrons are described by Eq. (12), which is solved by successive approximations of a Fourier series.

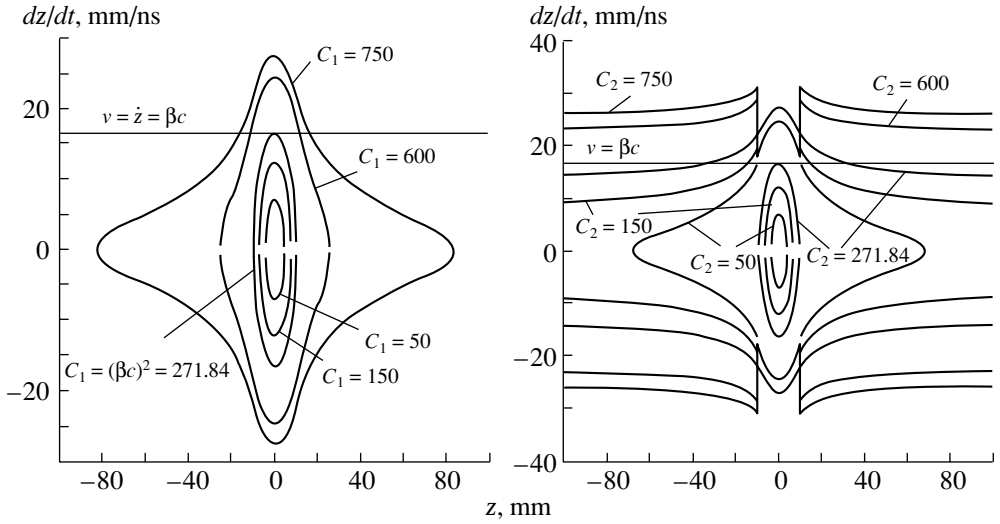


**Fig. 2.** The motion of the electron in the electric field of the moving homogeneous (left) and parabolic (right) charged bunch.

## 4. INFLUENCE OF THE FIELD OUTSIDE THE BUNCH

Because the field outside the bunch is always attracting, the electron moves in close orbits in the phase plane taking into account also the external field according to Eq. (5), which is the same for the homogeneously charged sphere and the parabolic one:

$$\ddot{z} = -\frac{R^3\omega^2}{z^2}. \qquad (16)$$

The solution is in both cases straightforward and the result for the homogeneous and parabolic charged sphere is shown in Fig. 2, taking $N^h_{\min} = 2.687 \times 10^9$ and $N^p_{\min} \sim 0.6N^h_{\min}$ for $U^{4+}$ ions. In both panels of Fig. 2, the three inner curves correspond to the motion within the bunch, while the two outer ones correspond to electrons moving also in the external field. Since such an electron moves with high speed through the bunch and may even be outside the bunch most of the time, we keep to our argumentation that those electrons will not contribute to neutralization. In addition, these electrons may be lost by the influence of other fields and distortions in the symmetry.

## CONCLUSION

The results presented may be useful for the beam diagnostics and determination of the longitudinal emittance. The partial neutralization within a bunch by capture of electrons freed by the residual gas ionization can reduce the signal of capacitive pickups or can change the required settings for focusing devices.

The estimation of the required number of ions within a single bunch for the catching of electrons gives the order of magnitude for the consideration of the neutralization of bunched beams. The investigation of the motion of the electrons and the space charge effect can be of interest for calculating the distortion of the beam profile measurements, which are based on residual gas ionization.

## REFERENCES

1. P. Strehl, in *Lecture Notes on Beam Instrumentation and Diagnostics of Courses on Accelerator Physics Technologies and Applications, Archamps, 1999,* Joint Universities Accelerator School (CERN, Switzerland, 1999), p. 104.
2. J. Struckmeier, J. Klabunde, and M. Reiser, Part. Accelerators **15**, 47 (1984).

*Physics of Atomic Nuclei, Vol. 66, No. 9, 2003, pp. 1646–1650. From Yadernaya Fizika, Vol. 66, No. 9, 2003, pp. 1694–1698.*


# Beryllium (Boron) Clustering Quest in Relativistic Multifragmentation (BECQUEREL Project)*

**V. Bradnova[1], M. M. Chernyavsky[2], L. Just[3], S. P. Kharlamov[2], A. D. Kovalenko[1], M. Haiduc[4], K. A. Kotel'nikov[2], V. A. Krasnov[2], V. G. Larionova[2], F. G. Lepekhin[5], A. I. Malakhov[1], G. I. Orlova[2], N. G. Peresadko[2], N. G. Polukhina[2], P. A. Rukoyatkin[1], V. V. Rusakova[1], N. A. Salmanova[2], B. B. Simonov[5], S. Vokal[6], and P. I. Zarubin[1]****

[1] *Laboratory of High Energies, Joint Institute for Nuclear Research, Dubna, Moscow oblast, 141980 Russia*

[2] *Lebedev Institute of Physics, Russian Academy of Sciences, Leninskiĭ pr. 53, Moscow, 117924 Russia*

[3] *Institute of Experimental Physics, SAS, Košice, Slovakia*

[4] *Institute of Space Sciences, Bucharest-Magurele, Romania*

[5] *Petersburg Institute of Nuclear Physics, Russian Academy of Sciences, Gatchina, 188350 Russia*

[6] *Šafarik University, Košice, Slovakia*

Received February 17, 2003

**Abstract**—A physical program of irradiation of emulsions in beams of relativistic nuclei named the BECQUEREL Project is reviewed. It is destined to study in detail the processes of relativistic fragmentation of light radioactive and stable nuclei. The expected results would make it possible to answer some topical questions concerning the cluster structure of light nuclei. Owing to the best spatial resolution, the nuclear emulsions would enable one to obtain unique and evident results. The most important irradiations will be performed in the secondary beams of He, Be, B, C, and N radioactive nuclei formed on the basis of JINR Nuclotron beams of stable nuclei. We present results on the charged state topology of relativistic fragmentation of the $^{10}$B nucleus at low energy–momentum transfers as the first step of the research.


## INTRODUCTION

The investigations of light nuclei situated around the boundary of neutron stability have recently developed a new direction of quest—physics of exotic nuclei. New phenomena have been established in the structure of light nuclei and in the course of nuclear reactions (see Introduction in [1]). In this domain of anomalously large radii of nuclei, the production of nucleon clusters separated in space has been observed (see Introduction in [2]). The low binding energy of nuclear clusters makes it possible to determine the structure of such nuclei as a molecular-like one.

Great progress has been made towards studying the structure of nuclei with excess and maximum number of neutrons, while research into the structure of proton-rich (or neutron-deficient) nuclei is merely being planned. The major goal of the appropriate experiments is to define the structural features of nuclei near the boundary of proton stability. Such nuclei are stable in the absence of electron shells. The structure of such nuclei can turn out to be another key in understanding the processes of nucleosynthesis. For instance, the presence of the proton halo (a proton far removed from the nucleus core) may serve as a "stringboard" for the isotope generation when advancing along the boundary of proton stability with a subsequent decay into stable isotopes.

One of the candidates for the system of the proton halo type is the $^8$B nucleus [3, 4]. We notice that the alternative transition to the solar CNO cycle can occur by the addition of a proton to the $^7$Be nucleus and a consecutive addition of the $^4$He nucleus. The produced $^{12}$N nucleus decays into a stable $^{12}$C isotope by electron capture. As compared with the well-known Hoyle version through $^8$Be, the advantage of the above-mentioned case consists in that the lifetime of the $^8$B nucleus even for a state with bound electrons is 16 orders of magnitude larger than that of the $^8$Be nucleus. Another example is the fusion of one more proton to the $^8$B nucleus resulting in the production of a $^9$C nucleus, which is also stable in the absence of bound electrons. The fusion of a $^4$He nucleus to a $^9$C one does lead to the formation of an isotope

*This article was submitted by the authors in English.

** e-mail: zarubin@lhe.jinr.ru

$^{13}$N nucleus intermediating in the CNO cycle. An unstable $^{6}$Be nucleus might play a mediator role like a $^{8}$Be one. Such examples of cluster nuclear systems may still be cited, including some nuclei in excited states.

Clustering in the above-mentioned nuclei might reflect possible paths of their synthesis. The proposed series of investigations is mostly aimed at elucidating the applicability of the picture of clustering in neutron-deficient nuclei. A program of further research of the fragmentation of neutron-deficient Be, B, C, and N isotopes by means of an emulsion technique is considered below.

## RESEARCH CONCEPT

The production of relativistic beams of radioactive light isotopes is currently under way at the JINR Nuclotron. The approaches based on the use of a charge exchange process or breakup of a lightest possible nuclide are most adequate for an emulsion technique. In this case, the mass number of an initial nucleus is conserved, beam losses in acceleration are lower, and a cluster nature of its intrinsic structure is partially set up. A certain advantage in the production of secondary beams toward increasing charge is a relative background reduction of other fragments with $Z/A$ closer to the stability region.

In general, experiments with nuclear beams at an energy of a few GeV are recognized to be one of the most promising ways for understanding the basic properties and the intrinsic structure of radioactive and unbound nuclei. Such beams can be employed to produce short-lived nuclear beams by means of breakup, charge-exchange, or fission (splitting) reactions. In the framework of such an approach, there is almost no restriction due to the lifetime of relativistic nuclei in question. A technical benefit in the analysis of relativistic proton-rich nuclei with respect to lower energy studies is a decrease in ionization to a minimum and closest to complete observation of the charge fragmentation process.

The limiting fragmentation of nuclei serves as a basis of the study of the nuclear structure. The fragmentation picture, i.e., isotopic composition and energy spectra, for one of the colliding nuclei was found to undergo a weaker dependence upon the properties of fragmentation of the other. The study of the fragmentation of relativistic nuclei may effectively supplement classical experiments on breakup of nuclei used as a target. In such an approach, the detection threshold is close to zero. It makes it possible to study fragmentation processes at rather weak nuclear excitations. The experimental approach based on the registration of the fragments of a projectile nucleus imposes a crucial requirement on the measuring technique on provision of the maximum angular resolution and the identification of fragments in a narrow forward cone (typically, a few degrees). In addition, the fragmentation process leads to a noticeably smaller ionization, which is due to the reaction products, as compared with the primary nucleus signal. This fact imposes a special requirement on the width of the sensitivity range starting from the primary nucleus down to particles with minimal ionization.

The emulsion technique can be implemented in the above-listed circumstances. In relativistic fragmentation, the nucleons produce with a large probability charged clusters, which, when decaying, are detected in emulsion as in a perfect 3D track detector. It should be stressed that emulsions are utilized in this way to register multiparticle decays of nuclei or multifragmentation events. Known cases are observations of coherent dissociation of relativistic $^{12}$C nuclei on three $\alpha$ particles and $^{16}$O on four $\alpha$ particles. We intend to extend coherent dissociation studies toward heavier stable nuclei like F, Ne, and Mg isotopes. The emulsion serves as a universal detector of the full fragmentation keeping permanent track information mostly in a single layer. This gradually reduces analysis work. Using perfect angular measurements, it is possible to get information about the excitation energy of a fragmenting nucleus.

Our approach to the study of clustering in nuclei is justified by the experience obtained when studying the relativistic $^{6}$Li in emulsion [5–7] and pilot results with a secondary beam of relativistic $^{6}$He and $^{3}$He nuclei ("beam cocktail") [8]. As development, we investigated the cluster structure of the stable isotope $^{10}$B, comparing probabilities of dissociation channels $^{10}\mathrm{B} \to (^{8}\mathrm{Be}) + d$, $\alpha + \alpha + d$, $^{6}\mathrm{Li} + \alpha$, $^{9}\mathrm{Be} + p$, etc.

## DISSOCIATION OF RELATIVISTIC $^{10}$B NUCLEI

We used a beam of $^{10}$B nuclei accelerated at the JINR Nuclotron to perform irradiation of an emulsion stack. The beam angular divergence was kept within an angle of 3 mrad. The beam profile for emulsion irradiations was formed in such a way that its horizontal size would correspond to irradiated emulsion width and the spatial beam density would be uniform enough. An emulsion irradiation dose was limited to $10^5$ beam tracks. The emulsion chamber was assembled as a stack of BR-2 type emulsion layers having sensitivity up to relativistic particles. Layers 550 $\mu$m thick had the dimensions $10 \times 20$ cm$^2$. During irradiation, the beam was directed in parallel to the emulsion plane. We present below pilot results of visual scanning that are important for the project major goal, i.e., determination of fragmentation probabilities.

**Table 1.** Charge-state distribution of the number of fragments in projectile fragmentation cone ($<15°$) in events of complete charge fragmentation (total number of events is 82)

| Total charge ($>4$) | Fragment charge $Z$ | | | | | Number of events |
|---|---|---|---|---|---|---|
| | 5 | 4 | 3 | 2 | 1 | |
| 6 | | – | – | 1 | 4 | 4 |
| 6 | | – | – | 2 | 2 | 1 |
| 6 | | – | – | – | 6 | 2 |
| 5 | | 1 | – | – | 1 | 2 |
| 5 | | – | 1 | 1 | – | 3 |
| 5 | | – | – | 1 | 3 | 26 |
| 5 | | – | – | 2 | 1 | 36 |
| 5 | 1 | – | – | – | – | 5 |
| 5 | | – | – | – | 5 | 3 |

**Table 2.** Charge-state distribution of the number of fragments in projectile fragmentation cone ($<15°$) in events of white star formation [no accompanying tracks in wide cone ($>15°$); total number of events is 35]

| Total charge ($>4$) | Fragment charge $Z$ | | | | Number of events |
|---|---|---|---|---|---|
| | 4 | 3 | 2 | 1 | |
| 6 | – | – | 1 | 4 | 3 |
| 5 | 1 | – | – | 1 | 2 |
| 5 | – | 1 | 1 | – | 1 |
| 5 | – | – | 1 | 3 | 9 |
| 5 | – | – | 2 | 1 | 18 |
| 5 | – | – | – | 5 | 2 |

All found charged tracks corresponding to relativistic boron ionization were followed to a nuclear interaction point or to an exit from the emulsion layer. In the first sample, 136 inelastic interactions were found over the scanned length of about 20 m of the initial particles. Within this sample, we defined a mean free path $\lambda = 14.7 \pm 1.2$ cm. This value is in good agreement with the mass number dependence established for uniform density nuclei like $^4$He, $^{12}$C, $^{16}$O, and $^{24}$Mg.

To clarify the general features, we concentrated current analysis on events of transfer of a total boron nucleus charge to relativistic fragments in a fragmentation cone of 15° ("complete charge fragmentation"). As correlation, such a selection gave dramatic suppression of mean target nucleus multiplicity. We have minimized the influence of interaction dynamic details in this way.

We describe a topological structure of 82 events having the total charge sum not less than five in a fragmentation cone. Table 1 presents the numbers of events with various fragment composition. The cases with total charge 6 correspond to the appearance of a relativistic meson in a fragmentation cone. As a further step, we selected 35 events (Table 2) containing neither target fragments nor produced mesons ("white stars," example shown in the figure). The obvious feature of both tables is a dominance of three-body charge states with respect to two-body ones. These data serve as a reference to explore features of $^7$Be, $^8$B, and $^9$C fragmentation.

A complete restoration of the charged fragmentation component in the rest of the events allowed us to assign additional tracks with minimal ionization to charged meson production. It is found that about 22% of complete charge fragmentation events contain a single charged meson and just 2–3% a couple. We plan to perform relativistic fragment identification

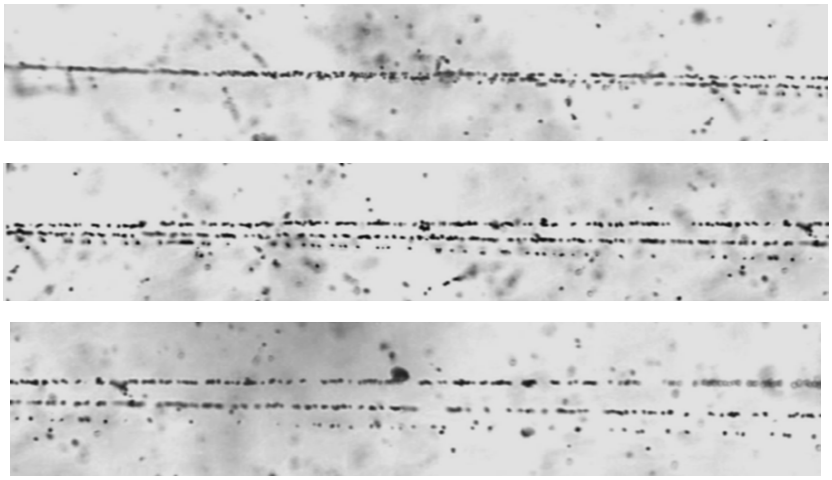

Event of dissociation of 1 $A$ GeV $^{10}$B nucleus into two double charged and one single charged tracks in sequential evaluation (top to bottom) as an example of white star. A 3D image is reconstructed as a projection by means of the FIAN PAVICOM automatic microscope.

and analyze the described statistics in the spirit of paper [6].

## FUTURE IRRADIATIONS IN SECONDARY BEAMS OF RELATIVISTIC NUCLEI

The cluster structure of $^7$Be can manifest itself in the fragmentation channels like $^7\mathrm{Be} \rightarrow {}^3\mathrm{He} + {}^4\mathrm{He}$, $^3\mathrm{He} + {}^3\mathrm{He} + n$, $^6\mathrm{Li} + p$, $\alpha + d + p$, and others. The study of $^7$Be nuclei is interesting from the point of view of its possible role of a core in $^8$B one. Using charge exchange of 1.23 $A$ GeV $^7$Li nucleus, the $^7$Be beam was produced at one of the Nuclotron beam lines. Emulsions irradiated by this beam are under analysis now

Table 1 contains an indication that a $^8$B nucleus beam may be produced in $^{10}$B nucleus fragmentation. Such an opportunity needs to be explored for this case and for $^9$C and $^{10}$C nuclei.

Being intended for investigations with the aid of the emulsion technique, the $^8$B beam could make the problem of proton-halo existence clearer. The particular feature of the $^8$B nucleus is the lowest binding energy of one of the protons (135 keV). Therefore, most probably, the $^8$B nucleus has a core in the form of a $^7$Be nucleus and a proton weakly coupled with the core. Their space distributions define the value of the $^8$B radius, the transverse momentum distributions for relativistic protons and $^7$Be, and the distribution with respect to the relative transverse momentum of the dissociation products. The probabilities of dissociation channels are suggested to be measured for $^8\mathrm{B} \rightarrow {}^7\mathrm{Be} + p$, $\alpha + {}^3\mathrm{He} + p$, $^3\mathrm{He} + {}^3\mathrm{He} + d$, $^6\mathrm{Li} + p + p$, $\alpha + d + p + p$, and others.

After that, the production of the $^9$C nucleus beam becomes a next logical step. Of all the nuclei that we have considered, this one has the largest ratio of number of protons to that of neutrons. This nucleus has an additional proton as compared with the $^8$B nucleus. The binding energy of this additional proton is far larger than that of the external proton in the $^8$B nucleus. Therefore, it appears that the $^9$C has no external two-proton shell. This nucleus is particularly interesting since the replacement of one of the protons by a neutron leads to the unstable $^9$B isotope in spite of the reduction of the Coulomb energy. One of the possible explanations to be verified is a hidden $^3$He clustering.

To do this, we suggest measuring the probabilities of dissociation channels like $^9\mathrm{C} \rightarrow {}^8\mathrm{B} + p$, $^3\mathrm{He} + {}^3\mathrm{He} + {}^3\mathrm{He}$, and others. An unavoidable feature of $^9$C beam formation is the presence of accompanying $^3$He nuclei having the same magnetic rigidity as in the case of our previous study with a triton and $^6$He beam "cocktail." The feasibility of emulsion application needs to be justified by a dedicated study.

To conclude, in the performed and suggested investigations of the interactions of light radioactive nuclei in emulsion, one and the same method is reviewed for systematic studies of the structure of several proton-rich nuclei. Attention is paid to the search for the manifestation of a structure like the proton halo and structures with an unstable nucleus core. Thus, the combination of new beams and the classical technique may result in new intriguing and conclusive finds. The results can be employed in planning further studies on the Nuclotron's beams, in particular, for forming reaction triggers in the detection of particles by electronic methods.

## ACKNOWLEDGMENTS

The development of this proposal would not have been possible without the scientific guidance and support of the late Academician A.M. Baldin. We are indebted to the late Prof. M.I. Adamovich for many years of leadership in the emulsion technique. Papers of the late Prof. G.M. Chernov on nuclear coherent dissociation have played an inspiring role in our research. Our manuscript is devoted to the memory of these outstanding scientists.

We express our warmest thanks to A.V. Pisetskaya from FIAN, Moscow, and I.I. Sosul'nikova, A.M. Sosul'nikova, N.A. Kachalova, and G.V. Stel'makh from JINR, Dubna, for their contribution in a microscope visual analysis, and I.I. Mar'in for perfect maintenance of the microscopes. Valuable contributions to our work have been provided by the JINR Synchrophasotron and Nuclotron personnel and LHE beam transport group.

This work was partially supported by the Russian Foundation for Basic Research (Scientific School of Academician A.M. Baldin) (project no. 96-15-96423), the Agency for Science at the Ministry of Education of Slovak Republic and the Slovak Academy of Sciences (grant no. VEGA 1/9036/22), and a grant from the Slovakian Plenary Representative at JINR.

## REFERENCES

1. P. G. Hansen and A. S. Jensen, Annu. Rev. Nucl. Part. Sci. **45**, 591 (1995).
2. A. H. Wuosamaa, R. R. Betts, M. Freer, and B. R. Fulton, Annu. Rev. Nucl. Part. Sci. **45**, 89 (1995).
3. W. Schwab *et al.*, Z. Phys. A **350**, 283 (1995).
4. M. H. Semdberg *et al.*, Phys. Lett. B **452**, 1 (1999).
5. M. El-Nadi *et al.*, in *Proceedings of International School of Cosmic Ray Astrophysics "Erice 1996, Towards the Millennium in Astrophysics," 1996,* p. 189.
6. M. I. Adamovich *et al.*, Phys. At. Nucl. **62**, 1378 (1999).
7. F. G. Lepekhin, D. M. Seliverstov, and B. B. Simonov, Eur. Phys. J. A **1**, 137 (1998).
8. M. I. Adamovich *et al.*, Part. Nucl. Lett., No. 1[110], 29 (2002).

*Physics of Atomic Nuclei, Vol. 66, No. 9, 2003, pp. 1651–1654. From Yadernaya Fizika, Vol. 66, No. 9, 2003, pp. 1699–1702.*


# Production of Exotic Λ Hypernuclei via Mesonic Beams*

**T. Yu. Tretyakova**[1)]** and **D. E. Lanskoy**[2)]***

[1)] *Frank Laboratory of Neutron Physics, Joint Institute for Nuclear Research, Dubna, Moscow oblast, 141980 Russia*

[2)] *Institute of Nuclear Physics, Moscow State University, Moscow, 119992 Russia*

Received August 28, 2002

**Abstract**—We study the production of neutron-rich hypernuclei ${}^{12}_{\Lambda}$Be, ${}^{16}_{\Lambda}$C, and ${}^{10}_{\Lambda}$Li by the $(\pi^-, K^+)$ and $(K^-, \pi^+)$ reactions in flight and treat two different mechanisms of production. The first mechanism is a two-step process with meson charge exchange (e.g., $\pi^- p \to \pi^0 n$, $\pi^0 p \to K^+\Lambda$). The other mechanism is one-step production ($\pi^- p \to K^+\Sigma^-$) proceeding via a small $\Sigma^-$ component, arising in Λ hypernuclei due to $\Lambda N$–$\Sigma N$ coupling, as a doorway state. Typically, the two-step mechanism is more productive. The forward differential cross section of the ${}^{10}\mathrm{B}(\pi^-, K^+){}^{10}_{\Lambda}\mathrm{Li}(2^-)$ reaction is about 70 nb/sr at an incident momentum of 1.05 GeV/$c$. On the other hand, the one-step process can serve as a direct measurement of the Σ admixture if the two-step contribution is suppressed by a suitable choice of the reaction kinematics.


## INTRODUCTION

Hypernuclei with neutron excess relate both to physics of exotic nuclei and to strangeness nuclear physics. On the one hand, neutron-rich hypernuclei give information about the response of loosely bound systems with neutron halo to Λ-induced perturbation. Some unbound neutron-rich nuclei can be bound by a Λ hyperon. Therefore, studying such systems can enrich our knowledge on exotic, especially neutron-halo, nuclei.

On the other hand, extension of the hypernuclear chart is of considerable importance for physics of hyperonic interactions. Properties of neutron-rich Λ hypernuclei appear to be sensitive to subtle features of $\Lambda N$ interaction in a nuclear medium hardly deduced from "usual" hypernuclei. We have studied theoretically [1] several examples of neutron-rich Λ hypernuclei (like ${}^{12}_{\Lambda}$Be, ${}^{16}_{\Lambda}$C, ${}^{11}_{\Lambda}$Li) and have shown that the last neutron separation energies are affected by a delicate interplay between the $\Lambda N$ density-dependent force, polarization of the nuclear core by a hyperon, and spin–orbit neutron–nucleus potential. Another interesting point related to structure of exotic hypernuclei is associated with $\Lambda N$–$\Sigma N$ coupling leading to admixtures of virtual Σ hyperons in Λ hypernuclei. In [2], the substantial contribution of the coupling, which is probably enhanced with neutron excess, to binding energies of neutron-rich Λ hypernuclei has been emphasized. Other aspects of neutron-rich Λ hypernuclei have been considered in [3, 4].

Earlier, only helium neutron-rich hyperisotopes (${}^{7}_{\Lambda}$He and ${}^{8}_{\Lambda}$He) were detected in old emulsion experiments [5] in a few events. Later, it was pointed out that a wide variety of interesting species can be produced by the $(K^-, \pi^+)$ reaction [6] at rest as well as in flight. Prospects of experimental studies of this reaction and also a similar $(\pi^-, K^+)$ reaction have been proposed currently [7, 8].

We presented some estimates for reaction $(K^-, \pi^+)$ at rest (with kaon capture from atomic levels) earlier [9]. Here, we report predictions for the $(\pi^-, K^+)$ and $(K^-, \pi^+)$ reactions in flight, mostly concerning in the first reaction in view of KEK proposal [8].

The reactions considered can proceed by different mechanisms. The evident mechanism is a two-step one with meson charge exchange, for instance, $\pi^- p \to \pi^0 n$ followed by $\pi^0 p \to K^+\Lambda$, or $\pi^- p \to K^0\Lambda$ and $K^0 p \to K^+ n$. This mechanism is similar to the simplest way of pion double charge exchange. The second possible process—one-step production via a $\Sigma^-$ admixture state as a doorway state—was the main point of concern in [9]. Here, we examine both mechanisms.

*This article was submitted by the authors in English.

** e-mail: ttretyak@nf.jinr.ru

*** e-mail: lanskoy@npi.msu.su

**Table 1.** $\Sigma^-$ admixture probabilities $p_\Sigma$

| Hypernucleus | $J^\pi$ | $p_\Sigma$ |
|---|---|---|
| ${}^{12}_{\Lambda}$Be | $1^-$ | $5.1 \times 10^{-4}$ |
| | $0^+$ | $4.0 \times 10^{-5}$ |
| ${}^{16}_{\Lambda}$C | $2^+$ | $8.1 \times 10^{-5}$ |
| | $0^+$ | $7.1 \times 10^{-6}$ |

## ONE-STEP PRODUCTION VIA $\Sigma^-$ ADMIXTURE

We consider a hypernuclear state as a superposition of the main $\Lambda$ component and the small $\Sigma^-$ admixture appearing from the $\Lambda n$–$\Sigma^- p$ coupling as follows:

$$|{}^A_\Lambda Z\rangle = \alpha|^{(A-1)}Z \otimes \Lambda\rangle + \beta|^{(A-1)}(Z+1) \otimes \Sigma^-\rangle.$$

The first (main) state can be produced in the $(\pi^-, K^+)$ and $(K^-, \pi^+)$ reactions only by the two-step process with subsequent $\Lambda$ production on one proton and meson charge exchange on another proton, whereas the second state is attainable in one step by elementary reaction $\pi^- p \to K^+\Sigma^-$ or $K^- p \to \pi^+\Sigma^-$. Normally, one-step productions are, of course, much more probable than two-step ones. However, the one-step production considered is strongly reduced by a small probability of the $\Sigma^-$ admixture $p_\Sigma = |\beta|^2$.

We calculate the $\Sigma^-$ admixture component in a simple two-channel approach as described in [9]. Due to the large difference between $\Sigma$ and $\Lambda$ masses, the $\Sigma$ wave function possesses some unusual properties (nonstandard asymptotic behavior and displacement from the center region), which have some implications for production probabilities [9].

Two target nuclei, ${}^{12}$C and ${}^{16}$O, are considered here, which give rise to hypernuclei ${}^{12}_{\Lambda}$Be and ${}^{16}_{\Lambda}$C, respectively. The host nuclei (${}^{11}$Be and ${}^{15}$C) possess a loosely bound external neutron moving in a compact core field. Each nucleus has two bound states ($1/2^+$ and $1/2^-$ in ${}^{11}$Be and $1/2^+$ and $5/2^+$ in ${}^{15}$C). Adding a $\Lambda$ hyperon in the $1s_{1/2}$ state, one accordingly obtains two natural-parity states in each hypernucleus ($0^+$ and $1^-$ in ${}^{12}_{\Lambda}$Be and $0^+$ and $2^+$ in ${}^{16}_{\Lambda}$C). Admixture probabilities $p_\Sigma$ in these states are displayed in Table 1. The probabilities are rather small relative to values obtained [10–13] in $s$-shell hypernuclei. It appears that the $\Lambda N$–$\Sigma N$ coupling involving $p$-shell nucleons is considerably weaker.

For differential cross sections of the $(\pi^-, K^+)$ and $(K^-, \pi^+)$ reactions within the one-step mechanism, we adopt the usual DWIA approach, which is widely applied to the similar $(\pi^+, K^+)$ and $(K^-, \pi^-)$ reactions (e.g., [14]). In Fig. 1, the differential cross sections of the ${}^{12}$C$(\pi^-, K^+)$ and ${}^{16}$O$(\pi^-, K^+)$ reactions at 1.05 GeV/$c$ are shown. The cross sections are typically less than 1 nb/sr and are in accordance with $p_\Sigma$ values listed in Table 1. Note that the cross sections of the $(\pi^+, K^+)$ reaction on the same targets are of order of units or tens of $\mu$b/sr. The $(\pi, K)$ reaction is characterized by a fairly high momentum transfer (about 350 MeV/$c$) even at zero angle, so the angular dependence of the cross sections is rather simple.

**Table 2.** Differential cross sections (in nb/sr) of the $(\pi^-, K^+)$ reaction at zero angle at $p_\pi = 1.05$ GeV/$c$

| Final hypernucleus | State | One-step mechanism | Two-step mechanism |
|---|---|---|---|
| ${}^{10}_{\Lambda}$Li | $2^-$ | | 66.8 |
| | $1^-$ | | 3.2 |
| ${}^{12}_{\Lambda}$Be | $1^-$ | 1.4 | 6.5 |
| | $0^+$ | 0.1 | 2.1 |
| ${}^{16}_{\Lambda}$C | $2^+$ | 0.3 | 0.4 |
| | $0^+$ | 0.01 | 0.1 |

In Fig. 2, the differential cross sections of the $(K^-, \pi^+)$ reactions are depicted at two incident kaon momenta. The momentum 500 MeV/$c$ corresponds to near-recoilless kinematics at zero angle (the momentum transfer is almost zero). Thus, the $0^+ \to 0^+$ transitions dominate at $\theta = 0$ despite less $p_\Sigma$. Nonzero-spin states can be produced at larger angles. At 900 MeV/$c$ (zero-angle momentum transfer is about 100 MeV/$c$), production of the $1^-$ and $2^+$ states with larger $\Sigma$ admixtures prevails in the whole range of angles considered.

The cross sections of the $(K^-, \pi^+)$ reaction reach 100 nb/sr. This does not mean that this reaction is more feasible, since available kaonic beams are much less intensive than pionic ones. However, comparison of Figs. 1 and 2 shows that the kinematics of the $(K^-, \pi^+)$ reaction is more selective due to wide possibilities of varying the momentum transfer.

## TWO-STEP MECHANISM OF THE $(\pi^-, K^+)$ REACTION

Treating the two-step mechanism ($\pi^- p \to \pi^0 n$, $\pi^0 p \to K^+\Lambda$ and $\pi^- p \to K^0\Lambda$, $K^0 p \to K^+ n$), we utilize the Glauber approach. For one-step reactions, it gives essentially the same description as the DWIA

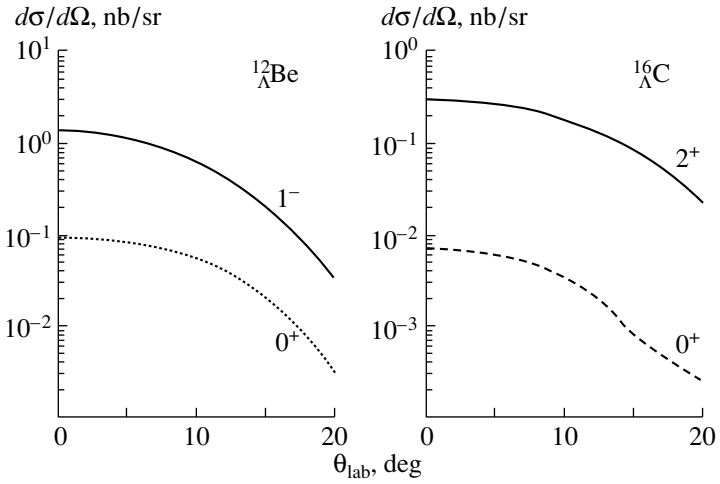


**Fig. 1.** Differential cross sections of the $^{12}$C $(\pi^-, K^+)^{12}_{\Lambda}$Be and $^{16}$O$(\pi^-, K^+)^{16}_{\Lambda}$C reactions at $p_\pi = 1.05$ GeV/$c$.

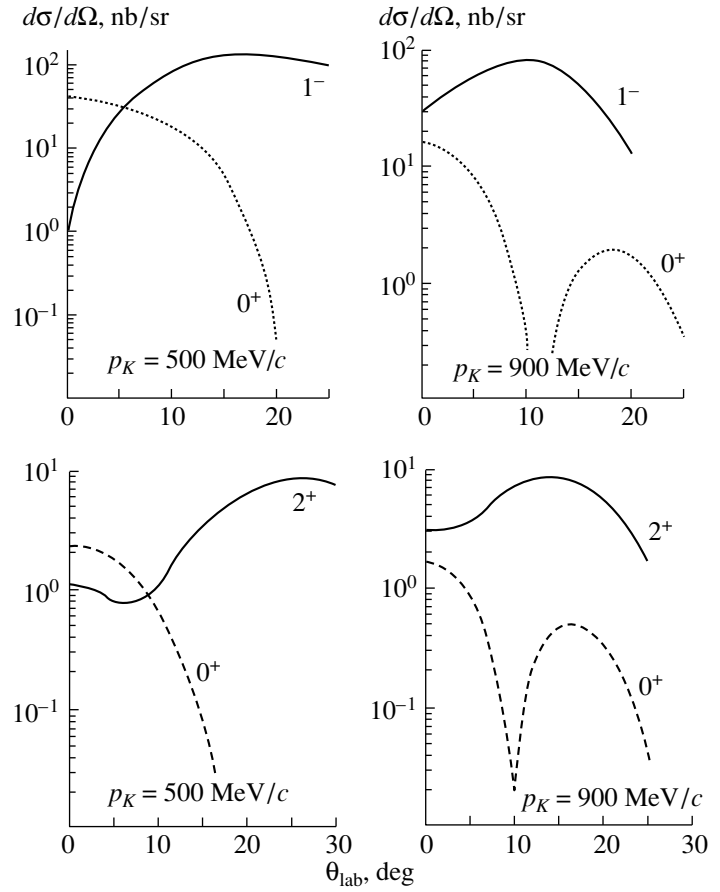


**Fig. 2.** Differential cross sections of the $^{12}$C$(K^-, \pi^+)^{12}_{\Lambda}$Be (top) and $^{16}$O$(K^-, \pi^+)^{16}_{\Lambda}$C (bottom) reactions.

at energies about 1 GeV, whereas its extension to two-step processes is straightforward.

The cross section of the $N(\pi, K)\Lambda$ elementary reaction is sharply peaked at the incident momentum 1.05 GeV/$c$ (whereas the cross section of the $p(\pi^-, K^+)\Sigma^-$ reaction varies smoothly with momentum), so the largest cross sections might be expected at this momentum value. As the momentum transfer in the $(\pi, K)$ reactions is high at zero angle and increases further with angle, we present here only the

results at $\theta = 0$ (the cross sections of the two-step mechanism also fall with angle). In Table 2, the cross sections calculated within the two-step mechanism are presented. The results for the one-step process (from Fig. 1) are also shown for comparison.

It is seen that the two-step cross sections exceed considerably (excepting ${}^{16}_{\Lambda}\mathrm{C}$ $(2^+)$ production) the one-step ones. Thus, it may be suggested that the two-step mechanism is more effective, at least for the hypernuclei considered.

Note that the cross sections exhibited in Table 2 are calculated for the two-step and one-step mechanisms separately. Strictly speaking, one should sum the amplitudes rather than the cross sections. However, the relative phase between the amplitudes of the two mechanisms is unknown and hardly deduced. While the contributions of the two mechanisms differ substantially from each other, this problem may be avoided.

In connection with the experiment recently proposed at KEK [8], we also calculate the cross section of the ${}^{10}\mathrm{B}(\pi^-, K^+){}^{10}_{\Lambda}\mathrm{Li}$ reaction within the two-step mechanism (it is presumed to be dominant). We consider two states ($1^-$ and $2^-$) built on the ground state of ${}^9\mathrm{Li}$ $(3/2^-)$. It is seen from Table 2 that the cross section for ${}^{10}_{\Lambda}\mathrm{Li}(2^-)$ production is much higher than that for all the other cases.

In ${}^{12}_{\Lambda}\mathrm{Be}$ and ${}^{16}_{\Lambda}\mathrm{C}$ production, a nucleon having undergone charge exchange is forced to change this state drastically. Quantum numbers of the external neutron always differ from quantum numbers of the protons. Moreover, the spatial distribution of the external (halo) neutron overlaps poorly with the distributions of the core protons. Such a drastic change is not needed for the ${}^{10}_{\Lambda}\mathrm{Li}$ production. Furthermore, in the two-step transition (e.g., ${}^{10}\mathrm{B}(3^+) \rightarrow {}^{10}_{\Lambda}\mathrm{Be}(2^-) \rightarrow {}^{10}_{\Lambda}\mathrm{Li}(2^-)$), the charge-exchange step can proceed without angular momentum changing. That is why production of ${}^{10}_{\Lambda}\mathrm{Li}(2^-)$ is greatly enhanced.

Hypernucleus ${}^{10}_{\Lambda}\mathrm{Li}$ is built on a relatively tightly bound ${}^9\mathrm{Li}$ core and does not represent extremely neutron-rich (halo) systems. However, this hypernucleus possesses a considerable neutron excess ($N/Z = 2$), and its detection might be of great interest. So far, ${}^{10}_{\Lambda}\mathrm{Li}$ has not been observed. The reaction ${}^{10}\mathrm{B}(\pi^-, K^+){}^{10}_{\Lambda}\mathrm{Li}$ can be a reasonable first step in the program studying neutron-rich $\Lambda$ hypernuclei [8].

## CONCLUSION

Investigations of production of neutron-rich $\Lambda$ hypernuclei are interesting from several viewpoints. Our study indicates that, searching for the largest experimental yields, one should mainly be concerned in the two-step mechanism of the $(\pi^-, K^+)$ and $(K^-, \pi^+)$ reactions with meson charge exchange. On the other hand, an attractive feature of the one-step mechanism is that the corresponding cross sections are proportional to the probabilities of the $\Sigma$ admixture. Though implications of the $\Lambda N$–$\Sigma N$ coupling in $\Lambda$ hypernuclei have been discussed intensively for a long time, no direct measurement of $\Sigma$ admixtures has been made so far. The reactions considered can give, in principle, such knowledge. But for this goal, otherwise, kinematical conditions should be chosen that suppress the two-step contribution. Maybe, selectivity of the $(K^-, \pi^+)$ reaction is useful from this point. Also, it is important to recognize $\Lambda$ hypernuclei attainable in the $(\pi^-, K^+)$ and $(K^-, \pi^+)$ reactions, in which $\Sigma^-$ admixtures are higher than those found here. Finally, we mention quite another way to produce neutron-rich $\Lambda$ hypernuclei—by heavy-ion beams [15, 16].

## ACKNOWLEDGMENTS

We are indebted to Y. Akaishi, T. Fukuda, Khin Swe Myint, and P.K. Saha for helpful discussions.

## REFERENCES

1. T. Yu. Tretyakova and D. E. Lanskoy, Eur. Phys. J. A **5**, 391 (1999).
2. Khin Swe Myint *et al.*, Few-Body Syst. Suppl. **12**, 383 (2000).
3. E. Hiyama *et al.*, Phys. Rev. C **53**, 2075 (1996).
4. D. Vretenar *et al.*, Phys. Rev. C **57**, R1060 (1998).
5. D. H. Davis and J. Pniewski, Contemp. Phys. **27**, 91 (1986).
6. L. Majling, Nucl. Phys. A **585**, 211c (1995).
7. H. Tamura, Eur. Phys. J. A **13**, 181 (2002).
8. T. Fukuda, P. K. Saha, and H. Noumi, *Production of Neutron-Rich Λ Hypernuclei by the $(\pi^-, K^+)$ Double-Charge Exchange Reaction* (KEK-PS Proposal, 2002).
9. T. Yu. Tretyakova and D. E. Lanskoy, Nucl. Phys. A **691**, 51c (2001).
10. Y. Akaishi *et al.*, Phys. Rev. Lett. **84**, 3539 (2000).
11. K. Miyagawa *et al.*, Phys. Rev. C **51**, 2905 (1995).
12. E. Hiyama *et al.*, Phys. Rev. C **65**, 011301 (2002).
13. A. Nogga, H. Kamada, and W. Glöckle, Phys. Rev. Lett. **88**, 172501 (2002).
14. H. Bandō, T. Motoba, and J. Žofka, Int. J. Mod. Phys. A **5**, 4021 (1990).
15. H. Bandō, Nuovo Cimento A **102**, 627 (1989).
16. J. Lukstins, Nucl. Phys. A **691**, 491c (2001).

*Physics of Atomic Nuclei, Vol. 66, No. 9, 2003, pp. 1655–1658. From Yadernaya Fizika, Vol. 66, No. 9, 2003, pp. 1703–1706.*


# Neutron Channel of the FOBOS Spectrometer for the Study of Spontaneous Fission*

**D. V. Kamanin[1)]**, Yu. V. Pyatkov[1),2)], E. A. Sokol[1)], S. V. Mitrofanov[1)], S. R. Yamaletdinov[2)], V. G. Tishchenko[1)], A. N. Tyukavkin[2)], B. V. Florko[1)], E. A. Kuznetsova[1)], and O. Yu. Gapienko[1)]**

[1)] *Joint Institute for Nuclear Research, Dubna, Moscow oblast, 141980 Russia*

[2)] *Moscow Engineering Physics Institute, Kashirskoe sh. 31, Moscow, 115409 Russia*

Received October 18, 2002

**Abstract**—The $4\pi$ spectrometer FOBOS has been completed with the multidetector system for registration of neutrons aimed at experiments to search for collinear tripartition of heavy spontaneously fissile nuclei. A simple empirical model developed for the description of the measured neutron multiplicity is tested on the data block comprising $6 \times 10^7$ events. © *2003 MAIK "Nauka/Interperiodica".*

The $4\pi$ spectrometer FOBOS [1] has been completed with the multidetector belt for registration of neutrons. Of course, the application of neutron detectors at the FOBOS setup is limited to some special experiments due to methodological problems, e.g., thick metallic and hydric matter constructions of the detectors, the large size of the spectrometer, an intensive neutron background from the U-400M cyclotron during in-beam experiments, etc. Bearing in mind these complications, we have found a suitable solution for experiments to search for collinear cluster tripartition (CCT) of heavy spontaneously fissile nuclei [2]. According to the model [3], such process should be accompanied by almost isotropic emission of postscission neutrons in the laboratory system of the multiplicity as high as ~10. This agrees with the previous results on spontaneous decay of $^{248}$Cm and $^{252}$Cf obtained at the FOBOS setup [3]. Therefore, the CCT events could be separated by considering those with a large number of fired neutron detectors, which reflects a high multiplicity.

The neutrons emitted from the moving fission fragments (FF) are focused along the fission axis. Hence, the optimal configuration of neutron detectors for the separation of the CCT events seems to be a belt of high-efficiency counters assembled in a plane perpendicular to the symmetry axis of the spectrometer configuration, which is obviously the mean fission axis under these conditions. The symmetry center of this belt must coincide with the location of the FF source [4]. This general disposition is illustrated in Fig. 1. Two groups containing five big and one small FOBOS modules each are used as a double-armed TOF-E spectrometer which covers ~29% of the hemisphere in each arm.

The neutron detector consists of 140 separate hexagonal modules [5] comprising a $^3$He-filled proportional counter, a moderator, a high-voltage input, and a preamplifier. The counters operate under a gas pressure of 7 bar, being 50 cm in length and 3.2 cm in diameter. The moderator is made of polyethylene. The spacing between the parallel planes of a module is 5 cm. The neutron counters are composed into eight arrangements of 16 counters each and one of 12 counters and they cover altogether effectively ~19% of the complete solid angle of $4\pi$. The electronics of the "neutron belt" is operated in the slave mode, being triggered by the event selector of the gas part of the FOBOS detector. The view of the spectrometer surrounded by the neutron belt is represented in Fig. 2.

In order to test the results obtained, in particular, the neutron multiplicity distribution, the following approach was used.

Three of a total of four different sources of neutrons have been taken into account and the partial contribution of each source to the experimental spectrum of the number of fired neutron detectors (i.e., experimental or measured multiplicity distribution) has been calculated. These sources are as follows:

(1) The moving FF originated from conventional binary fission and detected in coincidence in the opposite arms of the spectrometer. Note that the time gate (128 $\mu$s) for the registration of neutrons

*This article was submitted by the authors in English.

**e-mail: kamanin@fobos.jinr.ru

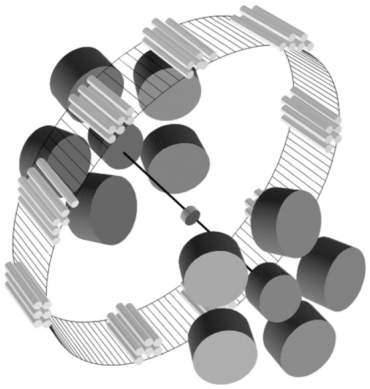

**Fig. 1.** The general layout of the modified FOBOS spectrometer. The spontaneous source inside the start detector is in the middle.

is opened just at the point of time when the FF fire the "stop" detectors.

(2) The FF originated from the fission events coinciding randomly with the gate. This source will be named below the "random source."

(3) The neutron background.

(4) The central fragment of the chainlike prescission nuclear configuration in CCT [3], which is almost at rest. This source has not been taken into consideration at the present stage of simulations.

The probability $P_k$ of registration of $k$ neutrons from the first source is given by the following expression [4]:

$$P_k = \sum_{N \geq k} P_N C_N^k \varepsilon^k (1-\varepsilon)^{N-k}, \qquad (1)$$

where $P_N$ is the emission probability of $N$ neutrons known from the literature and $\varepsilon$ is the detection efficiency. In the first approximation, $\varepsilon$ can be estimated directly from the measured multiplicity distribution.

In order to take into account the influence of the second (random) source, let us imagine that, at some time point $t_0$ (Fig. 3), the gate $[0; T]$ for detecting of neutrons is already opened as a result of registering the coincident FF. At any point of time $\tau$, an independent fission event can occur. This event is then interpreted as a random coincidence and each neutron emitted by the corresponding FF spends some time $t_d$ until it is detected. The latter is under the condition that the neutron hits the detector belt covering $\eta$ part of the whole sphere. From the physical point of view, the time $t_d$ is spent both for moderation and for secondary diffusion until absorption in one of the $^3$He counters. Time intervals $t_d$ are distributed by an exponential low with the timing constant $\lambda$. The parameter $\lambda$ was derived from the experimental spectrum of neutron detection times (Fig. 4). It should be noted that the neutron registration efficiency is

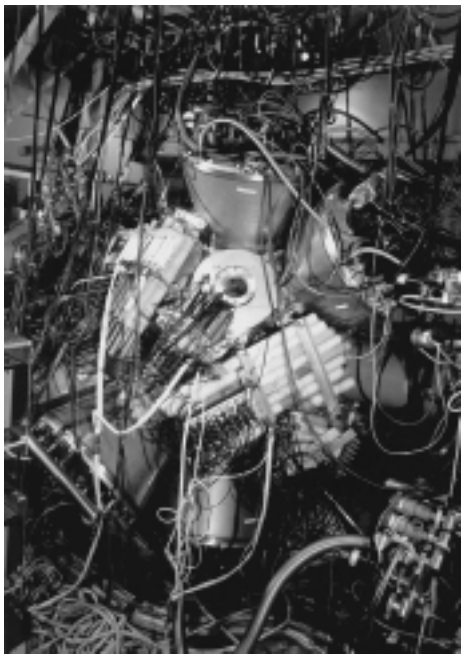

**Fig. 2.** The overall view of the spectrometer FOBOS surrounded by the belt of neutron counters during the February 2001 experimental session.

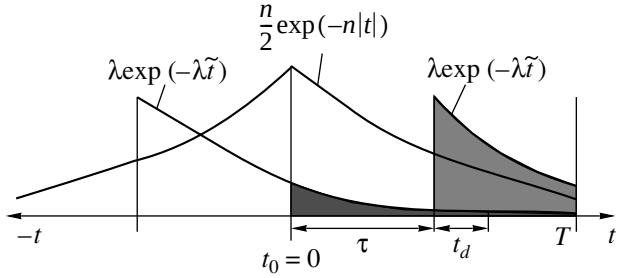


**Fig. 3.** The temporal scheme illustrating the contribution of the random source.

appreciably lower than the geometrical one due to the leaking-out and absorption of neutrons in the moderator. Using the well-known MCNP code, we have estimated the registration efficiency $f$ of the neutron belt during infinite time for an isotropic source. The obtained value of $f$ for the neutron energy of 0.5 MeV is about 60%. The value of $f$ decreases slightly with increasing neutron energy to 1 MeV.

Let us investigate how the experimental multiplicity is formed. Let $k$ neutrons originated from the fission event opening the gate be detected during the gate $[0; T]$. Let during the same gate $r$ neutrons emitted from the FF of the random fission event be detected as well. Then, the number $k_\Sigma = k + r$ is written by the data acquisition system. The distribu-

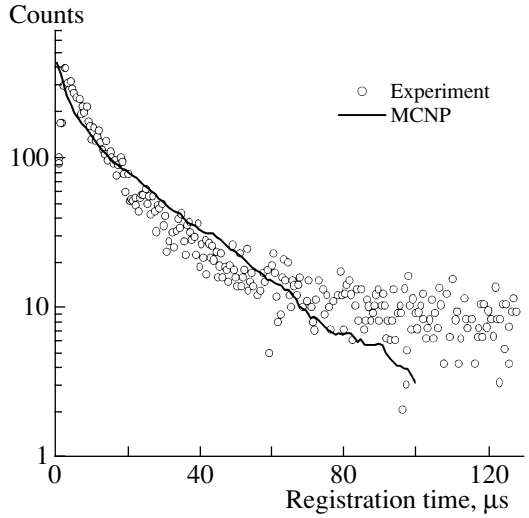


**Fig. 4.** Distribution of the capture time for neutrons in a 16-detector array.

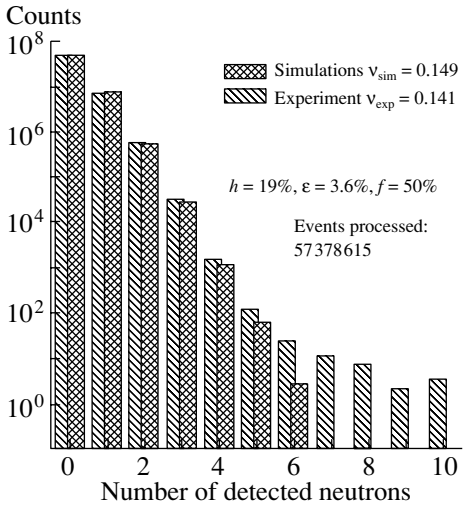


**Fig. 5.** The spectrum of frequency vs. number of tripped neutron counters for the recorded fission events. This picture represents a different experimental session than in [2].

tion $P_\Sigma(k_\Sigma)$ should be a convolution:

$$P_\Sigma = P_k * P_r, \tag{2}$$

where the function $P_k$ is calculated by the expression (1). The function $P_r$ can be obtained by the serial threefold application of the binomial transformation (1) to the function $P_N$ (which is the probability of emission of $N$ neutrons in fission of a $^{252}$Cf nucleus) using $\eta$, $f$, and $\eta_r(t)$, respectively, as the parameters. As the probability $\eta_r(t)$ of registration of the neutron hitting the detector at the time point $\tau$ (Fig. 3) depends on time according the expression

$$\eta_r = \int_0^{T-\tau} \lambda \exp(-\lambda t) dt,$$

it is necessary to integrate function $P_r$ with the weight function $n\exp(-nt)$ within the limits [0; $T$], where $n$ is the fission rate of the source. The function $P_\Sigma$ obtained above deals with positive times only. At the same time, those neutrons emitted earlier, i.e., at negative times (Fig. 3), can also be detected in the frame of the gate. One can obtain the distribution $P_\Sigma$-conditioned by such events in the same way as above. The full contribution from the random source $P_{\Sigma\Sigma}$ is obtained as the sum

$$P_{\Sigma\Sigma} = P_\Sigma + P_\Sigma\text{-}. \tag{3}$$

The third source of neutrons, namely, the background, was estimated experimentally. As can be judged from Fig. 4, the count rate at a time later than 80 $\mu$s looks like a plateau specified by the contributions of both the background of the experimental hall and the fission neutrons appearing formerly at a negative time and roaming in the neutron belt until the time gate under discussion. In our case, the background is low enough to be omitted.

The proposed model still does not include a contribution of the CCT as a source of neutrons. The existence of such a source itself could be tested by a comparison of the calculated and experimental multiplicity distribution with the calculated one.

Summarizing, the model multiplicity distribution is calculated according the formula:

$$P_{\text{fin}} = (1-c)P_k + cP_{\Sigma\Sigma}, \tag{4}$$

where $c$ is the probability of the random coincident fission events. In the framework of such a definition, the function $(n/2)\exp(-n|t|)$ should be normalized to unity and $c$ is the integral of this function in the limits $[-\infty; T]$.

The calculated spectrum $P_{\text{fin}}$ is compared with the experimental one in Fig. 5. A good agreement for the major contribution of low multiplicity observed can appraise us of evidence of the model adequacy. The discrepancy observed for high multiplicity seems to be consistent with the idea of an isotropic neutron source, which was not considered in the simulations.

The most critical point for the results of simulations with the model discussed is the efficiency of registration. Therefore, as was already mentioned, in addition to its empirical estimate, numerical simulations by the MCNP code have been performed. These simulations are also aimed at the optimization of the experimental conditions. The overall registration efficiency for neutrons from ordinary fission and from CCT events amounted to 4.1 and 10.8%, respectively. The latter is in good agreement with an empirical

estimate, bearing in mind that the efficiency of the 16-detector array is close to 60%.

The reliability of our MCNP simulations are checked by reproducing the experimental values of the timing constant $\lambda$ of $\sim$20 $\mu$s (Fig. 4) and the count ratio of 1.3 for the detectors from inner and outer layers of the 16-detector array. The simulation delivers 1.25, 1.35, and 1.3 for detector arrays positioned at angles of 79° and 101° with respect to the direction of the FF motion and on the average, respectively.

Such good agreement of MCNP simulations with the experimental data already at the preliminary phase together with success of our empirical modeling ensures the reliability of the measured distribution of the neutron multiplicity for the analysis. Although further simulations are in progress, the multiplicity filter is already being successfully applied for the analysis of the FF data [2].

## ACKNOWLEDGMENTS

This work is supported in part by the Russian Foundation for Basic Research, project no. 00-02-16577, and by the CRDF, grant no. Mo-011-0.

## REFERENCES

1. H.-G. Ortlepp *et al.*, Nucl. Instrum. Methods Phys. Res. A **403**, 65 (1998).

2. Yu. V. Pyatkov *et al.*, this Proceedings.

3. Yu. V. Pyatkov *et al.,* in *Proceedings of the International Conference on Nuclear Physics "Nuclear Shells—50 Years," Dubna, 1999*, Ed. by Yu. Ts. Oganessian and R. Kalpakchieva (World Sci., Singapore, 2000), p. 144.

4. A. Alexandrov *et al.*, FLNR JINR Scientific Report 1999–2000, "Heavy-Ion Physics," Ed. by A. G. Popeko (Dubna, 2001), E7-2001-173, p. 159.

5. E. A. Sokol *et al.,* Nucl. Instrum. Methods Phys. Res. A **400**, 96 (1997).

*Physics of Atomic Nuclei, Vol. 66, No. 9, 2003, pp. 1659–1662. From Yadernaya Fizika, Vol. 66, No. 9, 2003, pp. 1707–1710.*


# Setup for Fission and Evaporation Cross-Section Measurements in Reactions Induced by Secondary Beams*

**A. A. Hassan[1),2)**], S. M. Lukyanov[1)], R. Kalpakchieva[1)], N. K. Skobelev[1)], Yu. E. Penionzhkevich[1)], Z. Dlouhý[3)], S. Radnev[4)], and N. V. Poroshin[5)]**

[1)] *Flerov Laboratory of Nuclear Reactions, Joint Institute for Nuclear Research, Dubna, Moscow oblast, 141980 Russia*

[2)] *Physics Department, Faculty of Science, Zagazig University, Egypt*

[3)] *NPI ASCR, Řež, Czech Republic*

[4)] *Laboratory for Technical Development, BAS, Sofia, Bulgaria*

[5)] *Moscow Engineering Physics Institute, Kashirskoe sh. 31, Moscow, 115409 Russia*

Received August 28, 2002

**Abstract**—A setup for studying reactions induced by secondary radioactive beams has been constructed. It allows simultaneous measurement of $\alpha$-particle and fission fragment energy spectra. By measuring the $\alpha$ particles, identification of evaporation residues is achieved. A set of three targets can be used so as to ensure sufficient statistics. Two silicon detectors, located at 90° to the secondary beam direction, face each target, thus covering 30% of the solid angle. This experimental setup is to be used to obtain excitation functions of fusion–fission reactions and of reactions leading to evaporation residue production.


## 1. INTRODUCTION

The presence in a nucleus of a neutron skin or halo is expected to have strong influence on the cross section of reactions induced by such nuclei. This cross section is enhanced due to the diffuse density distribution of the valence neutrons. On the other hand, reactions induced by nuclei with neutron excess may have large $Q$ values and, therefore, fusion can lead to a highly excited compound nucleus. A question may arise whether the valence neutrons can serve as a bridge for nucleon transfer with the consequence of enhancing the fusion cross section below the barrier or whether they will be lost in a breakup process before fusion takes place, by this decreasing the total complete fusion cross section at and below the barrier.

One of the surprises in the physics of secondary radioactive beams was the observation of enhanced fusion–fission cross sections. Theoretical and experimental efforts have been devoted to study this phenomenon. However, a full understanding remains elusive since the various experiments had been performed to study different interaction channels.

A few experiments have been carried out with a $^6$He beam [1–5]. The increased interest in the $^6$He nucleus lies in the fact that it has a neutron skin. If the structure of this nucleus influences the reaction parameters, one should, comparing the results to similar results obtained with a $^4$He beam, find a difference. One way to look for any such effect is to measure the characteristics of the evaporation residues produced after complete fusion in $xn$-evaporation channels. Another way is to measure the fusion–fission excitation function in a wide energy range.

Formerly, we studied $^6$He-induced fission using a stack of thin $^{209}$Bi targets (0.5–0.7 mg/cm$^2$) separated by solid-state Mylar track detectors [4], allowing the detection of fission fragments with high efficiency (about 80%). The excitation function for the fission of $^{209}$Bi and the cross section for the $^{209}$Bi($^6$He, $4n$)$^{215}$At reaction were measured in a wide energy range.

Later, a similar experiment [5] was carried out at two values of the excitation energy equal to 32 and 34 MeV. Despite the conclusion of the authors of [5] that there was disagreement between their experimental fission data and ours, we should point out that, taking into account the large experimental errors characteristic of experimental data at low values of the cross sections, the difference between the data is not large. Moreover, their conclusion was qualitatively consistent with the statistical-model calculations [6]

*This article was submitted by the authors in English.

** e-mail: asmr1711@lnr.jinr.ru

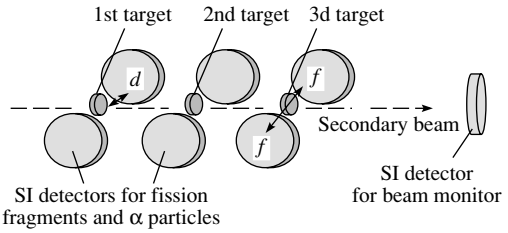


**Fig. 1.** Layout of the experimental setup.

in that the $^6$He-induced fission yield is smaller than that for $^4$He. However, this type of calculation has not been able to reproduce some experimental data, for instance, the experimental data on $^4$He + $^{209}$Bi fission [7]. We have found out that the behavior of the fission excitation function for the $^6$He + $^{209}$Bi reaction is the same as for the $^4$He + $^{209}$Bi reaction, but the fission cross section for the $^6$He isotope is significantly higher than that for $^4$He nuclei. In [2], it was suggested that this enhancement depends mainly on the entrance channel and is connected with the neutron skin of $^6$He nuclei. In order to get a clearer idea of the interaction, one should in principle measure all channels of the interaction: complete fusion, few-nucleon transfers, fission after complete and incomplete fusion, etc.

In the present paper, we describe a new experimental setup designed for simultaneous measurement of fission and neutron-evaporation cross sections in reactions induced by secondary beams.

## 2. THE EXPERIMENTAL SETUP

A schematic view of the experimental setup is presented in Fig. 1. The setup has been built for detecting both evaporation residues and fission fragments in parallel. The setup can hold up to three targets. The targets are placed at 45° with respect to the secondary beam direction. Two silicon detectors (diameter 5 cm), located at 90° to the beam direction, face each target from either side. This makes it possible to increase the effective solid angle up to 30% and thus get sufficient statistics in a shorter period of irradiation. The $^{209}$Bi targets were about 330 $\mu$g/cm$^2$ thick on a 2.5-$\mu$m-thick Mylar backing. This array of three targets allows increasing the statistics by a factor of three, as the maximum energy loss of the beam particles between the three targets is less than 1 MeV. If energy degraders are inserted between the targets, it would be possible to get measurements at three different energies of the beam in one run.

The silicon detectors measure the energy of the $\alpha$ particles emitted by various evaporation residues and also the energy of the fission fragments. The signals from the silicon detectors are divided for the fission fragments and for the decay of the evaporation residues. For this purpose, for each detector channel, two spectroscopic amplifiers (operating at various gains) are used.

Because of the quite large solid angle, this setup is suitable for use in studies of secondary-beam-induced reactions as it makes possible the investigation of reactions with cross sections less than $10^{-26}$ cm$^2$ at a mean beam intensity of about $10^4$ pps.

### *2.1. Secondary Beam Production*

The bombardment of a thick $^9$Be primary (production) target with an intense $^7$Li beam at about 35$A$ MeV has led to the production of relatively intense ($10^4$–$10^6$ pps) secondary beams of $^6$He with energies of 10–30$A$ MeV at the U400M cyclotron of the Flerov Laboratory of Nuclear Reactions [8]. The separation of the products produced in the target to form the secondary beam is achieved using the main beam-transport line of the accelerator. It has been specially modernized and supplemented with some new elements according to the ion optical calculations for the transport of the aforementioned light ions. Slits, a beam profiler (a multiwire proportional chamber), and a polypropylene degrader are used to control and improve the quality of the secondary beam. Its energy dispersion and angular convergence are thus minimized with only a small loss of intensity. The purity of the beam usually obtained is not worse than 98%. Using two profilers for diagnostics makes it possible to focus the beam on the physical target, located in the reaction chamber, as well as to control the size of the beam spot.

The secondary beam is monitored by means of position-sensitive Si detectors installed downstream of the targets.

### *2.2. Registration of $\alpha$ Particles and Fission Fragments*

This experimental setup has been tested using a Pu–Am–Cm source. The energy spectrum of the emitted $\alpha$ particles, measured with one of the detectors, is shown in Fig. 2 (left panel) as an example. We observe three peaks, corresponding to the strongest $\alpha$ transitions of 5.12, 5.42, and 5.84 MeV in the decay of $^{239}$Pu, $^{241}$Am, and $^{244}$Cm, respectively. On the basis of this measurement, we have been able to determine the energy resolution for $\alpha$ particles equal to FWHM $\approx$280 keV. The spectrum of the fission fragments is also shown in Fig. 2 (right panel). We can see that the energy distribution for the fission fragments allows distinguishing the two mass groups characteristic for the spontaneous fission of $^{244}$Cm.

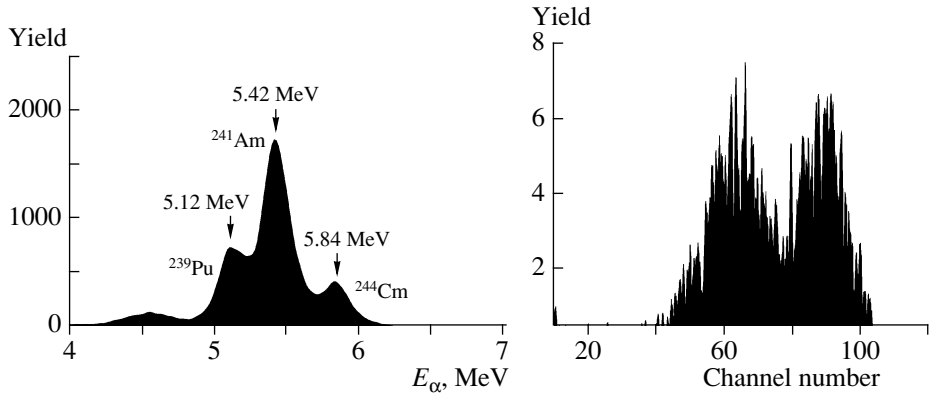


**Fig. 2.** Energy spectrum of $\alpha$ particles emitted by a Pu–Am–Cm source (left panel) and energy distribution of fission fragments from the spontaneous fission of $^{244}$Cm (right panel).

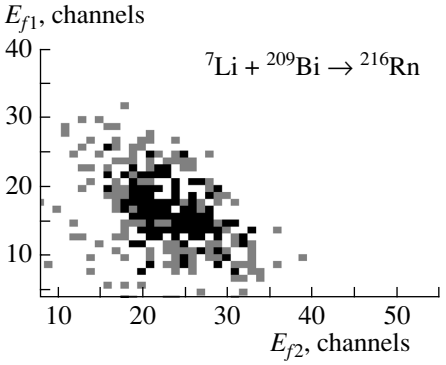


**Fig. 3.** The two-dimensional plot of the energies of the two correlated fission fragments obtained in the $^{7}$Li + $^{209}$Bi reaction.

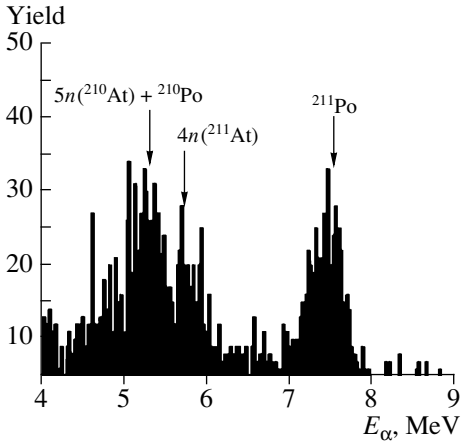


**Fig. 4.** Experimental $\alpha$-particle energy spectrum measured after the emission of different number of neutrons from the compound nucleus $^{215}$At.

## 3. EXPERIMENTAL RESULTS

### *3.1. Fission Fragments in the $^{7}Li + {}^{209}Bi$ Reaction*

We have tested the setup at the U400M accelerator using a $^{7}$Li beam with an energy $E = 80 \pm 1$ MeV. The $^{7}$Li-beam energy was chosen by tuning the magnetic rigidity of the beam line. Two correlated fission fragments were registered in coincidence by each couple of silicon detectors, located at 90° to the direction of the beam line (see Fig. 1). These detectors were calibrated with fission fragments from a thin $^{244}$Cm source and $\alpha$ particles from a $^{226}$Ra source. The two-dimensional plot of the energies of the fragments corresponding to the fission of the compound nucleus $^{216}$Rn is presented in Fig. 3.

### *3.2. Alpha Particles of Evaporation Recoil in the $^{6}He + {}^{209}Bi$ Reaction*

The described setup was also used to study the interaction of the secondary $^{6}$He beam with the $^{209}$Bi target nuclei. The energy of the beam was $50 \pm 3$ MeV. At this bombarding energy, the excitation energy of the formed compound nucleus $^{215}$At is $E^* \approx 49 \pm 3$ MeV. Thus, we can expect the formation of evaporation residues with the emission of up to six neutrons.

Most of the residual nuclei produced in He-induced reactions on $^{209}$Bi, due to their closeness to the $N = 126$ and $Z = 82$ closed shells, are short-lived $\alpha$-particle emitters. The characteristics [9] of the main $\alpha$-decay modes of the nuclei, which can be formed in our case in the $^{6}$He-induced reaction, are shown in the table. It is seen that the $\alpha$-decay half-lives of these nuclei are generally short and the $\alpha$-decay energy is reasonably well spaced in the energy region 6–10 MeV.

In Fig. 4, the $\alpha$-particle energy spectrum measured in the reaction $^{6}$He + $^{209}$Bi is shown. The $4n$-evaporation channel, with the formation of $^{211}$At, can be identified in two ways. The isotope $^{211}$At ($T_{1/2} =$

Alpha-decay characteristics of the nuclei formed in the $^{6}\mathrm{He} + {}^{209}\mathrm{Bi} \rightarrow {}^{215-xn}\mathrm{At}$ reaction

| $xn$ | Evaporation residue | $T_{1/2}$ | $E_\alpha$, MeV |
|---|---|---|---|
| $1n$ | $^{214}$At | 558 ns | 8.82 |
| $2n$ | $^{213}$At | 125 ns | 9.08 |
| $3n$ | $^{212}$At | 314 ms | 7.68 |
| $4n$ | $^{211}$At | 7.21 h | 5.87 |
| | | | 7.28 ($^{211}$Po, 516 ms) |
| $5n$ | $^{210}$At | 8.1 h | 5.36–5.52 |
| | | | 5.3 ($^{210}$Po, 138.4 d) |

7.21 h) undergoes $\alpha$ decay with $E_\alpha = 5.87$ MeV with a probability of 41.8%. In 58.2% of the cases, it decays by electron capture into short-lived $^{211}$Po ($T_{1/2} = 0.516$ s), which in turn undergoes $\alpha$ decay with $E_\alpha = 7.28$ MeV. In fact, two lines are observed in the energy spectrum of the $\alpha$ particles, which can be attributed to the decay of $^{211}$At: the first one ($E_\alpha \approx 5.74$ MeV) is located in the energy region where other nuclei contribute, whereas the second peak ($E_\alpha \approx 7.53$ MeV), corresponding to the decay of $^{211}$Po, allows good identification.

The evaporation of five neutrons leads to the production of the isotope $^{210}$At ($T_{1/2} = 8.1$ h). With about 99.8% probability, it decays by electron capture to $^{210}$Po ($T_{1/2} = 138.4$ d), and only in 0.18% of the cases does it undergo $\alpha$ decay with an average energy $E_\alpha \approx 5.4$ MeV. The $^{210}$Po isotope is an $\alpha$ emitter with $E_\alpha = 5.3$ MeV. As we can see in Fig. 4, there is a third peak in the spectrum at $E_\alpha \approx 5.28$ MeV, which can be explained by the decay of $^{210}$At and its daughter isotope $^{210}$Po.

## 4. CONCLUSIONS AND PERSPECTIVES

We have reported here on a set of measurements of prompt $^{7}$Li-induced fission of $^{209}$Bi and various evaporation residues produced in the $^{6}\mathrm{He} + {}^{209}\mathrm{Bi}$ reaction, performed by detection of fission fragments and $\alpha$ particles emitted from the produced nuclei. The described setup is to be used in excitation function measurements. We plan to measure the excitation functions of fission and fusion reactions. The fusion cross sections are determined from the sum of the $xn$-evaporation cross sections and the fission cross sections.

For better performance, we plan to improve the described setup by introducing CsI detectors and position-sensitive parallel-plate avalanche counters for the control of the spot size and the quality of the secondary beam, and for the identification of the reaction products. Also, some experiments of this type using other secondary beams are to be carried out at the DRIBs facility at JINR.

## ACKNOWLEDGMENTS

This work has been carried out with financial support from INTAS (grant no. 00-00463) and the Russian Foundation for Basic Research (project no. 01-02-22001), as well as from Bulgaria and the Czech Republic in the framework of the collaboration with JINR.

## REFERENCES

1. Yu. E. Penionzhkevich, Nucl. Phys. A **588**, 259c (1995).
2. A. S. Fomichev *et al.*, Z. Phys. A **351**, 129 (1995).
3. P. A. DeYoung *et al.*, Phys. Rev. C **58**, 3442 (1998).
4. N. K. Skobelev *et al.*, JINR Rapid Commun., No. 4[61]-93, 36 (1993).
5. J. J. Kolata *et al.*, Phys. Rev. C **57**, R6 (1998).
6. C. Signorini, Nucl. Phys. A **616**, 262c (1997).
7. J. R. Huizenga, R. Chaudhury, and R. Vandenbosch, Phys. Rev. **126**, 210 (1962).
8. S. M. Lukyanov *et al.*, Preprint No. P13-2000-283, JINR (Dubna, 2000).
9. http://atom.kaeri.re.kr/ton/nuc6.html.

*Physics of Atomic Nuclei, Vol. 66, No. 9, 2003, pp. 1663–1665. From Yadernaya Fizika, Vol. 66, No. 9, 2003, pp. 1711–1713.*


# Energy-Loss Spectrometer for Precise RIB Experiments in the Vicinity of the Coulumb Barrier*

**V. Z. Maidikov[1),2)**], V. V. Bashevoy[1)], and V. N. Melnikov[1)]**

[1)] *Flerov Laboratory of Nuclear Reactions, Joint Institute for Nuclear Research, Dubna, Moscow oblast, 141980 Russia*

[2)] *Institute for Nuclear Research, National Academy of Sciences of Ukraine, Kiev, Ukraine*

Received August 28, 2002

**Abstract**—Magnetic spectrometers of charged nuclear reaction products, properly matched with an accelerator beam line, have become a very effective setup for the performance of precise nuclear experiments involving ultrasensitive accelerator-based mass spectrometry and investigation of rare events, as well as experiments with radioactive nuclear beams. The procedure for increasing the efficiency and resolution of the available magnetic spectrometer at the Flerov Laboratory of Nuclear Reactions by a few orders of magnitude by means of its matching with the beam line is described. © *2003 MAIK "Nauka/Interperiodica"*.

## INTRODUCTION

During the last years, the main interest in radioactive ion beam (RIB) experiments has shifted to the intermediate- and high-energy region, since in these experiments RIBs are produced mainly using projectile fragmentation reactions. Thus, traditional nuclear reaction studies in the vicinity of the Coulomb barrier are scarce with regard to the use of RIBs.

The realization of the DRIBS project [1] will give rise to a rather unique possibility of precise experiments with RIBs that can be performed in the same manner as with accelerated beams of stable nuclei. According to this project, the U-400 cyclotron serves as a postaccelerator of RIBs produced at the U-400M cyclotron and at the MT-25 microtron.

An energy-loss spectrometer—a very effective setup for precise nuclear reaction studies based on magnetic analysis of the primary beam and charged nuclear reaction products—can be built on the basis of the existing magnetic analyzer at the U-400 cyclotron beam switchyard at the Flerov Laboratory of Nuclear Reactions (FLNR), namely, the broad-range magnetic spectrometer MSP-144 [2].

The solid angle acceptance of the MSP-144 spectrometer is about 5 msr and the momentum acceptance is ≈250% with the focal plane length of 1.5 m. The energy dispersion of the spectrometer is about 1 cm/%. It is installed on the first floor of the U-400 beam switchyard. The cyclotron beam is transported from the second floor to the spectrometer target through the beam downing and commutation setup (DCS) [3]. The DCS consists of two 90° bending magnets; the lower one is rotatable around the vertical beam axis to direct the beam either to the spectrometer or to other setups located on the first floor. The DCS could serve as a monochromator of the accelerated beam directed onto the spectrometer target.

Due to the orthogonality of the dispersive planes of the monochromator and spectrometer, the beam passing through the DCS is further focused onto the MSP-144 spectrometer target with a beam intensity loss of about 90%. To avoid this loss, it is necessary to realize the energy loss operation mode of the spectrometer by means of dispersion matching between the monochromator and the spectrometer [4]. The dispersion matching [5–7] permits one to increase the overall efficiency by a few orders of magnitude, preserving the main advantage of the magnetic spectrometer—the very high energy resolution.

## DISPERSION MATCHING

The dispersion matching conditions of the beam line with the magnetic spectrometer in the first-order approximation using the TRANSPORT computing code [8] notation for the ion optics matrix elements are given by

$$b_{16} = -s_{16}/s_{11} \quad \text{for the lateral dispersion,}$$

$$b_{26} = s_{21}s_{16} - s_{11}s_{26} \quad \text{for the angular dispersion,}$$

where $b_{16}$ and $b_{26}$ are the primary beam lateral and angular dispersion coefficients created by the beam

*This article was submitted by the authors in English.

** e-mail: maidikov@flnr.jinr.ru

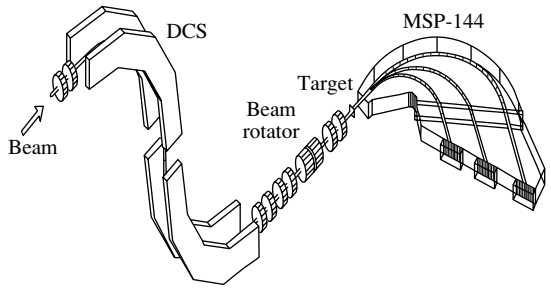


**Fig. 1.** Scematic layout of the matching of the beam downing and commutation system with the spectrometer.

line at the spectrometer target position with respect to the lateral $s_{16}$ dispersion and angular $s_{26}$ dispersion, and the lateral $s_{11}$ magnification coefficients of the spectrometer. Under these conditions, the energy resolution of the magnetic spectrometer becomes independent of the energy spread of the primary beam and its spot size at the target (in a first-order approximation).

At the U-400 cyclotron beam switchyard, such conditions can be achieved by means of a beam rotator [9] introduced into the beam line between the DCS and the spectrometer (see figure). The beam path length of about 15 m between the DCS and MSP-144 is long enough for the beam rotator and the necessary focusing elements to be installed. Such a rotator consists of five standard quadrupole lenses capable of turning the vertically oriented DCS dispersion plane to the horizontal plane, where the dispersion plane of the spectrometer is situated.

In this way, it is possible to use practically the total RIB energy and angular spread (even in the case of extracting the beam from a few cyclotron orbits simultaneously) for precise nuclear reaction experiments using the magnetic spectrometer, including precise nuclear structure studies, because, for the spectrometer, properly matched with the beam line, the energy loss of the particle in the target strongly corresponds to the nuclear excitation energy. In this case, all particles leading to the population of a specific state in a nuclear reaction are brought to the same point in the focal plane of the spectrometer. The position of this point along the focal plane is independent of the energy of the particle that initiated the reaction.

## KINEMATIC COMPENSATION

The accomplishment of the dispersion matching gives an additional opportunity for the compensation of the kinematic broadening of the spectrograph spectral line arising from the angular dependence $dE/d\Theta$ of the energy of the reaction products in the spectrometer acceptance solid angle [10–19]. At the first step, such compensation is performed by means of primary beam spot defocusing at the target through proper beam line tuning for obtaining better resolution in the focal plane of the spectrometer at the maximum counting rate. This defocusing procedure includes the matching of the spectrometer acceptance with the cyclotron emmitance so as to obtain optimal conditions for the relation between the counting rate and the energy resolution. The kinematic defocusing changes the above-mentioned matching conditions together with the focusing conditions by the following kinematic factors:

$$K = (1/P)(dP/d\Theta) \text{ and } C = (P_b/P)(dP/dP_b),$$

where $P_b$ and $P$ are the moments of the beam and nuclear reaction product under consideration, respectively. The final beam focusing conditions on the spectrometer target in the dispersive plane in the first-order approximation for the beam particle coordinate shift $x$ and its trajectory deviation angle $\theta$ from the central reference trajectory in the horizontal plane in the target position together with the target effect taken into account are

$$x = x_0(s_{11}b_{11}T + s_{12}b_{21}) + \theta_0(s_{11}b_{12}T + s_{12}b_{22}) + \delta_0(s_{11}b_{16}T + s_{12}b_{26} + s_{16}C) + \Theta(s_{12} + s_{16}K),$$

$$\theta = x_0(s_{21}b_{11}T + s_{22}b_{21}),$$

where $T = x_{\text{out}}/x_{\text{in}}$ and $\Theta = \theta_{\text{out}} - \theta_{\text{in}}$ are target functions [9] giving the change in particle trajectories due to the scattering or reaction at the target, and $x_0$, $\theta_0$, and $\delta_0$ are arbitrary beam particle initial coordinate, angle, and momentum divergence from the central reference trajectory at the accelerator exit, respectively. They determine the geometrical and momentum emmitance of the accelerator. Similar expressions are valid for the particle trajectory coordinate $y$ and its angle $\phi$ at the vertical plane.

The realization of all these conditions by means of proper beam line tuning brings the net experimental resolution of such a system to the first-order resolving power of the spectrometer with a simultaneous increase in its efficiency by a factor of about 100. In addition, such matching strongly eliminates (to a few orders of magnitude) the parasitic background of scattered particles due to the absence of collimators in the vicinity of the target. For compensation of the higher order effects, it is necessary to make a higher order aberration correction of the beam line, particularly for the DCS.

An additional increase in spectrometer efficiency can be made by means of the detector array around the spectrometer target solid angle increasing particularly for the correlation experiments with the magnetic spectrometer.

## CONCLUSION

The proper matching of existing facilities at the FLNR U-400 cyclotron beam switchyard gives them a new quality: the energy loss mode of operation for precise nuclear reaction experiments.

The resulting gain in their efficiency of about two orders of magnitude together with the net resolution increasing is very important for registering rare events in nuclear reaction studies, for precise ultrasensitive accelerator-based mass spectrometry (AMS), and in experiments with radioactive nuclear beams having low intensity and rather large energy spread.

## REFERENCES


1. G. G. Gulbekyan and Yu. Ts. Oganessian, in *Proceedings of the International Conference on Nuclear Physics "Nuclear Shells—50 Years," Dubna, 1999* (World Sci., Singapore, 2000), p. 61.
2. V. Z. Maidikov *et al.*, Prib. Tekh. Éksp., No. 4, 68 (1979).
3. G. G. Gulbekyan *et al.*, Preprint No. 9-85-346, JINR (Dubna, 1985).
4. V. Z. Maidikov, FLNR JINR Scientific Report 1999–2000, "Heavy-Ion Physics" (Dubna, 2001), p. 191.
5. B. L. Cohen, Rev. Sci. Instrum. **30**, 415 (1959); **33**, 85 (1962).
6. H. G. Blosser *et al.*, Nucl. Instrum. Methods Phys. Res. **91**, 61 (1971).
7. B. W. Ridley *et al.*, Nucl. Instrum. Methods Phys. Res. **130**, 79 (1975).
8. K. L. Brown, CERN Report 80-04 (1980).
9. S. Kowalski and H. Enge, in *Proceedings of the 4th International Conference on Magnet Technology, Berkeley, 1972,* p. 182.
10. H. Enge, Nucl. Instrum. Methods **49**, 181 (1967); **105**, 205 (1972); **162**, 161 (1979).
11. G. Hinderer *et al.*, Nucl. Instrum. Methods Phys. Res. **160**, 449 (1979).
12. H. Ikegami *et al.*, Nucl. Instrum. Methods Phys. Res. **175**, 335 (1980).
13. H. Ikegami *et al.*, Nucl. Instrum. Methods Phys. Res. **187**, 13 (1981).
14. Y. Sugiyama *et al.*, Nucl. Instrum. Methods Phys. Res. **187**, 25 (1981).
15. S. A. Martin *et al.*, Nucl. Instrum. Methods Phys. Res. **214**, 281 (1983).
16. Y. Fujita *et al.*, Nucl. Instrum. Methods Phys. Res. **225**, 298 (1984).
17. H. J. Gils *et al.*, Nucl. Instrum. Methods Phys. Res. **276**, 151 (1989); **276**, 169 (1989).
18. L. Bianchi *et al.*, Nucl. Instrum. Methods Phys. Res. **276**, 519 (1989).
19. T. Ichihara *et al.*, Nucl. Phys. A **569**, 287 (1994).

*Physics of Atomic Nuclei, Vol. 66, No. 9, 2003, pp. 1666–1670. From Yadernaya Fizika, Vol. 66, No. 9, 2003, pp. 1714–1718.*


# Analysis of Rare Events in Heavy-Ion Experiments*

**V. B. Zlokazov****

*Joint Institute for Nuclear Research, Dubna, Moscow oblast, 141980 Russia*

Received August 28, 2002

**Abstract**—Experiments in both high- and low-energy physics are planned so that physically interesting effects mathematically are rare (or small probability) events, compared to others, whose probabilities are not small. Correspondingly, the purpose of the paper was the development of the formalism for the treatment of rare events, which could be an inevitable alternative to methods requiring too much a priori information about the studied effect, in a situation when such information is absent, but, instead, background information is available, e.g., from calibration measurements. The main topics of the paper were as follows: (1) To what extent are the methods of Poisson time-event streams suitable for the goal declared? (2) What information can be extracted from the calibration measurement that detected zero interesting events? The method described is illustrated by the analysis of data registered in the experiment on the synthesis of element 114. © *2003 MAIK "Nauka/Interperiodica"*.

The outcome of the most advanced exploratory physical experiments is the observation of single events, which, on one hand, promise an exhilarating and innovative scientific interpretation, but, on the other hand, suffer from the lack of objective arguments for its justification. The low data statistics and absence of reliable theoretical forecasts necessitate a very cautious strategy, trying, first, to get answers to the basic questions such as: Is the observed event a random signal combination, or does it represent an interesting physical phenomenon?

Both signals of interest and those of the background normally are results of some radioactive decays, statistically independent of each other, and the only feature identifying the interesting event is that its constituent decays are genetically (not statistically) linked according to a certain pattern.

One can build two approaches to tackle the problem of signal identification:

(1) Formalize the concept of a background signal combination (BSC) and test whether the signal sequence analyzed does fit in this concept or not.

(2) Formalize the concept of a linked decay signal combination and test whether the signal sequence analyzed does fit in this concept or not.

In cases of extremely indefinite and poor experimental outcomes, we do not know the structure of the decay chain a priori; neither is reliable information about the half-lives of members of this chain available. In this situation, the first approach is inevitable and the most natural: to see whether the signal group analyzed corresponds to the BSC pattern or not, and thereby get the answer to the basic question mentioned above.

The most important advantage of this approach is the fact that, for building a BSC pattern, we can use objective sources of information—data of the background calibration measurement, which, in addition, are not affected by poor statistics [1].

**Philosophy of rare events.** Mathematically, we face here the following problems:

What is formally a static small probability event? It is not an impossible event; it is one occurring with a (negligibly) small probability compared to alternative events that could occur in the situation considered. Such a definition is not related to the absolute value of this probability. "Small" in mathematics is always used in a comparative context. If the distribution of signals is uniform, then we can observe situations paradoxical to the common sense of the majority of people. Namely, the probabilities of arbitrary event combinations are equal however exotic these combinations might be. For example, molecules of ideal gas under no gravity conditions with the same probability can form a completely chaotic figure, say, a human-body-like one. The basis for distinguishing patterns is a deterministic constituent of the Universe and specific features of certain random distributions.

What is formally a dynamic (proceeding in time) small probability event? All the aforesaid applies here too, but, in addition, we have here an effect of occurrence of ever greater deviation from the mean, while the observation goes on. A widespread error is connected with this effect—many people observing,

*This article was submitted by the author in English.

** e-mail: zlokazov@nf.jinr.ru

e.g., a hurricane that has never been registered before conclude that "the climate has changed." In fact, this event itself is not yet a reason for such a conclusion. In the observation of outcomes of a random number generator in the case of even such an "almost-deterministic" distribution as the normal one, ever larger deviations from the mean will be encountered (though with ever smaller probability), but, certainly, this is not evidence that "the generator has changed."

However cumbersome a signal combination shape might be and small probability it might have, it can occur in both static and dynamic situations. Certainly, conclusions made on such a weak basis do not have the convincibility of classical statistics, and the correct scientific decision becomes a matter of clever will and lucky chance. We build up not the "true" world image, but a "probable" one. The science based on small statistics is no longer knowledge of actual reality, but rather that of a virtual one.

**Mathematics of random event time processes.** Stochastic Poisson time processes, which proved to be perfect in many scientific and technical application fields as models of random event streams while the necessary a priori information about their origin is absent, seem to be the best means for the description of the background decays.

These processes are the time functions $k(t_1, t_2)$—numbers of random events occurring during a time interval $(t_1, t_2)$ with a probability $Q_k(t_1, t_2)$ and having the following properties:

(i) stationarity: $Q_k(t_1, t_2) = Q_k(t_2 - t_1)$ for arbitrary $t_1, t_2$;

(ii) $Q_k(t_1, t_2)$ independence of the event prehistory: $Q_k(t_1, t_2|C) = Q_k(t_1, t_2)$, where $C$ means events that happened before $t_1$;

(iii) rareness of events: $Q_{k>1}(\delta t) = o(\delta t)$.

These properties allow us to write simply $k(t)$ and $Q_k(t)$ bearing in mind that $t$ means the duration of $(0, t)$ = the time interval considered.

Incidental radioactive decays, as a rule, satisfy the above-numbered requirements; therefore, we can indeed use the Poisson processes for modeling both static and dynamic backgrounds. Further on, we shall use the term "signal" instead of "event," and event will mean a signal combination.

The function of probability distribution of $k(t)$ is

$$Q_k(t) = \frac{(lt)^k}{k!}\exp(-lt), \quad t \in (0, \infty), \qquad (1)$$

where $l$ is parameter of the Poisson distribution and $t$ is time. Note that $l = \ln(2)/T_{1/2}$, where $T_{1/2}$ is the half-life. The quantity $lt$ is the expectation and at the same time the variance of $k(t)$ at a moment $t$.

If the signals are of different type, formula (1) describes only probabilities of their sums irrespective of their order and configuration. If the event is made up of time-independent signal combinations of $m$ kinds, the probability distribution of the definite configuration is

$$Q_{sk}(t) = p_s \prod_{i=1}^{m} Q_{k_i}(t), \quad t \in (0, \infty), \qquad (2)$$

where $p_s$ is the probability of combination of the $s$th kind. An independent characteristic of the random signal sequence is $\tau$—the time between the two subsequent signals. It is subject to the exponential distribution

$$P(\tau < t) = 1 - \exp(-lt), \quad t \in (0, \infty),$$

where $l$ is the same parameter as above. The expectation $T_m$ and the variance $T_v$ are

$$T_m = \frac{1}{l}, \quad T_v = \frac{1}{l^2}.$$

The estimates of $l$ obtained from the data on the basis of (1) and of $T_m$ from the differences of these data on the basis of (2) are almost uncorrelated and can serve as independent statistical characteristics of the data analyzed.

In the case of a chain of genetically linked decays, the average distances between the times are predetermined, but they can be seen only if the statistics are large. For the case of rare signals, these distances do not play any role, whereas average minimax time distance estimates are rather informative quantities for distinguishing the background from the interesting phenomenon,

$$T_{\max} = \int_0^\infty tnl(1 - \exp(-lt))^{n-1}\exp(-lt)dt,$$

$$T_{\min} = \int_0^\infty tnl\exp(-lnt)dt,$$

where $n$ is the number of items in the signal sequence.

Thus, an event is set of $n$ signals of a specified configuration having occurred within a time interval $(0, t)$ with the probability $Q_{sn}(t)$ (2). If the measurement is dynamic and occupies the $(0, T)$ time span, $T \gg t$, then $N$—the number of event occurrences during $(0, T)$—will have a multinomial distribution $P_N$ with the mean $N_m$ and the variance $N_v$, where

$$N_m = Q_{sn}(t)\frac{T}{t}, \quad N_v = Q_{sn}(t)(1 - Q_{sn}(t))\frac{T}{t}. \qquad (3)$$

These quantities are very important for deciding whether the observation trajectory is rare or not.

The signals can be falsely identified or detected with probability (efficiency) less than 1. This makes the calculation of frequencies and probabilities like (2) and (3) more complicated; also, the estimation of quantities $l$, $N_m$, and $N_v$ from the calibration data becomes less reliable.

Spatial characteristics are another important means for background/phenomenon distingishability: if the places of a decay chain are significantly the same, it is a serious objection against the background hypothesis. The following test can be used for checking place coincidence.

Let $x_i$, $i = 1, 2, \ldots, n$, be signal locations and $\mathrm{var}(x_i)$ their variances. Bearing in mind that coordinates $x_i$ are in fact differences between zero (which is also a random quantity) and the registered coordinates, one can check whether the quadratic form

$$S_n = \sum_{i=1}^{n} y_i^2,$$

$$y_i = (x_i - x_{i+1})/\sqrt{\mathrm{var}(x_i) + \mathrm{var}(x_{i+1})},$$

has a distribution relevant for this case. Here, $y_i$ have zero expectation and unit variance, and the pairs $y_i$, $y_{i+1}$ are correlated with the coefficient $-0.5$. The probability distribution function of $S_n$ is not a usually assumed $\chi^2$ one even in the case of the normal distribution of $x$: one can show that the expectation of $S_n = n$; the variance $= 3n - 1$.

Similar tests can be elaborated for other quantities (energy of the decay products, etc.) if their means and variances are available.

**What information does detecting zero events contain?** This is a very important problem for both high- and low-energy physics. Within the framework considered here, we can say the following. The probabilities $P_0$ to detect within the time interval $(0, T)$ zero events, each characterized by $n$ signals defined at the time interval $(0, t)$, is

$$P_0 = (1 - p_s(lt)^n \exp(-lt)/n!)^{T/t}, \quad t \in (0, \infty). \tag{4}$$

Unfortunately, from this, it is impossible to estimate $l$. One can only solve a couple of problems of planning an experiment: for given $P_0$, $p_s$, and $l$ (or $T$), calculate $T$ (or $l$). Still, the most interesting problem is how to extract the information from "zero event" calibration, at least, about the lower limits of the quantities $T$ or $T_{1/2}$.

If during a long time period $T$ no event was registered, one can use a heuristic rule of "equal chances for the event to occur or not to occur," which corresponds to our complete absence of a priori information about the event and mathematically is a consequence of the principle of maximum entropy applied to this case:

$$P_0 = P_{\neq 0}. \tag{5}$$

From this, we get the estimate of $l$: $\hat{l} = \ln(2)/T$.

**Treating a physical effect as a rare event.** The event is rare if the probability of its constituent signal combination is small compared with the probability of other combinations that we call typical. Here, the comparison is stressed: the widespread habit to deal with absolute probabilities has no mathematical substantiation; probabilities of "typical" events can also be however small.

A typical event does not always mean background, just as a rare event should not necessarily be an interesting phenomenon. However, physical experiments are normally planned so that an event is a physical effect if it is rare.

In the static case—if a set of patterns is registered, each of which is characterized by $n$ signals, and we should decide which of them are rare and which are typical—comparison of $l$, $n(lt)$, $T_{\max}$, $T_{\min}$, and $S_{n-1}$ derived from background calibration and those calculated for the checked event is enough to make such decision: if the latters significantly (in the sense of mathematical statistics) differ from the formers, the event is rare and, thereby, not a background one.

In the dynamic case—if the measurement continues for a long time—the situation is more complicated. As stated above, rare signal combinations can occur, at least once, however small their probability might be, assuming that the observation time lasts sufficiently long, the only restriction being that the combination should not contradict physical or mathematical laws.

Here, one should define what a rare trajectory of a time process is.

Summarizing all the aforesaid, we state that, if $N_e$—the number of event occurrences in the experiment data—is much greater than $N_b$—the number of event occurrences in the background calibration data of the same registration period—then the trajectory is rare and, thus, the event is not a background one (in the physical sense). Statistical definition means by "much greater" no intersection of confidence intervals for $N_e$ and $N_b$.

Within the framework of such an approach under conditions of absence of qualitative and quantitative information about the decay time, there is not an appropriate characteristic for testing the event for randomness; as such, the number of occurrences of events of known types (in the case of element 114 the combination of recoil implantation and alpha-decay imitators, followed by final spontaneous fission) within a definite time interval should be used.

The selection of the time interval has to be optimal; it should be large enough so that the events occurring in it make up a combination suitable for physical interpretation if this combination turns out not to look random. And it should not be too large, since otherwise even numbers of actually linked decays referred to too large an interval make the statistical criteria to consider them random.

**Analysis of data from experiments on the synthesis of element 114.** The recorded locations of the decaying nucleus from the $^{48}Ca + {}^{244}Pu$ reaction are [2]

$x_{evr} = 16.5$ mm (position of the implantation signal);

$x_{\alpha 1} = 15.6$ mm, $x_{\alpha 2} = 16.5$ mm, $x_{\alpha 3} = 17.0$ mm (positions of alpha signals);

$x_{sf} = 17.1$ mm (position of spontaneous fission signal);

evr–alpha resolution $= 1.4$ mm, $\sigma_{evr-\alpha} = 0.59$ mm;

alpha–alpha resolution $= 1.0$ mm, $\sigma_{\alpha-\alpha} = 0.42$ mm;

evr–sf resolution $= 1.2$ mm, $\sigma_{evr-sf} = 0.51$ mm.

Times:

$t$ of implantation signal $= 0$;

$t$ of alpha signals $= 0.5, 15.9, 17.5$ min;

$t$ of spontaneous fission signal $= 34.0$ min.

The experiment and calibration duration was about 48 800 min [3]. Thus, our pattern of the interesting event is a time interval of 34 min, containing the recoil implantation signal, three alpha signals, and that of spontaneous fission; this event was observed in the time period of 48 800 min.

To illustrate the method described above in operation, we will proceed as follows.

The reliability of alpha-particle identification (by energy of 8.5–10 MeV in a detector strip for a position-correlation window of 1.6 mm) and that of spontaneous fission (by large energies) is justified only qualitatively, so we cannot involve it in quantitative calculations. The detection efficiency is known (about 0.87), but at this stage of analysis it is not appropriate to use it.

Calibration measurement of chance signals of recoil implantation and alpha particles with energy of 8.5–10 MeV gave the following: implantation $= 1.3$ per hour; alpha particle $= 1$ per hour; the fact that no spontaneous fissions were detected in the total calibration measurement is one of the most important facts for our analysis.

From this data, we can derive the probability of the events: one imitator of the implantation signal 34 min before the spontaneous fission and three imitators of alpha particles between them.

The time interval of 34 min was the minimum possible, but, certainly, it is not optimal. The real event pattern should be longer, at least, by one-quarter of this time—$(n+1)/n =$ normal maximum likelihood estimate of the interval size; neglecting the first signal as the interval starting point, we have $n = 4$, so that the interval can be taken to be 42.5 min long. These events represent a typical time process of the Poisson type. We can estimate its parameters for implantation and alpha-particle imitators on the basis of calibration data as follows:

$$l_i \cdot 60 = 1.3; \quad l_a \cdot 60 = 1,$$

which gives us $l_i = 1.3/60$ and $l_a = 1/60$.

On the basis of (5), we can set $l_{sf} = \ln(2)/48800$ for the spontaneous fission. Then, we get the following probabilities:

$$Q_{1_i}(42.5) = \frac{(42.5 \cdot 1.3/60)^1}{1!}\exp(-42.5/60)$$
(implantation),

$$Q_{3_\alpha}(42.5) = \frac{(42.5 \cdot 1/60)^3}{3!}\exp(-42.5/60)\ \text{(alpha)},$$

$$Q_{1_{sf}}(42.5) = \frac{(42.5\ln(2)/48\,800)^1}{1!}$$
$$\times \exp(-42.5\ln(2)/48\,800)\ \text{(spont. fission)}.$$

Using the probability of the signal order $p_s = 0.05$, we have the total probability

$$P_{total} = p_s Q_{1_i} Q_{3_\alpha} Q_{1_{sf}} \sim 0.3226 \times 10^{-6}.$$

To make a statistically correct decision, it is necessary to compare it with the probabilities of other random signal combinations. We have the following:

| Implantation | Alpha | Spont. fission | Probability |
|---|---|---|---|
| 0 | 0 | 0 | 0.19597461 |
| 0 | 1 | 0 | 0.13881535 |
| 0 | 2 | 0 | 0.04916377 |
| 1 | 1 | 0 | 0.12782580 |
| 1 | 2 | 0 | 0.04527164 |

It is seen that the largest is the probability to observe the combinations $0+0+0, 0+1+0, 1+2+0$, but the probability of the combination $1+3+1$ is really small as compared with them and belongs to the region of small probabilities, and that our event is a very little probable random static event.

Other calculations confirm this statement. Namely, let us compare the minimax time differences $T_m$ for the background and the event of interest:

background: $T_m = 26.09$ min,

$$\text{tested event: } T_m = 8.5 \pm 3.7 \text{ min};$$

$$\text{background: } T_{\max} = \frac{25}{12} T_m = 54.4 \text{ min},$$

$$T_{\min} = \frac{1}{4} T_m = 6.5 \text{ min};$$

$$\text{tested event: } T_{\max} = \frac{25}{12} T_m = 17.7 \text{ min},$$

$$T_{\min} = \frac{1}{4} T_m = 2.1 \text{ min}.$$

Then, let us calculate spatial test quantity $S_n$: $S_4 = 9.56$. Let us build the table of values of $S_4$ probabilities:

| | | | | | | | | | | |
|---|---|---|---|---|---|---|---|---|---|---|
| $P$ | 0.05 | 0.10 | 0.15 | 0.20 | 0.25 | 0.30 | 0.35 | 0.40 | 0.45 | 0.50 |
| $S_4$ | 0.6 | 0.9 | 1.1 | 1.4 | 1.6 | 1.9 | 2.2 | 2.5 | 2.8 | 3.1 |
| $P$ | 0.55 | 0.60 | 0.65 | 0.70 | 0.75 | 0.80 | 0.85 | 0.90 | 0.95 | |
| $S_4$ | 3.4 | 3.8 | 4.2 | 4.7 | 5.3 | 6.0 | 6.9 | 8.2 | 10.3 | |

Here, $P$ are probabilities with the step 0.05 for the corresponding values of $S_4$. We can construct the 67% confidence interval of $S_4$ as $n \pm \sigma$; corrected for the asymmetry, it is 1.8–10.8. Thus, we see that our value of 9.56 is covered by the 67% confidence interval 1.8–10.8, which means the validity of the hypothesis that decays took place at the same place of the detector.

Next, we can estimate the dynamic characteristics $N_m$ and $N_v$:

$$N_m = (48\,800/42.5) P_{\text{total}} \sim 0.0004; \quad N_v \sim N_m.$$

In other words, during the interval (0, 48 800), the expectation of the number of such events is equal to zero, the implication being that the event considered is a really rare event in both static and dynamic senses; therefore, these four signals, followed by the spontaneous fission, do not contradict the hypothesis that they are not background.

This implication does not change even if we suppose that some alpha particle was falsely identified.

## REFERENCES

1. V. B. Zlokazov, Eur. Phys. J. A **8**, 81 (2000).
2. Yu. Ts. Oganessian, V. K. Utyonkov, *et al.*, Preprint No. E7-99-53, JINR (Dubna, 1999).
3. N. J. Stoyer, M. A. Stoyer, J. F. Wild, *et al.*, Nucl. Instrum. Methods Phys. Res. A **455**, 443 (2000).

*Physics of Atomic Nuclei, Vol. 66, No. 9, 2003, pp. 1671–1679. From Yadernaya Fizika, Vol. 66, No. 9, 2003, pp. 1719–1727.*


# Fragmentation of Nuclei at Intermediate and High Energies in Modified Cascade Model*

**G. Musulmanbekov**[1)]** **and** **A. Al-Haidary**[2)]***

[1)] *Joint Institute for Nuclear Research, Dubna, Moscow oblast, 141980 Russia*

[2)] *Cairo University, Cairo, Egypt*

Received August 28, 2002

**Abstract**—The process of nuclear multifragmentation has been implemented, together with evaporation and fission channels of the disintegration of excited remnants, in nucleus–nucleus collisions using percolation theory and the intranuclear cascade model. Colliding nuclei are treated as face-centered-cubic lattices with nucleons occupying the nodes of the lattice. The site-bond percolation model is used. The code can be applied for calculation of the fragmentation of nuclei in spallation and multifragmentation reactions.


## 1. INTRODUCTION

The intranuclear cascade model is one of the basic tools for analyzing spallation and multifragmentation processes in nuclear collisions. In the traditional cascade model of hadron–nucleus and nucleus–nucleus interactions, particle production is treated in two stages. In the first, fast, stage, an intranuclear cascade occurs inside the target and (or) the projectile nuclei and some nucleons from the target and projectile nuclei are knocked out, together with mesons. In the second stage, residual nuclei (generally, in an excited state) divide into two remnants in the fission channel or evaporate protons, neutrons, and (or) light nuclei, including helium isotopes. However, experimental data indicate that, at intermediate energies, a third competing process, multifragmentation, comes into play, in which excited remnants break up into intermediate mass fragments (IMFs). There are two approaches to theoretical description of multifragmentation: dynamical and statistical. In statistical multifragmentation models, an excited remnant achieves a thermal equilibrium state and then expands, eventually reaching the freeze-out volume. At this point, it disintegrates into neutrons, light charged particles, and IMFs. In dynamical models, IMFs are formed at the fast stage of nuclear collision via dynamical forces between nucleons during the evolution of the total system of interacting projectile and target. In this case, the whole system and its parts (projectile and target remnants) never pass through states of thermal equilibrium.

There is one more approach to describing the process of multifragmentation: percolation theory. Percolation models treat the nucleus as a lattice with nucleons located at nodes of the lattice. It has been found that results of percolation calculations depend significantly upon the details of the lattice structure. For reasons of computational convenience, the simple cubic lattice has been most frequently used in multifragmentation simulations [1], but several studies have found [2, 3] that the face-centered-cubic (FCC) lattice more accurately reproduces the experimental distributions of fragment masses and their energy spectra.

Although lattice simulations have been found to reproduce multifragmentation data surprisingly well, there has been little examination of the role of the lattice arrangement of nucleons inside nuclei. That is, lattices were employed more as computational techniques, rather than as formal nuclear models. The appearance of solid-state models of nuclear structure [4–6] can be dated from the paper of L. Pauling in 1965. The most attractive lattice model is the FCC model proposed by Cook and Dallacasa [6] because it brings together shell, liquid-drop, and cluster characteristics, as found in the conventional models, within a single theoretical framework. Unique among the lattice models, the FCC reproduces the entire sequence of allowed nucleon states as found in the shell model.

In the present paper, we further develop the modified intranuclear cascade-evaporation code (MCAS), elaborated by one of the authors [7], with the aim of inclusion of multifragmentation channels. The word

*This article was submitted by the authors in English.

** e-mail: genis@jinr.ru

*** e-mail: a_alhaydari@yahoo.com

1063-7788/03/6609-1671$24.00 

"modified" relates to the implementation of the concept of "formation time" into traditional cascade calculations, as described in Section 3. The goodness of fit of the MCAS to experimental data has been reported in previous papers [7, 8] concerning multiparticle production in nucleus–nucleus collisions at intermediate and moderately high energies (up to 10–20 GeV/nucleon). Since traditional cascade models consider nuclear structure as a dilute Fermi gas, we reconstructed the model in the framework of the lattice nuclear model. For this purpose, we implemented the FCC lattice arrangement of nucleons for the colliding nuclei according to the algorithm proposed in [9] (Section 2). Calculations of multifragmentation channels are performed on the basis of the site-bond model of percolation theory (Section 4). Comparisons with experimental data are given in Section 5.

## 2. FCC LATTICE MODEL OF NUCLEAR STRUCTURE

The FCC packing of nucleons, with protons and neutrons occupying lattice sites in alternating layers, can be seen as consisting of four interpenetrating cubes. A nearest-neighbor distance of about 2.0262 fm reproduces the known core density of nuclei (0.17 nucleon/fm$^3$). The essence of the geometry of the FCC model can be shown using the quantum numbers that are assigned to each nucleon in the conventional shell model [9]. It is known that a nucleon's distance from the center of the nucleus determines its principal quantum number $n$. The distance of the nucleon from the "nuclear spin axis" determines its total angular momentum (quantum number $j$). Finally, the distance of each nucleon from the $y$–$z$ plane determines its magnetic quantum number $m$. The inherent simplicity of the FCC model is evident in the FCC definitions of the eigenvalues:

$$n = (|x| + |y| + |z| - 3)/2, \quad (1)$$

$$j = (|x| + |y| - 1)/2, \quad (2)$$

$$|m| = |x|/2, \quad (3)$$

where the sign of the $m$ value is determined by the intrinsic spin orientation of the nucleon in the antiferromagnetic lattice (spin up $= 1/2$ and spin down $= -1/2$). Conversely, the coordinate values can be determined solely from the nucleon eigenvalues:

$$x = |2m|\,(-1)^{m+1/2}, \quad (4)$$

$$y = (2j + 1 - |x|)(-1)^{i+j+m+1/2}, \quad (5)$$

$$z = (2n + 3 - |x| - |y|)(-1)^{i+n-j-1}, \quad (6)$$

where $i$ is the isospin quantum number. Therefore, knowing the full set of eigenvalues for a given set of nucleons, the configuration of those nucleons in 3D space relative to the nuclear center can be determined unambiguously. Using the Fermi coordinates of each nucleon, the mean radius of the nucleus with $A$ nucleons is defined as

$$R[A] = R_{\text{nucl}} + \frac{1}{A}\sum^{A} r_j, \quad (7)$$

where $r$ is the Euclidean distance of each nucleon, $\sqrt{x_j^2 + y_j^2 + z_j^2}$, from the origin, and $R_{\text{nucl}}$ is the nucleon radius. The calculated charged radii for various nuclei are in good agreement with experiment.

## 3. INTRANUCLEAR CASCADE WITH THE NUCLEAR LATTICE MODEL

Nucleon coordinates (4)–(6) for the target (projectile) nucleus are generated in accordance with the algorithm [9, 10]. For each nuclear collision, lattices of target and projectile nuclei are oriented randomly in relation to the collision axes. This random orientation of the nuclear lattice in 3D space mimics the Woods–Saxon distribution of nuclear density for medium and heavy nuclei. Nucleon momenta inside the nucleus, **p,** are generated uniformly in the space $0 \le |\mathbf{p}| \le p_{\text{F}}$. The bound Fermi momentum $p_{\text{F}}$ relates to the local nucleon density as

$$p_{\text{F}} = (3\pi^2)^{1/3} h \rho^{1/3}(r). \quad (8)$$

An inelastic collision of two nuclei is an incoherent superposition of baryon–baryon, meson–baryon, and meson–meson elastic and inelastic interactions. Elastic and inelastic cross sections and kinematical features of the elastic scattering are taken from experiments.

All interactions are arranged into four groups.

Group C: interactions of the nucleons of the projectile nucleus with those from the target nucleus; all secondary particles produced in any group of interactions are considered as cascade particles.

Group A: interactions of the cascade particles with the nucleons of the target nucleus.

Group B: interactions of the cascade particles with the nucleons of the incident nucleus.

Group D: so called "cascade–cascade" interactions—interactions of cascade particles with each other.

The probability of interaction of particles $i$ and $j$ is defined by a black disk approximation:

$$P(b_{ij}^2) = \Theta(b_{ij}^2 - \sigma_{\text{tot}}/\pi), \quad (9)$$

where $b_{ij}$ is the impact parameter between hadrons $i$ and $j$, and $\sigma_{\text{tot}}$ is their total cross section. Cross sections of resonances in subsequent interactions are

taken to be the same as for stable particles. The evolution of the interacting system is considered as follows. At some instant of time $t$, all possible interacting pairs in each group (A, B, C, and D) are determined. Among all possible interactions, that one is chosen to be the first if it occurs before others, i.e., $\Delta t = \min\{t_i\}$; then, the positions of both nuclei and all cascade particles are moved to new positions corresponding to a new instant of time $t_i \to t_i + \Delta t$. Since the formation of hadronic states of secondary particles takes some time, we apply the concept of formation time (zone) for consideration of their subsequent interactions. The formation time relates to the development of the cross section of the produced particle during its propagation inside the nuclear medium. We use the exponential form of the evolution of cross sections until the subsequent collision occurs,

$$\sigma_2^l = \sigma_1^I(1 - (1 - x^l)e^{-\tau/(\gamma\tau_0)}) \qquad (10)$$

for the leading particle,

$$\sigma_2^m = \sigma_1^m - (\sigma_1^m - x^m\sigma_1^I)e^{-\tau_1/(\gamma\tau_0)} \qquad (11)$$

for the $m$th produced particle, where $\sigma_1^I$ is the normal cross section of the incident particle in the first collision, $\sigma_2^l$ is the cross section of the remnant of the projectile (leading particle) in the second collision, $\sigma_2^m$ is the cross section of the $m$th produced particle, $\sigma_1^m$ is the cross section for this type of particle in the normal state, $\gamma$ is the Lorentz factor, and $\tau_0$ is an adjustable parameter corresponding to the mean value of the formation time in the rest frame of the particle. For $(r+1)$th inelastic rescattering of the incident particle, the cross section is defined as

$$\sigma_{r+1}^l = \sigma_1^I \prod_{i=1}^{r}(1 - (1 - x_i^l)e^{-\tau_i/(\gamma_i\tau_0)}). \qquad (12)$$

Among secondaries, $s$-wave resonances (deltas, rho and omega mesons) can be produced. The hadronic event generator is briefly described in the Appendix. During the evolution of the system, the produced resonances may decay before their subsequent interactions. A check is made whether the Pauli principle is satisfied both for all interactions and for the decay of resonances. The cascade stage of particle generation is completed when all cascade particles have left both nuclei or have been partly absorbed by them. In this way, the first, fast, stage of multiparticle production of the nuclear collision has been completed. After replacing the Fermi gas nuclear model by the FCC lattice, we compared the results of simulations using both models on multiparticle production in intermediate- and high-energy nuclear collisions and have found that they are identical. The first measurable characteristic of nucleus–nucleus collisions is the reaction cross section. In intranuclear cascade models, the cross section is defined by the ratio of the number of realized inelastic collisions $N^{\rm in}$ to the total number of trials $N^{\rm trial}$:

$$\sigma^{\rm reac} = \frac{N^{\rm in}}{N^{\rm trial}}\pi(R_A + R_B + \Delta)^2, \qquad (13)$$

where $R_A$ and $R_B$ are the radii of the colliding nuclei and $\Delta$ is the radius of the strong interaction. The Fermi gas and FCC lattice models are in agreement to within an accuracy of 5%.

## 4. FRAGMENTATION OF EXCITED REMNANTS

The number and total charge of the remaining nucleons in each remnant specify the mass and charge numbers of the residual nuclei. In general, remnants are in excited states and possess angular momentum. The excitation energy of each remnant nucleus is determined by the energy of the absorbed particles and the "holes" remaining after nucleons have been knocked out during the intranuclear cascade process. The momentum and angular momentum of the residual nucleus are evaluated in light of the conservation of momentum and sequentially followed for each intranuclear interaction. Thus, there are three competing processes for the disintegration of the excited remnant nucleus: evaporation, fission, and multifragmentation. In the standard intranuclear cascade model, only the first two processes are taken into account [11]. The purpose of the present study was to implement multifragmentation on the basis of percolation theory and to determine the relative weights of the above three competing processes. We have done this by applying the site-bond percolation model. We assume that nucleons occupying lattice sites are connected with their neighbors via bonds which schematically represent two-body nuclear forces. In the fast stage, during the development of an intranuclear cascade, some nucleons occupying the sites of the FCC lattice of the target (projectile) nucleus are knocked out, leaving holes at those sites. We say that these sites are broken. The ratio of the number of broken sites to the total number of sites (the mass number of the target or projectile) characterizes the degree of destruction of the target (projectile) nucleus after the cascade stage. This ratio depends on the collision energy, on the mass numbers of colliding nuclei, and, particularly, on the impact parameter of the collision. In peripheral collisions, mainly peripheral nucleons are knocked out, meaning that, with high probability, the remaining nucleons form one cluster in which all sites are occupied. In collisions with more centrality, corresponding to intermediate or small impact parameters, nucleons are knocked out mainly from the nuclear interior

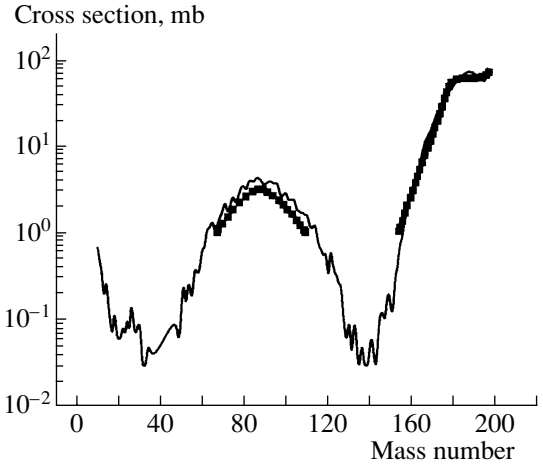


**Fig. 1.** Mass distribution of residues produced in a 0.5-GeV proton-induced reaction on $^{197}$Au; $p_{\rm bond} = 0.5$. Data are from [13].

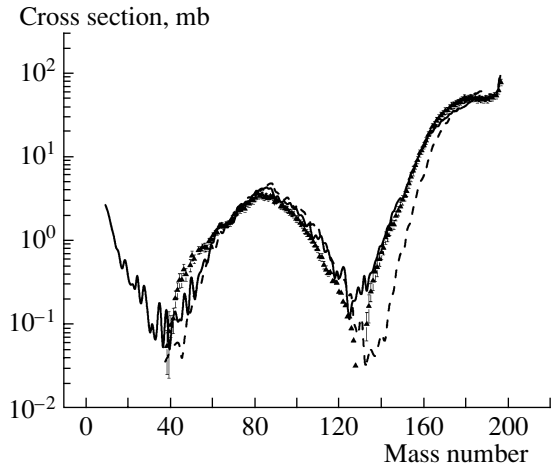


**Fig. 2.** Mass distribution of residues in the reaction $^{197}\mathrm{Au} + p$ at 800 $A$ MeV; $p_{\rm bond} = 0.57$. Dashed curve is the outcome of calculations without the contribution of multifragmentation channels. Data are taken from [14].

and the target (projectile) remnant represents the lattice with some sites broken. As mentioned above, remnants, in general, are in excited states. The larger the impact parameter, the smaller the number of broken sites and the less the excitation energy of the remnant. This initial condition is preferable for equilibration and thermalization of excited nuclear media and allows one to use evaporation and fission mechanisms for subsequent disintegration of the excited remnant. With increasing centrality of the collision, the number of broken sites increases (large destruction), leading to increasing excitation energy of the remnant nucleus. For this case, there is no conventional understanding of the mechanism of disintegration of an excited remnant (thermal breakup with statistical multifragmentation, liquid–gas phase transition, sequential evaporation, cold shattering breakup, etc.). However, it is obvious that, when there is considerable destruction of the remnant, there is no possibility for equilibration and thermalization over the whole volume of the remnant.

For excited remnant disintegration, we specify the bond-breaking probability, as an input parameter $p_{\rm bond}$, in the form of an impact parameter dependence:

$$p_{\rm bond}(b) = p_{\rm bond}(0)\sqrt{1 - \frac{b^2}{(R_A + R_B)^2}}, \qquad (14)$$

where $R_A$ and $R_B$ are the radii of the colliding nuclei. This ansatz can be derived from considerations of the collision geometry. The cluster counting algorithm developed by the authors looks for clusters (fragments): whether neighboring nucleons are connected via bonds or not. Only first nearest and second nearest neighbors are taken into account in the counting algorithm. In the initial FCC lattice, each nucleon has 12 first nearest neighbors at a distance of 2.0262 fm and 6 second nearest neighbors at 2.8655 fm. As a result of this counting algorithm, we obtain the mass and charge distribution of the fragments. Although this approach is statistical and the probability of any bond being broken does not depend on its position, the probability of disintegration of the remnant on multiple clusters (fragments) will be higher in the vicinity of regions with many broken sites. From this, it follows that the process of multifragmentation is influenced by the dynamics of the collision; i.e., according to our scenario, it is not purely a statistical process.

Next, we specify the energetic characteristics of the radiated fragments. In general, in its proper frame, the remnant possesses rotational energy $E^{\rm rot}$ and excitation energy $E^*$, which are used in the summation of the rotational $E^{\rm rot}_{\rm fr}$ and kinetic $E^{\rm kin}_{\rm fr}$ energies of fragments, their excitation energies $E^*_{\rm fr}$, and the energy of the Coulomb interactions of the fragments $E^{\rm Coul}_{\rm fr}$:

$$E^{\rm rot} + E^* = E^{\rm rot}_{\rm fr} + E^{\rm kin}_{\rm fr} + E^*_{\rm fr} + E^{\rm Coul}_{\rm fr} \qquad (15)$$
$$= \sum E^{\rm rot}_i + \sum E^{\rm kin}(A_i, Z_i) + \sum E^*(A_i, Z_i) + \frac{1}{2}\sum \frac{Z_i Z_j}{r_{ij}}.$$

In the standard intranuclear cascade model, the contribution of rotational energy $E^{\rm rot}_{\rm fr}$ is small compared with other terms, at least for light nuclei as projectiles. Whether or not this is the case in reality is unknown. Large rotational energies could be realized in this approach if we included nuclear viscosity. In the current calculations, we neglect the first term. Moreover,

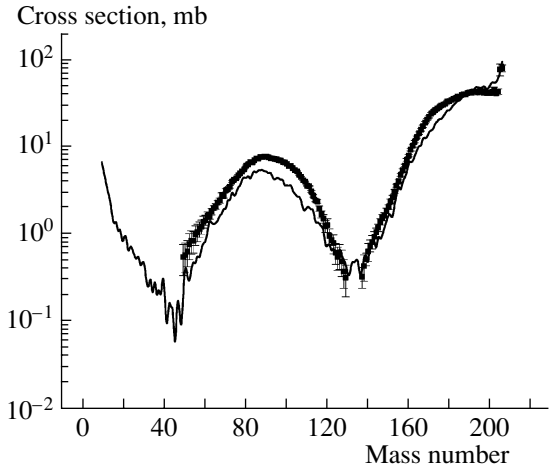


**Fig. 3.** Mass distribution of residues in the reaction $^{208}\mathrm{Pb} + p$ at 1 $A$ GeV; $p_{\mathrm{bond}} = 0.6$. Data are taken from [15].

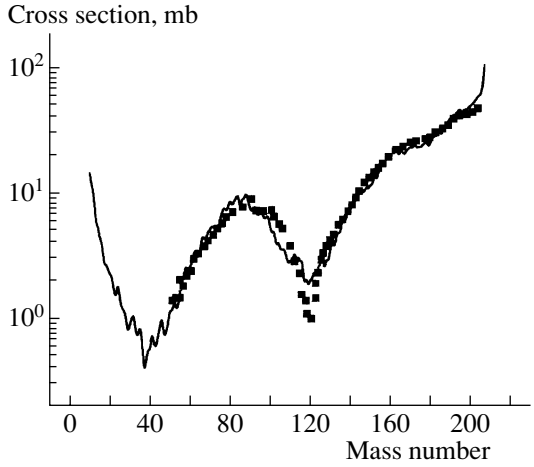


**Fig. 4.** Mass distribution of residues in the reaction $^{208}\mathrm{Pb} + d$ at 2 $A$ GeV; $p_{\mathrm{bond}} = 0.62$. Data are taken from [16].

for computational convenience, we make additional simplifications in Eq. (15). Since the Coulomb repulsion of the charged fragments increases their kinetic energies, we define the resulting kinetic energies of the fragments as follows:

$$E_{\mathrm{fr}}^{\mathrm{kin}} + E_{\mathrm{fr}}^{\mathrm{Coul}} = \sum E^{\mathrm{kin}}(A_i, Z_i) \qquad (16)$$
$$+ \frac{1}{2}\sum \frac{Z_i Z_j}{r_{ij}} = \sum \varepsilon_i(A_i, Z_i).$$

Another simplification concerns the excitation of the fragments: we assume that only one fragment among others is excited, the mass number of which is maximal. It is justified, particularly, when the model is compared with data obtained through inverse kinematics because the experimental setup registers a majority of radioactive fragments as well. Therefore, the excitation energy of the remnant $E^*$ is converted into the kinetic energies of the fragments and the excitation energy of the fragment with maximal mass:

$$E^* = \sum \varepsilon_i(A_i, Z_i) + E^*(A_{\max}, Z_{\max}). \qquad (17)$$

With these simplifications, we generate the energy distribution of fragments applying considerations proposed in [12]. Before the collision, the nucleons have a momentum distribution that is uniform inside the Fermi sphere of radius $p_{\mathrm{F}}$. After the collision, the distribution in the vicinity of the beam propagation is wider because of intranuclear interactions accompanied by local excitation of the nuclear medium. This can be written in the form

$$n(\varepsilon) \propto \left(1 + \exp\left[\frac{\varepsilon - \varepsilon_{\mathrm{F}}}{T_{\mathrm{eff}}}\right]\right)^{-1}, \qquad (18)$$

where $\varepsilon = p^2/2m$ and $\varepsilon_{\mathrm{F}}$ is the boundary Fermi energy. The effective temperature is given by

$$T_{\mathrm{eff}} = cE^*/N_{\mathrm{br}}, \qquad (19)$$

where $c$ is an adjustable parameter and $N_{\mathrm{br}}$ is the number of broken sites. Kinetic energies of nucleons composing the fragment are generated according to distribution (18), and, summing up all vector momenta directed randomly in 3D space, we obtain the momentum of the fragment. In such a way, we generate momenta of all produced fragments. The remaining part of the remnant excitation energy (17) is assigned to the fragment with maximal mass number. And, of course, we take into account the conservation of energy and momentum for the whole reaction.

## 5. COMPARISON WITH EXPERIMENT

Observation of residues emerging from spallation reactions in direct kinematics still remains a difficult task. Collisions of protons and light nuclei with heavy ions performed at GSI in inverse kinematics allows one to determine the production of residues prior to $\beta$ decay. This provides a good opportunity to compare the available data with theoretical models to achieve a better understanding of the mechanisms of reactions, which is today far from satisfactory. Until now, calculations have been performed by different versions of intranuclear cascade followed by the evaporation model. As seen from the previous section, our model also includes multifragmentation channels in the framework of the percolation approach. Here, we define the values of the input parameters, which are the bond-breaking probability $p_{\mathrm{bond}}(0)$ in Eq. (14) and the constant $c$ in Eq. (19). The probability $p_{\mathrm{bond}}(0)$ depends on the energy of the collision

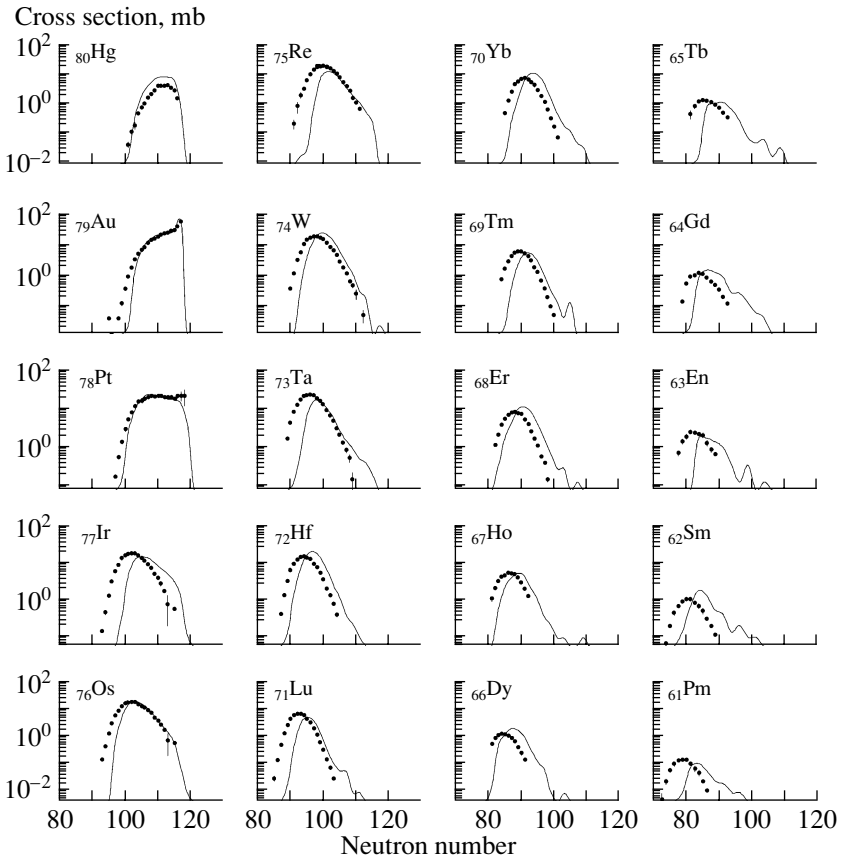


**Fig. 5.** Isotopic distribution of spallation residues in the reaction $^{197}\mathrm{Au} + p$ at 800 $A$ MeV; $p_{\mathrm{bond}} = 0.57$. Data are taken from [14].

and the type of reaction. For a specific reaction, it is obvious that site and bond-breaking probabilities are small at low energies and start growing with increasing energy, reaching constant values at the regime called "limiting fragmentation." Limiting fragmentation is reached at different energies for different reactions. Therefore, at low energies, the dominating mechanisms of disintegration of excited remnants are evaporation and fission. As the energy of the collision grows, the contribution of multifragmentation processes increases, depending on the site and bond-breaking probabilities. Since the number of broken sites is defined automatically during the development of the intranuclear cascade, only the bond-breaking probability remains to be input as a parameter. For proton-induced reactions, $p_{\mathrm{bond}}(0)$ changes from 0 at an incident proton energy of a few tens of MeV to 0.77 at the limiting fragmentation energy of 3–4 GeV. With regard to the parameter $c$ in Eq. (19), its value is chosen to be 0.7, energy independent, for all types of reactions. Comparison of the model calculations for mass distributions in spallation reactions $p$Au at 0.5 and 0.8 GeV, $p$Pb at 1 GeV, and $d$Pb at 2 GeV are shown in Figs. 1–4. As seen from the figures, at energies lower than those corresponding to the limiting fragmentation regime, mass yield distributions of residues in proton-induced reactions have well-pronounced bell-shaped curves in the central part, corresponding to the contribution of fission channels. Evaporation channels give a dominating contribution in the right peak of the distribution with a plateau at high-mass residues. The values of the level density parameters for evaporation and fission are taken to be $0.1A$ MeV$^{-1}$, the same for both and independent of the type of reaction and collision energy. Figures 5–7 show the isotopic distributions of residues produced in the following reactions: $p$Au at 0.8 GeV, $p$Pb at 1 GeV, and $d$Pb at 2 GeV. Calculated distributions are shifted toward neutron-rich isotopes for lighter residues. We think that underestimation of the proton-rich isotopes and overestimation of the neutron-rich isotopes could be corrected by better description of proton–neutron competition in fission–evaporation channels.

As the bombarding energy increases, so does the contribution of multifragmentation channels and, correspondingly, the contribution of evaporation and fission channels decreases. This leads to filling of

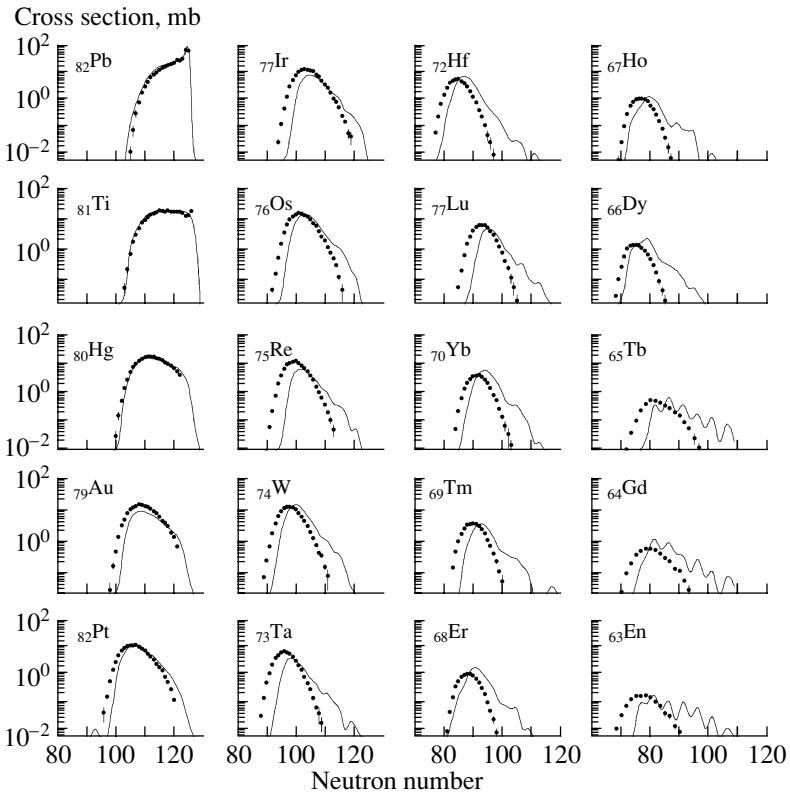


**Fig. 6.** Isotopic distribution of spallation residues in the reaction $^{208}$Pb + $p$ at 1 $A$ GeV; $p_{\mathrm{bond}} = 0.6$. Data are from [15].

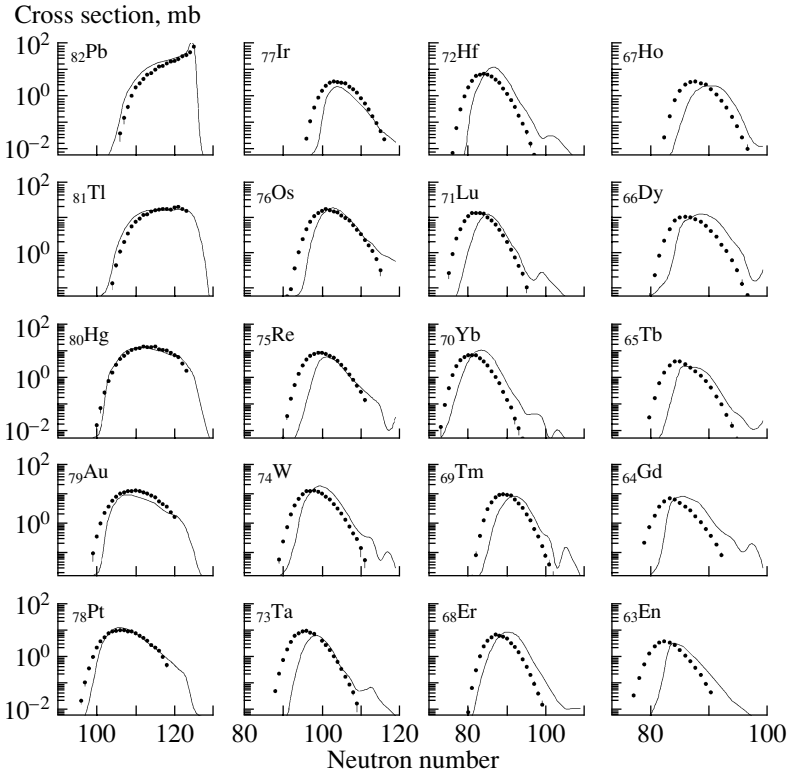


**Fig. 7.** Isotopic distribution of spallation residues in the reaction $^{208}$Pb + $d$ at 2 $A$ GeV; $p_{\mathrm{bond}} = 0.62$. Data are from [16].

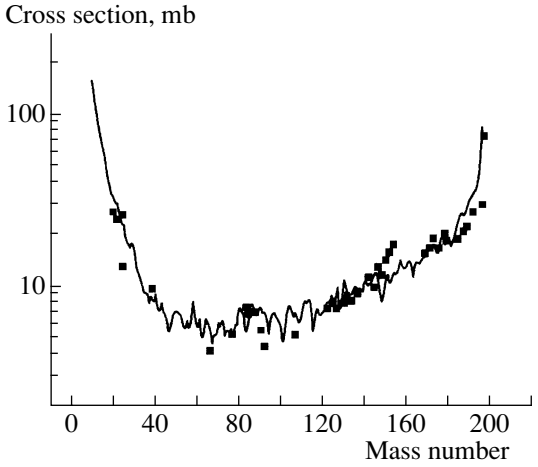


**Fig. 8.** Mass distribution of fragments in the reaction p + $^{197}$Au at 11.5 GeV; $p_{\mathrm{bond}} = 0.77$. Data are taken from [17].

the dips on both sides of the central bell-shaped curve and a decrease in the height of the right peak. As mentioned above, rising collision energy leads to an increasing number of broken sites and bonds in the nuclear lattices. This, in turn, results in an increasing yield in multifragmentation channels. This tendency is already evident in the reaction $\mathrm{Au} + p$ at 0.8 $A$ GeV (Fig. 2). The mass distribution of fragments in proton-induced reaction on Au at energies of 11.5 GeV corresponding to the limiting fragmentation regime is shown in Fig. 8.

## 6. CONCLUSIONS

A new version of the modified cascade model for intermediate- and high-energy nucleus–nucleus collisions including multifragmentation channels has been developed. Colliding nuclei are represented as face-centered-cubic lattices. Multifragmentation is calculated in the framework of percolation theory with usage of a site-bond percolation model. This version is able to reproduce reasonably well both spallation and multifragmentation processes.

## ACKNOWLEDGMENTS

This research was partly supported by the Russian Foundation for Basic Research, project no. 01-07-90144.

## APPENDIX

### *Hadronic Event Generator*

Monte Carlo simulation of inelastic events is performed in several steps. The first step in the generation of an exclusive event is the evaluation of the initial c.m. energy portion available for production of secondaries,

$$W = \sum E_i = k\sqrt{s}, \tag{A.1}$$

where $E_i$ is the energy of the $i$th particle (excluding leading particles) and $k$ is inelasticity. Fluctuation of the inelasticity from event to event leads to the distribution $P(k)$. There are no comparable theoretical methods for calculation of $P(k)$. It has been shown in [18] that one may fit the inelasticity distribution with a beta distribution

$$P(k,s) = k^{a-1}(1-k)^{b-1}/B(a,b), \tag{A.2}$$

$$B(a,b) = \Gamma(a)\Gamma(b)/\Gamma(a,b), \tag{A.3}$$

$$\langle k(s)\rangle = a/(a+b), \tag{A.4}$$

where $\Gamma(a)$, $\Gamma(b)$, and $\Gamma(a,b)$ are gamma functions; $s$ is the dependence of $P(k,s)$; and $\langle k(s)\rangle$ is enclosed in parameters $a$ and $b$. Up to 20–30 GeV/nucleon energies, one can neglect this $s$ dependence. In the second step, the energy $W$ is distributed between secondary particles whose kinematical characteristics are generated in correspondence to a cylindrical phase-space model. Parameters of the cylindrical phase-space model are adjusted by comparing the results of simulation of pion–nucleon and nucleon–nucleon interactions with experimental data. The remaining part of c.m. energy $(1-k)\sqrt{s}$ is distributed between remnants of the interacting particles (so-called leading particles) according to the conservation of energy and momentum:

$$\overline{P}_{\mathrm{I}} + \overline{P}_{\mathrm{II}} = \sum \overline{P}_i, \tag{A.5}$$

$$E_{\mathrm{I}} + E_{\mathrm{II}} = (1-k)\sqrt{s}, \tag{A.6}$$

where $\overline{P}_i$ is the momentum of the $i$th produced particle, and $\overline{P}_{\mathrm{I}}$, $\overline{P}_{\mathrm{II}}$ and $E_{\mathrm{I}}$, $E_{\mathrm{II}}$ are momenta and energies of leading particles. Interacting nucleons (mesons) can transform into nucleons (mesons) and $s$-wave resonances ($\Delta$ isobars and $\rho$, $\omega$ mesons). Transition probabilities are calculated with the use of a one-pion-exchange model.

## REFERENCES

1. W. Bauer *et al.*, Nucl. Phys. A **452**, 699 (1986).
2. N. C. Chao and K. C. Chung, J. Phys. G **17**, 1851 (1991).
3. A. J. Santiago and K. C. Chung, J. Phys. G **19**, 349 (1993).
4. L. Pauling, Science **150**, 297 (1965).
5. G. Anagnostatos, Can. J. Phys. **51**, 998 (1973).

6. N. D. Cook, Atomkernenergie **28**, 195 (1976); V. Dallacasa, Atomkernenergie **37**, 143 (1981); V. Dallacasa and N. D. Cook, Nuovo Cimento A **97**, 157, 184 (1987); N. D. Cook and V. Dallacasa, Phys. Rev. C **35**, 1883 (1987).
7. G. Musulmanbekov, in *Proceedings of the 11th EMU01 Collaboration Meeting, Dubna, Russia, 1992,* Ed. by V. Bradnova (JINR, Dubna, 1992), p. 288.
8. S. A. Krasnov *et al.*, Czech. J. Phys. **46**, 531 (1996).
9. N. D. Cook, Comput. Phys. **3**, 73 (1989).
10. N. D. Cook, J. Phys. G **23**, 1109 (1997).
11. V. S. Barashenkov and V. D. Toneev, *Interactions of High-Energy Particles and Nulcei with Atomic Nuclei* (Atomizdat, Moscow, 1972).
12. X. Campi and J. Desbois, in *Proceedings of the 23rd International Winter Meeting on Nuclear Physics, Bormio, 1985,* p. 707.
13. S. B. Kaufman *et al.*, Phys. Rev. C **22**, 1897 (1980).
14. F. Rejmund *et al.*, Nucl. Phys. A **683**, 540 (2001); J. Benlliure *et al.*, Nucl. Phys. A **683**, 513 (2001).
15. W. Wlazlo *et al.*, Phys. Rev. Lett. **84**, 5736 (2000); T. Enqvist *et al.*, Nucl. Phys. A **686**, 481 (2001).
16. J. Taïeb, PhD Thesis (IPN, Orsay, France, 2000).
17. S. B. Kaufman *et al.*, Phys. Rev. C **14**, 1121 (1976).
18. G. N. Fowler, R. M. Weiner, and G. Wilk, Phys. Rev. Lett. **55**, 173 (1985).

*Physics of Atomic Nuclei, Vol. 66, No. 9, 2003, pp. 1680–1682. From Yadernaya Fizika, Vol. 66, No. 9, 2003, pp. 1728–1730.*


# Nuclear-Induced Autoionization of Radioactive Atoms*

**V. Z. Maidikov[1),2)]****

[1)] *Flerov Laboratory of Nuclear Reactions, Joint Institute for Nuclear Research, Dubna, Moscow oblast, 141980 Russia*

[2)] *Institute for Nuclear Research, National Academy of Sciences of Ukraine, Kiev, Ukraine*

Received August 28, 2002

**Abstract**—In the experiment, where the atomic electron cloud serves as an indicator of nuclear isomeric transitions, measurements of the perturbation of the ionic charge-state distribution from the known isomeric transition of the $^{173}$Hf nucleus obtained in a heavy-ion-induced reaction, were carried out. As a result, a definite experimental confirmation has been obtained for the effect of nuclear forbidden transitions on their atomic electron cloud. The importance and possibilities of this effect for the study of the interplay of nuclear and atomic excitations are discussed. © *2003 MAIK "Nauka/Interperiodica"*.

## INTRODUCTION

The effect of nuclear transitions on the ionization of heavy atoms that undergo nuclear transformations (the perturbation in their electron clouds by the shake-off of many electrons caused by the decay of nuclear excited states via internal conversion) was widely studied among the heavy products of radioactive decay [1, 2], the fission isomers obtained in $\alpha$-induced reactions [3, 4], and among light [5, 6] and heavy fractions of fission fragments [7] from thermal neutron fission and heavy-ion fusion recoils [8–13].

The overwhelming majority of investigated recoils reveal a significant divergence of their charge-state distributions from the equilibrium value. The ionic charge-state distributions of the investigated nuclear reaction products strongly depend on the atomic number $Z$ and the mass number $A$ of the investigated nuclei (see, for example, the isotopic dependence of the ionization time of Dy isotopes [9]), which indicates that the nuclear structure influences the electron clouds. Similar results were obtained in other groups for Er isotopes [12] and Ni + Sn evaporation residues [13]. But until recently, only in the radioactive decay [1, 2] was it possible to establish the correlation of the electron shell ionization with a certain nuclear transition.

In this work, measurements of the perturbation of the ionic charge-state distribution from the known isomeric transition of the $^{173}$Hf nucleus obtained in a heavy-ion-induced reaction were carried out. As a result, a definite experimental confirmation has been obtained for the effect of nuclear forbidden transitions on their atomic electron cloud.

## EXPERIMENT

Some years ago, we supposed [10] that the equilibration of the disturbed electron structure of heavy nuclear reaction products by an additional charge-resetting foil at some distance downstream of the target [8, 14, 15] may be ineffective if the recoil nuclei have isomeric states with lifetime of the same order of magnitude as the time of flight of recoils in the electromagnetic separator, or spectrometer, or even in its part. In this case, the ionic charge-state distribution of recoils disturbed by the continuous internal conversion and the following Auger and Coster–Kronig transitions in their electron cloud will still be very broad and shifted to higher charge states.

The experimental procedure for measuring the atomic electron cloud ionization by nuclear transitions of heavy-ion fusion recoils with the broad-range magnetic spectrograph MSP-144 [16] was described elsewhere [8–11]. In this experiment, heavy-ion fusion $^{173}$Hf evaporation residues from the $^{164}$Dy($^{12}$C, $3n$) reaction emitted from the target (the enriched $^{164}$Dy isotope with 270 $\mu$g/cm$^2$ thickness deposited on a 50-$\mu$m Al backing) at $\Theta = 0°$ with recoil energy of about 3 MeV were analyzed by an MSP-144 broad-range magnetic spectrograph according to their momentum $P/q$ and collected by an Al catcher at the spectrograph focal plane whose length was 1.5 m.

The ionic charge-state distributions of evaporation residues were analyzed by scanning piece-by-piece the 1.5-m catcher at a $\gamma$ spectrometer taking

*This article was submitted by the author in English.

** e-mail: maidikov@flnr.jinr.ru

1063-7788/03/6609-1680$24.00 

into account the spectrograph dispersion and the energy spread of evaporation residues. The lifetime of $^{173}$Hf is about 24 h and it has a $\gamma$ line with $E =$ 123.6 keV (81.4%), allowing good identification of the isotope embedded into the catcher. The authentic identification of the $^{173}$Hf isotope ensures reliable study of the behavior of its charge-state distributions.

The experiment was performed in two runs—without and with charge resetting of recoil ions. In the second run, a carbon foil with thickness of 10 $\mu$g/cm was installed 20 cm downstream of the target at the spectrograph gap entrance. The resulting ionic charge-state distributions of $^{173}$Hf ions ($a$) without and ($b$) with charge resetting are shown in the Fig. 1. For the recoil energy of Hf $E_{\text{res}} = 3.3$ MeV, the expected mean equilibrium charge state has to be $5^+$, as estimated by the formulas of Nikolaev–Dmitriev [17] and Shima [18]. However, in the experiment, we did not see any activity of $^{173}$Hf gammas at the place (and nearby) of this charge state at the catcher and may conclude that a very small part of the evaporation residues leave the target with the equilibrium ionic charge-state distribution. The experimental distribution is so broad that we could not collect it completely at the 1.5-m catcher in a single spectrograph magnetic field setting. Thus, we could estimate neither the mean charge nor the width of the charge-state distribution.

As can be seen from Fig. 1$b$, the charge resetting is truly ineffective in this case because the $^{173}$Hf decay to the ground state is delayed by 180 and 160 ns by two isomeric states at 69.73 keV ($3/2^-$) and 107.16 keV ($5/2^-$) [19]. The total internal conversion coefficient of transitions from these and nearest levels is so great that almost all recoil ions suffer from continuous "nuclear-induced autoionization." The time of flight of 110 ns between the target and carbon foil is too short for the disturbed electron cloud equilibration. The charge-resetting foil may only clarify the charge-state distribution: to cut off the stochastic charge exchange of recoil ions at the exit boundary of the target (including the low-charge part of the distribution) and effects from the shorter converted nuclear transitions. A lot of investigated recoil atoms still ionize in flight by the continuous delayed nuclear-induced ionization in a much longer time interval according to the lifetime of the nuclear isomeric states. As is seen from the figure, in both experiments (with charge resetting and without it), the abundance of the equilibrium charge state $q_{\text{eq}} = 5^+$ is very low.

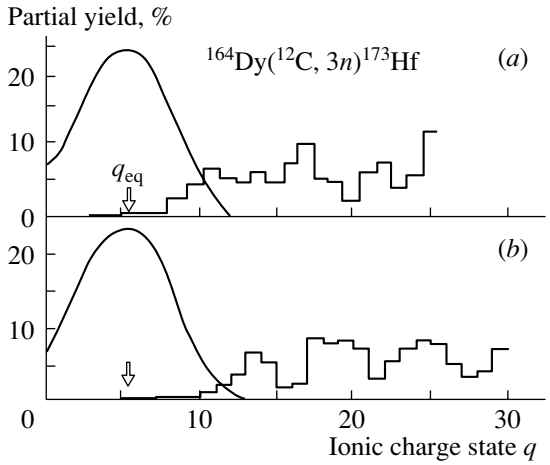


**Fig. 1.** Ionic charge-state distribution of $^{173}$Hf recoils ($a$) without any charge resetting and ($b$) with an additional charge resetting at the distance $d = 20$ cm (time of flight $\tau = 110$ ns) downstream of the target: measured distribution (histogram) and equilibrium distribution simulated by the formulas of [17] (solid curve). Arrows indicate the mean equilibrium charge state $q_{\text{eq}}$.

## DISCUSSION AND CONCLUSION

In heavy-ion reactions as well as in any nuclear perturbation, the atomic cloud formation strongly depends on the structure of the final nucleus, especially on the forbidden nuclear transitions via internal conversion at the inner electron shells. The filling of inner-shell vacancies by electrons from the outer shells causes a drastic rearrangement in the atomic cloud surrounding the nucleus, with the emission of a large number of outer electrons—so-called nuclear-induced autoionization.

Although this effect is of interest from the viewpoint of fundamental research and for solving a number of applied problems, experimental data obtained thus far are scanty. And so far there is no quantitative theory of this effect.

The study of this effect in many laboratories [1–13] shows that it is very common in nature and has very large probability. It determines the atomic physical and chemical properties of radioactive atoms all the time throughout the existence of nuclear excited states until the moment when the nuclear ground state is populated and the processes of filling its atomic electron shells is completed. This effect can play a dominant role in the excitation and ionization of radioactive atoms in stellar plasmas and in interstellar space.

The high probability and large effects of nuclear-induced ionization may serve as a good experimental tool for the study of both nuclear and atomic structure and for investigations of the interplay between the nuclear and atomic phenomena in atoms with an excited nucleus and an excited (and ionized) electron cloud.

The electron cloud of radioactive atoms affected by nuclear-induced autoionization, in turn, may cause the excitation of nuclei by inverse internal conversion [20] or by electron transitions (NEET) [21–23] and may change the nuclear lifetime by ionic charge state blocking of the nuclear decay [24–28] or change the nuclear decay properties of highly ionized atoms [29, 30], as well as change the nuclear reaction conditions due to electron screening corrections [31–33].

In the experimental practice of separation, transport, acceleration, or storing of radioactive ions, this effect may cause some problems due to the uncontrolled change of their ionic charge.

## ACKNOWLEDGMENTS

I am grateful to N.T. Surovitskaja and D.V. Bugaev for their very important assistance in the experiment and G.N. Koseratskaja for the target and foil preparation.

## REFERENCES

1. F. Pleasonton and A. H. Snell, Proc. R. Soc. London, Ser. A **241**, 141 (1957).
2. W. De Wieclawik, C. R. Acad. Sci. B **266**, 577 (1968).
3. V. Metag *et al.*, Hyperfine Interact. **1**, 405 (1976).
4. G. Ulfert, D. Habs, V. Metag, and H.-J. Specht, Nucl. Instrum. Methods Phys. Res. **148**, 369 (1978).
5. H. Wohlfarth *et al.*, Z. Phys. A **287**, 153 (1978).
6. C. Schmitt *et al.*, Nucl. Phys. A **430**, 21 (1984).
7. A. D. Belyaev, V. Z. Maidikov, *et al.*, Nucl. Instrum. Methods Phys. Res. B **35**, 156 (1988).
8. N. K. Skobelev, V. Z. Maidikov, and N. T. Surovitskaya, Z. Phys. A **314**, 5 (1983).
9. V. Z. Maidikov and N. T. Surovitskaya, Yad. Fiz. **60**, 218 (1997) [Phys. At. Nucl. **60**, 160 (1997)].
10. V. Z. Maidikov, Z. Phys. A **321**, 563 (1985).
11. V. Z. Maidikov, in *Heavy-Ion Physics* (World Sci., Singapore, 1998), p. 585.
12. T. M. Cormier *et al.*, Phys. Rev. C **30**, 1953 (1984).
13. W. S. Freeman *et al.*, Phys. Rev. C **28**, 919 (1983).
14. G. Munzenberg *et al.*, Nucl. Instrum. Methods Phys. Res. **161**, 65 (1979).
15. N. V. S. V. Prasad *et al.*, Nucl. Phys. A **603**, 176 (1996).
16. V. Z. Maidikov *et al.*, Prib. Tekh. Éksp., No. 4, 68 (1979).
17. V. S. Nikolaev and I. S. Dmitriev, Phys. Lett. A **28A**, 277 (1968).
18. K. Shima, T. Ishichara, and T. Mikumo, Nucl. Instrum. Methods Phys. Res. **200**, 605 (1982).
19. V. S. Shirley, Nucl. Data Sheets **75**, 377 (1995).
20. V. I. Goldansky and V. A. Namiot, Yad. Fiz. **33**, 319 (1981) [Sov. J. Nucl. Phys. **33**, 169 (1981)].
21. Y. Izawa and C. Yamanaka, Phys. Lett. B **88B**, 59 (1979).
22. S. Kishimoto *et al.*, Phys. Rev. Lett. **85**, 1831 (2000).
23. I. Ahmad *et al.*, Phys. Rev. C **61**, 051304 (2000).
24. B. Budik, Phys. Rev. Lett. **51**, 1034 (1983).
25. A. Krasznahorkay *et al.*, Z. Phys. A **323**, 12 (1986).
26. W. R. Phillips *et al.,* Phys. Rev. Lett. **62**, 1025 (1989).
27. F. Attallah *et al.*, Phys. Rev. Lett. **75**, 1715 (1995).
28. T. Carrere *et al.*, Phys. Rev. C **62**, 024311 (2000).
29. M. Jung *et al.*, Phys. Rev. Lett. **69**, 2164 (1992).
30. F. Bosch *et al.*, Phys. Rev. Lett. **77**, 5190 (1996).
31. J. S. Blair *et al.*, Phys. Rev. Lett. **41**, 1712 (1978).
32. J. F. Chemin *et al.*, Phys. Rev. A **24**, 1218 (1981).
33. C. Angulo *et al.*, Z. Phys. A **345**, 231 (1993).

Physics of Atomic Nuclei, Vol. 66, No. 9, 2003, pp. 1683–1690. From Yadernaya Fizika, Vol. 66, No. 9, 2003, pp. 1731–1738.


NUCLEI
Experiment

# Measurement of the Astrophysical $S$ Factor for $dd$ Interaction at Ultralow Deuteron-Collision Energies Using the Inverse $Z$ Pinch*

**Vyach. M. Bystritsky[1], V. V. Gerasimov[1], A. R. Krylov[1], S. S. Parzhitski[1], F. M. Pen'kov[1], O. M. Shvyryaev[1], V. A. Stolupin[1], G. N. Dudkin[2], B. A. Nechaev[2], V. M. Padalko[2], J. Wozniak[3], G. A. Mesyats[4], Vit. M. Bystritskii[5], V. I. Makhrin[6], and N. A. Ratakhin[6]**

[1] *Joint Institute for Nuclear Research, Dubna, Moscow oblast, 141980 Russia*

[2] *Research Institute of Nuclear Physics, Tomsk State University, Tomsk, Russia*

[3] *Department of Physics and Nuclear Techniques, University of Mining and Metallurgy, Cracow, Poland*

[4] *Institute of Electrophysics, Yekaterinburg, Russia*

[5] *University of California, Irvine, USA*

[6] *Institute of High-Current Electronics, Tomsk, Russia*

Received October 16, 2002

**Abstract**—This paper is devoted to measurement of the astrophysical $S$ factor and cross sections of the $d + d \rightarrow {}^3\mathrm{He} + n$ reaction at ultralow deuteron-collision energies. Formation of the flow of the accelerated deuterons incident on the $CD_2$ solid-state target was made within the scheme of the inverse $Z$ pinch. The liner in the initial state was a hollow supersonic deuterium jet of radius of 15 mm and length of 20 mm. The experiment was carried out at the pulsed high-current accelerator ($I = 950$ kA, $\tau = 80$ ns) of the Institute of High-Current Electronics (Tomsk, Russia). Measurement of the deuteron energy distribution was performed through an analysis of the time distributions of the intensity of the liner radiation ($H_\alpha$ and $H_\beta$ lines) generated during the liner radial movement from the axis. Recording of this radiation was carried out by optical detectors placed along the direction of the liner moving from its axis. The measured value of the astrophysical $S$ factor for the $dd$ reaction at the average deuteron collision energy $E_{\mathrm{coll}} = 3.69$ keV was equal to $S(E_{\mathrm{coll}} = 3.69\,\mathrm{keV}) = 58.2 \pm 18.1$ keV b. The $dd$-reaction cross section calculated using the found value of the $S$ factor and known representation of the reaction cross section as the product of the barrier factor and the astrophysical $S$ factor was $\sigma^n_{dd}(E_{\mathrm{coll}} = 3.69\,\mathrm{keV}) = (1.33 \pm 0.41) \times 10^{-30}$ cm$^2$.


## 1. INTRODUCTION

The importance of studying reactions between light nuclei in the ultralow-energy range is emphasized in many papers [1–7], for this may allow a possibility of verifying fundamental symmetries in strong interactions [1–4] and solving some astrophysical problems [5–7]. However, it is very difficult to carry out such research at classical accelerators because cross sections for nuclear reactions in the ultralow-energy range are extremely small.

A new method for investigation of nuclear reactions by using radially converging powerful fluxes of ions generated in the course of liner plasma implosion (formation of a direct $Z$ pinch) was proposed in [7–10].

This method allowed the effective cross sections for the $dd$ reaction

$$d + d \rightarrow {}^3\mathrm{He} + n(2.5\,\mathrm{MeV}) \qquad (1)$$

and the astrophysical $S$ factor to be estimated for the first time in the deuteron-collision energy range 1.8–2.3 keV [10–16] (see Fig. 1).

It is of interest to study nuclear reactions between light nuclei at higher deuteron collision energies (3–7 keV) because these studies will make it possible not only to measure the $dd$-reaction cross sections in the above energy range for the first time but also to compare them correctly with the calculations and the experimental results at collision energies of 6–7 keV [17, 18].

For these investigations, we proposed a method based on inverse $Z$-pinch formation [19].

The inverse $Z$-pinch scheme has a few advantages over the direct $Z$-pinch configuration:

(i) The density of the incident plasma flux decreases.

(ii) The processes of the electrodynamic liner acceleration and liner–target interaction are better discriminated in time.

*This article was submitted by the authors in English.

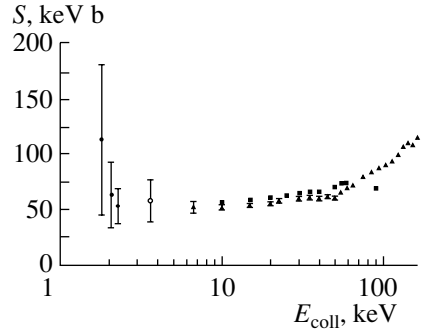


**Fig. 1.** Astrophysical $S$ factor for $dd$ reactions as a function of the deuteron-collision energy. Closed circles, closed triangles, and closed squares are the data from [16], [17], and [18], respectively; the open circle is the result of the present paper.

(iii) The method of measuring the energy distribution of accelerated liner ions with optical detectors, which detect radiation from the liner in the course of its acceleration, becomes technically much simpler.

Characteristics of the deuterium liner accelerated to $(2.8–7.2) \times 10^7$ cm/s were first experimentally investigated within the inverse $Z$-pinch scheme in [19].

The results of investigating the inverse $Z$-pinch formation [19–21] indicate that the proposed method can be used to study nuclear reactions in the ultralow-energy range.

Another point is worth mentioning. To use a liner plasma for precise investigation of nuclear reactions (measurement of cross sections, astrophysical $S$ factors), one should know the energy distribution of accelerated liner ions and the liner–target interaction model because the cross sections of the reactions in question are sharply dependent on the particle-collision energy in the entrance channel.

In this connection, an investigation [21] was carried out to develop a method for measuring the energy distribution of accelerated deuterons in experiments on the study of the $dd$ reaction by using the inverse $Z$-pinch scheme.

That methodological investigation was carried out with a deuterium liner and a deuterated polyethylene target and involved a few shots (by a shot is meant a single operation of the high-current accelerator). The present paper reports the results of analyzing the experimental information gained in these shots ($S$ factor and $dd$-reaction cross sections).

## 2. MEASUREMENT METHOD

Experimental determination of the astrophysical $S$ factor is based on measurement of the neutron yield from reaction (1) and parametrization of the dependence of the $dd$-reaction cross section on the deuteron collision energy

$$\sigma(E) = \frac{S(E)}{E} e^{-2\pi\eta}, \tag{2}$$

$$2\pi\eta = 2\pi\frac{(Ze)^2}{\hbar V} = 31.29\left(\frac{1}{E}\right)^{1/2},$$

where $\eta$ is the Sommerfeld parameter, $Ze$ is the deuteron charge, $E$ is the c.m. deuteron collision energy (in keV), and $V$ is the velocity of the relative deuteron motion.

As was found in [22], the total yield of detected neutrons $N_n^{\exp}$ from reaction (1) can be represented as

$$N_n^{\exp} = N_d n_t \varepsilon_n \overline{S(E)} \int_0^\infty e^{-2\pi\eta} D(E) dE \int_E^\infty f(E') dE', \tag{3}$$

where the average $S$ factor value is given by the expression

$$\overline{S(E)} = \int_E S(E) P(E) dE \tag{4}$$

corresponding to the distribution function

$$P(E) = \frac{e^{-2\pi\eta} D(E) \int_E^\infty f(E') dE'}{\int_0^\infty e^{-2\pi\eta} D(E) dE \int_E^\infty f(E') dE'}, \tag{5}$$

$$D(E) = -\frac{1}{E}\frac{dx}{dE}.$$

In addition, energies averaged over the distribution functions $f(E)$ and $P(E)$,

$$\overline{E} = \int_E E f(E) dE, \tag{6}$$

$$E_{\text{coll}} = \int_E E P(E) dE, \tag{7}$$

will be used below. Here, $f(E)$ is the energy distribution function of the liner deuterons incident on the target; $P(E)$ is the differential deuteron-collision energy distribution function of the probability for yield of neutrons from reaction (1) normalized to unity; $\varepsilon_n$ is the detection efficiency for 2.5-MeV neutrons; $\overline{E}$ is the average deuteron-collision energy corresponding to the distribution function $f(E)$; $N_d$ is the number of deuterons incident on the target; $n_t$ is the deuteron density in the target; $dE/dx = -(\pi n_t e^4)L/(2E)$ is

**Table 1.** Experimental conditions

| Shot | $E^p$, keV | $\overline{E}$, keV | $m$, $\mu$g/cm | $l$, cm | $N_d$, $10^{18}$ | $n_t$, $10^{22}$ cm$^{-3}$ | $d_l^{\text{in}}$, mm | $d_l^{\text{ex}}$, mm | $r_t$, mm | $t$, mm | $N_n^{\text{cal}}$ |
|---|---|---|---|---|---|---|---|---|---|---|---|
| 1 | 2.24 | 2.52 | 6.2 | 2 | 3.72 | 8.0 | 30 | 32 | 185 | 0.25 | 15.5 |
| 2 | 1.20 | 1.42 | 5.3 | 2 | 3.18 | 8.0 | 30 | 32 | 185 | 0.25 | 0.077 |

Note: $\overline{E}$ and $E^p$ are the average and the most probable c.m. deuteron energies corresponding to the distribution function $f(E)$, $m$ is the liner mass per unit length, $l$ is the liner length, $n_t$ is the density of target atoms, $d_l^{\text{in}}$ is the internal diameter of the liner, $d_l^{\text{ex}}$ is the external diameter of the liner, $r_t$ is the target arrangement radius, $t$ is target thickness, and $N_n^{\text{cal}}$ is the yield of detected neutrons calculated by (3) with the $S$ factor equal to 53.8 keV b [18].

the specific Coulomb energy loss of liner deuterons because of their collisions with target deuterons [23]; $e$ is the elementary electric charge; $L$ is the Coulomb logarithm for the deuterium plasma conforming to the experimental conditions [23]; $E_{\text{coll}}$ is the average deuteron collision energy determined by the function $P(E)$.

Reaction-cross-section parametrization (2) assumes that the Coulomb potential corresponds to interaction of bare deuterons.

In addition, the following is worth mentioning:

(i) Expression (3) was derived with allowance made for the energy spread of incident deuterons and Coulomb energy loss at their interaction with the target.

(ii) Further replacement $\overline{S(E)} \to S(E_{\text{coll}})$ is assumed in the energy interval determined by the deuteron energy spread and Coulomb energy loss.

This is because the $S$ factor is a slightly varying function in the given deuteron collision energy interval.

Thus, measuring the neutron yield from the $dd$ fusion reaction and the energy distribution of incident deuterons in a particular shot, one can find by (3) the average value of the $S$ factor for the $dd$ reaction. This value corresponds to the average deuteron-collision energy $E_{\text{coll}}$ determined by the distribution function $P(E)$. Note that, for finding $\overline{S(E)}$ from (3), one should also know the total number of incident deuterons $N_d$ and the neutron-detection efficiency $\varepsilon_n$ of the experimental setup.

The quantity $N_d$ can be found by calculation within the zero-dimensional model of the inverse $Z$-pinch-formation dynamics with use of the data obtained with magnetic $dB/dt$ probes. The detection efficiency for 2.5-MeV neutrons can be found both experimentally with use of standard $^{252}$Cf, Po–Be sources of neutrons and by Monte Carlo calculation. As to $n_t$, its values fully depend on the procedure used to apply deuterated polyethylene on the target backing.

## 3. EXPERIMENT

The experiment was carried out with the pulsed high-current accelerator SGM (generator current $I = 950$ kA, high-voltage pulse duration $\tau = 80$ ns [24]) at the Institute of High-Current Electronics. The experimental setup consisting of a high-current generator, a load module, and detecting and diagnostic equipment is schematically shown in Fig. 2.

The initial deuterium liner was formed with a fast electromagnetic valve and a supersonic Laval nozzle. The average liner radius was 15 mm. A current-intercepting structure (CIS) in the form of a squirrel cage of 45-mm radius made of rods 1 mm in diameter was installed on the way of the radially diverging plasma shell. The CIS installation radius determines the liner acceleration path. The current through the liner was measured with the Rogovsky coils.

Three light detectors LD1, LD2, and LD3 were installed behind the CIS along the radius in the direction of the liner's motion away from the axis. The

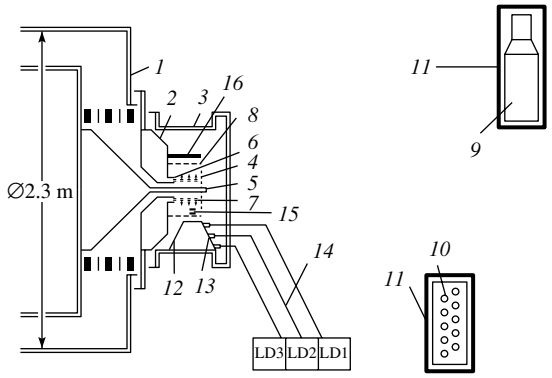


**Fig. 2.** Experimental setup: (*1*) high-current generator, (*2*) accelerator load module, (*3*) measuring chamber, (*4*) grid cathode, (*5*) return conductor, (*6*) supersonic Laval nozzle, (*7*) liner, (*8*) current-intercepting structure, (*9*) scintillator detector D1, (*10*) thermal-neutron detector D2, (*11*) Pb shielding, (*12*) light-protecting cone, (*13*) collimators, (*14*) light guides, (*15*) magnetic $dB/dt$ probes, (*16*) $CD_2$ target; the electromagnetic valve is not shown.

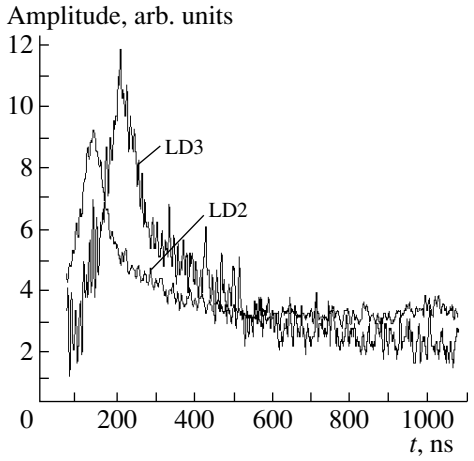


**Fig. 3.** Oscillogram of signals from the light detectors LD2 and LD3 in shot 1.

distance between the CIS and LD1, LD1 and LD2, and LD2 and LD3 was 50 mm. Each light detector consisted of a collimator, a quartz light guide, and fast photomultiplier.

The target was placed around the liner. It was a cylindrical copper shell with a radius of 185 mm and a length of 40 mm. The inner surface of the target was coated with a $CD_2$ layer 0.25 mm thick.

Fast neutrons were detected by a time-of-flight method with using the plastic scintillator detector D1 ($d = 10$ cm, $l = 20$ cm).

The total flux of neutrons emitted upon interaction of the deuterium liner with the target was measured by thermal-neutron detector D2. It consisted of ten proportional $BF_3$ counters enclosed in polyethylene moderator. The detectors D1 and D2 were installed at the respective distances of 410 and 277 cm from the liner axis. They were shielded with 5 cm of Pb to suppress the effect of powerful x-ray radiation and bremsstrahlung on them. The neutron detection efficiency was $4.5 \times 10^{-6}$ for D1 and $4.0 \times 10^{-6}$ for D2.

Pulses from the three light detectors and the neutron scintillator spectrometer arrived at the inputs of the TEKTRONIX oscilloscopes. The high-voltage generator current pulse was a trigger signal.

The experimental setup is described in more detail in [19–21].

Table 1 presents the $CD_2$ target and deuterium liner parameters in shots 1 and 2.

The liner mass was found by using the zero-dimensional model of liner motion and the information on the current through the liner and the instants of appearance of signals from the magnetic $dB/dt$ probes detecting passage of the liner current shell through them. Liner acceleration was monitored with two $dB/dt$ probes placed at the radii of 23 and 34 mm.

The mass of the liner and its velocity over the radius at which the CIS was placed were taken to be such that the calculated times of arrival of the liner at the positions of the magnetic $dB/dt$ probes coincided with their real readings within the measurement error.

## 4. ANALYSIS OF THE RESULTS

The energy distribution of liner ions incident on the target was measured by means of recording optical radiation of the liner ($H_\alpha$ and $H_\beta$ lines) moving radially away from the axis.

The times of appearance of signals from the light detectors (placed at certain distances from the CIS) and the durations of these signals (dictated by the duration of the light pulse) are related to the distance from the CIS by the equation

$$\Delta t = 16.15 \frac{L_d}{\sqrt{(E^p)_{\rm lab}}} \frac{(\Delta E)_{\rm lab}}{(E^p)_{\rm lab}}, \qquad (8)$$

where $\Delta t$ (in ns) is the full width at half-maximum of the light pulse from the detector placed at the distance $L_d$ (in cm) from the CIS (it is assumed that, after the liner reaches the CIS, its further motion is free motion of the currentless shell); $(E^p)_{\rm lab}$ is the most probable energy of liner ions in the laboratory system (in keV); and $(\Delta E)_{\rm lab}$ is the total width of deuteron energy distribution in the laboratory system (in keV) at the distance $L_d$ from the CIS.

Thus, broadening of light signals with increasing distance between the liner and the CIS characterizes the corresponding liner ion-energy spread.

Note that changing over from the time dependence of the liner light intensity measured by the detectors LD1–LD3 to the energy distribution of liner ions is based on some assumptions concerning motion dynamics of an expanding liner plasma (deuterium liner).

One of the major assumptions is that thermodynamic equilibrium is established between ions and excited neutrals in the expanding plasma and its stable acceleration takes place.[1)]

By way of example, Fig. 3 displays oscillograms of signals from the light detectors LD2 and LD3 in a shot with the deuterium target (shot 1).

Table 2 presents results of processing oscillograms of LD2 and LD3 pulses in shots 1 and 2.

Figure 4 displays deuteron energy distributions $f(E)$ and $P(E)$ measured in shot 1 and corresponding to the time distributions in Fig. 3.

[1)] As shown in [21], the assumptions mentioned hold if the liner is accelerated in the inverse $Z$-pinch scheme at distances larger than 10 cm from the CIS. Therefore, oscillograms of pulses from the detectors LD2 and LD3 are dealt with in what follows.

**Table 2.** Results of analyzing LD2 and LD3 oscillograms

| Shot | $T_3 - T_2$, ns | $(\mathrm{FWHM})^t$ LD2, ns | $(\mathrm{FWHM})^t$ LD3, ns | $V_d$, $10^7$ cm/s | $E^p$, keV | $(\mathrm{FWHM})^E$ LD2, keV | $(\mathrm{FWHM})^E$ LD3, keV |
|---|---|---|---|---|---|---|---|
| 1 | 69 | 49.2 | 84.4 | 7.1 | 2.24 | 1.62 | 1.86 |
| 2 | 98.6 | 55.2 | 139 | 5.07 | 1.20 | 0.90 | 1.39 |

Note: $T_2$ and $T_3$ are the times of signals appearing at the output of the detectors LD2 and LD3, respectively; $(\mathrm{FWHM})^t$ LD2 and $(\mathrm{FWHM})^t$ LD3 are the full widths at half-maximum of the LD2 and LD3 pulses, respectively; $V_d$ is the deuteron velocity in the laboratory system found from the time shift of the positions of the LD2 and LD3 pulse vertices; $E^p$ is the most probable c.m. deuteron energy corresponding to the velocity $V_d$; $(\mathrm{FWHM})^E$ LD2 and $(\mathrm{FWHM})^E$ LD3 are the full widths at half-maximum of the deuteron energy distributions derived for the LD2 and LD3 through changing over from time distributions to energy distributions by formula (8).

**Table 3.** Experimental data analysis results

| Experiment | | | | | | | | |
|---|---|---|---|---|---|---|---|---|
| Shot | $E^p$, keV | $\overline{E}$, keV | $E_{\mathrm{coll}}$, keV | $E^p_{P(E)}$, keV | $\sigma_{P(E)}$, keV | $N_n^{\mathrm{exp}}$ | $S(E_{\mathrm{coll}})$, keV b | $\Delta S(E_{\mathrm{coll}})$, keV b |
| 1 | 2.24 | 2.52 | 3.69 | 3.56 | 0.57 | $18.2 \pm 3.6$ | 58.2 | 18.1 |
| 2 | 1.20 | 1.42 | 2.45 | 2.33 | 0.34 | – | – | – |

| Calculations | | | | |
|---|---|---|---|---|
| Shot | $N_n^{\mathrm{cal}}$ | $\sigma^n_{dd}(E_{\mathrm{coll}})$, cm$^2$ | $\sigma^n_{dd}(E_{\mathrm{coll}} + \sigma_{P(E)})$, cm$^2$ | $\sigma^n_{dd}(E_{\mathrm{coll}} - \sigma_{P(E)})$, cm$^2$ |
| 1 | 15.5 | $1.33 \times 10^{-30}$ | $3.55 \times 10^{-30}$ | $3.84 \times 10^{-31}$ |
| 2 | 0.077 | $4.24 \times 10^{-32}$ | $1.31 \times 10^{-31}$ | $1.04 \times 10^{-32}$ |

Note: $E^p_{P(E)}$ is the most probable c.m. deuteron energy corresponding to the energy distribution $P(E)$; $\Delta S(E_{\mathrm{coll}})$ is the root-mean-square deviation of the astrophysical $S$ factor; $\sigma^n_{dd}$ is the $dd$-reaction cross section with neutron production.

For finish processing of the experimental data, the energy distributions $f(E)$ and $P(E)$ (see Figs. 3 and 4) found by averaging the corresponding distributions obtained with the detectors LD2 and LD3 were used for shots 1 and 2.

In Fig. 5, deuteron energy distributions $f(E)$ and $P(E)$ measured in shot 2 are displayed for illustration and comparison with results of the analysis of the data from shot 1 with the $CD_2$ target.

The astrophysical $S$ factor was found by formula (3) with the deuteron energy distribution $f(E)$ averaged over the LD2 and LD3 data and the measured yield of detected neutrons $N_n^{\mathrm{exp}}$ substituted into it.

The yield of detected neutrons was found as follows.

Figure 6 displays the oscillogram of the neutron spectrometer signals in shot 1. The right and left arrows indicate the limits of the time interval within which detection of neutrons from the $dd$ reaction is possible. These limits are dictated by the energy distribution $f(E)$ of accelerated deuterons incident on the target: the right limit corresponds to liner deuteron energy $E^p - 2\sigma_E$ and the left limit to $E^p + 2\sigma_E$, where $\sigma_E$ is the root-mean-square deviation of the deuteron collision energy over the distribution $f(E)$.

The middle arrow corresponds to the most probable initial deuteron energy $E^p$ for the distribution $f(E)$.

As is evident from Fig. 6, in this time interval, there are two distinct neutron peaks caused by detection of neutrons from reaction (1) in shot 1. Note that these peaks result from time overlap of individual events of neutron detection by the scintillation spectrometer D1.

Therefore, there arises a problem of finding the average number of detected $dd$ fusion neutrons from the shape of the spectrometer D1 signal resulting from pileup of a few pulses from individual neutron detection events.

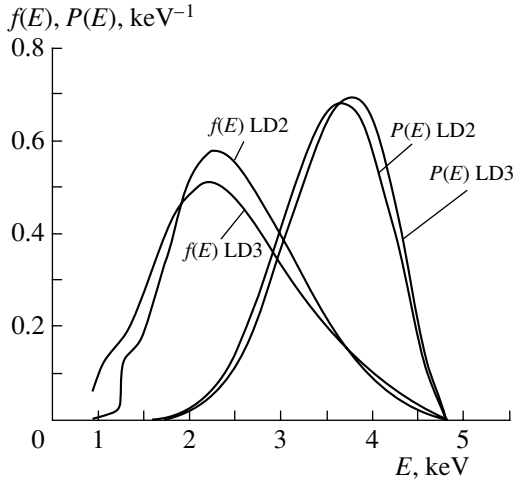


**Fig. 4.** Liner deuteron energy distributions $f(E)$ and $P(E)$ measured in shot 1 with the light detectors LD2 and LD3.

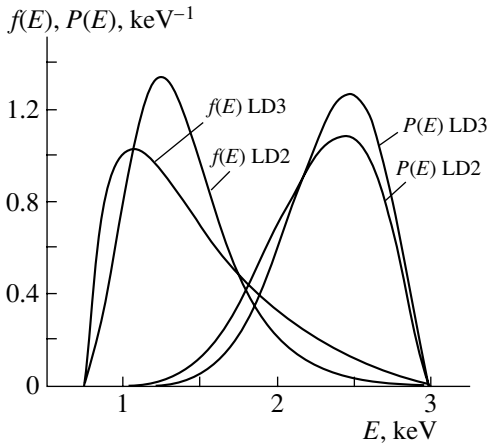


**Fig. 5.** Liner deuteron energy distributions $f(E)$ and $P(E)$ measured in shot 2 with the light detectors LD2 and LD3.

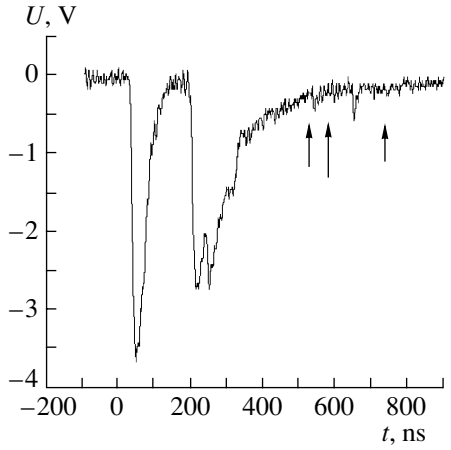


**Fig. 6.** Oscillogram of the pulses from the scintillation neutron detector D1 in shot 1.

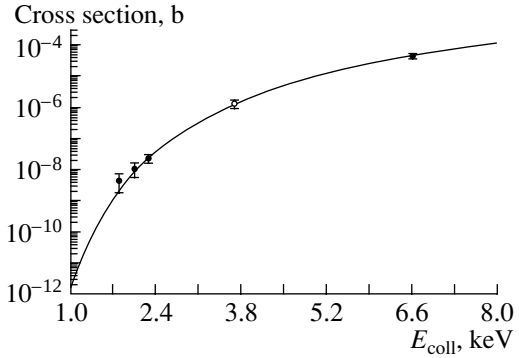


**Fig. 7.** Dependence of the *dd*-reaction cross section on the deuteron-collision energy: the solid curve is the calculation by formula (2) with $S = 53.8$ keV b [18]; closed circles and closed square are the experimental $S$-factor values found in [16] and [17], respectively; the open circle is the result of the present paper.

To solve the problem, we analyzed the shape of the signals from the neutron spectrometer exposed to $\gamma$ quanta and neutrons from standard sources ($^{137}$Cs, $^{60}$Co, Po–Be, $^{252}$Cf, Pu–Be) with varying intensity. The plastic scintillator light output due to $\gamma$ quanta and recoil protons[2)] coupling in the energy range corresponding to the maximum recoil proton energy of 2.5 MeV was used. Using the Monte Carlo method and taking into account the shape of the neutron spectrometer scintillation pulse and the time distribution of the neutron radiation intensity, we found the average number of detected neutrons in the time interval shown in Fig. 6: $N_n^{\exp} = 18.2 \pm 3.6$ (see Table 3). The astrophysical $S$-factor value was derived by substituting the experimental neutron yield $N_n^{\exp}$ of reaction (1) into (3). It came out to $S(E_{\rm coll} = 3.69\ \text{keV}) = 58.2 \pm 18.1$ keV b (see Table 3).

As to *dd* reaction cross sections, we calculated them by (2) with the above $S$ factor for the deuteron-collision energies

$$E_{\rm coll} + \sigma_{P(E)}, \quad E_{\rm coll}, \quad E_{\rm coll} - \sigma_{P(E)}$$

($\sigma_{P(E)}$ is the root-mean-square deviation of the deuteron-collision energy corresponding to the $P(E)$ distribution).

Table 3 presents basic characteristics of the energy distributions $f(E)$ and $P(E)$ for shots 1 and 2, measured yields of neutrons from reaction (1), astrophysical $S$ factors, and *dd*-reaction cross sections.

The value of the astrophysical $S$ factor found by us (see Fig. 1) in shot 1 is its average corresponding

[2)]Fast neutrons are detected by the plastic scintillator through detecting recoil protons arising from elastic *np* scattering.

to the average deuteron-collision energy determined by the function $P(E)$. As is evident from Fig. 1, the measured value of the $S$ factor agrees within the statistical error with its expected value derived by extrapolation from the region of "higher" deuteron-collision energies (7–45 keV) to the region under consideration.

Figure 7 displays cross sections for the neutron-yielding $dd$ reaction at deuteron-collision energies $E_{\text{coll}}$, $E_{\text{coll}} + \sigma_{P(E)}$, $E_{\text{coll}} - \sigma_{P(E)}$ calculated by formula (2) with the $S$-factor value from [18].

As is evident from the figure, the results are quite well described by dependence (2).

As to analysis of shot-2 data, we did not observe any excess of the neutron yield over the background level. This agrees with the measured liner deuteron energy distribution in shot 2 (see Fig. 5). The expected yield of detected neutrons in shot 2 ($N_n \approx 2 \times 10^4$ into the solid angle of $4\pi$), calculated by formula (3) with the function $f(E)$ found for this shot, turned out to be well below the neutron detection system sensitivity threshold $N_{\text{thresh}} = 5 \times 10^5$.

Some of the most significant factors giving rise to uncertainties of the measured $S$ factor and $dd$-reaction-cross-section values should be pointed out:

(i) uncertainty of the position of the light detectors LD2 and LD3 in space with respect to the CIS: 0.5 mm;

(ii) inaccuracy in determination of the liner mass (and thus the number of incident deuterons) within the zero-dimensional model by analysis of the data from the magnetic $dB/dt$ probes: 15%;

(iii) inaccuracy in the neutron detection efficiency of the scintillation spectrometer found by measurements with standard $^{252}$Cf and Pu–Be sources and by Monte Carlo calculations: 10%;

(iv) inaccuracy in the number of incident liner deuterons caused by angular divergence of the radially expanding plasma flux on the way between the CIS and the $CD_2$ target (on the basis of bolometric investigations of the liner acceleration dynamics [2]): 5%;

(v) errors in determination of the parameters of liner deuteron energy distributions arising from transformation of time distributions of signals from optical detectors LD2 and LD3 into energy distributions, the average errors in determination of $E^p$, $\overline{E}$, $E_{\text{coll}}$, and $E^p_{P(E)}$ and the dispersions of the deuteron energy distribution functions $f(E)$ and $P(E)$ amounting to about 10%;

(vi) inaccurate knowledge of the ion–ion collision temperature in the determination of the liner deuteron path in a solid target, this error amounting to about 7%.

Considering all the above causes of uncertainties, we found the resulting errors in the quantities of interest (see Table 3).

Finally, the following should be mentioned. The results of the present experiment indicate that the use of the liner plasma in the inverse $Z$-pinch scheme and the proposed method for measuring the energy distribution of accelerated deuterons allow reactions between light nuclei to be investigated in the ultralow-energy region, which is practically inaccessible with use of classical accelerators.

With a higher generator current (and thus a larger number of accelerated liner ions) and a larger number of light detectors and magnetic $dB/dt$ probes, it will undoubtedly be possible to obtain more precise information on characteristics of nuclear reactions in such a poorly studied region of ultralow-energy collisions of strongly interacting particles.

## ACKNOWLEDGMENTS

We are grateful to the collaborators from the Institute of High-Current Electronics S.A. Sorokin for fruitful discussions on dynamics of the dense $Z$-pinch formation and E.N. Volkov and V.A. Sinebryukhov for providing uninterruptible operation of the accelerator and for assistance in measurements.

The investigation was supported by the Russian Foundation for Basic Research (project no. 00-02-17203) and the Fund of the Plenipotentiary of Poland at JINR.

## REFERENCES

1. S. P. Merkuriev *et al.*, in *Proceedings of the International Conference on the Theory of Few-Body and Quark–Hadronic Systems, Dubna, 1987,* D4-87-692, p. 6.
2. H. Paetz gen. Schieck, Few-Body Syst. **5**, 171 (1988).
3. V. F. Kharchenko *et al.*, Yad. Fiz. **55**, 86 (1992) [Sov. J. Nucl. Phys. **55**, 49 (1992)].
4. G. S. Chulick *et al.*, Nucl. Phys. A **551**, 255 (1993).
5. J. N. Bachall and M. N. H. Pinsonneault, Rev. Mod. Phys. **64**, 885 (1992).
6. W. A. Fowler, Rev. Mod. Phys. **56**, 149 (1984).
7. V. B. Belyaev, A. Bertin, Vit. M. Bystritsky, *et al.*, Nukleonika **40**, 85 (1995).
8. V. B. Belyaev, V. M. Bystritsky, O. I. Kartavtsev, *et al.*, Preprint No. D15-92-324, JINR (Dubna, 1992).
9. V. B. Belyaev, V. M. Bystritsky, V. M. Grebenyuk, *et al.*, Preprint No. D15-95-378, JINR (Dubna, 1995); Vit. M. Bystritskii *et al.*, IEEE **2**, 1215 (1995).
10. V. M. Bystritsky *et al.*, Nukleonika **42**, 775 (1997).
11. T. L. Bulgakov, Vit. M. Bystritskii, Vyach. M. Bystritsky, *et al.*, Yad. Fiz. **60**, 1349 (1997) [Phys. At. Nucl. **60**, 1217 (1997)].

12. Vit. M. Bystritskii, V. M. Bystritsky, V. M. Grebenyuk, *et al.*, Preprint No. D15-96-11, JINR (Dubna, 1996).
13. T. Bulgakov, Vit. M. Bystritskii, G. Mesyats, *et al.*, in *Proceedings of the XI International Conference on High-Power Particle Beams "Beams 96," Prague, 1996,* Vol. 2, p. 917.
14. V. M. Bystritsky, V. M. Grebenyuk, S. S. Parzhitski, *et al.*, Laser Part. Beams **18**, 325 (2000).
15. Vit. M. Bystritskii, V. M. Bystritsky, S. A. Chaikovsky, *et al.*, Yad. Fiz. **64**, 920 (2001) [Phys. At. Nucl. **64**, 855 (2001)].
16. V. Bystritskii, V. Bystritsky, S. Chaikovsky, *et al.*, Kerntechnik **66**, 42 (2001).
17. A. Krauss, H. W. Becker, H. P. Trautvetter, *et al.*, Nucl. Phys. A **465**, 150 (1987).
18. R. E. Brown and N. Jarmie, Phys. Rev. C **41**, 1391 (1990).
19. V. M. Bystritsky, V. M. Grebenyuk, S. S. Parzhitski, *et al.*, Nucl. Instrum. Methods Phys. Res. A **455**, 706 (2000).
20. V. M. Bystritsky, Vit. M. Bystritskii, V. M. Grebenyuk, *et al.*, in *Proceedings of the 28th IEEE International Conference on Plasma Science and 13th IEEE International Pulse Power Conference, Las Vegas, Nevada, 2001,* Ed. by R. Reinovsky and M. Newton, Vol. 2, p. 1031-1-34.
21. Vit. M. Bystritskii, Vyach. M. Bystritsky, V. M. Grebenyuk, *et al.*, Zh. Tekh. Fiz. **9**, 29 (2002).
22. V. M. Bystritsky and F. M. Pen'kov, Preprint No. D15-2000-293, JINR (Dubna, 2000); Phys. At. Nucl. **66**, 75 (2003).
23. D. V. Sivukhin, *Voprosy Teorii Plazmy* (Atomizdat, Moscow, 1964), Vol. 4, p. 81.
24. A. V. Luchinski, V. I. Makhrin, N. A. Ratakhin, *et al.*, Izv. Vyssh. Uchebn. Zaved., Ser. Fiz., No. 38, 52 (1995).

*Physics of Atomic Nuclei, Vol. 66, No. 9, 2003, pp. 1691–1699. Translated from Yadernaya Fizika, Vol. 66, No. 9, 2003, pp. 1739–1748.*


**NUCLEI**
**Theory**

# Parity Nonconservation in Binary and Ternary Nuclear Fission Induced by Polarized Neutrons

**S. G. Kadmensky**

*Voronezh State University, Universitetskaya pl. 1, Voronezh, 394693 Russia*

Received July 15, 2002; in final form, October 24, 2002

**Abstract**—Within the quantum-mechanical theory of the nuclear-fission process, the conditions of the emergence of coherent effects in the angular distributions of fragments originating from the binary and ternary fission of polarized nuclei are analyzed with allowance for the properties of transition fission states. In the case of ternary fission, the coefficients of $P$-odd asymmetry in the angular distributions of a light particle and a third particle, which is taken here to be an alpha particle, are calculated under the assumption that the third particle and two fragments are produced through a one-step mechanism. In order to confirm the ideas developed here, it is proposed to repeat, at a higher level of statistical accuracy, experiments devoted to seeking $P$-odd asymmetries for alpha particles in the ternary fission of nuclei.


## 1. INTRODUCTION

Parity violation in binary nuclear fission (we label relevant quantities with the index $b$) induced by polarized thermal neutrons was discovered by Danilyan *et al.* [1] in analyzing the $P$-odd-asymmetry coefficient $\alpha_{\mathrm{LF}}^b$ defined in a standard way. This asymmetry is associated with the emergence of the $P$-odd correlation $(\boldsymbol{\sigma}_n \cdot \mathbf{k}_{\mathrm{LF}})$ in the normalized (to unity) angular distributions of fission fragments, $\boldsymbol{\sigma}_n$ and $\mathbf{k}_{\mathrm{LF}}$ being, respectively, the neutron spin and the light-fission-fragment wave vector. For $^{233}$U target nuclei, this coefficient proved to be [2]

$$\alpha_{\mathrm{LF}}^b = (4 \pm 0.17) \times 10^{-4}. \quad (1)$$

Investigation of similar correlations in the ternary fission of $^{233}$U nuclei (here, the index $t$ is used to label quantities associated with this fission channel) that is induced by polarized thermal neutrons was performed in [3, 4]. For the relevant asymmetry coefficient $\alpha_{\mathrm{LF}}^t$, this yielded a value close to that of the coefficient $\alpha_{\mathrm{LF}}^b$ for the binary fission of the same nucleus; that is,

$$\alpha_{\mathrm{LF}}^t = \alpha_{\mathrm{LF}}^b (1.05 \pm 0.10). \quad (2)$$

Petrov *et al.* [5] and Goennenwein *et al.* [6] investigated $P$-odd correlations of the form $(\boldsymbol{\sigma}_n \cdot \mathbf{k}_3)$ in the angular distributions of a third particle emerging in ternary nuclear fission induced by polarized thermal neutrons, $\mathbf{k}_3$ being the wave vector of the third particle, an alpha particle here. For $^{233}$U target nuclei, the asymmetry coefficient $\alpha_3^t$ defined in a standard way proved to be

$$\alpha_3^t = (0.60 \pm 0.40) \times 10^{-4}; \quad (3)$$

$$\alpha_3^t = (0.9 \pm 1.3) \times 10^{-4}.$$

Thus, we see that the coefficient $\alpha_3^t$ (3) is much less in magnitude than the coefficient $\alpha_{\mathrm{LF}}^t$ (2), the value of $\alpha_3^t$ remaining uncertain at the level of precision achieved in the experiments reported in [5, 6].

Parity-nonconservation effects in binary nuclear fission induced by polarized resonance neutrons were theoretically investigated by Sushkov and Flambaum [7] and by Bunakov and Gudkov [8], the effect of dynamical enhancement in the mixing of opposite-parity states because of the influence of weak nucleon–nucleon forces being taken into account at the stage of compound-nucleus formation in both of these studies.

The asymmetry coefficient $\alpha_{\mathrm{LF}}^b$ was estimated in [7] under some assumptions, and the result proved to be in agreement with its experimental value in (1).

A qualitative analysis of $P$-odd effects in the ternary fission of nuclei revealed [9] that the coefficients $\alpha_{\mathrm{LF}}^b$ and $\alpha_{\mathrm{LF}}^t$ are expected to have close values. At the same time, it follows from the analysis in [9] that, depending on the mechanism of ternary nuclear fission, two versions of values are possible for the coefficient $\alpha_3^t$. For the one-step mechanism consisting in the simultaneous rupture of the fissile-nucleus neck in two sections, with the result that two fragments and a third particle emerge at the same instant, it was concluded that the asymmetry coefficients $\alpha_{\mathrm{LF}}^t$ and $\alpha_3^t$ take similar values. For the two-step (sequential) mechanism of ternary fission, in which case a single rupture of the fissile-nucleus

1063-7788/03/6609-1691$24.00 

neck at the first step, with the formation of two fission fragments, is followed by the emission of a third particle from one of the fragments at the second stage, the conclusion drawn in [9] is that the coefficient $\alpha_3^t$ must be close to zero because there are a great number of statistically independent channels of the emission of the third particle.

In [10], it was argued that the experimental values of the coefficient $\alpha_3^t$ in (3) are indicative of its proximity to zero, whence it was deduced, in accordance with the ideas developed in [9], that the ternary fission of nuclei proceeds through the two-step mechanism.

On the basis of the theory of open Fermi systems [11], methods developed in analyzing the angular distributions of protons emitted by polarized nuclei [12, 13], and A. Bohr's concept of transition fission states [14], a quantum-mechanical approach was developed in [15, 16] that made it possible to describe the binary fission of nuclei. This approach, supplemented with the adiabatic approximation for the asymptotic region of the fissile system, permitted obtaining the explicit dependence of the amplitudes of partial fission widths and of potential fission phase shifts on spins, relative orbital angular momenta, and the orientation of the symmetry axes of fission fragments. In [17], this approach was generalized to the case of ternary nuclear fission.

The objective of the present study is to analyze parity-nonconservation effects in binary and ternary nuclear fission by using the results obtained in [15–17] and to explore, on this basis, the mechanism of ternary nuclear fission.

## 2. CONDITIONS OF THE EMERGENCE OF COHERENT INTERFERENCE EFFECTS IN BINARY NUCLEAR FISSION

Binary nuclear fission is characterized by a great number of open fission channels (about $10^{10}$) where fission fragments may differ in atomic weight, charge, and structure. In order to explain coherent interference effects in the energy dependence of cross sections for nuclear-fission processes induced by resonance and thermal neutrons, as well as in the angular distributions of fragments originating from the fission of polarized nuclei, in $P$-even- and $P$-odd-asymmetry coefficients, and in other features of the fission process, A. Bohr [14] proposed a quantum-mechanical concept according to which a moderately small number of transition fission states that are formed at the saddle point of the deformation potential of a fissile nucleus play a dominant role in the fission process, controlling basic properties of nuclear fission, including the scission of the nucleus undergoing fission into fragments and the structure of its states in the asymptotic region of large relative distances $\mathbf{R} = \mathbf{R_1} - \mathbf{R_2}$ between the centers of mass, $\mathbf{R_i}$, of a light ($i = 1$) and the complementary heavy ($i = 2$) fission fragment. However, a consistent application of this concept brings about questions concerning the properties of the amplitudes of partial fission widths and of potential fission phase shifts for various fission channels since these are the quantities that determine the character of interference effects in fission. No solution to relevant problems can be obtained without describing the fission process within a quantum-mechanical approach that would explicitly employ the concepts of fission phase shifts and widths. A version of such a theory for binary nuclear fission was developed in [15, 16].

Our further consideration will deal with the example of binary nuclear fission induced by resonance neutrons. In this case, the initial stage of the fission process involves the formation of compound-nucleus states that are characterized by a spin $J$; its projection $M$ onto the $z$ axis in the laboratory frame; a parity $\pi$; and other quantum numbers $\sigma$, including the atomic weight $A$ and the charge of the nucleus, and which are described by the wave functions $\Psi_\sigma^{JM\pi}$. Since the effect of Coriolis interaction on the structure of states of the axisymmetric deformed compound nucleus is dynamically enhanced, there occurs the mixing of compound-nucleus states having a fixed value of the projection $K$ of the nuclear spin $J$ onto the symmetry axis (the corresponding wave functions are denoted by $\Psi_{\sigma K}^{JM\pi}$) [18], which is taken to be coincident with the $z'$ axis of the intrinsic coordinate system of the nucleus. In view of this, it is convenient to represent the fissile-nucleus wave function $\Psi_\sigma^{JM\pi}$ in the form [18, 19]

$$\Psi_\sigma^{JM\pi} = \sum_K \alpha_{\sigma K}^J \Psi_{\sigma K}^{JM\pi}, \qquad (4)$$

where the signs of the coefficients $\alpha_{\sigma K}^J$ are distributed at random, while their absolute values are equal to $(2J+1)^{-1/2}$.

Using A. Bohr's concept of transition fission states [14], we single out, in the wave function $\Psi_{\sigma K}^{JM\pi}$, the component associated with the wave functions $\Psi_{r_K K}^{JM\pi}$ describing the aforementioned transition states [7]; that is, we write it as

$$\Psi_{\sigma K}^{JM\pi} = \sum_{\nu_K} \gamma_{\sigma K \nu_K}^{J\pi} \varphi_{\nu_K K}^{JM\pi} + \sum_{r_K} \gamma_{\sigma K r_K}^{J\pi} \Psi_{r_K K}^{JM\pi}, \quad (5)$$

where $N_\sigma$ wave functions $\varphi_{\nu_K K}^{JM\pi}$ that are associated with particle–hole nucleon excitations of nucleus $A$ form a nucleon basis of Wigner random matrices [14].

The wave functions $\Psi_{r_K K}^{JM\pi}(\beta_\lambda)$ for transition fission states describe the evolution of an axisymmetric

fissile nucleus in its collective deformation variables $\beta_\lambda$ ($\lambda = 2, 3, \ldots$) from the saddle point of the deformation potential $V(\beta_\lambda)$ of the nucleus, where $\beta_\lambda$ has a single value $\beta_\lambda = \beta_\lambda^{\rm sad}$, to the scission point of the nucleus ($R = R_{\rm sc}$), where it disintegrates into fission fragments. Since a path from the point $\beta_\lambda = \beta_\lambda^{\rm sad}$ to the scission point may lie in $n$ different valleys of the deformation potential, which lead to different values of $\beta_{\lambda n}^{\rm sc}$, the wave function for the $J\pi r_K K$ transition fission state at $R = R_{\rm sc}$ can be represented as the superposition

$$\Psi_{r_K K}^{JM\pi}(\beta_\lambda^{\rm sc}) = \sum_n S_{r_K K n}^{J\pi} \Psi_{nK}^{JM\pi}, \qquad (6)$$

where the coefficients $S_{r_K K n}^{J\pi}$ have a dynamical character and the wave function $\Psi_{nK}^{JM\pi}$ for the $J\pi nK$ fission state corresponds to a specific shape of the fissile nucleus at its scission point, this shape being determined by the deformation parameters $\beta_{\lambda n}^{\rm sc}$.

The coefficients $\gamma_{\sigma K \nu_K}^{J\pi}$ and $\gamma_{\sigma K r_K}^{J\pi}$ in (5) have a random character, the mean values of their squares being approximately given by [7]

$$\langle (\gamma_{\sigma K \nu_K}^{J\pi})^2 \rangle \approx \langle (\gamma_{\sigma K r_K}^{J\pi})^2 \rangle \approx \frac{1}{N_\sigma}.$$

In the asymptotic region of the fissile system—that is, at large distances between fission fragments—the behavior of the wave function for the transition fission state in question is [15, 16]

$$\Psi_{r_K K}^{JM\pi} \to \sum_{cJ_1J_2jL} U_{cJ_1J_2jL}^{JM\pi} \frac{e^{ik_{cJ_1J_2}R}}{R} \times e^{i\delta_{cJ_1J_2jL}^{J\pi}} \sqrt{\frac{\Gamma_{r_K K c J_1 J_2 j L}^{J\pi}}{\hbar v_{cJ_1J_2}}}, \qquad (7)$$

where the index $c$ comprises spin projections $K_i$; parities $\pi_i$; and other quantum numbers $\sigma_i$, including the atomic weights $A_i$, charges $Z_i$, and deformations $\beta_{\lambda i}$ of primary fission fragments, while $k_{cJ_1J_2}$ and $v_{cJ_1J_2}$ are, respectively, the wave vector and the velocity of the relative motion of fragments in the $cJ_1J_2$ channel. The term "primary fission fragments" reflects the fact that, upon the scission of a fissile nucleus, these fragments are produced in states characterized by strongly nonequilibrium values of the deformation parameters $\beta_{\lambda i}$. In the course of the subsequent evolution of these fragments, they appear to be in highly excited states and then deexcite through the emission of prompt neutrons and photons, transforming into final fission fragments that occur in ground or long-lived isomeric states, which are usually recorded by detectors. In the following, we restrict our consideration to the first stage of the fission process—that is, a stage that results in the formation of primary fission fragments.

Expression (7) involves the channel function $U_{cJ_1J_2jL}^{JM\pi}$, which possesses correct transformation properties under time inversion [20],

$$U_{cJ_1J_2jL}^{JM\pi} = \left\{ \Psi_{\sigma_1 K_1}^{J_1 M_1 \pi_1} \{ \Psi_{\sigma_2 K_2}^{J_2 M_2 \pi_2} i^L Y_{LM_L}(\Omega) \}_{jm_j} \right\}_{JM}, \qquad (8)$$

where $\Omega \equiv (\theta, \varphi)$ is a solid angle that is associated with the direction of the radius vector $\mathbf{R}$ in the laboratory frame, the braces denote the vector coupling of angular momenta, $L$ is the relative orbital angular momentum of primary fission fragments, the parity $\pi$ is found from the parity-conservation law $\pi = \pi_1\pi_2(-1)^L$, and the index $c$ is defined as $c \equiv \sigma_1 K_1 \pi_1 \sigma_2 K_2 \pi_2$.

Expression (7) also involves the amplitude $\sqrt{\Gamma_{r_K K c J_1 J_2 j L}^{J\pi}}$ of the partial fission width of a transition fission state. This amplitude is defined as [15, 16]

$$\sqrt{\Gamma_{r_K K c J_1 J_2 j L}^{J\pi}} = \sqrt{2\pi} \times \left\langle U_{cJ_1J_2jL}^{JM\pi} \frac{\varphi_{cJ_1J_2jL}^{J\pi}(R)}{R} |H_A| (\Psi_{r_K K}^{JM\pi})_{\rm sh} \right\rangle. \qquad (9)$$

Here, $H_A$ is the total Hamiltonian of the fissile nucleus in question and the function $(\Psi_{r_K K}^{JM\pi})_{\rm sh}$ describes the transition fission state in the internal (shell) region of the fissile nucleus (from the saddle point to the point at which nucleus $A$ undergoes scission into fragments), where nucleus $A$ has a simply connected shape and where the ideas of a generalized model of a nucleus are valid with allowance for the shell properties of the nucleon modes of motion. In (9), $\varphi_{cJ_1J_2jL}^{J\pi}(R)$ is a regular radial wave function that describes the relative motion of fission fragments in the region of a continuous spectrum and which is normalized to a delta function of energy, its asymptotic behavior for $R \to \infty$ being

$$\varphi_{cJ_1J_2jL}^{J\pi}(R) \to \sqrt{\frac{2}{\pi\hbar v_{cJ_1J_2}}} \times \sin\left( k_{cJ_1J_2}R - \frac{L\pi}{2}| + \delta_{cJ_1J_2jL}^{J\pi} \right). \qquad (10)$$

This asymptotic behavior determines the fission phase $\delta_{cJ_1J_2jL}^{J\pi}$, which appears in (7) and which coincides with the phase shift for the potential scattering of fragments on each other, since, by construction [15,16], the function $\varphi_{cJ_1J_2jL}^{J\pi}(R)$ does not involve resonances associated with the formation of a compound nucleus.

From the structure of the integral formula (9), where the function $(\Psi^{JM\pi}_{r_KK})_{\rm sh}$ decreases exponentially beyond the shell region, while the function $\varphi^{J\pi}_{cJ_1J_2jL}(R)$ decreases exponentially toward the interior of this region, it follows that the main contribution to the partial-width amplitude (9) comes from the region of $R$ values that is adjacent to the point $R = R_{\rm sc}$, at which the parent nucleus undergoes breakup into fission fragments.

Considering primary fission fragments as axisymmetric nuclei, we can represent, in the strong-coupling approximation, their wave functions $\Psi^{J_iM_i\pi_i}_{\sigma_iK_i}$, which appear in the definition (8) of the channel function, in the form [14]

$$\Psi^{J_iM_i\pi_i}_{\sigma_iK_i} = \sqrt{\frac{2J_i+1}{16\pi^2}}\left[1+\delta_{K_i,0}\left(\frac{1}{\sqrt{2}}-1\right)\right] \times\left\{D^{J_i}_{M_iK_i}(\omega_i)\chi^{\pi_i}_{\sigma_iK_i}(q_i(\omega_i)) + (-1)^{J_i+K_i}D^{J_i}_{M_i-K_i}(\omega_i)\chi^{\pi_i}_{\overline{\sigma_iK_i}}(q_i(\omega_i))\right\}, \quad (11)$$

where $D^J_{MK}(\omega_i)$ is a generalized spherical harmonic depending on the Euler angles $(\alpha_i,\beta_i,\gamma_i)\equiv\omega_i$ that determine the orientation of the axes of the intrinsic coordinate frame of the $i$th fragment with respect to the axes of the laboratory frame, $\chi^{\pi_i}_{\sigma_iK_i}$ is the intrinsic wave function describing this fragment and depending on the set of its internal coordinates $q_i(\omega_i)$, and $\chi^{\pi_i}_{\overline{\sigma_iK_i}}$ is its time-reversed counterpart.

The asymptotic behavior (7) of transition fission states makes it possible to conclude that, because of the orthogonality of the intrinsic wave functions $\chi^{\pi_i}_{\sigma_iK_i}$ describing fission fragments and corresponding to different values of the indices $\pi_i\sigma_iK_i$, it is necessary for the emergence of coherent interference effects in the angular distributions of fission fragments that, for a fixed transition fission state characterized by the quantum numbers $J\pi r_KK$, the reduced-width amplitudes (9) be dependent on the indices $J_1J_2jL$ dynamically rather than statistically in a chaotic way. But for coherent interference effects to emerge in the coefficients of $P$-odd asymmetries, it is also necessary that the $J\pi r_KK$ transition fission states that are characterized by opposite parities, $\pi$ and $\overline{\pi}=-\pi$, and which are involved in the formation of these asymmetries have the same structure of intrinsic wave functions.

Sushkov and Flambaum [7] relied on the assumption that, even at the saddle point $\beta_\lambda=\beta^{\rm sad}_\lambda$ of the deformation potential, the $J\pi r_KK$ transition fission states correspond to a pearlike axisymmetric shape of the fissile nucleus, in which case the octupole-deformation parameter $\beta^{\rm sad}_3$ has a static character and differs from zero significantly. In this case, the wave functions for transition fission states can be represented in the form [20]

$$\Psi^{JM\pi}_{r_KK} = \sqrt{\frac{2J+1}{16\pi^2}}\left[1+\delta_{K,0}\left(\frac{1}{\sqrt{2}}-1\right)\right] \times\left\{D^J_{MK}(\omega)\chi_{r_KK}(q(\omega)) + (-1)^{J+K}\pi D^J_{M-K}(\omega)\chi_{\overline{r_KK}}(q(\omega))\right\}i^{\frac{1-\pi}{2}}, \quad (12)$$

where $\omega\equiv(\alpha,\beta,\gamma)$ are the Euler angles for the fissile nucleus and the functions $\chi_{r_KK}(q(\omega))$, which are determined by the total set of internal coordinates $q(\omega)$ of nucleus $A$, correspond to values of $\beta^{\rm sad}_3>0$ and are independent of the parity $\pi$. This assumption was severely criticized by Bunakov and Gudkov [8], who indicated that it is in conflict with the results deduced from an analysis of experiments devoted to the low-energy photofission of nuclei [14]: according to this analysis, the static octupole deformations at the saddle point of the deformation potential are $\beta^{\rm sad}_3=0$, as a rule. It follows that, at the saddle point $\beta^{\rm sad}_\lambda$, a fissile nucleus may have only dynamical values of the parameter $\beta^{\rm sad}_3$ that correspond to octupole vibrations of the nucleus.

It is physically clear, however, that, for the case of strongly asymmetric fission, the fission states $\Psi^{JM\pi}_{nK}$ (6) in the vicinity of the scission point $R=R_{\rm sc}$ (where the fissile nucleus being considered disintegrates into fragments) correspond to pearlike shapes of the fissile nucleus at nonzero static values of the octupole-deformation parameters $\beta^{\rm sc}_{3n}$. In this case, formula (12), with the subscript $nK$ being substituted for the subscript $r_KK$, can be used to describe the fission states $\Psi^{JM\pi}_{nK}$. Considering that, in the fission of a nucleus from $J\pi nK$ prescission states characterized by different values of $n$, there arise fission fragments in states where the indices $c$ differ significantly, we can then represent the fission width of the $J\pi\sigma$ compound state in the form

$$\Gamma^{J\pi}_\sigma = \sum_{r_KK}(\alpha^J_{\sigma K})^2(\gamma^{J\pi}_{\sigma Kr_K})^2\Gamma^{J\pi}_{r_KK}, \quad (13)$$

where the fission width $\Gamma^{J\pi}_{r_KK}$ of the $J\pi nK$ transition fission state is

$$\Gamma^{J\pi}_{r_KK} = \sum_n (s^{J\pi}_{r_KKn})^2\Gamma^{J\pi}_{nK}; \quad (14)$$

$$\Gamma^{J\pi}_{nK} = \sum_c \Gamma^{J\pi}_{nKc} = \sum_{cJ_1J_2jL}\Gamma^{J\pi}_{nKcJ_1J_2jL}.$$

Here, the amplitude $\sqrt{\Gamma^{J\pi}_{nKcJ_1J_2jL}}$ of the width with respect to fission from the fission state $\Psi^{JM\pi}_{nK}$ is given by (9), with the corresponding component of the function $(\Psi^{JM\pi}_{nK})_{\rm sh}$ being substituted for $(\Psi^{JM\pi}_{r_KK})_{\rm sh}$.

For $s$- and $p$-wave neutron resonances, the coefficients $\alpha^J_{\sigma_sK}$ and $\alpha^J_{\sigma_pK}$ coincide in magnitude, while the coefficients $\gamma^{J\pi}_{\sigma_sKr_K}$ and $\gamma^{J\pi}_{\sigma_pKr_K}$ have close absolute values and variances owing to the proximity of the numbers $N_{\sigma_s}$ and $N_{\sigma_p}$ of basis nucleon states. If the differences $\Delta E^J_{r_KK}$ of the energies of the $J\pi r_KK$ transition fission states characterized by opposite parities, $\pi$ and $\overline{\pi}=-\pi$, are so small at the saddle point that they affect only slightly factors that describe the penetrability of the potential fission barrier, the mean values of the coefficients $s^{J\pi}_{r_KKn}$ (they control the transition from the above fission states to the $J\pi nK$ states) will be weakly dependent on the parities $\pi$ and $\overline{\pi}$ and on the spins $J$. In this case, it follows from (13) that the total fission widths $\Gamma^{J\pi}_{\sigma_s}$ and $\Gamma^{J\pi}_{\sigma_p}$ of the $s$- and $p$-wave neutron resonances are rather close, and so are the variances of these widths. It would be of interest to verify this conclusion in analyzing $P$-even and $P$-odd correlations in the binary fission of nuclei, since the idea that the fission widths of $s$- and $p$-wave neutron resonances are close is used in estimating the coefficients of the corresponding asymmetries in [7–9].

In order to obtain the dynamical dependence of the partial-fission-width amplitudes $\sqrt{\Gamma^{J\pi}_{ncJ_1J_2jL}}$ on the indices $J_1J_2jL$, one can use the adiabatic approximation for the asymptotic region of the fissile nucleus, where primary fission fragments have already been formed. This approximation is based on fulfillment of two conditions whose validity was analyzed in [15, 16]:

(i) The first requires that the centrifugal potential $\dfrac{\hbar^2(L+1)L}{2\mu_cR^2}$, where $\mu_c$ is the reduced mass of fission fragments, be much smaller than the kinetic energy $E_{\rm kin}(R_{\rm sc})$ of the fragments at the scission point $R=R_{\rm sc}$, where the nucleus disintegrates into fragments.

(ii) The second requires that the excitation energies $E^{\pi_i}_{\sigma_iJ_iK_i}$ of the rotational bands built in the fission fragments on the basis of the fixed intrinsic states $\chi^{\pi_i}_{\sigma_iK_i}$ of these fragments be much smaller than $E_{\rm kin}(R_{\rm sc})$.

If these conditions are satisfied, the potential fission phase shifts $\delta^{J\pi}_{cJ_1J_2jL}$ are independent of the indices $J\pi J_1J_2jL$, while the partial-fission-width amplitudes $\sqrt{\Gamma^{J\pi}_{ncJ_1J_2jL}}$ are independent of the index $\pi$ and are dependent on the indices $JJ_1J_2jL$ only through Clebsch–Gordan coefficients and through simple dynamical factors [15, 16].

In order to describe the normalized (to unity) angular distributions $dP^J_{MK}(\Omega)/d\Omega$ of fragments originating from the binary fission of nuclei and having a spin $J$ and its projections $M$ and $K$, use is traditionally made of the A. Bohr formula [14]

$$\frac{dP^J_{MK}(\Omega)}{d\Omega} = \frac{2J+1}{4\pi}[|D^J_{MK}(\omega)|^2+|D^J_{M-K}(\omega)|^2]_{\beta=\theta}. \quad (15)$$

This formula corresponds to the simple physical assumption that, in the intrinsic coordinate frame, fragments emerging from the fission of an arbitrary $J\pi nK$ fission state through any physical channel $c$ are emitted in a direction that is parallel or antiparallel to the symmetry axis of the fissile nucleus. Since the solid-angle element $d\Omega'$ specifying the direction of the radius vector $\mathbf{R}$ in the intrinsic coordinate frame can be represented in the form $d\Omega'=\sin\theta' d\theta d\varphi'=-d\xi' d\varphi'$, where $\xi'=\cos\theta'$, the amplitudes of the angular distributions of fragments in the intrinsic coordinate frame of the fissile nucleus are then described by delta functions of the form $\delta(\xi'\pm1)$. These delta functions can be represented as

$$\delta(\xi'\pm1)=\sum_{L=0}^{L_m}2\pi Y_{L0}(\xi')Y_{L0}(\pm1) = \sum_{L=0}^{L_m}\sqrt{(2L+1)\pi}Y_{L0}(\xi')P_L(\pm1), \quad (16)$$

where the spherical harmonic $Y_{L0}(\Omega')=Y_{L0}(\theta')$ is written in the form $Y_{L0}(\xi')$, which is related to the Legendre polynomial $P_L(\xi')$ [recall that $P_L(+1)=1$ and $P_L(-1)=(-1)^L$], and where the quantity $L_m$ must be considered in the limit $L_m\to\infty$. Formula (16) reflects the quantum-mechanical uncertainty principle relating the operator $(\hat{\mathbf{L}})^2$ and the square of the angle $\theta'$.

As was shown in [15, 16], formula (15) is approximately valid if the adiabaticity conditions considered above and two more conditions are satisfied. First, the symmetry axes of primary fission fragments must be approximately parallel at the first stage of fission to the symmetry axis of the fissile nucleus—that is, $\omega_1\approx\omega_2\approx\omega$. Second, the amplitude of the angular distribution of fission fragments in the intrinsic coordinate frame of the fissile nucleus must have the form (16) at finite but large values of $L_m$—that is, the angular part of the wave function describing the relative motion of

fission fragments must be a coherent superposition of the form

$$F_{L_m}(\theta') = b(L_m) \times \left\{ \sum_{L=0}^{L_m} \sqrt{(2L+1)\pi} Y_{L0}(\xi')[1+(-1)^L \pi\pi_1\pi_2] \right\}, \quad (17)$$

where the constant $b(L_m)$ is determined from the condition requiring that the function $|F_{L_m}(\theta')|^2$ be normalized to unity. For finite values of $L_m$, angular distributions of fission fragments deviate from those that are predicted by formula (15). The analysis performed in [21], where the angular distributions of fragments originating from the subthreshold photofission of nuclei were investigated with allowance for the mean values obtained for the spins of primary fission fragments from the examination of the multiplicities and multipolarities of prompt photons emitted by these fragments, revealed, however, that $L_m$ values are quite large ($20 < L_m < 25$). Owing to this, the A. Bohr (15) formula proves to be quite accurate in many cases.

Using the approximation specified by the A. Bohr formula (15) and following the methods developed in [15,16], we can represent the asymptotic expression for the fission-state wave function $\Psi_{nK}^{JM\pi}$ in the form

$$\Psi_{nK}^{JM\pi} \sim \sum_c \{D_{MK}^J(\omega) f_c + (-1)^{J+K} \pi D_{M-K}^J(\omega) f_{\overline{c}}\}_{\theta=\beta} \times \sqrt{\frac{\Gamma_{nKc}^J}{\hbar v_c}} \frac{e^{ik_c R}}{R}, \quad (18)$$

where the width $\Gamma_{nKc}^{J\pi}$, which is given by Eq. (14), is denoted by $\Gamma_{nKc}^J$ since it is independent of parity and where the function $f_c$ is written as

$$f_c = \chi_{\sigma_1 K_1}^{\pi_1} \chi_{\sigma_2 K_2}^{\pi_2} + (-1)^{J_1+K_1} \chi_{\overline{\sigma_1 K_1}}^{\pi_1} \chi_{\sigma_2 K_2}^{\pi_2} + (-1)^{J_2+K_2} \chi_{\sigma_1 K_1}^{\pi_1} \chi_{\overline{\sigma_2 K_2}}^{\pi_2} + (-1)^{J_1+J_2+K_1+K_2} \chi_{\overline{\sigma_1 K_1}}^{\pi_1} \chi_{\overline{\sigma_2 K_2}}^{\pi_2} \quad (19)$$

and is nonzero under the condition that the indices $K_i$ on the functions $\chi_{\sigma_i K_i}^{\pi_i}$ and $\chi_{\overline{\sigma_i K_i}}^{\pi_i}$ satisfy the equality $\sum_i K_i = K$. The function $f_{\overline{c}}$ is the time-conjugate counterpart of $f_c$.

## 3. PARITY-NONCONSERVATION EFFECTS IN THE BINARY-FISSION OF NUCLEI

It was shown in [7, 8] that, in the case where the fission of unpolarized target nuclei having a spin $I$ and a parity $\pi$ is induced by polarized neutrons whose polarization vector $\boldsymbol{\sigma}_n$ is aligned with the $z$ axis of the laboratory coordinate frame, $P$-odd asymmetries in the angular distributions of fission fragments are the most pronounced if the fission process is initiated by $s$-wave neutrons of orbital angular momentum $l_n = 0$ and total spin $j_n = 1/2$ that are captured by the target nucleus with the formation of $s$-wave neutron resonance states of spin $J = J_\pm = I \pm 1/2$ and parity $\pi$ that are described by the wave functions $\Psi_{\sigma_s}^{JM\pi}$ of the form (4). Owing to weak nucleon–nucleon forces, the wave functions $\Psi_{\sigma_p}^{JM\pi}$ of neighboring $p$-wave resonances of spin $J$ and parity $\overline{\pi} = -\pi$ are admixed to the wave function for the $s$-wave resonance formed, with the result that the wave function $\Psi_{\sigma_s}^{JM\pi}$ assumes the form

$$\Psi_{\sigma_s}^{JM\pi} \to \Psi_{\sigma_s}^{JM\pi} + \beta_{\sigma_s\sigma_p}^J \Psi_{\sigma_p}^{JM\overline{\pi}}, \quad (20)$$

where

$$\beta_{\sigma_s\sigma_p}^J = \frac{\langle \Psi_{\sigma_p}^{JM\overline{\pi}} | H_W | \Psi_{\sigma_s}^{JM\pi} \rangle}{E - E_{\sigma_p J} + i\Gamma_{\sigma_p J}/2}. \quad (21)$$

Here, $E_{\sigma_p J}$ and $\Gamma_{\sigma_p J}$ are, respectively, the energy and the total width of a $p$-wave resonance; $E$ is the energy of the incident neutron; and $H_W$ is the Hamiltonian of weak nucleon–nucleon interaction.

In the wave functions of $s$- and $p$-wave neutron resonances, we isolate fission states (which are specified by the index $n$) by using Eqs. (5) and (6). In order to obtain $P$-odd coherent interference effects in the angular distributions of fission fragments, we restrict our consideration, for the sake of simplicity, to the case where the fission process involves only one $s$- and one $p$-wave resonance of fixed spin $J$, disregarding the interference between resonance states of spin $J = J_+$ and $J = J-$. To take into account a greater number of $s$- and $p$-wave neutron resonances and the interference between the $J = J_+$ and $J = J_-$ spin states, one can make use of the methods developed in [7]. Following the same line of reasoning as in [7], we can represent the cross section for binary nuclear fission induced by polarized $s$-wave neutrons in the form

$$\frac{d\sigma^b(\Omega)}{d\Omega} \equiv \sigma^b(\theta) \sim \sum_{r_K nK} \Gamma_{nK}^{Jb} \{A_{0r_K Kn}^J + P_1(\xi) A_{1r_K Kn}^J\}, \quad (22)$$

where

$$A_{0r_K Kn}^J = (\gamma_{\sigma_s K r_k}^{J\pi}\, \alpha_{\sigma_s K}^J\, s_{r_K Kn}^{J\pi})^2; \quad (23)$$

$$A_{1r_K Kn}^J = 2\mathrm{Re}(\beta_{\sigma_s\sigma_p}^J) \frac{K(-1)^{J-I-1/2}}{I+1/2} \times \gamma_{\sigma_s K r_K}^{J\pi} \gamma_{\sigma_p K r_K}^{J\overline{\pi}} \alpha_{K\sigma_s}^J \alpha_{K\sigma_p}^J s_{r_K Kn}^{J\pi} s_{r_K Kn}^{J\overline{\pi}}. \quad (24)$$

Defining the coefficient of $P$-odd asymmetry in the angular distribution of binary-fission fragments, $\alpha^b_{\rm LF}$, as

$$\alpha^b_{\rm LF} = \frac{\sigma^b_+ - \sigma^b_-}{\sigma^b_+ + \sigma^b_-},$$

where $\sigma^b_+ = \dfrac{d\sigma^b(0^\circ)}{d\Omega}$ and $\sigma^b_- = \dfrac{d\sigma^b(180^\circ)}{d\Omega}$, and using Eq. (22), we then obtain

$$\alpha^b_{\rm LF} = \frac{\sum\limits_{r_K nK} \Gamma^{Jb}_{nK} A^J_{1r_K Kn}}{\sum\limits_{r_K nK} \Gamma^{Jb}_{nK} A^J_{0r_K Kn}}. \qquad (25)$$

Retaining, in (25), only one state characterized by fixed values of $r_K$, $n$, and $K$, one can go over to the analogous formula obtained in [7] for $\alpha^b_{\rm LF}$.

## 4. $P$-ODD ASYMMETRIES IN THE TERNARY FISSION OF NUCLEI

By employing the concept of the one-step ternary-fission mechanism and the results presented in [17], we can write the double-differential cross section for ternary nuclear fission induced by polarized resonance neutrons in the form

$$\frac{d^2\sigma^t}{d\Omega d\Omega_3} = \frac{d\sigma^t(\Omega)}{d\Omega}(M(\widetilde{\theta}_3))^2, \qquad (26)$$

where $\Omega_3 \equiv (\theta_3, \varphi_3)$ is the solid angle specifying the direction of third-particle emission in the laboratory frame and the differential cross section $\dfrac{d\sigma^t(\Omega)}{d\Omega}$ is given by expression (22) in which the amplitude $\sqrt{\Gamma^{Jb}_{nK}}$ of the width with respect to binary fission from the $J\pi nK$ fission state is replaced by the amplitude $\sqrt{\Gamma^{Jt}_{nK}}$ of the width with respect to ternary fission occurring from the same state and leading to the emission of a third particle. The function $M(\widetilde{\theta}_3)$ is defined as

$$M(\widetilde{\theta}_3) = \sum_l b_l Y_{l0}(\widetilde{\theta}_3), \qquad (27)$$

where $l$ is the orbital angular momentum of the third particle with respect to the center of mass of the light and heavy fission fragments and $\widetilde{\theta}_3$ is the angle between the momenta of the third particle and the heavy fragment. The spherical harmonic $Y_{l0}(\widetilde{\theta}_3)$ can be represented in the form

$$Y_{l0}(\widetilde{\theta}_3) = \sum_m Y^*_{lm}(\Omega_3) Y_{lm}(\Omega)\sqrt{\frac{4\pi}{2l+1}} \qquad (28)$$
$$= (-1)^l \{Y_{lm}(\Omega) Y_{l-m}(\Omega_3)\}_{00}\sqrt{4\pi},$$

where the braces denote the vector composition of the angular momenta of the spherical harmonics involved, the total angular momentum formed in this way being zero. It follows that the function $M(\widetilde{\theta}_3)$ is a scalar function, so that the inclusion of this function does not change the total spin of the fissile system.

If we disregard parity-nonconservation effects in (22), in which case $\beta^J_{\sigma_s\sigma_p} = 0$, the angular distribution (26) assumes the form

$$\frac{d^2\sigma^t}{d\Omega d\Omega)_3} = \frac{d\sigma^t_0(\Omega)}{d\Omega_3 \lambda}(M(\widetilde{\theta}_3))^2, \qquad (29)$$

where $\dfrac{d\sigma^t_0(\Omega)}{d\Omega}$ is given by (22) with $A^J_{1r_K Kn} = 0$ and is independent of either the solid angle $\Omega$ or the polarization vector $\boldsymbol{\sigma}_n$ of incident neutrons. Choosing the $z$ axis in the laboratory frame to be aligned with the direction of light-fragment emission, we then obtain the normalized (to unity) angular distribution of the third particle in the form

$$\frac{dW_3(\theta_3)}{d\Omega_3} = \left(\sum_l b_l Y_{l0}(\theta_3)\right)^2, \qquad (30)$$

where, by virtue of the orthonormality of the spherical harmonics $Y_{l0}(\theta_3)$, the coefficients $b_l$ satisfy the normalization condition

$$\sum_l b_l^2 = 1. \qquad (31)$$

For the resonance-neutron-induced ternary fission of $^{235}$U target nuclei, the coefficients $b_l$ from formula (27) were calculated in [17] with the aid of representation (30) for the normalized (to unity) experimental angular distribution $\dfrac{dW^{\rm expt}(\theta_3)}{d\Omega_3}$ of a third particle, which was taken to be an alpha particle. The results of that calculation were presented in the table of [17]. Since the experimental angular distributions of alpha particles, $\dfrac{dW^{\rm expt}(\theta_\alpha)}{d\Omega_\alpha}$, for the ternary fission of $^{235}$U target nuclei are close to the analogous angular distributions for ternary fission of $^{235}$U nuclei, those results can also be used for $^{235}$U target nuclei. As can be seen from the table of [17], the coefficients $b_l$ for the even values of $l = 0$, 2, and 4 are much greater in magnitude than those for odd values of $l$ because the angle of $\theta^m_\alpha \approx 82.4^\circ$, which corresponds to a maximum in the angular distribution $\dfrac{dW(\theta_\alpha)}{d\Omega_\alpha}$, is close to the angle of 90°, for which the values of the spherical harmonics $Y_{l0}(\theta_\alpha)$ for odd $l$ are strictly equal to zero.

In order to describe $P$-odd asymmetry that is associated with a correlation of the form $(\boldsymbol{\sigma}_n \cdot \mathbf{k}_{\mathrm{LF}})$ in the angular distribution of fragments originating from ternary nuclear fission induced by polarized resonance neutrons, it is convenient to fix the direction of light-fragment emission along or against the $z$ axis of the laboratory frame, this axis being aligned with the direction of the neutron-polarization vector $\boldsymbol{\sigma}_n$, and to record an alpha particle at an angle of 90° with respect to the $z$ axis. In this case, we have $\theta_3 = 90°$, and none of the odd harmonics in $l$ contributes to the angular distribution $\dfrac{dW_3(90°)}{d\Omega_3} = \left(\sum_l b_l Y_{l0}(90°)\right)^2$ of the third fragment. Since this distribution is identical for the directions of light-fragment emission along and against the $z$ axis, the angular-asymmetry coefficient $\alpha^t_{\mathrm{LF}}$ assumes the form

$$\alpha^t_{\mathrm{LF}} = \frac{\sum\limits_{r_K nK} \Gamma^{Jt}_{nK} A^J_{1r_K Kn}}{\sum\limits_{r_K nK} \Gamma^{Jt}_{nK} A^J_{0r_K Kn}}. \qquad (32)$$

The expression obtained for $\alpha^t_{\mathrm{LF}}$ differs from expression (25) for the analogous asymmetry coefficient $\alpha^b_{\mathrm{LF}}$ in the case of binary nuclear fission only by the replacement of the amplitudes $\sqrt{\Gamma^{Jb}_{nK}}$ of the widths with respect to binary fission from the $J\pi nK$ fission states by the analogous amplitudes $\sqrt{\Gamma^{Jt}_{nK}}$ of widths with respect to ternary fission proceeding from the same fission states and leading to the emission of an alpha particle. It follows that, if the ratios $q_\alpha = \dfrac{\Gamma^{J\alpha}_{nK}}{\Gamma^{Jb}_{nK}}$ are identical for all fission states characterized by fixed values of $J$ and different values of $\pi nK$, then the $P$-odd-asymmetry coefficient $\alpha^t_{\mathrm{LF}}$ (32) for the ternary fission of nuclei is coincident with the asymmetry coefficient $\alpha^b_{\mathrm{LF}}$ (25) for the binary fission of nuclei. Since the experimental values of the coefficients $\alpha^t_{\mathrm{LF}}$ and $\alpha^b_{\mathrm{LF}}$ are close, as can be seen from (1) and (2), the above implies that $q_\alpha$ depends only slightly on the type of $J\pi nK$ state. This result indicates that the angular distributions of a third particle in ternary fission are determined primarily by the character of its nuclear and Coulomb interactions with fission fragments and are universal for all $vJ_1J_2\beta jL$ channels [17] of ternary nuclear fission that possess close values of the mass-asymmetry coefficient $R_0 = \dfrac{A_H}{A_L}$, where $A_H$ and $A_L$ are the masses of, respectively, a heavy and the complementary light fission fragment. With the aim of examining the dependence of the ratio $q_\alpha$ on the properties of $J\pi nK$ fission states, it would be of interest to continue experimentally studying the coefficients $\alpha^t_{\mathrm{LF}}$ for the case of those target nuclei for which the coefficients $\alpha^b_{\mathrm{LF}}$ have already been determined.

For the ternary fission of nuclei that is induced by polarized resonance neutrons, we will now consider the asymmetry coefficient $\alpha^t_3$ associated with correlations of the form $(\mathbf{k_3} \cdot \boldsymbol{\sigma}_\mathbf{n})$ in the angular distributions of a third particle. The most convenient way to explore this asymmetry is to detect the emission of alpha particles along or against the vector $\boldsymbol{\sigma}_n$ without recording the first and second fission fragments, which corresponds to integrating the angular distribution in (26) with respect to all emission angles of the light fragment. Upon employing formulas of the type

$$Y_{lm}(\Omega)Y_{l'-m}(\Omega) = \sum_\lambda \left[\frac{(2l+1)(2l'+1)}{(2\lambda+1)4\pi}\right]^{1/2} \times Y_{\lambda 0}(\Omega) C^{\lambda 0}_{ll'm-m} C^{\lambda 0}_{ll'00}$$

and taking into account the orthonormality condition for Clebsch–Gordan coefficients,

$$\sum_m C^{10}_{ll'm-m} C^{\lambda 0}_{ll'm-m} = \delta_{\lambda,1},$$

the angular distribution (26) then reduces to a distribution of the form

$$\frac{dW(\Omega_\alpha)}{d\Omega_\alpha} \sim \sum_{r_K nK} \Gamma^{J\alpha}_{nK} \{A^J_{0r_K Kn} + P_1(\xi_\alpha)\eta_\alpha A^J_{1r_K Kn}\}, \qquad (33)$$

where the factor $\eta_\alpha$ is given by

$$\eta_\alpha = \sum_{ll'} b_l b_{l'} (C^{10}_{ll'00})^2 \left[\frac{(2l+1)(2l'+1)}{9}\right]^{1/2}. \qquad (34)$$

Under the condition that the third particle is an alpha particle, the coefficient $\alpha^t_3$ then takes the form

$$\alpha^t_3 = \eta_\alpha \alpha^t_{\mathrm{LF}}, \qquad (35)$$

where the coefficient $\alpha^t_{\mathrm{LF}}$ is given by (32).

A calculation of the coefficient $\eta_\alpha$ for $^{233}$U and $^{235}$U target nuclei with the values of the coefficients $b_l$ from the table of [17] yields a value of $\eta_\alpha = 0.116$. We note that, if only the $l, l' = 0, 1$ terms are retained in expression (34), the result becomes $\eta_\alpha = 0.11$. If, for $^{233}$U, the value in (2) is used for the coefficient $\alpha^t_{\mathrm{LF}}$, the result for the coefficient $\alpha^t_3$ is

$$\alpha^t_3 = (0.44 \pm 0.02) \times 10^{-4}. \qquad (36)$$

A comparison of the coefficient in (36) with its experimental values obtained in [5, 6] and presented in (3) makes it possible to conclude that, for the

nonzero value of the coefficient $\alpha_3^t$ in (36) to be detected experimentally, it is sufficient to improve the statistical accuracy of the experiment by a factor of 4.

Since, with increasing mass-asymmetry coefficient $R_0$, the angle $\widetilde{\theta}_\alpha^m$ at which the angular distribution of alpha particles with respect to the direction of light-fragment emission has a maximum is shifted toward angles smaller than 90° [22], it would be of interest to discover experimentally a change in the $P$-odd-asymmetry coefficient $\alpha_3^t$ from zero value at $R_0 = 1$ to maximum values at $R_0 = 2$.

In our theoretical investigation of the coefficient $\alpha_3^t$, we used the concept of the one-step ternary-nuclear-fission mechanism according to which a third particle and two fission fragments emerge simultaneously upon the scission of the fissile-nucleus neck in two sections; therefore, an experimental corroboration of the value in (36), which was calculated theoretically for the coefficient $\alpha_3^t$, would validate the one-step mechanism of ternary nuclear fission.

## 5. CONCLUSION

The present analysis of the nature of coherent interference effects in the nuclear-fission process and the investigation of the $P$-odd-asymmetry coefficients in binary and ternary nuclear fission induced by polarized resonance neutrons confirm the potential of the proposed quantum-mechanical theory of nuclear fission.

It is of interest to study, within this approach, $P$-even and $T$-odd asymmetries in binary and ternary nuclear fission induced by polarized resonance neutrons, since this may furnish additional information about the mechanisms of ternary nuclear fission.

## ACKNOWLEDGMENTS

I am grateful to V.E. Bunakov, W.I. Furman, and L.A. Barabanov for stimulating discussions and to L.V. Rodionova for assistance in performing numerical calculations.

This work was supported by INTAS (project no. 99-00229) and by the Universities of Russia Foundation (project no. UR-02.01.011).

## REFERENCES

1. G. V. Danilyan *et al.*, Pis'ma Zh. Éksp. Teor. Fiz. **26**, 68 (1977) [JETP Lett. **26**, 186 (1977)].
2. A. Koetzle *et al.*, Nucl. Instrum. Methods Phys. Res. A **440**, 750 (2000).
3. A. M. Belozerov, G. V. Danilyan, *et al.*, Pis'ma Zh. Éksp. Teor. Fiz. **54**, 136 (1991) [JETP Lett. **54**, 132 (1991).
4. F. Goennenwein *et al.*, Nucl. Phys. A **567**, 303 (1994).
5. G. A. Petrov, G. Val'ski, *et al.*, Nucl. Phys. A **502**, 297 (1989).
6. F. Goennenwein *et al.*, in *Proceedings of the International Conference on Nuclear Physics, St. Petersburg, 2000,* p. 147.
7. O. P. Sushkov and V. V. Flambaum, Usp. Fiz. Nauk **136**, 3 (1982) [Sov. Phys. Usp. **25**, 1 (1982)].
8. V. E. Bunakov and V. P. Gudkov, Nucl. Phys. A **401**, 93 (1993).
9. V. E. Bunakov and V. P. Gudkov, Z. Phys. A **321**, 277 (1985).
10. V. E. Bunakov, F. Goennenwein, *et al.*, Preprint ILL 01BU03T (Grenoble, 2001).
11. S. G. Kadmensky, Yad. Fiz. **64**, 478 (2001) [Phys. At. Nucl. **64**, 423 (2001)].
12. S. G. Kadmensky and A. A. Sanzogni, Phys. Rev. C **62**, 054601 (2000).
13. S. G. Kadmensky, Yad. Fiz. **65**, 863 (2002) [Phys. At. Nucl. **65**, 831 (2002)].
14. A. Bohr, in *Proceedings of the International Conference on Peaceful Uses of Atomic Energy, United Nations, 1955,* Vol. 5, p. 200.
15. S. G. Kadmensky, in *Matherials of IX International Seminar on the Interaction of Neutrons with Nuclei, Dubna, 2001,* p. 128.
16. S. G. Kadmensky, Yad. Fiz. **65**, 1424 (2002) [Phys. At. Nucl. **65**, 1390 (2002)].
17. S. G. Kadmensky, Yad. Fiz. **65**, 1833 (2002) [Phys. At. Nucl. **65**, 1785 (2002)].
18. S. G. Kadmenskiĭ, V. P. Markushev, and V. I. Furman, Yad. Fiz. **35**, 300 (1982) [Sov. J. Nucl. Phys. **35**, 166 (1982)].
19. W. I. Furman and J. Kliman, in *Proceedings of the International Symposium on Nuclear Physics, Gaussig, 1987,* p. 86.
20. A. Bohr and B. Mottelson, *Nuclear Structure* (Benjamin, New York, 1969, 1975; Mir, Moscow, 1971, 1977), Vols. I, II.
21. S. G. Kadmensky and L. V. Rodionova, Yad. Fiz. **66**, 1259 (2003) [Phys. At. Nucl. **66**, 1219 (2003)].
22. M. Mutterer and J. P. Theobald, *Dinuclear Decay Modes* (IOP, Bristol, 1996), Chap. 12.

*Translated by A. Isaakyan*

*Physics of Atomic Nuclei, Vol. 66, No. 9, 2003, pp. 1700–1704. Translated from Yadernaya Fizika, Vol. 66, No. 9, 2003, pp. 1749–1753.*


**NUCLEI**
**Theory**

# Photofission Accompanied by Pion Emission

**A. S. Iljinov and L. N. Latisheva**

*Institute for Nuclear Research, Russian Academy of Sciences,*
*pr. Shestidesyatiletiya Oktyabrya 7a, Moscow, 117312 Russia*

Received May 28, 2002; in final form, September 9, 2002

**Abstract**—For the nuclear-fission process induced by photons of energy in the range $150 < E_\gamma < 600$ MeV and accompanied by pion emission, the total cross section; the angular and differential distributions of pions; the excitation-energy, mass, and charge distributions of compound nuclei; and the mass distribution of the fission fragments are predicted on the basis of the cascade–evaporation–fission model. These features are compared for the cases of nuclear fission induced by photons and protons of initial energy in the same range. © *2003 MAIK "Nauka/Interperiodica".*

## 1. INTRODUCTION

It is well known that the fission of nuclei into two fragments is accompanied by the emission of neutrons, photons, protons, and extremely light nuclei ($d$, $t$, $\alpha$, ...) [1]. Since a rather large amount of energy (about 200 MeV) is released in the fission of a heavy nucleus, the emission of a pion is also possible, however. The emission of a pion upon the spontaneous fission of heavy transuranium nuclei was predicted in [2]. Only an upper bound on the ratio of the $\pi$-channel probability[1)] to the total spontaneous-fission probability was established in the experiments reported in [3], $w_{\pi f}/w_{\mathrm{SF}} < 10^{-11}$.

In [4], it was shown that the probability of the $\pi$ channel is many orders of magnitude higher in induced fission than in spontaneous fission, and basic features of $\pi$ fission induced by protons of energy in the range $150 < E_p < 600$ MeV were predicted there. Thus, it is reasonable, both from the experimental and the theoretical point of view, to begin studying $\pi$ fission at projectile energies in the vicinity of the pion-production threshold, where the pion-production mechanism is well known.

In the present study, which is a continuation of that in [4], we predict the features of the $\pi$ channel of photofission in the energy range $150 < E_\gamma < 600$ MeV. This is done on the basis of the cascade–evaporation–fission model, which was previously found to reproduce faithfully a broad variety of experimental data on fission cross sections, mass–energy distributions of fission fragments, spectra of secondary particles, and isotope yields from experiments in the beams of intermediate-energy protons [5], neutrons [6], antiprotons [7], and photons [8].

## 2. CASCADE–EVAPORATION–FISSION MODEL

The inelastic interaction of an intermediate-energy photon with a nucleus proceeds in a few stages. At the first stage, a photon of energy in excess of the pion-production threshold, $E_\gamma > 140$ MeV, interacts with an individual intranuclear nucleon, producing one or a few pions, $\gamma N \to i\pi N$ ($i \geq 1$). The products of this $\gamma N$ interaction generate a cascade of successive $\pi N$ and $NN$ collisions in the target nucleus. This stage, within which continuous-spectrum particles produced in such collisions escape from the target nucleus, is rather short: $\tau_{\mathrm{cas}} \sim \tau_0$, where $\tau_0 \sim 10^{-22}$ s is the time it takes for a fast particle to traverse the nucleus. The first stage will be described on the basis of the intranuclear-cascade model [9, 10], which is a numerical method for solving the kinetic equation for a multiparticle distribution function [10, 11]. The calculations were performed within the model version described in [12].

Upon the completion of the intranuclear cascade, the residual nucleus reaches thermodynamic equilibrium within a relatively short time of $\tau_{\mathrm{eq}} \sim (5\text{–}10)\tau_0$ [10, 11]. At the next, slow, stage ($\tau_{\mathrm{ev}} \gg \tau_0$), the compound nucleus evaporates particles sequentially or undergoes fission. This stage will be described within the evaporation model [9, 10], which takes into account, at each step of the evaporation cascade, the competition between the evaporation of different particles ($n, p, d, t$, $^3$He, $\alpha$) and fission. The calculations were performed within the model modified in [13] by correctly including collective and pairing effects

[1)] Hereafter, we will refer to nuclear fission accompanied by pion emission as $\pi$ fission and to the corresponding fission channel as the $\pi$ channel.

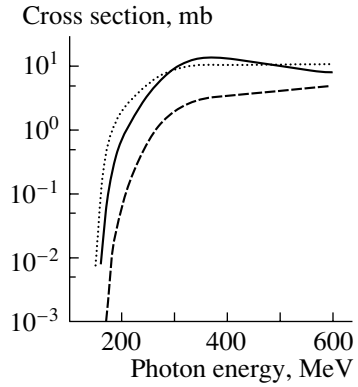


**Fig. 1.** Cross section for $^{238}$U photofission accompanied by the emission of a pion in a given charge state as a function of the initial photon energy. The solid, dashed, and dotted curves correspond to the $\pi^0$, $\pi^+$, and $\pi^-$ channels, respectively.

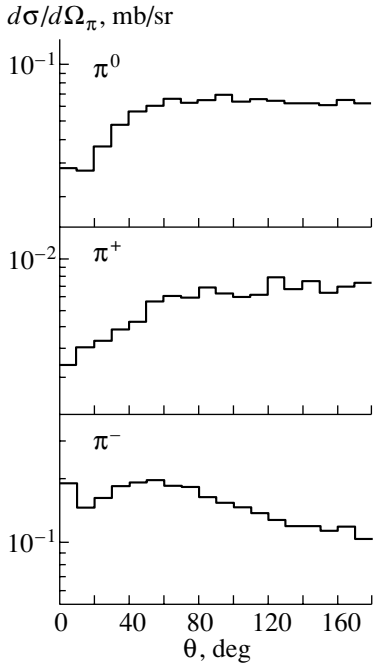


**Fig. 2.** Angular distribution $d\sigma/d\Omega_\pi$ of $\pi^0$, $\pi^+$, and $\pi^-$ mesons emitted in the reaction $^{238}$U$(\gamma, \pi f)$ at an energy of $E_\gamma = 200$ MeV.

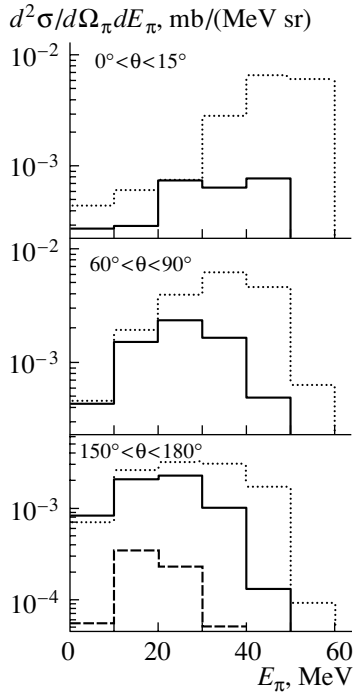


**Fig. 3.** Double-differential distribution $d^2\sigma/dE_\pi d\Omega_\pi$ of pions emitted into the angular intervals $0° \le \theta_\pi \le 15°$, $60° \le \theta_\pi \le 90°$, and $150° \le \theta_\pi \le 180°$ in the reaction $^{238}$U$(\gamma, \pi f)$ at an energy of $E_\gamma = 200$ MeV. The solid-, dashed-, and dotted-line histograms correspond to $\pi^0$, $\pi^+$, and $\pi^-$ mesons, respectively.

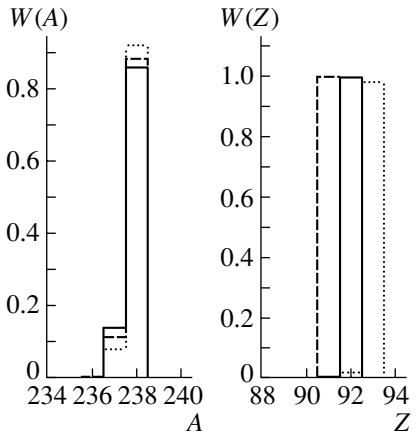


**Fig. 4.** Distributions (normalized to unity) of compound nuclei produced in the reaction $^{238}$U$(\gamma, \pi f)$ at an energy of $E_\gamma = 200$ MeV with respect to the mass $(A)$ and charge $(Z)$ numbers. The solid-, dashed-, and dotted-line histograms correspond to the $\pi^0$, $\pi^+$, and $\pi^-$ channels, respectively.

and the thermal damping of shell effects in the level density of the compound nucleus.

The evaporation cascade terminates either when the evaporated particles carry away the entire excitation energy $E^*$ of the compound nucleus or when this nucleus undergoes fission. At high excitation energies of $E^* > 50$ MeV, the damping of shell effects results in that the nuclear-potential-energy surface assumes the shape of that in the liquid-drop model, exhibiting only one valley, that of symmetric fission. In this case, we use a diffusion model based on the Fokker–Planck equation [14] to describe the dynamics of the descent of a fissile nucleus from the saddle to the scission point.

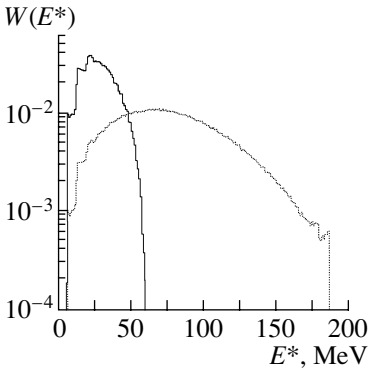


**Fig. 5.** Excitation-energy distributions (normalized to unity) of compound nuclei produced upon the exposure of $^{238}$U nuclei to photons of energy $E_\gamma = 200$ MeV (solid-line histogram) in the $\pi$ channel and (dotted-line histogram) in other fission channels.

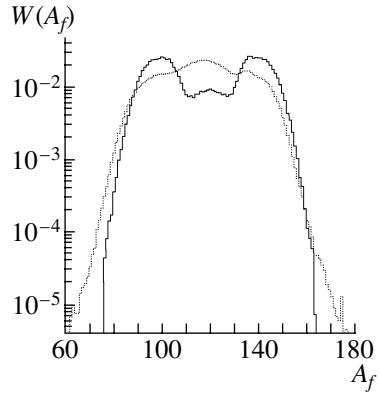


**Fig. 6.** Mass distributions (normalized to unity) of fission fragments produced in the reaction $^{238}$U$(\gamma, \pi f)$ at an energy of $E_\gamma = 200$ MeV (solid-line histogram) in the $\pi$ channel and (dotted-line histogram) in other fission channels.

In the fission of low-excited ($E^* < 50$ MeV) nuclei, shell effects play a significant role, leading, in particular, to the existence of two or more fission valleys on the nuclear-potential-energy surface. As a result, the symmetric-fission mode coexists with one or a few modes of asymmetric fission [15]. We will perform our calculations for low-energy fission, relying on the empirical approximation from [5] for the mass–energy distribution of fission fragments, where the coexistence of symmetric fission with two modes of asymmetric fission is taken into account.

Given a fission event in one of the links of the evaporation chain, we calculate the mass and charge numbers ($A_f$ and $Z_f$), the kinetic ($E_f$) and excitation ($U_f$) energies, and the evaporation cascade for each fission fragment.

Thus, the cascade–evaporation–fission model describes the evolution of a nuclear system over a broad time interval from $10^{-23}$ to $10^{-13}$ s, correctly taking into account all stages of the nuclear reaction (the intranuclear cascade, the evaporation of particles from the excited residual nucleus, its subsequent fission, and the evaporation of particles from fission fragments), and provides an exclusive description of the nuclear reaction, making it possible to calculate the features of all emitted particles (including pions) and the fission fragments. Within this model, the events of pion emission and nuclear fission are clearly separated in time, occurring at the opposite extreme edges of the time scale ($\tau_\pi \sim 10^{-23}$–$10^{-22}$ s versus $\tau_f \sim 10^{-18}$–$10^{-13}$ s).

## 3. BASIC FEATURES OF THE $\pi$ CHANNEL OF PHOTOFISSION

The cascade–evaporation–fission model was used to calculate the photofission of $^{238}$U nuclei at the photon energy $E_\gamma$ ranging between 150 and 600 MeV. For the $\pi$ channel of photofission, we have calculated the total cross section $\sigma(\gamma, \pi f)$; the angular distribution $d\sigma/d\Omega_\pi$ and the differential distribution $d^2\sigma/d\Omega_\pi dE_\pi$ for pions of different charges; the distributions of compound nuclei with respect to the excitation energy $E^*$, the mass number $A$, and the charge number $Z$; and the distribution of fission fragments with respect to the mass number $A_f$. In [4], the analogous features were calculated for $^{238}$U fission induced by protons of energy in the same range. This allows us to compare the features of the $\pi$ channel in nuclear fission induced by photons and protons.

Figure 1 displays the total cross section for the reaction $^{238}$U$(\gamma, \pi f)$ as a function of energy. The cross section for $\pi$ fission grows fast as the energy $E_\gamma$ increases from the pion-production threshold $E_{\gamma N}^{\text{thr}} \approx 140$ MeV to a value of $E_\gamma \approx 300$ MeV, whereupon this growth becomes slow. For the $(p, \pi f)$ reaction in question, the energy dependence of the cross section near the threshold of pion production on a free nucleon, $E_{pN}^{\text{thr}} \approx 290$ MeV, is considerably weaker [4]. This can be explained by a stronger effect of the Fermi motion of intranuclear nucleons on pion production in nuclear fission induced by protons.

Thus, it is reasonable to begin experimental searches for the $\pi$ channel of photofission at a photon energy of $E_\gamma \approx 300$ MeV, where the cross sections for the $\pi^0$ and $\pi^-$ channels amount to about 10 mb, while the cross section for the $\pi^+$ channel is about 2 mb (see Fig. 1). Concurrently, it should be noted that, at $E_\gamma$ values close to the pion-production threshold, $150 < E_\gamma < 250$ MeV, the cross section takes the largest (smallest) value for the $\pi^-$ ($\pi^+$) channel, the

cross section for the $\pi^0$ channel having an intermediate value (see Fig. 1). In nuclear fission induced by protons, the hierarchy of the cross sections is different: the largest cross-section value corresponds to the $\pi^0$ channel, while the smallest corresponds to the $\pi^-$ channel [4]. This distinction is due to the excitation of different isospin states of the $\Delta(1232)$ isobar in the elementary interactions $\gamma N \to \Delta \to \pi N$ and $pN \to \Delta N \to \pi NN$.

Figure 2 presents the angular distributions $d\sigma/d\Omega_\pi$ of pions emitted in the reaction $^{238}\mathrm{U}(\gamma, \pi f)$ at an energy of $E_\gamma = 200$ MeV. It can be seen that $\pi^0$ and $\pi^+$ mesons are emitted predominantly into the backward hemisphere, but that $\pi^-$ mesons are emitted into the forward hemisphere.

Figure 3 shows the double differential distributions of pions emitted in the reaction $^{238}\mathrm{U}(\gamma, \pi f)$ at an energy of $E_\gamma = 200$ MeV. Naturally, the spectrum is harder for pions emitted into the forward than for pions emitted into the backward hemisphere.

At a photon energy of $E_\gamma = 200$ MeV, compound nuclei formed in the $\pi$ channel have a very narrow nucleon-composition distribution (see Fig. 4). In $\pi$ fission, the product pion is emitted from the target nucleus, while cascade nucleons are predominantly absorbed in it after rescattering. Only in approximately 10% of the cases does one of the cascade neutrons escape from the nucleus. Thus, the $\pi^+$ channel most often produces $^{238}$Pa compound nuclei, while the $\pi^0$ and $\pi^-$ channels result in the production of $^{238}$U and $^{238}$Np nuclei, respectively.

Compound nuclei produced in the $\pi$ channel are cold (see Fig. 5): the excitation-energy distribution of compound nuclei is narrow, peaking at $E^* = 20$ MeV. Therefore, shell effects are very important in $\pi$ fission, and the contribution of asymmetric fission to the mass distribution of fission fragments is decisive (see Fig. 6).

Owing to the smallness of the cross section for $\gamma N$ interaction, photon absorption is of a volume character. In this case, the product pion and cascade nucleons are efficiently captured by a heavy nucleus, with the main part of the initial energy $E_\gamma$ being transferred to this nucleus. Therefore, the excitation-energy ($E^*$) distribution of compound nuclei in the $\pi$ channel is drastically different from those in other channels (see Fig. 5). Highly excited compound nuclei produced in these channels undergo symmetric fission and exhibit the corresponding mass distribution of fission fragments (see Fig. 6).

## 4. CONCLUSION

The investigation of the $\pi$ channel in the proton-induced fission of nuclei in [4] has been generalized to the photofission case. As in [4], we have considered the simplest $\pi$-fission mechanism, which is dominant at energies close to the pion-production threshold and above. It is reasonable to begin seeking $\pi$ fission in this energy region, where its cross section is rather large [about 10 to 100 mb in $(p, \pi f)$ reactions and about 1 to 10 mb in $(\gamma, \pi f)$ reactions] and where theoretical predictions are quite reliable. Despite smaller values of relevant cross sections and lower intensities of quasimonochromatic beams, experiments with photons may be more advantageous than experiments with proton beams owing to more clear-cut distinctions between the features of the $\pi$ channel and other photofission channels and better background conditions for detecting pions and other charged particles.

In the future, attention will be given primarily to advancements toward the region of initial energies below 140 MeV, where the above mechanism is not operative. The existence of other pion-production mechanisms that could be dominant in this region is suggested by data from experiments devoted to pion production in nuclear fission induced by heavy ions of energy in the range 20–30 MeV/nucleon [16].

## ACKNOWLEDGMENTS

We are grateful to E.S. Golubeva and I.A. Pshenichnov for stimulating discussions.

This work was supported in part by the Russian Foundation for Basic Research (project no. 98-02-17171).

## REFERENCES

1. R. Vandenbosch and J. R. Huizenga, *Nuclear Fission* (Academic, New York, 1973).
2. D. B. Ion *et al.*, Ann. Phys. (N.Y.) **171**, 237 (1986); Rev. Roum. Phys. **31**, 205, 209, 551 (1986); **32**, 1037 (1987); **33**, 239, 1071 (1988); **34**, 261, 359 (1989).
3. J. R. Beene *et al.*, Phys. Rev. C **38**, 569 (1988); C. Cerruti *et al.*, Z. Phys. A **329**, 383 (1988); Yu. V. Adamchuk *et al.*, Yad. Fiz. **49**, 932 (1989) [Sov. J. Nucl. Phys. **49**, 579 (1989)]; S. Stanislaus *et al.*, Phys. Rev. C **39**, 295 (1989); J. R. Knudson *et al.*, Phys. Rev. C **44**, 2869 (1991).
4. A. S. Iljinov and M. V. Mebel, Yad. Fiz. **64**, 1463 (2001) [Phys. At. Nucl. **64**, 1386 (2001)].
5. G. D. Adeev *et al.*, Preprint No. 816/93, IYaI (Inst. for Nuclear Research, Moscow, 1993).
6. C. M. Zoller *et al.*, Report IKDA 95/25 (Darmstadt, 1995).

7. P. Hoffman *et al.*, Phys. Rev. C **49**, 2555 (1994); Y. S. Kim *et al.*, Phys. Rev. C **54**, 2469 (1996); W. Schmid *et al.*, Phys. Rev. C **55**, 2965 (1997).
8. V. Lucherini *et al.*, Phys. Rev. C **39**, 911 (1989); A. S. Iljinov *et al.*, Phys. Rev. C **39**, 1420 (1989); Nucl. Phys. A **539**, 263 (1992); N. Bianchi *et al.*, Phys. Rev. C **48**, 1785 (1993).
9. V. S. Barashenkov and V. D. Toneev, *Interaction of High-Energy Particles and Nuclei with Nuclei* (Atomizdat, Moscow, 1972).
10. A. S. Iljinov, M. V. Kazarnovsky, and E. Ya. Paryev, *Intermediate-Energy Nuclear Physics* (CRC, Boca Raton, 1994).
11. V. E. Bunakov, Fiz. Élem. Chastits At. Yadra **11**, 1285 (1980) [Sov. J. Part. Nucl. **11**, 507 (1980)].
12. A. S. Iljinov *et al.*, Nucl. Phys. A **616**, 575 (1997).
13. A. S. Iljinov *et al.*, Nucl. Phys. A **543**, 517 (1992).
14. G. D. Adeev *et al.*, Fiz. Élem. Chastits At. Yadra **19**, 1229 (1988) [Sov. J. Part. Nucl. **19**, 529 (1988)].
15. M. G. Itkis *et al.*, Fiz. Élem. Chastits At. Yadra **19**, 701 (1988) [Sov. J. Part. Nucl. **19**, 301 (1988)].
16. Z. Rudy *et al.*, Z. Phys. A **351**, 217 (1995); **354**, 445 (1995).

*Translated by O. Chernavskaya*

*Physics of Atomic Nuclei, Vol. 66, No. 9, 2003, pp. 1705–1714. Translated from Yadernaya Fizika, Vol. 66, No. 9, 2003, pp. 1754–1762.*


**NUCLEI**
**Theory**

# Inversion of the $K^\pi = 1^-$ States in $^{156}$Gd and $^{170}$Yb

**E. P. Grigoriev**

*Institute of Physics (Petrodvorets Branch), St. Petersburg State University, Ul'yanovskaya ul. 1, Petrodvorets, 198904 Russia*

Received April 26, 2002; in final form, December 15, 2002

**Abstract**—For the $^{156}$Gd and $^{170}$Yb nuclei, where the inversion of levels in the $K^\pi = 1^-$ bands is observed, the energies of rotational levels are calculated on the basis of the Coriolis interaction model for the states of two bands whose quantum numbers are $K^\pi = 1^-$ and $0^-$. New $J^\pi K = 3^-0$ and $3^-3$ levels are introduced in $^{170}$Yb, and the structure of $^{170}$Er is refined. The interaction parameters calculated for six nuclei are considered within the structure predicted by the quasiparticle–phonon model. © *2003 MAIK "Nauka/Interperiodica".*

## 1. INTRODUCTION

Among even–even rare-earth nuclides, the $^{156}$Gd and $^{170}$Yb nuclei possess unique properties. In the $K^\pi = 1^-$ rotational bands, the signature splitting—that is, the shift of even-spin levels in a rotational band with respect to the sequence of odd-spin levels—proved to be so great that it resulted in the inversion of levels. For either nuclide, it was found that the $J^\pi = 2^-$ states lie higher than the $J^\pi = 3^-$ states, that the $4^-$ states lie higher than the $5^-$ states, and so on. In the present study, we attempt to explain this effect as a particular case of signature splitting within the Coriolis interaction model. Our calculations have demonstrated the applicability of this model, the reason behind the shift of levels in the $J^\pi = 1^-$ bands being the effect of the $K^\pi = 0^-$ bands, which contain only odd-spin levels.

Preceding calculations on the basis of the model in question [1] revealed that this model is applicable to the $^{162}$Dy and $^{172}$Yb nuclei and that, for $^{168}$Er, it is applicable to taking into account the interaction of the $K^\pi = 1^-$ and $0^-$ bands, as in the present study. In taking into account the mixing of the $K = 1$ and 0 bands, it is possible here to use a simplified version of the relevant formula; that is,

$$E_{K,K+1} = X/2 + AJ(J+1) \pm 1/2[Y^2 + 4b^2 J(J+1)]^{1/2}, \quad (1)$$

where four parameters of the model, $X$, $A$, $Y$, and $b$, are determined from a fit to the experimental values of the energies of the $J^\pi K = 1^-0$, $1^-1$, $3^-0$, and $3^-1$ levels. The plus (minus) sign in front of the square root in Eq. (1) refers to levels of the band that lies higher (lower) on the energy scale. This corresponds to a repulsion rather than an attraction of levels having equal spins. By using the parameter values found in this way, we can calculate, by formula (1), the energies $E_{K=0}$ and $E_{K=1}$ of the levels in both bands.

Rotational states of deformed nuclei can be traced in heavy-ion (HI) reactions up to states characterized by very high spins $J$ ($J = 40\hbar$ or higher). Such states are generated in (HI, $xn$, $yp$) nuclear reactions. It is not always possible, however, to observe, in such processes, a bandhead and two to three levels close to it. This is because intraband transitions are dominant in the deexcitation of high-spin states, while interband transitions deexcite low-spin states; as a result, the population of low-lying levels of a band proves to be very small, so that such levels are not observed in the aforementioned processes. However, they can manifest themselves in beta decay.

A second feature peculiar to heavy-ion reactions is that, in the same band, states of one signature are often populated to a greater extent than states of the other signature; that is, the sequence of only even-spin states or the sequence of only odd-spin states is seen in relevant experiments.

## 2. BANDS IN $^{170}$Yb

### *2.1. $K^\pi = 1^-$ Band*

Features mentioned in the Introduction manifested themselves in the $^{170}$Yb nucleus, where a band having a bandhead at 1364.41 keV with spin–parity $1^-$ and including odd-spin levels up to the $17^-$ level at 4017.5 keV is known at present [1–5] (see Fig. 1). For this band, there was an uncertainty in the value of the quantum number $K$: 0 versus 1. Although Baglin [2] assigned the sequence of odd-spin levels $K = 1$, he did not indicate the sequence of even-spin levels.

1063-7788/03/6609-1705$24.00 

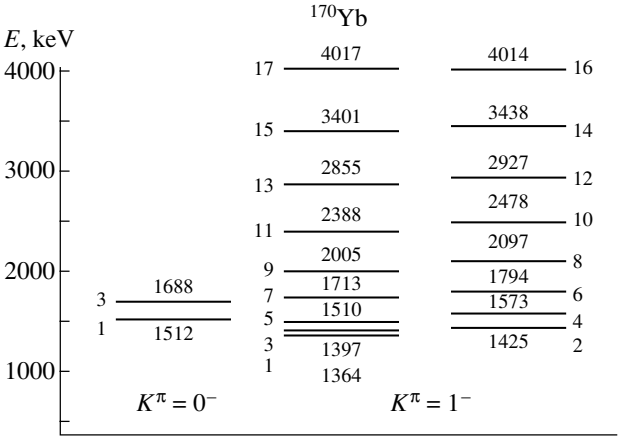


**Fig. 1.** $K^\pi = 0^-$ and $1^-$ rotational bands in $^{170}$Yb.

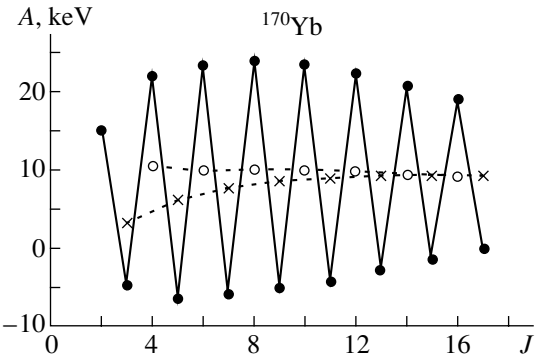


**Fig. 2.** Inertia parameters of the $K^\pi = 1^-$ rotational band in $^{170}$Yb: (closed circles) $\Delta J = 1$; (open circles) $\Delta J = 2$, even $J$; and (inclined crosses) $\Delta J = 2$, odd $J$.

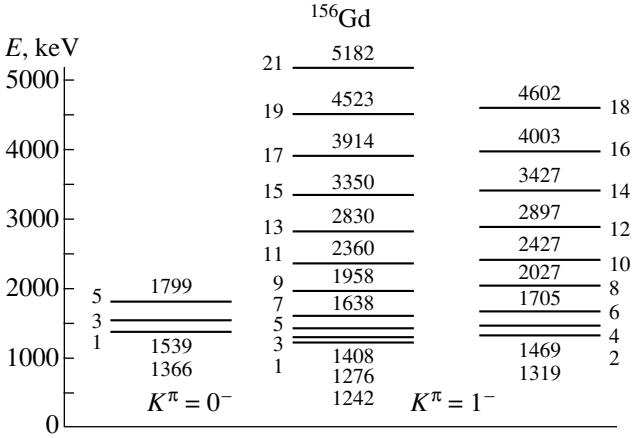


**Fig. 3.** $K^\pi = 0^-$ and $1^-$ rotational bands in $^{156}$Gd.

In 1998 (see [5]), there appeared information about a new band that includes even-spin levels ($J^\pi = 4^- - 16^-$). The lowest of the levels observed in this band has an energy of 1573.3 keV and a spin–parity of $J^\pi = 4^-$. The value of $K$ was not established.

The $K^\pi = 1^-$ band is identified in the present study. One branch of this band is formed by the known half-band containing odd-spin levels and having the signature of $a = 1$. The other branch involves even-spin levels and has the signature of $a = 0$ (Fig. 1). These statements are based on a few experimental facts.

(i) In the spectrum of $^{170}$Yb, there is the $2^-$ state at 1425.09 keV. This state, known from data on the beta decay of $^{170}$Lu [4], supplements that branch of the band which is formed by even-spin levels and which was observed in [5].

(ii) In general, the inertia parameters $A^+$ determined for even-spin states show a rather smooth behavior over a band. The inertia parameters $A^-$ refer to odd-spin levels. The values of $A^+$ and $A^-$ were calculated for each pair of levels on the basis of the formula

$$A^+(J \to J-2) = [E(J) - E(J-2)]/2(2J-1)$$

and are shown in Fig. 2. Here, one can see that the point for $A^+$ ($J = 4$) lies higher than what would be expected from a smooth dependence of $A^+$ on $J$: $A^+(4) = 10.59$ keV, but $A^+(6) = 10.02$ keV. This feature has a simple explanation if one takes into account the repulsion of levels in the $K = 1$ and 3 bands. In the $K = 3$ band, there is no $J = 2$ state, and it has no effect on the position of the $J^\pi K = 2^-1$ state. At the same time, the $J = 4$ levels proved to be closely lying. The experimental value of $E(4^-1) = 1573.3$ keV is known. A $4^-3$ level has not yet been discovered in the $K = 3$ band. The corresponding calculated energy value of $E(4^-3) = 1559(5)$ keV was obtained by extrapolating the values of $A$ in the $K = 3$ band [2]. The repulsion of two closely spaced $J = 4$ levels leads to a shift of the $4^-1$ state toward higher energy values and, hence, to an increase in $A^+(4)$. An estimation reveals that this shift is about 10 keV.

(iii) There is a clear analogy (see below) between the behavior of the $K^\pi = 1^-$ band in the $^{170}$Yb nucleus, which is considered here, and the behavior of the well-known $K^\pi = 1^-$ band in the $^{156}$Gd nucleus. Both nuclei exhibit the following feature: in the $K^\pi = 1^-$ bands, there is an inversion of levels—that is, the $2^-$ states lie higher than the $3^-$ states, the $4^-$ states lie higher than the $5^-$ states, and so on (see Figs. 1, 3). These features of the bands in question can be explained by the Coriolis interaction between the $K^\pi = 1^-$ and $0^-$ bands. In the $^{156}$Gd nucleus, the $K^\pi = 0^-$ band has been well established, while, in the $^{170}$Yb nucleus, only the $1^-$ level at 1512.35 keV has been associated with the analogous band.

**Table 1.** Levels and gamma transitions from [4] that determine the $3^-0$ state at 1687.51(31) keV in $^{170}$Yb

| $J^\pi K_f$ | $J^\pi K_i$ | $E_f$, keV | $E_i$, keV | $E_\gamma$, keV | $E(\Delta E)$, keV | $I_K$, arb. units | $I_\gamma$, arb. units |
|---|---|---|---|---|---|---|---|
| $2^+0$ | $3^-0$ | 84.3 | – | 1603.8 | 1688.1(5) | 0.33(10) | 5.9 (calc.) |
| $4^+0$ | $3^-0$ | 277.4 | – | 1410.4 | 1687.8(4) | 0.40(20) | 2.8(3) |
| $3^-0$ | $1^-$ | – | 2939.56 | 1252.1 | 1687.5(4) | 0.53(14) | 2.7 (calc.) |
| $3^-0$ | $1^-$ | – | 3179.7 | 1492.1 | 1687.6(6) | 0.5(3) | 3.5 (calc.) |
| $3^-0$ | $1^-$ | – | 3195.30 | 1507.80 | 1687.50(20) | $< 0.3$ | 1.00(15) |
| $3^-0$ | $1^-$ | – | 3273.2 | 1585.8 | 1687.4(4) | 0.16(10) | 0.20(2) |

Note: A parenthetical label "calc." indicates calculated values; it was assumed that $\alpha_K(E1; 1603.53) = 5.6 \times 10^{-4}$; for the $1^- \to 3^-$ transitions, use was made of the theoretical values of the conversion coefficients $\alpha_K(E2)$; and $I_K$ is the intensity of the conversion $K$ line.

### *2.2. $K^\pi = 0^-$ Band: Determination of the Position of the $3^-0$ Level at 1687.5 keV,*

In order to perform correct calculations, it is necessary to know at least the position of the $3^-0$ level in the $K = 0$ band, but there has been no information about this so far. The first step in calculating the energies of the levels in question with allowance for Coriolis interaction was the assumption that the inertia parameter is identical in the two bands, taking the value of $A = 10.2$ keV, which was obtained for the half-band containing even-spin levels in the $K = 1$ band (see Fig. 2). For states of spin values up to $J = 8$, the calculated energies proved to be close to their experimental counterparts, the maximum discrepancy being 19 keV for the $J = 7$ level. The energy of the $3^-0$ level was 1684 keV. It served as a guideline in searches for this level in the spectrum of states that are formed upon the decay of the $J^\pi = 0^+$ state of $^{170}$Lu [4]. An observation of a state at $E = 1690$ keV in the relevant $(d, t)$ reaction is a piece of evidence for the existence of a level at a close energy: its cross section is very small, and no $J^\pi K$ assignment was made. The $3^-0$ level is expected to decay via gamma transitions to the $2^+$ and $4^+$ levels of the ground-state band, and it can be populated via transitions from the $1^-$, $2^-$, or $2^+$ levels. An analysis of the spectrum of gamma radiation from $^{170}$Lu revealed that the level at 1687.51(32) keV satisfies such conditions.

The energies of two gamma transitions from this level and four gamma transitions populating it are quoted in Table 1, along with the respective relative intensities in terms of the scale adopted in [4]. From Table 1, it can be seen that the possible gamma transitions give close values of its energy. However, consistency in energy in the very complicated spectrum of $^{170}$Lu does not prove conclusively that the transitions in question are disposed precisely in this segment of the diagram of excited levels. That this is indeed the case was experimentally shown in [6] by means of the method of gamma–gamma coincidences that was combined with summation of the amplitudes of pulses. Unfortunately, the review article of 1996 given in [2] ignored the earlier studies of Dzhelepov *et al.* [4] and Vasi'eva *et al.* [6], whereas the present analysis employs, for the energies and the intensities of the transitions, the values averaged in [4].

That the energy of the level was established on the basis of six gamma transitions gives sufficient grounds to believe that this result is quite reliable, especially if one considers that the level in question manifested itself in the relevant $(d, t)$ reaction at energies where the level density is not very high. The existence of a level at 1687.51 keV is also supported by the balance of gamma-transition intensities. The intensity of deexcitation of the level is 8.7 arb. units according to [4], and the intensity of its population is in agreement with this value within the errors, 7.4 arb. units. For the $3^-1$ level at 1396.6 keV, which is somewhat lower—this level is also known from data on the decay of $^{170}$Lu—the intensity of deexcitation is 11 arb. units, while the intensity of its population is 9 arb. units, which is compatible with that within the errors. It should be recalled that, because of a large difference in spin, the $J = 3$ levels cannot be directly populated in the beta decay of the $J^\pi = 0^+$ state of $^{170}$Lu.

### *2.3. Determination of the Position of the $3^-3$ Level at 1494.7 keV*

States of $J \geq 5$ have been traced in the $K = 3$ band. It can be expected that an as-yet-undiscovered $J = 3$ state will manifest itself in the decay of $^{170}$Lu. At the same time, the calculation that has been performed with allowance for Coriolis interaction yields a value of 1492 keV for the $3^-3$ level. A level at

**Table 2.** Experimental ($E_{\text{expt}}$) and theoretical ($E_{\text{theor}}$) energies of levels in the $^{170}$Yb nucleus; their difference $E_{\text{expt}} - E_{\text{theor}}$ in the $K^\pi = 1^-$ and $0^-$ bands; inertia parameters $A$; and contribution $\Delta$ to the energy of a level from Coriolis interaction

| $J$ | $A_{\text{expt}}$, keV | $E_{\text{expt}}$, keV | $E_{\text{theor}}$, keV | $E_{\text{expt}} - E_{\text{theor}}$, keV | | | $\Delta$, keV |
|---|---|---|---|---|---|---|---|
| | | | | a | b | c | |
| $K^\pi = 1^-$ | | | | | | | |
| 1 | – | 1364.41 | ≡ 1364.41 | ≡ 0 | | −0.01 | 26 |
| 2 | 15.17 | 1425.09 | 1431.4 | −6.3 | −6.3 | | |
| 3 | −4.70 | 1396.91 | ≡ 1396.91 | ≡ 0 | | −0.5 | 97 |
| 4 | 22.05 | 1573.3 | 1576.8 | −3.5 | −2.6 | | |
| 5 | −6.31 | 1510.4 | 1507.2 | 3.2 | | −0.3 | 174 |
| 6 | 23.63 | 1793.8 | 1805.2 | −11.8 | −7 | | |
| 7 | −5.79 | 1712.7 | 1699.4 | 13 | | −1 | 252 |
| 8 | 24.03 | 2097.1 | 2116.7 | −20 | −6 | | |
| 9 | −5.04 | 2005.3 | 1974.1 | 31 | | 1 | 330 |
| 10 | 23.59 | 2478.1 | 2512 | −33 | −1 | | |
| 11 | −4.06 | 2387.9 | 2331.6 | 56 | | −8 | 409 |
| 12 | 22.45 | 2927.5 | 2989 | −61 | 4 | | |
| 13 | −2.73 | 2855.4 | 2772.0 | 83 | | 39 | 488 |
| 14 | 20.78 | 3438.1 | 3550 | −112 | 6 | | |
| 15 | −1.29 | 3401.3 | 3295.5 | 106 | | 108 | 557 |
| 16 | 19.19 | 4013.7 | 4193 | −180 | 19 | | |
| 17 | 0.11 | 4017.5 | 3902.0 | 115 | | 231 | 646 |
| $K^\pi = 0^-$ | | | | | | | |
| 1 | – | 1512.35 | ≡ 1512.35 | ≡ 0 | – | – | 26 |
| 3 | 17.53 | 1687.51 | ≡ 1687.51 | ≡ 0 | – | – | 97 |
| 5 | – | – | 1951 | – | – | – | 174 |
| 7 | – | – | 2299 | – | – | – | 252 |

Note: The model parameters were set to the following values: $X = 2835.2$ keV, $A = 10.38$ keV, $Y = 96.94$ keV, and $b = 39.51$ keV; (a) $B = 0$, (b) $B = -2.7$ eV, and (c) $B = +3.7$ eV.

1494.7 keV can be revealed by examining the spectrum of gamma rays emitted by $^{170}$Lu [4, 6]. This level is deexcited via transitions to the $2^+$ and $4^+$ levels of the ground-state band and is populated by a number of gamma transitions from higher lying levels. Conclusions on whether levels in $^{170}$Yb at $E \geq 2.35$ MeV are reliable or questionable were drawn in [6].

### *2.4. Calculation with Allowance for Coriolis Interaction*

The position of the $3^-0$ level has been established, and the calculated energies $E_{\text{theor}}$ of the levels have been determined with allowance for the Coriolis interaction of levels belonging to the $K^\pi = 0^-$ and $1^-$ bands (see Table 2). It is necessary to indicate the limitations of the model.

(i) The calculations have been performed under the assumption of the interplay of only two bands.

(ii) The inertia parameter $A$ was taken to have identical values for the two bands in question and for all levels of a band.

The second assumption contradicts the well-known statement that the moment of inertia of band states increases with increasing spin, reaching the rigid-body limit [7]. In all probability, this is the

**Table 3.** Experimental ($E_{\text{expt}}$) and calculated ($E_{\text{theor}}$) energies of levels in the $^{156}$Gd nucleus; their difference $E_{\text{expt}} - E_{\text{theor}}$ in the $K^\pi = 1^-$ and $0^-$ bands; inertia parameters $A$; and contribution $\Delta$ to the energy of a level from Coriolis interaction

| $J$ | $A_{\text{expt}}$, keV | $E_{\text{expt}}$, keV | $E_{\text{theor}}$, keV | $E_{\text{expt}} - E_{\text{theor}}$, keV | $\Delta$, keV |
|---|---|---|---|---|---|
| | | | $K^\pi = 1^-$ | | |
| 1 | – | 1242.50 | $\equiv$ 1242.50 | $\equiv$ 0 | 28 |
| 2 | 19.31 | 1319.74 | 1312 | 8 | – |
| 3 | −7.27 | 1276.11 | $\equiv$ 1276.11 | $\equiv$ 0 | 103 |
| 4 | 24.05 | 1468.51 | 1456 | 12 | – |
| 5 | −6.04 | 1408.13 | 1390 | 18 | 175 |
| 6 | 24.79 | 1705.61 | 1683 | 23 | – |
| 7 | −4.83 | 1637.96 | 1585 | 53 | 248 |
| 8 | 24.34 | 2027.42 | 1992 | 35 | – |
| 9 | −3.83 | 1958.46 | 1862 | 96 | 321 |
| 10 | 23.44 | 2427.24 | 2383 | 44 | – |
| 11 | −3.04 | 2360.37 | 2221 | 139 | 394 |
| 12 | 22.35 | 2896.8 | 2857 | 40 | – |
| 13 | −2.58 | 2829.6 | 2663 | 167 | 467 |
| 14 | 21.32 | 3427 | 3413 | 14 | – |
| 15 | −2.57 | 3350 | 3188 | 162 | 540 |
| 16 | 20.41 | 4003 | 4052 | −49 | – |
| 17 | −2.62 | 3914 | 3794 | 120 | 614 |
| 18 | 19.11 | 4602 | 4772 | −170 | – |
| 19 | −2.08 | 4523 | 4483 | 40 | 687 |
| 20 | – | – | 5576 | – | – |
| 21 | – | 5182 | 5254 | −72 | 760 |
| | | | $K^\pi = 0^-$ | | |
| 1 | – | 1366.5 | $\equiv$ 1366.5 | $\equiv$ 0 | 28 |
| 3 | 17.24 | 1538.9 | $\equiv$ 1538.9 | $\equiv$ 0 | 103 |
| 5 | 14.43 | 1798.7 | 1796.5 | 2.2 | 175 |
| 7 | – | – | 2133 | – | 248 |
| 9 | – | – | 2561 | – | 321 |

Note: The model parameters were set to the following values: $X = 2567.8$ keV, $A = 10.30$ keV, $Y = 68.1$ keV, and $b = 36.6$ keV.

reason why the difference $E_{\text{expt}} - E_{\text{theor}}$ grows with increasing spin in the case where the interaction is disregarded and where the calculation is performed by the formula $E_{\text{theor}} = E_0 + AJ(J+1)$ with a constant value of $A$; in fact, this parameter must decrease, leading to an increase in $E_{\text{theor}}$, and this does indeed occur, as can be seen from Table 2. An increase in the difference $E_{\text{expt}} - E_{\text{theor}}$ for odd-spin levels can be understood if one assumes that the interaction is in fact weaker than what is predicted by the Coriolis model for high-spin levels. It should be borne in mind that the $K = 1$ band lies lower than the $K = 0$ band and that it is necessary to use formula (1) with a minus sign in front of the square root. The influence of other bands may underlie an alternative explanation of the observed effect.

**Table 4.** Experimental ($E_{\text{expt}}$) and calculated ($E_{\text{theor}}$) energies of levels in the nucleus $^{170}$Er; their difference $E_{\text{expt}} - E_{\text{theor}}$ in the $K^\pi = 1^-$ and $0^-$ bands; inertia parameters $A$; and contribution $\Delta$ to the energy of a level from Coriolis interaction

| $J$ | $A_{\text{expt}}$, keV | $E_{\text{expt}}$, keV | $E_{\text{theor}}$, keV | $E_{\text{expt}} - E_{\text{theor}}$, keV | $\Delta$, keV |
|---|---|---|---|---|---|
| | | | $K^\pi = 1^-$ | | |
| 1 | – | 1266.64 | $\equiv 1266.64$ | $\equiv 0$ | 7 |
| 2 | 9.64 | 1305.23 | 1307.4 | −2.2 | – |
| 3 | 5.83 | 1340.20 | $\equiv 1340.20$ | $\equiv 0$ | 22 |
| 4 | 11.59 | 1432.95 | 1436.5 | −3.5 | – |
| 5 | 5.77 | 1483.72 | 1476.3 | 7 | 52 |
| 6 | 12.29 | 1631.2 | 1639.3 | −8.1 | – |
| 7 | 5.26 | 1704.8 | 1676 | 29 | 92 |
| 8 | – | – | 1916 | – | – |
| | | | $K^\pi = 0^-$ | | |
| 1 | – | 1824.60 | $\equiv 1824.60$ | $\equiv 0$ | 7 |
| 3 | 11.08 | 1935.44 | $\equiv 1935.44$ | $\equiv 0$ | 22 |
| 5 | 11.97 | 2150.9 | 2133.3 | 18 | 52 |
| 7 | – | – | 2413 | – | 92 |

Note: The model parameters were set to the following values: $X = 3054.4$ keV, $A = 9.22$ keV, $Y = 550.2$ keV, and $b = 32.78$ keV.

Given in the last column of Table 2 are values of $\Delta$ that represent the contributions to the energies of the levels belonging to the $K = 0$ and 1 bands from the interaction of these bands. These contributions are defined as the differences of the energies obtained for the levels in question with $b = 0$ and with the value of $b$ derived from the calculations. For the $^{170}$Yb nucleus, it turned out that $b = 39.51$ keV. The values of $\Delta$ for the $^{156}$Gd and $^{170}$Er nuclei in Tables 3 and 4 were determined in the same way. For the $J = 13$ level in the $^{170}$Yb nucleus, the contribution $\Delta$ from the interaction of the bands is 488 keV and is five times as great as the discrepancy $E_{\text{expt}} - E_{\text{theor}} = 83$ keV (see Table 2). The results for the $J = 15$ and 17 levels are similar. From this comparison, it follows that, for deformed-nucleus states in which the spin values are not very high (up to $J \approx 10\hbar$), the model employing Coriolis interaction can be considered as quite an acceptable model within the resulting limits.

### *2.5. Refinement of the Calculation*

In order to attain better agreement between the results of the calculations and experimental data and to take into account, to some extent, the reduction of pair forces with increasing spin, formula (1), which involves the rotational term $AJ(J+1)$, was supplemented with the term $BJ^2(J+1)^2$. Here, the value of the parameter $B$ is usually less in magnitude than the value of $A$ by a factor of $10^2$ to $10^3$ and is negative. The traditional formula extended in this way was used to calculate the energies $E_{\text{theor}}$ of even-spin levels, and the resulting values of the difference $E_{\text{expt}} - E_{\text{theor}}$ are given in Table 2. The new-parameter value of $B = -2.7$ eV was obtained upon averaging over the $J = 10$–$16$ levels. Astonishingly good agreement with experimental data was achieved over the range between $-7$ and $+6$ keV for all levels with the exception of the $J = 16$ one, which is the last in this series. A moderate deviation for the $J = 2$ level was explained above (see Subsection 2.1) in terms of the effect of the $J = 3$ band. It should be emphasized that only one free parameter, $B$, has been used here—the remaining four parameters were determined from a fit to data on odd-spin levels.

A similar procedure was applied to the half-band containing odd-spin levels and having a signature of $a = 0$. The parameter value of $B = +3.7$ keV was determined on the basis of data on the $J = 5$–$11$ levels. As one can see, it proved to be positive, and excellent agreement with experimental data on the $J = 1$–$11$ levels was obtained with this parameter value (see Table 2). However, the positive sign of the parameter $B$ contradicts both the idea that pair correlations must decrease and results that concern the half-band containing even-spin levels. As was

indicated above, the effect of band interaction is exaggerated for some reason, and the positive sign of $B$ additionally supports this conjecture.

A more complicated pattern is observed for other nuclei (see Tables 3, 4). In what is concerned with the effect of the correction term, no definitive conclusion, such as that for the $^{170}$Yb nucleus, could be drawn for the $^{156}$Gd and $^{170}$Er nuclei.

## 3. BANDS IN $^{156}$Gd

### *3.1. $K^\pi = 1^-$ Band*

The $^{156}$Gd nucleus provides a second example where there are a signature splitting and an inversion of levels in the $K^\pi = 1^-$ band. There, this band was observed up to the $J^\pi = 21^-$ state [3, 8] (see Figs. 3, 4; Table 3). In a recent study, Sugawara *et al.* [9] observed high-spin states that manifested themselves in the reaction $^{150}$Nd($^{13}$C, $\alpha 3n$) induced by a 65-MeV beam of $^{13}$C ions. Gamma rays and gamma–gamma coincidences were recorded in that study by the GEMINI facility including 12 detectors from pure germanium that were equipped with anti-Compton shielding.

The use of modern techniques for accelerating heavy ions of $^{13}$C and, what is more important, of a facility that, in addition to performing a highly efficient detection of gamma rays, is capable of performing computer-based analysis of the recorded multiple gamma–gamma coincidences permitted advancing toward previously unknown high-spin states. New data were obtained not only for positive-parity bands, including the ground-state band, but also for both branches of the $K^\pi = 1^-$ band. Data from [9] were used in Table 3.

### *3.2. Calculation with Allowance for Coriolis Interaction*

The $J = 1$, 3, and 5 levels are known in the $K^\pi = 0^-$ band (see Table 3). With these data, one can compute theoretical values for the energies of levels with allowance for mixing due to Coriolis interaction, employing a procedure that is similar to that applied to the $^{170}$Yb nucleus. The same assumptions of two-band mixing and of the invariability of the inertia parameter $A$ were made here. The greatest discrepancy between the experimental and the theoretical values of the energies of odd-spin levels is observed at $J = 9$–19. The greatest values of $A^-$ correspond to the same odd-spin values (see Fig. 4).

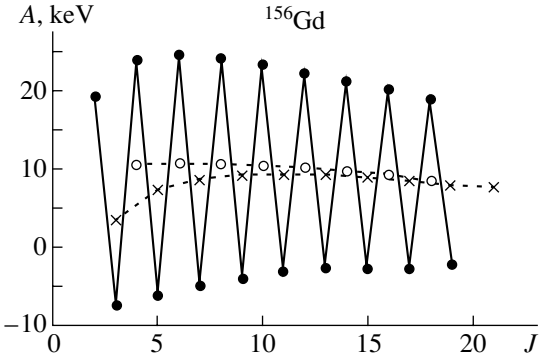


**Fig. 4.** Inertia parameters of the $K^\pi = 1^-$ rotational band in $^{156}$Gd: (closed circles) $\Delta J = 1$; (open circles) $\Delta J = 2$, even $J$; and (inclined crosses) $\Delta J = 2$, odd $J$.

## 4. GENERALIZATION TO A WIDER CLASS OF OCTUPOLE BANDS

In the two nuclei considered here, $^{156}$Gd and $^{170}$Yb, the $K^\pi = 0^-$ and $1^-$ bands were identified as vibrational octupole excitations. Their structure was calculated on the basis of the quasiparticle–phonon model and was presented in [10]. It is of interest to generalize information obtained for the interaction of bands to other nuclei and to compare this information with model concepts.

### *4.1. $K^\pi = 0^-$ and $1^-$ Bands in the $^{170}$Er Nucleus*

The $^{170}$Er nucleus, whose structure was recently established in [11] on the basis of an analysis of the gamma-ray spectra measured in the beta decay of $^{170}$Ho isomers and in various nuclear reactions, predominantly those of the $(n, n'\gamma)$ type, is one of the nuclides close to $^{170}$Yb. The calculation with allowance for Coriolis interaction is motivated by the following two factors. First, it can be seen from Tables 2 and 3 that the calculation for the $J = 1$–7 states reproduces their energies fairly well. Second, a conclusion on the structure of bands can be drawn from a simultaneous analysis of the mixing parameters $b$ for a number of nuclei. For these reasons, a calculation has been performed for the mixing of the $K^\pi = 0^-$ and $1^-$ bands in the $^{170}$Er nucleus. The results of this calculation are given in Table 4. It can be seen that the energies of the states in $^{170}$Er and in $^{170}$Yb and even the differences of the experimental and calculated values of these energies are close; even for the level of spin as high as $J = 7$, the differences in question are only 29 and 13 keV, respectively. This similarity can be considered as a strong argument in support of the conclusions on the structure of the $^{170}$Er nucleus that were drawn in [11].

### *4.2. Interaction Parameters in the $^{158}$Gd, $^{168}$Er, and $^{162}$Dy Nuclei*

By examining the interaction of the $1^-$ and $0^-$ bands in a number of nuclei simultaneously, one can reveal special features of the signature shift and of the inversion of levels in the $1^-$ bands. For the sake of generality, data on the $^{158}$Gd, $^{168}$Er, and $^{162}$Dy nuclei were included in the analysis. The $K^\pi = 0^-$ and $1^-$ bands are also known in these nuclei, and there is a Coriolis interaction between them, which leads to the signature splitting of the $K^\pi = 1^-$ band; for one reason or another, however, this splitting is not as great as that in the $^{156}$Gd or in the $^{170}$Yb nucleus. No inversion of levels occurs here.

An analysis has been performed for all additional nuclei, and the calculated energies of levels have been obtained on the basis of the same model as that used above. It turned out that the model leads to approximately the same deviation from experimental data for the different nuclei: for states of the same spin, the differences of the experimental and theoretical values of the energies of levels fall within the same range for the $^{156}$Gd, $^{170}$Er, and $^{170}$Yb nuclei (see Tables 2–4). For the $^{168}$Er nucleus, relevant data can be found in [1]. The values of the model parameters $A$ and $b$ and basic experimental data are given in Table 5.

### *4.3. Analysis of the Results*

Listed immediately below are similar features of the bands considered above and distinctions between them.

(i) The $K = 1$ bands lie lower than the $K = 0$ bands in all nuclei, with the exception of $^{162}$Dy. The excitation energy $E(1^-1)$ is 1.0–1.4 MeV, while the differences of the energies of the bandheads of the $K = 0$ and 1 bands are below 0.4 MeV.

(ii) The inertia parameters $A$ obtained from the present calculations lie in the narrow range 10.0–10.4 keV, but, for the $^{162}$Dy and $^{170}$Er nuclei, they are noticeably lower: $A = 9.185$ and 9.22 keV, repectively.

(iii) The correction to the energy of a spin-$J$ level due to band interaction takes close values for the $^{156}$Gd and the $^{170}$Yb nucleus (see Tables 2, 3).

(iv) The interaction parameter $b$ proved to be close for five nuclei: $b = 35$–$40$ keV; for the $^{162}$Dy nucleus, it is sizably less, $b = 19.41$ keV. This distinction can be explained by using the results obtained on the basis of the quasiparticle–phonon model due to V.G. Soloviev [10]. The intense two-quasiparticle neutron components of the wave functions for the $K^\pi = 0^-$ and $1^-$ collective quadrupole states are quoted in Table 5, along with the weights of these components, which vary between 19 and 93%; however, the actual values of the weights may be different for a more correct choice of values for the model parameters. Other components of two-quasiparticle wave functions differ by the quantum numbers of both nucleons and do not contribute to the interaction parameter $b$. The distinctions between the structures of the bands are associated with the difference in the quantum numbers of one of the unpaired neutrons: $642\uparrow$ versus $651\uparrow$ in $^{156}$Gd and $^{158}$Gd and $633\uparrow$ versus $642\uparrow$ in $^{168}$Er and $^{170}$Yb. The second unpaired neutron, $521\uparrow$, $512\uparrow$, or $523\downarrow$, is the same in both bands. It follows that values in the range $b = 35$–$40$ keV are due to the interaction of neutrons whose principal quantum number is $N = 6$. No significant effect of the fraction of the two-quasiparticle component on the content of the wave function has been found. The situation in the $^{162}$Dy nucleus is different. The quantum numbers of the identical unpaired nucleon are $642\uparrow$; the distinction between the bands is due here to the $523\downarrow$ and $521\uparrow$ neutrons. A reduction of the interaction parameter $b$ by a factor of 2 is observed in this case.

Of particular interest is the $^{170}$Er nucleus. The interaction-parameter value of $b = 32.78$ keV for this nucleus is less than those for the other nuclei considered here, but it is much greater than that in $^{162}$Dy. From the general point of view, this result can be understood if one considers the structure of the $1^-$ and $0^-$ states in this nucleus, following the ideas developed in [10]. In the $1^-$ band, the weight of the $nn633 \uparrow 512 \uparrow$ two-quasiparticle state is 93%. In the $0^-$ state, the contribution of the structure that would lead to a greater value of $b$, $nn642 \uparrow 512 \uparrow$, is as small as 10%, which is one-half as great as that in the nuclei considered above. The weight of the other component of the wave function for the $K = 0$ states, $nn633 \uparrow 514 \downarrow$, is 67%, but its interaction with the wave function for the $K = 1$ state is due to neutrons occurring in the $n512 \uparrow$ and $n514 \downarrow$ states—that is, neutrons whose principal quantum number is $N = 5$ rather than 6. One can conjecture that it is precisely this structural feature that reduces the interaction parameter in $^{170}$Er.

In order to verify these conclusions, it is necessary to study different nuclides, but the two bands in question—that is, the $K = 1$ and 0 ones—are not known in all of them. Data on the energies in these bands are necessary for calculating the values of the mixing parameter. The list of nuclides for which the content of the wave functions for collective octupole states was calculated in [10] is not very large.

Additional investigations were performed for four more nuclides: $^{154}$Gd, $^{154}$Sm, $^{160}$Dy, and $^{162}$Er. The results proved to be similar to those that are quoted

**Table 5.** Properties of the $K^\pi = 1^-$ and $0^-$ bands in some deformed nuclei

| Nucleus, keV | $E(1^-1)$, keV | $E(1^-0)$, keV | $A$, keV | $b$, keV |
|---|---|---|---|---|
| $^{156}$Gd | 1242.50 | 1366.5 | 10.30 | 36.6 |
| $^{158}$Gd | 977.08 | 1263.46 | 10.195 | 34.82 |
| $^{168}$Er | 1358.90 | 1786.11 | 10.018 | 35.44 |
| $^{170}$Yb | 1364.41 | 1512.35 | 10.38 | 39.51 |
| $^{170}$Er | 1266.64 | 1824.60 | 9.22 | 32.78 |
| $^{162}$Dy | 1637.1 | 1276.1 | 9.185 | 19.41 |

| Nucleus | $nn$ structure [10] | |
|---|---|---|
| | $K^\pi = 1^-$ | $K^\pi = 0^-$ |
| $^{156}$Gd | $642\uparrow - 521\uparrow$ 19% | $651\uparrow - 521\uparrow$ 50% |
| $^{158}$Gd | $642\uparrow - 521\uparrow$ 55% | $651\uparrow - 521\uparrow$ 21% |
| $^{168}$Er | $633\uparrow - 523\downarrow$ 93% | $642\uparrow - 523\downarrow$ 26% |
| $^{170}$Yb | $512\uparrow - 523\downarrow$ 93% | $642\uparrow - 512\uparrow$ 25% |
| $^{170}$Er | $633\uparrow - 512\uparrow$ 93% | $642\uparrow - 512\uparrow$ 10% |
| | | $633\uparrow - 514\downarrow$ 67% |
| $^{162}$Dy | $521\uparrow - 642\uparrow$ 50% | $523\downarrow - 642\uparrow$ 74% |

in Tables 2–5, but, among features that were revealed in these investigations, there are those that remained unexplained.

In the $^{154}$Gd nucleus, an inversion of even- and odd-spin levels is observed in the $K = 1$ band. However, the spacing between the $J = 1$ and 3 levels in the $K = 0$ band proved to be very small: 10 keV instead of the expected spacing of 100 keV. The calculation led to a very large value of $b = 51$ keV for the interaction parameter and to much poorer agreement between the calculated and the experimental values of the energies of levels.

In the $^{162}$Er nucleus, the $1^-$ and $3^-$ levels proved to be even more closely spaced: the gap between them is 4.6 keV. The parameter $A$ there, 6.07 keV, is much less than in the other nuclei, this value also leading to a large distinction between the calculated and the experimental values of the energies of levels. The reason behind the effects observed in these two nuclei has not been established conclusively, but one can conjecture that these effects stem from different deformations of octupole-band levels and from the proximity of these nuclei to the boundary of deformations. This idea is suggested by the systematics of the $K = 0$ bands in the $N = 88$ isotones (see [3]). In the majority of them, the $3^-$ levels lie lower than the $1^-$ levels, and these nuclei also occur in the vicinity of the boundary of deformations, but they lie on the other side of it and do not belong to the class of deformed nuclei.

For the $^{154}$Sm and $^{160}$Dy nuclei, the experimental values of the energies of levels are reproduced fairly well, but, there, other bands lie quite closely and may have a nontrivial effect. Of course, this must be taken into account in further calculations.

## 5. CONCLUSION

An analysis of the effect of inversion of levels in the $K^\pi = 1^-$ octupole vibrational bands in the $^{156}$Gd and $^{170}$Yb nuclei has revealed that the inclusion of Coriolis interaction makes it possible to explain, in a natural way, the observed features of these nuclei. The model parameters have been calculated, and it appears that the interaction parameter $b$ has close values not only

in the bands featuring the inversion of levels but also in the neighboring nuclides of $^{158}$Gd and $^{168}$Er, where there is no inversion, but where a significant signature splitting is observed.

A comparison with the bands in the $^{162}$Dy nucleus has made it possible to relate the numerical value of $b$ with the structure of octupole bands that is determined within the quasiparticle–phonon model.

The present calculations of the energies of rotational levels have demonstrated the scale of the discrepancy between the theoretical and experimental results. The well-known effect of the reduction of pair correlations, which is not included in the Coriolis interaction model and which is not taken into account in the calculations, is a natural reason for the growth of discrepancies with increasing spin $J$. This is not so only for the $^{170}$Yb nucleus (see Table 2). However, the effect in question can be traced as the experimental values of the inertia parameter $A^+$, which are given in Figs. 2 and 4 and in Tables 2–4, become smaller.

## REFERENCES


1. E. P. Grigoriev, Yad. Fiz. **65**, 673 (2002) [Phys. At. Nucl. **65**, 641 (2002)].
2. G. M. Baglin, Nucl. Data Sheets **77**, 125 (1996).
3. V. M. Belen'kiĭ and E. P. Grigoriev, *Structure of Even Nuclei* (Énergoatomizdat, Moscow, 1987).
4. B. C. Dzhelepov *et al.*, *Radioactive Nuclei A = 169, 170 Decay Schemes* (Nauka, Leningrad, 1988).
5. D. E. Archer *et al.*, Phys. Rev. C **57**, 2924 (1998).
6. É. V. Vasil'eva *et al.*, Izv. Akad. Nauk, Ser. Fiz. **56** (5), 2 (1992).
7. E. P. Grigoriev, Fiz. Élem. Chastits At. Yadra **31**, 1496 (2000).
8. R. G. Helmer, Nucl. Data Sheets **65**, 65 (1992).
9. M. Sugawara *et al.*, JAERI-Review **018**, 27 (2000).
10. E. P. Grigoriev and V. G. Soloviev, *Structure of Even Deformed Nuclei* (Nauka, Moscow, 1974).
11. E. P. Grigoriev and I. A. Gladkova, Yad. Fiz. **63**, 773 (2000) [Phys. At. Nucl. **63**, 705 (2000)].


*Translated by A. Isaakyan*

*Physics of Atomic Nuclei, Vol. 66, No. 9, 2003, pp. 1715–1718. From Yadernaya Fizika, Vol. 66, No. 9, 2003, pp. 1763–1766.*


## ELEMENTARY PARTICLES AND FIELDS
## Experiment

# Observation of a Baryon Resonance with Positive Strangeness in $K^+$ Collisions with Xe Nuclei*,**

**V. V. Barmin[1], V. S. Borisov[1], G. V. Davidenko[1], A. G. Dolgolenko[1]***, C. Guaraldo[2], I. F. Larin[1], V. A. Matveev[1], C. Petrascu[2], V. A. Shebanov[1], N. N. Shishov[1], L. I. Sokolov[1], and G. K. Tumanov[1]**

**The DIANA Collaboration**

[1] *Institute of Theoretical and Experimental Physics, Bol'shaya Cheremushkinskaya ul. 25, Moscow, 117259 Russia*

[2] *Laboratori Nazionali di Frascati dell' INFN, Italy*

Received May 14, 2003

**Abstract**—The status of our investigation of low-energy $K^+$Xe collisions in the xenon bubble chamber DIANA is reported. In the charge-exchange reaction $K^+\mathrm{Xe} \to K^0 p\mathrm{Xe}'$, the spectrum of $K^0p$ effective mass shows a resonant enhancement with $M = 1539 \pm 2$ MeV/$c^2$ and $\Gamma \leq 9$ MeV/$c^2$. The statistical significance of the enhancement is near $4.4\sigma$. The mass and width of the observed resonance are consistent with expectations for the lightest member of the antidecuplet of exotic pentaquark baryons, as predicted in the framework of the chiral soliton model. 

This paper reports an investigation of low-energy $K^+$–nucleus collisions aimed at testing the hypothesis of an antidecuplet of exotic pentaquark baryons, as proposed by Diakonov, Petrov, and Polyakov [1] in the framework of the chiral soliton model. Under the assumption that the known nucleon resonance $P_{11}(1710)$ belongs to the hypothesized antidecuplet, predictions for the masses and decay widths of its other members have been obtained [1]. Of these, the lightest is the exotic pentaquark state $uudd\bar{s}$ with mass near 1530 MeV/$c^2$ and decay width $\Gamma <$ 15 MeV/$c^2$. This spin-1/2 isospin-zero state with positive strangeness, referred to as the $Z^+$ baryon, is expected to decay to $K^0p$ and $K^+n$.

Two different methods may be employed in the search for formation of the $Z^+$ baryon in $K^+$Xe collisions. The first and straightforward approach is to analyze the effective mass of the $K^0p$ system in the reaction $K^+\mathrm{Xe} \to K^0 p\mathrm{Xe}'$ for the $Z^+$ peak near 1530 MeV/$c^2$. The second approach is to measure the cross sections for formation of the final states $K^0p$ and $K^+n$ as functions of $K^+$ momentum. Given a target nucleon bound in the Xe nucleus, formation of the $Z^+$ baryon should manifest itself as an enhancement of partial cross sections of elementary processes $K^+n \to K^+n$ and $K^+n \to K^0p$ at $K^+$ momentum near 480 MeV/$c$. Measurements of these partial cross sections in the interval $400 < P_{K^+} < 700$ MeV/$c$ are in progress and should finally reach a statistical accuracy of 3–6% with $K^+$ momentum pitch of 30–40 MeV/$c$. The latter measurements are also important for clarifying some problems arising in the analysis of low-energy $K^+$–nucleus collisions [2–4].

The bubble chamber DIANA filled with liquid xenon has been exposed to a separated $K^+$ beam with momentum of 850 MeV/$c$ from the ITEP proton synchrotron. The density and radiation length of the fill are 2.2 g/cm$^3$ and 3.7 cm, respectively. The chamber has a total volume of $70 \times 70 \times 140$ cm$^3$ viewed by photographic cameras and operates without a magnetic field [5]. Charged particles are identified by ionization and momentum-analyzed by range in xenon. In total, some $10^6$ tracks of incident $K^+$ mesons are recorded on film. Half of the collected film has been scanned, and nearly 25 000 events with visible $K^0$ decays, $K^0_S \to \pi^+\pi^-$ and $K^0_S \to \pi^0\pi^0$, have been found.

In the fiducial volume of the bubble chamber, $K^+$ momentum is a function of longitudinal coordinate and varies from 750 MeV/$c$ for entering kaons to zero for those that range out through ionization. (A 150-mm-thick layer of xenon downstream of the front

*This article was submitted by the authors in English.

**Based on a talk at Session of Nuclear Division of Russian Academy of Sciences, Dec. 3, 2002.

***e-mail: dolgolenko@vitep1.itep.ru

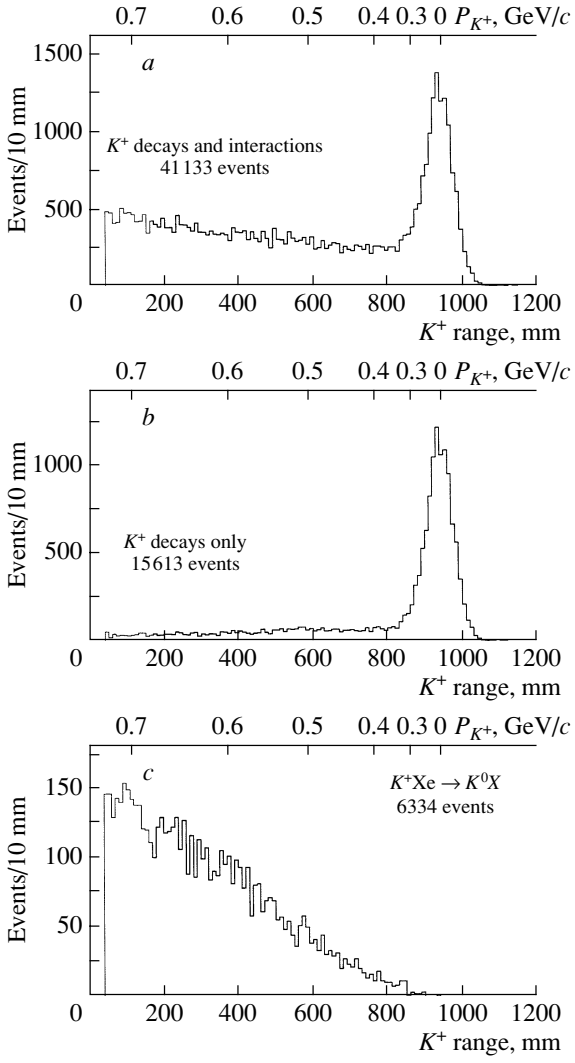


**Fig. 1.** Range and equivalent momentum (top scale) of the incident $K^+$ for different event categories: (*a*) for all $K^+$ decays and interactions; (*b*) only for $K^+$ decays; (*c*) only for the charge-exchange reaction $K^+\mathrm{Xe} \to K^0X$.

wall is beyond the selected fiducial volume and is only used for detecting the secondaries that travel in the backward hemisphere.) Throughout this interval of $K^+$ momentum, partial cross sections for formation of various final states of $K^+$Xe collisions can be measured thanks to efficient detection of the decays and interactions of incident kaons in the xenon bubble chamber. The momentum of an interacting $K^+$ is determined from the longitudinal coordinate of the interaction vertex with respect to the central position of the observed maximum due to decays of stopping $K^+$ mesons. The uncertainty on $K^+$ momentum is near 20 MeV/$c$ for $P_{K^+}$ in the range of $500 \pm 50$ MeV/$c$.

The methodology of this work is illustrated by Fig. 1, where the measured $K^+$ range before interaction or decay is plotted for different event categories (the upper scale shows the corresponding $K^+$ momentum). These data are based on a throughput measurement of 41 000 tracks of incident kaons. The distribution of all incident $K^+$ mesons in track length is shown in Fig. 1*a*, and the distribution of those $K^+$ mesons that have decayed either in flight or at rest is shown in Fig. 1*b*. The enhancement near 945 mm is due to decays of stopping kaons. All $K^+$ decays have been uniquely identified in the bubble chamber, and observed branching fractions are in agreement with tabulated values. The distribution of selected events of the charge-exchange reaction $K^+\mathrm{Xe} \to K^0X$ is illustrated in Fig. 1*c*. This includes events with a $K^0_S$ detected by decay to $\pi^0\pi^0$ or $\pi^+\pi^-$ and a $K^0_L$ whose presence is inferred from nonobservation of strange particles in the final state.[1)] Apart from $K^+$ decays and the charge-exchange reaction $K^+\mathrm{Xe} \to K^0X$, the inclusive distribution of Fig. 1*a* picks contributions from elementary scattering processes $K^+n \to K^+n$ and $K^+p \to K^+p$ and from electromagnetic interactions with the Coulomb field of the Xe nucleus. The extraction of corresponding partial cross sections is in progress. As indicated above, comparing the partial cross sections of elementary reactions $K^+n \to K^+n$, $K^+n \to K^0p$, and $K^+p \to K^+p$ as functions of $K^+$ momentum may provide a clue to formation of the hypothesized $Z^+$ baryon in $K^+$Xe collisions.

In this paper, we adopt an alternative approach that consists in analyzing the $K^0p$ effective mass in the charge-exchange reaction $K^+n \to K^0p$ on a bound nucleon. The events of this reaction are fully measured and reconstructed in space using specially designed stereoprojectors similar to those proposed in [6]. Of the 25 000 events with visible $K^0_S$ decays, selected for complete reconstruction are those with a single proton and a $K^0_S \to \pi^+\pi^-$ candidate in the final state. The distance between the primary and $K^0$ vertices is required to exceed 2.5 mm. In a selected event, we measure the $K^0_S$ and proton emission angles with respect to the $K^+$ direction, $\pi^+$ and $\pi^-$ emission angles with respect to the parent $K^0_S$ direction, and proton and pion paths in xenon. The momentum is estimated by range for the proton and by pion ranges and emission angles for the $K^0_S$. Proton and $K^0_S$ momenta are required to exceed 180 and 170 MeV/$c$, respectively. Further details on the experimental procedure can be found in [7, 8].

[1)] Note that, of some 6300 events in the latter distribution, 3100 are part of the aforementioned subsample of 25 000 events with detected $K^0_S$ decays. Measuring the $K^+$ track length in all such events will significantly increase the statistics of the charge-exchange reaction.

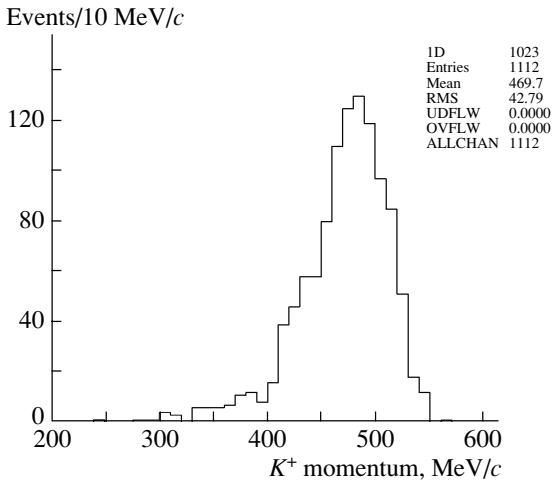


**Fig. 2.** Incident $K^+$ momentum for measured events of the reaction $K^+\mathrm{Xe} \to K^0 p\mathrm{Xe}'$.

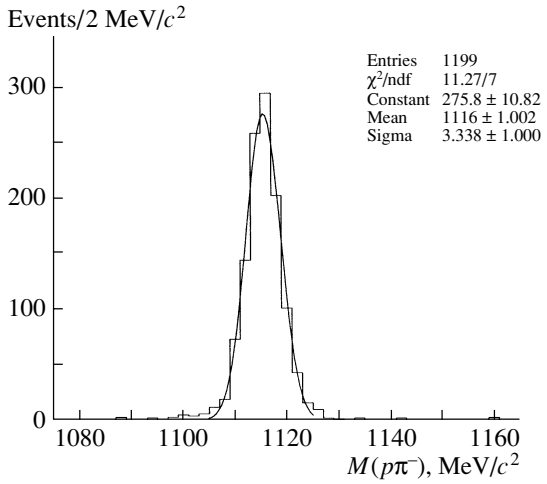


**Fig. 3.** Effective mass of the $p\pi^-$ system for secondary vertices of the type $V \to p\pi^-$.

In order to reduce the total volume of measurements, the $K^+$ range before interaction is required to exceed 550 mm. On average, this corresponds to the selection $P_{K^+} < 530$ MeV/$c$.[2)] The distribution of measured events of the reaction $K^+\mathrm{Xe} \to K^0 p\mathrm{Xe}'$ in $P_{K^+}$ is shown in Fig. 2. The mean value of $K^+$ momentum is close to 470 MeV/$c$. At present, we have fully measured 1112 events of the charge-exchange reaction $K^+\mathrm{Xe} \to K^0 p\mathrm{Xe}'$; measuring all selected events will nearly double the available statistics of this reaction.

In order to estimate the uncertainty on effective mass of the $K^0 p$ system, we invoke our earlier measurements [9] of two-prong secondary vertices (or Vees) formed by a proton and a charged pion, which relied on same techniques. The distribution of effective mass of such Vees, illustrated in Fig. 3, shows a prominent $\Lambda^0$ peak at the expected mass of $M(p\pi^-) = 1116 \pm 1$ MeV/$c^2$ with instrumental width of $\sigma = 3.3 \pm 1.0$ MeV/$c^2$. Note that distributions of the total momentum and the proton momentum are very similar for the $p\pi^-$ system from $\Lambda^0$ decay and for the $K^0 p$ system formed in the reaction $K^+\mathrm{Xe} \to K^0 p\mathrm{Xe}'$. At the same time, the $K^0$ and $\pi^-$ momenta are measured with very similar precision. We may conclude that effective mass of the $K^0 p$ system, like that of the $p\pi^-$ system, is measured to a precision of a few MeV/$c^2$.

Effective mass of the $K^0 p$ system formed in the charge-exchange reaction is plotted in Fig. 4*a* for all measured events. Qualitatively, a narrow enhancement is seen at the expected mass of the $Z^+$ baryon ($M \simeq 1530$ MeV/$c^2$). To estimate the level of background, the mass spectrum of Fig. 4*a* has been fitted to a linear combination of two regular distributions:

(i) the $K^0 p$ mass spectrum expected for the nonresonant charge-exchange reaction $K^+ n \to K^0 p$, obtained through a simulation that takes into account the momentum distribution of interacting $K^+$ mesons, the Fermi motion and binding energy of the target nucleon, the differential cross section for $K^0$ emission in the charge-exchange reaction [10], and actual conditions of the discussed experiment; and

(ii) a distribution obtained by the method of random stars.

The results of the fit are illustrated by the dashed line in Fig. 4*a*. In the mass interval of 1535–1545 MeV/$c^2$, populated by 107 events, the estimated background amounts to 83 events, resulting in a statistical significance of $2.6\sigma$.

It is interesting to see whether the observed enhancement is affected by rescattering of reaction products in nuclear matter. In order to remove the events worst affected by rescatterings, additional topological selections[3)] are applied:

(i) $\theta_p < 100^\circ$ and $\theta_K < 100^\circ$ for the proton and $K^0$ emission angles with respect to the $K^+$ direction in the laboratory frame;

(ii) $\cos\Phi_{pK} < 0$ for the azimuthal angle between the proton and $K^0$ directions (that is, the proton and $K^0$ are required to be back-to-back in the plane transverse to the beam direction).

According to a simulation that accounts for Fermi motion of the target neutron, these selections keep

[2)] Mean momentum of incident $K^+$ beam varied by some $\pm 15$ MeV/$c$ in different exposures.

[3)] At this stage of the analysis, no kinematic selections based on constraining measured events to $K^+ n \to K^0 p$ are used.

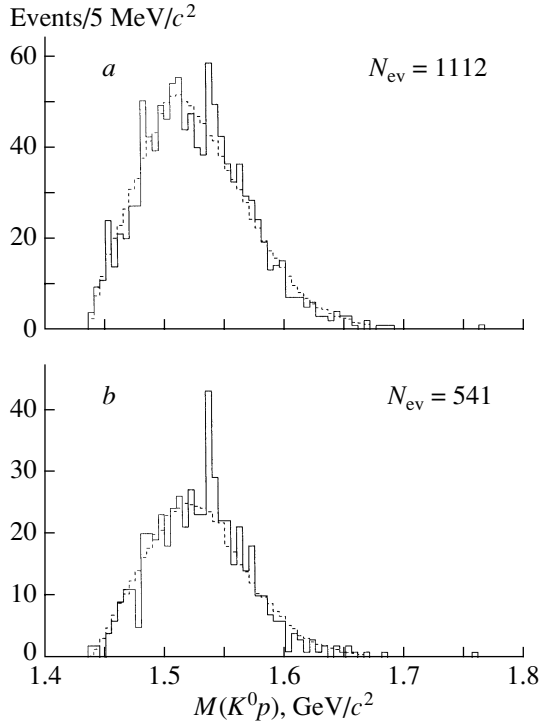


**Fig. 4.** Effective mass of the $K^0p$ system formed in the reaction $K^+\mathrm{Xe} \to K^0p\mathrm{Xe}'$: (*a*) for all measured events, (*b*) for events that pass additional selections aimed at suppressing proton and $K^0$ reinteractions in nuclear matter (see text). The fit to the expected functional form is depicted by the dashed line.

the bulk of events of the charge-exchange reaction that are not affected by proton and $K^0$ rescattering in nuclear matter. Of the 1112 measured events of the reaction $K^+\mathrm{Xe} \to K^0p\mathrm{Xe}'$, nearly half (541 events) survive the additional selections. In the $K^0p$ mass spectrum for these events shown in Fig. 4*b*, the enhancement near 1540 MeV/$c^2$ becomes more prominent. In the mass interval of 1535–1545 MeV/$c^2$, the total number of events is 73 with an estimated background of 44 events, resulting in a statistical significance of $4.4\sigma$. In order to estimate the mass and width of the observed resonance, a Gaussian with floating position and rms is added to the fitting function. The latter fit yields the values $M = 1539 \pm 2$ MeV/$c^2$ and $\sigma = 3$ MeV/$c^2$.

To summarize, a baryon resonance with mass $M = 1539 \pm 2$ MeV/$c^2$ and width $\Gamma \leq 9$ MeV/$c^2$ has been observed in the $K^0p$ effective-mass spectrum for the reaction $K^+\mathrm{Xe} \to K^0p\mathrm{Xe}'$. The statistical significance of the signal is estimated at $4.4\sigma$. The resonance is a strong indication for formation of the exotic pentaquark $Z^+$ baryon.[4)] Our work is still in progress.

## ACKNOWLEDGMENTS

We wish to thank A.E. Asratyan for useful comments and discussions. This work is supported by the Russian Foundation for Basic Research (project no. 01-02-16465).

## REFERENCES

1. D. Diakonov, V. Petrov, and M. Polyakov, Z. Phys. A **359**, 305 (1997).
2. C. B. Dover and G. E. Walker, Phys. Rep. **89**, 1 (1982).
3. R. Weiss *et al.*, Phys. Rev. C **49**, 2569 (1994).
4. N. Kaiser *et al.*, Nucl. Phys. A **594**, 325 (1995).
5. V. V. Barmin *et al.*, Prib. Tekh. Éksp., No. 4, 61 (1984).
6. J. W. Cronin *et al.*, Phys. Rev. Lett. **18**, 25 (1967).
7. V. V. Barmin *et al.*, Nucl. Phys. A **566**, 409 (1993).
8. V. V. Barmin *et al.*, Phys. At. Nucl. **57**, 1655 (1994).
9. V. V. Barmin *et al.*, Nucl. Phys. A **683**, 305 (2001).
10. U. Casadei *et al.*, CERN–HERA 75-1 (1975).

[4)]The existence of a baryon resonance with positive strangeness looks even more reliable in connection with the recent paper by Y. Nakano *et al.* (hep-ex/0301020) which reports the observation of a baryon resonance in the $K^+n$ system with $M = 1.54 \pm 0.01$ GeV/$c^2$, $\Gamma < 25$ MeV/$c^2$, and significance of $4.6\sigma$ in the reaction $\gamma n \to K^+K^-n$ on $^{12}$C.

Physics of Atomic Nuclei, Vol. 66, No. 9, 2003, pp. 1719–1729. Translated from Yadernaya Fizika, Vol. 66, No. 9, 2003, pp. 1767–1777.


ELEMENTARY PARTICLES AND FIELDS
Theory

# One-Loop Corrections of Orders $(Z\alpha)^6 m_1/m_2$ and $(Z\alpha)^7$ to the Fine Structure of Muonium

**A. P. Martynenko[1)]* and R. N. Faustov[2)]****

[1)] *Samara State University, ul. Akademika Pavlova 1, Samara, 443011 Russia*

[2)] *Scientific Council for the Interdisciplinary Problem Cybernetics, Russian Academy of Sciences, ul. Vavilova 40, Moscow, 117967 Russia*

Received June 14, 2002; in final form, November 26, 2002

**Abstract**—Corrections of orders $(Z\alpha)^6 m_1/m_2$ and $(Z\alpha)^7$ from one-loop two-photon amplitudes to the energy spectra of hydrogen-like atoms are calculated by expanding the relevant integrand in a Taylor series. A method for averaging the resulting quasipotential in the $d$-dimensional coordinate representation is formulated. Numerical values are obtained for the corresponding contributions to the fine structure of the muonium, hydrogen, and positronium atoms. © *2003 MAIK "Nauka/Interperiodica".*

## 1. INTRODUCTION

Investigation of high-order perturbative effects in $\alpha$ (where $\alpha$ is the fine-structure constant) in the energy spectra of the positronium and muonium atoms is of paramount importance for testing the theory of bound states in QED. In recent years, considerable advances have been made in these realms [1]. First of all, this was due to the improvement of accuracy in measuring the fine and the hyperfine structure in the energy spectra of these lepton systems. For example, the experimental error in measuring the hyperfine structure of the muonium atom was reduced by a factor of 3 [2]:

$$\Delta\nu^{\rm expt}_{\rm HFS}({\rm Mu}) = 4\,463\,302\,765(53)\ {\rm Hz}. \qquad (1)$$

An even more significant improvement of accuracy was achieved in measuring the $1S{-}2S$ interval in the muonium atom on the basis of Doppler-free two-photon spectroscopy [3]:

$$\Delta\nu^{\rm expt}_{\rm Mu}(2^3S_1{-}1^3S_1) = 2\,455\,528\,941.0(9.8)\ {\rm MHz}. \qquad (2)$$

For the analogous interval in the positronium atom, measurements performed a decade ago yielded [4]

$$\Delta\nu^{\rm expt}_{\rm Ps}(2^3S_1{-}1^3S_1) = 1\,233\,607\,216.4(3.2)\ {\rm MHz}. \qquad (3)$$

In the spectroscopy of extremely simple atomic systems, one of the most precise experimental results was obtained by measuring the frequency of the $1S{-}2S$ transition in the hydrogen atom [5]:

$$\Delta\nu^{\rm expt}_{\rm H}(2S{-}1S) = 2\,466\,061\,413\,187.34(84)\ {\rm kHz}. \qquad (4)$$

On the other hand, the aforementioned advances were associated with the refinement of computer methods for calculating Feynman amplitudes and with the advent of nonrelativistic QED formulated as an effective theory of electromagnetic particle interaction for calculating the energy spectra of bound states in the nonrelativistic region [6–8]. Calculations on this basis yielded contributions of order $(Z\alpha)^6 m_1^2/m_2$ [$m_1$ and $m_2$ are the masses of bound particles; $Z$ is the charge of the second particle (nucleus); the parameter $Z\alpha$ specifies the order of relativistic corrections and of binding effects] to the fine structure of the muonium atom [9–14], corrections of order $m\alpha^6$ to the fine and the hyperfine structure of the positronium atom [15–19], the first logarithmic contributions of the form $O(m\alpha^7\ln^2\alpha)$ to the spectrum of the positronium atom [20, 21], and $O(m\alpha^7\ln\alpha)$ logarithmic corrections to the hyperfine structure of the muonium and positronium atoms [22, 23]. It is more difficult to calculate loop integrals specifying corrections to the Coulomb potential in perturbation theory since a few significantly different energy regions control the behavior of the relevant integrand. In terms of the loop energy $p^0$ and the loop momentum $\mathbf{p}$, these regions can be characterized as follows [24, 25]:

$$\text{hard-momentum region, } p^0 \sim \mu, |\mathbf{p}| \sim \mu; \qquad (5)$$

$$\text{potential region, } p^0 \sim \mu\alpha^2, |\mathbf{p}| \sim \mu\alpha; \qquad (6)$$

$$\text{soft region, } p^0 \sim \mu\alpha, |\mathbf{p}| \sim \mu\alpha; \qquad (7)$$

* e-mail: mart@info.ssu.samara.ru
** e-mail: faustov@theory.sinp.msu.ru

1063-7788/03/6609-1719$24.00 

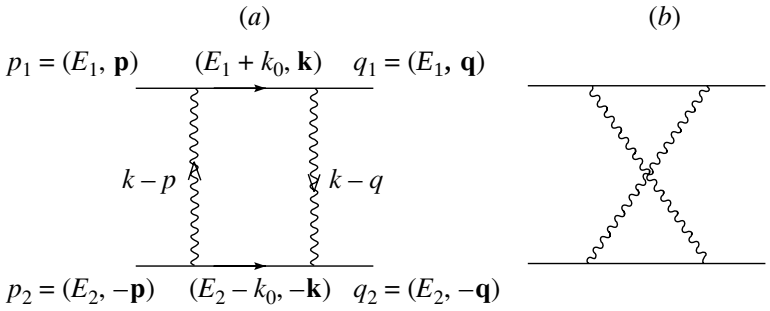


**Fig. 1.** Two-photon exchange Feynman diagrams, where $P = p_1 + p_2$ is the total momentum of the bound state of two particles, while $p$ and $q$ are the 4-momenta of the relative motion of, respectively, the initial- and the final-state particles.

$$\text{ultrasoft region, } p^0 \sim \mu\alpha^2, |\mathbf{p}| \sim \mu\alpha^2. \qquad (8)$$

Here, the mass parameter $\mu$ is determined by the particle masses $m_1$ and $m_2$. There are two possibilities for calculating contributions of a specific order in $\alpha$. The first possibility consists in explicitly specifying a small parameter and constructing, in one of the regions in (5)–(8), a series expansion of relevant QED Feynman amplitudes [14, 26–28]. The second possibility implemented within nonrelativistic QED is to formulate this procedure at the stage as early as that of the Lagrangian [6–8]. In the present study, which is a continuation of that reported in [14], we examine contributions of orders $(Z\alpha)^6$ and $(Z\alpha)^7$ to the spectra of the muonium and positronium atoms, relying on the first method, which, if it is used along with the dimensional-regularization procedure, enables us to construct the particle-interaction operator both in the momentum and in the coordinate representation. Since we have $(Z\alpha)^6 m_e^2/m_\mu = 0.0902$ MHz and $m_e\alpha^7 = 0.136$ MHz, it is of crucial importance to calculate such contributions, especially for the quantities in (1) and (4).

## 2. CONTRIBUTIONS OF ORDER $(Z\alpha)^6 m_1/m_2$ TO THE FINE STRUCTURE OF THE MUONIUM ATOM

By merely counting the powers of $Z\alpha$ in the two-photon exchange diagrams shown in Fig. 1, it can be shown that these diagrams can make contributions of order $(Z\alpha)^2 \times (Z\alpha)^3 = (Z\alpha)^5$. Here, the first factor owes its existence to exchange photons, while the second stems from the wave functions for the bound system. At the same time, the fact that the momenta of the relative motion of the initial- and final-state particles ($\mathbf{p}$, $|\mathbf{p}| \sim \mu\alpha$, and $\mathbf{q}$, $|\mathbf{q}| \sim \mu\alpha$, respectively) are present in these $2\gamma$ amplitudes leads to the emergence of contributions whose order in $\alpha$ is still higher. Here, we formulate the computational procedure to be employed in the ensuing analysis and calculate corrections involving an additional power of $Z\alpha$ and the electron-to-muon mass ratio $m_1/m_2 = 0.004836$. We note that the approach in question is applicable to the positronium atom as well if some simplifications associated with the smallness of the ratio $m_1/m_2$ are not used in the two-photon Feynman amplitudes. The general structure of integrals that determine the quasipotential remains unchanged.

Our calculations are based on a local quasipotential equation of the Schrödinger type [14],

$$\left(\frac{b^2}{2\mu_R} - \frac{\mathbf{p}^2}{2\mu_R}\right)\psi_M(\mathbf{p}) = \int \frac{d\mathbf{q}}{(2\pi)^3} V(\mathbf{p}, \mathbf{q}, M)\psi_M(\mathbf{q}). \qquad (9)$$

Here, $b^2 = E_1^2 - m_1^2 = E_2^2 - m_2^2$, $\mu_R = E_1E_2/M$ is the relativistic reduced mass, $M = E_1 + E_2$ is the bound-state mass, and $\psi_M(\mathbf{p})$ is the quasipotential wave function for the bound state. As an input approximation to the quasipotential $V(\mathbf{p}, \mathbf{q}, M)$ for the bound system, we choose an ordinary Coulomb potential.

In constructing the particle-interaction operator corresponding to the $2\gamma$ amplitudes being considered, we also use the operators $\hat{P}_{S=0}$ and $\hat{P}_{S=1}$ of projection onto the states in which the total spin of the $S$-wave $(e^-\mu^+)$ bound state is equal to 0 and 1, respectively,

$$\hat{P}_{S=0} = \frac{\hat{P} + M}{2\sqrt{2}M}\gamma_5, \quad \hat{P}_{S=1} = \frac{\hat{P} + M}{2\sqrt{2}M}\hat{\epsilon}, \qquad (10)$$

where $\hat{\epsilon} = \epsilon^\mu\gamma_\mu$, $\epsilon^\mu$ being the polarization vector of the ${}^3S_1$ state, and $P = p_1 + p_2$ is the total 4-momentum of the bound state of the two particles in question.

The contribution of the diagram in Fig. 1*a* to the quasipotential is determined with the aid of formulas (10) and is given by (only the ${}^3S_1$ triplet states are considered below)

$$V^{(a)}_{2\gamma}(\mathbf{p}, \mathbf{q}) = \frac{i(Z\alpha)^2}{\pi^2} \qquad (11)$$

$$\times \int \frac{f_1(k,m_1,m_2)d^4k}{(k-p)^2(k-q)^2 D_1(k)D_2(-k)},$$

$$f_1(k,m_1,m_2) = m_2(4m_1+2k_0)+2m_1k_0 - 2{k_0}^2+\frac{2}{3}\mathbf{k}^2.$$

The denominator of the electron propagator is $D_1(k) = k^2 + 2m_1k_0 + b^2$, while the corresponding muon denominator can be simplified by taking into account the smallness of the ratio $m_1/m_2$, in which case one can disregard the kinetic energy of the muon atom in the intermediate state: $D_2(-k) \approx 2m_2(-k_0+i0)$. The crossed two-photon diagram in Fig. 1*b* makes a similar contribution to the quasipotential; that is,

$$V_{2\gamma}^{(b)}(\mathbf{p},\mathbf{q}) = \frac{i(Z\alpha)^2}{\pi^2} \times \int \frac{f_2(k,m_1,m_2)d^4k}{(k-p)^2(k-q)^2 D_1(k)D_2(-k+p+q)}, \quad (12)$$

$$f_2(k,m_1,m_2) = m_2(4m_1+2k_0)+2m_1k_0 + 6{k_0}^2+\frac{10}{3}(\mathbf{p}\cdot\mathbf{k}+\mathbf{q}\cdot\mathbf{k}-\mathbf{k}^2).$$

The direct two-photon amplitude corresponding to Fig. 1*a* involves a lower order contribution ($\alpha^3$), which is canceled by the iteration term of the quasipotential $V_{1\gamma}\times G^f \times V_{1\gamma}$ [14] ($G^f = (\mathbf{p}^2-b^2)/2\mu_R$ is the free two-particle Green's function). In order to isolate this contribution, we transform the product of the electron and the muon denominator as follows [25]:

$$\frac{1}{D_1(k)D_2(-k)} = \frac{-2\pi i\delta(k_0)}{-2E(\mathbf{k}^2-b^2)} - \frac{1}{2E}\left[\frac{1}{(k_0+i0)D_1(k)}+\frac{1}{(-k_0+i0)D_2(-k)}\right]. \quad (13)$$

Omitting the first term on the right-hand side of Eq. (13)—it corresponds to the free two-particle propagator—we can represent the sum of the potentials, $V_{2\gamma}^{(a)}+V_{2\gamma}^{(b)}$, in the form

$$V_{2\gamma}(\mathbf{p},\mathbf{q}) = V_{2\gamma}^{(a)}(\mathbf{p},\mathbf{q})+V_{2\gamma}^{(b)}(\mathbf{p},\mathbf{q}) = \frac{i(Z\alpha)^2}{6m_2\pi^2}\int\frac{d^4k}{(k-p)^2(k-q)^2} \times \left[\frac{12m_1^2+18m_1k_0+24{k_0}^2-12\mathbf{k}^2+10\mathbf{k}(\mathbf{p}+\mathbf{q})}{(k_0+i0)D_1(k)} - \frac{6m_1+3k_0}{(-k_0+i0)^2}\right]. \quad (14)$$

In the operator in (14), we will first consider the contribution of order $(Z\alpha)^6 m_1/m_2$ arising in the potential region (6). Here, the integral with respect to $k_0$ is determined by the residue at the pole of the electron propagator, which can be written in the form

$$\frac{1}{{k_0}^2-\mathbf{k}^2+2m_1k_0+b^2} = \sum_{n=0}^{\infty}\frac{(-{k_0}^2)^n}{(-\mathbf{k}^2+2m_1k_0+b^2)^{n+1}}. \quad (15)$$

The corresponding expansions of the photon propagators in series are given by

$$\frac{1}{{k_0}^2-(\mathbf{k}-\mathbf{p})^2} = \sum_{n=0}^{\infty}\frac{(-{k_0}^2)^n}{[-(\mathbf{k}-\mathbf{p})^2]^{n+1}}. \quad (16)$$

Multiplying the expansions in (15) and (16), we can see that expression (14) assumes the form

$$V_{2\gamma}^{pot}(\mathbf{p},\mathbf{q}) \sim \int d^4k\left[\frac{1}{-(\mathbf{k}-\mathbf{p})^2} - \frac{{k_0}^2}{(\mathbf{k}-\mathbf{p})^4} - \frac{{k_0}^4}{(\mathbf{k}-\mathbf{p})^6} - \cdots\right]\left[\frac{1}{-(\mathbf{k}-\mathbf{q})^2} - \frac{{k_0}^2}{(\mathbf{k}-\mathbf{q})^4} - \frac{{k_0}^4}{(\mathbf{k}-\mathbf{q})^6} - \cdots\right]\frac{1}{(k_0+i0)} \times \left[\frac{1}{-\mathbf{k}^2+2m_1k_0+b^2} - \frac{{k_0}^2}{(-\mathbf{k}^2+2m_1k_0+b^2)^2} - \frac{{k_0}^4}{(-\mathbf{k}^2+2m_1k_0+b^2)^3} - \cdots\right]. \quad (17)$$

The integral in (17) involves corrections of different orders in $Z\alpha$. The order of individual terms in (17) is determined by counting the powers of this parameter after taking the residue at the pole in the variable $k_0$. Contributions of order $(Z\alpha)^6$ are present in expression (17) and are determined by integrals of the type

$$J(\mathbf{p},\mathbf{q}) = \int\frac{d\mathbf{k}}{(2\pi)^3}\frac{(\mathbf{k}^2)^\alpha}{(\mathbf{k}^2-2\mathbf{k}\mathbf{p}+\mathbf{p}^2)^\beta(\mathbf{k}^2-2\mathbf{k}\cdot\mathbf{q}+\mathbf{q}^2)^\gamma}, \quad (18)$$

where the exponents $\alpha$, $\beta$, and $\gamma$ can take different values that satisfy the relation $2\alpha+3-2\beta-2\gamma = 1$. The contribution to the spectrum of a hydrogen-like system is obtained upon averaging $J(\mathbf{p},\mathbf{q})$ with the Coulomb wave functions. Integrals of the type in (18)

**Table 1.** Results obtained by calculating some integrals in (18) [$\mathbf{t} = (\mathbf{p} - \mathbf{q})$]

| $\alpha$ | 0 | 1 | 2 |
|---|---|---|---|
| $\beta = 1, \gamma = 1$ | $\dfrac{1}{8t}$ | $\dfrac{\mathbf{p}^2 + \mathbf{q}^2 - \mathbf{t}^2}{16t}$ | – |
| $\beta = 1, \gamma = 2$ | – | $\dfrac{\mathbf{p}^2 - \mathbf{q}^2 + \mathbf{t}^2}{16t^3}$ | $\dfrac{\mathbf{p}^4 - 3(\mathbf{q}^2 - \mathbf{t}^2)^2 + 2\mathbf{p}^2(\mathbf{q}^2 + \mathbf{t}^2)}{32t^3}$ |
| $\beta = 1, \gamma = 3$ | – | – | $\dfrac{3\mathbf{p}^4 + 3(\mathbf{q}^2 - \mathbf{t}^2)^2 + \mathbf{p}^2(-6\mathbf{q}^2 + 2\mathbf{t}^2)}{64t^5}$ |
| $\beta = 2, \gamma = 2$ | – | – | $\dfrac{\mathbf{t}^4 + 2\mathbf{t}^2(\mathbf{p}^2 + \mathbf{q}^2) - 3(\mathbf{p}^2 - \mathbf{q}^2)^2}{32t^5}$ |

are divergent both in the ultraviolet and in the infrared region. These divergences are caused by that reduction of the integrand in (14) which was performed in order to isolate the contribution of the required order in $\alpha$. The original integral in (14) is finite; therefore, all divergences arising in intermediate expressions of the type in (18) must cancel in the final total expression. The quantity $\langle J(\mathbf{p}, \mathbf{q}) \rangle$ can be calculated by the following two methods:

(i) The integral in (18) with respect to $\mathbf{k}$ is calculated by using the dimensional-regularization procedure. Upon isolating a finite part, one constructs its Fourier transform, which is then averaged with the Coulomb wave functions in coordinate space.

(ii) One performs the Fourier transformation of expression (18), whereupon the result is averaged in coordinate space.

We used both methods to calculate contributions of order $(Z\alpha)^6 m_1/m_2$ to the energy spectrum of the muonium atom. A transition to $d$-dimensional space enables one to regularize the expression for the quasipotential both in the relativistic and in the nonrelativistic region of intermediate momenta. The results obtained by calculating some integrals of the type in (18) are presented in Table 1.

Corrections of the required order to the spectrum of $S$-wave states of the muonium atom also come from the soft-momentum region (7). There, the integral in (14) is determined by the residues at the photon poles. The expansion of the electron propagator in the soft-momentum region (7) has the form

$$\frac{1}{{k_0}^2 - \mathbf{k}^2 + 2m_1 k_0 + b^2} = \sum_{n=0}^{\infty} \frac{({k_0}^2 - \mathbf{k}^2 + b^2)^n}{(2m_1 k_0)^{n+1}}. \tag{19}$$

As a result, integrals of the following type arise in (14):

$$I^{\mathrm{soft}}(\mathbf{p}, \mathbf{q}) \sim \sum_{n=0}^{\infty} \int \frac{d^4k}{(k-p)^2(k-q)^2} \times \frac{1}{(k_0 + i0)} \frac{({k_0}^2 - \mathbf{k}^2 + b^2)^n}{(2m_1 k_0)^{n+1}}. \tag{20}$$

Since the function appearing in the numerator on the right-hand of (14) involves terms of orders 1, $\alpha$, and $\alpha^2$, it turns out that, in the sum in (20), an $O(\alpha^6)$ contribution comes from the $n = 1$, 2, and 3 terms, which are further calculated in just the same way as in the potential region.

## 3. CALCULATING MATRIX ELEMENTS OF THE OPERATOR $r^{-\nu}$ IN $d$-DIMENSIONAL COORDINATE SPACE

In many cases, it is convenient to perform averaging of the two-photon-interaction quasipotential with Coulomb wave functions in the coordinate representation. Indeed, the results obtained by calculating the integrals $J(\mathbf{p}, \mathbf{q})$ and given in Table 1 show that their averaging in three-dimensional momentum space leads to divergent expressions. Naturally, these divergences appeared for the same reason as above—namely, because of resort to expanding the integrand in a Taylor series. In just the same way as in performing integration with respect to the loop momentum $\mathbf{k}$, we can again use here the dimensional-regularization procedure—that is, a transition to $d$-dimensional momentum space. In order to do this, it is necessary to know the form of the wave functions in the $d$-dimensional momentum representation [29, 30]. A different approach to calculating the expectation value $\langle V_{2\gamma} \rangle$ involves determining the Fourier transform of the potential (14) in $d$-dimensional coordinate space and subsequently evaluating relevant expectation values for the Coulomb wave functions in this space. The Fourier transform of the power-law potential $V(p) = 1/p^m$ is given by [31]

$$V(r) = \frac{1}{(2\pi)^{d-1}} \prod_{k=1}^{d-3} \frac{\Gamma\left(\dfrac{k+1}{2}\right)\Gamma(1/2)}{\Gamma\left(\dfrac{k+2}{2}\right)} \tag{21}$$

$$\times \int_0^\pi \int_0^\infty \sin^{d-2}\theta e^{ipr\cos\theta} d\theta p^{d-1-m} dp$$

$$= \frac{\Gamma\left(\frac{d-m}{2}\right)}{2^m \pi^{d/2} r^{d-m} \Gamma\left(\frac{m}{2}\right)}.$$

It follows that, in $d = 3$ coordinate space, there arise potentials whose matrix elements are divergent for $S$-wave states. In order to isolate these singular terms, which are proportional to $1/\epsilon$ ($d = 3 + 2\epsilon$), we formulate an auxiliary Coulomb problem in $d$-dimensional coordinate space—namely, we formally consider a Coulomb potential in $d$-dimensional space, representing the Hamiltonian in the form [29, 30]

$$H = \frac{\mathbf{p}^2}{2} + V_C(r) = \frac{p_r^2}{2} + \frac{1}{2r^2} \times \left[\mathbf{L}^2 + \frac{(d-1)(d-3)}{4}\right] - \frac{a}{r}, \quad a = \mu Z\alpha, \tag{22}$$

$$r = \sqrt{\sum_{i=1}^{d} x_i^2},$$

where $p_r$ is the radial-momentum operator and $\mathbf{L}^2$ is the angular component of the Laplace operator $\Delta$ in $d$-dimensional space; the eigenfunctions of the operator $\mathbf{L}^2$, which are homogeneous harmonic polynomials of degree $l$ on a sphere $S^{d-1}$, correspond to the eigenvalues $\lambda = l(l+d-2)$ [32]. For the case of a discrete spectrum, an exact solution to the $d$-dimensional Coulomb problem was first obtained in [30]. In particular, it was shown that the Coulomb energy levels are given by

$$\epsilon_n = -\frac{1}{2\left(n + \frac{d-3}{2}\right)^2}, \tag{23}$$

where $n = 1, 2, 3, \ldots$ is the principal quantum number (see Appendix). The Coulomb Green's function for the $d$-dimensional problem—this function is necessary for calculating corrections in higher orders of perturbation theory—was derived in [33]. Recursion equations that relate the matrix elements of the operators $r^{-\nu}$ for different values of the exponent $\nu$ play an important role in calculating the expectation values of the quasipotential $V_{2\gamma}$. In order to derive these equations in $d$-dimensional space, we consider the operator

$$p_r = \frac{1}{2}\left\{\frac{r_i}{r}, p_i\right\} = \frac{r_i}{r} p_i - \frac{i(d-1)}{2r} = -i\left(\frac{\partial}{\partial r} + \frac{d-1}{2r}\right), \tag{24}$$

where the braces $\{\ldots, \ldots\}$ denote the anticommutator of the operators enclosed by these braces. The radial-momentum operator satisfies the commutation relations

$$[r, p_r] = i \cdot I, \quad \left[\frac{1}{r^\nu}, p_r\right] = \frac{-i\nu}{r^{\nu+1}}. \tag{25}$$

After a direct calculation, we find from relations (24) and (25) that

$$\left[H, \frac{1}{r^{\nu-1}}\right] = \frac{\nu-1}{2}\left(-\frac{\nu}{r^{\nu+1}} + \frac{2i}{r^\nu} p_r\right), \tag{26}$$

$$[H, ip_r] = \frac{\Delta_0}{r^3} - \frac{a}{r^2}, \quad \Delta_0 = \mathbf{L}^2 + \frac{(d-1)(d-3)}{4}.$$

From relations (24)–(26), it also follows that [34]

$$\left[\frac{1}{r^\nu}[r, H], H\right] + \frac{\nu}{2}\left[\frac{1}{r^{\nu+1}}, H\right] = \frac{2\nu}{r^{\nu+1}} H - \frac{\nu+1}{r^{\nu+3}}\left[\mathbf{L}^2 + \frac{(d-1)(d-3)}{4}\right] + \frac{(2\nu+1)a}{r^{\nu+2}} + \frac{\nu(\nu+1)(\nu+2)}{4}\frac{1}{r^{\nu+3}}. \tag{27}$$

The recursion relation for the matrix elements of $1/r^\nu$ arises upon averaging (27) with the wave functions $\psi_{nlm}$, for which we have

$$H\psi_{nlm} = E_n \psi_{nlm}, \tag{28}$$

$$E_n = a^2 \epsilon_n = -\frac{a^2}{2\left(n + \frac{d-3}{2}\right)^2},$$

$$\mathbf{L}^2 \psi_{nlm} = l(l+d-2)\psi_{nlm}.$$

The matrix element of the left-hand side of Eq. (27) between $\psi_{nlm}$ is equal to zero; therefore, we arrive at the recursion relation

$$0 = 2\nu E_n \left\langle \frac{1}{r^{\nu+1}} \right\rangle - (\nu+1) \times \left[l(l+d-2) + \frac{(d-1)(d-3)}{4}\right] \left\langle \frac{1}{r^{\nu+3}} \right\rangle + a(2\nu+1)\left\langle \frac{1}{r^{\nu+2}} \right\rangle + \frac{\nu(\nu+1)(\nu+2)}{4}\left\langle \frac{1}{r^{\nu+3}} \right\rangle. \tag{29}$$

In the case of $S$-wave states, $l = 0$, and it follows from (29) that

$$\left\langle \frac{1}{r^{\nu+3}} \right\rangle = -\frac{8E_n\nu}{(\nu+1)[\nu(\nu+2) - (d-1)(d-3)]}\left\langle \frac{1}{r^{\nu+1}} \right\rangle - \frac{4a(2\nu+1)}{(\nu+1)[\nu(\nu+2) - (d-1)(d-3)]}\left\langle \frac{1}{r^{\nu+2}} \right\rangle. \tag{30}$$

With the aid of relation (30), we can go over from calculating the matrix elements of $1/r^\nu$ at high negative values of the exponent—in $d = 3$ space, these matrix elements are singular—to calculating the matrix elements of lower negative powers of $r$, explicitly isolating the singular factors $1/\epsilon$ ($d = 3 + 2\epsilon$). In order to illustrate the use of the recursion relation (30), we consider a typical integral in (14),

$$I(\mathbf{p},\mathbf{q}) = \int \frac{d\mathbf{k}}{(2\pi)^d} \frac{(4\pi\alpha)^2(\mathbf{k}^2 - b^2)}{(\mathbf{k}-\mathbf{p})^2(\mathbf{k}-\mathbf{q})^2 \cdot 2\mu}, \quad (31)$$

where we have introduced the factors $(4\pi\alpha)^2$ and $1/2\mu$ to simplify the ensuing transformations, and calculate this integral by two independent methods. In the momentum representation, the Coulomb wave function satisfies Eq. (9) [35]. With the aid of this equation, the expectation value of the integral in (31) can then be reduced to the form

$$\langle I(\mathbf{p},\mathbf{q})\rangle = \left\langle \left(\frac{\mathbf{k}^2 - b^2}{2\mu}\right)^3 \right\rangle \quad (32)$$

$$= \left\langle (\mathbf{k}^6 + 3\mathbf{k}^4 W^2 + 3\mathbf{k}^2 W^4 + W^6)\frac{1}{8\mu^3} \right\rangle,$$

$$W^2 = -b^2.$$

The expectation values of the individual terms in (32) can be immediately found in $d = 3$ space. We have

$$\langle \mathbf{k}^2\rangle = \langle 2\mu(E_n - V_\mathrm{C})\rangle = \frac{(\mu\alpha)^2}{n^2}, \quad (33)$$

$$\langle W^6\rangle = \frac{(\mu\alpha)^6}{n^6},$$

$$\langle \mathbf{k}^4\rangle = \langle (E_n - V_\mathrm{C})(E_n - V_\mathrm{C})4\mu^2\rangle \quad (34)$$

$$= (\mu\alpha)^4 \left[-\frac{3}{n^4} + \frac{8}{n^3}\right].$$

In averaging $\mathbf{k}^6$, there arises a different situation; that is,

$$\left\langle \frac{\mathbf{k}^6}{8\mu^3} \right\rangle = \left\langle (E_n - V_\mathrm{C})\frac{\mathbf{k}^2}{2\mu}(E_n - V_\mathrm{C}) \right\rangle \quad (35)$$

$$= \langle E_n^2(E_n - V_\mathrm{C})\rangle - 2\langle E_n(E_n - V_\mathrm{C})V_\mathrm{C}\rangle$$

$$- \left\langle \frac{W^2}{2\mu} V_\mathrm{C}^2 \right\rangle - \langle V_\mathrm{C}^3\rangle + \left\langle \frac{\alpha^2}{2r^4} \right\rangle.$$

It follows that, in (35), we have two matrix elements that are divergent in 3-dimensional space, those proportional to $\langle 1/r^3\rangle$ and $\langle 1/r^4\rangle$. By using the recursion relation (30), we can show that, in the $d = 3$ case, the singular terms in (35) cancel. As a result, we arrive at the following finite result:

$$\left\langle \frac{\mathbf{k}^6}{8\mu^3} \right\rangle = \mu^3\alpha^6 \left[\frac{5}{8n^6} - \frac{7}{3n^5} - \frac{8}{3n^3}\right]. \quad (36)$$

Upon the substitution of (33), (34), and (36) into expression (32) and subsequent summation, we obtain the sought integral

$$\langle I(\mathbf{p},\mathbf{q})\rangle = \mu^3\alpha^6 \left[\frac{2}{3n^5} - \frac{8}{3n^3}\right]. \quad (37)$$

Let us consider an alternative method for evaluating the integral in (31). We perform integration in (31) by using the dimensional-regularization procedure. Going over to the limit $d \to 3$, we find the following contribution to the quasipotential in momentum space:

$$I(\mathbf{p},\mathbf{q}) = \frac{(4\pi\alpha)^2}{2\mu}\left[\frac{\mathbf{p}^2 - b^2}{8t} - \frac{t}{16}\right], \quad \mathbf{t} = (\mathbf{p} - \mathbf{q}). \quad (38)$$

As in deriving expression (21), we further calculate the Fourier transform of (38) in $d$-dimensional space. The result is

$$I(r) = \frac{\alpha^2}{2\mu}\left[(\mathbf{p}^2 - b^2)\frac{1}{r^2} + \frac{1}{r^4}\right]. \quad (39)$$

The expectation values of the individual terms in this expression can be simplified by using the equation for the wave function and the recursion relation (30). As a result, we obtain

$$\left\langle \frac{(\mathbf{p}^2 - b^2)}{2\mu}\frac{\alpha^2}{r^2} \right\rangle = \left\langle \frac{\alpha^3}{r^3} \right\rangle = \mu^3\alpha^6 \quad (40)$$

$$\times \left[\frac{2}{\epsilon n^3} - \frac{6}{n^4} - \frac{6}{n^3}\right],$$

$$\left\langle \frac{\alpha^2}{2\mu r^4} \right\rangle = \frac{\mu^3\alpha^6}{2}\left[-\frac{4}{\epsilon n^3} + \frac{20}{3n^3} + \frac{12}{n^4} + \frac{4}{3n^5}\right], \quad (41)$$

where the contributions of order $1/\epsilon$ in the last two divergent matrix elements differ only in sign. As a result, the sum of expressions (40) and (41) appears to be finite and coincident with (37). Both methods for calculating integrals belonging to the same type as $I(\mathbf{p},\mathbf{q})$ were used in this study to determine the $(Z\alpha)^6 m_1/m_2$ contributions to the spectrum of the muonium atom. Upon averaging (14), the sum of all contributions of this order in the potential and soft regions assumes the form

$$\langle V_{2\gamma}\rangle = \frac{m_1(Z\alpha)^6}{m_2}\left[-\frac{37}{9n^3} - \frac{1}{6n^4} + \frac{7}{9n^5}\right]. \quad (42)$$

## 4. CORRECTIONS OF ORDER $(Z\alpha)^7$ TO $S$-WAVE ENERGY LEVEL

As was mentioned above, the main contribution of two-photon amplitudes to the energy spectrum is of order $\alpha^5$. In the hard-momentum region,

**Table 2.** Results obtained by calculating basic integrals of the type in (48): $\int \frac{d^4k}{16i\pi^2} \frac{S(k)}{(k^2)^\alpha (k^2+2k_0E_1)^\beta (k^2-2k_0E_2)^\gamma}$

| $S(k)$ | 1 | $k_0$ | $\mathbf{k}^2$ | $k_0^2$ |
|---|---|---|---|---|
| $\alpha=2,\beta=1,\gamma=1$ | $\frac{E_1E_2-E_1^2-E_2^2}{96E_1^3E_2^3}$ | $\frac{E_1-E_2}{32E_1^2E_2^2}$ | $\frac{1}{32E_1E_2}$ | – |
| $\alpha=2,\beta=2,\gamma=1$ | $\frac{2E_1^2E_2-3E_1E_2^2-E_1^3+4E_2^3}{960E_1^5E_2^4}$ | $\frac{2E_1E_2-E_1^2-3E_2^2}{192E_1^4E_2^3}$ | – | $\frac{E_1^2-E_2^2-E_1E_2}{128E_1^3E_2^2(E_1+E_2)}$ |
| $\alpha=3,\beta=1,\gamma=1$ | – | $\frac{(E_1^2+E_2^2)(E_1-E_2)}{192E_1^4E_2^4}$ | $\frac{E_1^2-E_1E_2+E_2^2}{144E_1^3E_2^3}$ | $\frac{E_1^2-E_1E_2+E_2^2}{64E_1^3E_2^3}$ |

the diagrams in Fig. 1 also make higher order contributions—those of order $(Z\alpha)^7$. In order to calculate these corrections to the $S$-wave levels of the bound state, we average the two-photon amplitudes over the particle spins. As a result, the quasipotentials corresponding to the amplitudes associated with the diagrams in Figs. 1*a* and 1*b* assume the form

$$V_{2\gamma}^{(a)}(\mathbf{p},\mathbf{q}) = \frac{i(Z\alpha)^2}{\pi^2} \times \int \frac{g_1(k,m_1,m_2)d^4k}{(k-p)^2(k-q)^2D_1(k)D_2(-k)}, \tag{43}$$

$$g_1(k,m_1,m_2) = 16m_1m_2 - 8m_1k_0 + 8m_2k_0 - 4W^2\left(\frac{m_1}{m_2}+\frac{m_2}{m_1}\right) + 8k_0W^2\left(\frac{1}{m_1}-\frac{1}{m_2}\right) - 16{k_0}^2 + 8\mathbf{k}^2,$$

$$V_{2\gamma}^{(b)}(\mathbf{p},\mathbf{q}) = \frac{i(Z\alpha)^2}{\pi^2} \times \int \frac{g_2(k,m_1,m_2)d^4k}{(k-p)^2(k-q)^2D_1(k)D_2(-k+p+q)}, \tag{44}$$

$$g_2(k,m_1,m_2) = 16m_1m_2 + 8m_1k_0 + 8m_2k_0 - 4W^2\left(\frac{m_1}{m_2}+\frac{m_2}{m_1}\right) - 8k_0W^2\left(\frac{1}{m_1}-\frac{1}{m_2}\right) + 16{k_0}^2 - 8\mathbf{k}^2 + 8\mathbf{k}\cdot\mathbf{p} + 8\mathbf{k}\cdot\mathbf{q},$$

$$D_{1,2}(k) = k^2 + 2E_{1,2}k_0 - W^2. \tag{45}$$

If $k_0 \sim \mu$ and $|\mathbf{k}| \sim \mu$, the expansions of the electron (muon) and photon propagators are given by

$$\frac{1}{D_{1,2}(k)} = \sum_{n=0}^{\infty} \frac{(W^2)^n}{(k^2+2E_{1,2}k_0)^{n+1}}, \tag{46}$$

$$\frac{1}{(k-p)^2} \approx \frac{1}{k^2} + \frac{\mathbf{p}^2 - 2\mathbf{p}\cdot\mathbf{k}}{(k^2)^2} + \frac{4(\mathbf{k}\cdot\mathbf{p})^2}{(k^2)^3}, \tag{47}$$

where, in the last expression, we have retained only terms of the required order. Substituting expressions (46) and (47) into (43) and (44), we can see that the hard component of the quasipotential $V_{2\gamma}$ is determined by the sum of integrals of the form

$$K(\mathbf{p},\mathbf{q}) = \int \frac{d^4k}{16i\pi^2} \frac{S(k)}{(k^2)^\alpha (k^2+2k_0E_1)^\beta (k^2\pm 2k_0E_2)^\gamma}, \tag{48}$$

where $S(k)$ is a power-law function of $k_0$ or $\mathbf{k}^2$. In calculating integrals of the form (48), we have employed the dimensional-regularization procedure. The results of the calculation are quoted in Table 2 (only the finite parts of the final expressions are given there).

In the two-photon quasipotential, the spin-independent component obtained by summing all terms in (43) and (44) upon integration in (48) involves a term of the form $(Z\alpha)^2\mathbf{p}^2F(m_1,m_2)$. The contribution of this term to the energy spectrum can be obtained by using the dimensional-regularization procedure and Eq. (9) [15, 31]. This yields

$$\langle \mathbf{p}^2 \rangle = \psi_M(0) \int \frac{d\mathbf{p}}{(2\pi)^d} \mathbf{p}^2 \psi_M(\mathbf{p}) = b^2 |\psi_M(0)|^2. \tag{49}$$

As a result, the exchange two-photon diagrams lead, in the hard-momentum region, to the following correction of order $(Z\alpha)^7$ to the positronium spectrum:

$$\Delta B_n(\mathrm{Ps}) = -\frac{(Z\alpha)^7}{\pi n^5} m_1 \frac{1129}{720}. \tag{50}$$

In the case of the muonium atom, one can perform an additional expansion in powers of $m_1/m_2$. Retaining linear corrections in $m_1/m_2$, we obtain

$$\Delta B_n(\mathrm{Mu}) = -\frac{(Z\alpha)^7}{\pi n^5} m_1 \left(\frac{16}{5} + 20\frac{m_1}{m_2}\right). \tag{51}$$

Here, we have calculated only power-law corrections of order $(Z\alpha)^7$. Logarithmic terms of order $\ln(m_{1,2}/\lambda)$ (where $\lambda$ is the mass parameter of dimensional regularization) were systematically discarded, although they are present in the intermediate expressions (48).

In the soft-momentum region, the general structure of the quasipotential that makes a contribution of order $(Z\alpha)^7$ is similar to that in (20). In the case of the muonium atom, we can, by using the additional expansion in $m_1/m_2$, represent the corresponding quasipotential in the form

$$V_{2\gamma}^{\rm soft}(\mathbf{p},\mathbf{q}) = \frac{i(Z\alpha)^2}{4\pi^2 m_1^3 m_2} \times \int \frac{d^4k}{(k-p)^2(k-q)^2k_0^2}\left\{\frac{(k^2-W^2)^4}{k_0^4} + \frac{(k^2-W^2)^3(k^2+2\mathbf{k}(\mathbf{p}+\mathbf{q})-\mathbf{t}^2-W^2)}{k_0^4} - \frac{3(k^2-W^2)^3}{k_0^2} + 8W^2(k^2-W^2) - \frac{(k^2-W^2)^2(k^2+2\mathbf{k}(\mathbf{p}+\mathbf{q})-\mathbf{t}^2-W^2)}{k_0^2} - \frac{W^2(k^2-W^2)(k^2+2\mathbf{k}(\mathbf{p}+\mathbf{q})-\mathbf{t}^2-W^2)}{k_0^2} - \frac{W^2(k^2-W^2)^2}{k_0^2} + \frac{4(2k_0^2-\mathbf{k}^2)(k^2-W^2)^2}{k_0^2} + \frac{2\mathbf{k}(\mathbf{p}+\mathbf{q})(k^2-W^2)^2}{k_0^2}\right\}. \quad (52)$$

The residues at the photon poles determine the integral with respect to $k_0$. Integration with respect to $\mathbf{k}$ can be performed by means of the dimensional-regularization procedure. As a result, the quasipotential (52) in the momentum representation takes the form

$$V_{2\gamma}^{\rm soft}(\mathbf{p},\mathbf{q}) = \frac{(Z\alpha)^2}{2m_1^3m_2}\left\{\frac{13}{4}\mathbf{p}^2 - \frac{W^2}{6} - \frac{(17\mathbf{p}^4-9W^4)}{2t^2} + \frac{8\mathbf{p}^6-4W^6+3\mathbf{p}^4(2\mathbf{q}^2+3W^2)+3\mathbf{p}^2W^2(\mathbf{q}^2-2W^2)}{3t^4} + \frac{16W^8-29\mathbf{p}^8+16\mathbf{p}^6(\mathbf{q}^2-2W^2)+3\mathbf{p}^4(12W^4-\mathbf{q}^4)+4W^4\mathbf{p}^2(8W^2-9\mathbf{q}^2)}{12t^6} + \frac{(44\mathbf{p}^2-5W^2)}{8}\ln(t/W) + \frac{14W^4-45\mathbf{p}^4+38\mathbf{p}^2\mathbf{q}^2+26W^2\mathbf{p}^2}{4t^2}\ln(t/W) + \frac{28W^6-8\mathbf{p}^6-53W^2\mathbf{p}^4+W^2\mathbf{p}^2\mathbf{q}^2-16W^4\mathbf{p}^2}{4t^4}\ln(t/W) + \frac{23\mathbf{p}^8-16W^8+16\mathbf{p}^6(2W^2-\mathbf{q}^2)+\mathbf{p}^4(9\mathbf{q}^4-12W^4)+4W^4\mathbf{p}^2(3\mathbf{q}^2-8W^2)}{4t^6}\ln(t/W)\right\}. \quad (53)$$

The singularity of the individual terms in the quasipotential (53) becomes stronger. In calculating the energy spectrum in the coordinate representation, there arise expectation values of higher negative powers of $1/r$ than in the case of $(Z\alpha)^6$ contributions: $\langle 1/r^3\rangle$, $\langle 1/r^4\rangle$, and $\langle 1/r^5\rangle$. These matrix elements were transformed with the aid of relations (24)–(26), (30), and (A.4)–(A.7) within the FeynCalc package for the Mathematica system [36, 37]. As a result, the $(Z\alpha)^7$ corrections to the $S$-wave levels of the muonium (hydrogen) atom reduce to the form

$$\Delta B_n^{\rm soft} = \frac{(Z\alpha)^7\mu^5}{m_1^3m_2\pi n^3}\left\{\frac{63565}{288} - \frac{8675}{72}C - \frac{38}{3}\pi^2 - \frac{2521}{72}\psi(n) + 38\psi'(n) + \frac{1}{n}\left[\frac{605147}{9216} - \frac{148257}{1024}C - \frac{360673}{6144}\psi(n)\right] + \frac{1}{n^2}\left[\frac{3698203}{36864} + \frac{7157}{6144}C + \frac{10757}{12288}\psi(n)\right] + \frac{1}{n^3}\left[-\frac{81}{64} + \frac{47}{16}C + \frac{47}{16}\psi(n)\right]\right\}, \quad (54)$$

where $\psi(z) = d\ln\Gamma(z)/dz$ and $C = 0.5772156649\ldots$ is the Euler constant.

## 5. DISCUSSION OF THE RESULTS

The calculation of high-order perturbative corrections in $\alpha$ to the energy spectra of hydrogen-like atoms is presently a very important problem in view of the improvement of accuracy in measuring

the energy levels of extremely simple atomic systems. Even for one-loop Feynman amplitudes, such calculations become more involved with increasing power of $\alpha$. The majority of computer methods for calculating Feynman diagrams were developed for on-shell particles. In the case of bound states, one has to expand the relevant amplitudes in a Taylor series in order to isolate contributions of the required order in $\alpha$ and $m_1/m_2$. In this study, the application of such expansions was illustrated in calculating corrections of orders $(Z\alpha)^6 m_1/m_2$ and $(Z\alpha)^7$. The dimensional-regularization procedure is the most important tool that makes it possible to use Taylor expansions. This procedure enables one to deal with ultraviolet and infrared divergences simultaneously. Apart from this, the dimensional-regularization procedure permits calculating the Fourier transforms of quasipotentials obtained in momentum space that have a high degree of singularity. Individual terms of the quasipotential in the coordinate representation that were obtained in this study also lead to expressions in the energy spectrum that are divergent for $S$-wave states [see (39), (53)]. In view of this, we formulated the recursion relations (30) in $d$-dimensional coordinate space that make it possible to take correctly into account all coefficients in divergent terms. By using expression (42) and the results obtained in [14], we can represent the total contribution of order $(Z\alpha)^6 m_1^2/m_2$ for an arbitrary value of $n$ as follows (in our calculations, we took into account the spin-dependent part of the quasipotential):

$$\Delta B_n^{\rm tot} = \left\{\frac{5}{2}\ln 2 - \frac{151}{36} - \frac{3}{n} + \frac{1}{2n^2} \right. \tag{55}$$
$$\left. + \frac{547}{72n^3} - \frac{7}{2}(-1)^n (C + \psi(n) - 1)\right\} \frac{m_1^2 (Z\alpha)^6}{m_2 n^3}.$$

It should be emphasized that our recoil correction of order $(Z\alpha)^6 m_1/m_2$ in (55) differs from the contributions of the same order to the Lamb shift in the hydrogen atom that were obtained in [10–13]. The quasipotential for the $S$-wave states of the hydrogenlike atom has the form

$$V(r) = V_1(r) + (\mathbf{s}_1 \cdot \mathbf{s}_2) V_2(r); \tag{56}$$

that is, it involves a component dependent on the particle spins $\mathbf{s}_1$ and $\mathbf{s}_2$ and a spin-independent term. The contribution to the Lamb shift is determined by the first term on the right-hand side of (56). But in our calculations, we took into account both the contribution induced by the first term $V_1(r)$ and the contribution of the second, spin-dependent, component for triplet energy levels. Therefore, the results that were obtained here supplement the results of the calculations performed by other authors for the recoil effects of order $(Z\alpha)^6 m_1/m_2$ in the Lamb shift of extremely simple atomic systems. The numerical values of the contribution in (55) to the $2^3S_1$–$1^3S_1$ fine-structure intervals in the muonium and hydrogen atoms are 0.045 MHz and 5.116 kHz, respectively. The methods used in the present study to calculate relevant Feynman amplitudes enable one to calculate power-law corrections of higher order in $\alpha$. The numerical values of the $(Z\alpha)^7$ contributions (50), (51), and (54), which were obtained in the hard- and soft-momentum regions for the "large"-structure interval $(2S$–$1S)$ in the muonium, hydrogen, and positronium atoms, are 0.092, 0.130, and 0.066 MHz, respectively.

## ACKNOWLEDGMENTS

We are grateful to A.S. Yelkhovsky for an enlightening discussion on the study reported in [15].

This work was financially supported by the program Universities of Russia—Basic Research (project no. UR.01.02.016) and by the Ministry for Higher Education of the Russian Federation (project no. EOO-3.3-45).

## APPENDIX

### *Matrix Elements of Potentials in the Coordinate Representation*

In order to calculate matrix elements of the form $\left\langle \frac{1}{r^m} \right\rangle$ or $\left\langle \frac{\ln r}{r^m} \right\rangle$, it is necessary to know radial wave functions in $d$-dimensional space and to use the recursion relation (30). The radial wave function satisfies the equation

$$R'' + \frac{d-1}{\rho} R' + \left( -\frac{1}{4} + \frac{B}{\sqrt{A}} \frac{1}{\rho} \right. \tag{A.1}$$
$$\left. - \frac{l(l+d-2)}{\rho^2} \right) R = 0,$$

where the dimensionless variable is given by $\rho = 2r\sqrt{A}$, $B = \mu Z\alpha$, and $A = -2\mu E$. In the case of $S$-wave states, the normalized solution to this equation—it is sought by a standard method—can be represented in the form [this solution leads to spectrum in (23)]

$$R_{n,l=0}(r) \tag{A.2}$$
$$= \sqrt{\frac{2^d W^d \Gamma(n)}{(2n+d-3)\Gamma(n+d-2)}} e^{-Wr} L_{n-1}^{d-2}(2Wr),$$
$$W = \frac{\mu Z\alpha}{n + \dfrac{d-3}{2}},$$

where

$$L_n^\lambda(z) = \frac{1}{n!} z^{-\lambda} e^z \frac{d^n}{dz^n}\left(e^{-z} z^{\lambda+n}\right) \qquad \text{(A.3)}$$

are Laguerre polynomials.

Apart from the matrix elements of power-law potentials, there arise the expectation values of operators involving $\ln\rho$: $\left\langle \frac{\ln\rho}{\rho^m} \right\rangle$. By using (30), we can obtain the following recursion relations for matrix elements of this type in $d$-dimensional space:

$$\left\langle \frac{\ln\rho}{\rho^3} \right\rangle = -\frac{8\epsilon_n}{(d-1)(d-3)} \left\langle \frac{1}{\rho} \right\rangle \qquad \text{(A.4)}$$
$$-\frac{4(d^2-4d+5)}{(d-3)^2(d-1)^2} \left\langle \frac{1}{\rho^2} \right\rangle + \frac{4}{(d-1)(d-3)} \left\langle \frac{\ln\rho}{\rho^2} \right\rangle,$$

$$\left\langle \frac{\ln\rho}{\rho^4} \right\rangle = -\frac{d^2-4d+24}{d^2(d-4)^2} \left\langle \frac{1}{\rho^3} \right\rangle \qquad \text{(A.5)}$$
$$+\frac{6}{d(d-4)} \left\langle \frac{\ln\rho}{\rho^3} \right\rangle - \frac{2\epsilon_n(d^2-4d+8)}{(d-4)^2 d^2} \left\langle \frac{1}{\rho^2} \right\rangle$$
$$+\frac{4\epsilon_n}{d(d-4)} \left\langle \frac{\ln\rho}{\rho^2} \right\rangle.$$

The expectation values $\left\langle \frac{\ln\rho}{\rho^2} \right\rangle$ and $\left\langle \frac{\ln\rho}{\rho} \right\rangle$ are finite in $d = 3$ space; nevertheless, we must calculate them with the aid of the wave functions (A.2), retaining terms proportional to $\epsilon = \frac{d-3}{2}$ in the limit $d \to 3$. The results are

$$\left\langle \frac{\ln\rho}{\rho} \right\rangle = \frac{\psi(n+d-2)}{(2n+d-3)}, \qquad \text{(A.6)}$$

$$\left\langle \frac{\ln\rho}{\rho^2} \right\rangle = \frac{1}{(d-2)(2n+d-3)} \qquad \text{(A.7)}$$
$$\times \left[\psi(d-1) + \psi(d-2) - \psi(n+d-3)\right].$$

We also note that, in $d$-dimensional space, the expectation values of $1/r^2$ and $1/r$ can be obtained by representing the Hamiltonian in the form

$$H = -\frac{1}{2}\left[\frac{\partial^2}{\partial r^2} + \frac{(d-1)}{r}\frac{\partial}{\partial r}\right] \qquad \text{(A.8)}$$
$$+\frac{1}{2r^2} l(l+d-2) - \frac{a}{r}.$$

By using relation (23) and formula (A.8), we arrive at

$$\left\langle \frac{1}{r^2} \right\rangle^d = \frac{2}{2l+d-2} \left\langle \frac{\partial H}{\partial l} \right\rangle \qquad \text{(A.9)}$$
$$= \frac{2}{(2l+d-2)} \frac{a^2}{\left(n+\frac{d-3}{2}\right)^3},$$

$$\left\langle \frac{1}{r} \right\rangle^d = \frac{a}{\left(n+\frac{d-3}{2}\right)^2}. \qquad \text{(A.10)}$$

## REFERENCES


1. P. J. Mohr and B. N. Taylor, Rev. Mod. Phys. **72**, 351 (2000).
2. W. Liu *et al.*, Phys. Rev. Lett. **82**, 711 (1999).
3. V. Meyer, S. N. Bagayev, P. E. G. Baird, *et al.*, Phys. Rev. Lett. **84**, 1136 (2000).
4. M. S. Fee *et al.*, Phys. Rev. Lett. **70**, 1397 (1993).
5. Th. Udem, A. Huber, B. Gross, *et al.*, Phys. Rev. Lett. **79**, 2646 (1997).
6. W. E. Caswell and G. P. Lepage, Phys. Lett. B **167B**, 437 (1986).
7. P. Labelle, Phys. Rev. D **58**, 093013 (1998).
8. M. Nio, in *Quantum Electrodynamics and Physics of the Vacuum,* Ed. by G. Cantatore; AIP Conf. Proc. **564**, 178 (2001).
9. M. I. Eides, H. Grotch, and V. A. Shelyuto, Phys. Rep. **342**, 62 (2001).
10. M. I. Eides and H. Grotch, Phys. Rev. A **55**, 3351 (1997).
11. V. M. Shabaev, Teor. Mat. Fiz. **63**, 394 (1985).
12. V. M. Shabaev, Phys. Rev. A **57**, 59 (1998).
13. A. S. Elkhovskiĭ, Zh. Éksp. Teor. Fiz. **110**, 431 (1996) [JETP **83**, 230 (1996)]; A. S. Yelkhovsky, Zh. Éksp. Teor. Fiz. **113**, 865 (1998) [JETP **86**, 472 (1998)].
14. A. P. Martynenko and R. N. Faustov, Zh. Éksp. Teor. Fiz. **115**, 1221 (1999) [JETP **88**, 672 (1999)].
15. A. Czarnecki, K. Melnikov, and A. Yelkhovsky, Phys. Rev. A **59**, 4316 (1999).
16. G. S. Adkins and J. Sapirstein, Phys. Rev. A **58**, 3552 (1998).
17. G. S. Adkins, R. N. Fell, and P. M. Mitrikov, Phys. Rev. Lett. **79**, 3383 (1997).
18. K. Pachucki and S. G. Karshenboim, Phys. Rev. Lett. **80**, 2101 (1998).
19. A. P. Burichenko, hep-ph/0004063.
20. K. Melnikov and A. S. Yelkhovsky, Phys. Lett. B **458**, 143 (1999).
21. B. A. Kniehl and A. A. Penin, Preprint DESY No. 00-123 (Hamburg, 2000).
22. S. G. Karshenboim, Zh. Éksp. Teor. Fiz. **103**, 1105 (1993) [JETP **76**, 541 (1993)].
23. K. Melnikov and A. Yelkhovsky, Phys. Rev. Lett. **86**, 1498 (2001).
24. D. R. Yennie, Preprint CLNS No. 88/857 (Cornell Univ., 1988).
25. G. T. Bodwin, D. R. Yennie, and M. A. Gregorio, Rev. Mod. Phys. **57**, 723 (1985).
26. A. Czarnecki and V. A. Smirnov, Phys. Lett. B **394**, 211 (1997).
27. F. V. Tkachov, Phys. Lett. B **412**, 350 (1997).
28. M. Beneke and V. A. Smirnov, Nucl. Phys. B **522**, 321 (1998).

29. V. S. Popov, in *Proceedings of the International School in Theoretical Physics "High Energy Physics and Elementary Particle Theory"* (Naukova Dumka, Kiev, 1967), p. 702.
30. S. P. Alliluev, Zh. Éksp. Teor. Fiz. **33**, 200 (1958) [Sov. Phys. JETP **6**, 156 (1958)].
31. P. Ramon, *Field Theory* (Benjamin, Reading, 1981; Mir, Moscow, 1984).
32. N. Ya. Vilenkin, *Special Functions and the Theory of Group Representations* (Nauka, Moscow, 1991; Am. Math. Soc., Providence, R.I., 1968, transl. 1st ed.).
33. A. M. Perelomov and V. S. Popov, Zh. Éksp. Teor. Fiz. **50**, 179 (1966) [Sov. Phys. JETP **23**, 118 (1966)].
34. A. Bohm, *Quantum Mechanics: Foundations and Applications* (Springer, Heidelberg, 1986; Mir, Moscow, 1990).
35. A. P. Martynenko and R. N. Faustov, Teor. Mat. Fiz. **64**, 765 (1985).
36. R. Mertig, *FeynCalc 4.0 Reference Guide* (2001); http://www.mertig.com.
37. S. Wolfram, *Mathematica: A System for Doing Mathematics by Computer* (Addison-Wesley, Reading, 1988).

*Translated by A. Isaakyan*

*Physics of Atomic Nuclei, Vol. 66, No. 9, 2003, pp. 1730–1736. Translated from Yadernaya Fizika, Vol. 66, No. 9, 2003, pp. 1778–1784.*


**ELEMENTARY PARTICLES AND FIELDS**
**Theory**

# Production of $\Omega_{scb}$ Baryons in Electron–Positron Collisions

**S. P. Baranov*** **and V. L. Slad****

*Lebedev Institute of Physics, Russian Academy of Sciences, Leninskiĭ pr. 53, Moscow, 117924 Russia*

Received July 5, 2002; in final form, November 19, 2002

**Abstract**—The total and differential cross sections for the production of $\Omega_{scb}$ baryons in electron–positron collisions are calculated at the $Z$-boson pole. © *2003 MAIK "Nauka/Interperiodica".*

## 1. INTRODUCTION

Baryons involving two or three heavy quarks $(c, b)$ have not yet been observed experimentally. Theoretical investigations into the mass spectra of hadrons that contain two or more heavy quarks, the cross sections for their production in various processes, and their lifetimes and decay modes form a rather new line of research in particle physics. For an overview of these investigations, the interested reader is referred to [1]. Calculations presented in the literature that are aimed at determining the production cross sections for baryons featuring two heavy quarks either rely on the fragmentation approach [2], or treat the production of unbound four-quark states in a bounded phase space [3], or consider (as is done in the majority of the most recent studies on this subject) the production of the relevant heavy diquark [4–9]. In particular, the production of doubly heavy baryons in electron–positron collisions was analyzed in [3, 9]. No attention has so far been given to the production of triply heavy baryons.

Investigation of the mechanisms responsible for the production of multiply heavy hadrons is of interest from the theoretical point of view since this provides the possibility of further verifying QCD (more precisely, of obtaining deeper insight into this theory). This involves testing both its perturbative aspect, which is used to describe the simultaneous production of a few quark pairs, and QCD-inspired nonperturbative models of bound states. We recall that, even in apparently obvious cases, the results of QCD calculations often unexpectedly prove to be at odds with experimental data, as was, for example, in the hadronic production of $J/\psi$ particles. On the other hand, a derivation of theoretical cross-section estimates is of importance from the point of view of applications to searches for such particles and investigation into their properties. The presence of two or more heavy quarks in a hadron substantially affects the properties of its weak decays. At the same time, the reliability of theoretical predictions is higher for such hadrons, and this makes it possible to test model concepts more thoroughly.

In the present study, we reveal some features of $\Omega_{scb}$-baryon production in electron–positron annihilation. The choice of a process where the initial state is purely leptonic was motivated, on one hand, by the fact that the relevant calculations are simpler here than in the case of hadronic production and, on the other hand, by the fact that the case of leptonic production offers a number of advantages in what is concerned with a possible experimental observation, which include favorable background conditions and a precisely known initial energy.

At the quark level, the subprocess $e^-e^+ \to s\bar{s}c\bar{c}b\bar{b}$, which is of order $\alpha^2\alpha_s^4$ in conventional perturbation theory, is associated with the process being considered. In evaluating the square of the relevant matrix element, use is made of the method that was proposed in [10] and which is referred to as the method of orthogonal amplitudes (previously, this method was employed, for example, in [7, 8]). The fusion of the product $s$, $c$, and $b$ quarks into a $\Omega_{scb}$ baryon is described within the standard nonrelativistic approximation [11–13]. A detailed account of the technical facet of our calculations is given in Section 2. The numerical results obtained on the basis of these calculations are discussed in Section 3.

## 2. COMPUTATIONAL PROCEDURE

Our calculations are based on considering the partonic process

$$e^-(p_{e^-}) + e^+(p_{e^+}) \to s(p_1,\xi) + c(p_2,\zeta) + b(p_3,\chi) + \bar{s}(p_4,\xi') + \bar{c}(p_5,\zeta') + \bar{b}(p_6,\chi'), \quad (1)$$

where the parentheses referring to the colliding particles enclose their 4-momenta, while the parentheses

*e-mail: baranov@sci.lebedev.ru
**e-mail: vslad@sci.lebedev.ru

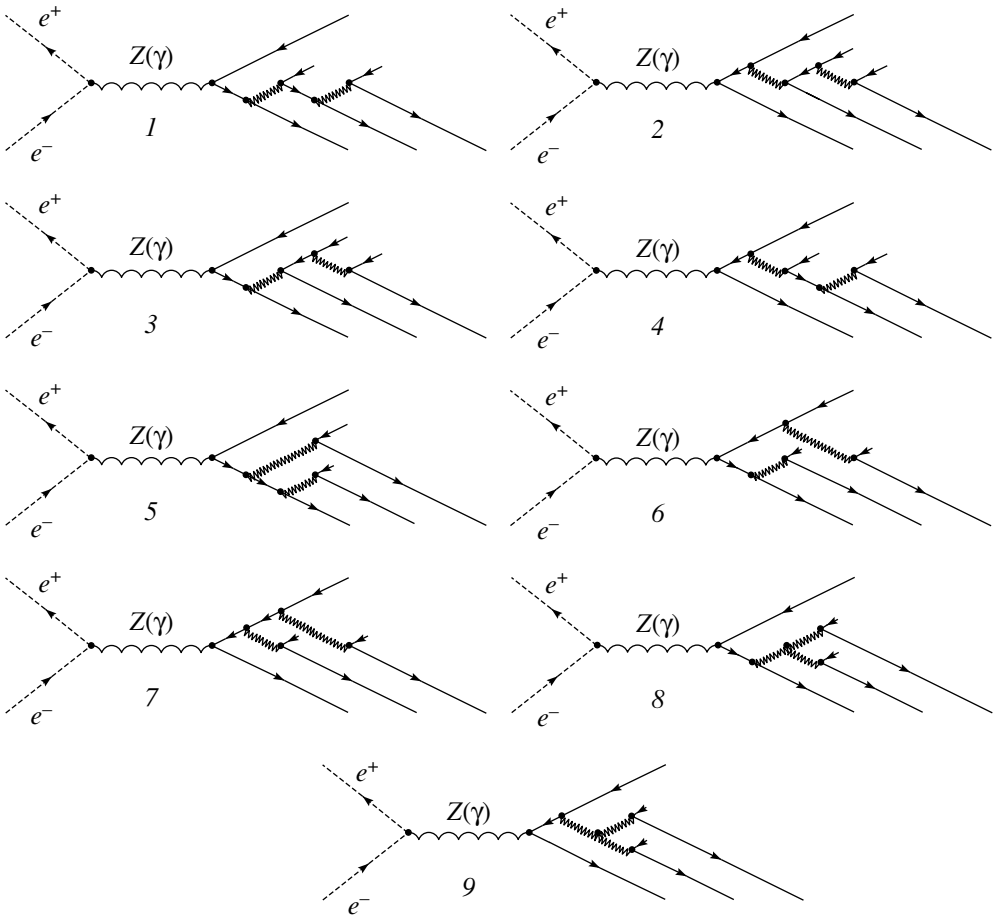


**Fig. 1.** Basic Feynman diagrams for the process $e^- + e^+ \to s + c + b + \bar{s} + \bar{c} + \bar{b}$.

referring to the product quarks and antiquarks enclose their 4-momenta and color indices. As usual, we disregard Feynman diagrams featuring the electroweak interaction of the quarks involved. In other words, we consider only those diagrams where the interaction between the quarks is mediated by gluons. For this class of diagrams, Fig. 1 shows nine basic diagrams in which quark and gluon lines are connected in different ways. Here, six (three) nonequivalent dispositions of the $s\bar{s}$, $c\bar{c}$, and $b\bar{b}$ lines correspond to each of the first seven (last two) diagrams in Fig. 1—that is, diagrams *1–7* (diagrams *8* and *9*). Considering that the annihilation channel may involve either a photon or a $Z$ boson, we conclude that the total number of diagrams in question is 96.

The matrix element for the process in (1) can be represented in the form

$$\mathcal{M} = \frac{g_s^4 g^2}{24\cos^2\theta_W(s - M_Z^2 + iM_Z\Gamma_Z)}\varepsilon^{\xi\zeta\chi}\varepsilon^{\xi'\zeta'\chi'} \quad (2)$$
$$\times A^Z_{\xi\xi'\zeta\zeta'\chi\chi'} - \frac{g_s^4 e^2}{6s}\varepsilon^{\xi\zeta\chi}\varepsilon^{\xi'\zeta'\chi'}A^\gamma_{\xi\xi'\zeta\zeta'\chi\chi'},$$

where

$$A^Z_{\xi\xi'\zeta\zeta'\chi\chi'} = B^{s\bar{s}c\bar{c}b\bar{b}}_{\xi\xi'\zeta\zeta'\chi\chi'} + B^{s\bar{s}b\bar{b}c\bar{c}}_{\xi\xi'\chi\chi'\zeta\zeta'} \quad (3)$$
$$+ B^{c\bar{c}s\bar{s}b\bar{b}}_{\zeta\zeta'\xi\xi'\chi\chi'} + B^{c\bar{c}b\bar{b}s\bar{s}}_{\zeta\zeta'\chi\chi'\xi\xi'} + B^{b\bar{b}s\bar{s}c\bar{c}}_{\chi\chi'\xi\xi'\zeta\zeta'} + B^{b\bar{b}c\bar{c}s\bar{s}}_{\chi\chi'\zeta\zeta'\xi\xi'},$$

$$B^{s\bar{s}c\bar{c}b\bar{b}}_{\xi\xi'\zeta\zeta'\chi\chi'} = \Big\{[(p_2 + p_1 + p_4)^2 - m_c^2]^{-1} \quad (4)$$
$$\times [(p_{e^+} + p_{e^-} - p_6)^2 - m_b^2]^{-1}(p_1 + p_4)^{-2}$$
$$\times (p_1 + p_2 + p_4 + p_5)^{-2}\bar{u}(\mathbf{p}_2)T^a_{\zeta l}T^b_{l\zeta'}\gamma^\nu(\hat{p}_2 + \hat{p}_1$$
$$+ \hat{p}_4 + m_c)\gamma_\delta v(-\mathbf{p}_5)\bar{u}(\mathbf{p}_3)T^b_{\chi\chi'}\gamma^\delta(\hat{p}_{e^+} + \hat{p}_{e^-}$$
$$- \hat{p}_6 + m_b)\gamma_\varepsilon(g_V^b - g_A^b\gamma_5)v(-\mathbf{p}_6) + [(p_5$$
$$+ p_1 + p_4)^2 - m_c^2]^{-1}[(p_{e^+} + p_{e^-} - p_3)^2 - m_b^2]^{-1}$$
$$\times (p_1 + p_4)^{-2}(p_1 + p_2 + p_4 + p_5)^{-2}$$
$$\times \bar{u}(\mathbf{p}_2)T^b_{\zeta l}T^a_{l\zeta'}\gamma_\delta(-\hat{p}_5 - \hat{p}_1 - \hat{p}_4 + m_c)\gamma^\nu$$
$$\times v(-\mathbf{p}_5)\bar{u}(\mathbf{p}_3)T^b_{\chi\chi'}\gamma_\varepsilon(-\hat{p}_{e^+} - \hat{p}_{e^-}$$
$$+ \hat{p}_3 + m_b)\gamma^\delta(g_V^b - g_A^b\gamma_5)v(-\mathbf{p}_6) + [(p_5$$
$$+ p_1 + p_4)^2 - m_c^2]^{-1}[(p_{e^+} + p_{e^-} - p_6)^2 - m_b^2]^{-1}$$
$$\times (p_1 + p_4)^{-2}(p_1 + p_2 + p_4 + p_5)^{-2}$$

$$\times \bar{u}(\mathbf{p}_2)T^b_{\zeta l}T^a_{l\zeta'}\gamma_\delta(-\hat{p}_5-\hat{p}_1-\hat{p}_4+m_c)\gamma^\nu$$
$$\times v(-\mathbf{p}_5)\bar{u}(\mathbf{p}_3)T^b_{\chi\chi'}\gamma^\delta(\hat{p}_{e^+}+\hat{p}_{e^-}$$
$$-\hat{p}_6+m_b)\gamma_\varepsilon(g^b_V-g^b_A\gamma_5)v(-\mathbf{p}_6)+[(p_2$$
$$+p_1+p_4)^2-m_c^2]^{-1}[(p_{e^+}+p_{e^-}-p_3)^2-m_b^2]^{-1}$$
$$\times(p_1+p_4)^{-2}(p_1+p_2+p_4+p_5)^{-2}$$
$$\times \bar{u}(\mathbf{p}_2)T^a_{\zeta l}T^b_{l\zeta'}\gamma^\nu(\hat{p}_2+\hat{p}_1+\hat{p}_4+m_c)\gamma_\delta$$
$$\times v(-\mathbf{p}_5)\bar{u}(\mathbf{p}_3)T^b_{\chi\chi'}\gamma_\varepsilon(-\hat{p}_{e^+}-\hat{p}_{e^-}$$
$$+\hat{p}_3+m_b)\gamma^\delta(g^b_V-g^b_A\gamma_5)v(-\mathbf{p}_6)+[(p_2$$
$$+p_5+p_3)^2-m_b^2]^{-1}[(p_{e^+}+p_{e^-}-p_6)^2-m_b^2]^{-1}$$
$$\times(p_1+p_4)^{-2}(p_2+p_5)^{-2}\bar{u}(\mathbf{p}_2)T^b_{\zeta\zeta'}\gamma_\delta$$
$$\times v(-\mathbf{p}_5)\bar{u}(\mathbf{p}_3)T^b_{\chi l}T^a_{l\chi'}\gamma^\delta(\hat{p}_2+\hat{p}_5$$
$$+\hat{p}_3+m_b)\gamma^\nu(\hat{p}_{e^+}+\hat{p}_{e^-}-\hat{p}_6+m_b)$$
$$\times\gamma_\varepsilon(g^b_V-g^b_A\gamma_5)v(-\mathbf{p}_6)+[(p_2+p_5+p_3)^2$$
$$-m_b^2]^{-1}[(p_1+p_4+p_6)^2-m_b^2]^{-1}(p_1+p_4)^{-2}$$
$$\times(p_2+p_5)^{-2}\bar{u}(\mathbf{p}_2)T^b_{\zeta\zeta'}\gamma_\delta v(-\mathbf{p}_5)$$
$$\times\bar{u}(\mathbf{p}_3)T^b_{\chi l}T^a_{l\chi'}\gamma^\delta(\hat{p}_2+\hat{p}_5+\hat{p}_3+m_b)\gamma_\varepsilon(-\hat{p}_1$$
$$-\hat{p}_4-\hat{p}_6+m_b)\gamma^\nu(g^b_V-g^b_A\gamma_5)v(-\mathbf{p}_6)+[(p_1$$
$$+p_4+p_6)^2-m_b^2]^{-1}[(p_{e^+}+p_{e^-}-p_3)^2-m_b^2]^{-1}$$
$$\times(p_1+p_4)^{-2}(p_2+p_5)^{-2}\bar{u}(\mathbf{p}_2)T^b_{\zeta\zeta'}\gamma_\delta$$
$$\times v(-\mathbf{p}_5)\bar{u}(\mathbf{p}_3)T^b_{\chi l}T^a_{l\chi'}\gamma_\varepsilon(-\hat{p}_{e^+}-\hat{p}_{e^-}$$
$$+\hat{p}_3+m_b)\gamma^\delta(-\hat{p}_1-\hat{p}_4-\hat{p}_6+m_b)\gamma^\nu(g^b_V$$
$$-g^b_A\gamma_5)v(-\mathbf{p}_6)-(i/2)[(p_{e^+}+p_{e^-}-p_6)^2$$
$$-m_b^2]^{-1}(p_1+p_4)^{-2}(p_2+p_5)^{-2}(p_1+p_2$$
$$+p_4+p_5)^{-2}f^{abd}[(-p_1^\delta-p_4^\delta+p_2^\delta+p_5^\delta)g^{\mu\nu}$$
$$+(-2p_2^\nu-2p_5^\nu)g^{\mu\delta}+(2p_1^\mu+2p_4^\mu)g^{\nu\delta}]\bar{u}(\mathbf{p}_2)$$
$$\times T^b_{\zeta\zeta'}\gamma_\mu v(-\mathbf{p}_5)\bar{u}(\mathbf{p}_3)T^d_{\chi\chi'}\gamma_\delta(\hat{p}_{e^+}+\hat{p}_{e^-}$$
$$-\hat{p}_6+m_b)\gamma_\varepsilon(g^b_V-g^b_A\gamma_5)v(-\mathbf{p}_6)-(i/2)$$
$$\times[(p_{e^+}+p_{e^-}-p_3)^2-m_b^2]^{-1}(p_1+p_4)^{-2}$$
$$\times(p_2+p_5)^{-2}(p_1+p_2+p_4+p_5)^{-2}f^{abd}[(-p_1^\delta$$
$$-p_4^\delta+p_2^\delta+p_5^\delta)g^{\mu\nu}+(-2p_2^\nu-2p_5^\nu)g^{\mu\delta}$$
$$+(2p_1^\mu+2p_4^\mu)g^{\nu\delta}]\bar{u}(\mathbf{p}_2)T^b_{\zeta\zeta'}\gamma_\mu v(-\mathbf{p}_5)\bar{u}(\mathbf{p}_3)T^d_{\chi\chi'}$$
$$\times\gamma_\varepsilon(-\hat{p}_{e^+}-\hat{p}_{e^-}+\hat{p}_3+m_b)\gamma_\delta(g^b_V-g^b_A\gamma_5)$$
$$\times v(-\mathbf{p}_6)\Big\}\bar{u}(\mathbf{p}_1)T^a_{\xi\xi'}\gamma_\nu v(-\mathbf{p}_4)\bar{v}(-\mathbf{p}_{e^+})$$
$$\times\gamma^\varepsilon(g^e_V-g^e_A\gamma_5)u(\mathbf{p}_{e^-}),$$

and where the expression for $A^\gamma_{\xi\xi'\zeta\zeta'\chi\chi'}$ is obtained from the expression for $A^Z_{\xi\xi'\zeta\zeta'\chi\chi'}$ by setting in it $g^e_V=1$, $g^e_A=0$, $g^q_V=Q_q$, and $g^q_A=0$, with $Q_q$ being the electric charge of the quark $q$ ($q=s,\ c,\ b$) in units of the electron charge $e$. Since the number of nonequivalent Feynman diagrams belonging to type *8* or *9* (Fig. 1) and differing from one another only by a permutation of the $s\bar{s}$, $c\bar{c}$, and $b\bar{b}$ lines is equal to three and since the quantity $A^Z_{\xi\xi'\zeta\zeta'\chi\chi'}$ from Eq. (3) involves six terms that are obtained from one another by permuting the quantum numbers of $s\bar{s}$, $c\bar{c}$, and $b\bar{b}$ quark–antiquark pairs, we introduce, in the eighth and the ninth term in expression (4), an additional (in relation to the Feynman formulation) factor of $1/2$, whereupon we arrive at the correct results for this quantity and for the matrix element in (2).

Let us consider in more detail the color structure of the matrix element given by Eqs. (2)–(4). Since any baryon is a color-singlet object, the *scb* state that is produced in process (1) must be an $SU(3)_c$ singlet that is contained in the tensor product of three $SU(3)_c$ triplets. It follows that the *scb* state must be fully antisymmetric in the color indices of the quarks; to take this into account, it is necessary to introduce, in the amplitude of the process, the antisymmetric tensor $\varepsilon^{\xi'\zeta'\chi'}/\sqrt{6}$, which is normalized to unity. Since the initial electron–positron state is also a color singlet, the state of three unbound $\bar{s}$, $\bar{c}$, and $\bar{b}$ antiquarks accompanying the product baryon must also be a singlet. We note in passing that the tensor $\varepsilon^{\xi\zeta\chi}T^a_{\xi\xi'}T^a_{\zeta l}T^b_{l\zeta'}T^b_{\chi\chi'}$ is already fully antisymmetric in its indices $\xi'$, $\zeta'$, and $\chi'$; therefore, it is not necessary that the projection operator $\varepsilon^{\xi'\zeta'\chi'}/\sqrt{6}$ be explicitly present there. The presence of this operator is technically useful, however, since this makes it possible to perform summation over color indices at the amplitude level—that is, prior to squaring the amplitude.

Further, it is straightforward to prove the identity[1)]

$$\varepsilon^{\xi\zeta\chi}\varepsilon^{\xi'\zeta'\chi'}f^{abd}T^a_{\xi\xi'}T^b_{\zeta\zeta'}T^d_{\chi\chi'}=0, \qquad (5)$$

from which it follows that the contributions of diagrams involving a three-gluon vertex [eighth and ninth term in Eq. (4)] vanish. At the same time, all

[1)] Of three indices $a$, $b$, and $d$ corresponding to nonzero values of the structure constant $f^{abd}$, two are always the numbers of Gell-Mann matrices such that they undergo no changes upon transposition, while the remaining index is associated with a Gell-Mann matrix that changes sign upon transposition. By simultaneously replacing the primed indices by unprimed ones and transposing the matrices $T^a$, $T^b$, and $T^d$, we arrive at

$$\varepsilon^{\xi\zeta\chi}\varepsilon^{\xi'\zeta'\chi'}T^a_{\xi\xi'}T^b_{\zeta\zeta'}T^d_{\chi\chi'}=-\varepsilon^{\xi\zeta\chi}\varepsilon^{\xi'\zeta'\chi'}T^a_{\xi'\xi}T^b_{\zeta'\zeta}T^d_{\chi'\chi}$$
$$=-\varepsilon^{\xi'\zeta'\chi'}\varepsilon^{\xi\zeta\chi}T^a_{\xi\xi'}T^b_{\zeta\zeta'}T^d_{\chi\chi'},$$

whence we immediately obtain relation (5).

of the remaining terms in Eqs. (2)–(4) have the same color structure. Summation over color indices yields

$$\frac{1}{6}\varepsilon^{\xi\zeta\chi}\varepsilon^{\xi'\zeta'\chi'}T^a_{\xi\xi'}T^a_{\zeta l}T^b_{l\zeta'}T^b_{\chi\chi'}=\frac{4}{9}. \quad (6)$$

In performing summation over fermion polarizations (with the aid of the REDUCE system [14] for analytic calculations), we employed the method of orthogonal amplitudes. Briefly, the essence of the method is as follows. Suppose that we have the quantity $\bar{u}(\mathbf{p}')Ru(\mathbf{p}'')$, where $u(\mathbf{p}')$ and $u(\mathbf{p}'')$ are spinors that obey the Dirac equation, while $R$ is an operator that is expressed in terms of the $\gamma$ matrices and their contractions with 4-vectors. In general, this quantity then admits a linear decomposition in terms of four orthogonal amplitudes $w_1=\bar{u}(\mathbf{p}')u(\mathbf{p}'')$, $w_2=\bar{u}(\mathbf{p}')\hat{K}u(\mathbf{p}'')$, $w_3=\bar{u}(\mathbf{p}')\hat{Q}u(\mathbf{p}'')$, and $w_4=\bar{u}(\mathbf{p}')\hat{K}\hat{Q}u(\mathbf{p}'')$. That two different amplitudes are orthogonal implies the vanishing of the quantity obtained by summing, over the polarizations of the two spinors, the product of one of these amplitudes and the complex conjugate of the other. This is so if the 4-vectors $K^\mu$ and $Q^\mu$ are orthogonal to the 4-momenta $p'^\mu$ and $p''^\mu$ and to each other—that is, $K_\mu p'^\mu=0$, $K_\mu p''^\mu=0$, $Q_\mu p'^\mu=0$, $Q_\mu p''^\mu=0$, and $K_\mu Q^\mu=0$; otherwise, the 4-vectors $K^\mu$ and $Q^\mu$ are arbitrary.

Let us apply the method of orthogonal amplitudes to the specific problem at hand. For this purpose, we introduce the quantities

$$w_{s1}=\bar{u}(\mathbf{p}_1)v(-\mathbf{p}_4),\quad w_{s2}=\bar{u}(\mathbf{p}_1)\hat{K}_s v(-\mathbf{p}_4), \quad (7)$$

$$w_{s3}=\bar{u}(\mathbf{p}_1)\hat{Q}_s v(-\mathbf{p}_4),\quad w_{s4}=\bar{u}(\mathbf{p}_1)\hat{K}_s\hat{Q}_s v(-\mathbf{p}_4),$$

$$w_{c1}=\bar{u}(\mathbf{p}_2)v(-\mathbf{p}_5),\quad w_{c2}=\bar{u}(\mathbf{p}_2)\hat{K}_c v(-\mathbf{p}_5),$$

$$w_{c3}=\bar{u}(\mathbf{p}_2)\hat{Q}_c v(-\mathbf{p}_5),\quad w_{c4}=\bar{u}(\mathbf{p}_2)\hat{K}_c\hat{Q}_c v(-\mathbf{p}_5),$$

$$w_{b1}=\bar{u}(\mathbf{p}_3)v(-\mathbf{p}_6),\quad w_{b2}=\bar{u}(\mathbf{p}_3)\hat{K}_b v(-\mathbf{p}_6),$$

$$w_{b3}=\bar{u}(\mathbf{p}_3)\hat{Q}_b v(-\mathbf{p}_6),\quad w_{b4}=\bar{u}(\mathbf{p}_3)\hat{K}_b\hat{Q}_b v(-\mathbf{p}_6),$$

$$w_{e_1}=\bar{v}(-\mathbf{p}_{e^+})\hat{K}_e u(\mathbf{p}_{e^-}),$$
$$w_{e_2}=\bar{v}(-\mathbf{p}_{e^+})\hat{Q}_e u(\mathbf{p}_{e^-}),$$

where

$$K^\mu_s=\varepsilon^{\mu\nu\rho\sigma}p_{1\nu}p_{4\rho}a_{s\sigma},\quad Q^\mu_s=\varepsilon^{\mu\nu\rho\sigma}p_{1\nu}p_{4\rho}K_{s\sigma}, \quad (8)$$
$$K^\mu_c=\varepsilon^{\mu\nu\rho\sigma}p_{2\nu}p_{5\rho}a_{c\sigma},\quad Q^\mu_c=\varepsilon^{\mu\nu\rho\sigma}p_{2\nu}p_{5\rho}K_{c\sigma},$$
$$K^\mu_b=\varepsilon^{\mu\nu\rho\sigma}p_{3\nu}p_{6\rho}a_{b\sigma},\quad Q^\mu_b=\varepsilon^{\mu\nu\rho\sigma}p_{3\nu}p_{6\rho}K_{b\sigma},$$
$$K^\mu_e=\varepsilon^{\mu\nu\rho\sigma}p_{e^+\nu}p_{e^-\rho}a_{e\sigma},$$
$$Q^\mu_e=\varepsilon^{\mu\nu\rho\sigma}p_{e^+\nu}p_{e^-\rho}K_{e\sigma},$$

the 4-vectors $a_{s\sigma}$, $a_{c\sigma}$, $a_{b\sigma}$, and $a_{e\sigma}$ being arbitrary. Our problem is then described in terms of 128 orthogonal amplitudes of the form

$$w_{ijkl}=w_{si}w_{cj}w_{bk}w_{el},\quad i,j,k=1,2,3,4,\quad l=1,2. \quad (9)$$

In order to find the coefficients $c_{ijkl}$ in the expansion of the matrix element (2) in the amplitudes specified by Eq. (9),

$$\mathcal{M}=\sum_{i,j,k=1}^{4}\sum_{l=1}^{2}c_{ijkl}w_{ijkl}, \quad (10)$$

we multiply both sides of this equality by the quantity $w^*_{i'j'k'l'}$, sum the result over the polarizations of all fermions, and make use of the orthogonality of the different amplitudes $w_{ijkl}$. Denoting by $|w_{ijkl}|^2$ the quantity obtained by summing, over the polarizations of all fermions, the squared modulus of the amplitude $w_{ijkl}$, we have

$$c_{ijkl}=\left\{\sum_{\text{polar}}\mathcal{M}w^*_{ijkl}\right\}\Big/|w_{ijkl}|^2. \quad (11)$$

For the squared modulus of the relevant matrix element, summation over the polarizations of product particles and averaging over the polarizations of colliding particles is performed by the formula

$$\overline{|\mathcal{M}|^2}=\frac{1}{4}\sum_{i,j,k=1}^{4}\sum_{l=1}^{2}|c_{ijkl}|^2|w_{ijkl}|^2. \quad (12)$$

We note that we did not include the quantities $\bar{v}(-\mathbf{p}_{e^+})u(\mathbf{p}_{e^-})$ and $\bar{v}(-\mathbf{p}_{e^+})\hat{K}_e\hat{Q}_e u(\mathbf{p}_{e^-})$ in the list of basic orthogonal amplitudes in (7), since the corresponding coefficients in the expansion of the matrix element [Eqs. (2)–(4)] vanish (this is because the traces that arise in performing summation over the polarizations of massless electrons and positrons involve an odd number of Dirac $\gamma$ matrices).

The question of why it is profitable to employ the method of orthogonal amplitudes is in order here. Upon directly squaring the matrix element specified by Eqs. (2)–(4), we would obtain, with allowance for the equality in (5), 3570 terms, and an individual operation of summation over particle polarizations would correspond to each of these terms. Within the method of orthogonal amplitudes, we compose one REDUCE code for evaluating traces and tensor contractions that corresponds to 84 terms in the quantity $\mathcal{M}w^*_{1111}$, whereupon we apply text editors (for example, joe or gedit) to perform obvious substitutions in this code, thereby obtaining REDUCE codes for evaluating all 128 coefficients $c_{ijkl}$. We note that analytic expressions for 128 coefficients $c_{ijkl}$ occupy 370 Mb.

Features of $\Omega_{scb}$-baryon production in electron–positron collisions at the $Z$-boson pole

| $m_s$, MeV | $\sigma_{\rm tot}$, fb | $A_{FB}$ |
|---|---|---|
| 300 | $0.0534 \pm 0.0014$ | $0.162 \pm 0.024$ |
| 500 | $0.0153 \pm 0.0004$ | $0.158 \pm 0.016$ |

## 3. NUMERICAL RESULTS

In order to describe a bound state of heavy quarks, we make use of the nonrelativistic approximation [11–13], according to which the relative velocities of the quarks in a heavy hadron are assumed to be low. In the case of $S$-wave states, these velocities can be set to zero. Accordingly, the velocities of all three quarks in the final state of process (1) are taken to be identical, while the momenta of the quarks are assumed to be proportional to their masses; that is,

$$p_1 = (m_s/M)p, \quad p_2 = (m_c/M)p, \qquad (13)$$
$$p_3 = (m_b/M)p, \qquad M = m_s + m_c + m_b.$$

Concurrently, the six-particle phase space of the final state of process (1) reduces to the four-particle phase space of the process

$$e^-(p_{e^-}) + e^+(p_{e^+}) \to \Omega_{scb}(p) + \bar{s}(p_4) \qquad (14)$$
$$+ \bar{c}(p_5) + \bar{b}(p_6),$$

while the probability of bound-state formation is controlled by the value of the baryon wave function at the origin of coordinates, the only model parameter in this approach. Eventually, the differential cross section for process (14) assumes the form

$$d\sigma = \frac{(2\pi)^4\overline{|\mathcal{M}|^2}}{2s}\,\frac{|\psi(0)|^2}{M^2}\delta^4(p_{e^-} + p_{e^+} \qquad (15)$$
$$- p_4 - p_5 - p_6 - p)\frac{d^3p_4}{(2\pi)^3 2E_4}\,\frac{d^3p_5}{(2\pi)^3 2E_5}$$
$$\times \frac{d^3p_6}{(2\pi)^3 2E_6}\,\frac{d^3p}{(2\pi)^3 2E}.$$

In evaluating the cross sections in question, we employed codes for integration that enter as ingredients into the CompHEP package [15]. As a necessary test, we first of all made sure that numerical values of the cross sections are identical for different choices of the 4-vectors $a_{s\sigma}$, $a_{c\sigma}$, $a_{b\sigma}$, and $a_{e\sigma}$, which are involved in the construction of the basic amplitudes. Having proven this, we prescribed ten iterations for the cross sections, each involving 100 000 steps of a Monte Carlo sampling of the integrand. The error in evaluating the total cross sections was 2.0–2.5%, while the error in the differential cross sections was about 10%, on average.

Among theoretical uncertainties that affect cross-section values, the choice of renormalization scale in the running coupling constant for strong interaction, the values of the baryon wave function at the origin, and numerical values of the quark masses are of greatest importance. In what is concerned with the quark masses, the results of the calculations are the most sensitive to the choice of value for the lightest quark (strange one), because, for some gluon propagators, the minimal values of the denominators are $4m_s^2$. To illustrate this dependence, we everywhere present the results obtained at two values of the strange-quark mass, $m_s = 300$ and 500 MeV. The remaining parameters were set to the following values: $m_c = 1500$ MeV, $m_b = 4800$ MeV, $\alpha = \alpha(M_Z) = 1/128.0$, $\alpha_s = \alpha_s(M_Z/2) = 0.134$, and $\sin^2\theta_{\rm W} = \sin^2\theta_{\rm W}(M_Z) = 0.2240$; the numerical value of the wave function for the spin-3/2 $\Omega_{scb}$ baryon at zero relative coordinates of its quarks was borrowed from [16]:

$$|\psi(0)|^2 = 0.90 \times 10^{-3}\ \text{GeV}^6. \qquad (16)$$

We note that the change in the characteristic energy scale $\mu$ in the running coupling constant $\alpha_s(\mu)$ from $\mu = M_Z/2$ to $\mu = M_Z$ leads to a change in the calculated cross sections by a common factor of $[\alpha_s(M_Z)/\alpha_s(M_Z/2)]^4 = 0.665$.

For electron–positron collisions at $\sqrt{s} = 91.2$ GeV, the table presents the values of the total cross sections $\sigma_{\rm tot}$ and of the forward–backward asymmetry at the $Z$-boson pole. This asymmetry is defined as

$$A_{FB} = (\sigma_F - \sigma_B)/(\sigma_F + \sigma_B), \qquad (17)$$

where $\sigma_F$ ($\sigma_B$) is the cross section for the production of $\Omega_{scb}$ baryons traveling in the forward (backward) direction with respect to the direction of the electron momentum.

Figure 2 displays the transverse-momentum ($p_T$) and rapidity ($Y$) distributions of $\Omega_{scb}$ baryons at the strange-quark-mass values of $m_s = 300$ and 500 MeV. For both values of the mass $m_s$, the differential cross sections $d\sigma/dp_T$ peak at $p_T$ values approximately equal to one-fourth of the total energy of colliding particles, while the quantities $d\sigma/dY$ peak at small positive values of the rapidity $Y$.

By using the concept of a fragmentation function, we can represent our numerical results in a simpler analytic form that is convenient for phenomenological applications. It is natural to break down the entire set of diagrams considered here into three groups that correspond to the fragmentation of $b$, $c$, and $s$ quarks (in accordance with the flavor of quarks that are produced at the $\gamma/Z$ vertex). Here, the fragmentation of $b$ quarks plays a dominant role, whence it

follows that, to a high precision, we can approximate the differential cross section as (see, for example, [4] and the discussion on the treatment of experimental data on electron–positron annihilation in [17, 18])

$$d\sigma/dz = \sigma_{b\bar{b}} D_{b\to\Omega_{scb}}(z), \tag{18}$$

where $\sigma_{b\bar{b}}$ is the total cross section for the process $e^-e^+ \to b\bar{b}$, $D_{b\to\Omega_{scb}}(z)$ is the function that describes the fragmentation of a $b$ quark into an $\Omega_{scb}$ baryon, and the variable $z$ is expressed in terms of the energy $E$ of the final hadron and its longitudinal momentum $p_{||}$ as

$$z = (E + p_{||})/(E + p_{||})_{\max}. \tag{19}$$

For reasons of practical convenience, the variable $z$ is often replaced by the variable $x_p = p/p_{\max}$ [17–20], which is close to it, or by $x_E = E/E_{\max}$ [21]. The distinction between these definitions vanishes in the limit of ultrahigh energies, but it can be sizable under actual conditions.

Experimental results obtained for electron–positron annihilation are usually contrasted against the Peterson fragmentation function [22]

$$D(z) \sim \frac{1}{z[1 - (1/z) - \varepsilon/(1-z)]^2}, \tag{20}$$

where $\varepsilon$ is a phenomenological parameter.

If one disregards the aforementioned small asymmetry in the angular distribution of $\Omega_{scb}$ baryons and sets $z \simeq x_E$, the relation between the differential distribution of the cross section with respect to the transverse momentum of the product baryon and the fragmentation function assumes the form

$$\frac{d\sigma}{dp_T} = \frac{4\sigma_{b\bar{b}} p_T}{s} \int\limits_{2\sqrt{(p_T^2+M^2)/s}}^{1} dz \times \frac{D_{b\to\Omega_{scb}}(z)}{\sqrt{[z^2 - 4M^2/s][z^2 - 4(M^2+p_T^2)/s]}}. \tag{21}$$

But if the variable $x_p$ is used instead of $z$, it is necessary to set $M = 0$ in relation (21).

The conclusions drawn from a comparison of relation (21) with our numerical results are as follows: if $z \simeq x_E$, the parameter values of $\varepsilon = 0.098 \pm 0.012$ and $0.132 \pm 0.018$ correspond to the strange-quark masses of $m_s = 300$ and 500 MeV, respectively; if $z \simeq x_p$, the corresponding parameter values are $\varepsilon = 0.108 \pm 0.016$ and $0.147 \pm 0.022$.

For the sake of comparison, we present values of the parameter $\varepsilon$ in the Peterson fragmentation function (20) that were obtained in experiments where electron–positron annihilation was explored at $\sqrt{s} = 10$ GeV: $\varepsilon = 0.236^{+0.068}_{-0.048}$ for $c$-quark fragmentation into $\Lambda_c$ [17]; $\varepsilon = 0.29 \pm 0.06$ for $c$-quark fragmentation into $\Sigma_c$ [19]; and $\varepsilon = 0.24 \pm 0.08$ and $0.23^{+0.09}_{-0.06}$ for $c$-quark fragmentation into $\Xi_c$ according to the results obtained in [18] and [20], respectively.

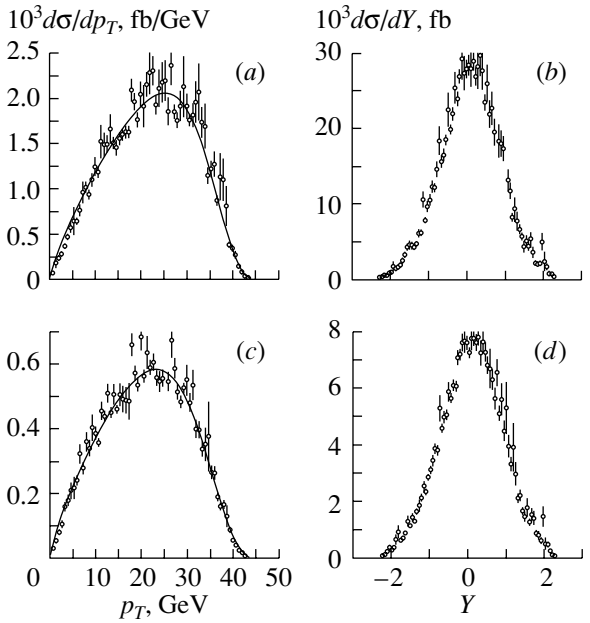


**Fig. 2.** Differential distributions of the cross section for $\Omega_{scb}$-baryon production in electron–positron collisions at the $Z$-boson pole with respect to ($a$, $c$) the transverse momentum $p_T$ and ($b$, $d$) the rapidity $Y$ at the strange-quark-mass values of $m_s =$ ($a$, $b$) 300 and ($c$, $d$) 500 MeV. Points represent the results of our Monte Carlo calculations. The solid curves correspond to the calculations by formula (21) with the Peterson fragmentation function whose parameter takes the value of $\varepsilon = 0.098$ for $m_s = 300$ MeV and the value of $\varepsilon = 0.132$ for $m_s = 500$ MeV.

## ACKNOWLEDGMENTS

We are grateful to A.E. Pukhov for assistance in adapting the problem considered in this article to the CompHEP package.

## REFERENCES

1. V. V. Kiselev and A. K. Likhoded, Usp. Fiz. Nauk **172**, 497 (2002).
2. A. Falk, M. Luke, M. Savage, and M. Wise, Phys. Rev. D **49**, 555 (1994).
3. V. V. Kiselev, A. K. Likhoded, and M. V. Shevlyagin, Phys. Lett. B **332**, 411 (1994).
4. A. V. Berezhnoy, V. V. Kiselev, and A. K. Likhoded, Yad. Fiz. **59**, 909 (1996) [Phys. At. Nucl. **59**, 870 (1996)].
5. A. V. Berezhnoy, V. V. Kiselev, A. K. Likhoded, and A. I. Onichshenko, Yad. Fiz. **60**, 2048 (1997) [Phys. At. Nucl. **60**, 1875 (1997)].

6. A. V. Berezhnoy, V. V. Kiselev, A. K. Likhoded, and A. I. Onishchenko, Phys. Rev. D **57**, 4385 (1998).
7. S. P. Baranov, Phys. Rev. D **54**, 3228 (1996).
8. S. P. Baranov, Phys. Rev. D **56**, 3046 (1997).
9. V. V. Braguta and A. E. Chalov, hep-ph/0005149.
10. R. E. Prange, Phys. Rev. **110**, 240 (1958).
11. C.-H. Chang, Nucl. Phys. B **172**, 425 (1980).
12. R. Baier and R. Rückl, Phys. Lett. B **102B**, 364 (1981).
13. E. L. Berger and D. Jones, Phys. Rev. D **23**, 1521 (1981).
14. A. C. Hearn, Preprint Utah University CP78 Rev. 4/84 (Rand Publ., Utah, 1984).
15. A. Pukhov *et al.*, hep-ph/9908288.
16. E. Bagan, H. G. Dosch, P. Godzinsky, *et al.*, Z. Phys. C **64**, 57 (1994).
17. ARGUS Collab. (H. Albrecht *et al.*), Phys. Lett. B **207**, 109 (1988).
18. ARGUS Collab. (H. Albrecht *et al.*), Phys. Lett. B **247**, 121 (1990).
19. ARGUS Collab. (H. Albrecht *et al.*), Phys. Lett. B **211**, 489 (1988).
20. CLEO Collab. (K. W. Edward *et al.*), Phys. Lett. B **373**, 261 (1996).
21. OPAL Collab. (G. Alexander *et al.*), Phys. Lett. B **364**, 93 (1995).
22. C. Peterson, D. Schlatter, I. Schmitt, and P. M. Zerwas, Phys. Rev. D **27**, 105 (1983).

*Translated by A. Isaakyan*

Physics of Atomic Nuclei, Vol. 66, No. 9, 2003, pp. 1737–1742. Translated from Yadernaya Fizika, Vol. 66, No. 9, 2003, pp. 1785–1790.


ELEMENTARY PARTICLES AND FIELDS
Theory

# Cancellation of Divergences in Rare Processes

**V. I. Kuksa**

*Rostov State University, Bol'shaya Sadovaya 105, Rostov-on-Don, 344006 Russia*

Received July 9, 2002; in final form, September 18, 2002

**Abstract**—The structure of divergences in effective vertices that generate flavor-changing neutral currents is considered. For extremely simple examples, it is shown that divergences are completely canceled in rare processes governed by such vertices. Methodological facets of the cancellation and renormalization process are discussed. © *2003 MAIK "Nauka/Interperiodica".*

## 1. INTRODUCTION

In recent years, much attention has been given to so-called rare processes occurring at the loop level that are caused by flavor-changing neutral currents (FCNC). Interest in rare processes is associated with performing precision tests of the Standard Model with allowance for radiative corrections. This resulted in the appearance of a considerable number of studies devoted to calculating and analyzing effective FCNC vertices [1–10].

A basic feature peculiar to effective vertices of the $q_\alpha q_\beta X$ form, where $X = \gamma, Z^0, g$ (penguin diagrams), and of the $q_\alpha q_\beta \bar{q}_\alpha \bar{q}_\beta$ and the $l\bar{l}q_\alpha\bar{q}_\beta$ form (box diagrams) is that they vanish at the tree level in the Standard Model. This fact is of fundamental importance for the renormalization procedure and is associated with the problem of introducing counterterms. In the available literature [8, 9, 11, 12], $q_\alpha q_\beta X$ and $l\bar{l}q_\alpha\bar{q}_\beta$ vertices are usually renormalized by introducing counterterms in the divergent amplitudes corresponding to the transitions in question, whereupon the renormalized vertices are intended for use as elements of more general diagrams in calculating specific processes. It should be emphasized here that, in FCNC amplitudes, the divergences cancel on the mass shell—that is, there is no need for introducing counterterms in this case [7–12]. In the general case, however, where an FCNC vertex appears to be a fragment of a more complicated diagram (that is, where some of its lines are off the mass shell, so that there is no cancellation of divergences inherent in this vertex), it is necessary to introduce a renormalization procedure. Thus, a traditional renormalization procedure developed for processes occurring at the tree level (bare terms) is mechanically extended to the special case where there are no bare terms—FCNC vertices are absent at the tree level. There then arises the question of whether such an extension is legitimate or reasonable. Since no detailed investigation of this question has been performed so far, the proposed methodological analysis is of importance and interest.

The objective of the present study is to show, by considering some specific examples, that, in FCNC vertices, counterterms are not needed even in the general case, where some external legs of these vertices are off the mass shell. Further, we will demonstrate that unrenormalized expressions in divergent FCNC amplitudes can be used as blocks in a more general expression for the amplitude of the total process. This results in that the divergences of various FCNC vertices appearing as elements of diagrams describing a physical process cancel each other in the total expression. All calculations are performed in the physical gauge, where, on one hand, the spectrum of divergences is the most diversified and, on the other hand, the analysis of the cancellation of divergences in terms of subdiagrams is the most convenient since there are no diagrams, in this case, involving unphysical degrees of freedom.

## 2. STRUCTURE OF DIVERGENCES IN FCNC VERTICES

In order to illustrate and to test the process of cancellation of divergences in physical FCNC amplitudes, we present the expressions for the coefficients of divergences appearing in input effective vertices. The total expressions for $q_\alpha q_\beta X$ amplitudes in the physical gauge—that is, the gauge coinciding with the unitary gauge for massive vector bosons and with the Feynman gauge for massless bosons—were obtained in [10].

The set of diagrams describing $d_\alpha d_\beta Z$ vertices in the one-loop approximation is shown in Fig. 1. (Obviously, $u_\alpha u_\beta Z$ vertices are described by the set of diagrams that is obtained from the preceding one upon the substitution of $u$ for $d$.)

In the expression for the total amplitude describing the $d_\alpha d_\beta Z$ transition in the case where all external

1063-7788/03/6609-1737$24.00 

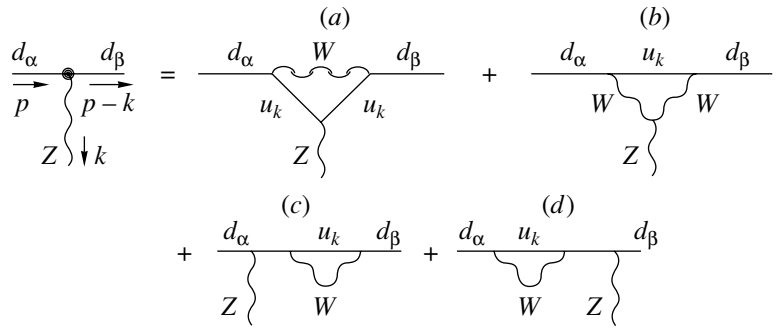


**Fig. 1.** Structure of $d_\alpha d_\beta Z$ vertices ($d_\alpha = d, s, b$; $u_k = u, c, t$).

legs of the vertex are off the mass shell, the coefficient $D_Z$ of the $(\gamma - 1/\varepsilon)$ divergence in the dimensional-regularization procedure, where $\varepsilon = 2 - d/2$, has the form

$$D_Z(\Gamma^\mu_{\alpha\beta}(p,k)) = a^Z_{\alpha\beta}\left[-2\cos^2\theta_\mathrm{W}\gamma^\mu L - \frac{\cos^2\theta_\mathrm{W}}{m_W^2}(k^2\gamma^\mu - k^\mu\hat{k})L\right. \quad (1)$$
$$\left. + \frac{3}{2}\gamma^\mu\frac{c_+ m_\beta\hat{p} + c_- p^2}{p^2 - m_\beta^2}L + \frac{3}{2}R\frac{c_+ m_\alpha(\hat{p}-\hat{k}) + c_-(p-k)^2}{(p-k)^2 - m_\alpha^2}\gamma^\mu\right],$$

where

$$a^Z_{\alpha\beta} = \frac{g^3 U^*_{\beta k}U_{\alpha k}\alpha_k}{2^7\pi^2\cos\theta_\mathrm{W}}, \quad \alpha_k = \frac{m_k^2}{m_W^2},$$
$$c_+ = -4\sin^2\theta_\mathrm{W}/3, \quad c_- = 2 - 4\sin^2\theta_\mathrm{W}/3.$$

Here, $U_{\alpha k}$ are elements of the Cabibbo–Kobayashi–Maskawa matrix, and summation is performed over the subscript $k$ (flavor of an internal quark). Terms that do not depend on $\alpha_k$ are not presented here, since their total contribution vanishes by virtue of the unitarity of the matrix $U$ [Glashow–Iliopoulos–Maiani (GIM) cancellation mechanism]. The first two terms in expression (1) arise from the diagrams in Figs. 1*a* and 1*b*, while the last two terms stem from the diagrams in Figs. 1*c* and 1*d*.

If $d_\alpha$ or $d_\beta$ is on the mass shell, the third or the fourth term becomes, respectively,

$$\frac{3}{2}\gamma^\mu\frac{c_+ m_\alpha m_\beta R + c_- m_\alpha^2 L}{m_\alpha^2 - m_\beta^2}; \quad (2)$$
$$\frac{3}{2}\frac{c_+ m_\alpha m_\beta L + c_- m_\beta^2 R}{m_\beta^2 - m_\alpha^2}\gamma^\mu.$$

In the case where $d_\alpha$ and $d_\beta$ are both on the mass shell, we have

$$D_Z(\Gamma^\mu_{\alpha\beta}(k)) = a^Z_{\alpha\beta}\left[\gamma^\mu - \frac{\cos^2\theta_\mathrm{W}}{m_W^2}(k^2\gamma^\mu - k^\mu\hat{k})\right]L. \quad (3)$$

If the $Z$ boson is on the mass shell, the first two terms in (1) are given by

$$-(1 + 2\cos^2\theta_\mathrm{W})\gamma^\mu L + (\cos^2\theta_\mathrm{W}/m_W^2)k^\mu\hat{k}L, \quad (4)$$

where the second term can be discarded by virtue of the transverseness condition. If $d_\alpha$, $d_\beta$, and $Z$ are on the mass shell simultaneously, we obtain

$$D_Z(\Gamma^\mu_{\alpha\beta}(k)) = a^Z_{\alpha\beta}\hat{k}L\frac{k^\mu}{m_Z^2} \quad (5)$$
$$= a^Z_{\alpha\beta}(m_\alpha R - m_\beta L)\frac{k^\mu}{m_Z^2}.$$

Since the quantity in (5) is proportional to $k^\mu$, it does not contribute to the amplitude of a physical process either.

The structure of the divergence in the $d_\alpha d_\beta\gamma$ vertex is also determined by the diagrams in Figs. 1*a*–1*d*, where the substitution $Z \to \gamma$ is made; the coefficient $D_\gamma$ of the divergence has the form

$$D_\gamma(\Gamma^\mu_{\alpha\beta}(p,k)) = a^\gamma_{\alpha\beta}\left[-\gamma^\mu L - \frac{k^2\gamma^\mu - k^\mu\hat{k}}{2m_W^2}L\right. \quad (6)$$
$$\left. + \gamma^\mu\frac{m_\beta\hat{p} + p^2}{p^2 - m_\beta^2}L + R\frac{m_\alpha(\hat{p}-\hat{k}) + (p-k)^2}{(p-k)^2 - m_\alpha^2}\gamma^\mu\right],$$

where $a^\gamma_{\alpha\beta} = eg^2 U^*_{\beta k}U_{\alpha k}\alpha_k/(2^6\pi^2)$. If $d_\alpha$ or $d_\beta$ is on the mass shell, the third or the fourth term in (6)

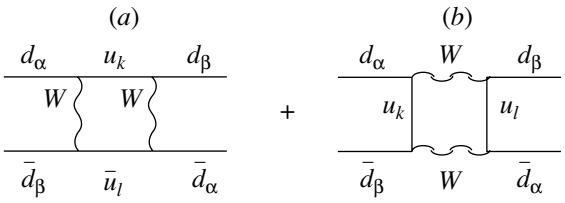


**Fig. 2.** Quark box diagrams ($d_\alpha \bar{d}_\beta \to \bar{d}_\alpha d_\beta$).

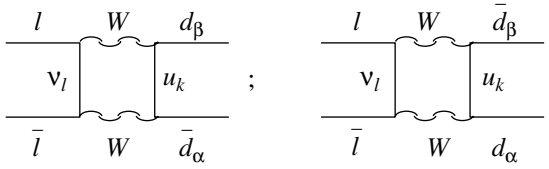


**Fig. 3.** Quark–lepton box diagrams ($l\bar{l} \to \bar{d}_\alpha d_\beta, \bar{d}_\beta d_\alpha$).

reduces to, respectively,

$$\gamma^\mu \frac{m_\alpha m_\beta R + m_\alpha^2 L}{m_\alpha^2 - m_\beta^2}; \quad \frac{m_\alpha m_\beta L + m_\beta^2 R}{m_\beta^2 - m_\alpha^2}\gamma^\mu. \quad (7)$$

In the case where $d_\alpha$ and $d_\beta$ are both on the mass shell, we have

$$D_\gamma\left(\Gamma^\mu_{\alpha\beta}(k)\right) = -\frac{a^\gamma_{\alpha\beta}}{m_W^2}(k^2\gamma^\mu - k^\mu \hat{k})L. \quad (8)$$

If $d_\alpha$, $d_\beta$, and $\gamma$ are on the mass shell, then $D_\gamma$ is proportional to $k^\mu \hat{k} L$ and does not contribute to the amplitude.

The structure of the divergences in the gluon vertex $d_\alpha d_\beta G$ is analogous to that specified by Eqs. (6) and (7), but, in the present case, expression (6) features no second term corresponding to the diagram in Fig. 1*b*. The coefficient $D_G$ is obtained from the expression for $D_\gamma$ (without the second term) upon substituting into (6) the quantity

$$a^{G^a}_{\alpha\beta} = -\frac{3}{2^7\pi^2} g^2 g_s U^*_{\beta k} U_{\alpha k} \alpha_k \lambda^a.$$

If $d_\alpha$ or $d_\beta$ is on the mass shell, the last two terms in the expression for $D_G$ are equal to the corresponding sign-reversed terms in (7), but, if $d_\alpha$ and $d_\beta$ are both on the mass shell, a complete cancellation of divergences occurs, irrespective of the gluon state; that is, $D_G = 0$.

We note that, on the mass shell, the coefficients $D_\gamma$ and $D_G$ satisfy the transverseness condition $k_\mu D(\Gamma^\mu) = 0$. As an additional test, we also verified fulfillment of the Ward–Slavnov–Taylor identity for these coefficients.

Let us consider the structure of divergences arising in box diagrams of two types corresponding to the transitions $q_\alpha \bar{q}_\beta \to \bar{q}_\alpha q_\beta$ and $l\bar{l} \to q_\alpha \bar{q}_\beta$. The quark box diagrams in Fig. 2 lead to the mixing effect in neutral meson systems, $M^0_{\alpha\beta} - \overline{M^0_{\alpha\beta}}$, where $M_{\alpha\beta} = M(q_\alpha \bar{q}_\beta)$.

In the unitary gauge, the amplitudes corresponding to the diagrams in Figs. 2*a* and 2*b* involve divergences arising in Feynman integrals with respect to the momenta of order from the fourth to the sixth inclusive. However, the coefficients of divergences associated with the fourth and the fifth order are free from the quantity $\alpha_k$ and are canceled by the GIM mechanism. The coefficients appearing upon integration of the six-order term with respect to momenta feature $\alpha_k$ and $\alpha_i$ in the form

$$D_{\text{box}} \sim \sum_{i,k} U^*_{k\beta} U_{k\alpha} U^*_{i\beta} U_{i\alpha}(\alpha_i + \alpha_k) \quad (9)$$

$$= 2\sum_k U^*_{k\beta} U_{k\alpha} \left(\sum_i U^*_{i\beta} U_{i\alpha} \alpha_i\right).$$

The parenthetical expression on the right-hand side of (9) is independent of the flavor index $k$; that is, the coefficient $D_{\text{box}}$ is eventually equal to zero by virtue of the double GIM mechanism of cancellation.

Transitions of the $l\bar{l} \to d_\alpha \bar{d}_\beta, d_\beta \bar{d}_\alpha$ types are described by the quark–lepton box diagrams in Fig. 3. In contrast to what occurs in the case of a purely quark transition, there is no complete cancellation of divergences here.

The operator structure of the coefficient of divergence in the $l\bar{l} \to d_\alpha \bar{d}_\beta$ amplitude has the form

$$D^{\text{box}}_{\alpha\beta} = -b_{\alpha\beta} \bar{d^+_\beta} \gamma^\mu L d^+_\alpha \bar{l}^- \gamma^\mu L l^-, \quad (10)$$

$$b_{\alpha\beta} = \frac{ig^4}{2^{10}\pi^4 m_W^2} U^*_{\beta k} U_{\alpha k} \alpha_k.$$

In the following, we will need this expression to illustrate the process of cancellation of divergences in physical amplitudes.

## 3. CANCELLATION OF DIVERGENCES IN AMPLITUDES FOR PHYSICAL PROCESSES

The simplest example of cancellation of divergences in physical amplitudes is provided by processes that can be completely described by the effective $q_\alpha q_\beta X$ vertex, such as the decays $Z \to q_\alpha \bar{q}_\beta$,

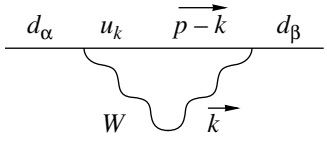


**Fig. 4.** Self-energy nondiagonal diagram for $\Sigma_{\alpha\beta}(p)$.

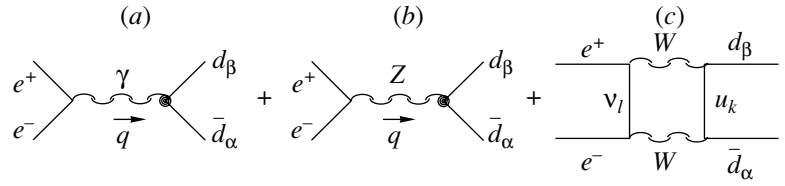


**Fig. 5.** Processes of nondiagonal quark production.

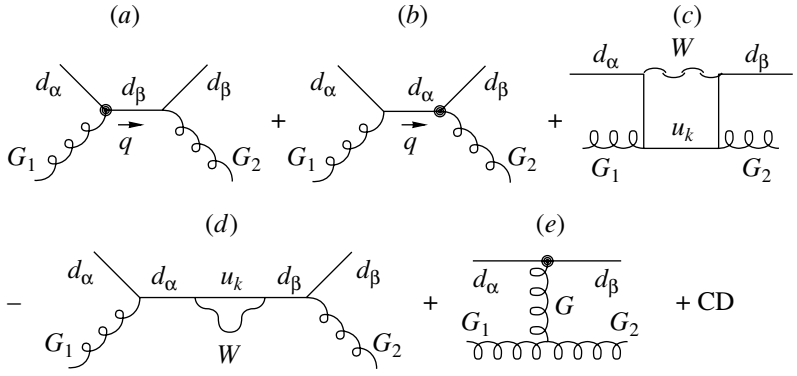


**Fig. 6.** Nondiagonal gluon scattering $G_1 d_\alpha \to G_2 d_\beta$ (CD stands for the crossed diagrams).

$q_\alpha \to q_\beta\gamma(G)$, and $t \to cZ, uZ$. It was indicated in Section 2 that, in this case, the coefficient of the divergence is $D \sim k^\mu$; since, for the amplitude $F$, we have $F \sim e_\mu k^\mu$ ($e_\mu$ is the boson polarization vector), $F_D$ then vanishes by virtue of the transverseness condition $e_\mu k^\mu = 0$. The mixing in the systems of neutral mesons, $M^0_{\alpha\beta} - \overline{M^0_{\alpha\beta}}$, which is described by the diagrams in Fig. 2, presents a similar trivial example, but, in this case, the external quarks are not bound to be on the mass shell.

The case of the $q_\alpha q_\beta X$ vertex also provides an extremely simple illustration of the "structural" cancellation of divergences. The divergent third-order diagrams in Fig. 1 include the divergent second-order self-energy subdiagram $\Sigma_{\alpha\beta}(p)$ presented in Fig. 4.

At $\alpha \neq \beta$, the $d_\alpha$ and $d_\beta$ external legs cannot be on the mass shell simultaneously, in which case the self-energy $\Sigma_{\alpha\beta}(p)$ involves an noncompensated divergence. Within the traditional method, one first renormalizes the self-energy $\Sigma_{\alpha\beta}(p)$ by introducing the corresponding counterterms and then substitutes it into the vertex $\Gamma^\mu_{\alpha\beta}(p, p-k)$, where $\Sigma_{\alpha\beta}(p)$ enters into the diagrams in Figs. 1*c* and 1*d* [8, 9, 11, 12]. As was shown above, however, there is no need for renormalizing $\Sigma_{\alpha\beta}(p)$ since, in the physical amplitudes associated with the vertex $\Gamma^\mu_{\alpha\beta}(p, p-k)$, the divergences that stem from the diagrams in Figs. 1*a* and 1*b* are canceled by the divergences in the self-energy $\Sigma_{\alpha\beta}(p)$ that appear in the diagrams in Figs. 1*c* and 1*d*. The next task is to demonstrate that divergences in FCNC vertices are canceled in processes described by fourth-order diagrams. In this case, some of the external legs of the $q_\alpha q_\beta X$ vertex must be off the mass shell, the divergences in question being exactly canceled by the divergences that arise in other diagrams involving higher order loops.

The nondiagonal production of quarks in the process $e^+e^- \to \bar{d}_\alpha d_\beta$, which is described by the diagrams in Figs. 5*a*–5*c*, where the shaded circle denotes the effective $d_\alpha d_\beta \gamma$ and $d_\alpha d_\beta Z$ vertices in the one-loop approximation, is the simplest example of this kind.

In the diagrams in Figs. 5*a*–5*c*, photons and $Z$ bosons are off the mass shell; with the aid of expressions (3), (8), and (10), the operator coefficients of the divergences in the amplitudes corresponding to the diagrams in Figs. 5*a*–5*c* are then found to have the form

$$\text{(a)}\ D_a = A\sin^2\theta_W \bar{e}^-\gamma^\mu e^- \cdot \bar{d}^+_\beta (q^2\gamma^\mu - q^\mu \hat{q}) L d^+_\alpha / q^2, \tag{11}$$

$$\text{(b)}\ D_b = \frac{1}{4} A \bar{e}^-\gamma^\mu (1 - 4\sin^2\theta_W - \gamma_5) e^- \cdot \bar{d}^+_\beta \gamma^\mu L d^+_\alpha,$$

$$\text{(c)}\ D_c = -\frac{1}{2} A \bar{e}^-\gamma^\mu L e^- \cdot \bar{d}^+_\beta \gamma^\mu L d^+_\alpha,$$

where $A = ig^4 U^*_{\beta k} U_{\alpha k} \alpha_k / (2^9 \pi^4 m^2_W)$. The sum of all

contributions, $D = D_a + D_b + D_c$, is

$$D = -A\sin^2\theta_W \bar{e}^-\hat{q}e^- \cdot \bar{d}^+_\beta \hat{q}Ld^+_\alpha/q^2. \qquad (12)$$

This sum makes zero contribution by virtue of lepton-current conservation. This can easily be verified with the aid of the relation $q = p_+ + p_-$, where $p_+$ and $p_-$ are, respectively, the electron and positron momentum:

$$\bar{e}^-\hat{q}e^- = \bar{e}^-(\hat{p}_+ + \hat{p}_-)e^- = 0. \qquad (13)$$

In (13), use was made of the Dirac equation for negative-frequency components of the field operators. The simple example considered above illustrates the cancellation of the divergences arising in vertices of the $q_\alpha q_\beta X$ type (third-order loop) by the divergences in the quark–lepton box diagram (fourth-order loop). Here, it is not necessary to invoke renormalized effective vertices.

Let us consider nondiagonal gluon scattering in the process $G_1 d_\alpha \to G_2 d_\beta$, which is represented by the diagrams in Figs. 6*a*–6*e*. In this figure, we omitted the crossed diagrams because the cancellation of divergences in these diagrams occurs independently of direct diagrams.

We note that the contribution of the diagram in Fig. 6*d* is subtracted from the total expression since it was twice taken into account in the diagrams in Figs. 6*a* and 6*b*. Thus, the shaded circles in Figs. 6*a* and 6*b* symbolize effective $Gd_\alpha d_\beta$ vertices by convention, and one must take into account the structure of these vertices in constructing more complicated diagrams. It can easily be shown, by means of a direct calculation, that all divergences in the diagram in Fig. 6*c* are independent of $\alpha_k$ and are therefore canceled by the GIM mechanism. According to the results presented in Section 2, the diagram in Fig. 6*e* also makes a finite contribution, and there remain the contributions of the diagrams in Figs. 6*a*, 6*b*, and 6*d*. The amplitudes for the direct and crossed diagrams are given by

$$(1)\quad F_a + F_b = a_{\alpha\beta}\bar{d}^+_\beta \hat{e}^i_2 \hat{O}_q \hat{e}^k_1 \lambda_i \lambda_k d^-_\alpha, \qquad (14)$$

$$(2)\quad (F_a + F_b)_{\text{cross}} = a_{\alpha\beta}\bar{d}^+_\beta \hat{e}^i_1 \hat{O}_q \hat{e}^k_2 \lambda_i \lambda_k d^-_\alpha,$$

where

$$a_{\alpha\beta} = -3ig_s^2 g^2 U^*_{\beta k} U_{\alpha k}\alpha_k/(2^{11}\pi^4\sqrt{p_1 p_2}).$$

The divergent part of the amplitude for the direct diagrams, $D(\hat{O}_q)$, has the form

$$D(\hat{O}_q) = -\frac{m_\alpha m_\beta \hat{q}L + (m_\alpha L + m_\beta R)q^2 + q^2\hat{q}R}{(q^2 - m^2_\alpha)(q^2 - m^2_\beta)}. \qquad (15)$$

The analogous expression for the coefficient $D(\hat{O}_k)$ is obtained from (15) upon the substitution $q \to k$. It can easily be proven, by means of a direct calculation, that the divergence in (15) is exactly cancelled by the divergence appearing in the diagram in Fig. 6*d*. The same occurs for the crossed diagrams. Thus, we see that, in the process being considered, all divergences cancel one another in the total expression, so that there is no need for renormalizing the divergent $Gd_\alpha d_\beta$ vertex. It is natural to expect a similar cancellation mechanism in more complicated cases.

## 4. CONCLUSION

The description of rare processes requires invoking a broad range of means, both of a conceptual and of a computational and a technical character. In particular, special features of FCNC bring about the question of the status of counterterms—more specifically, the question of whether it is necessary to introduce them in divergent input effective vertices of the penguin and the box type. In the present study, the statement that divergences cancel automatically in physical amplitudes is illustrated by considering a rather narrow range of extremely simple examples. In this case, a finite part is isolated unambiguously and an arbitrary mass parameter $\mu$ is fixed at a scale that is convenient for calculations (for example, $\mu = m_W$), the result being independent of the choice of this scale.

The cancellation of divergences in FCNC-induced processes, which has been demonstrated here for the simplest one-loop diagrams, must be of a general character. A rigorous proof of this statement would make it possible to simplify the renormalization procedure and to establish the relationship between the symmetry properties of the Standard Model Lagrangian at the tree level and the cancellation mechanism. The problem considered here is of importance in the case where the application of different renormalization schemes yields different results [13, 14].

It is planned that the present simplified method for calculating rare processes without renormalization will be applied in the future to more complicated cases—for example, the case of $e^+e^- \to d_\alpha \bar{d}_\beta \gamma_1\gamma_2 (G_1G_2)$ or $\gamma_1 d_\alpha \to \gamma_2 d_\beta$—with a simultaneous determination of finite contributions to the amplitude. A comparison of cross sections obtained by different methods with one another (and, if possible, with experimental values) would be of great importance for analyzing the methodological facet of computational techniques that was considered above.

## REFERENCES

1. M. K. Gaillard and B. W. Lee, Phys. Rev. D **10**, 897 (1974).

2. E. E. Bogomol'nyĭ, V. A. Novikov, and M. A. Shifman, Yad. Fiz. **23**, 825 (1976) [Sov. J. Nucl. Phys. **23**, 435 (1976)].
3. M. K. Gaillard, B. W. Lee, and R. E. Shrok, Phys. Rev. D **13**, 2674 (1976).
4. A. I. Vaĭnshteĭn and I. B. Khriplovich, Pis'ma Zh. Éksp. Teor. Fiz. **18**, 141 (1973) [JETP Lett. **18**, 83 (1973)].
5. E. Ma, Phys. Rev. D **9**, 3103 (1974).
6. E. Ma and A. Promudita, Phys. Rev. D **22**, 214 (1980).
7. T. Inami and C. S. Lim, Prog. Theor. Phys. **65**, 297 (1981).
8. N. G. Deshpande and G. Eilam, Phys. Rev. D **26**, 2463 (1982).
9. J. M. Soares and A. Barroso, Phys. Rev. D **39**, 1973 (1989).
10. V. A. Beilin, G. M. Vereshkov, and B. I. Kuksa, Yad. Fiz. **61**, 1649 (1998) [Phys. At. Nucl. **61**, 1538 (1998)].
11. A. Barroso, Phys. Rev. D **42**, 901 (1990).
12. A. Barroso, M. A. Doncheski, *et al.*, Phys. Lett. B **261**, 123 (1991).
13. M. Cinchini, E. Franko, *et al.*, Phys. Lett. B **316**, 127 (1993).
14. M. Demidov and A. Slavnov, Mod. Phys. Lett. A **14**, 993 (1999).

*Translated by A. Isaakyan*

*Physics of Atomic Nuclei, Vol. 66, No. 9, 2003, pp. 1743–1759. Translated from Yadernaya Fizika, Vol. 66, No. 9, 2003, pp. 1791–1806.*


**ELEMENTARY PARTICLES AND FIELDS**
**Theory**

# Contribution of the $\pi\pi$ Components of the Sigma and Rho Mesons to Pion–Nucleon Scattering

**A. N. Almaliev, I. V. Kopytin, and M. A. Shehalev***

*Voronezh State University, Universitetskaya pl. 1, Voronezh, 394693 Russia*

Received August 12, 2002

**Abstract**—For elastic pion–nucleon scattering at a collision energy below the threshold for the production of two pions, dynamical effects are studied that are induced by the presence of a $\pi\pi$ component in the structure of the $\sigma(400–1200)$ and $\rho(770)$ resonances. These effects manifest themselves both in the Green's functions for the sigma and rho mesons and in the form factors for the interaction of these mesons with nucleons. The scattering amplitude is calculated on the basis of the $K$-matrix formalism, the mechanism of dressing being taken into account in the $\pi NN$ and $\pi N\Delta$ form factors and in the nucleon and delta-isobar Green's functions. The method of dispersion relations is used to calculate the real parts of the form factors and functions that parametrize self-energy operators. It is shown that, if strong interaction is taken explicitly into account in the $\pi\pi$ system, elastic pion–nucleon scattering can be described satisfactorily without introducing a sigma meson as an elementary particle. © *2003 MAIK "Nauka/Interperiodica"*.

## 1. INTRODUCTION

Pion–nucleon interaction plays a significant role in low- and intermediate-energy nuclear physics. On one hand, it is of interest in and of itself, appearing to be one of the vivid examples of strong hadron–hadron interactions. On the other hand, it is an important ingredient in many other hadronic processes—for instance, in pion photoproduction on nucleons, in pion scattering on nuclei, and in the formation of three-body nucleon–nucleon–nucleon ($NNN$) forces.

The problem of revealing dominant interaction mechanisms that control specific properties of observables is one of the main problems in constructing a phenomenological description of processes involving hadrons. Concurrently, a theory to be developed must rely on a sound microscopic basis for the resulting free parameters to have specific physical meaning and, in an ideal case, must serve for testing more microscopic models. The first dynamical models of pion–nucleon interaction isolated, in the scattering amplitude, a resonance component associated with the exchange of one nucleon and a delta isobar in the $s$ channel and a nonresonance background, which was simulated, in the majority of cases, by an arbitrary separable function [1, 2]. Although such models reproduced experimental phase shifts fairly well, the free-parameter values obtained as the result of fitting did not have a clear physical meaning and could be used only within a given model.

Presently, QCD is a fundamental microscopic theory that makes it possible, in principle, to describe, within a unified conceptual framework, the majority of hadronic processes, including pion–nucleon scattering. In performing specific investigations into the physics of low-energy processes, one has to invoke, however, because of a nonperturbative origin of confinement, various effective means for describing hadron interactions. In choosing such a description, it is desirable that the effective model used be as close to a fundamental model as possible and that it obey the same symmetries—in particular, chiral symmetry. In view of this, strong-interaction models where the quark–gluon Lagrangian is replaced by an effective chiral Lagrangian featuring mesons and baryons for degrees of freedom became especially popular. In this approach, the physics of all subhadronic processes not included explicitly in the Lagrangian is taken into account either by introducing terms that involve higher powers of meson fields and their derivatives (chiral perturbation theory) or by using phenomenological form factors in hadron-interaction potentials (so-called meson-exchange models). This makes it possible to study dynamical features (such as a dynamical mass or a magnetic moment) that hadrons develop upon being dressed with a meson cloud. The approach in question was successfully used in describing nucleon–nucleon ($NN$) interactions [3], meson–meson and meson–nucleon scattering (see [4] and [5–9], respectively), and some other processes involving mesons and baryons.

The effects of correlation in the exchange of two

*e-mail: shehalev@phys.vsu.ru

or more mesons also play a significant role in hadron physics. Frequently, such effects lead to the emergence of various resonances. In pion–nucleon scattering, correlated two-pion exchange is of greatest importance. Very often, it is simulated as the exchange of a scalar–isoscalar sigma meson and a vector–isovector rho meson. While the rho meson is a distinct resonance of the two-pion system, the sigma meson has not yet been observed as a resonance in data on pion–pion scattering, so that its existence has not been proven definitively [10]. From the majority of the latest analyses of experimental data on pion–pion scattering, as well as on some other processes (see, for example, data of the recent experiment devoted to studying the decay process $D^+ \to \pi^-\pi^+\pi^+$ and reported in [11]), it follows that, in the complex plane of mass, the amplitude of pion–pion scattering has a pole that can be associated with a sigma meson. However, there is presently no consensus on the parameters of this pole, values found for its real and imaginary parts varying, respectively, within the range $\mathrm{Re}\sqrt{s} = 400$–$600$ MeV and within the range $\mathrm{Im}\sqrt{s} = 150$–$350$ MeV (as to the effective mass $m_\sigma$ and the effective width $\Gamma$, they range between 500 and 850 MeV, being approximately equal to each other). At the moment, a physical interpretation of the pole in question is an unresolved problem that is closely related to the problem of describing the properties of the entire nonet of scalar mesons [12]. It is well known that mesons having vacuum quantum numbers are of crucial importance for understanding mechanisms behind the violation of QCD symmetries. However, the question of which of these mesons are quark–antiquark states and which are meson–meson molecules and the question of whether there is a glueball admixture among the lightest of them have been the subject of much controversy. In theories that are based on a linear realization of chiral $SU(2)_L \times SU(2)_R$ symmetry [13]—for example, in the Nambu–Jona-Lasinio model—the sigma meson of mass approximately equal to the mass of two constituent quarks ($m_\sigma \approx 700$ MeV) is assumed to be a chiral partner of the pion. Its nonzero vacuum expectation value is responsible for the breakdown of chiral symmetry; for the formation of a sigma condensate; and, as a consequence, for the mass difference between the constituent and current quarks. From this point of view, the sigma meson is analogous to the Higgs particle in the theory of electroweak interaction. However, the situation is complicated in the present case by the fact that, because of strong coupling to the pion–pion channel, the decay width of the sigma meson is very large, which hinders the investigation of the quark–antiquark component.

An alternative point of view on the nature of the sigma resonance relies on results that were obtained on the basis of nonrelativistic QCD. According to this theory, $S$-wave quark–antiquark states correspond to vector and pseudoscalar states, while $P$-wave states correspond to scalar mesons, $f_0(1370)$ being the lightest of them. Moreover, the bosonization of the Nambu–Jona-Lasinio model with allowance for confinement may lead, as was shown in [14], to a shift of the lightest scalar meson to a mass region around 1 GeV. It follows that, if there are no low-lying $0^{++}$ quark–antiquark states, a nonlinear sigma model may be a theory that describes the dynamics of low-energy processes. In the case of a nonlinear realization of (spontaneously broken) local chiral symmetry [15, 16], the rho meson plays the role of a vector gauge boson, but there is no need for introducing a scalar sigma meson (if, in the $\pi N$ vertex, use is made of a pseudovector-type interaction). In that case, the pole in the amplitude of pion–pion scattering has a dynamical origin associated with a strong attraction in the pion–pion channel. Indeed, it follows from [17, 18] that the required behavior of the scalar spectral function for the amplitude of pion–pion scattering can be obtained if the exchange of a vector (rho) and a scalar [$f_0(980)$] meson in the $t$ and $u$ channels is taken into account along with the unitarity condition. However, the need for explicitly taking into account the exchange of a sigma meson was highlighted in a number of other studies (see, for example, [19, 20]), where it was treated as a $0^{++}$ quark–antiquark state. Thus, the question of whether there is an admixture of quark–antiquark states at the pole that is present in the amplitude for pion–pion scattering and which is associated with the sigma resonance remains open (for a discussion on the problem of revealing a sigma resonance in analyzing experimental data, see also the review article of Vereshchagin *et al.* [21]).

Irrespective of whether there exists (or there does not exist) a sigma meson as a fundamental particle, models of two-nucleon interaction that are based on the dispersion-relation approach [22–24] and investigations of the central component of the nucleon–nucleon potential within chiral perturbation theory [25] revealed that $\sigma$ can be treated as an effective degree of freedom that parametrizes the exchange of two pions. Within chiral perturbation theory, it was also noticed [26] that the values of the constants appearing in the effective pion–nucleon Lagrangian to order $p^2$ in the pion momentum can be obtained on the basis of the resonance-exchange mechanism; that is, they can be expressed in terms of the rho- and sigma-meson masses and coupling constants.

In the majority of meson-exchange models constructed to describe pion–nucleon scattering, the rho and the sigma meson are considered as particles of

fixed mass [5–8]. For the rho meson, this approximation may prove to be justified because of a small width of its spectral function, but, for the sigma meson, it may appear to be overly crude. Moreover, phenomenological form factors are used in relevant interaction vertices, and the parameters of these form factors may be arbitrarily varied with the aim of obtaining the best agreement between theoretical and experimental results. Meson-exchange theories enable one to take into account, at least partly, those processes that make a dominant contribution to the long-range part of the form factors.

In the present study, we explore the effects of pion–pion correlations in the exchange of sigma and rho mesons. These effects may manifest themselves both in the Green's functions for the sigma and the rho meson (if one goes beyond the fixed-mass approximation) and in the form factors for the interaction of these mesons with nucleons. The last circumstance makes it possible to examine mesons for the presence of a quark–antiquark component in them. By way of example, we indicate that, if the sigma meson is only an effective reflection of a strong interaction in the pion–pion channel, its coupling to nucleons must occur via a two-pion state. If this mechanism is taken explicitly into account, there arises no need for introducing an effective Lagrangian that would describe the interaction of scalar and nucleon fields. One of the main goals pursued in this study is to obtain an answer to the question of whether it is possible to describe satisfactorily experimental data on pion–nucleon scattering without introducing a direct sigma–nucleon–nucleon interaction.

The proposed approach is based on the use of analytic properties of the Green's functions for all participant particles and analytic properties of the vertices for sigma- and rho-meson interaction with nucleons. Form factors and functions that parametrize self-energy parts are complex-valued. Their imaginary parts are associated with open multiparticle channels and are determined by the discontinuities of these quantities at the unitary cut in the complex plane of energy. In order to calculate the relevant real parts, we employ the dispersion-relation method [27, 28]. Direct and exchange diagrams involving a nucleon and a delta isobar are also included in the consideration. The delta isobar is described in terms of the Rarita–Schwinger vector–spinor representation. The amplitude for pion–nucleon scattering is calculated on the basis of the $K$-matrix formalism, which makes it possible to take into account the unitarity requirement in the most straightforward way. However, this approach is applicable only in the region of low collision energies, at which there are no effects associated with the production of two or more pions.

## 2. EQUATION OF SCATTERING

In meson-exchange models, emphasis is placed on taking into account multiple-scattering effects and ensuring exact fulfillment of the unitarity condition for the $S$ matrix. Within this conceptual framework, a solution to the problem of pion–nucleon scattering is constructed in three steps that involve (i) specifying an effective interaction Lagrangian, (ii) finding a pion–nucleon potential with the aid of this Lagrangian, and (iii) solving the relevant Bethe–Salpeter equation and determining the $T$ matrix for the scattering process in question.

In principle, the pion–nucleon potential must be an infinite sum of terms corresponding to all possible irreducible Feynman diagrams constructed on the basis of a given Lagrangian. In practice, however, one naturally has to take into account only a finite number of diagrams. In the collision-energy region where effects associated with the possible production of two or more pions are absent or small, only the requirement of two-particle unitarity is imposed on the $S$ matrix. In this case, the potential is usually represented as the sum of terms corresponding to diagrams of the lowest nonvanishing order. The condition of two-particle unitarity then makes it possible to write the Bethe–Salpeter equation in the form

$$T(q_2, q_1; P) = V(q_2, q_1; P) + \int \frac{d^4q}{(2\pi)^4} V(q_2, q; P) G_{\pi N}(q|P) T(q, q_1; P), \quad (1)$$

where $q_1 = (p_1 - k_1)/2$ and $q_2 = (p_2 - k_2)/2$ are, respectively, the initial and the final relative 4-momentum in the system being considered; $p_1$ ($k_1$) and $p_2$ ($k_2$) are, respectively, the initial and the final 4-momentum of the nucleon (pion) involved; $P = p_1 + k_1 = p_2 + k_2$ is the c.m. 4-momentum;

$$G_{\pi N}(q|P) = \frac{i}{(P/2 - q)^2 - m_\pi^2 + i\varepsilon} \times \frac{\not P/2 + \not q + m_N}{(P/2 + q)^2 - m_N^2 + i\varepsilon}$$

is the two-particle relativistic pion–nucleon Green's function (here and below, we use the notation adopted in [27]); $T$ is the scattering matrix; and $V$ is the pion–nucleon potential. For the sake of completeness, we also introduce the Mandelstam variables

$$s = P^2, \quad t = (p_2 - p_1)^2, \quad u = (p_2 - k_1)^2,$$

which we will need below.

Any integral involving $G_{\pi N}$ can be broken down into a pole part and a part that contains its principal values. For this, we represent the Green's function in the form

$$G_{\pi N} = G^R + iG^i, \quad (2)$$

where $G^R$ is its real part, which determines virtual (off-shell) states. The imaginary part $G^i$, which corresponds to the propagation of a real nucleon and a real pion, is determined by the discontinuity of the Green's function at the cut $(m_N + m_\pi)^2 \le s < \infty$ along the real axis in the complex plane of energy; that is,

$$G^i(q|P) = -2\pi^2\left(\frac{\not{P}}{2} + \not{q} + m_N\right) \times \delta\left(\left[\frac{P}{2} - q\right]^2 - m_\pi^2\right)\delta\left(\left[\frac{P}{2} + q\right]^2 - m_N^2\right) \times \theta\left(\frac{P_0}{2} - q_0\right)\theta\left(\frac{P_0}{2} + q_0\right), \quad (3)$$

where $\theta(x)$ is a Heaviside step function.

Substituting (2) into (1) and introducing the real $K$ matrix as

$$K(q_2, q_1; P) = V(q_2, q_1; P) + \int \frac{d^4q}{(2\pi)^4} V(q_2, q; P) G^R(q|P) K(q, q_1; P), \quad (4)$$

we obtain an equation for the $T$ matrix in the operator form

$$T = K + iKG^iT.$$

The simplest way to solve this equation is to employ the partial-wave expansions of the $T$ and $K$ matrices. Taking into account relation (3), we find for the relevant components in the c.m. frame that

$$T^{JLI}(W) = \frac{K^{JLI}(W)}{1 + i\alpha_s K^{JLI}(W)},$$

where $W = \sqrt{s}$;

$$\alpha_s = \frac{m_N}{2s}([s - (m_N + m_\pi)^2][s - (m_N - m_\pi)^2])^{1/2};$$

and the superscripts $J$, $L$, and $I$ represent, respectively, the total angular momentum, the orbital angular momentum, and the isospin of the pion–nucleon system. The form of the imaginary part of the Green's function, $G^i$, is unambiguously determined by the requirement that the $S$ matrix be unitary. Indeed, it can be proven that the $S$ matrix

$$S^{JLI}(W) = 1 - 2i\alpha_s T^{JLI}(W)$$

satisfies this requirement. However, no stringent constraints are imposed on the form of the real part $G^R$. In principle, it must be arbitrary (what is of crucial importance is that no additional unphysical poles arise in the Green's function—that is, $G^R$ must be analytic in the complex plane of energy), and this circumstance is frequently employed in approaches based on applying, as an equation of scattering, various three-dimensional quasipotential reductions of the Bethe–Salpeter equation.

As a matter of fact, mathematical difficulties associated with integration with respect to the variable $q_0$ arise in solving Eq. (4). Moreover, the equation itself has a number of significant flaws: in particular, the single-particle limit corresponding to the case where the mass of one of the particles tends to infinity is incorrect [29]; in addition, some symmetries present in the pion–nucleon potential—such as crossing and chiral symmetries—may be violated in solving this equation.[1)] As applied to pion–nucleon scattering, Eq. (4) has so far been solved directly only in [7, 32]. In other cases, use was made of various approximations based on either a delta-function-like behavior of $G^R$ as a function of $q_0$ [5, 6] or on the disregard of the dependence of the $K$ matrix (and, often, the pion–nucleon potential) on this variable [8]. As a result, integration with respect to $q_0$ was performed straightforwardly, and the resulting equations proved to be formally similar to the Lippmann–Schwinger equation. Because of available freedom in choosing $G^R$, there are an infinite number of such three-dimensional reductions, and there are no strong reasons, in principle, for giving preference to any of them. Moreover, it turned out that the behavior of the pion–nucleon–nucleon and pion–nucleon–delta form factors, as well as the behavior of the off-shell $T$ matrix, depends greatly on the choice of equation of scattering [6].

In view of the uncertainty in choosing an equation of scattering, one sometimes sets $G^R = 0$ (so-called $K$-matrix approximation) in order to simplify ensuing calculations. In this approximation, the $K$ matrix is equivalent to the pion–nucleon potential. At low collision energies, the approach in question was used in a number of studies [33–35], and a fairly good description of experimental data was obtained on this basis for pion–nucleon scattering and for $\gamma N \to \pi N$ reactions. This was because the main contribution to the $K$ matrix came from the first Born term at such energies, rescattering effects being expected to be relatively small in this case.

In the present study, we will also rely on the $K$-matrix approximation, but we will employ it in a somewhat modified form. In accordance with the requirement of two-particle unitarity, the pion–nucleon potential is represented as the sum of second-order diagrams featuring the exchanges of a nucleon and a delta isobar in the $s$ and the $u$ channel and the $t$-channel exchanges of a sigma and a rho meson (see

[1)] This concerns the majority of meson-exchange models. A rigorous inclusion of crossing symmetry and exact consistency with low-energy theorems for the amplitude of pion–nucleon scattering are achieved in models based on chiral perturbation theory [30, 31].

Fig. 1). In the $s$ channel, the interaction has a resonance structure that is associated with the possibility for an intermediate nucleon and an intermediate delta isobar to approach the respective mass shell. Taking this circumstance into account, we can represent the pion–nucleon potential in the form

$$V(q_2, q_1; P) = \sum_{B=N,\Delta} \Gamma^{\dagger}_{B0}(q_2; P) G_{B0}(P) \Gamma_{B0}(q_1; P) + V_{\rm NP}(q_2, q_1; P),$$

where $\Gamma_{B0}$ and $G_{B0}$ are, respectively, the bare vertex and the bare propagator for the baryon $B$ and $V_{\rm NP}$ stands for the entire remaining nonpole part of the potential (diagrams in Figs. 1$b$, 1$c$). Instead of Eq. (4), we then obtain

$$K(q_2, q_1; P) = \sum_{B=N,\Delta} \Gamma^{\dagger}_{B}(q_2; P) G_{B}(P) \Gamma_{B}(q_1; P) + K_{\rm NP}(q_2, q_1; P). \quad (5)$$

Here,

$$K_{\rm NP}(q_2, q_1; P) = V_{\rm NP}(q_2, q_1; P) + \int \frac{d^4q}{(2\pi)^4} V_{\rm NP}(q_2, q; P) G^R(q|P) K_{\rm NP}(q, q_1; P), \quad (6)$$

while $\Gamma_B$ and $G_B$ are the dressed vertex and the dressed propagator for the baryon $B$; for these two quantities, we have

$$\Gamma_B(q_1; P) = \Gamma_{B0}(q_1; P) + \int \frac{d^4q}{(2\pi)^4} \Gamma_{B0}(q; P) G^R(q|P) K_{\rm NP}(q, q_1; P),$$

$$G_B^{-1}(P) = G_{B0}^{-1}(P) - \Sigma_B(P),$$

where

$$\Sigma_B(P) = \int \frac{d^4q}{(2\pi)^4} \Gamma_{B0}(q; P) G^R(q|P) \Gamma^{\dagger}_B(q; P) \quad (7)$$

is the mass operator. The main distinction between our approach and the standard $K$-matrix approximation is that we set $G^R = 0$ only in Eq. (6) and take explicitly into account both the effects of dressing in the pion–nucleon–nucleon and pion–nucleon–delta form factors and the dynamical components in the nucleon and delta-isobar masses.

## 3. INTERACTION LAGRANGIANS

### *3.1. Chiral Lagrangian for the System Formed by a Nucleon, a Pion, and a Rho Meson*

For the system consisting of a nucleon, a pion, and a rho meson, we took an effective Lagrangian

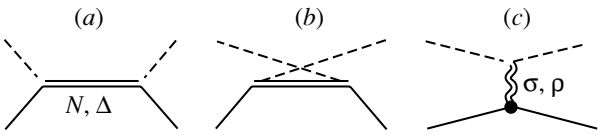


**Fig. 1.** Diagrams representing the pion–nucleon potential: ($a$) $s$-channel exchange of a nucleon and a delta isobar, ($b$) $u$-channel exchange of a nucleon and a delta isobar, and ($c$) $t$-channel exchange of a sigma and a rho meson. The double wavy line represents the renormalized Green's function. The point at the $\rho(\sigma)NN$ vertex denotes that the contribution of two-pion states is taken into account.

that, to second-order terms in the pion field inclusive, coincides with the Wess–Zumino Lagrangian [16] and which involves a nonlinear realization of chiral symmetry and determined the respective interaction potential from this Lagrangian. The specific form of the Lagrangian is

$$\mathcal{L}_{\rm WZ} = \frac{g_{\pi NN}}{2m_N} \bar{N} \gamma^{\mu} \gamma_5 \boldsymbol{\tau} \cdot \partial_{\mu} \boldsymbol{\pi} N - g_{\rho NN} \bar{N} \left\{ \gamma^{\mu} - \frac{\kappa_{\rho}}{2m_N} \sigma^{\mu\nu} \partial_{\nu} \right\} \frac{\boldsymbol{\tau}}{2} \cdot \boldsymbol{\rho}_{\mu} N - g_{\rho\pi\pi} \boldsymbol{\rho}_{\mu} \cdot [\boldsymbol{\pi} \times \partial^{\mu} \boldsymbol{\pi}] - \frac{g_{\rho\pi\pi}}{4m_{\rho}^2} (\delta - 1) \boldsymbol{\rho}_{\mu\nu} \cdot [\partial^{\mu} \boldsymbol{\pi} \times \partial^{\nu} \boldsymbol{\pi}], \quad (8)$$

where $N$, $\boldsymbol{\pi}$, and $\boldsymbol{\rho}_{\mu}$ ($\boldsymbol{\rho}_{\mu\nu} = \partial_{\mu}\boldsymbol{\rho}_{\nu} - \partial_{\nu}\boldsymbol{\rho}_{\mu}$) are, respectively, the nucleon-, the pion-, and the rho-meson-field operator; $\boldsymbol{\tau}$ are the Pauli matrices; and $\sigma_{\mu\nu} = i[\gamma_{\mu}, \gamma_{\nu}]/2$. Of all of the parameters appearing in the Lagrangian $\mathcal{L}_{\rm WZ}$, the particle masses and the pion–nucleon–nucleon coupling constant are known to the highest degree of precision (the coupling constant is set here to $g^2_{\pi NN}/4\pi = 13.6$ [36]). As to terms in the Lagrangian that describe the interaction of the rho meson, there are presently no reliable direct experimental data (maybe, with the exception of data on the $\rho \to \pi\pi$ decay width) that would make it possible to determine the respective coupling constants to a fairly high degree of precision. In performing calculations, one therefore has either to fit these parameters to available experimental information or to employ values that were obtained on the basis of different theoretical models.

At first glance, the Lagrangian in (8) is not an appropriate choice. First, preference has recently been given to the tensor coupling of the rho meson to the pion field [$\delta$ term in (8)]. This is based on the assumption that vector mesons must be associated with the divergences of tensor quark currents [37]. Second, this Lagrangian does not involve a contact interaction with four pion legs. It is well known that the behavior of the amplitude for pion–pion scattering

in the soft-pion approximation [38] is determined by precisely this interaction, which is contained in the Lagrangian [39]

$$\mathcal{L}_{\pi\pi} = \frac{F_\pi^2}{4}\mathrm{tr}(\partial_\mu U^\dagger \partial^\mu U) + \frac{F_\pi^2}{4} m_\pi^2 \mathrm{tr}(U^\dagger + U - 2), \tag{9}$$

where $U(x) = \xi\xi = \exp(2i\pi(x)/F_\pi)$, $\pi \equiv (\boldsymbol{\pi}\cdot\boldsymbol{\tau})/2$, $F_\pi = 92.4$ MeV is the pion decay constant, and the trace tr is taken over the $SU(2)$ isospin indices. But if we assume that the amplitude for pion–pion scattering receives a dominant contribution from the rho-meson-exchange mechanism, as follows from Eq. (8), we will arrive at the relation (in the fixed-mass approximation)

$$\frac{3g_{\rho\pi\pi}^2}{m_\rho^2} = \frac{1}{F_\pi^2}, \tag{10}$$

which leads to a rho-meson decay width that is much less than the experimentally observed value.

We will show, however, that, in the case of a renormalized rho-meson field, the Lagrangian in Eq. (8) is not worse than any other effective Lagrangian that satisfies the requirements of chiral symmetry, Lorentz invariance, and parity conservation. Our argument is based on the statement (known as the theorem of equivalence) that physical observables are independent of the specific choice of interacting fields [40]. In other words, any combinations of fields (but not of their derivatives) characterized by the same quantum numbers and taken at the same point may themselves be considered as physical particles; that is, they can generate the corresponding in- and out-states and satisfy the required commutation relations.

According to the general rules for constructing an effective Lagrangian [41], the Lagrangian for the system consisting of a nucleon, a rho meson, and a pion can be represented in the form

$$\mathcal{L}(x) = \mathcal{L}_0 + \mathcal{L}_{\mathrm{int}} + \mathcal{L}_{\pi\pi} + \mathcal{L}_c + \mathcal{L}_4, \tag{11}$$

where

$$\mathcal{L}_0 = \bar{N}\left[i\gamma^\mu\partial_\mu - m_N\right]N - \frac{1}{2}\mathrm{tr}(\rho_{\mu\nu}\rho^{\mu\nu}) + m_\rho^2\mathrm{tr}(\rho_\mu\rho^\mu)$$

is the Lagrangian for the free nucleon and rho-meson fields;

$$\mathcal{L}_{\mathrm{int}} = \bar{N}[\frac{g_{\pi NN}}{m_N}\gamma^\mu\gamma_5\partial_\mu\pi - \gamma^\mu v_\mu - g_{\rho NN}\gamma^\mu\rho_\mu]N - g_{\rho NN}\frac{\kappa_\rho}{4m_N}\bar{N}\rho_{\mu\nu}\sigma^{\mu\nu}N - \frac{\kappa_\pi}{4m_N}\bar{N}v_{\mu\nu}\sigma^{\mu\nu}N - g'_{\rho\pi\pi}\frac{2F_\pi^2}{m_\rho^2}\mathrm{tr}(\rho_{\mu\nu}v^{\mu\nu})$$

is the component that describes the interaction between the nucleon, the rho meson, and the pion involved; $\mathcal{L}_{\pi\pi}$ is given by (9); and

$$\mathcal{L}_c = (1 - Z_\rho)\left(\frac{1}{2}\mathrm{tr}(\rho_{\mu\nu}\rho^{\mu\nu}) - m_\rho^2\mathrm{tr}(\rho_\mu\rho^\mu)\right) - \delta m_\rho^2 Z_\rho \mathrm{tr}(\rho_\mu\rho^\mu)$$

corresponds to counterterms of the renormalized rho-meson field (we have not written here the counterterms of the renormalized nucleon field since they do not affect the ensuing consideration). In $\mathcal{L}_4$, we have collected terms involving fourth-order and higher order derivatives of the pion field. We have also used the following notation: $\rho_\mu \equiv (\boldsymbol{\rho}_\mu\cdot\boldsymbol{\tau})/2$, $Z_\rho$ is the renormalization constant for the rho-meson wave function, and $\delta m_\rho^2$ is the renormalization constant for the rho-meson mass. The vector field $v_\mu(x)$ is defined as $v_\mu = -(i/2)(\xi^\dagger\partial_\mu\xi + \xi\partial_\mu\xi^\dagger)$; in the leading order, we have

$$v_\mu = -\frac{i}{2F_\pi^2}[\pi, \partial_\mu\pi] + \ldots, \tag{12}$$

$$v_{\mu\nu} = \partial_\mu v_\nu - \partial_\nu v_\mu + i[v_\mu, v_\nu] = -\frac{i}{F_\pi^2}[\partial_\mu\pi, \partial_\nu\pi] + \ldots$$

We now redefine the rho-meson field in (11), making the substitution $\rho_\mu \to \rho_\mu - v_\mu/g_{\rho NN}$ and, accordingly, the substitution $\rho_{\mu\nu} \to \rho_{\mu\nu} - v_{\mu\nu}/g_{\rho NN}$; in view of the theorem of equivalence [40], this will not change the values of physical observables. As a result, the structure of the Lagrangians $\mathcal{L}_{\mathrm{int}}$ and $\mathcal{L}_4$ will change: $\mathcal{L}_{\mathrm{int}} \to \mathcal{L}'_{\mathrm{int}}$ and $\mathcal{L}_4 \to \mathcal{L}'_4$. For $\mathcal{L}'_{\mathrm{int}}$, we obtain

$$\mathcal{L}'_{\mathrm{int}} = \bar{N}\left[\frac{g_{\pi NN}}{m_N}\gamma^\mu\gamma_5\partial_\mu\pi - g_{\rho NN}\gamma^\mu\rho_\mu\right]N \tag{13}$$

$$- g_{\rho NN}\frac{\kappa_\rho}{4m_N}\bar{N}\rho_{\mu\nu}\sigma^{\mu\nu}N - \frac{\kappa_\pi - \kappa_\rho}{4m_N}\bar{N}v_{\mu\nu}\sigma^{\mu\nu}N - \frac{2Z_\rho}{g_{\rho NN}}(m_\rho^2 - \delta m_\rho^2)\mathrm{tr}(\rho_\mu v^\mu) + (\frac{Z_\rho}{g_{\rho NN}} - g'_{\rho\pi\pi}\frac{2F_\pi^2}{m_\rho^2})\mathrm{tr}(\rho_{\mu\nu}v^{\mu\nu}) + \frac{Z_\rho}{g_{\rho NN}^2}(m_\rho^2 - \delta m_\rho^2)\mathrm{tr}(v_\mu v^\mu).$$

Assuming vector-meson dominance, setting $\kappa_\pi = \kappa_\rho$ in (13), and taking into account (12), we then arrive at

$$\mathcal{L}'_{\mathrm{int}} = \mathcal{L}_{\mathrm{WZ}} + \frac{Z_\rho}{g_{\rho NN}^2}(m_\rho^2 - \delta m_\rho^2)\mathrm{tr}(v_\mu v^\mu). \tag{14}$$

Concurrently, the following relations hold for the rho-meson coupling constants:

$$g_{\rho NN} = \frac{Z_\rho(m_\rho^2 - \delta m_\rho^2)}{2F_\pi^2 g_{\rho\pi\pi}}, \qquad (15)$$

$$\frac{g_{\rho\pi\pi}}{4m_\rho^2}(1-\delta) = \left(\frac{Z_\rho}{2F_\pi^2 g_{\rho NN}} - \frac{g'_{\rho\pi\pi}}{m_\rho^2}\right). \qquad (16)$$

We note that relation (15) is the analog of the well-known Kawarabayashi–Suzuki–Riazuddin–Fayazuddin relation [42] for the case of the renormalized rho-meson field. For the Lagrangians in Eqs. (8) and (11) to lead to the same rho-meson decay width, the following relation must also be valid:

$$g'_{\rho\pi\pi} = \frac{5-\delta}{4} g_{\rho\pi\pi}.$$

Taking into account relations (15) and (16), we then find for the parameter $\delta$ that

$$\delta = 1 - \frac{2\delta m_\rho^2}{m_\rho^2 - \delta m_\rho^2}. \qquad (17)$$

For small values of $\delta m_\rho^2$, this parameter is obviously close to unity.

It can now be proven that, if the relation

$$\frac{3Z_\rho(m_\rho^2 - \delta m_\rho^2)}{4g_{\rho NN}^2 F_\pi^2} = 1$$

or the relation

$$\frac{3g_{\rho\pi\pi}^2 F_\pi^2}{Z_\rho(m_\rho^2 - \delta m_\rho^2)} = 1, \qquad (18)$$

which is equivalent to it with allowance for (15), holds, the last term in (14) and the analogous term in the Lagrangian $\mathcal{L}_{\pi\pi}$ cancel each other completely. The $\pi^4(x)$ interaction remaining in $\mathcal{L}_{\pi\pi}$ and violating chiral symmetry can further be taken into account by introducing an effective scalar field associated with the sigma meson.

Let us compare expressions (18) and (10). Since $\delta m_\rho^2$ is always negative, the equality in (18) may now be in agreement with the experimental value of the rho-meson decay width. This circumstance highlights the importance of renormalization in field theory.

### *3.2. Lagrangian for a Scalar Field*

For the Lagrangian describing the interaction of a scalar field, we took

$$\mathcal{L}_\sigma = -\frac{g_{\sigma\pi\pi}}{2m_\pi}\sigma(\partial_\mu\boldsymbol{\pi}\cdot\partial_\mu\boldsymbol{\pi}) + \frac{g_{\sigma\pi\pi}}{2}c_\sigma m_\pi\sigma(\boldsymbol{\pi}\cdot\boldsymbol{\pi}), \qquad (19)$$

with $\sigma$ being the scalar-field operator. We emphasize that, in (19), there is no term corresponding to the direct interaction of a scalar and a nucleon field.[2)] The value of the coupling constant $g_{\sigma\pi\pi}$ is determined from the presumed decay width of the sigma meson. The second term in (19) introduces a breakdown of chiral symmetry. The value of $c_\sigma = 1$ corresponds to the absence of the contributions to the pion–pion and pion–nucleon $S$-wave scattering lengths from the mechanism of sigma-meson exchange. According to the low-energy theorem for pion–nucleon scattering [38], the main contribution to the $S$-wave amplitude must come from the exchange of a vector rho meson. However, the value of the parameter $c_\sigma$ may slightly differ from unity in our study, since sigma-meson exchange also parametrizes here $\pi^4(x)$ interaction, which contributes to the pion–pion scattering amplitude in the soft-pion approximation.

### *3.3. Lagrangian for the Interaction of a Pion, a Nucleon, and a Delta Isobar*

Because of available freedom in the choice of interacting fields, various forms of delta-isobar coupling to a nucleon and a pion are possible. As a matter of fact, all of them differ only in the strength of nucleon and pion coupling to the component of the delta-isobar spin equal to 1/2 [43]. It was shown in [44] that, apart from the contact pion–pion–nucleon–nucleon interaction, which may be absorbed in the mechanism of sigma-meson exchange, the respective Lagrangians are equivalent to one another. Thus, there inevitably arises an uncertainty in the scalar-field parameters that depends on the form of the pion–nucleon–delta interaction used. Since the contribution of the sigma-meson-exchange mechanism to the pion–nucleon scattering length is small in the proposed model, the delta-isobar contribution must also be insignificant. This condition is satisfied in the case of the gauge-invariant Lagrangian that was proposed in [45]. It has the form

$$\mathcal{L}_{\pi N\Delta} = \frac{g_{\pi N\Delta}}{m_\pi m_\Delta}\varepsilon^{\mu\nu\alpha\beta}(\partial_\mu\bar{\Delta}_\nu)\gamma_5\gamma_\alpha\mathbf{T}\cdot\partial_\beta\boldsymbol{\pi}N + \text{h.c.}, \qquad (20)$$

where $m_\Delta$ is the delta-isobar mass, $\Delta_\mu$ is a vector–spinor field, $\mathbf{T}$ is a $4\times 2$ matrix that determines transitions between isospin-1/2 and isospin-3/2 states, $\varepsilon^{\mu\nu\alpha\beta}$ is an antisymmetric tensor, and h.c. stands for the Hermitian conjugate term. The coupling constant

[2)] We recall that a scalar-type contact $\pi\pi NN$ interaction, which could be taken into account by introducing a direct $\sigma NN$ interaction, is absent if use is made of a pseudovector pion–nucleon coupling, as in (8).

$g_{\pi N\Delta}$ is determined on the basis of the known delta-isobar decay width. This Lagrangian is invariant under the Rarita–Schwinger gauge transformation

$$\Delta_\mu(x) \to \Delta_\mu(x) + \partial_\mu u(x),$$

where $u(x)$ is a bispinor; therefore, it rules out the possible appearance of spin-1/2 states in the delta-isobar Green's function.

## 4. FORM FACTORS

In order to specify the pion–nucleon potential definitively, the vertices constructed on the basis of the Lagrangians in Eqs. (8), (19), and (20) must be supplemented with phenomenological form factors that reflect the dynamics of processes not included in the consideration explicitly. These form factors are also necessary for regularizing the renormalized Green's functions and vertex operators for hadrons. For the rho–pion–pion and sigma–pion–pion vertices, we used the parametrization

$$F_x(t) = \frac{\Lambda_x^4}{\Lambda_x^4 + (t - m_x^2)^2},$$

where $x$ stands for a sigma or a rho meson. For the exchange of a baryon $B$ in the $u$ channel (see Fig. 1*b*), the form factor corresponding to the bare vertex $\Gamma_{B0}$ is given by

$$F_{B0}(u) = \left(\frac{\Lambda_{B0}^4}{\Lambda_{B0}^4 + (u - m_B^2)^2}\right)^2.$$

The invariant structure of the renormalized vertices $\Gamma_B$ is assumed to be identical to that of the bare vertices $\Gamma_{B0}$. However, the effects of dressing are taken into account by using different form factors; that is,

$$F_N(s) = \left(\frac{\Lambda_N^4}{\Lambda_N^4 + (s - m_N^2)^2}\right)^2$$

in the pion–nucleon–nucleon vertex and

$$F_\Delta(s) = \left(\frac{\Lambda_\Delta^4}{\Lambda_\Delta^4 + (s - \widetilde{m}_\Delta^2)^2 - (m_\Delta - \widetilde{m}_\Delta)^2}\right)^2$$

in the pion–nucleon–delta vertex. The last form factor is somewhat asymmetric with respect to the delta-isobar mass, but this was necessary for reproducing the $P_{33}$-wave phase shift [34, 46]. The cutoff parameters $\Lambda_i$ and $\widetilde{m}_\Delta$ are free parameters of the model and are determined from a fit to experimental data. We have also performed calculations with different parametrizations of the form factors, but they have not provided a better description of the phase shifts.

The form of the vertex functions and the dependence of the form factor on the kinematical variables are dictated by Lorentz invariance. In the case where both nucleons are on the mass shell, the sigma–nucleon–nucleon and the rho–nucleon–nucleon vertex are given by

$$\Gamma_{\sigma NN} = ig_{\sigma NN} F_{\sigma NN}(t),$$

$$\Gamma^{\mu a}_{\rho NN} = -ig_{\rho NN}\frac{\tau^a}{2}\Big(\gamma^\mu F_{\rho NN1}(t) - i\frac{\kappa_\rho}{2m_N}\sigma^{\mu\nu}k_\nu F_{\rho NN2}(t)\Big),$$

where $k_\nu$ is the sigma- or the rho-meson momentum, $t = k^2$, $a$ is the isotopic index, and the form factors $F_i(t)$ for the sigma- and rho-meson interaction with a nucleon (here, $i$ stands for $\rho NN1$, $\rho NN2$, or $\sigma NN$) are normalized by the condition $F_i(0) = 1$. The dispersion-relation method is used to calculate $F_i(t)$.

In practice, dispersion-relation calculations always rely on an approximation where one takes into account only the contributions from the simplest intermediate states. We will assume that the main contribution to the long-range part of the form factors $F_i(t)$ comes from sigma- and rho-meson coupling to a dipion state. The corresponding diagrams are shown in Fig. 2. For the form factors $F_i(t)$ where one or a few arguments are analytically continued from their physical values, the region of analyticity can be found on the basis of the microcausality condition. If $t$ is chosen for a dispersion variable, then, for a singularity to emerge in $F_i(t)$, there must exist a reduced graph in which a virtual sigma or rho meson is coupled to a real intermediate dipion state. However, this graph is meaningful in the unphysical region, for $t \geq 4m_\pi^2$, whereas the annihilation process $\pi^+ + \pi^- \to \bar{N} + N$ is allowed only above the threshold of $4m_N^2$. As a result, it becomes necessary to perform an analytic continuation of the annihilation amplitude and of the unitarity condition as well, which is used in calculating the absorptive parts of the form factors. In order to avoid invoking such assumptions, we use here a somewhat different approach.

Let us consider a more general case where, in the sigma–nucleon–nucleon and rho–nucleon–nucleon vertices, only one line corresponds to a real nucleon, which, for example, has a momentum $p'$, the variable $p^2$ being analytically continued from its physical value of $p^2 = m_N^2$. It was rigorously proven in [47] that, in this case, the dispersion relation

$$\widetilde{F}_i(t) = \frac{1}{\pi}\int\limits_{p_{\text{thr}}^2}^{\infty} \frac{\mathrm{Im}\widetilde{F}_i(p^2, t)dp^2}{p^2 - m_N^2},$$

where the notation $\widetilde{F}$ means that the form factor in question has yet to be normalized, holds for any

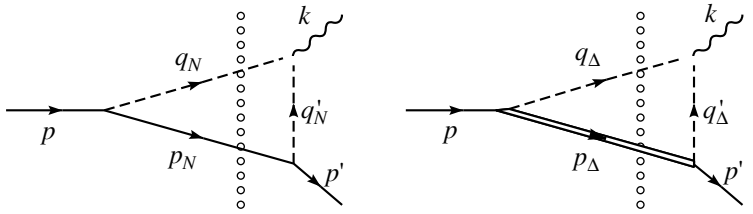


**Fig. 2.** Contribution of dipion states to the vertices for sigma- and rho-meson interaction with nucleons. The single solid, double solid, dashed, and wavy lines represent, respectively, a nucleon, a delta isobar, a pion, and a sigma or a rho meson. The dotted line denotes a unitary cut in calculating the imaginary parts of the respective form factors.

spacelike vector $k_\nu$. In this formulation, the imaginary part of the form factor is due to the existence of real pion–nucleon and pion–delta states, the lower boundary of the region where a singularity may occur intersecting the real axis at $p^2_{\rm thr} = (m_\pi + m_N)^2$. The procedure for deriving the imaginary parts $\mathrm{Im}\widetilde{F}_i(p^2, t)$ is described in the Appendix.

Under the assumption that a sigma meson is coupled to a nucleon via a dipion state exclusively, the respective form factor is normalized by the condition $F_{\sigma NN}(t) = \widetilde{F}_{\sigma NN}(t)/\widetilde{F}_{\sigma NN}(0)$, and the coupling constant is given by $g_{\sigma NN} = \widetilde{F}_{\sigma NN}(0)$. The coupling of a rho meson to a nucleon is determined by the Lagrangian in Eq. (8), where $g_{\rho NN}$ and $\kappa_\rho$ are parameters that characterize the interaction of the renormalized rho-meson field. Therefore, the normalization of the rho-meson form factors is performed by means of one subtraction:

$$F_{\rho NN1}(t) = 1 + \frac{\widetilde{F}_{\rho NN1}(t) - \widetilde{F}_{\rho NN1}(0)}{g_{\rho NN}},$$

$$F_{\rho NN2}(t) = 1 + \frac{\widetilde{F}_{\rho NN2}(t) - \widetilde{F}_{\rho NN2}(0)}{\kappa_\rho g_{\rho NN}}.$$

## 5. MESON AND BARYON GREEN'S FUNCTIONS

Effects of pion–pion correlations are also taken into account by using the renormalized sigma- and rho-meson Green's functions in the pion–nucleon potential, which satisfy the Dyson equation and which have the form

$$G_\sigma(t) = \frac{1}{t - m_\sigma^2 - \Pi_{\sigma,R}(t)},$$

$$G_{\rho,\mu\nu}(t) = -\frac{P^1_{\mu\nu}}{t - m_\rho^2 - \Pi_{\rho,R}(t)} + \frac{P^0_{\mu\nu}}{m_\rho^2},$$

where $P^1_{\mu\nu} = g_{\mu\nu} - k_\mu k_\nu/t$ and $P^0_{\mu\nu} = k_\mu k_\nu/t$ are the operators of projection onto, respectively, spin-1 states and states of spin zero, while $\Pi_{x,R}(t)$ is the renormalized polarization operator. The polarization operator is renormalized via the subtraction of counterterms that are contained in the free-field Lagrangian; that is,

$$\Pi_{x,R}(t) = \Pi_x(t) - (t - m_x^2)(Z_x - 1) - Z_x \delta m_x^2,$$

where

$$Z_x = 1 + \frac{d}{dt}\mathrm{Re}\Pi_x(t)\Big|_{t=m_x^2}, \quad \delta m_x^2 = \frac{1}{Z_x}\mathrm{Re}\Pi_x(m_x^2)$$

are the renormalization constants for, respectively, the wave function and the mass of the meson $x$.

The polarization operator $\Pi_x$ is represented by the diagram having the shape of a two-pion loop (see Fig. 3). Its imaginary part, which corresponds to sigma- or rho-meson decay into two real photons, which is followed by their annihilation, can be found from the condition requiring that the $S$ matrix be unitary [48]. As a result, we obtain

$$\mathrm{Im}\Pi_\sigma(t) = -\frac{3g^2_{\sigma\pi\pi}}{128\pi}\frac{(t - 2m_\pi^2(1 - c_\sigma))^2}{m_\pi^2} \times \sqrt{1 - \frac{4m_\pi^2}{t}}F_\sigma^2(t),$$

$$\mathrm{Im}\Pi_\rho(t) = -\frac{g^2_{\rho\pi\pi}}{48\pi}(t - 4m_\pi^2)\sqrt{1 - \frac{4m_\pi^2}{t}}F_\rho^2(t)$$

for $t \geq 4m_\pi^2$ and $\mathrm{Im}\Pi_x(t) = 0$ for $t < 4m_\pi^2$.

At collision energies below the threshold for the production of two pions, the $K$ matrix is real, and the effects of pion–pion correlations are taken into account through the real part of the polarization operator exclusively. By using the analytic properties

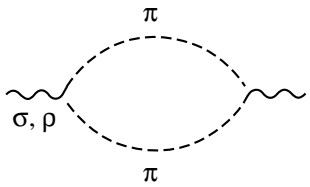


**Fig. 3.** Diagram corresponding to the sigma- and rho-meson polarization operators.

**Table 1.** Model parameters

| Particle | Coupling constant | Particle mass and cutoff parameter, GeV |
|---|---|---|
| $N$ | $\frac{g^2_{\pi NN}}{4\pi} = 13.6$ | $m_N = 0.939,\ \Lambda_{N0} = 1.75$ |
| | | $\Lambda_N = 1.15$ |
| $\pi$ | | $m_\pi = 0.138$ |
| $\Delta$ | $\frac{g^2_{\pi N\Delta}}{4\pi} = 0.35$ | $m_\Delta = 1.231,\ \widetilde{m}_\Delta = 1.02$ |
| | | $\Lambda_{\Delta 0} = 1.4,\ \Lambda_\Delta = 1.2$ |
| $\rho$ | $\frac{g^2_{\rho\pi\pi}}{4\pi} = 2.86,\ \frac{g^2_{\rho NN}}{4\pi} = 4.84$ | $m_\rho = 0.77,\ \Lambda_\rho = 1.5$ |
| | $\kappa_\rho = 1.2,\ \delta = 1$ | |
| $\sigma$ | $\frac{g^2_{\sigma\pi\pi}}{4\pi} = 0.54$ | $m_\sigma = 0.65,\ \Lambda_\sigma = 1.1$ |
| | $c_\sigma = 1.14$ | |

of the operator $\Pi_x$, we obtain for it the dispersion relation

$$\mathrm{Re}\Pi_x(t) = \frac{1}{\pi} P \int\limits_{4m_\pi^2}^{\infty} \frac{\mathrm{Im}\Pi_x(t')dt'}{t'-t},$$

where the symbol $P$ means the principal-value prescription for the integral involved.

The baryon propagator $G_B$ in (5) is calculated by a method similar to that used to calculate the sigma- and rho-meson propagators. The problem here consists in calculating the mass operator $\Sigma_B$ (7), which takes into account the dressing of the baryon with a meson cloud.

We define the operator

$$\widetilde{\Sigma}_B(P) = \int \frac{d^4q}{(2\pi)^4} \Gamma_{B0}(q;P) G_{\pi N}(q|P) \Gamma^\dagger_B(q;P),$$

which, in contrast to $\Sigma_B$, includes an intermediate state featuring two real particles. We have $\Sigma_B = \mathrm{Re}\widetilde{\Sigma}_B$. By virtue of Lorentz invariance, the following relation also holds:

$$\widetilde{\Sigma}_N = a_N(s)\not{P} + b_N(s) m_N.$$

If delta-isobar interaction with a pion and a nucleon is specified by the Lagrangian in Eq. (20), then, in order to determine the Green's function $G_\Delta$, it is sufficient to find only that part of the mass operator which corresponds to a spin-3/2 state [46]; that is,

$$\widetilde{\Sigma}_{\Delta\mu\nu} = (a_\Delta(s)\not{P} + b_\Delta(s) m_\Delta) P^{3/2}_{\mu\nu},$$

where

$$P^{3/2}_{\mu\nu} = g_{\mu\nu} - \frac{1}{3}\gamma_\mu\gamma_\nu - \frac{1}{3P^2}(\not{P}\gamma_\mu P_\nu + P_\mu \gamma_\nu \not{P})$$

is the operator of projection onto the spin-3/2 state of the delta isobar.

By using the unitarity condition, we obtain

$$\mathrm{Im}\widetilde{\Sigma}_B(P) = -\frac{\alpha_s}{2(4\pi)^2 m_N} \times \int \Gamma_{B0}(q;P)(\not{q} + m_N)\Gamma^\dagger_B(q;P) d\Omega_{\mathbf{q}},$$

whence it follows that

$$\mathrm{Im}a_N(s) = C_N(2m_N^2 - \beta_s(s+m_N^2)),$$
$$\mathrm{Im}b_N(s) = C_N m_\pi^2;$$
$$\mathrm{Im}a_\Delta(s) = -C_\Delta \frac{m_\Delta}{m_N}\beta_s, \quad \mathrm{Im}b_\Delta(s) = -C_\Delta,$$

where

$$C_N = \left(\frac{g_{\pi NN}}{2m_N}\right)^2 \frac{3\alpha_s}{8\pi m_N} F_{N0}(s) F_N(s),$$

$$C_\Delta = \left(\frac{g_{\pi N\Delta}}{m_\pi m_\Delta}\right)^2 \frac{s^2\alpha_s^3}{24\pi m_\Delta m_N^2} F_{\Delta 0}(s) F_\Delta(s),$$

and

$$\beta_s = \frac{s + m_N^2 - m_\pi^2}{2s}.$$

Further, we reduce the real parts to the form

$$\mathrm{Re}a_B(s) = \frac{1}{\pi} P \int\limits_{(m_N+m_\pi)^2}^{\infty} \frac{\mathrm{Im}a_B(s')ds'}{s'-s}$$

and derive a similar relation for the coefficient $b_B(s)$.

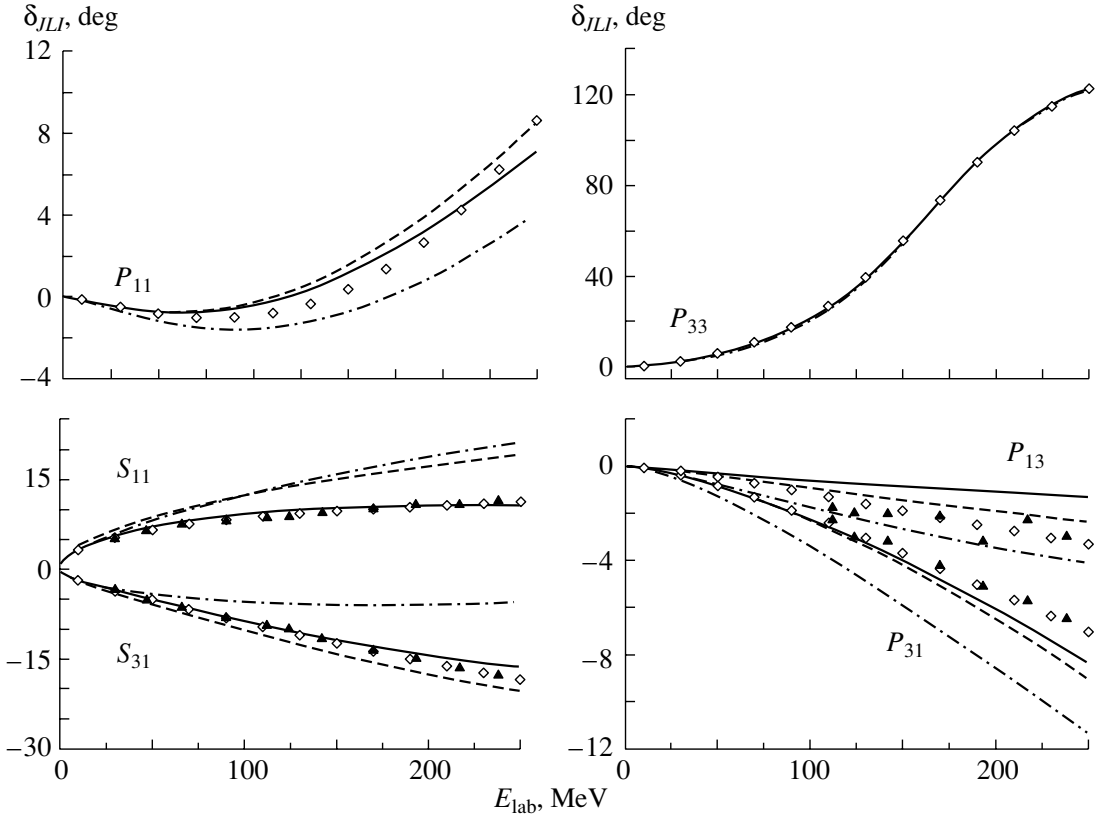


**Fig. 4.** Pion–nucleon phase shifts (theoretical curves and experimental points): (solid curve) results of the calculation taking into account the effects of pion–pion correlations, (dashed curve) results of the calculation disregarding pion–pion correlations in rho-meson exchange, (dash-dotted curve) results of the calculation not including sigma-meson exchange, (open diamonds) SM95 data from [50], and (closed triangles) KH80 data from [51].

Renormalization is performed as

$$\Sigma_{B,R}(P) = \Sigma_B(P) + (1 - Z_B)(\not{P} - m_B) - Z_B\delta m_B,$$

where the renormalization constants for the wave function and mass are

$$Z_B = 1 + \mathrm{Re}a_B(m_B^2) + 2m_B^2\frac{d}{dp^2}(\mathrm{Re}a_B(p^2) + \mathrm{Re}b_B(p^2))\Big|_{p^2=m_B^2},$$

$$\delta m_B = \frac{m_B}{Z_B}(\mathrm{Re}a_B(m_B^2) + \mathrm{Re}b_B(m_B^2)).$$

## 6. RESULTS OF THE CALCULATIONS AND DISCUSSION

Values of all of the parameters used in the present model are quoted in Table 1. Some of them are not free. In addition to the known value of the pion–nucleon coupling constant $g_{\pi NN}$, the parameters $g_{\pi N\Delta}$ and $g_{\rho\pi\pi}$ were determined from the experimental decay widths of the delta isobar and the rho meson [10]. In doing this, we used the value of $\delta = 1$, which is in accord with formula (17); that is, we completely disregarded the tensor coupling of the rho meson to the pion field. We have also performed calculations with a value of $\delta$ differing slightly from unity, but we have not found any noticeable distinctions between the two cases in the behavior of the phase shifts. The sigma-meson mass and the coupling constant $g_{\sigma\pi\pi}$ were determined from the analysis of the scalar spectral amplitude for pion–

**Table 2.** Scattering lengths and volumes in units of $m_\pi^{-2L-1}$ as obtained within the present model, along with the SM95 experimental data from [50] and the KH80 experimental data from [51]

| $L_{2I2J}$ | Present model | SM95 | KH80 |
|---|---|---|---|
| $S_{11}$ | 0.173 | 0.175 | 0.173 |
| $S_{31}$ | −0.087 | −0.087 | −0.101 |
| $P_{11}$ | −0.076 | −0.068 | −0.081 |
| $P_{13}$ | −0.021 | −0.022 | −0.030 |
| $P_{31}$ | −0.040 | −0.039 | −0.045 |
| $P_{33}$ | 0.205 | 0.209 | 0.214 |

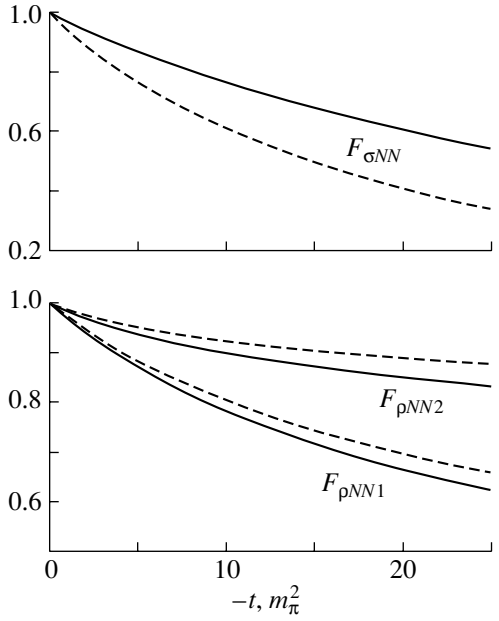


**Fig. 5.** Form factors for (upper panel) the sigma and (lower panel) the rho meson versus the momentum transfer squared in $m_\pi^2$ units: (solid curves) results obtained with allowance for the contributions that arise, at the unitary cut, from pion–nucleon and pion–delta states and (dashed curves) results obtained with allowance for only pion–nucleon states.

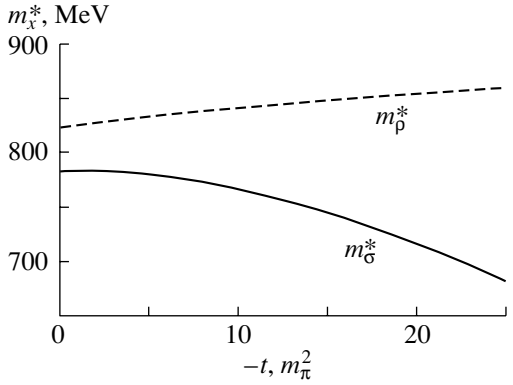


**Fig. 6.** Effective masses of (solid curve) the sigma and (dashed curve) the rho meson versus the momentum transfer squared in $m_\pi^2$ units.

nucleon scattering, this amplitude being calculated on the basis of pseudoempirical data on the reaction $N\bar{N} \to \pi\pi$, which, in turn, were obtained as an analytic continuation of experimental data on pion–pion and pion–nucleon scattering [49]. The value of $g^2_{\sigma\pi\pi}/4\pi = 0.54$ corresponds to the sigma-meson decay width of $\Gamma_\sigma \simeq 680$ MeV. There are also some constraints on the cutoff parameters $\Lambda_i$—namely, an upper bound on the possible values that is determined by the convergence of the respective polarization or mass operator exists for each of them. For example, the value of the parameter $\Lambda_\sigma$ lies in the vicinity of its upper bound.

Free-parameter values are usually determined from a fit to experimental data. In the case of elastic pion–nucleon scattering, this means that the present model must reproduce phase shifts fairly well, along with low-energy features, such as scattering lengths and volumes. In the channel characterized by the orbital angular momentum $L$, the total angular momentum $J$, and the isospin $I$, the phase shifts are expressed in terms of the partial-wave $K$ matrix as

$$\tan\delta_{JLI} = -\alpha_s K_{JLI}.$$

At very low collision energies, the momentum dependence of $K_{JLI}$ has the form $p^{2L}$, where $p = \sqrt{s}\alpha_s/m_N$. In this case, it is more convenient to explore the scattering length ($L = 0$) or the scattering volume ($L = 1$) rather than the phase shifts; that is,

$$a_{JLI} = p^{-2L-1}\tan\delta_{JLI}.$$

The calculated scattering lengths and volumes are quoted in Table 2, while the phase shifts are displayed in Fig. 4 versus the pion kinetic energy in the laboratory frame; also given there for the sake of comparison are the corresponding results of the partial-wave analysis of the SM95 data from [50] and the KH80 data from [51]. It can be seen that the present model reproduces the experimental data fairly well, at least up to a collision energy of $E_{\rm lab} \approx 250$ MeV.

In order to investigate effects due to pion–pion correlations, the results of the calculations in which the contribution of dipion states are disregarded both in the vertices of sigma- and rho-meson interaction with nucleons and in the sigma- and rho-meson Green's functions are also shown in Fig. 4. Two cases are considered individually: that in which virtual dipion states are disregarded in rho-meson exchange and that in which the mechanism of sigma-meson exchange is switched off, the latter being singled out because, in the present study, the sigma meson is considered as a dynamical effect in the dipion system. On the basis of the data in Fig. 4, it can be concluded that the sigma-meson-exchange mechanism, which parametrizes the strong pion–pion interaction in the $S$ wave, plays a significant role in pion–nucleon scattering. This is not so only for the resonance $P_{33}$ wave, which receives the main contribution from the $s$-channel exchange of a delta isobar and a somewhat smaller contribution from the $u$-channel exchange of a nucleon. The effect of pion–pion correlations is sizable in rho-meson exchange as well—it is especially pronounced in the $S_{11}$ wave.

For the interaction of the scalar and the nucleon field, the coupling constant is found to be $g_{\sigma NN} = 12$.

Thus, we see that, with allowance for the signs in the Lagrangian specified by Eq. (19), the potential corresponding to sigma-meson exchange is repulsive in the $S$ wave and is attractive in the $P$ wave. The same result was obtained in [52] from an analysis of pion–pion correlations. It is interesting to note that the value of $m_\sigma/\sqrt{g_{\sigma NN}} = 187$ is in good agreement with the value of $m_\sigma/\sqrt{g_{\sigma NN}} = 180$, which was derived within chiral perturbation theory [26]. In calculating the sigma–nucleon–nucleon form factor, the much smaller value of $g_{\sigma NN} = 4.5$ is obtained for the coupling constant without taking into account an intermediate pion–delta state. The effect of pion–delta states on the behavior of the form factors in the vertices of sigma- and rho-meson interaction with nucleons is illustrated in Fig. 5. For the case of a sigma meson, its inclusion leads to a considerable increase in the contribution of states characterized by a high momentum transfer, whereas, for the rho-meson form factors, the effect is qualitatively inverse and is much weaker quantitatively. This indicates that the mechanism of delta-isobar excitation plays an important role in studying nucleon interaction with a dipion system in the $S$-wave state. Here, one can trace an analogy with the nucleon–nucleon interaction, where the isoscalar central component of the potential—this component is often parametrized in terms of sigma-meson exchange—is determined primarily by the excitation of a virtual delta isobar in two-pion exchange [53].

That the dynamical components of the masses of the sigma and the rho meson are significant is suggested by the values of the renormalization constants for the wave functions and masses of these mesons. The calculated values of these features are compiled in Table 3. It can be concluded that the effects of pion–pion correlations play a crucial role for the sigma meson. For example, a value of a few GeV units is obtained for the bare sigma-meson mass. This means that the physical mass of $m_\sigma = 0.65$ GeV is of an almost completely dynamical origin that is associated with correlation effects in the exchange of two pions. The effective masses of the sigma and the rho meson behave differently. The behavior of the effective masses of the sigma and the rho meson, $m_x^* = \sqrt{m_x^2 + \Pi_{x,R}(t)}$, versus energy transfer is shown in Fig. 6 for values of the variable $t$ that are of importance for elastic pion–nucleon scattering. While the effective mass $m_\rho^*$ increases with increasing energy transfer, $m_\sigma^*$ decreases quite fast. It is worth noting here that neither the form factors nor the effective masses are observable; therefore, they may depend on the representation of interacting fields. By way of example, we indicate that, in the Lagrangians specified by Eqs. (8) and (11), the rho mesons feature different weights of dipion states; these are different rho mesons—their form factors will behave differently, and their normalization constants will take different values. In the present study, we employ a specific representation where dynamics in the pion–pion system is entirely absorbed in the properties of the rho and sigma mesons.

**Table 3.** Renormalization constants obtained in the model used in the present study

| Particle | $Z_x$ | $\delta m_x^2$, GeV$^2$ | Particle | $Z_B$ | $\delta m_B$, MeV |
|---|---|---|---|---|---|
| $\rho$ | 1.02 | −0.2 | $N$ | 0.87 | −50.3 |
| $\sigma$ | 0.09 | −17.3 | $\Delta$ | 0.93 | −121.8 |

The value found for the parameter $\kappa_\rho$, which characterizes the strength of the tensor coupling of a nucleon to a rho meson, is much less than the value of $\kappa_\rho \approx 6$, which is used in nucleon–nucleon potentials, and is even less than the value of $\kappa_\rho = 3.7$, which is dictated by the model of vector-meson dominance in nucleon electromagnetic form factors. However, the smallness of this parameter is peculiar to the majority of models for describing pion–nucleon scattering, its specific value being greatly dependent, as was shown in [7], on the form of the equation of scattering used.

With allowance for the values found for the constants of renormalization of the rho-meson field and the value found for the parameter $g_{\rho NN}$ by means of fitting, one can assess the accuracy to which relations (15) and (18) hold. By using values from Tables 1 and 3, we obtain

$$\frac{Z_\rho(m_\rho^2 - \delta m_\rho^2)}{2F_\pi^2 g_{\rho\pi\pi} g_{\rho NN}} = 1.01,$$

$$\frac{3g_{\rho\pi\pi}^2 F_\pi^2}{Z_\rho(m_\rho^2 - \delta m_\rho^2)} = 1.13.$$

Thus, the present model complies well with the requirements of chiral theory and has quite a sound microscopic basis.

## 7. CONCLUSION

While the rho meson can be represented as a superposition of quark–antiquark and dipion states, no definitive and noncontradictory conclusions on the structure of the sigma resonance, which manifests itself in the dipion system in the $S$ wave, have been drawn so far. In the present study, the effect of the pion–pion component of the sigma and rho resonances on the features of elastic pion–nucleon scattering at collision energies below the threshold for the production of two pions has been examined within a dynamical resonance model. In doing this, it has

been assumed that the sigma resonance involves no quark–antiquark component and that it completely parametrizes the scalar part of strong interaction in the pion–pion system. It has been shown that a satisfactory description of experimental data can be obtained without introducing a sigma meson as a fundamental particle.

## APPENDIX

Let us now proceed to describe a specific calculation of the imaginary parts of the form factors $\widetilde{F}_i(p^2,t)$. In doing this, we make use of the condition requiring that the $S$ matrix that corresponds to the sigma–nucleon–nucleon vertex involving two two-particle intermediate states, $\pi N$ and $\pi\Delta$, be unitary. In the reference frame where $\mathbf{p}=0$, we then obtain

$$\begin{aligned}\mathrm{Im}\widetilde{F}_{\sigma NN} = &-\frac{|\mathbf{q}_N|}{2(4\pi)^2 p_0}\int \Gamma^{ab}_{\sigma\pi\pi}\Gamma^{b}_{\pi NN}\frac{i(\not{p}_N+m_N)}{q_N'^2-m_\pi^2}\Gamma^{a}_{\pi NN}d\Omega_{\mathbf{q}_N}\\ &+\frac{|\mathbf{q}_\Delta|}{2(4\pi)^2 p_0}\int \Gamma^{ab}_{\sigma\pi\pi}\Gamma^{\alpha b}_{\Delta N\pi}\frac{i(\not{p}_\Delta+m_\Delta)}{q_\Delta'^2-m_\pi^2}P^{3/2}_{\alpha\beta}\Gamma^{\beta a}_{N\Delta\pi}d\Omega_{\mathbf{q}_\Delta}.\end{aligned} \tag{A.1}$$

Here,

$$\begin{aligned}|\mathbf{q}_B|^2 &= \frac{(p^2+m_B^2-m_\pi^2)^2-4p^2m_B^2}{4p^2},\\ q_B'^2 &= m_N^2+m_B^2\\ &-\frac{(p^2+m_N^2-t)(p^2+m_B^2-m_\pi^2)}{2p^2}\\ &+2|\mathbf{q}_B||\mathbf{k}|\cos(\theta_{\mathbf{q}_B}),\\ |\mathbf{k}|^2 &= \frac{(p^2+m_N^2-t)^2-4p^2m_N^2}{4p^2},\end{aligned} \tag{A.2}$$

where $B=N,\Delta$ and $\theta_{\mathbf{q}_B}$ is the angle between the vectors $\mathbf{q}_B$ and $\mathbf{k}$. The first term in (A.1) differs from zero for $p^2>(m_\pi+m_N)^2$, while the second does not vanish in the region $p^2>(m_\pi+m_\Delta)^2$. The vertex functions appearing in (A.1) have the following meaning:

$$\Gamma^{ab}_{\sigma\pi\pi}=i\frac{g_{\sigma\pi\pi}}{2m_\pi}(t-q_B'^2-m_\pi^2(1-2c_\sigma))F_\sigma(t)\delta^{ab}$$

is the vertex of sigma-meson interaction with a pion pair ($\pi\pi\to\sigma$);

$$\Gamma^{a}_{\pi NN}=\frac{g_{\pi NN}}{2m_N}\not{q}_N\gamma_5\tau^a F_{N0}(p^2)$$

is the vertex of pion–nucleon interaction ($N\to\pi N$); and

$$\Gamma^{\beta a}_{N\Delta\pi}=\frac{g_{\pi N\Delta}}{m_\pi m_\Delta}\not{p}_\Delta(P^{3/2})^{\beta\alpha}q_{\Delta\alpha}T^aF_{N0}(p^2)$$

corresponds to the vertex for the decay process $N\to\pi\Delta$ and satisfies to the transverseness condition $p_{\Delta\beta}\Gamma^{\beta}_{N\Delta\pi}=0$. In the above expressions, $a$ and $b$ are isotopic indices, and the following relation holds:

$$T^{\dagger a}T^b=\frac{2}{3}\delta^{ab}-\frac{1}{3}i\varepsilon^{abc}\tau^c.$$

With the aid of relation (A.2), integration over the solid angles in (A.1) can be replaced by integration with respect to $q_B'^2$. Each of the integrals in (A.1) can be broken down into two parts; that is,

$$I_B=\gamma_\mu I^\mu_{1B}+I_{2B},$$

where the integral $I^\mu_{1B}$ involving the timelike 4-vector $p^\mu_B$ must be expressed in terms of the 4-vector $P^\mu=p^\mu+p'^\mu$, because we have only two independent 4-vectors at our disposal, $P^\mu$ and $k^\mu$, only one of these, $P^\mu$, being timelike. Therefore, we have $I^\mu_{1B}=A_BP^\mu$. Multiplying this equality by $P^\mu$, we can obtain $A_B$. Further, we transfer, in the integrals $I_B$, the factors $\not{p}$ to the right and the factors $\not{p}'$ to the left and [implying that, eventually, expression (A.1) is sandwiched between $\overline{u}(p')$ and $u(p)$] make the substitutions $\not{p},\not{p}'\to m_N$. As a result, we find that $\mathrm{Im}\widetilde{F}_{\sigma NN}(p^2,t)$ takes the form

$$\begin{aligned}\mathrm{Im}\widetilde{F}_{\sigma NN}(p^2,t) &= \frac{g_{\sigma NN}}{2m_\pi}\\ &\times\frac{F_{\sigma\pi\pi}(t)F_{N0}(p^2)}{8\pi((p^2+m_N^2-t)^2-4p^2m_N^2)^{1/2}}\\ &\times\left(\frac{3g^2_{\pi NN}}{4m_N}K_N^{(\sigma)}+\left(\frac{g_{\pi N\Delta}}{m_\pi m_\Delta}\right)^2K_\Delta^{(\sigma)}\right),\end{aligned}$$

where

$$K_N^{(\sigma)} = \int\limits_{q_{N-}^2}^{q_{N+}^2} \frac{t - m_\pi^2(1-2c_\sigma) - q_N'^2}{q_N'^2 - m_\pi^2} \times (2m_N^2 - C_{N1}(p^2 + 3m_N^2))dq_N'^2,$$

$$K_\Delta^{(\sigma)} = \int\limits_{q_{\Delta-}^2}^{q_{\Delta+}^2} \frac{t - m_\pi^2(1-2c_\sigma) - q_\Delta'^2}{q_\Delta'^2 - m_\pi^2} \times \left[\frac{m_\Delta^2}{2}(2C_{\Delta1}m_N + m_\Delta)(p^2 + m_N^2 - t) + \frac{m_N m_\Delta}{6}(2C_{\Delta1}m_N - m_\Delta)(p^2 + m_\Delta^2 - m_\pi^2) + \frac{m_\Delta}{6}(C_{\Delta1}(p^2 + m_N^2) - m_N m_\Delta) \times ((m_N + m_\Delta)^2 - q_\Delta'^2) - \frac{1}{3}(C_{\Delta1}m_N + m_\Delta) \times (p^2 + m_\Delta^2 - m_\pi^2)(m_N^2 + m_\Delta^2 - q_\Delta'^2)\right] dq_\Delta'^2,$$

$$C_{B1} = \frac{p_B P}{P^2},$$

with the limits of integration being given by

$$q_{B\pm}^2 = m_N^2 + m_B^2 - \frac{(p^2 + m_N^2 - t)(p^2 + m_B^2 - m_\pi^2)}{2p^2} \pm 2|\mathbf{k}||\mathbf{q}_B|.$$

The procedure for determining the imaginary parts of the form factors for the rho–nucleon–nucleon vertex is analogous, in many respects, to that in the preceding case. We have

$$\mathrm{Im}(-i\Gamma_{\rho NN}^{\mu c}) = -\frac{|\mathbf{q}_N|}{2(4\pi)^2 p_0}\int \Gamma_{\rho\pi\pi}^{\mu cba}\Gamma_{\pi NN}^{b}\frac{i(\not{p}_N + m_N)}{q_N'^2 - m_\pi^2}\Gamma_{\pi NN}^{a} d\Omega_{\mathbf{q}_N} + \frac{|\mathbf{q}_\Delta|}{2(4\pi)^2 p_0}\int \Gamma_{\rho\pi\pi}^{\mu cba}\Gamma_{\Delta N\pi}^{\alpha b}\frac{i(\not{p}_\Delta + m_\Delta)}{q_\Delta'^2 - m_\pi^2}P_{\alpha\beta}^{3/2}\Gamma_{N\Delta\pi}^{\beta a} d\Omega_{\mathbf{q}_\Delta}, \quad (A.3)$$

where

$$\Gamma_{\rho\pi\pi}^{\mu cba} = g_{\rho\pi\pi}\varepsilon^{cba}(q_B' - q_B)^\mu F_\rho(t)$$

is the vertex for rho-meson interaction with a pion pair ($\pi\pi \to \rho$). Here, we have used the coupling-constant value of $\delta = 1$.

Each of the two integrals in (A.3) can be represented as the sum of a few terms; that is,

$$I_B^\mu = P^\mu(I_{1B}^\nu\gamma_\nu + I_{2B}) + I_{3B}^\mu + I_{4B}^{\mu\nu}\gamma_\nu,$$

where the integrals $I_{1B}^\mu$ and $I_{3B}^\mu$ involving the 4-momentum $p_B^\mu$ in the integrands can be expressed in terms of the 4-vector $P^\mu$, while the integral $I_{4B}^{\mu\nu}$ involving the combination $p_B^\mu p_B^\nu$ can be represented in the form

$$I_{4B}^{\mu\nu} = A_{1B}P^2\delta^{\mu\nu} + A_{2B}P^\mu P^\nu.$$

In order to determine the coefficients $A_{1B}$ and $A_{2B}$, it is sufficient to calculate the integrals $(I_{4B})_\mu^\mu$ and $I_{4B}^{\mu\nu}P_\mu P_\nu$.

Considering that the rho–nucleon–nucleon vertex has the form

$$\Gamma_{\rho NN}^{\mu c} = -i\widetilde{F}_{\rho NN1}(p^2,t)\gamma^\mu\tau^c - \frac{\widetilde{F}_{\rho NN2}(p^2,t)}{2m_N}\sigma^{\mu\nu}k_\nu\tau^c$$

and replacing $P^\mu$ by a term that becomes equivalent to it upon sandwiching the respective expression between relevant state vectors,

$$P^\mu \to 2m_N\gamma^\mu + i\sigma^{\mu\nu}k_\nu,$$

we eventually reduce the imaginary parts of the form factors $\widetilde{F}_{\rho NN1(2)}(p^2,t)$ to

$$\mathrm{Im}\widetilde{F}_{\rho NN1(2)}(p^2,t) = \frac{g_{\rho NN}F_\rho(t)F_{N0}(p^2)m_N}{2\pi((p^2 + m_N^2 - t)^2 - 4p^2m_N^2)^{1/2}} \times \left(\frac{g_{\pi NN}^2}{4m_N}K_{N1(2)}^{(\rho)} - \left(\frac{g_{\pi N\Delta}}{m_\pi m_\Delta}\right)^2\frac{K_{\Delta1(2)}^{(\rho)}}{6}\right).$$

Here,

$$K_{Ni}^{(\rho)} = \lambda_i \int\limits_{q_{N-}^2}^{q_{N+}^2} \frac{(p^2+3m_N^2)(2C_{N3}-C_{N1})+2m_N^2(1-2C_{N1})+2C_{N2}P^2\delta_{1i}}{q_N'^2-m_\pi^2} dq_N'^2,$$

$$K_{\Delta i}^{(\rho)} = \lambda_i$$

$$\times \int\limits_{q_{\Delta-}^2}^{q_{\Delta+}^2} \Big[\Big(1-2C_{\Delta1}\Big)\Big(m_\Delta^3(p'p) - \frac{1}{3}m_N m_\Delta^2(p_\Delta P) - \frac{1}{3}m_\Delta^3 m_N^2 - \frac{4}{3}m_\Delta(p_\Delta p')(p_\Delta p)\Big)$$

$$+ \Big(C_{\Delta1}-2C_{\Delta3}\Big)\Big(2m_N m_\Delta^2(p'p) + \frac{1}{3}m_N m_\Delta^2 p^2 + \frac{1}{3}m_N^3 m_\Delta^2 - \frac{4}{3}m_N(p_\Delta p')(p_\Delta p) + \frac{2}{3}m_\Delta m_N^2(p_\Delta p) + \frac{1}{3}m_\Delta p^2(p_\Delta p') + \frac{1}{3}m_N^2 m_\Delta(p_\Delta p')\Big) - C_{\Delta2}\frac{P^2}{m_N}$$

$$\times \Big(m_\Delta^2(p'p) + \frac{1}{3}m_N^2 m_\Delta^2 - \frac{2}{3}(p_\Delta p')(p_\Delta p) + \frac{1}{3}m_\Delta m_N(p_\Delta P)\Big)\delta_{1i}\Big]\Big[q_\Delta'^2 - m_\pi^2\Big]^{-1} dq_\Delta'^2,$$

where $i = 1, 2$; $\lambda_{1(2)} = 1(-1)$; $\delta_{1i}$ is a Kronecker delta symbol;

$$C_{B2} = \frac{m_B^2P^2 - (p_BP)^2}{3P^4},$$

$$C_{B3} = \frac{4(p_BP)^2 - m_B^2P^2}{3P^4};$$

and

$$p_Bp' = \frac{1}{2}(m_N^2 + m_B^2 - q_B'^2),$$

$$p_Bp = \frac{1}{2}(p^2 + m_B^2 - m_\pi^2),$$

$$p'p = \frac{1}{2}(p^2 + m_N^2 - t), \quad P^2 = 2p^2 + 2m_N^2 - t.$$

## REFERENCES


1. S. Nozawa, B. Blankleider, and T.-S. H. Lee, Nucl. Phys. A **513**, 459 (1990).
2. R. Wittman, Phys. Rev. C **37**, 2075 (1988).
3. R. Machleidt, Adv. Nucl. Phys. **19**, 189 (1989).
4. D. Lohse, J. W. Durso, K. Holinde, and J. Speth, Nucl. Phys. A **516**, 513 (1990).
5. B. C. Pearce and B. K. Jennings, Nucl. Phys. A **528**, 655 (1991).
6. C. T. Hung, S. N. Yang, and T.-S. H. Lee, J. Phys. G **20**, 1531 (1994); Phys. Rev. C **64**, 034309 (2001).
7. A. D. Lahiff and I. R. Afnan, Phys. Rev. C **60**, 024608 (1999).
8. V. Pascalutsa and J. A. Tjon, Phys. Rev. C **61**, 054003 (2000).
9. C. Schütz, J. Haidenbauer, J. Speth, and J. W. Durso, Phys. Rev. C **57**, 1464 (1998).
10. K. Hagiwara *et al.* (Particle Data Group), Phys. Rev. D **66**, 010001 (2002).
11. E. M. Aitala *et al.*, Phys. Rev. Lett. **86**, 770 (2001).
12. *Proceedings of Possible Existence of the σ-Meson and Its Implications to Hadron Physics, Kyoto, Japan, 2000,* KEK-Procs. 2000 4.
13. T. Hatsuda and T. Kunihiro, Phys. Rep. **247**, 221 (1994); J. Bijnens, Phys. Rep. **265**, 369 (1996).
14. L. S. Celenza, H. Wang, and C. M. Shakin, Phys. Rev. C **63**, 025209 (2001).
15. S. Weinberg, Phys. Rev. **166**, 1568 (1968).
16. J. Wess and B. Zumino, Phys. Rev. **163**, 1727 (1967).
17. C. Schütz, K. Holinde, J. Speth, *et al.*, Phys. Rev. C **51**, 1374 (1995).
18. J. A. Oller, E. Oset, and J. R. Peláez, Phys. Rev. D **59**, 074001 (1999).
19. K. Igi and K. Hikasa, Phys. Rev. D **59**, 034005 (1999).
20. Z. Xiao and H. Zheng, Nucl. Phys. A **695**, 273 (2001).
21. V. V. Vereshchagin, K. N. Mukhin, and O. O. Patarakin, Usp. Fiz. Nauk **170**, 353 (2000) [Phys. Usp. **43**, 315 (2000)].
22. W. N. Cottingham, M. Lacombe, B. Loiseau, *et al.*, Phys. Rev. D **8**, 800 (1973).
23. J. W. Durso, A. D. Jackson, and B. J. Verwest, Nucl. Phys. A **345**, 471 (1980).
24. A. Reuber, K. Holinde, H.-C. Kim, and J. Speth, Nucl. Phys. A **608**, 243 (1996).
25. C. M. Maekawa, J. C. Pupin, and M. R. Robilotta, Phys. Rev. C **61**, 064002 (2000).
26. V. Bernard, N. Kaiser, and U.-G. Meißner, Nucl. Phys. A **615**, 483 (1997).
27. J. D. Björken and S. D. Drell, *Relativistic Quantum Fields* (McGraw-Hill, New York, 1965; Nauka, Moscow, 1978).
28. G. Barton, *Introduction to Dispersion Techniques in Field Theory* (Benjamin, New York, 1965; Atomizdat, Moscow, 1968).
29. F. Gross, Phys. Rev. C **26**, 2203 (1982).
30. P. J. Ellis and H.-B. Tang, Phys. Rev. C **57**, 3356 (1998).
31. N. Fettes, U.-G. Meißner, and S. Steininger, Nucl. Phys. A **640**, 199 (1998).
32. H. M. Nieland and J. A. Tjon, Phys. Lett. B **27B**, 309 (1968).

33. P. F. A. Goudsmit, H. J. Leisi, E. Matsinos, *et al.*, Nucl. Phys. A **575**, 673 (1994).
34. T. Feuster and U. Mosel, Phys. Rev. C **58**, 457 (1998).
35. A. Yu. Korchin, O. Scholten, and R. G. E. Timmermans, Phys. Lett. B **438**, 1 (1998).
36. V. Stoks, R. G. E. Timmermans, and J. J. de Swart, Phys. Rev. C **47**, 512 (1993).
37. E. P. Shabalin, Yad. Fiz. **63**, 659 (2000) [Phys. At. Nucl. **63**, 594 (2000)].
38. S. Weinberg, Phys. Rev. Lett. **17**, 616 (1966).
39. J. Gasser and H. Leutwyler, Ann. Phys. (N.Y.) **158**, 142 (1984).
40. S. Coleman, J. Wess, and B. Zumino, Phys. Rev. **177**, 2239 (1969); S. Kamefuchi, L. O'Raifeartaigh, and A. Salam, Nucl. Phys. **28**, 529 (1961).
41. C. G. Callan, S. Coleman, J. Wess, and B. Zumino, Phys. Rev. **177**, 2247 (1969).
42. K. Kawarabayashi and M. Suzuki, Phys. Rev. Lett. **16**, 255 (1966); Riazuddin and Fayazuddin, Phys. Rev. **147**, 1071 (1966).
43. M. Benmerrouche, R. M. Davidson, and N. C. Mukhopadhyay, Phys. Rev. C **39**, 2339 (1989).
44. V. Pascalutsa, Phys. Lett. B **503**, 85 (2001).
45. V. Pascalutsa, Phys. Rev. D **58**, 096002 (1998).
46. A. N. Almaliev, I. V. Kopytin, and M. A. Shehalev, J. Phys. G **28**, 233 (2002).
47. A. M. Bincer, Phys. Rev. **118**, 855 (1960).
48. V. B. Berestetskiĭ, E. M. Lifshitz, and L. P. Pitaevskiĭ, *Quantum Electrodynamics* (Fizmatlit, Moscow, 2001; Pergamon, Oxford, 1982 (translation of 2nd ed., Nauka, Moscow, 1980)).
49. G. Höhler, in *Pion–Nucleon Scattering,* Ed. by H. Schopper (Springer-Verlag, New York, 1983).
50. R. A. Arndt, I. I. Strakovsky, R. L. Workman, and M. M. Pavan, Phys. Rev. C **52**, 2120 (1995).
51. R. Koch and E. Pietarinen, Nucl. Phys. A **336**, 331 (1980).
52. C. Schütz, J. W. Durso, K. Holinde, and J. Speth, Phys. Rev. C **49**, 2671 (1994).
53. N. Kaiser, S. Gerstendörfer, and W. Weise, Nucl. Phys. A **637**, 395 (1998).

*Translated by A. Isaakyan*

*Physics of Atomic Nuclei, Vol. 66, No. 9, 2003, pp. 1760–1772. Translated from Yadernaya Fizika, Vol. 66, No. 9, 2003, pp. 1807–1819.*


**ELEMENTARY PARTICLES AND FIELDS**
**Theory**

# Electroproduction of $J/\psi$ Mesons within the Semihard QCD Approach and the Color-Singlet Model

**N. P. Zotov[*] and A. V. Lipatov[1)**]**

*Institute of Nuclear Physics, Moscow State University, Vorob'evy gory, Moscow, 119899 Russia*
*[1)] Moscow State University, Vorob'evy gory, Moscow, 119899 Russia*

Received July 9, 2002

**Abstract**—The deep-inelastic production of $J/\psi$ mesons in electron–proton interactions at the HERA collider is considered within the semihard ($k_T$-factorization) QCD approach and within the color-singlet model. The dependence of the $Q^2$, $\mathbf{p}_T^2$, $z$, $y^*$, and $W$ distributions of $J/\psi$ mesons on various sets of unintegrated gluon distributions and the dependence of the spin parameter $\alpha$ on $\mathbf{p}_T^2$ and $Q^2$ are investigated. The results of the calculations are compared with the latest experimental data obtained by the H1 and ZEUS Collaborations at the HERA collider. It is shown that experimental investigations of the polarization properties of $J/\psi$ mesons over the kinematical region $Q^2 < 1$ GeV$^2$ may provide an additional test of the statement that the dynamics of gluon distributions is governed by the Balitsky–Fadin–Kuraev–Lipatov equations. © *2003 MAIK "Nauka/Interperiodica".*

## 1. INTRODUCTION

Investigation of processes involving the production and photoproduction of heavy quarks and quarkonia is a rich source of information both about the dynamics of parton interaction and about the distribution of gluons in the proton [1–4]. Strong interest in the distribution of gluons is motivated, in particular, by the fact that they play a key role in determining cross sections for many processes that will be examined at next-generation colliders (such as LHC).

In the energy region of present-day colliders, processes involving the production and photoproduction of heavy quarks and quarkonia are classified among so-called semihard processes [5]. With such processes, one usually associates reactions whose characteristic scale $\mu \sim m_Q$ (where $m_Q$ is the heavy-quark mass) of the hard parton-scattering subprocess is much less than the total energy of colliding particles in the c.m. frame, $\sqrt{s}$, but is much greater than the parameter $\Lambda_{\mathrm{QCD}}$—that is, $\Lambda_{\mathrm{QCD}} \ll \mu \ll \sqrt{s}$—in which case the running QCD coupling constant remains small: $\alpha_{\mathrm{QCD}}(\mu^2) \ll 1$. The condition $\mu \ll \sqrt{s}$ means that the cross sections for such processes are determined by the behavior of the gluon structure functions in the proton at low values of the variable $x$, $x \simeq m_Q/\sqrt{s} \ll 1$. In view of a high density of gluon distributions at such values of $x$, the assumption of the parton model that the cross sections for the relevant subprocesses and hadron structure functions factorize is violated, so that it is necessary to take into account the dependence of the amplitude for a hard subprocess on the virtuality, transverse momentum, and longitudinal polarization of gluons, whose contribution to the cross section is dominant [6–8].

The distributions of gluons in the proton, $xG(x,\mu^2)$, can be derived from the Dokshitzer–Gribov–Lipatov–Altarelli–Parisi (DGLAP) evolution equations [9] in the leading-logarithm approximation [in which case contributions of the form $\alpha_S^n \ln^n(\mu^2/\Lambda^2_{\mathrm{QCD}})$ are taken into account] or in the double logarithmic approximation [in which case contributions of the form $\alpha_S^n \ln^n(1/x) \ln^n(\mu^2/\Lambda^2_{\mathrm{QCD}})$ are included]. As the c.m. energy of colliding particles, $\sqrt{s}$, increases, however, contributions of order $\alpha_S^n \ln^n(s/\Lambda^2_{\mathrm{QCD}}) \sim \alpha_S^n \ln^n(1/x)$, which are disregarded in the DGLAP equations, begin to play an ever more pronounced role. Summation of diagrams involving terms of orders $\alpha_S^n \ln^n(\mu^2/\Lambda^2_{\mathrm{QCD}})$, $\alpha_S^n \ln^n(1/x) \ln^n(\mu^2/\Lambda^2_{\mathrm{QCD}})$, and $\alpha_S^n \ln^n(1/x)$ leads to unintegrated gluon distributions (that is, distributions that are dependent on the transverse momentum $\mathbf{q}_T$) $\Phi(x,\mathbf{q}_T^2,\mu^2)$ satisfying the Balitsky–Fadin–Kuraev–Lipatov (BFKL) evolution equations [10]. These distributions are related to conventional (collinear) gluon distributions $xG(x,\mu^2)$ by the

[*] e-mail: zotov@theory.sinp.msu.ru
[**] e-mail: artem_lipatov@mail.ru

equation

$$xG(x,\mu^2) = xG(x,Q_0^2) + \int_{Q_0^2}^{\mu^2} \Phi(x,\mathbf{q}_T^2,\mu^2)d\mathbf{q}_T^2. \quad (1)$$

Cross sections for physical processes are determined by a convolution of unintegrated gluon distributions with the off-shell matrix element for the relevant hard subprocess [6–8]. In addition, the semihard approach [5] prescribes, for virtual gluons, the choice of the polarization tensor $L^{\mu\nu}$ in the matrix element for the subprocess of gluon–gluon fusion in the form

$$L^{\mu\nu}(q) = \frac{q_T^\mu q_T^\nu}{\mathbf{q}_T^2}. \quad (2)$$

The semihard approach was previously used to describe a number of processes [6, 11–25]—in particular, processes involving the production and photoproduction of heavy quarks [6, 11, 14, 16, 20–23] and quarkonia [13, 15, 19, 24, 25]. We note that calculations within the theory of semihard processes lead to some observable effects that do not emerge in other approaches—namely, a faster growth of cross sections in relation to what is obtained from calculations within the usual parton model [13, 15] and a broadening of transverse-momentum spectra in relation to the results produced by the parton model, this flattening becoming more significant as the energy increases [6, 11, 13–21].

We emphasize that calculations of cross sections for the production of heavy quarks and quarkonia within the usual parton model to a fixed order of perturbative QCD prove to be unable to reproduce experimental data as they become vaster and more precise. For example, it was found that, for the production of $J/\psi$ and $\Upsilon$ mesons in proton–antiproton interactions, the cross sections calculated within the usual parton model fall short of experimental data by more than one order of magnitude [26, 27]. This circumstance gave impetus to intensive theoretical investigations into such processes—in particular, it was required to introduce additional mechanisms through which $c\bar{c}$ states undergo transitions into $J/\psi$ mesons. The so-called color-octet model [28], which was proposed to include such mechanisms, claimed to provide a complete description of quarkonium-production processes both in proton–antiproton and in electron–proton interactions, but it immediately ran into the problem of describing the photoproduction of $J/\psi$ mesons [29, 30] at the HERA collider energies, where the contribution of the color-octet mechanism is insignificant or is even at odds with experimental data [31, 32]. Another feature peculiar to the color-octet model is associated with the polarization properties of $J/\psi$ mesons produced in proton–antiproton interactions at the Tevatron. If, as is expected, a leading contribution to the production of $J/\psi$ mesons comes from gluon fragmentation into octet $c\bar{c}$ pairs, then $J/\psi$ mesons must predominantly have a transverse polarization at high transverse momenta, but this contradicts experimental data, which are indicative of the absence of polarization of product $J/\psi$ mesons or of their longitudinal polarization.

The color-octet model was also used in [33, 34] to describe the deep-inelastic electroproduction of $J/\psi$ mesons at the HERA collider, but the results obtained in those two studies contradict each other [34]. The results of the calculations performed in [35–38] within the usual parton model to a fixed order of perturbation theory and within the color-singlet model differ from experimental results by a factor greater than 2.

First attempts at solving the problem of $J/\psi$-meson polarization in proton–antiproton interactions within the $k_T$-factorization approach were made in [24, 39, 40]. The theoretical predictions obtained in [19] within the semihard approach stimulated an experimental analysis of the polarization properties of $J/\psi$ mesons at the HERA collider energies. However, this problem calls for a further theoretical and experimental examination.

The present study is devoted to a continuation of investigations into the deep-inelastic electroproduction of $J/\psi$ mesons at the HERA collider within the semihard QCD approach. Relying on the color-singlet model and employing the formalism of projection operators [41], we will calculate the $Q^2$, $\mathbf{p}_T^2$, $z$, $y^*$, and $W$ distributions of $J/\psi$ mesons within the semihard QCD approach and compare the results of our calculations with the latest experimental data obtained by the H1 and ZEUS Collaborations (see [42] and [43], respectively), as well as with the results of calculations performed within the usual parton model in the leading order of perturbation theory. With the aim of seeking a universal distribution of gluons, we also analyze the sensitivity of the calculated quantities to the choice of various sets of unintegrated distributions of gluons and to variations in the parameters of the semihard approach. Particular attention will be given to unintegrated gluon distributions that are obtained by solving the BFKL evolution equations and which were previously used in [15–18]. In addition, we will explore the polarization properties of the final $J/\psi$ meson versus its transverse momentum squared, $\mathbf{p}_{J/\psi T}^2$, and versus the virtuality of the primary photon, $Q^2$.

The ensuing exposition is organized as follows. In Section 2, we derive simple analytic expressions describing the differential cross section for the deep-inelastic electroproduction of $J/\psi$ mesons within the

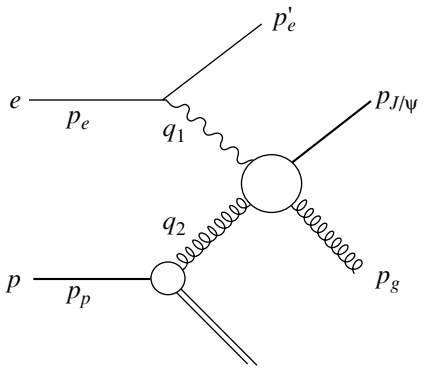


**Fig. 1.** Diagram for deep-inelastic production of $J/\psi$ mesons in electron–proton interactions.

$k_T$-factorization approach and within the usual parton model. In Section 3, we discuss some features of the parametrizations used for unintegrated distributions of gluons in the proton. In Section 4, we calculate matrix elements for the relevant hard subprocess on the basis of the color-singlet model within the semihard QCD approach and on the basis of the usual parton model without recourse to previous studies. In Section 5, we present the results of our numerical calculations and compare them with the latest experimental data of the H1 and ZEUS Collaborations (see [42] and [43], respectively). In Section 6, we briefly summarize the basic results and conclusions obtained in the present study.

## 2. CROSS SECTION FOR THE DEEP-INELASTIC ELECTROPRODUCTION OF $J/\psi$ MESONS IN THE SEMIHARD QCD APPROACH

Relying on the semihard QCD approach, we will calculate here the differential cross section for the process involving the deep-inelastic electroproduction of $J/\psi$ mesons and proceeding through the subprocess of photon–gluon fusion (Fig. 1). In these calculations, we will use expression (2) for the polarization tensor $L^{\mu\nu}$ of initial virtual gluons. The Sudakov decomposition for the process $ep \to e'J/\psi X$ (Fig. 1) has the form

$$\begin{aligned} p_{J/\psi} &= \alpha_1 p_e + \beta_1 p_p + p_{J/\psi T}, \\ p_g &= \alpha_2 p_e + \beta_2 p_p + p_{gT}, \\ q_1 &= x_1 p_e + q_{1T}, \\ q_2 &= x_2 p_p + q_{2T}, \end{aligned} \tag{3}$$

where

$$\begin{aligned} p_{J/\psi}^2 = m_{J/\psi}^2, \quad p_g^2 = 0, \\ q_1^2 = q_{1T}^2 = -Q^2, \quad q_2^2 = q_{2T}^2. \end{aligned} \tag{4}$$

Here, $p_{J/\psi}$ and $p_g$ are the 4-momenta of the $J/\psi$ meson and the final gluon, respectively; $q_1$ and $q_2$ are the 4-momenta of the initial virtual photon and the initial gluon, respectively; and $p_{J/\psi T}$, $p_{gT}$, $q_{1T}$, and $q_{2T}$ are the transverse 4-momenta of the corresponding particles. In the c.m. frame of colliding particles, we have

$$p_e = (E, 0, 0, E), \quad p_p = (E, 0, 0, -E), \tag{5}$$

where

$$E = \frac{\sqrt{s}}{2}, \quad p_e^2 = p_p^2 = 0, \quad (p_e \cdot p_p) = \frac{s}{2}. \tag{6}$$

The Sudakov variables have the form

$$\begin{aligned} \alpha_1 = \frac{m_{J/\psi T}}{\sqrt{s}} \exp(y_{J/\psi}), \quad \alpha_2 = \frac{|\mathbf{p}_{gT}|}{\sqrt{s}} \exp(y_g), \\ \beta_1 = \frac{m_{J/\psi T}}{\sqrt{s}} \exp(-y_{J/\psi}), \quad \beta_2 = \frac{|\mathbf{p}_{gT}|}{\sqrt{s}} \exp(-y_g), \end{aligned} \tag{7}$$

where $m_{J/\psi T}^2 = m_{J/\psi}^2 + \mathbf{p}_{J/\psi T}^2$, $m_{J/\psi}$ being the $J/\psi$-meson mass, and $y_{J/\psi}$ and $y_g$ are the rapidities of, repectively, the $J/\psi$ meson and the final gluon in the c.m. frame of colliding particles. The differential cross section for the process $ep \to e'J/\psi X$ can be represented in the form

$$\begin{aligned} d\sigma(ep \to e'J/\psi X) = \frac{dx_2}{x_2} \\ \times \Phi(x_2, \mathbf{q}_{2T}^2, \mu^2) \frac{d\phi_2}{2\pi} d\mathbf{q}_{2T}^2 d\hat{\sigma}(eg^* \to e'J/\psi g'), \end{aligned} \tag{8}$$

where $\phi_2$ is the azimuthal angle of the initial virtual gluon; $\Phi(x_2, \mathbf{q}_{2T}^2, \mu^2)$ is the unintegrated distribution of gluons; and

$$\begin{aligned} d\hat{\sigma}(eg^* \to e'J/\psi g') \\ = \frac{(2\pi)^4}{2x_2 s} \sum |M|_{\mathrm{SHA}}^2 (eg^* \to e'J/\psi g') \\ \times \frac{d^3 p'_e}{(2\pi)^3 2p'^0_e} \frac{d^3 p_{J/\psi}}{(2\pi)^3 2p^0_{J/\psi}} \frac{d^3 p_g}{(2\pi)^3 2p^0_g} \\ \times \delta^{(4)}(p_e + q_2 - p'_e - p_{J/\psi} - p_g), \end{aligned} \tag{9}$$

with $\sum |M|_{\mathrm{SHA}}^2 (eg^* \to e'J/\psi g')$ being the matrix element calculated for the hard scattering subprocess $eg^* \to e'J/\psi g'$ within the semihard QCD approach. In (9), the summation sign means averaging over the polarizations of initial particles and summation over the polarizations of final particles. From expressions (8) and (9), one can easily obtain the differential cross section for the process $ep \to e'J/\psi X$ within the semihard QCD approach. The eventual result has the form

$$d\sigma(ep \to e'J/\psi X) \tag{10}$$

$$= \frac{1}{128\pi^3}\frac{\Phi(x_2,\mathbf{q}_{2T}^2,\mu^2)}{(x_2 s)^2(1-x_1)}\frac{dz}{z(1-z)}dy_{J/\psi} \times \sum |M|^2_{\mathrm{SHA}}(eg^* \to e'J/\psi g')d\mathbf{p}^2_{J/\psi T} \times dQ^2 d\mathbf{q}^2_{2T}\frac{d\phi_1}{2\pi}\frac{d\phi_2}{2\pi}\frac{d\phi_{J/\psi}}{2\pi},$$

where

$$x_1 = \alpha_1 + \alpha_2, \qquad x_2 = \beta_1 + \beta_2, \qquad (11)$$
$$\mathbf{q}_{1T} + \mathbf{q}_{2T} = \mathbf{p}_{J/\psi T} + \mathbf{p}_{gT};$$

$\phi_1$ and $\phi_{J/\psi}$ are the azimuthal angles of the initial virtual photon and the $J/\psi$ meson, respectively; and $z = (p_{J/\psi}\cdot p_p)/(q_1\cdot p_p)$. Considering the limit $\mathbf{q}^2_{2T} \to 0$ and averaging expression (10) over transverse directions, which are specified by the vector $\mathbf{q}_{2T}$, we obtain the differential cross section for the process $ep \to e'J/\psi X$ within the usual parton model; that is,

$$d\sigma(ep \to e'J/\psi X) \qquad (12)$$
$$= \frac{1}{128\pi^3}\frac{1}{(x_2 s)^2(1-x_1)}\frac{dz}{z(1-z)}x_2 G(x_2,\mu^2) \times \sum |M|^2_{\mathrm{PM}}(eg \to e'J/\psi g')dy_{J/\psi} \times d\mathbf{p}^2_{J/\psi T}dQ^2\frac{d\phi_1}{2\pi}\frac{d\phi_{J/\psi}}{2\pi},$$

where $\sum |M|^2_{\mathrm{PM}}(eg \to e'J/\psi g')$ is the matrix element calculated for the hard subprocess $eg \to e'J/\psi g'$ within the usual parton model and the summation sign means, as before, averaging over the polarizations of initial particles and summation over the polarizations of final particles. In performing averaging over the azimuthal angle $\phi_2$ and integration with respect to $\mathbf{q}^2_{2T}$, we have used the relation

$$\int d\mathbf{q}^2_{2T}\int \frac{d\phi_2}{2\pi}\Phi(x_2,\mathbf{q}^2_{2T},\mu^2) \qquad (13)$$
$$\times \sum |M|^2_{\mathrm{SHA}}(eg^* \to e'J/\psi g') = x_2 G(x_2,\mu^2)\sum |M|^2_{\mathrm{PM}}(eg \to e'J/\psi g'),$$

where

$$\int_0^{2\pi}\frac{d\phi_2}{2\pi}\frac{q^\mu_{2T}q^\nu_{2T}}{\mathbf{q}^2_{2T}} = \frac{1}{2}g^{\mu\nu}. \qquad (14)$$

## 3. UNINTEGRATED DISTRIBUTIONS OF GLUONS

In performing the ensuing calculations, we will employ various parametrizations of unintegrated gluon distributions. In this section, we consider some special features of the parametrizations used.

The first is the so-called JB parametrization, which was obtained by solving the BFKL equations on the basis of the method proposed in [44]. This method for deriving unintegrated gluon distributions relies on directly solving the BFKL equations in the leading approximation, with the collinear gluon density $xG(x,\mu^2)$ from the Glück–Reya–Vogt set [45] being taken for the initial condition. Technically, the unintegrated gluon distributions are calculated in this case as the convolution of the collinear gluon distribution $xG(x,\mu^2)$ with a universal weight factor [44]; that is,

$$\Phi(x,\mathbf{q}_T^2,\mu^2) = \int_x^1 \varphi(\eta,\mathbf{q}_T^2,\mu^2)\frac{x}{\eta}G\left(\frac{x}{\eta},\mu^2\right)d\eta, \qquad (15)$$

where

$$\varphi(\eta,\mathbf{q}_T^2,\mu^2) = \begin{cases}\dfrac{\bar\alpha_S}{\eta\mathbf{q}_T^2}J_0\left(2\sqrt{\bar\alpha_S\ln(1/\eta)\ln(\mu^2/\mathbf{q}_T^2)}\right) & \text{for } \mathbf{q}_T^2 \le \mu^2\\ \dfrac{\bar\alpha_S}{\eta\mathbf{q}_T^2}I_0\left(2\sqrt{\bar\alpha_S\ln(1/\eta)\ln(\mathbf{q}_T^2/\mu^2)}\right) & \text{for } \mathbf{q}_T^2 > \mu^2.\end{cases} \qquad (16)$$

Here, $J_0$ and $I_0$ are Bessel functions of, respectively, a real and an imaginary argument. The parameter $\bar\alpha_S = 3\alpha_S/\pi$, which appears in (16), is related to the Pomeron intercept $\Delta$: in the leading order of perturbation theory, we have $\Delta = 4\bar\alpha_S\ln 2 \simeq 0.53$, but, in the next-to-leading order, the expression for the Pomeron intercept in terms of the parameter $\bar\alpha_S$ assumes the form $\Delta = 4\bar\alpha_S\ln 2 - N\bar\alpha_S^2$ and takes negative values since $N \sim 18$ [46, 47]. However, various summation procedures proposed in recent years (see [47, 48]) lead to positive values of $\Delta \sim 0.2$–$0.3$. In our calculations, we will use the value of $\Delta = 0.35$ from [20].

A different parametrization of unintegrated gluon distributions (here, it will be referred to as the KMS parametrization) was obtained in [49] by solving the generalized BFKL–DGLAP equation with allowance for additional kinematical constraints in the evolution of the gluon cascade [50]. As was shown in [51], this approach makes it possible to take effectively into

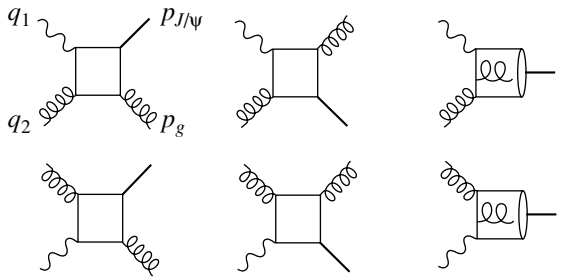


**Fig. 2.** Diagrams representing the subprocess $\gamma g^* \to J/\psi g'$ in the leading order of perturbation theory.

account about 70% of next-to-leading-order corrections to the Pomeron intercept $\Delta$.

In our calculations, we will also employ the phenomenological gluon distribution that was proposed by the authors of the model where the gluon distribution is assumed to be saturated at low values of the variable $x$ [52, 53]. This model was successfully used to describe the processes of inclusive and diffractive deep-inelastic scattering (see [52] and [53], respectively) at the HERA collider energies. The expression for $\Phi(x, \mathbf{q}_T^2, \mu^2)$ has the form

$$\Phi(x, \mathbf{q}_T^2, \mu^2) = \frac{3\sigma_0}{4\pi^2}\frac{1}{\alpha_S}R_0^2(x)\mathbf{q}_T^2 \exp(-R_0^2(x)\mathbf{q}_T^2), \tag{17}$$

where

$$R_0^2(x) = \frac{1}{\mathrm{GeV}^2}\left(\frac{x}{x_0}\right)^{\lambda/2}. \tag{18}$$

The parameter values of $\sigma_0 = 23.03$ mb, $\lambda = 0.288$, and $x_0 = 3.04 \times 10^{-4}$ were obtained in describing the behavior of the proton structure function $F_2$ in the region $x < 0.01$ [52]. In the present article, we will refer to this parametrization as the GBW parametrization of unintegrated gluon distributions.

The effective gluon distribution $xG(x, \mu^2)$ is related to the unintegrated distribution functions $\Phi(x, \mathbf{q}_T^2, \mu^2)$ by Eq. (1). In (1), the contribution of the low-$\mathbf{q}_T^2$ region ($0 < \mathbf{q}_T^2 < Q_0^2$) is taken into account with the aid of the collinear gluon density $xG(x, Q_0^2)$, where $Q_0^2 = 1$ GeV$^2$ for all parametrizations.

## 4. MATRIX ELEMENTS FOR THE SUBPROCESS $eg^* \to e'J/\psi g'$

In this section, we will calculate the squared matrix element $\sum |M|^2_{\mathrm{SHA}}(eg^* \to e'J/\psi g')$ for the relevant hard scattering subprocess within the theory of semihard processes and also obtain the expression for $\sum |M|^2_{\mathrm{PM}}(eg \to e'J/\psi g')$ in the leading order of perturbative QCD; we will employ this expression in the calculations based on the usual parton model. As was indicated above, expression (10), which describes the differential cross section for the electroproduction of $J/\psi$ mesons within the semihard QCD approach, presumes the dependence of the matrix element for the relevant hard subprocess on the initial-gluon virtuality $q_2^2 = -\mathbf{q}_{2T}^2 \neq 0$.

Within the color-singlet model, which is considered in the present study, $J/\psi$ mesons are described by nonrelativistic wave functions representing the $c\bar{c}$ quark system in the color-singlet state characterized by the orbital angular momentum $L = 0$; the spin $S = 1$; and the mass $m_{J/\psi} = 2m_c$, where $m_c$ is the $c$-quark mass. The amplitude of the subprocess of photon–gluon fusion, $\gamma g^* \to J/\psi g'$, is described by the set of six diagrams in Fig. 2 and can be obtained, within the formalism of projection operators [41], from the amplitude of the subprocess $\gamma g^* \to c\bar{c}g'$ by means of the substitution

$$v(p_{\bar{c}})\bar{u}(p_c) \to \hat{J}(p_{J/\psi}) = \frac{\psi(0)}{2\sqrt{m_{J/\psi}}}\hat{\epsilon}(p_{J/\psi})(\hat{p}_{J/\psi} + m_{J/\psi})\frac{1}{\sqrt{3}}, \tag{19}$$

where $\hat{\epsilon}(p_{J/\psi}) = \epsilon_\mu(p_{J/\psi}), \gamma^\mu\epsilon(p_{J/\psi})$ is the polarization 4-vector of the product $J/\psi$ meson, $1/\sqrt{3}$ is a color factor, and $\psi(0)$ is the value of the nonrelativistic $J/\psi$-meson wave function at the origin. By using standard Feynman rules for QCD, we represent the amplitude for the subprocess $\gamma g^* \to J/\psi g'$ in the form

$$M = e_c g^2 \epsilon_\mu(q_1)\epsilon_\sigma(q_2)\epsilon_\rho(p_g)\mathrm{Sp}\left[\hat{J}(p_{J/\psi})\gamma^\mu\frac{\hat{p}_c - \hat{q}_1 + m_c}{(p_c - q_1)^2 - m_c^2}\gamma^\sigma\frac{-\hat{p}_c - \hat{p}_g + m_c}{(-p_c - p_g)^2 - m_c^2}\gamma^\rho\right] \tag{20}$$

plus five permutations of all gauge bosons. Here, $\epsilon_\mu(q_1)$ and $\epsilon_\mu(q_2)$ are the polarization 4-vectors of, respectively, the initial photon and the initial gluon; $\epsilon_\mu(p_g)$ is the polarization 4-vector of the final gluon; and $p_c = p_{J/\psi}/2$. Summation over the polarizations of the $J/\psi$ meson and the final real gluon is performed in a conventional way:

$$\sum \epsilon^\mu(p_{J/\psi})\epsilon^{*\nu}(p_{J/\psi}) = -g^{\mu\nu} + \frac{p^\mu_{J/\psi}p^\nu_{J/\psi}}{m^2_{J/\psi}}, \tag{21}$$

$$\sum \epsilon^{\mu}(p_g)\epsilon^{*\nu}(p_g) = -g^{\mu\nu}. \quad (22)$$

For the sum over the polarizations of the initial virtual photon, $\sum \epsilon^{\mu}(q_1)\epsilon^{*\nu}(q_1)$, we employ the total lepton tensor (which also includes the photon propagator and the relevant vertex factor) in the form

$$\sum \epsilon^{\mu}(q_1)\epsilon^{*\nu}(q_1) = 2\frac{e^2}{Q^2}\left(-g^{\mu\nu} + \frac{4p_e^{\mu}p_e^{\nu}}{Q^2}\right). \quad (23)$$

In calculating $\sum |M|^2_{\mathrm{PM}}(eg \to e'J/\psi g')$ within the parton model, we will make use of a conventional gluon polarization tensor of the form

$$\sum \epsilon^{\mu}(q_2)\epsilon^{*\nu}(q_2) = -g^{\mu\nu}. \quad (24)$$

In order to investigate the polarization properties of $J/\psi$ mesons, we take the longitudinal-polarization 4-vector $\epsilon_L^{\mu}(p_{J/\psi})$ in the form [54]

$$\epsilon_L^{\mu}(p_{J/\psi}) = \frac{(p_{J/\psi}\cdot p_p)}{\sqrt{(p_{J/\psi}\cdot p_p)^2 - m^2_{J/\psi}s}} \times \left(\frac{p^{\mu}_{J/\psi}}{m_{J/\psi}} - \frac{m_{J/\psi}p_p^{\mu}}{(p_{J/\psi}\cdot p_p)}\right). \quad (25)$$

In the limiting case of $s \gg m^2_{J/\psi}$, this 4-vector satisfies conventional conditions: $(\epsilon_L \cdot \epsilon_L) = -1$ and $(\epsilon_L \cdot p_{J/\psi}) = 0$.

The calculations of $\sum |M|^2_{\mathrm{SHA}}(eg^* \to e'J/\psi g')$ and $\sum |M|^2_{\mathrm{PM}}(eg \to e'J/\psi g')$ within the parton model were performed with the aid of the REDUCE system for analytic calculations.

## 5. RESULTS OF THE CALCULATIONS

In this section, we present our results obtained both within the theory of semihard processes and within the usual parton model in the leading order of perturbative QCD; we also compare our theoretical results with the latest experimental data of the H1 and ZEUS Collaborations (see [42] and [43], respectively).

We note that the absolute normalization of the cross sections calculated by formulas (10) and (12) depends on the choice of values for the $J/\psi$-meson wave function at the origin, $\psi(0)$; the $c$-quark mass, $m_c$; and the factorization scale, $\mu$. The wave-function value at the origin, $\psi(0)$, can be calculated within the potential model or can be obtained from the experimentally measured leptonic-decay width $\Gamma(J/\psi \to \mu^+\mu^-)$. Following [55], we will use the value of $|\psi(0)|^2 = 0.0876\ \mathrm{GeV}^3$ in our calculations.

At present, the problem of choosing values for the $c$-quark mass remains open. On one hand, we have $m_c = m_{J/\psi}/2 = 1.55$ GeV in the nonrelativistic QCD approximation, which is used for the $J/\psi$ wave function in the color-singlet model. On the other hand, however, there exist grounds to take a somewhat lower value of $m_c$—for example, $m_c = 1.4$ GeV [33, 56]. In our study, we will use both of these values for the $c$-quark mass.

Following [57], we will set the factorization scale to $\mu^2 = \mathbf{q}^2_{2T}$ in the ensuing calculations.[1)]

As was indicated above, the calculations within the theory of semihard processes were performed by formula (10), while the calculations within the usual parton model were based on formula (12). The limits of integration with respect to $\mathbf{p}^2_{J/\psi T}$ were derived from the requirement that the reaction in question be of a deep-inelastic character: $1\ \mathrm{GeV}^2 \le \mathbf{p}^2_{J/\psi T} \le s/4 - m^2_{J/\psi}$. In accordance with (1), the domain of integration with respect to $\mathbf{q}^2_{2T}$ was broken down into two parts. For $\mathbf{q}^2_{2T} \ge Q_0^2$, we performed calculations by formula (10), while, for $\mathbf{q}^2_{2T} < Q_0^2$, we set $\mathbf{q}^2_{2T} = 0$ in the scattering amplitude and replaced $\sum |M|^2_{\mathrm{SHA}}(eg^* \to e'J/\psi g')$ by $\sum |M|^2_{\mathrm{PM}}(eg \to e'J/\psi g')$. The choice of the critical value $Q_0^2$ was based on the requirement that the coupling constant $\alpha_S(\mathbf{q}^2_{2T})$ be small in the region $\mathbf{q}^2_{2T} \ge Q_0^2$. In our calculations, we used the value of $Q_0^2 = 1\ \mathrm{GeV}^2$, in which case $\alpha_S(\mathbf{q}^2_{2T}) \le 0.26$. The limits of integration with respect to $Q^2$, the rapidity $y_{J/\psi}$, and the variable $z$ are related to the boundaries of two kinematical regions in which the H1 Collaboration obtained experimental data on the inelastic electroproduction of $J/\psi$ mesons [42]: $2 \le Q^2 \le 80\ \mathrm{GeV}^2$, $40 \le W \le 180$ GeV, $z > 0.2$, and $M_X \ge 10$ GeV (first region) and $\mathbf{p}^2_{J/\psi T} \ge 4\ \mathrm{GeV}^2$, $4 \le Q^2 \le 80\ \mathrm{GeV}^2$, $40 \le W \le 180$ GeV, $z > 0.2$, and $M_X \ge 10$ GeV (second region).

The results of our calculations are displayed in Figs. 3–8. The distributions of $J/\psi$ mesons with respect to the variables $Q^2$, $\mathbf{p}^2_{J/\psi T}$, $z$, $y^*_{J/\psi}$ (rapidity of $J/\psi$ mesons in the c.m. frame of the $\gamma^* p$ system), and $W$ in the kinematical region specified by the inequalities $2 \le Q^2 \le 80\ \mathrm{GeV}^2$, $40 \le W \le 180$ GeV, $z > 0.2$, and $M_X \ge 10$ GeV are displayed in Fig. 3 for $\sqrt{s} = 314$ GeV, $m_c = 1.55$ GeV, and $\Lambda_{\mathrm{QCD}} = 250$ MeV. Curve *1* corresponds to the calculations on the basis of the usual parton model with the gluon distribution $xG(x,\mu^2)$ from the Glück–Reya–Vogt set, while curves *2*, *3*, and *4* represent the results

[1)] We note that our preliminary results in [58] correspond to $\mu^2 = m^2_{J/\psi} + \mathbf{p}^2_{J/\psi T}$.

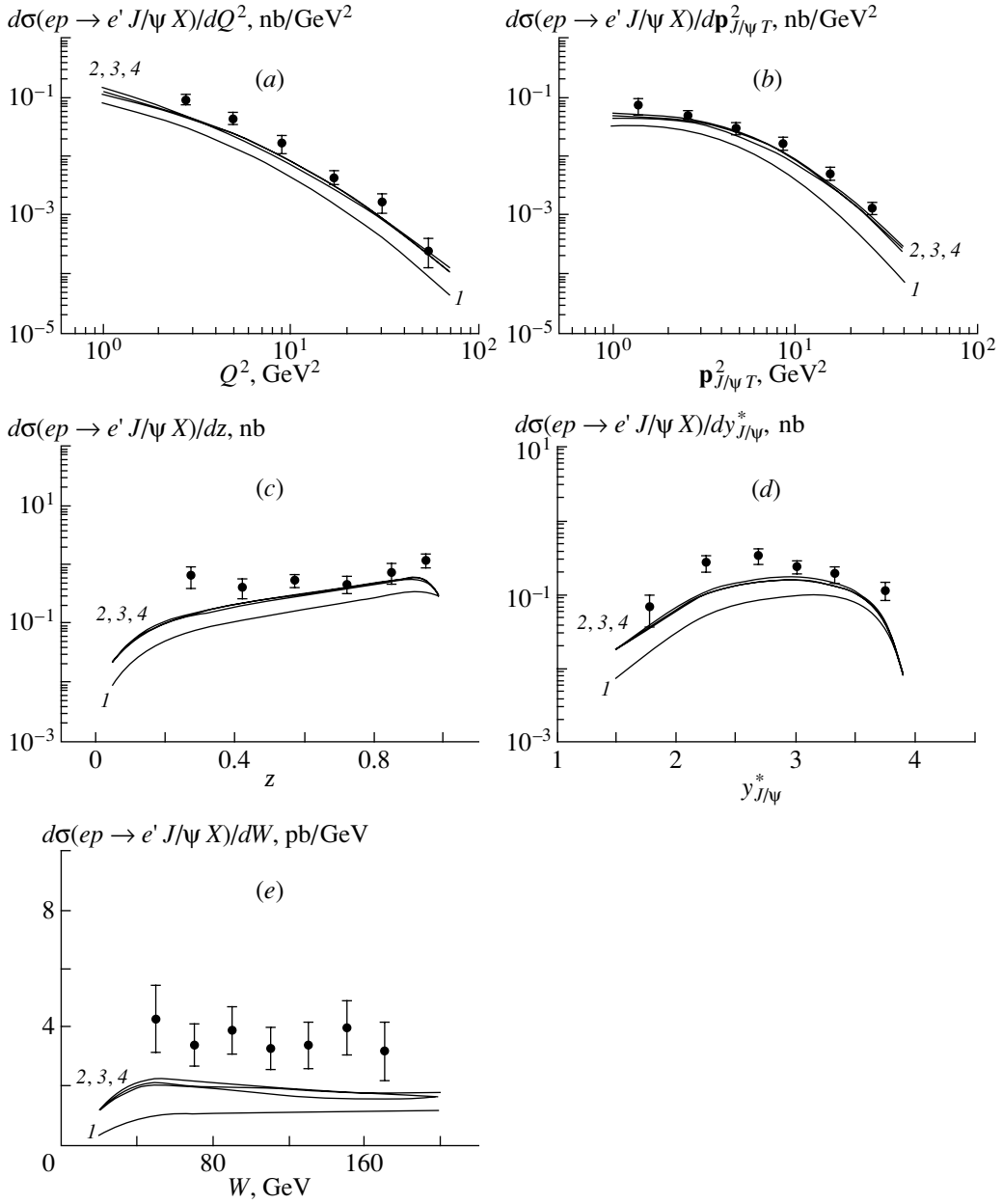


**Fig. 3.** Distributions of $J/\psi$ mesons with respect to $Q^2$, $\mathbf{p}^2_{J/\psi T}$, $z$, $y^*_{J/\psi}$ and $W$ in the kinematical region specified by the inequalities $2 \le Q^2 \le 80$ GeV$^2$, $40 \le W \le 180$ GeV, $z > 0.2$, and $M_X \ge 10$ GeV at $\sqrt{s} = 314$ GeV, $m_c = 1.55$ GeV, and $\Lambda_{\rm QCD} = 250$ MeV. Curve *1* corresponds to the calculations within the usual parton model that employ the gluon distribution $xG(x, \mu^2)$ from the Glück–Reya–Vogt set, while curves *2*, *3*, and *4* represent the results of the calculations performed within the theory of semihard processes by using, respectively, the JB, KMS, and GBW unintegrated gluon distributions at $Q_0^2 = 1$ GeV$^2$. Points show experimental data of the H1 Collaboration [42].

obtained within the theory of semihard processes by using, respectively, the JB, KMS, and GBW unintegrated gluon distributions at $Q_0^2 = 1$ GeV$^2$. It can easily be seen that, for all distributions calculated within the semihard QCD approach (curves *2*, *3*, *4*), their shapes comply well with experimental data of the H1 Collaboration. It should be noted that the calculations on the basis of the parton model in the leading order of perturbative QCD (curves *1*) disagree with experimental data of the H1 Collaboration (the discrepancy is about a factor of 2 in absolute value).

In Fig. 4, the distributions of $J/\psi$ mesons with respect to the variables $z$, $y^*_{J/\psi}$, and $W$ at $\sqrt{s} =$ 314 GeV, $m_c = 1.55$ GeV, and $\Lambda_{\rm QCD} = 250$ MeV are shown for a different kinematical region, that which

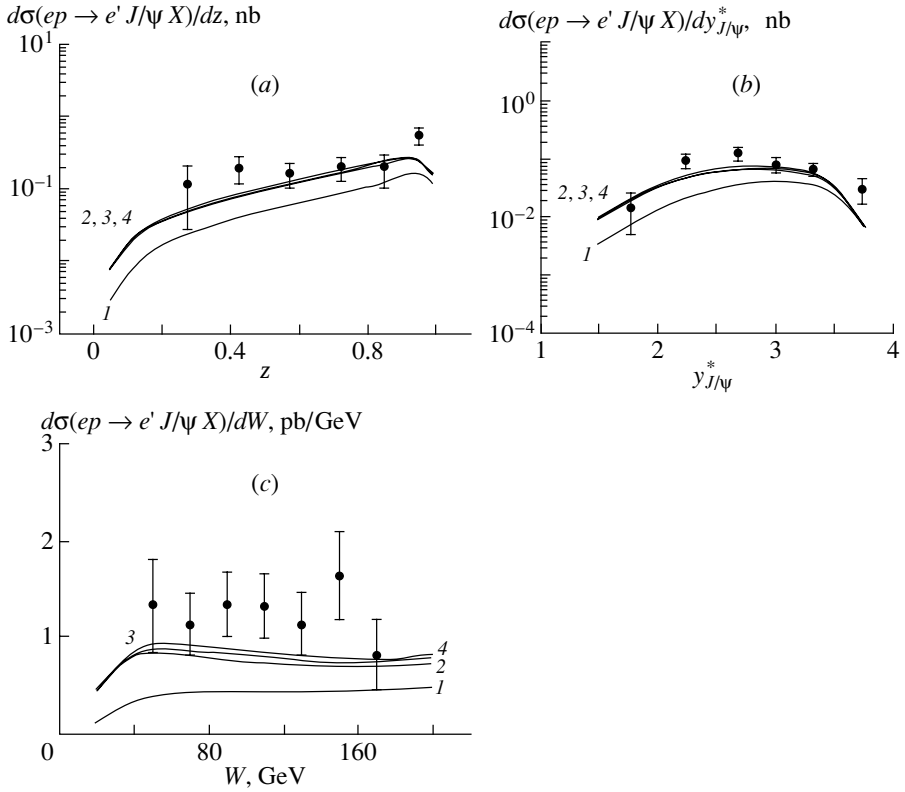


**Fig. 4.** Distributions of $J/\psi$ mesons with respect to $z$, $y^*_{J/\psi}$, and $W$ in the kinematical region specified by the inequalities $\mathbf{p}^2_{J/\psi T} \geq 4\,\mathrm{GeV}^2, 4 \leq Q^2 \leq 80\,\mathrm{GeV}^2, 40 \leq W \leq 180\,\mathrm{GeV}, z > 0.2$, and $M_X \geq 10\,\mathrm{GeV}$ at $\sqrt{s} = 314\,\mathrm{GeV}$, $m_c = 1.55\,\mathrm{GeV}$, and $\Lambda_{\mathrm{QCD}} = 250\,\mathrm{MeV}$. The notation is identical to that in Fig. 3.

is specified by the inequalities $\mathbf{p}^2_{J/\psi T} \geq 4\ \mathrm{GeV}^2$, $4 \leq Q^2 \leq 80\ \mathrm{GeV}^2$, $40 \leq W \leq 180\,\mathrm{GeV}$, $z > 0.2$, and $M_X \geq 10\ \mathrm{GeV}$; here, the notation for the curves is identical to that in Fig. 3. It can easily be seen that agreement between experimental data from [42] and the results of the calculations performed within the theory of semihard processes is better in the second than in first kinematical region (where, for example, the constraint $\mathbf{p}^2_{J/\psi T} \geq 4\,\mathrm{GeV}^2$ is not imposed).

The $Q^2$, $\mathbf{p}^2_{J/\psi T}$, $z$, $y^*_{J/\psi}$, and $W$ distributions of $J/\psi$ mesons at $\sqrt{s} = 314\,\mathrm{GeV}$, $m_c = 1.4\,\mathrm{GeV}$, and $\Lambda_{\mathrm{QCD}} = 250$ MeV are shown in Fig. 5 for the kinematical region specified by the inequalities $2 \leq Q^2 \leq 80\ \mathrm{GeV}^2$, $40 \leq W \leq 180\,\mathrm{GeV}$, $z > 0.2$, and $M_X \geq 10\,\mathrm{GeV}$ and in Fig. 6 for the kinematical region specified by the inequalities $\mathbf{p}^2_{J/\psi T} \geq 4\ \mathrm{GeV}^2$, $4 \leq Q^2 \leq 80\,\mathrm{GeV}^2$, $40 \leq W \leq 180\,\mathrm{GeV}$, $z > 0.2$, and $M_X \geq 10\,\mathrm{GeV}$; as before, the notation here for the curves is identical to that in Fig. 3. As can be seen from these graphs, the change in the $c$-quark mass from $m_c = 1.55\,\mathrm{GeV}$ to $m_c = 1.4\,\mathrm{GeV}$ leads to an approximately 1.5-fold increase in the magnitude of the calculated distributions.

If only the color-singet state of $J/\psi$ mesons is taken into account, their distributions with respect to the variable $z$ at $m_c = 1.4\,\mathrm{GeV}$ are reproduced in the region $z \geq 0.4$ but not beyond it, because, in the region $z < 0.4$, the contribution of other mechanisms—such as those that are associated with the QCD structure of the photon and with the production of $J/\psi$ mesons in the octet state [59]—becomes significant.

We have investigated the $m_c$ dependence of the results of our calculations in greater detail and found that the 1.5-fold change in the magnitude of the calculated distributions in response to the shift of the $c$-quark mass from $m_c = 1.55\,\mathrm{GeV}$ to $m_c = 1.4\,\mathrm{GeV}$ is due to the change in the phase space corresponding to the final $J/\psi$ meson, a variation of $m_c$ in the amplitude of the subprocess $eg \to e'J/\psi g'$ affecting the results of the calculations only slightly. However, the value of $m_c = 1.4\,\mathrm{GeV}$ in the phase space of the final state corresponds to an unphysical value of the $J/\psi$-meson mass.[2)]

[2)]We are grateful to S.P. Baranov, who proposed that we examine this issue in greater detail.

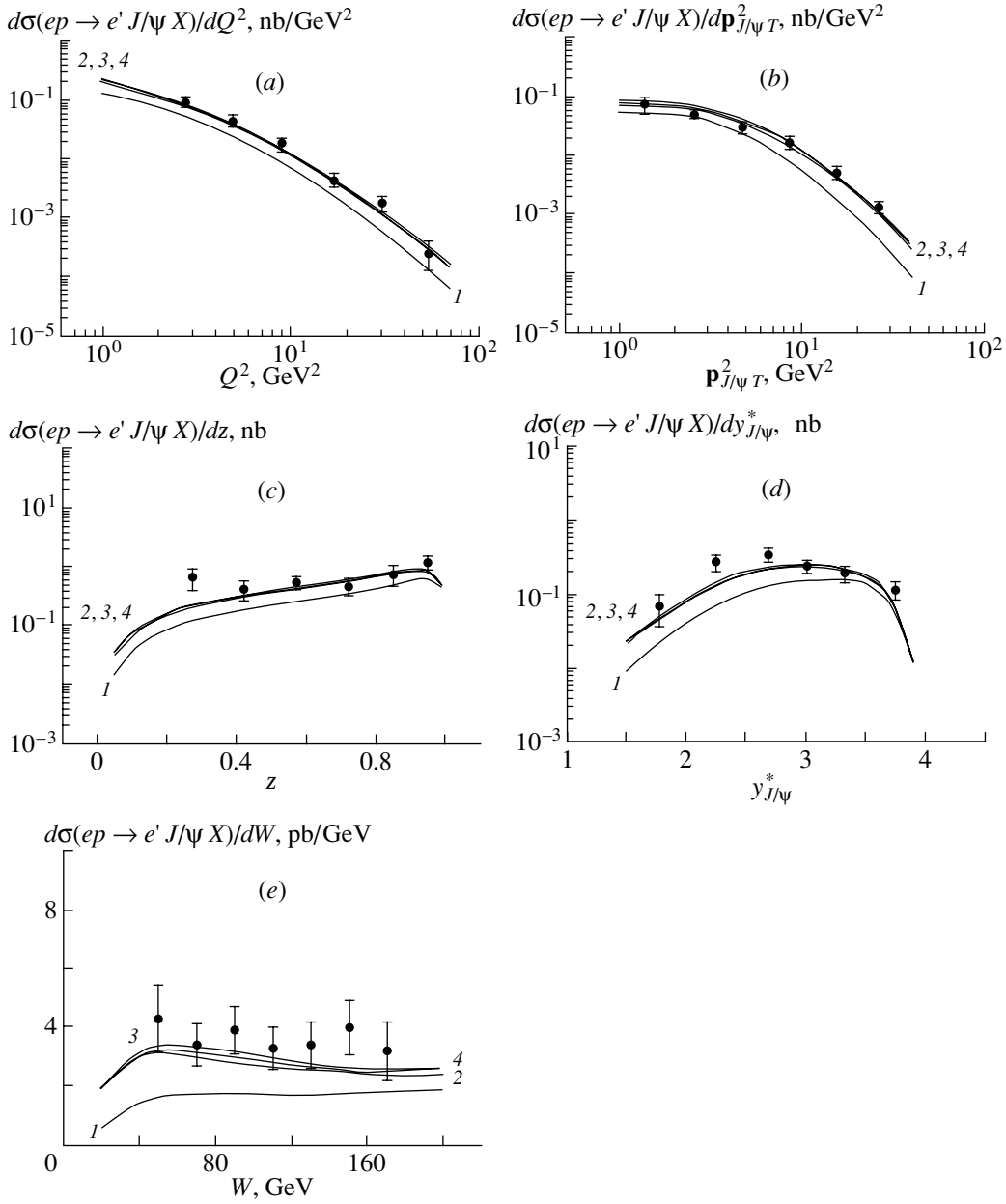


**Fig. 5.** Distributions of $J/\psi$ mesons with respect to $Q^2$, $\mathbf{p}^2_{J/\psi T}$, $z$, $y^*_{J/\psi}$, and $W$ in the kinematical region specified by the inequalities $2 \le Q^2 \le 80$ GeV$^2$, $40 \le W \le 180$ GeV, $z > 0.2$, and $M_X \ge 10$ GeV at $\sqrt{s} = 314$ GeV, $m_c = 1.4$ GeV, and $\Lambda_{\rm QCD} = 250$ MeV. The notation is identical to that in Fig. 3.

As can be seen from Figs. 5 and 6, the inclusion of effects associated with the saturation of gluon distributions in the low-$x$ region (GBW parametrization) does not disturb the agreement with experimental data.

Our calculations reveal that, within the semihard QCD approach to describing the inelastic electroproduction of $J/\psi$ mesons at the HERA collider, agreement with experimental data is reached at a rather low value of the c-quark mass, $m_c = 1.4$ GeV. At the more realistic value of $m_c = 1.55$ GeV, the predictions of the $k_T$-factorization approach differ in magnitude from experimental data of the H1 Collaboration [42] by a factor of about 1.5.

In order to investigate the polarization properties of final $J/\psi$ mesons, we will calculate, within the semihard approach and within the usual parton model, the spin parameter $\alpha$ [19, 60],

$$\alpha(\omega) = \frac{d\sigma/d\omega - 3d\sigma_L/d\omega}{d\sigma/d\omega + d\sigma_L/d\omega}, \qquad (26)$$

where $\sigma_L$ is the cross section for the electropro-

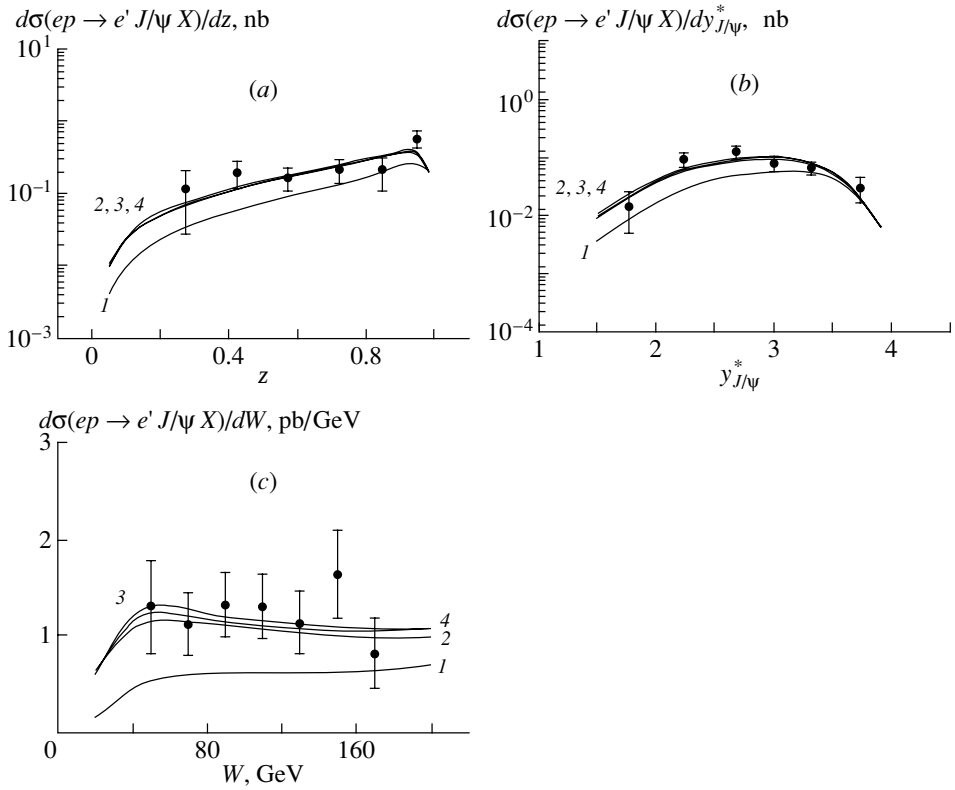


**Fig. 6.** Distributions of $J/\psi$ mesons with respect to $z$, $y^*_{J/\psi}$, and $W$ in the kinematical region specified by the inequalities $\mathbf{p}^2_{J/\psi T} \geq 4$ GeV$^2$, $4 \leq Q^2 \leq 80$ GeV$^2$, $40 \leq W \leq 180$ GeV, $z > 0.2$, and $M_X \geq 10$ GeV at $\sqrt{s} = 314$ GeV, $m_c = 1.4$ GeV, and $\Lambda_{\rm QCD} = 250$ MeV. The notation is identical to that in Fig. 3.

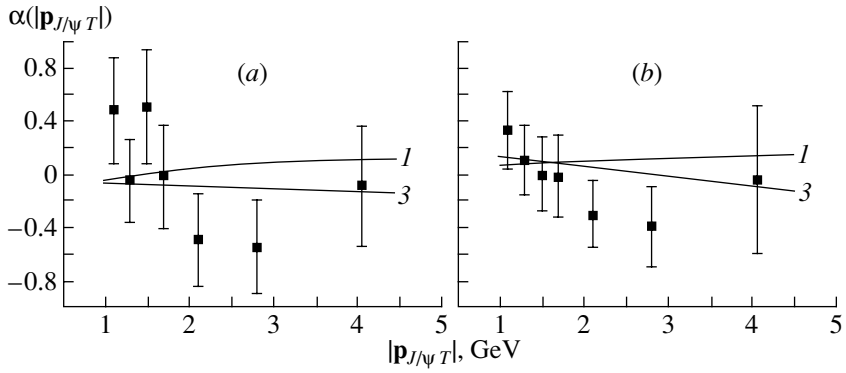


**Fig. 7.** Parameter $\alpha$ as a function of $|\mathbf{p}_{J/\psi T}|$ in the kinematical regions $(a)$ $0.4 < z < 0.9$ and $(b)$ $0.4 < z < 1$ at $\sqrt{s} =$ 314 GeV, $m_c = 1.4$ GeV, and $\Lambda_{\rm QCD} = 250$ MeV: (curve *1*) results of the calculation on the basis of the usual parton model with the gluon distribution $xG(x, \mu^2)$ from the Glück–Reya–Vogt model, (curve *3*) results of the calculation based on the theory of semihard processes and performed with the KMS unintegrated gluon distribution ($Q_0^2 = 1$ GeV$^2$), and (points) experimental data of the ZEUS Collaboration [43].

duction of longitudinally polarized $J/\psi$ mesons and $\omega = \mathbf{p}^2_{J/\psi T}, Q^2$, considering it as a function of $\mathbf{p}^2_{J/\psi T}$ and $Q^2$. The parameter $\alpha$ is related to the angular distribution of leptons from the decay process $J/\psi \to \mu^+\mu^-$ by the equation

$$\frac{d\Gamma(J/\psi \to \mu^+\mu^-)}{d\cos\theta} \sim 1 + \alpha\cos^2\theta, \qquad (27)$$

where $\theta$ is the polar angle of emission of the final muon $\mu^+$ in the $J/\psi$ rest frame.

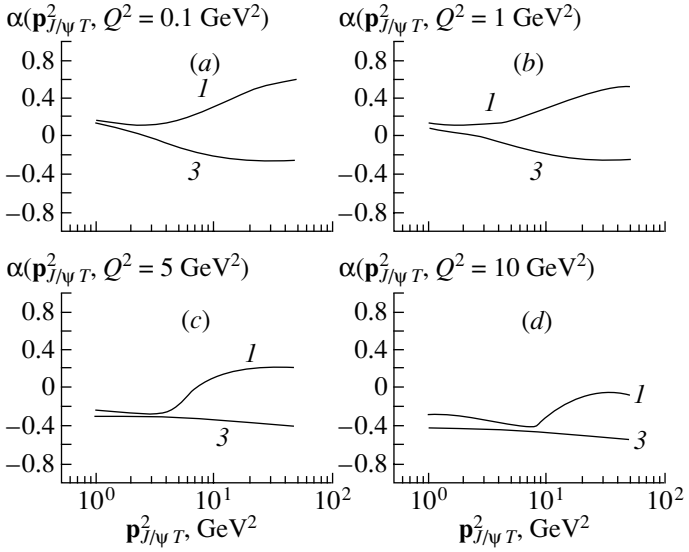


**Fig. 8.** Parameter $\alpha$ as a function of $\mathbf{p}^2_{J/\psi T}$ for $40 \le W \le 180$ GeV, $z > 0.2$, $M_X \ge 10$ GeV, $\sqrt{s} = 314$ GeV, $m_c = 1.4$ GeV, and $\Lambda_{\rm QCD} = 250$ MeV at fixed values of $Q^2$. The notation for the curves is identical to that in Fig. 7.

In Fig. 7, the parameter $\alpha$ as a function of $|\mathbf{p}_{J/\psi T}|$ at $\sqrt{s} = 314$ GeV, $m_c = 1.4$ GeV, and $\Lambda_{\rm QCD} = 250$ MeV is presented for the kinematical regions (*a*) $0.4 < z < 0.9$ and (*b*) $0.4 < z < 1$; the experimental data displayed there (points) were obtained by the ZEUS Collaboration [43]. In that figure, curve *1* corresponds to the calculation on the basis of the usual parton model with the gluon distribution $xG(x, \mu^2)$ from the Glück–Reya–Vogt set, while curve *3* represents the results obtained within the theory of semihard processes by using the KMS unintegrated gluon distribution ($Q_0^2 = 1$ GeV$^2$). We note that, in view of large experimental uncertainties and in view of the additional contribution to the cross section for the production of $J/\psi$ mesons of helicity $\lambda = 0$ from longitudinally polarized initial virtual photons, it is very difficult to draw definitive conclusions on the degree to which the virtuality of the initial gluon affects the cross section for the production of longitudinally polarized $J/\psi$ mesons. At photon-virtuality values in the region $Q^2 < 1$ GeV$^2$, the contribution of longitudinally polarized photons is insignificant, however, which must lead to qualitative distinctions between the polarization properties of product $J/\psi$ mesons within the usual parton model and those within the semihard QCD approach [19, 58]. By way of example, Fig. 8 displays the parameter $\alpha$ as a function of $\mathbf{p}^2_{J/\psi T}$ for $40 \le W \le 180$ GeV, $z > 0.2$, $M_X \ge 10$ GeV, $\sqrt{s} = 314$ GeV, $m_c = 1.4$ GeV, and $\Lambda_{\rm QCD} = 250$ MeV at various fixed values of $Q^2$: $Q^2 =$ (*a*) 0.1, (*b*) 1, (*c*) 5, and (*d*) 10 GeV$^2$; the notation for the curves here is identical to that in Fig. 7. From Fig. 8, it can be seen that, for $Q^2 < 1.0$ GeV$^2$, the dependence $\alpha_{\rm SHA}(\mathbf{p}^2_{J/\psi T})$ calculated within the semihard approach differs significantly, both in shape and in magnitude, from the dependence $\alpha_{\rm PM}(\mathbf{p}^2_{J/\psi T})$ found on the basis of the parton model in the leading order of perturbative QCD. Thus, we conclude that, if next-to-leading-order corrections to the predictions of the parton model for the cross section describing the production of longitudinally polarized $J/\psi$ particles (these corrections have yet to be calculated) do not introduce significant changes in the behavior of the parameter $\alpha_{\rm PM}(\mathbf{p}^2_{J/\psi T})$ for $Q^2 < 1$ GeV$^2$, experimental investigations of the polarization properties of $J/\psi$ mesons in this region would provide yet another test of the BFKL dynamics of gluon distributions.

## 6. CONCLUSION

Within the semihard QCD approach, we have considered the inelastic electroproduction of $J/\psi$ mesons at the HERA collider. We have investigated the sensitivity of the $Q^2$, $\mathbf{p}_T^2$, $z$, $y^*$, and $W$ distributions of $J/\psi$ mesons to the choice of unintegrated gluon distributions and analyzed the behavior of the spin parameter $\alpha$ as a function of $\mathbf{p}_T^2$ and $Q^2$. Particular attention has been given to gluon distributions obtained by solving the BFKL evolution equations. It has been shown that, at the values of $m_c = 1.4$ GeV and $|\psi(0)|^2 = 0.0876$ GeV$^3$ for, respectively, the $c$-quark mass and the squared modulus of the $J/\psi$-meson wave function at the origin ($\Lambda_{\rm QCD} = 250$ MeV, $\Delta = 0.35$), the results

of the calculations performed within the semihard QCD approach and within the color-singlet model by using the JB, KMS, and GBW gluon distributions agree fairly well with experimental data obtained by the H1 Collaboration at the HERA collider. At the more realistic value of $m_c = 1.55$ GeV, however, the predictions of the $k_T$-factorization approach differ in magnitude from experimental data by a factor of about 1.5.[3)] The inclusion of effects associated with the saturation of gluon distributions in the low-$x$ region (GBW parametrization) does not contradict the existing experimental data. It has been shown that experimental investigations into the polarization properties of $J/\psi$ mesons in the kinematical region $Q^2 < 1$ GeV$^2$ may provide an additional test of the BFKL dynamics of gluon distributions.

## ACKNOWLEDGMENTS

We are grateful to S.P. Baranov for enlightening discussions on various aspects of the semihard QCD approach. A.V. Lipatov gratefully acknowledges the assistance of V.A. Saleev at the initial stage of this research.

This work was supported by the Russian Foundation for Basic Research (project no. 02-02-17513) and by INTAS (grant no. YSF 2002-399).

## REFERENCES

1. E. L. Berger and D. Jones, Phys. Rev. D **23**, 1521 (1981).
2. S. S. Gershteĭn, A. K. Likhoded, and S. R. Slabospitskiĭ, Yad. Fiz. **34**, 227 (1981) [Sov. J. Nucl. Phys. **34**, 128 (1981)].
3. R. Baier and R. Rückl, Nucl. Phys. B **218**, 289 (1983).
4. A. D. Martin, C. K. Ng, and W. J. Stirling, Phys. Lett. B **191**, 200 (1987).
5. L. Gribov, E. Levin, and M. Ryskin, Phys. Rep. **100**, 1 (1983).
6. E. M. Levin, M. G. Ryskin, Yu. M. Shabel'skiĭ, and A. G. Shuvaev, Yad. Fiz. **53**, 1059 (1991) [Sov. J. Nucl. Phys. **53**, 657 (1991)].
7. S. Catani, M. Ciafaloni, and F. Hautmann, Nucl. Phys. B **366**, 135 (1991).
8. J. C. Collins and R. K. Ellis, Nucl. Phys. B **360**, 3 (1991).
9. V. N. Gribov and L. N. Lipatov, Yad. Fiz. **15**, 781 (1972) [Sov. J. Nucl. Phys. **15**, 438 (1972)]; L. N. Lipatov, Yad. Fiz. **20**, 181 (1974) [Sov. J. Nucl. Phys. **20**, 94 (1975)]; G. Altarelli and G. Parisi, Nucl. Phys. B **126**, 298 (1977); Yu. L. Dokshitser, Zh. Éksp. Teor. Fiz. **73**, 1216 (1977) [Sov. Phys. JETP **46**, 641 (1977)].
10. É. A. Kuraev, L. N. Lipatov, and V. S. Fadin, Zh. Éksp. Teor. Fiz. **71**, 840 (1976) [Sov. Phys. JETP **44**, 443 (1976)]; Zh. Éksp. Teor. Fiz. **72**, 377 (1977) [Sov. Phys. JETP **45**, 199 (1977)]; Ya. Ya. Balitskiĭ and L. N. Lipatov, Yad. Fiz. **28**, 1597 (1978) [Sov. J. Nucl. Phys. **28**, 822 (1978)].
11. M. G. Ryskin and Yu. M. Shabelski, Z. Phys. C **69**, 269 (1996).
12. M. G. Ryskin and Yu. M. Shabelski, Z. Phys. C **61**, 517 (1994); **66**, 151 (1995).
13. V. A. Saleev and N. P. Zotov, Mod. Phys. Lett. A **9**, 151 (1994).
14. V. A. Saleev and N. P. Zotov, Mod. Phys. Lett. A **11**, 25 (1996).
15. A. V. Lipatov and N. P. Zotov, Mod. Phys. Lett. A **15**, 695 (2000).
16. A. V. Lipatov, V. A. Saleev, and N. P. Zotov, Mod. Phys. Lett. A **15**, 1727 (2000).
17. A. V. Lipatov and N. P. Zotov, in *Proceedings of the 8th International Workshop on DIS and QCD (DIS'2000), Liverpool, 2000*, p. 157.
18. A. V. Kotikov, A. V. Lipatov, G. Parente, and N. P. Zotov, hep-ph/0107135; Eur. Phys. J. C **26**, 51 (2002).
19. S. P. Baranov, Phys. Lett. B **428**, 377 (1998).
20. S. P. Baranov and N. P. Zotov, Phys. Lett. B **458**, 389 (1999); **491**, 111 (2000).
21. S. P. Baranov and M. Smizanska, Phys. Rev. D **62**, 014012 (2000).
22. Ph. Hägler, R. Kirschner, A. Schäfer, *et al.*, Phys. Rev. D **62**, 071502 (2000).
23. H. Jung, Phys. Rev. D **65**, 034015 (2002); hep-ph/0110034.
24. Ph. Hägler, R. Kirschner, A. Schäfer, *et al.*, Phys. Rev. D **63**, 077501 (2001); F. Yuan and K.-T. Chao, Phys. Rev. D **63**, 034006 (2001); hep-ph/0009224.
25. H. Jung, hep-ph/0110345; Phys. Rev. D **65**, 034015 (2002).
26. E. Braaten and S. Fleming, Phys. Rev. Lett. **74**, 3327 (1995); E. Braaten and T. C. Yuan, Phys. Rev. D **52**, 6627 (1995).
27. P. Cho and A. K. Leibovich, Phys. Rev. D **53**, 150, 6203 (1996).
28. G. T. Bodwin, E. Braaten, and G. P. Lepage, Phys. Rev. D **51**, 1125 (1995); **55**, 5853 (1997).
29. M. Cacciari and M. Kramer, Phys. Rev. Lett. **76**, 4128 (1996).
30. P. Ko, J. Lee, and H. S. Song, Phys. Rev. D **54**, 4312 (1996); **60**, 119902 (1999).
31. H1 Collab. (S. Aid *et al.*), Nucl. Phys. B **472**, 3 (1996).

[3)]When this article was prepared for publication, new experimental data were reported by the H1 Collaboration in [61] (which are characterized by vaster statistics and a higher level of experimental accuracy in relation to the data in [42]) in two other kinematical regions: $\mathbf{p}^{*2}_{J/\psi T} \geq 1$ GeV$^2$, $2 \leq Q^2 \leq 100$ GeV$^2$, $50 \leq W \leq 225$ GeV, and $0.3 \leq z \leq 0.9$ (first region) and $\mathbf{p}^2_{J/\psi T} \geq 6.4$ GeV$^2$, $12 \leq Q^2 \leq 100$ GeV$^2$, $50 \leq W \leq 225$ GeV, and $0.3 \leq z \leq 0.9$ (second region). Our preliminary results obtained within the $k_T$-factorization approach and the color-singlet model reveal that experimental data presented in [61] can be reproduced at the value of $m_c = 1.55$ GeV.

32. ZEUS Collab. (J. Breitweg *et al.*), Z. Phys. C **76**, 599 (1997).
33. S. Fleming and T. Mehen, Phys. Rev. D **57**, 1846 (1998).
34. B. A. Kniehl and L. Zwirner, hep-ph/0112199; Nucl. Phys. B **621**, 337 (2002).
35. J. C. Korner, J. Cleymans, M. Kuroda, and G. J. Gounaris, Phys. Lett. B **114B**, 195 (1982).
36. J.-Ph. Guillet, Z. Phys. C **39**, 75 (1988).
37. H. Merabet, J. F. Mathiot, and R. Mendez-Galain, Z. Phys. C **62**, 639 (1994).
38. F. Yuan and K.-T. Chao, Phys. Rev. D **63**, 034017 (2001).
39. F. Yuan and K.-T. Chao, Phys. Rev. Lett. **87**, 022002 (2001).
40. Ph. Hägler *et al.*, Phys. Rev. Lett. **86**, 1446 (2001).
41. B. Guberina *et al.*, Nucl. Phys. B **174**, 317 (1980).
42. H1 Collab. (C. Adloff *et al.*), DESY-99-026.
43. ZEUS Collab. (B. Brugnero *et al.*), in *Proceedings of the 9th International Workshop on DIS and QCD (DIS'2001), Bologna, Italy, 2001*.
44. J. Blumlein, DESY-95-121.
45. M. Glück, E. Reya, and A. Vogt, Z. Phys. C **67**, 433 (1995).
46. V. Fadin and L. Lipatov, Phys. Lett. B **429**, 127 (1998); M. Ciafaloni and G. Camici, Phys. Lett. B **430**, 349 (1998).
47. G. Salam, J. High Energy Phys. **9807**, 019 (1998); hep-ph/9806482.
48. S. J. Brodsky, V. S. Fadin, V. T. Kim, *et al.*, hep-ph/9901229.
49. J. Kwiecinski, A. Martin, and A. Stasto, Phys. Rev. D **56**, 3991 (1997).
50. J. Kwiecinski, A. Martin, and A. Sutton, Phys. Rev. D **52**, 1445 (1995); Z. Phys. C **71**, 585 (1996).
51. J. Kwiecinski, A. Martin, and J. Outhwaite, Eur. Phys. J. C **9**, 611 (2001).
52. K. Golec-Biernat and M. Wusthoff, Phys. Rev. D **59**, 014017 (1999).
53. K. Golec-Biernat and M. Wusthoff, Phys. Rev. D **60**, 114023 (1999).
54. M. Beneke and M. Kramer, Phys. Rev. D **55**, 5269 (1997).
55. M. Kramer, Nucl. Phys. B **459**, 3 (1996).
56. P. Ball, M. Beneke, and V. Braun, Phys. Rev. D **52**, 3929 (1995).
57. E. M. Levin, M. G. Ryskin, Yu. M. Shabelskiĭ, and A. G. Shuvaev, Yad. Fiz. **54**, 1420 (1991) [Sov. J. Nucl. Phys. **54**, 867 (1991)].
58. A. V. Lipatov, *Talk at International School "Heavy Quark Physics" (HQP'2002), Dubna, Russia, 2002*; N. P. Zotov, *Talk at "Small x Collaboration" Meeting, Lund, Sweden, 2002*.
59. H1 Collab., in *Proceedings of the International Europhysics Conference on High Energy Physics (HEP'99), Tampere, Finland, 1999*.
60. S. P. Baranov, A. V. Lipatov, and N. P. Zotov, in *Proceedings of the 9th International Workshop on DIS and QCD (DIS'2001), Bologna, Italy, 2001*; hep-ph/0106229.
61. H1 Collab., DESY-02-060; hep-ex/0205065.

*Translated by A. Isaakyan*

*Physics of Atomic Nuclei, Vol. 66, No. 9, 2003, pp. 1773–1777. From Yadernaya Fizika, Vol. 66, No. 9, 2003, pp. 1820–1824.*


**ELEMENTARY PARTICLES AND FIELDS**
**Theory**

# Uncertainty of the Two-Loop RG Upper Bound on the Higgs Mass*

**Yu. F. Pirogov** and **O. V. Zenin*****

*Institute for High Energy Physics, Protvino, Moscow oblast, 142284 Russia*

Received August 8, 2002

**Abstract**—A modified criterion of the SM perturbative consistency is proposed. It is based on the analytic properties of the two-loop SM running couplings. Under the criterion adopted, the Higgs mass up to 380 GeV might not give rise to strong coupling prior to the Planck scale. This means that the light Higgs boson is possibly preferred for reasons other than the SM perturbative consistency, i.e., for reasons beyond the SM. © *2003 MAIK "Nauka/Interperiodica"*.

## 1. INTRODUCTION

The current experimental data restrict the Higgs mass in the Standard Model (SM) within the range $114.1 < M_{\rm H} < 194$ GeV. The lower bound on $M_{\rm H}$ comes from the absence of the Higgs production signal at LEP II at the 95% C.L. [1]. The upper bound is derived at the same C.L. from the fit to the precision electroweak data [2]. On the other hand, the upper bound on the Higgs mass can be obtained from the requirement of the SM perturbative consistency up to a cutoff energy scale $\Lambda$ at which the SM might get into the strong coupling regime. The two-loop renormalization group (RG) gives typical upper bounds $M_{\rm H} < 200$ GeV at $\Lambda = M_{\rm GUT} = 10^{14}$ GeV and $M_{\rm H} < 180$ GeV at $\Lambda = M_{\rm Pl} = 10^{19}$ GeV (see, e.g., [3]). Thus, both the electroweak precision data and the SM perturbative consistency up to the GUT scale exclude the Higgs mass $M_{\rm H} \geq 200$ GeV. This could be interpreted as though the Higgs should be light due to the self-suppression of the strong coupling in the SM. But the question is to what extent the Higgs upper bound from the SM perturbative consistency is reliable.

A clear-cut criterion of the strong coupling in the Higgs sector of the SM exists only in one loop. In this case, the one-loop quartic coupling $\lambda$ develops the Landau pole at a finite energy scale $\Lambda$. In two loops, the pole is compensated, but $\lambda$ becomes large, $\lambda/4\pi^2 \simeq 1$, nearly at the same energy scale $\Lambda$. Taken alone, this does not give an unambiguous criterion of the nonperturbative regime anymore. In the conventional assumption that the higher loops become comparable with the first and second ones at the same scale $\Lambda$, the results of [3, 4] follow (see also [5] for a review). On the other hand, the contributions of the higher loops might be either small or large but mutually compensated. This would not change drastically the two-loop running of $\lambda$ and may relax the conventional upper bound on the Higgs mass.

Presently, the full set of the SM $\beta$ functions is known only up to two loops. This forces one to study the reliability of the self-consistency criterion of the two-loop RG approximation in the SM. This is the purpose of the present paper. The method proposed in the paper relies on the subtracted RG and the analytic properties of the running couplings. It is similar in spirit to methods applied to resolve the Landau singularity problem in QED [6] and, later, to improve the infrared behavior of the QCD running coupling $\alpha_S(\mu^2)$ [7, 8].

## 2. SUBTRACTED FINITE-LOOP RG

Let us consider the system of the SM two-loop RG equations (RGE)

$$\mu^2 \frac{da_i(\mu^2)}{d\mu^2} = \beta_i(\{a_j(\mu^2)\}). \qquad (1)$$

Here and in what follows, $a_i(\mu^2)$ are the SM running couplings vs. the energy squared scale $\mu^2$, and $\beta_i$ are the respective $\beta$ functions calculated at the given number of loops. We disregard the mass effects here. Conventionally, the system (1) is integrated numerically along the real axis $\mathrm{Re}\mu^2 < 0$:

$$a_i(\mu^2) = a_i(\mu_0^2) + \int_{\mu_0^2}^{\mu^2} \frac{d\mu'^2}{\mu'^2} \beta_i(\{a_j(\mu'^2)\}), \qquad (2)$$

*This article was submitted by the authors in English.

**e-mail: pirogov@mx.ihep.su
***e-mail: zenin_o@mx.ihep.su

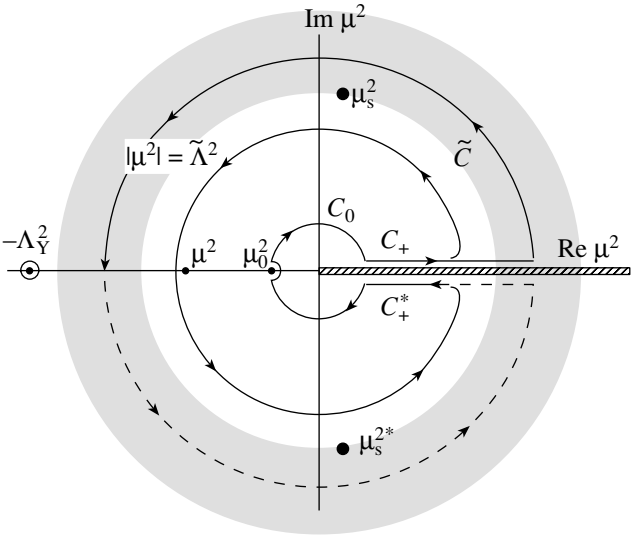


**Fig. 1.** The integration contour $C$ and the generic complex-conjugate singularity points $\mu_s^2, \mu_s^{2*}$ with $|\mu_s^2| = \Lambda_s^2$. $C_+$ is the part of the contour $C$ that goes along the real positive semiaxis from above, $C_+^*$ being its complex conjugate, and $\tilde{C}$ is the total outer circle of the contour. All these parts vary with the radius $\tilde{\Lambda}$ of $\tilde{C}$, while the inner circle $C_0$ stays invariable. The real point $-\Lambda_\Upsilon^2$ corresponds to the $U(1)_\Upsilon$ singularity. All the complex singularities are assumed to reside within the shadowed area at $\Lambda_s^2 \leq |\mu^2| < \Lambda_\Upsilon^2$. The hatched line designates the physical cut.

where $\mu_0^2 < 0$ is a reference point, $|\mu_0| \sim M_Z$. The $\beta$ functions can now be defined as functions of the real negative $\mu^2$:

$$\beta_i(\mu^2) \equiv \beta_i\left(\{a_j(\mu^2)\}\right). \tag{3}$$

Equations (1)–(3) preserve their meaning for the complex $\mu^2$ as well. But the numerical solution obtained says nothing about the analytic properties of the running couplings with respect to $\mu^2$. In two loops, despite the absence of real singularities of the Higgs quartic coupling $\lambda$, there could be complex ones. They influence the strong coupling regime $\lambda/4\pi^2 \geq 1$ at large enough real $\mu^2$. The extension of the two-loop RG analysis onto the complex $\mu^2$ plane allows one to find the position of the singularities implicitly.

To this end, let us continue analytically the $\beta$ functions and running couplings onto the complex $\mu^2$ plane with the cut along the real axis $\mathrm{Re}\,\mu^2 > 0$ (Fig. 1). The cut is chosen so that $-\pi < \mathrm{Im}\ln(-\mu^2) < \pi$. All the running couplings are assumed to satisfy the hermiticity condition $a_i(\mu^{2*}) = a_i^*(\mu^2)$. Let us first choose the closed contour $C = C_0 \cup C_+ \cup \tilde{C} \cup C_+^*$ (Fig. 1) so that $C$ encircles the given point $\mu^2$ and all the singularities of the running couplings $a_i(\mu^2)$ reside outside $C$. Then, $\beta_i(\mu^2)$ satisfy the identity

$$\beta_i(\mu^2) \equiv \frac{1}{2\pi i}\int\limits_C \frac{\beta_i(s)\,ds}{s-\mu^2}, \tag{4}$$

where $\beta_i(s) \equiv \beta_i(\{a_j(s)\})$. Substituting Eq. (4) into Eq. (2), one gets

$$a_i(\mu^2) = a_i(\mu_0^2) + \frac{1}{2\pi i}\int\limits_{\mu_0^2}^{\mu^2}\frac{d\mu'^2}{\mu'^2}\int\limits_C \frac{\beta_i(s)ds}{s-\mu'^2}, \tag{5}$$

where the integration path between points $\mu_0^2$ and $\mu^2$ should lie inside $C$. In what follows, the square root $\tilde{\Lambda}$ of the radius of the outer contour $\tilde{C}$ is referred to as the modification radius.

Now let us spread the outer contour $\tilde{C}$ so that at least some of the implicit singularities of $a_i(\mu^2)$ become located inside $C$. In general, identity (5) ceases to be valid. Moreover, the integration of the RG system (1) from the reference point $\mu_0^2$ to the real point $(-\tilde{\Lambda}^2)$, $\tilde{\Lambda} > \Lambda_s$, along the real axis and the upper half of the contour $C$ (shown in solid in Fig. 1) does not give the same results. Remarkably, in the latter case, the couplings $a_i(-\tilde{\Lambda}^2)$ acquire nonzero complex parts, while in the former case they are real by construction. This discrepancy reflects the contribution of the implicit complex singularities. The minimal radius $\Lambda_s^2$ of the external contour $\tilde{C}$ at which all these irregularities take place gives an estimate of the upper range of the reliability of the RG in the given loops. The value of $\Lambda_s$ corresponds to crossing the nearest singularities of $a_i(\mu^2)$. At scales larger than $\Lambda_s$, the original finite-loop approximation is definitely unreliable. It is at $|\mu^2| \geq \Lambda_s^2$, where the contributions of higher loops are needed to improve the analytic properties of the conventional running couplings $a_i(\mu^2)$.

The above procedure suffices to give the clear-cut numerical criterion of the self-consistency of the finite-loop RG. But to visualize it, let us modify Eq. (5) and define the new running couplings $a_i^{(\tilde{\Lambda})}(\mu^2)$ as follows:

$$a_i^{(\tilde{\Lambda})}(\mu^2) = a_i(\mu_0^2) + \int\limits_{\mu_0^2}^{\mu^2}\frac{d\mu'^2}{\mu'^2}\beta_i^{(\tilde{\Lambda})}(\mu'^2),$$

with the once subtracted $\beta$ functions

$$\beta_i^{(\tilde{\Lambda})}(\mu^2) \equiv \beta_i(\mu_0^2) + \frac{1}{2\pi i} \tag{6}$$

$$\times \int\limits_C ds\, \beta_i(s) \left( \frac{1}{s-\mu^2} - \frac{1}{s-\mu_0{}^2} \right).$$

Here, the point $\mu_0^2$ is shifted infinitesimally inside $C$, and $\beta_i(s)$, restricted to contour $C$, are obtained by integrating the RG system (1) along the contour $C$ itself. By their very construction, the modified couplings $a_i^{(\tilde\Lambda)}(\mu^2)$ exactly coincide with $a_i(\mu^2)$ at $|\mu| < \tilde\Lambda$ if the integration contour does not encompass the complex singularities, i.e., $\tilde\Lambda < \Lambda_s$. Due to hermiticity, the couplings are real at the real negative $\mu^2$. If the complex singularities get inside the contour, the procedure is not uniquely defined. In particular, $a_i^{(\tilde\Lambda)}(\mu^2)$ cease generally to be Hermitian. To improve this, we redefine the integral in Eq. (6) as the contribution of the upper half of the contour $C$ minus the contribution of the symmetric lower half of the contour calculated in a similar manner. This does not change the results at $\tilde\Lambda < \Lambda_s$. So defined $a_i^{(\tilde\Lambda)}(\mu^2)$ are regular and Hermitian and differ from $a_i(\mu^2)$ by the contribution of singularities and normalization constants. The constants are chosen so that $\beta_i^{(\tilde\Lambda)}(\mu_0^2) \equiv \beta_i(\mu_0^2)$ and, hence, $a_i^{(\tilde\Lambda)}(\mu^2) = a_i(\mu^2) + \mathcal{O}((\mu^2-\mu_0^2)^2)$ in a vicinity of $\mu_0^2$, where the finite-loop RG is believed to be reliable. The large difference between the couplings arises as soon as the singular parts of $a_i(\mu^2)$ become large.

## 3. MODIFICATION OF THE SM TWO-LOOP COUPLINGS

The SM ultraviolet behavior has been extensively studied by the conventional RG method up to two loops [3–5]. An important outcome of this study is the range of the Higgs mass for which the SM remains perturbatively consistent up to the given cutoff scale $\Lambda$. The consistency can be broken either by a sufficiently heavy Higgs, whose quartic coupling $\lambda$ "blows up" at the scale $\Lambda$, or by a light Higgs, whose coupling $\lambda$ dumps below zero at the scale $\Lambda$.[1)] Thus, quite a narrow corridor is retained for the Higgs mass (see, e.g., Fig. 4 in [3]). These bounds are of special interest because the Higgs mass remains the last undetermined SM parameter.

In two loops, the Higgs quartic coupling $\lambda$, as well as the other SM couplings, develops no singularities prior to the Landau singularity of the $U(1)_Y$ gauge coupling at $\Lambda \geq 0.2 \times 10^{41}$ GeV, the latter corresponding to the Higgs mass $M_H \geq 114.1$ GeV [3]. The situation is obscured by the fact that the SM two-loop RG equations can be solved only numerically. The numerical solution vs. real $\mu^2$ provides no information about the analytic properties of the SM two-loop running couplings.

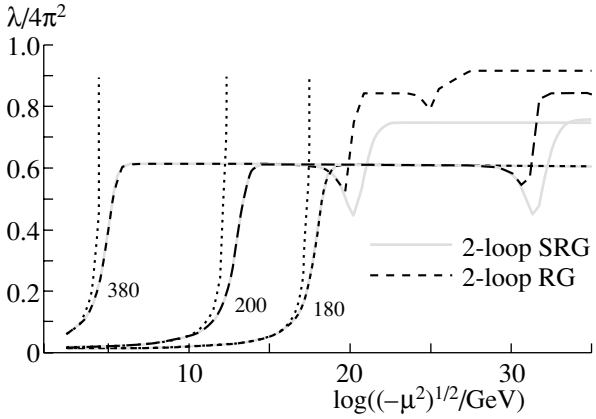


**Fig. 2.** The conventional (RG) and subtracted (SRG) two-loop running of the SM Higgs quartic coupling $\lambda$ at $M_H = 180$–$380$ GeV. The SRG lines correspond to the proper RG ones from which they deviate minimally. For comparison, the one-loop RG running of $\lambda$ is shown by dots.

The method of analytic modification studies the evolution of the running couplings vs. complex $\mu^2$. The variation of the modification radius $\tilde\Lambda$ (Fig. 1) allows one to determine the two-loop singularity scale $\Lambda_s$ without finding the unphysical singularities explicitly. Thus, one can judge the self-consistency of the two-loop RG at the given energy scale $\mu$. It is sufficient to calculate the modified couplings $a_i^{(\tilde\Lambda)}(\mu^2)$ and compare them to the conventional ones Eq. (2). This enables one to determine the radius $\Lambda_s$ at which the singularity is located, making the numerical analysis rather productive. If $\tilde\Lambda < \Lambda_s$, then the conventional and the modified SM running couplings are identical within the routine accuracy, $a_i(\mu^2) \equiv a_i^{(\tilde\Lambda)}(\mu^2)$, $|\mu| < \tilde\Lambda$. As soon as $\tilde\Lambda$ exceeds $\Lambda_s$, the modified couplings depart from the respective conventional ones.

To illustrate, consider the two-loop RG evolution of the SM with the maximally heavy Higgs, $M_H = 200$ GeV, nearly allowed by the electroweak precision data [2]. Varying the modification radius $\tilde\Lambda$ in the range $10^{19} < \tilde\Lambda < 10^{42}$ GeV,[2)] we find numerically the scale of the two-loop hidden singu-

[1)] The upper and lower bounds on the Higgs mass are also known in the literature as the triviality bound and the vacuum stability bound, respectively.

[2)] That is, well below the Landau singularity of the $U(1)_Y$ gauge coupling at $\Lambda_s \simeq 5 \times 10^{50}$ GeV for this $M_H$.

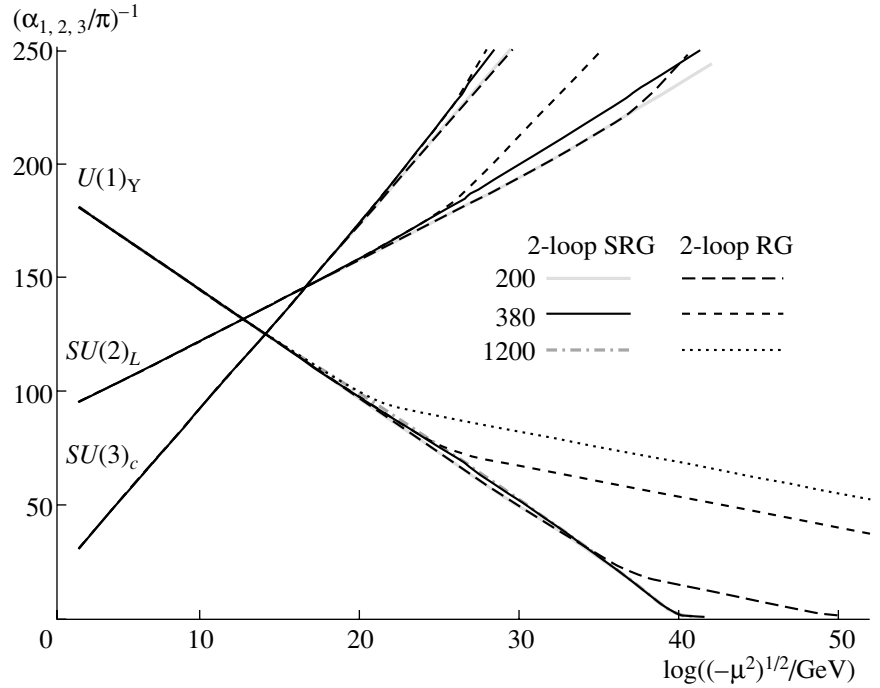


**Fig. 3.** The conventional (RG) and subtracted (SRG) two-loop running of the SM gauge couplings at $M_H = 200$ and 380 GeV. $M_H = 380$ GeV corresponds to $\Lambda_s = M_{Pl}$. The running of the $U(1)_Y$ gauge coupling at $M_H \simeq 1.2$ TeV corresponding to $\Lambda_s = M_{GUT}$ is also shown.

larity to be $\Lambda_s \simeq 10^{31}$ GeV. This can be seen from Fig. 2, showing the conventional (RG) and subtracted (SRG) two-loop running of the Higgs quartic coupling $\lambda$. Note that $\lambda$ gets in fact a rather large decrement, of 10% or so, when the integration contour encompasses the implicit singularities. For the lighter Higgs (not shown), $\lambda$ actually stays unmodified.[3)] Figure 3 shows the conventional and modified two-loop evolution of the SM gauge couplings. In these figures, the modification radius is $\tilde{\Lambda} = 10^{42}$ GeV and $|\mu_0|$ is equal to the Higgs VEV, $v = 246.2$ GeV. The extension of $\tilde{\Lambda}$ even beyond the position of the Landau singularity results in the relative variation of the modified running couplings at the level of $10^{-3}$. The case $M_H = 380$ GeV corresponds to $\Lambda_s = M_{Pl} = 10^{19}$ GeV. Also shown in Fig. 3 is the evolution of $\alpha_1(\mu^2)$ at $M_H \simeq 1.2$ TeV, which corresponds to $\Lambda_s = M_{GUT} = 10^{14}$ GeV.

**The upper Higgs bound.** An important conclusion follows hereof. For the 200-GeV Higgs, all the SM couplings demonstrate very close conventional and modified two-loop running up to the two-loop singularity scale $\Lambda_s$. The Higgs mass $M_H = 200$ GeV spoils the analytic properties of the SM two-loop running couplings only at the scale $\Lambda_s \simeq 10^{31}$ GeV, i.e., well above the Planck scale. This can imply that, to improve the analytic properties of the SM two-loop couplings, the contributions of the third and higher loops are needed only at scales $\mu > M_{Pl}$. To break down the perturbativity of the SM prior to the Planck scale $M_{Pl} = 10^{19}$ GeV, the Higgs mass $M_H > 380$ GeV is required. This raises the commonly accepted upper bound on the Higgs mass $M_H \leq 180$ GeV derived in the conventional manner from the same requirement. Moreover, to guarantee the SM perturbativity up to the GUT scale, $M_{GUT} = 10^{14}$ GeV, it is not actually necessary to impose any upper bound on $M_H$. Thus, the Higgs is light probably for reasons other than the absence of strong coupling in the SM. These reasons might lie beyond the SM. For example, the Higgs could be the composite pseudo-Goldstone boson having the natural mass $\sim M_Z$ [9].

To resolve the uncertainty of the Higgs upper bound, the third and fourth loops in the SM are urgently needed. Two extreme possibilities can be envisaged. First, the higher loops are large and do not compensate each other. In this case, the conservative conventional upper bound $M_H < 180$ GeV at $\Lambda = M_{Pl}$ would follow. Second, the higher loops are either small or large but mutually compensated. In this case, the more liberal modified upper bound is appropriate, and $M_H$ up to 380 GeV would be allowed

[3)] For the 380-GeV Higgs, the modification of the $t$, $b$, and $\tau$ Yukawa couplings (not shown) cancels the unification of the latter ones [3] above the singularity scale $\Lambda_s$.

at the same $\Lambda$. More realistically, an intermediate case may be realized, so that the upper bound on $M_{\rm H}$ should lie somewhere in between 180 and 380 GeV.

**The lower Higgs bound.** The low Higgs masses, $M_{\rm H} \leq 138.1$ GeV,[4)] give rise to the electroweak vacuum instability prior to the Planck scale. However, at the vacuum instability scale, the SM running couplings develop no singularities and hence require no subtractions. Thus, the analytic modification method taken as it is cannot clarify the electroweak vacuum instability problem.

## 4. CONCLUSION

The subtracted RG is applied to study the two-loop self-consistency of the SM. It is found that, at the Higgs mass $M_{\rm H} < 380$ GeV, the two-loop singularity scale is $\Lambda_s > M_{\rm Pl}$. This implies that $M_{\rm H} < 380$ GeV does not necessarily give rise to strong coupling prior to the Planck scale. Even allowing $\Lambda_s$ as low as $M_{\rm GUT}$, the SM self-consistency may actually impose no upper bound on $M_{\rm H}$. In other words, the light Higgs might be preferred for reasons other than the SM perturbativity, i.e., for reasons beyond the SM. To clarify the issue, the third and fourth loops in the SM RG are needed. On the other hand, the method cannot resolve the SM vacuum instability problem arising, in two loops, at $M_{\rm H} < 138.1$ GeV. Thus, out of the entire experimentally allowed range for the Higgs mass $114.1 < M_{\rm H} < 194$ GeV, only the lowest Higgs masses $114.1 < M_{\rm H} < 138.1$ GeV could definitely give rise to the SM inconsistency prior to the Planck scale and would require new physics.

## ACKNOWLEDGMENTS

We are grateful to A.I. Alekseev and V.V. Kabachenko for useful discussions.

## REFERENCES

1. F. Cerutti, in *Proceedings of the 16th Rencontres de Physique de la Vallee d'Aoste: Results and Perspectives in Particle Physics, La Thuile, Aosta Valley, Italy, 2002,* CERN-ALEPH-PUB-2002-003; hep-ex/0205095.
2. U. Baur *et al.*, Summary Report of the Precision Measurement Working Group at Snowmass 2001; hep-ph/0202001.
3. Yu. F. Pirogov and O. V. Zenin, Eur. Phys. J. C **10**, 629 (1999); hep-ph/9808396.
4. J. A. Casas *et al.*, Nucl. Phys. B **436**, 3 (1995); Erratum: *ibid.* **439**, 466 (1995); hep-ph/9407389; P. Q. Hung and G. Isidori, Phys. Lett. B **402**, 122 (1997); hep-ph/9609518; P. Q. Hung, Phys. Rev. Lett. **80**, 3000 (1998); hep-ph/9712338; D. Dooling, K. Kang, and S. K. Kang, Int. J. Mod. Phys. A **14**, 1605 (1999); hep-ph/9710258; Phys. Rev. D **60**, 017701 (1999); hep-ph/9904412.
5. P. Frampton, P. Q. Hung, and M. Sher, Phys. Rep. **330**, 263 (2000); hep-ph/9903387.
6. N. N. Bogolyubov, A. A. Logunov, and D. V. Shirkov, Zh. Éksp. Teor. Fiz. **37**, 805 (1959).
7. A. I. Alekseev and B. A. Arbuzov, Yad. Fiz. **61**, 314 (1998) [Phys. At. Nucl. **61**, 264 (1998)]; Mod. Phys. Lett. A **13**, 1747 (1998); A. I. Alekseev, J. Phys. G **27**, L117 (2001); hep-ph/0105338; in *Proceedings of the Workshop on Nonperturbative Methods in Quantum Field Theory, Adelaide, Australia, 1998* (World Sci., Singapore, 1998), p. 104; hep-ph/9808206.
8. I. L. Solovtsov and D. V. Shirkov, Theor. Math. Phys. **120**, 1220 (1999); A. V. Nesterenko, Mod. Phys. Lett. A **15**, 2401 (2000); hep-ph/0102203; Phys. Rev. D **64**, 116009 (2001); hep-ph/0102124; A. V. Nesterenko and I. L. Solovtsov, Mod. Phys. Lett. A **16**, 2517 (2001); hep-ph/0111067.
9. Yu. F. Pirogov, Int. J. Mod. Phys. A **7**, 6473 (1992).
10. Particle Data Group (K. Hagiwara *et al.*), Phys. Rev. D **66**, 010001 (2002).

[4)]This corresponds to the recalculated result of [3] for the central value 174.3 GeV [10] of the top mass.